



**HAL**  
open science

# Rupture et instabilités : sismicité et mouvements de terrain

Agnès Helmstetter

► **To cite this version:**

Agnès Helmstetter. Rupture et instabilités : sismicité et mouvements de terrain. Géophysique [physics.geo-ph]. Université Joseph-Fourier - Grenoble I, 2002. Français. NNT : . tel-00010935

**HAL Id: tel-00010935**

**<https://theses.hal.science/tel-00010935>**

Submitted on 11 Nov 2005

**HAL** is a multi-disciplinary open access archive for the deposit and dissemination of scientific research documents, whether they are published or not. The documents may come from teaching and research institutions in France or abroad, or from public or private research centers.

L'archive ouverte pluridisciplinaire **HAL**, est destinée au dépôt et à la diffusion de documents scientifiques de niveau recherche, publiés ou non, émanant des établissements d'enseignement et de recherche français ou étrangers, des laboratoires publics ou privés.

Thèse de Doctorat de  
l'Université Joseph Fourier - Grenoble I

Spécialité : Géophysique

**Agnès HELMSTETTER**

---

---

RUPTURES ET INSTABILITÉS :  
SISMICITÉ ET MOUVEMENTS GRAVITAIRES

---

---

Thèse soutenue à Grenoble le 16 septembre 2002 devant le jury composé de :

James Dieterich ..... Rapporteur  
Stéphane Roux ..... Rapporteur  
Ralph Archuleta ..... Examineur  
Pascal Bernard ..... Examineur  
Henri-Claude Nataf ..... Président  
Didier Sornette ..... Examineur  
Jean-Robert Grasso ..... Directeur de thèse  
Jérôme Weiss ..... Directeur de thèse

---

Thèse préparée au Laboratoire de Géophysique Interne et Tectonophysique et au Laboratoire de Glaciologie et Géophysique de l'Environnement (Observatoire de Grenoble)



# Avant Propos

Je tiens avant tout à remercier Jean-Robert Grasso et Jérôme Weiss pour avoir accepté de diriger ma thèse et m'avoir fait bénéficier d'excellentes conditions de travail. Je les remercie surtout pour la liberté qu'ils m'ont laissé dans mon travail et dans le choix de mes sujets de recherche.

Le titre de cette thèse aurait du être "Etude des tremblements de glace comme analogue des tremblements de terre". Malgrès plus d'un an consacré à des expériences d'étude sismique des tremblements de glace, sur le terrain et en laboratoire, qui m'ont permis de faire quelques descentes à ski des vallons de la Meije, mais qui n'ont pas donné les résultats scientifiques espérés, le mot tremblement de glace n'apparaît finalement pas dans cette thèse. Je tiens néanmoins à remercier tous les membres du LGIT, du laboratoire de glaciologie, et de l'université de Pau, et le personnel des remontés mécaniques de La Grave qui m'ont aidés à réaliser ces expériences.

Je remercie Stéphane Roux et James Dieterich pour avoir accepté d'être rapporteurs de ce mémoire, et tous les membres du jury pour l'intérêt qu'ils ont porté à cette thèse.

J'ai une profonde reconnaissance pour Didier Sornette, avec qui j'ai réalisé l'essentiel de ce travail de thèse. Son aide et son enthousiasme sans faille ont été essentielles à la réalisation de cette thèse. Je le remercie aussi pour m'avoir accueillie plusieurs mois à UCLA, et plusieurs semaines à Nice... et pour m'offrir la possibilité de continuer à travailler avec lui en post-doc à UCLA.

Je remercie aussi Ludovic Margerin, Christophe Voisin, Art McGarr, Michel Bouchon, Guy Ouillon avec qui j'ai eu des discussions scientifiques très enrichissantes, et pour leur relecture de plusieurs manuscrits.

Merci enfin à tous les grimpeurs, skieurs, taroteurs et buveurs de bière que j'ai eu la chance de connaître pendant ces 5 années passées au LGIT : merci à ludo, sabine, christophe, morgane, pascal, marielle, nicolas, martin, bruno, jerome, david, hugo, caroline, daniel.



# Résumé

On s'intéresse à la rupture associée à deux classes de phénomènes naturels, les séismes et les instabilités gravitaires.

Pour les séismes, on étudie un modèle stochastique de sismicité, basé sur les deux lois les mieux établies pour la sismicité, la décroissance en loi de puissance du taux de sismicité après un séisme, et la distribution en loi de puissance des énergies des séismes. Dans ce modèle, on suppose que chaque séisme déclenche d'autres séismes, dont le nombre augmente avec l'énergie du choc principal. Le taux de sismicité global résulte de la cascade de déclenchements de séismes directs et indirects. On analyse l'organisation spatiale et temporelle de la sismicité dans les différents régimes sous- et sur-critiques du modèle. Ce modèle permet de reproduire un grand nombre de propriétés de l'activité sismique, telles que la variabilité de la décroissance des séquences d'aftershocks, l'augmentation de l'activité sismique avant un séisme, la diffusion des aftershocks, la migration des foreshocks et la modification de la distribution des magnitudes avant un séisme. On obtient avec ce modèle une bonne prédictabilité d'une fraction des séismes qui sont déclenchés à court terme après un grand séisme. Nos résultats démontrent le rôle essentiel des cascades de déclenchement de séismes à toutes les échelles dans l'organisation de l'activité sismique.

Concernant l'étude des instabilités gravitaires, une étude statistique de plusieurs catalogues d'éboulements rocheux montre que la distribution des volumes de roches suit une loi de puissance. On propose que cette distribution en loi de puissance résulte soit de l'hétérogénéité initiale de la matrice rocheuse, soit de la dynamique d'un système critique auto-organisé.

Certains glissements de terrains sont précédés par une accélération de la vitesse de glissement avant la rupture finale. On peut reproduire l'évolution temporelle du glissement à l'aide d'un modèle de bloc rigide avec une loi de friction dépendante de la vitesse de glissement et de l'état de contact entre le bloc et sa surface de glissement. L'analyse de deux glissements de terrains avec ce modèle permet de distinguer une accélération du glissement dans le régime stable, d'une accélération instable qui évolue vers une rupture catastrophique.



# Abstract

We analyze the rupture associated with two natural phenomena, earthquakes and landslides.

In the first part, we study a simple stochastic model of seismicity, based on the two best-established empirical laws for earthquakes, the power law decay of seismicity after an earthquake and the power law distribution of earthquake energies. This model assumes that each earthquake can trigger aftershocks, with a rate increasing with its magnitude. The seismicity rate is in this model the result of the whole cascade of direct and secondary aftershocks. We analyze the space-time organization of the seismic activity in the different sub- and super-critical regimes of the model. We show that this simple model can reproduce many properties of real seismicity, such as the variability of the aftershocks decay law, the acceleration of the seismic activity before large earthquakes, the diffusion of aftershocks, the migration of foreshocks, and the modification of the magnitude distribution before large earthquakes. We find that this model provides a good predictability for a fraction of earthquakes that are triggered by a previous large event. We demonstrate the essential role played by the cascades of earthquake triggering at all scales in controlling the seismic activity.

The second part is devoted to the analysis of landslides. A study of several catalogs of rock falls shows that the distribution of rockfall volumes follows a power-law distribution, arising either from the scale invariant heterogeneity of the rock-mass, or from the dynamics of a self-organized critical system.

We propose that the precursory acceleration of the displacement before some catastrophic landslides can be reproduced using a slider block model with a rate-and-state dependent friction law. Application of this model to two landslide slip histories suggests that we can distinguish an acceleration of the sliding velocity in the stable regime from an unstable acceleration leading to a catastrophic collapse.



# Table des matières

<b>Avant Propos</b>	<b>1</b>
<b>Résumé</b>	<b>3</b>
<b>Abstract</b>	<b>5</b>
<b>Introduction générale</b>	<b>11</b>
<b>I Interactions entre séismes et leur déclenchement</b>	<b>21</b>
<b>1 Introduction</b>	<b>23</b>
1.1 Déclenchement des séismes . . . . .	23
1.2 Mécanismes physiques pour le déclenchement des séismes . . . . .	26
1.3 Un modèle générique de déclenchement de séismes . . . . .	27
1.4 Synthèse des résultats obtenus avec le modèle de déclenchement de séismes . . . . .	28
<b>2 Rôle dominant des petits séismes dans le déclenchement de la sismicité</b>	<b>33</b>
2.1 Introduction . . . . .	33
2.2 Mesure du nombre d'aftershocks en fonction de la magnitude du mainshock . . . . .	35
2.3 Modèle . . . . .	37
2.4 Conclusion . . . . .	38
<b>3 Mécanismes physiques du déclenchement des aftershocks</b>	<b>41</b>
3.1 Processus d'affaiblissement sous contrainte . . . . .	41
3.2 Loi de friction dépendante de la vitesse . . . . .	49
3.3 Relaxation visco-élastique dans la croûte inférieure . . . . .	51
3.4 Transfert de fluides dans un milieu poreux . . . . .	52
3.5 Géométrie et interactions multi-échelles dans les réseaux de failles . . . . .	53
3.6 Effet des variations de contraintes statiques et dynamiques . . . . .	54

3.7	Synthèse . . . . .	55
<b>4</b>	<b>Observations et modélisation de la variabilité de la loi d’Omori</b>	<b>57</b>
4.1	Modèles de corrosion sous contrainte . . . . .	58
4.2	Modèle d’Arrhenius . . . . .	63
<b>5</b>	<b>Régimes sous-critiques et sur-critiques dans un modèle de sismicité</b>	<b>67</b>
5.1	Introduction . . . . .	68
5.2	Description du modèle . . . . .	71
5.3	Solution analytique . . . . .	76
5.4	Discussion . . . . .	83
5.5	Conclusion . . . . .	94
5.6	Appendix : dérivation de la solution analytique . . . . .	95
<b>6</b>	<b>Singularité en temps fini dans un modèle stochastique de sismicité</b>	<b>103</b>
<b>7</b>	<b>Prédictabilité dans le modèle ETAS de déclenchement de séismes</b>	<b>111</b>
7.1	Introduction . . . . .	112
7.2	Déclenchement de la sismicité et prédiction . . . . .	113
7.3	Le modèle ETAS de déclenchement des séismes . . . . .	118
7.4	Interprétations physiques du taux de branchement $n$ . . . . .	122
7.5	Solution formelle pour la prédiction de la sismicité . . . . .	125
7.6	Tests de prédiction . . . . .	129
7.7	Conclusions . . . . .	148
7.8	Appendix A : Solutions limites pour le progagateur hypermétrape $K_u^*(t)$ . . . . .	149
<b>8</b>	<b>Diffusion des aftershocks</b>	<b>151</b>
8.1	Introduction . . . . .	152
8.2	Modèle épidémique de cascades d’aftershocks . . . . .	160
8.3	Correspondance entre les modèles ETAS et CTRW . . . . .	165
8.4	Résultats dans le régime critique $n = 1$ . . . . .	172
8.5	Discussion . . . . .	187
8.6	Conclusion . . . . .	192
<b>9</b>	<b>Observations de la diffusion des aftershocks</b>	<b>193</b>
9.1	Limites de l’approche analytique . . . . .	194
9.2	Méthode . . . . .	195

9.3	Catalogue de sismicité . . . . .	197
9.4	Résultats . . . . .	198
9.5	Conclusion . . . . .	199
<b>10</b>	<b>Mainshocks are aftershocks of conditional foreshocks</b>	<b>205</b>
10.1	Introduction . . . . .	206
10.2	Définition du modèle ETAS et dérivation de l'équation maitresse . . . . .	211
10.3	Dérivation de la loi d'Omori inverse et conséquences . . . . .	217
10.4	Prédiction de la distribution des magnitudes des foreshocks . . . . .	229
10.5	Migrations des foreshocks vers le mainshock . . . . .	230
10.6	Discussion . . . . .	234
10.7	Conclusion . . . . .	242
10.8	Appendix A : Ecart au taux de sismicité moyen . . . . .	243
10.9	Appendix B : Conditionnement de variables à la réalisation de leur somme . . . . .	244
<b>11</b>	<b>Observations de la loi d'Omori inverse des foreshocks</b>	<b>247</b>
11.1	Catalogues de sismicité . . . . .	247
11.2	Sélection des foreshocks et des aftershocks . . . . .	247
11.3	Loi d'Omori inverse . . . . .	248
11.4	Modification de la distribution des magnitudes avant un mainshock . . . . .	253
11.5	Migration des foreshocks . . . . .	254
11.6	Conclusion . . . . .	258
<b>12</b>	<b>Chocs endogènes et exogènes dans les systèmes à mémoire</b>	<b>259</b>
12.1	Introduction . . . . .	260
12.2	Chocs endogènes et exogènes . . . . .	262
12.3	Classification des réponses pour différentes classes de fonctions mémoire . . . . .	269
12.4	Conclusion . . . . .	272
<b>13</b>	<b>Conclusions</b>	<b>273</b>
<b>II</b>	<b>Instabilités gravitaires</b>	<b>275</b>
<b>14</b>	<b>Analyse statistique des éboulements rocheux</b>	<b>277</b>
14.1	Introduction . . . . .	278
14.2	Données . . . . .	279
14.3	Analyse statistique de la distribution des volumes . . . . .	285

14.4 Discussion . . . . .	290
14.5 Conclusion . . . . .	297
<b>15 Loi de friction et modélisation des glissements de terrain</b>	<b>299</b>
15.1 Introduction . . . . .	300
15.2 Modèle de bloc avec une loi de friction dépendante de la vitesse . . . . .	305
15.3 Glissement de terrain de Vaiont . . . . .	310
15.4 Glissement de terrain de la Clapière . . . . .	322
15.5 Discussion et conclusion . . . . .	338
15.6 Appendix A : Dérivation de la solution complète du modèle de friction . . . . .	339
15.7 Appendix B : Méthode de renormalisation appliquée au modèle de friction . . . . .	341
15.8 Appendix C : Méthode de renormalisation pour la prédiction de $t_c$ . . . . .	344
<b>Conclusion générale et perspectives</b>	<b>347</b>
<b>Références</b>	<b>350</b>

# Introduction générale

La rupture des objets géologiques existe à toutes les échelles, depuis l'échelle des liaisons interatomiques ( $10^{-9}$  m) jusqu'à des ruptures de 1000 km associées aux plus gros séismes. La rupture est responsable d'un grand nombre de risques naturels : séismes, éruptions volcaniques, instabilités gravitaires. Comprendre l'organisation de la rupture dans l'espace et dans le temps revêt donc une importance fondamentale.

Deux types de modèles génériques de physique statistique ont été proposés pour décrire la rupture. Les modèles de point-critique considèrent la rupture globale d'un système comme un point critique, au sens des transitions de phase, et décrivent l'approche vers la rupture globale d'un matériau hétérogènes soumis à un chargement externe (augmentation de la force appliquée ou de la déformation). Le concept de système critique auto-organisé (CAO) décrit au contraire l'auto-organisation d'un système dans un état stationnaire hors équilibre, caractérisé par des avalanches (rupture instantanées d'éléments du système) en lois de puissances.

A l'échelle globale, la dynamique des objets géologiques semble s'organiser dans un état stationnaire, caractérisé par des ruptures (séismes, éruptions volcaniques, éboulements rocheux, glissement de terrains) de toutes tailles, souvent distribuées en loi de puissance. Ce comportement est caractéristique des systèmes critiques auto-organisés.

Les ingrédients essentiels d'un système CAO sont [Bak et al., 1987 ; Vespignani et Zapperi, 1998] :

- un chargement externe constant du système aux temps longs,
- une dynamique à seuil, caractérisée par la rupture instantanée d'un élément quand son énergie dépasse un seuil,
- une redistribution quasi-instantanée (par rapport au temps long du chargement externe) de l'énergie due à la rupture d'un élément, qui peut induire des phénomènes d'avalanches lorsque la rupture d'un élément se propage aux sites voisins,
- un guérissement immédiat après la rupture d'un élément, qui peut immédiatement être rechargé (pas d'endommagement),
- l'absence d'inertie.

Un système critique auto-organisé est caractérisé par [Bak et al., 1987 ; Vespignani et Zapperi, 1998] :

- l'évolution spontanée du système vers un état stationnaire hors d'équilibre,

- une distribution en loi de puissance de la taille des avalanches induites par la rupture quasi-simultanée de plusieurs éléments,
- des corrélations spatiales à longue portée.

Il est important de noter ici que la simple observation de distributions en lois de puissance ne suffit pas à caractériser un système comme étant un système critique auto-organisé, car de nombreux autres phénomènes peuvent générer des distribution en loi de puissance (cf chapitre 14 de [Sornette, 2000a]).

Le concept de systèmes critique auto-organisé a été appliqué pour décrire les séismes [Bak et Tang, 1989 ; Sornette et Sornette, 1989], les éruptions volcaniques [Lahaie et Grasso, 1998] et les mouvements de terrains [Noever, 1993 ; Hergarten et Neugebauer, 1998 ; et chapitre 14 de ce travail].

Le premier modèle de système critique auto organisé a été proposé par Bak et al. [1987] (voir Figure 1). Ils considèrent une grille à  $d$  dimensions. Chaque site  $i$  est caractérisé par une variable  $z_i$ , qui représente la hauteur locale du tas de sable, ou la contrainte sur chaque élément dans le contexte des séismes. On charge le système en choisissant un site aléatoirement et en augmentant son énergie d'une unité  $z_i \rightarrow z_i + 1$ , reflétant par exemple l'ajout d'un grain de sable sur le tas ou l'augmentation de la contrainte sur une portion de la faille due au chargement tectonique. Lorsqu'un site atteint le seuil de rupture  $z_c = 2d$ , on relaxe le système en redistribuant équitablement l'énergie aux sites voisins. Les sites voisins peuvent alors devenir instables à leur tour s'ils atteignent le seuil de rupture, et engendrer ainsi une avalanche de redistribution d'énergie. Le système dissipe de l'énergie uniquement sur les bords du système quand des grains sortent de la grille. Ce modèle est quasiment imprédictible (les avalanches sont quasiment indépendantes), dû au chargement stochastique du système. N'importe quelle avalanche peut dégénérer en une avalanche majeure.

Suite aux travaux de [Bak et al., 1987], de nombreuses variantes du modèle de plus en plus complexes ont été proposées. On citera ici simplement le modèle d'Olami et al. [1992] qui diffère du modèle de Bak et al. [1987] par un chargement continu et uniforme sur tout le système, et une dissipation de l'énergie lors de la rupture d'un élément du système. La dissipation introduite dans ce modèle induit une variation de l'exposant de la distribution des tailles d'avalanches par rapport au modèle de Bak et al. [1987], qui devient une fonction continue de la dissipation [Christensen et Olami, 1992]. Ce modèle produit aussi des interactions temporelles à longue portée [Christensen et Olami, 1992], et une plus grande prédictabilité des plus grandes avalanches [Pepke et Carlson, 1994] que dans le modèle de Bak et al. [1987]. La prédictabilité de ce modèle reste néanmoins très faible. Ces modèles ont aussi été utilisés pour modéliser les systèmes biologiques ou économiques, pour rationaliser les distributions en lois de puissances observées.

Si dans les modèles d'état critique auto-organisé la dynamique du système est (quasiment) imprédictible (il n'existe pas de phénomène précurseur des plus grosses avalanches), de nom-

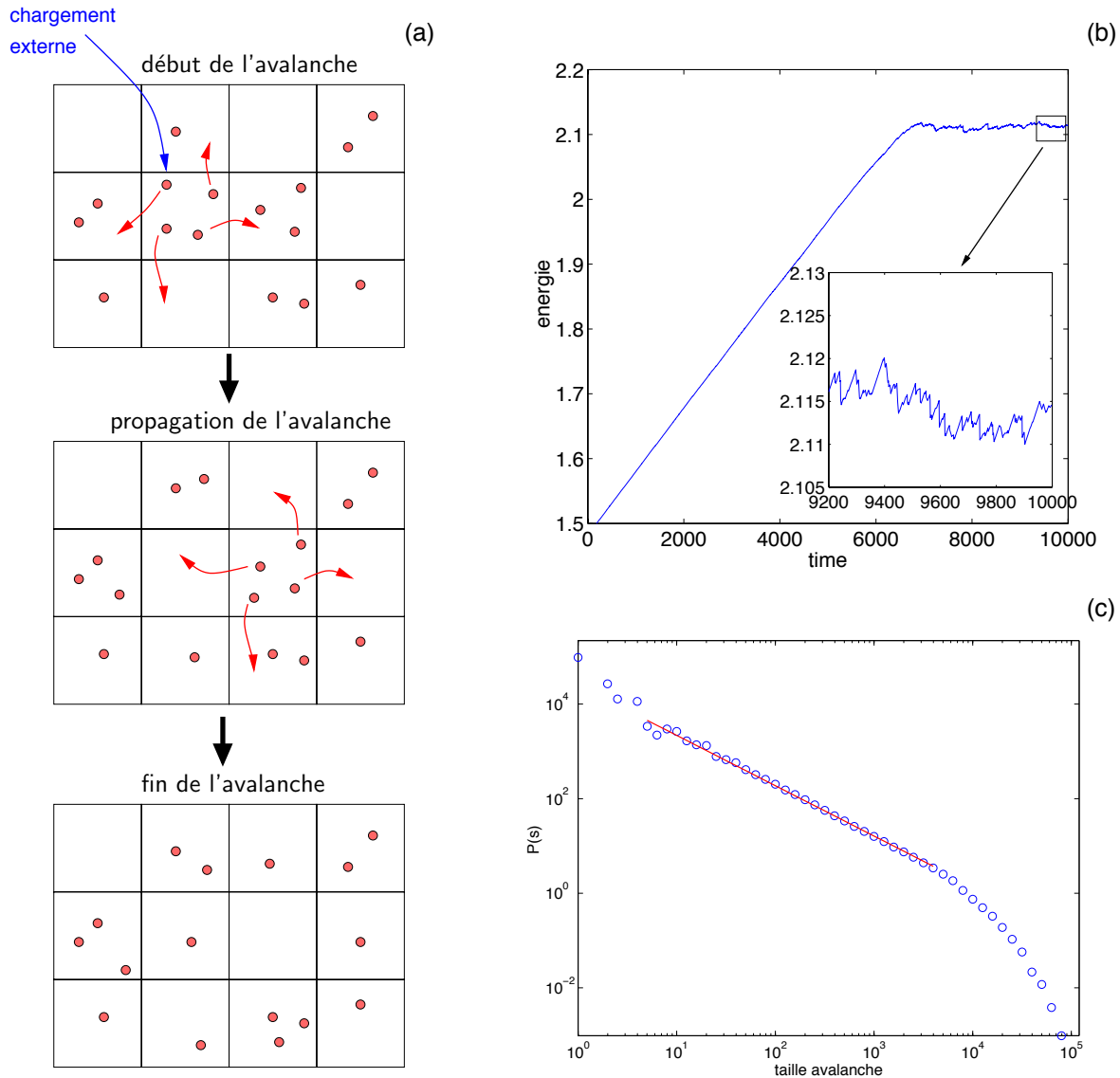


FIG. 1 – (a) Illustration des règles de redistribution de l'énergie entre plus proches voisins pendant une avalanche dans le modèle de Bak et al. [1987]. (b) évolution du système vers un état stationnaire. En partant d'un état initial déchargé  $z_i = 0$ , l'énergie moyenne du système (nombre de grains moyen par case) évolue vers un état stationnaire avec des avalanches de toutes tailles. (c) distribution (différentielle) des tailles d'avalanches dans le régime stationnaire. La taille d'une avalanche est définie comme le nombre total de relaxations. La ligne continue est un fit par une loi de puissance  $P(s) \sim s^{-1.06}$ . La coupure pour les grandes tailles est due à la taille finie du système (grille de taille  $128 \times 128$ ).

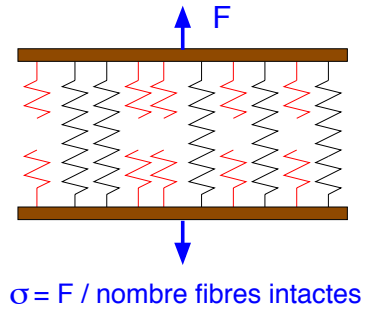
breuses catastrophes naturelles (séismes, éruptions, mouvements de terrains) sont parfois précédées par une accélération de la déformation ou de l'activité sismique. Les mêmes phénomènes précurseurs sont parfois aussi observés dans les expériences de rupture ou de fluage en laboratoire [Anifrani et al., 1995 ; Guarino et al., 2002]. Cette accélération de la déformation peut être interprétée comme l'approche vers un point critique en physique statistique. Dans ces modèles, la rupture d'un matériau hétérogène est précédée d'avalanches dont le nombre et la taille moyenne divergent au moment de la rupture (point critique). De nombreux modèles mécaniques (réseaux de ressorts, par exemple) reproduisent un comportement critique de la déformation précédant la rupture macroscopique du système [cf Sammis et Sornette, 2002, pour une revue]. Le modèle le plus simple de rupture critique est le modèle démocratique de fibres illustré sur la Figure 2. La différence fondamentale entre ces modèles de rupture critique et les modèles de systèmes CAO décrits plus haut vient du fait que dans les modèles de point critique il y a un endommagement permanent d'un élément après chaque rupture. Un élément qui atteint le seuil de rupture ne peut plus soutenir de charge, ce qui produit une augmentation de la contrainte sur les autres éléments, et conduit à une accélération de la déformation jusqu'à la rupture globale du système si on augmente la force exercée sur le système.

Ce modèle de point critique a été appliqué aux séismes par Sornette [1994] et Sornette et Sammis [1995], et largement utilisé par la suite pour essayer de prédire les plus gros séismes [Sornette et Sammis, 1995 ; Bowman et al., 1998 ; Jaumé et Sykes, 1999 ; Sammis et Sornette, 2002]. Néanmoins, ces études sont pour la plupart des "prédictions" réalisées à posteriori, et la validité statistique de ces "prédictions" reste encore à prouver [Zöller et al., 2002]. La prédiction d'un séisme particulier en terme de date, position et magnitude est pour le moment inaccessible.

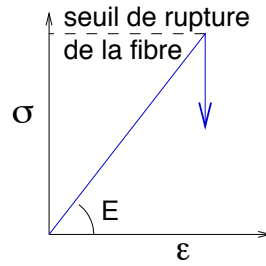
Les deux concepts de point critique et de système CAO ne sont pas contradictoires, mais peuvent coexister dans un même système. Par exemple, le modèle numérique de sismicité étudié par Huang et al. [1998], caractérisé par une géométrie fractale des failles, présente à la fois un comportement CAO aux grandes échelles de temps (état stationnaire avec une distribution en loi de puissance des tailles de séismes), et un comportement caractéristique de l'approche vers un point critique avant les plus gros séismes (accélération en loi de puissance de l'énergie dissipée avant les séismes dont la taille est comparable à celle du système).

On s'intéresse dans ce travail aux tremblements de terre et aux instabilités gravitaires, mais les mêmes modèles ou concepts utilisés dans ce travail pourraient aussi s'appliquer à d'autres objets géologiques, comme les éruptions volcaniques, ou de façon plus générique à la modélisation de la rupture en laboratoire.

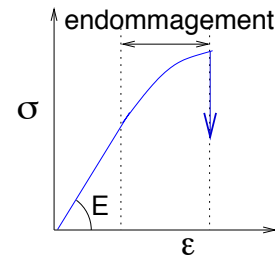
Modèle démocratique de fibres



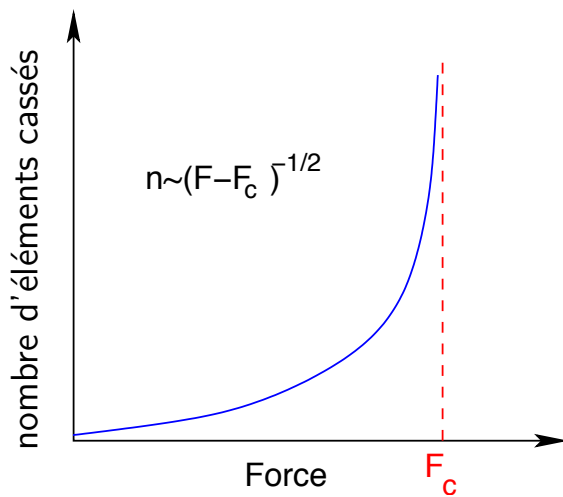
comportement d'une fibre



comportement du système



Evolution du nombre de fibres cassées avant la rupture globale



Distribution des tailles d'avalanches

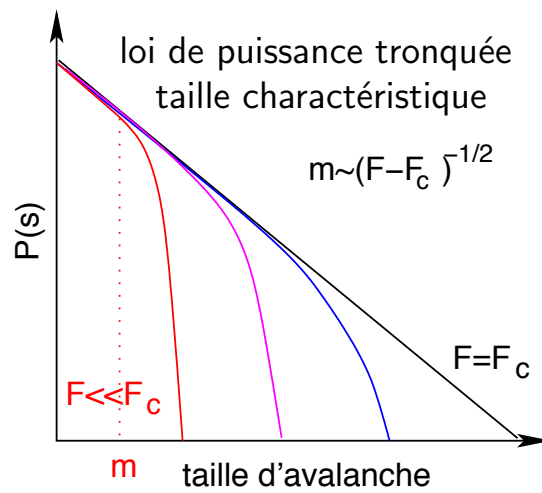


FIG. 2 – Illustration du modèle démocratique de fibres. On augmente la force appliquée sur un réseau de fibres élastiques en parallèle. On considère une distribution initiale de seuils de rupture de chaque fibre. La contrainte est distribuée démocratiquement sur les fibres intactes. La rupture d'une fibre augmente instantanément la contrainte sur les autres fibres, et peut donc déclencher une avalanche de ruptures. Le nombre de ruptures accélère jusqu'à la rupture globale du système. Si le matériau est peu hétérogène, la rupture de la première fibre provoque la rupture matériau. Pour une distribution de seuils de rupture suffisamment large, la rupture globale du système est précédée d'avalanches, dont le nombre et la taille moyenne augmentent en loi de puissance avant la rupture.

## Observations et modélisations des interactions entre séismes et de leur déclenchement

La sismicité existe à toutes les échelles, depuis les ruptures à l'échelle du monocristal, jusqu'à des tailles de rupture qui atteignent 1000 km pour les plus gros séismes. Ces plus gros séismes sont heureusement beaucoup moins fréquents que les plus petits séismes. Spécifiquement, la distribution des magnitudes  $P(m)$  suit la loi de Gutenberg-Richter  $P(m) \sim 10^{-bM}$ , avec  $b \approx 1$ . Cette loi correspond à une distribution en loi de puissance des énergies des séismes ou des longueurs de rupture.

La distribution de la sismicité n'est pas uniforme ni en temps en espace, mais présente de fortes concentrations. Les plus gros séismes sont toujours suivis d'une augmentation de sismicité ("aftershocks"), et parfois précédés d'une accélération du nombre de séismes ("foreshocks"). Le nombre d'aftershocks décroît en loi de puissance en fonction du temps après le choc principal. Cette loi a été observée par Omori dès 1894, et a été validée sur de nombreuses séquences depuis. La même loi ("loi d'Omori inverse") a aussi été proposée pour décrire l'accélération de l'activité sismique avant un choc principal [Papazachos, 1975a,b ; Kagan et Knopoff, 1978 ; Jones et Molnar, 1979].

On montre dans le deuxième chapitre que les aftershocks et la loi d'Omori existent à toutes les échelles ; les séquences d'aftershocks des plus gros séismes étant plus facilement observées parce que le nombre d'aftershocks augmente avec la magnitude du choc principal. On montre pour un catalogue de sismicité de la Californie que l'augmentation du nombre de séismes  $P(m)$  lorsque la magnitude  $m$  diminue (loi de Gutenberg-Richter,  $P(m) \sim 10^{-bm}$  avec  $b \approx 1$ ) est plus rapide que l'augmentation du nombre d'aftershocks avec la magnitude du mainshock ( $N_{aft.} \sim 10^{\alpha m}$ , avec  $\alpha \approx 0.8$ ). Ce résultat implique que le déclenchement de la sismicité est dominé par les plus petits séismes. Les plus petits séismes déclenchent individuellement moins d'aftershocks que les plus gros séismes, mais ils déclenchent globalement plus d'aftershocks parce qu'ils sont beaucoup plus nombreux. Ce résultat remet en cause un certain nombre d'études qui tentent de comprendre et de modéliser les interactions entre événements en prenant en compte uniquement les plus gros séismes.

Le troisième chapitre est une synthèse des mécanismes physiques qui permettent de reproduire la loi d'Omori pour les aftershocks. Les observations ne permettent pas d'identifier le modèle physique le plus pertinent pour décrire la sismicité. Ces modèles font intervenir un grand nombre de propriétés mécaniques qui ne sont pas accessibles par les observations, surtout pour les plus petits séismes, qui sont trop petits pour être enregistrés mais qui dominent le déclenchement des séismes.

A cause du grand nombre de modèles physiques qui reproduisent les deux principales lois de la sismicité, la loi de Gutenberg-Richter et la loi d'Omori, et de l'impossibilité de tenir compte des interactions à toutes les échelles dans ces modèles mécaniques, on utilise dans ce travail un modèle

stochastique de sismicité qui utilise la loi d’Omori et la loi de Gutenberg-Richter pour décrire la sismicité et les interactions entre séismes à toutes les échelles. On utilise le modèle ETAS (“Epidemic Type Aftershock Sequence”) de déclenchement de sismicité introduit par [Hawkes, 1971 ; Kagan et Knopoff, 1987 ; Ogata, 1988 ; Kagan, 1991]. Ce modèle est basé uniquement sur la loi de Gutenberg-Richter pour décrire la distribution des magnitudes, et la loi d’Omori pour modéliser les séquences d’aftershocks. La loi d’Omori est introduite pour décrire les interactions “locales” directes, entre un séisme et les séismes déclenchés par ce séisme (“aftershocks”). On suppose que chaque séisme déclenche sa propre séquence d’aftershocks suivant la “loi locale” qui décroît en temps suivant la loi d’Omori, et dont le nombre augmente avec la magnitude du séisme. On suppose aussi que la magnitude de chaque séisme suit la loi de Gutenberg-Richter. Le taux de sismicité est la somme d’un taux de sismicité constant qui modélise le chargement tectonique, des séismes directement déclenchés par un séisme et de toutes les cascades de sismicité prenant en compte les “aftershocks secondaires” déclenchés par tous les séismes de la séquence. Ce modèle est le modèle statistique de déclenchement le plus parsimonieux permettant de prendre en compte les propriétés de l’activité sismique. Ce modèle, introduit il y a plus de 30 ans, a été surtout utilisé pour décrire l’activité sismique et pour fournir des prédictions à court terme.

Connaissant les interactions locales entre séismes (distributions des temps et distances entre un séisme et ses aftershocks), on cherche à caractériser la distribution temporelle et spatiale de la sismicité globale. Le modèle présente différents régimes en fonction des paramètres du modèle, qui permettent de reproduire de nombreuses propriétés de l’activité sismique. On démontre le rôle essentiel des cascades de déclenchement à toutes les échelles dans l’organisation de l’activité sismique. Ces cascades de déclenchement induisent une renormalisation de la loi d’Omori locale qui décrit les interactions directes entre événements : la loi d’Omori globale prenant en compte les cascades de déclenchement est fondamentalement différente de la loi locale. Le paramètre essentiel du modèle est le taux de branchement  $n$  (nombre moyen de séismes déclenchés par séisme), qui contrôle la transition entre un régime sous-critique pour  $n < 1$  et le régime sur-critique pour  $n > 1$ . Avant ce travail très peu d’études ont tenté de comprendre analytiquement ce modèle pour caractériser les différents régimes. Un premier pas a été réalisé par Kagan [1991] qui a estimé le taux de branchement  $n$  en fonction des paramètres du modèle. Sornette et Sornette [1999a] ont ensuite étudié analytiquement un cas particulier du modèle ETAS sans dépendance en magnitude, en considérant uniquement le régime sous-critique  $n < 1$ .

Les chapitres 5 et 6 décrivent les différents régimes sous-critique et sur-critique de la sismicité dans le modèle ETAS à l’aide d’études analytiques et numériques. Dans le chapitre 7, on étudie la prédictabilité du modèle, et on propose une méthode de prédiction prenant en compte les cascades de sismicité déclenchées par chaque séisme. Cette méthode améliore sensiblement les méthodes précédentes [Kagan et Jackson, 1998, 2000 ; Vere-Jones, 1998] qui négligeaient les aftershocks secondaires.

Le chapitre 8 généralise les résultats obtenus dans le chapitre 5 au modèle ETAS temporel

et spatial. On montre en particulier que les cascades de sismicité induisent un couplage entre les distributions spatiales et temporelles de la sismicité et peuvent induire dans certains régimes une diffusion des séquences d'aftershocks par rapport au choc principal comparable aux observations.

Dans le chapitre 10, on étudie l'évolution de la sismicité avant un séisme majeur. On montre que la loi d'Omori inverse observée par [Papazachos, 1975a,b ; Kagan et Knopoff, 1978 ; Jones et Molnar, 1979] résulte de la loi d'Omori directe introduite pour décrire les aftershocks. D'autres propriétés souvent observées pour les foreshocks, telles que la diminution apparente du paramètre  $b$  de la loi de Gutenberg-Richter avant un séisme majeur, ou la migration de l'activité sismique vers le choc principal, sont aussi reproduites par le modèle ETAS. Le chapitre 12 généralise les résultats obtenus dans le chapitre 10 aux systèmes à mémoire, dans le but de distinguer la réponse d'un système à un choc endogène ou exogène.

Les prédictions du modèle ETAS, concernant la diffusion de la sismicité et les propriétés des foreshocks, sont comparées aux données de sismicité de la Californie dans les chapitres 9 et 11.

## Observation et modélisation des instabilités gravitaires

Les instabilités gravitaires partagent un certain nombre de propriétés avec les séismes : des tailles de ruptures à toutes les échelles, depuis des éboulements rocheux ou des glissements de terrains de moins d'un  $m^3$  jusqu'à des ruptures qui impliquent tout un massif rocheux ( $10^{10} m^3$ ), et un chargement externe (tectonique et érosion) très lent par rapport à la durée d'une rupture. De plus, les glissements de terrains résultent comme les séismes d'instabilités de glissement. L'analogie entre les glissement de terrains et les séismes a déjà été notée par Gombert [1995].

Dans le chapitre 14, on étudie la distribution des tailles d'éboulement rocheux, pour plusieurs jeux de données à différentes échelles de temps et d'espace. On montre que les 3 catalogues étudiés sont caractérisés par une distribution en loi de puissance des volumes de roches, avec le même exposant. Cette distribution en loi de puissance avait auparavant été observée uniquement pour des éboulements rocheux sur des falaises artificielles en bordure des routes, ou pour des glissements de terrain sur des pentes beaucoup plus faibles. Cette distribution en loi de puissance des éboulements rocheux permet d'extrapoler la distribution des volumes pour des volumes plus grands que ceux observés, et donne ainsi une estimation du temps de retour d'un événement en fonction de son volume. On propose ensuite différents modèles pour expliquer la distribution en loi de puissance des volumes d'éboulements rocheux. Cette distribution en loi de puissance peut provenir de la distribution initiale de l'hétérogénéité de la matrice rocheuse (distribution en loi de puissance de la taille des fragments) ; ou elle peut résulter de la dynamique d'un système critique auto-organisé.

Comme pour les séismes, ils existent parfois un certain nombre de phénomènes précurseurs ou d'interactions entre événements, qui permettent d'aller au delà de l'estimation du risque indépendante du temps. En particulier, de nombreux exemples de glissements de terrains "ca-

tastrophiques” (glissements très rapides pouvant atteindre 20 m/sec) ont été précédés par une accélération du glissement pendant une période de quelques jours à plusieurs dizaines d’années avant la rupture finale. Dans le chapitre 15, on propose d’utiliser un modèle de bloc avec une loi de friction dépendante de la vitesse pour modéliser les mouvements de terrains, et distinguer un glissement stable d’un glissement instable qui risque d’évoluer vers une rupture catastrophique. La loi de friction qu’on utilise a été établie en laboratoire [Dieterich, 1978 ; Ruina, 1983] et largement utilisée pour modéliser les séismes (voir [Scholz, 1998] pour une revue). On montre que ce modèle permet de décrire l’accélération du glissement qui a précédé l’effondrement du glissement de terrain de Vaiont en 1963 (Alpes italiennes). Ce modèle permet de prédire la rupture 20 jours à l’avance, et justifie par un modèle physique le fit par une loi de puissance de la vitesse de glissement  $v \sim 1/(t_c - t)$  qui était utilisée avant empiriquement pour prédire les glissements de terrain [Voight, 1988]. Appliquée au glissement de terrain de La Clapière (Alpes françaises), le modèle suggère que l’accélération transitoire du déplacement pendant la période 1983-1988 était dans le régime stable de la loi de friction. Le modèle ne permet pas de décrire la restabilisation du système depuis 1989, à moins d’invoquer une variation de la géométrie du glissement ou une variation des paramètres de la loi de friction.



Première partie

Intéractions entre séismes et leur  
déclenchement



# Chapitre 1

## Introduction

In its richness and complexity, seismicity has been compared with the turbulence of solids [Kagan, 1992, 1994] and is in fact arguably more varied, multi-faceted and complicated. What are the space-time characteristics of seismicity? What are the physical mechanisms controlling the space-time properties of seismicity? How does past seismicity influence seismicity in the future? Is there a significant degree of space-time dependence in seismicity and can we understand it to provide useful skills for earthquake forecasting? How can we reduce the societal risk of earthquake hazard?

There are only a few solidly documented stylized facts in seismicity :

- spatial clustering of earthquakes,
- power law Gutenberg-Richter distribution of released seismic energies and
- clustering in time following large earthquakes, quantified by Omori's  $\approx 1/t^p$  law for after-shocks (with  $p \approx 1$ ) [Omori, 1894].

These “laws” are however only the beginning of a full model of seismic activity and earthquake triggering. It is not an exaggeration to state that a major portion of research in seismology deals with various ways formulated in different forms of characterizing and understanding the nature of earthquakes, their space-time organization and their inter-dependence.

The question addressed here is to describe, to model and to understand how earthquakes interact and how past seismicity impacts on future seismicity. The target of this work is thus 1) to develop a class of simple but powerful physically-based models of spatio-temporal seismicity and 2) to apply and test it against seismicity data, in order to provide a basis for further improvements and for testing of new hypotheses.

### 1.1 Earthquake triggering

This is a growing awareness and an intense research activity based on the fact that a significant fraction of earthquakes are events triggered (in part) by preceding events. In the simple textbook view of a single isolated fault loaded at a constant stress rate, characteristic earth-

quakes occur periodically by rupturing the whole fault, with a period equal to the ratio of the stress drop divided by the rate of stress loading. These earthquakes are “witnesses” or signatures of the tectonic loading.

However, a look at any geological map confirmed by sophisticated statistical tools (multifractal, wavelets, geostatistics) show that faults are complex structures organized into complex networks (see [Bonnet et al., 2001] for a review). There are many evidences that such faults (and therefore earthquakes) interact, as suggested by calculations of stress redistribution (see Harris [2000] for a review), elastodynamic propagation of ruptures using laboratory-based friction law [Dieterich, 1994; Cochard and Madariaga, 1994; Ben-Zion and Rice, 1993, 1995; Rice and Ben-Zion, 1996; Lapusta et al., 2000], simplified models of multiple faults [Cowie et al., 1993; Miltenberger et al., 1993; Cowie et al., 1995; Sornette et al., 1994, 1995; Panza et al., 1997; Soloviev et al., 1999, 2000; Gorshkov et al., 1997; Lee et al., 1999; Ben-Zion et al., 1999; Robinson and Benites, 1995; Narteau et al., 2000], as well as general constraints of kinematic and geometric compatibility of the deformations [Gabriellov et al., 1996]. This dependence between earthquakes implies that any earthquake may have a (partial) role of triggering other earthquakes.

The existence of earthquake triggering is particularly obvious after large shallow earthquakes, for which the seismicity rate increases strikingly for time period up to one hundred years [Utsu et al., 1995], and distances up to several hundred km [Tajima and Kanamori, 1985a,b; Steeples and Steeples, 1996; Kagan and Jackson, 1998; Meltzner and Wald, 1999; Dreger and Savage, 1999]. The rate of the triggered events usually decays in time as the modified Omori law  $n(t) = K/(t + c)^p$  [Omori, 1894], where the  $p$  exponent is found to vary between 0.3 and 2 [Davis and Frohlich, 1991a; Kisslinger and Jones, 1991; Guo and Ogata, 1995; Utsu et al., 1995] and is often close to 1 (see however [Kisslinger, 1993; Gross and Kisslinger, 1994] for alternative decay laws such as the stretched exponential).

These triggered events are usually called aftershocks if their magnitude is smaller than the first event. However, the definition of an aftershock contains unavoidably a degree of arbitrariness because the qualification of an earthquake as an aftershock requires the specification of time and space windows. In this spirit, several alternative algorithms for the definition of aftershocks have been proposed [Gardner and Knopoff, 1974; Reasenber, 1985; Davis and Frohlich, 1991a; Molchan and Dmitrieva, 1992] and there is no consensus. Since the underlying physical processes are not fully understood, the qualifying time and space windows are more based on common sense than on hard science. Particularly, there is no agreement about the duration of the aftershock sequence and the maximum distance between aftershock and mainshock. If one event occurs with a magnitude larger than the first event, it becomes the new mainshock and all preceding events are retrospectively called foreshocks. Thus, there is no way to identify foreshocks from usual aftershocks in real time. There is also no way to distinguish aftershocks from individual earthquakes [Hough and Jones, 1997]. The aftershock magnitude distribution follows the Gutenberg-Richter distribution with similar  $b$ -value as other earthquakes [Ranalli,

1969; Knopoff et al., 1982]. They have also similar rupture process. Moreover, an event can be both an aftershock of a preceding large event, and a mainshock of a following larger earthquake. For example, the  $M=6.5$  Big Bear event is usually considered as an aftershock of the  $M=7.3$  Landers event, and has clearly triggered its own aftershock sequence. One can trace the difficulty of the problem from the long-range nature of the interactions between faults in space and time resulting in a complex self-organized crust.

These observations taken together pose many challenging questions. What is the role of earthquake interactions and triggering compared with the underlying tectonic driving forces? Specifically, is there a way to define and distinguish triggered earthquakes from untriggered ones? Can one use the physics of earthquake triggering to understand the spatio-temporal seismicity beyond the narrow definition of aftershocks? Can it be used to distinguish foreshocks from mainshocks and from aftershocks? Can it be useful for improving the forecast of future seismicity? What are the fundamental limits of predictability imposed by the interplay between the physics of triggering, of tectonic loading and of their interplay?

These questions are essential because there is growing evidence that a large fraction of earthquakes in seismic catalogs are triggered events. The identification of aftershocks is often driven by the need to “decluster” catalogs. This obviously provides only a lower bound to the total fraction of triggered events. Gardner and Knopoff [1974] propose to detect aftershocks according to a windowing method. Applied to the Southern California catalog, they find that  $2/3$  of the events in the catalog are aftershocks. Reasenbergs [1985] analyzes the central California catalog over the period 1969-1982, and identifies aftershocks from the constraint of obtaining a declustered catalog with a constant seismic rate. In this way, he finds that 48% of the events belong to a seismic cluster. Davis and Frolich [1991a] use a single link cluster analysis to identify aftershocks in the ISC catalog. They obtain a smaller proportion of dependent events equal to 30%. Kagan [1991a] estimates the ratio of dependent events in various catalogs (California and worldwide) using an inversion by the maximum likelihood method of a simple cascade model of aftershock seismicity. The proportion of dependent earthquakes of the first generation that he estimates ranges between 0.1% for deep events to 90%, but is often close to 20%. Knopoff [2000] revisits a windowing method applied to the Southern California catalog over the period 1944-1990, for magnitudes  $M \geq 4$ . He finds again that clustered events constitute about  $2/3$  of the whole catalog.

Among an aftershock sequence, a large proportion of aftershocks may be triggered indirectly by the mainshock, that is, they may be secondary aftershocks of the mainshock triggered by a previous aftershock. Secondary aftershock sequences are often observed following major aftershocks. For instance, the  $M = 6.5$  Big-Bear earthquake occurred a few hours following the Landers  $M = 7.3$  event and has clearly triggered its own aftershock sequence. Smaller aftershocks at any scale may also trigger their own aftershocks, but may be much more difficult to observe. Therefore, it is very difficult to distinguish between direct and secondary aftershocks

and to quantify the proportion of secondary aftershocks.

Correig et al. [1997] study the aftershock sequence of a  $M = 5.2$  mainshock in eastern Pyrenees. They separate aftershocks as either leading aftershocks or cascades. Leading aftershocks represent only 10% of the aftershocks sequences. Cascade aftershocks are clusters of aftershocks following these leading aftershocks. If we identify leading aftershocks with direct aftershocks of the mainshock, we obtain a proportion of secondary aftershocks equal to 90%. Felzer et al. [2002] estimated the rate of secondary aftershocks from a comparison of the Landers aftershock sequence with numerical simulations of a simple model of aftershock sequence. They find that about 85% of the aftershocks of the Landers event were secondary aftershocks. They concluded that the 1999  $M_W$  7.1 Hector Mine earthquake was triggered, not by the 1992  $M_W$  7.3 Landers earthquake itself [Felzer et al., 2002], but by some of its aftershocks.

There is a large evidence that aftershocks occur at all scales, from the laboratory scale to the worldwide seismicity. However, common belief is that aftershock triggering is controlled by the largest earthquakes, which trigger more aftershocks than smaller earthquakes. Using the SCEC catalog for the time 1932-2001, we show in section 2 that all earthquakes, whatever their magnitudes  $M$  in the range 3–7, trigger aftershocks with the same Omori law, but with a rate  $n_M$  that increases exponentially with the mainshock magnitude  $M$  as  $n_M \sim 10^{\alpha M}$ , with  $\alpha = 0.8$ . This exponent  $\alpha$  is therefore significantly smaller than the exponent of the magnitude distribution  $P(M) \sim 10^{-bM}$ , with  $b = 0.95$  for the southern California seismicity. The finding that  $\alpha < b$  for the southern California seismicity implies that small earthquakes are more important than large earthquakes in triggering aftershocks. Small earthquakes taken individually have a very low probability of triggering a larger earthquake. But because they are much more numerous than larger earthquakes, collectively, they trigger more aftershocks.

To sum up, there seems to be overwhelming evidence that seismicity can only be understood by taking into account earthquake interactions at all scales and their mutual triggering. We propose here to explore a hierarchy of increasingly realistic models of earthquake triggering. In order to define our research strategy, we must first ponder over the possible underlying physical mechanisms.

## 1.2 Physical mechanisms for earthquake interactions and triggering

It is fair to state that there is no consensus on the underlying cause(s) of aftershocks and more generally of earthquake triggering. A review of the mechanisms proposed either for aftershocks and/or for foreshocks is presented in chapter 3, and include weakening processes, rate and state dependent friction law, dynamics of stress distribution on pre-existing hierarchical structures of faults or tectonic blocks, visco-elastic response of the crust and on delayed transfer of fluids. All these mechanisms are fundamentally based on processes associated with or activated by

stresses changes, both static and dynamical [see for a review Harris, 2000] associated with a given earthquake modeled as a set of dislocations or cracks. In this simple mechanical view, earthquakes cast stress shadows [Harris and Simpson, 1992, 1996, 1998 ; Harris, 2000] in lobes of stress unloading and advance the clock towards rupture in zones of stress increase, according to the laws of elasticity [Harris et al., 1995]. These calculations have large uncertainties stemming from the poorly known geometry of the rupture surfaces, the unconstrained homogeneity and amplitude of the stress drop, the use of simplified models of the crust (3D semi-infinite, or thin elastic plate, or plate coupled to a semi-infinite visco-elastic asthenosphere, etc.), and the unknown direction and amplitude of the absolute stress field that pre-existed before the event. These models are mostly limited to direct influences and, apart from rare exceptions, have not attempted to develop of a consistent description of seismicity taking into account of the succession of earthquake triggering processes.

Most of these mechanisms, apart from rare exceptions, give an Omori exponent equal to one, while observations of aftershock decay suggest that the Omori exponent ranges between 0.3 and 2. What determines the variability of  $p$  value? Is  $p$  universal, as proposed by many physical models of aftershocks, or a function of the material properties of the crust, which are different from one location to another? We discuss in chapter 4 possible mechanisms to explain the variability of  $p$ -value, and we propose two new mechanisms to reproduce a variability of the Omori exponent.

In the following, we describe a stochastic model of earthquake triggering and then describe the results that we have obtained using this model. We also compare our numerical and analytical studies of this model with observations of seismic activity. Finally, we propose possible extensions and applications of this model.

### 1.3 The simplest statistical model of earthquake triggering

Why should we consider statistical models? Should not mechanical models such as those discussed above be preferred? The answer is an emphatic yes, ..., if (1) we knew precisely what are the relevant physical processes and (2) we could adequately account for the effect of the multitude of small earthquakes. With respect to the first point, as we recalled in section 1.2, we have a list of reasonable mechanisms and a partial understanding of them but are far from fully understanding their relative importance and even further from being able to develop a consistent formulation of their interplay, if any. In the face of this stalemate, a coarse-grained description of the lumped effect of the different possible mechanisms seems to be a reasonable way to make progress for understanding the space and time organization of earthquakes. With respect to the second point, there is growing evidence, as we discuss in section 2, that the numerous small and intermediate-sized earthquakes may have a significant effect on the future seismicity, when taken together. A systematic counting of them using mechanical calculations seems completely

out of range in the near future and in addition this operation would be poorly constrained. The standard strategy in this case, inherited from the celebrated approach of statistical physics and condensed-matter theory to tackle the so-called many-body problem, is to coarse-grained the dynamics and obtain an effective physical representation at the scale of an individual event, allowing us to investigate the consequences of the interaction between earthquakes.

As we said above, the best-documented law of earthquake interaction and triggering is the Omori's decay rate  $K/(t+c)^p$  of aftershocks following a mainshock. This law provides an effective statistical description of what is sometimes considered to be a special type of earthquake triggering (mainshock  $\rightarrow$  aftershocks). In view of the difficulties in classifying sometimes an earthquake as a foreshock, a mainshock or an aftershock, it is natural to investigate the parsimonious hypothesis in which this distinction is removed and to study its observable consequences. We thus take the Omori's law as our coarse-grained physical formulation of earthquake interactions. Specifically, we assume that the rate of aftershocks following a mainshock of magnitude  $m$  decays according to the local law  $\Psi_m(t)$  defined by

$$\Psi_m(t) = \frac{K 10^{\alpha m}}{(t+c)^{1+\theta}}. \quad (1.1)$$

We assume that all earthquakes whatever their magnitude trigger aftershocks with a rate increasing with their magnitude. The seismicity rate is the sum of all direct and secondary aftershocks sequences triggered by all events. We also assume that all earthquake magnitudes follow the Gutenberg-Richter distribution, independently of the previous history of seismicity. This very simple model is nothing but the so-called epidemic type aftershock (ETAS) model [Kagan and Knopoff, 1987; Ogata, 1988], which was initially introduced for modeling temporal seismic clustering. We prefer call this model "triggering model" instead of ETAS model, because this model is not restricted to the description of aftershock sequences, but can also describe general seismicity and foreshock sequences, as we shall see in chapter 10.

In this model, all earthquakes can be simultaneously mainshocks, aftershocks and possibly foreshocks. An observed "aftershock" sequence is the result of the activity of all events triggering events triggering themselves other events, and so on, taken together. The background seismicity rate is often modeled by a stationary Poisson process with a constant occurrence rate. This provides a structureless source term describing the average effect of tectonic loading. In this description, the observed spatio-temporal richness results from the cascade of triggering processes. As data is going to accumulate with the present quality of recording stations, the previously discussed evidences strongly suggest that such scenarios are going to be recognized as more and more ubiquitous and essential in order to make sense of the observed spatio-temporal seismicity. The situation is not unlike the fault slips inverted from seismograms, which become more and more heterogeneous and complex as the quality of the recordings improve. The model we use is described in more details in chapter 5.

## 1.4 Description of the new results obtained with the triggered-seismicity model

This triggering model has been used to give short-term probabilistic forecast of seismic activity [Kagan and Knopoff, 1987; Kagan and Jackson, 2000], to describe temporal and spatial clustering of seismic activity [Ogata, 1988; Kagan, 1991a; Guo and Ogata, 1997; Console and Murru, 2001; Felzer et al., 2002] and to identify periods of precursory quiescence [Ogata, 1989, 1992, 2001]. However, no attempt has been made until our work to study this model analytically in order to obtain a deeper understanding of the model. The key parameter of this model is the average number  $n$  of daughter-earthquakes created per mother-event. This average is performed over time and over all possible mother magnitudes. For  $\alpha < b$  and  $\theta > 0$ ,  $n$  is finite and given by  $n = \frac{K}{\theta c^\theta} \frac{b}{b-\alpha}$ , where the parameters  $K$ ,  $\alpha$ ,  $c$  and  $\theta$  are parameters of the local law (1.1) and  $b$  is the parameter of the magnitude distribution. This parameter controls the nature of the seismic activity. The different regimes and the full analytical solutions for  $\alpha < b$  are given in section 5 and illustrated in Figure 1.1.

We summarize below the main results :

- For  $n < 1$  (sub-critical regime), a crossover from an Omori exponent  $p = 1 - \theta$  for  $t < t^*$  to  $p = 1 + \theta$  for  $t > t^*$  is found [Sornette and Sornette, 1999a; Helmstetter and Sornette, 2002a], where  $t^* \sim c/(1 - n)^{1/\theta}$  is a characteristic time controlled by the distance from  $n$  to 1. For  $n = 1$ ,  $t^* \rightarrow +\infty$  and only the early times  $t < t^*$  Omori exponent  $p = 1 - \theta$  is observed.
- For  $n > 1$  and  $\theta > 0$  (super-critical regime), one finds a transition from an Omori decay law with exponent  $p = 1 - \theta$  to an explosive exponential increase of the seismicity rate. Of course, the super-critical process can only be transient and has to cross-over to another regime, due to energy conservation.

In the case  $\theta < 0$ ,  $n$  becomes formally infinite. However, the model stills describes an interesting seismicity which initially decays after a mainshock according to an Omori law with exponent  $1 - |\theta|$  similar to the local law and then grows exponentially at large times.

The case  $b < \alpha$  requires a special attention. In absence of truncation or cut-off in the GR distribution, it leads to a power law acceleration culminating in a finite-time singularity due to the interplay between long-memory and extreme fluctuations [Sornette and Helmstetter, 2002]. This case is described in section 6. It is more common to introduce a truncation or roll-off of the GR law at an upper “corner” magnitude, such as given by a power-law distribution tapered by an exponential tail [Kagan, 1999b; Sornette and Sornette, 1999b]. Then,  $n$  becomes finite again and the above classification holds. However, a transient power-law acceleration of the seismicity rate still holds when the maximum observed magnitude is smaller than the corner magnitude.

A stationary seismicity corresponds to  $n < 1$  such that any sequence triggered by an earthquake eventually dies out. A value  $n < 1$  should not lead to the belief that  $n$  gives the typical

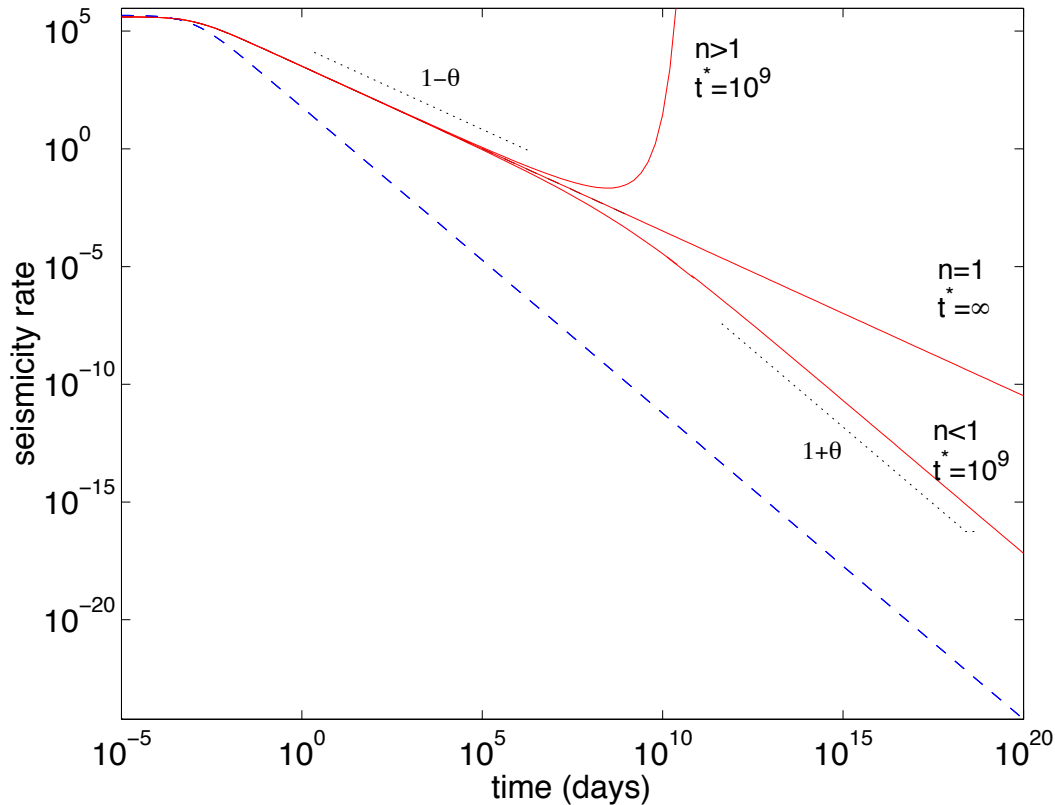


FIG. 1.1 – Seismicity rate  $N(t)$  for the temporal triggering model calculated for  $\theta = 0.3$  and  $c = 0.001$  day. The local law  $\Psi(t) \propto 1/t^{1+\theta}$ , which gives the probability distribution of times between an event and its (first-generation) aftershocks is shown as a dashed line. The global law  $N(t)$ , which includes all secondary and successive aftershocks generated by all the aftershocks of the first event, is shown as a solid line for the three regimes,  $n < 1$ ,  $n = 1$  and  $n > 1$ . We have chosen for pedagogical purpose values of  $n = 0.9997 < 1$  and  $n = 1.0003 > 1$  very close to 1 such that the crossover time  $t^* = 10^9$  days is very large.

number of daughters to a given earthquake, because this  $\rho(m)$  number is extremely sensitive to the specific value of its magnitude  $m$ , as seen from the dependence  $\rho(m) \propto 10^{\alpha m}$ . As an example, for  $\alpha = 0.8$ ,  $b = 1$ ,  $m_0 = 0$  and  $n = 0.9$ , a mainshock of magnitude  $M = 7$  will have on average 80000 direct aftershocks, compared to only 2000 direct aftershocks for an earthquake of magnitude  $M = 5$  and less than 0.2 aftershocks for an earthquake of magnitude  $M = 0$ .

In section 7 we give two observable meanings to  $n$  as the ratio of triggered events over total seismicity and the ratio of secondary aftershocks over all aftershocks. We also offer an analytical approach to account for the yet unobserved triggered seismicity adapted to the problem of forecasting future seismic rates at varying horizons from the present.

The triggering model can be extended to describe the spatio-temporal distribution of seismic activity. In section 8 we study numerically and analytically the spatio-temporal model and we present an exact mapping between the triggering model and a class of continuous time

random walk (CTRW) models. We provide a classification of the different regimes of diffusion of seismic activity triggered by a mainshock. Specifically, we derive the relation between the average distance between aftershocks and the mainshock as a function of the time from the mainshock and the joint probability distribution of the times and locations of the aftershocks. We show that the triggering model can account for the (non-systematic) observation of seismicity diffusion [Mogi, 1968; Imoto and Kishimoto, 1977; Imoto, 1981; Chatelain et al., 1983; Tajima and Kanamori, 1985a,b; Wesson, 1987; Ouchi and Uakawa, 1986; Noir et al., 1997; Di Luccio et al., 1997; Jacques et al., 1999]. Our theory predicts that seismic diffusion or sub-diffusion should be observable only when the observed Omori's exponent is less than 1, because this signals the operation of the renormalization of the bare Omori's law  $\Psi(t)$  (1.1) due to multiple cascades, which can be shown to be also at the origin of seismic diffusion in the triggering model [Helmstetter and Sornette, 2002b]. The mechanism for the diffusion relies on the cascade process of events triggering their aftershocks which trigger their own aftershocks, and so on. This is a remarkable example where a simple model with decoupled space and time leads to a non-trivial coupled process. These results are compared with real seismicity data in section 9.

An even more remarkable property concerning foreshocks can be derived in a very economical way from the triggered-seismicity model in the normal sub-critical stationary regime  $n < 1$  (see section 10). Recall that the inverse Omori's law for foreshocks discovered in the 1970s [Papazachos, 1973; Kagan and Knopoff, 1978; Jones and Molnar, 1979] states that the rate of earthquakes prior to a mainshock increases on average as a power law  $\propto 1/(t_c - t)^{p'}$  of the time to the mainshock occurring at  $t_c$ . Our work [Helmstetter et al., 2002] shows that the inverse Omori's law for foreshocks emerges as the expected (in a statistical sense) trajectory of seismicity, conditioned on the fact that it leads to the burst of seismic activity accompanying the mainshock. In other words, a power law acceleration of seismicity does not require the super-critical regime, the singular regime  $\alpha > b$  or even the critical earthquake concept, but may result from intermittent cascades of triggered earthquakes in the normal sub-critical regime. However, this inverse Omori law is an average statistical law, that is clearly observed only when averaging the seismicity rate over a large number of foreshock sequences. We also show that the often documented apparent decrease of the  $b$ -value of the GR law at the approach to the main shock results straightforwardly from the conditioning of the path of seismic activity culminating at the mainshock. However, we predict that the GR law is not modified simply by a change of  $b$ -value but that a more accurate statement is that the GR law gets an additive (or deviatoric) power law contribution with exponent smaller than  $b$  and with an amplitude growing as a power law of the time to the mainshock. In the space domain, we predict that the phenomenon of aftershock diffusion must have its mirror process reflected into an inward migration of foreshocks towards the mainshock. Using this model, we show that foreshock sequences are special aftershock sequences which are modified by the condition to end up in a burst of seismicity associated with the mainshock. Foreshocks are not just statistical creatures, they are genuine forerunners of large

shocks as shown by the large prediction gains obtained using several of their qualifiers. These results are in good agreement with observations of foreshocks and aftershocks presented in section 11.

In section 12, we use a generalization of the triggering model to describe systems with long-range persistence and memory, such as financial crashes, biological extinctions or climate change. We show that the existence of long memory processes may lead to specific signatures in the precursory and in the relaxation/recovery/adaptation of a system after a large fluctuation of its activity, after a profound shock or even after a catastrophic event, that may allow one to distinguish an endogenous origin from an exogenous source. The recovery after an endogenous shock is in general slower than after an exogenous perturbation. The difference between recovery following endogenous and exogenous shocks results from the same mechanism than the difference between the direct Omori's law and the inverse Omori's law for earthquakes described in section 10. This offers the possibility of distinguishing between an endogenous versus exogenous cause of a given shock even when there is no "smoking gun".

## Chapitre 2

# Earthquake triggering driven by small earthquakes ?

Agnès Helmstetter

Laboratoire de Géophysique Interne et Tectonophysique,  
Université Joseph Fourier, BP 53X, 38041 Grenoble Cedex, France.

Submitted to *Geophys. Res. Letts.*, 2002.

### Abstract

Using a seismicity catalog for California, we measure how the number of triggered earthquakes increases with the earthquake magnitude. The trade-off between this scaling and the distribution of earthquake magnitudes controls the relative role of small compared to large earthquakes. We show that seismicity triggering is driven by the smallest earthquakes, which trigger fewer aftershocks than larger earthquakes, but which are much more numerous. We propose that the non-trivial scaling of the number of aftershocks emerges from the fractal spatial distribution of aftershocks.

### 2.1 Introduction

Large shallow earthquakes are always followed by aftershocks, that are due to the redistribution of the stress induced by the mainshock. The number of aftershocks  $n_M$  triggered by a mainshock of magnitude  $M$  has been proposed to scale with  $M$  as [Utsu, 1969; Kagan and Knopoff, 1987; Kagan, 1991a; Reasenber, 1985; Reasenber, 1999; Singh and Suarez, 1988; Ogata, 1988; Reasenber and Jones, 1989; Yamanaka and Shimazaki, 1990; Davis and Frohlich, 1991b;

Molchan and Dmitrieva, 1992; Hainzl et al., 2000; Drakatos et al., 2001; Felzer et al., 2002]

$$n_M \sim 10^{\alpha M} . \quad (2.1)$$

This relation accounts for the fact that large earthquakes trigger much more aftershocks than small earthquakes. A similar relation holds for the distribution of earthquake magnitudes [Gutenberg and Richter, 1949] given by

$$\rho(M) \sim 10^{-bM} , \quad (2.2)$$

with  $b \approx 1$ , which implies that small earthquakes are much more frequent than large earthquakes.

Because large earthquakes release more energy and trigger more aftershocks than smaller earthquakes, it is usually accepted that interactions between earthquakes and earthquake triggering are dominated by the largest earthquakes. However, because they are much more frequent than larger earthquakes, small earthquakes are also just as important as large earthquakes in redistributing the tectonic forces if  $b = 1$  [Hanks, 1992]. Other quantities, such as the Benioff strain  $\epsilon \sim 10^{0.75M}$ , are dominated by small earthquakes.

The  $\alpha$ -exponent is an important parameter of earthquake interaction that is used in many stochastic models of seismicity or prediction algorithms [Kagan and Knopoff, 1987; Kagan, 1991a; Reasenber, 1985; Reasenber, 1999; Ogata, 1988; Reasenber and Jones, 1989; Console and Murru, 2001; Felzer et al., 2002]. The parameter controls the nature of the seismic activity, that is, the relative role of small compared to large earthquakes. While there is a significant amount of literature on the  $b$ -value, very few studies have measured accurately the  $\alpha$  exponent in real seismicity data. Many studies use  $\alpha = b$  without justification [Kagan and Knopoff, 1987; Reasenber and Jones, 1989; Davis and Frohlich, 1991b; Console and Murru, 2001; Felzer et al., 2002]. In this case, small earthquakes are just as important as large earthquakes for the triggering process. Using (2.1) and (2.2), the global number of aftershocks triggered by all earthquakes of magnitude  $M$  scales as

$$N(M) \sim \rho(M) n_M \sim 10^{(\alpha-b)M} , \quad (2.3)$$

and is indeed independent of  $M$  in the case  $\alpha = b$ . In the case  $\alpha < b$ , aftershock triggering is controlled by the smallest earthquakes, while the largest earthquakes dominate if  $\alpha > b$ .

A few studies measured directly  $\alpha$  from aftershocks sequences, using a fit of the number of aftershocks as a function of the mainshock magnitude [Singh and Suarez, 1988; Yamanaka and Shimazaki, 1990; Molchan and Dmitrieva, 1992; Drakatos et al., 2001]. These studies yield  $\alpha$ -value close to 1, but the limited range of the mainshock magnitude considered and the large scatter of the number of aftershocks per mainshock do not allow an accurate estimation of  $\alpha$ . The case  $\alpha = b$  also explains another well documented property of aftershocks, known as Bath's Law [Bath, 1965; Drakatos et al., 2001; Felzer et al., 2002], which states that the difference between the mainshock magnitude and its largest aftershock is on average equal to 1, independently of the mainshock magnitude. Again, the limited range of mainshock magnitudes used in these

studies and possible biases in the method of data selection [Vere-Jones, 1969] does not allow one to test the dependence of the magnitude difference as a function of the mainshock magnitude.

Other studies measured  $\alpha$  indirectly using the ETAS stochastic triggering model [Ogata, 1988; Kagan, 1991a; Guo and Ogata, 1997] based only on the Gutenberg-Richter and Omori laws [Kagan and Knopoff, 1987; Ogata, 1988]. This model assumes that each earthquake above a magnitude threshold  $m_0$  can trigger aftershocks, with a rate that increases with its magnitude according to (2.1), and decays with time according to Omori's law [Omori, 1894]. In this model, the seismicity rate is the result of the whole cascade of direct and secondary aftershocks, that is, aftershocks of aftershocks, aftershocks of aftershocks of aftershocks, and so on. Using this model,  $\alpha$  can be measured using a maximum likelihood method [Ogata, 1988; Kagan, 1991a; Guo and Ogata, 1997]. The  $\alpha$ -values obtained from the inversion of the this model are not well constrained and show large fluctuations from one sequence to another. For instance, one study [Guo and Ogata, 1997] analyzed 34 aftershock sequences in Japan and measured  $\alpha$  in the range [0.2-1.9] with a mean value of 0.86.

The behavior of the ETAS model model is controlled by the branching ratio  $\nu$ , defined as the average over all mainshock magnitudes of the number of aftershocks per mainshock [Helmstetter and Sornette, 2002a]. The sub-critical regime  $\nu < 1$  is a stable stationary regime, while the seismicity blows up exponentially in the super-critical regime if  $1 < \nu < \infty$ . The case  $\alpha \geq b$  yields  $\nu = \infty$  [Helmstetter and Sornette, 2002a]. In this singular regime, the seismicity rate goes to infinity in finite time  $t_c$  as  $1/(t_c - t)^m$  [Sornette and Helmstetter, 2002]. Such a power-law increase of seismic activity can describe the acceleration of the deformation preceding material failure, as well as a starquake sequence [Sornette and Helmstetter, 2002]. This explosive regime cannot however describe a stationary seismic activity. Thus, the  $\alpha$ -value should not be fixed equal to  $b$  in order to predict or to model seismic activity. Because  $\alpha$  is a crucial parameter of stochastic seismicity models, it is very important to have an accurate estimation of  $\alpha$ . In the sequel, we propose a new efficient method to measure  $\alpha$  directly from earthquake catalogs.

## 2.2 Estimation of $\alpha$ for California seismicity

We use a superposed epoch analysis [Davis and Frohlich, 1991a] to estimate the rate of aftershocks triggered on average by a mainshock of magnitude between  $M$  and  $M + \Delta M$ , for different ranges of the mainshock magnitude  $M$ . In each magnitude range  $[M, M + \Delta M]$ , we superpose all aftershock sequences whose mainshock magnitude is in the range  $[M, M + \Delta M]$ . We use the seismicity catalog of Southern California Data Center, which covers the time period 1932-2000, and which is almost complete above  $M = 3$  for this time period.

The definition of an aftershock contains unavoidably a degree of arbitrariness because the qualification of an earthquake as an aftershock requires the specification of time and space windows. Since there is no widely accepted criteria to define aftershocks [Gardner and Knopoff,

1974; Reasenberg, 1985; Davis and Frohlich, 1991b; Molchan and Dmitrieva, 1992], we test different proposed criteria.

1. We select all earthquakes that occurred at a distance from the mainshock less than  $R$ , where  $R$  is independent of  $M$ . This method has the advantage of not introducing by hand any scaling between the aftershock zone and the mainshock magnitude. However, it may overestimate of the number of aftershocks of the smallest mainshocks if  $R$  is too large, or underestimate the number of aftershocks of the largest mainshock if  $R$  is too small.
2. We use a distance  $R$  increasing with the mainshock magnitude, because the aftershock zone is usually found to scale with the rupture length [Utsu, 1961; Kagan, 2002]. We use  $R = 0.01 \cdot 10^{0.5M}$  km, which is close to the rupture length of a mainshock of magnitude  $M$ . For small mainshock magnitudes, this choice would lead to unacceptable values of  $R$  smaller than the location error, and thus underestimate the number of aftershocks of small mainshocks. Therefore, we impose  $R > 10$  km, larger than the location error.

There is also no consensus on the definition of an earthquake as a mainshock. We need to select aftershocks triggered directly or indirectly by a mainshock, but not affected by the seismic activity preceding this mainshock. Therefore, we do not consider as a mainshock an earthquake which was preceded by a larger earthquake in a time  $T$  and at a distance smaller than  $D$ . We use the same time window  $T$  to define aftershocks and mainshocks. The results are not sensitive to the choice of  $T$  in the range 0.1-1 year. The value of  $D$  is fixed equal to 50 km, roughly the size of the aftershock zone of the largest earthquake in the catalog, to remove the influence of all large earthquakes that have occurred before the mainshock. We do not reject mainshocks that are followed by a larger event, and which would usually be considered as a foreshock, because it would lead to underestimate the number of aftershocks of small mainshocks.

The results obtained for  $T = 1$  year,  $R = 0.01 \cdot 10^{0.5M}$  km and  $D = 50$  km are presented on Figure 2.1. We estimate the aftershock rate  $n_M(t)$  using all earthquakes that occurred in the space-time window  $R, T$  after an earthquake of magnitude in the range  $[M, M + 0.5]$ . The same decay rate with time is observed for all magnitudes, but the number of aftershocks increases exponentially with  $M$ . All the curves for different magnitudes can be collapsed onto a single master curve by dividing the seismicity rate by the factor  $10^{\alpha M}$  with  $\alpha = 0.81$ . This confirms that the scaling of the rate of aftershocks with  $M$  follows (2.1). This method is much more accurate than previous studies which determined the scaling of  $n_M$  with  $M$  using the cumulative number of aftershocks [Singh and Suarez, 1988; Yamanaka and Shimazaki, 1990; Molchan and Dmitrieva, 1992; Drakatos et al., 2001]. Selecting aftershocks within a disk of fixed radius  $R = 50$  km for all mainshock magnitudes yields a slightly smaller value  $\alpha = 0.75$ . Decreasing  $R$  leads to a smaller value of  $\alpha$  because it underestimates the number of aftershocks of the largest mainshocks. When increasing  $R$  between 5 and 100 km, the value of  $\alpha$  first increases with  $R$  and then saturates around  $\alpha = 0.75$  for  $R \geq 30$  km.

In order to test our method of estimation of  $\alpha$ , and the effect of the selection rules for

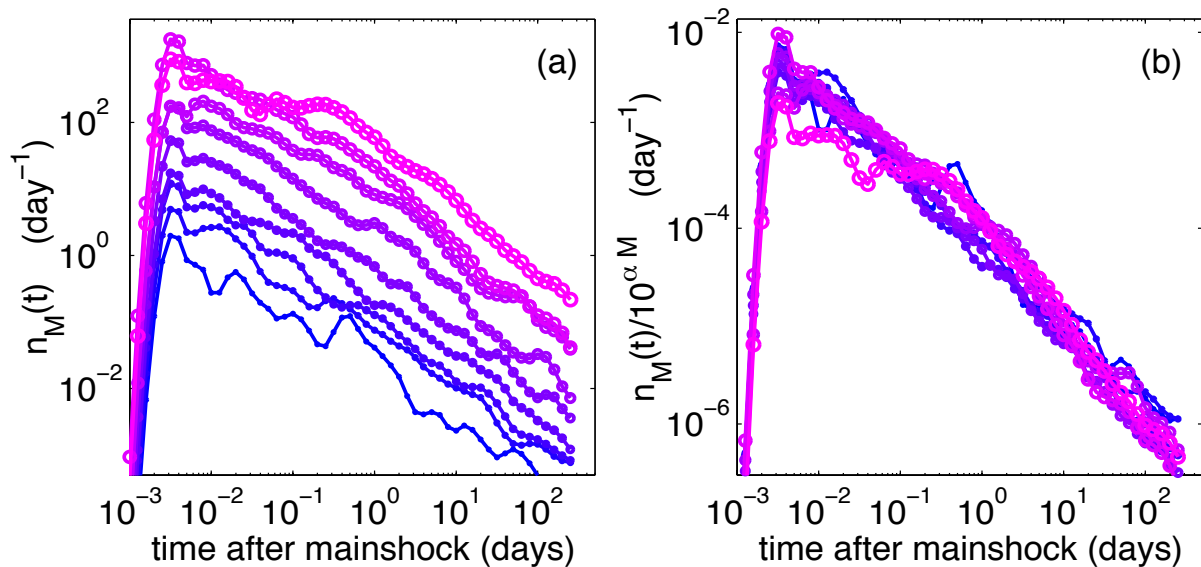


FIG. 2.1 – Aftershock rate  $n_M(t)$  before (a) and after (b) collapse of the curves for different values of the mainshock magnitude between 3 (dark line, small circles) and 7 (grey line, large symbols) with a magnitude step  $\Delta M = 0.5$ . The best collapse in the time range 0.01-100 days is obtained for  $\alpha = 0.81$ . The roll-off of the seismicity rate for  $M \geq 7$  mainshocks at times smaller than 1 day is due to the incompleteness of the catalog after large mainshocks, caused by the saturation of the seismic network.

aftershocks and mainshocks, we have generated synthetic catalogs of seismicity following the ETAS model, which incorporate most properties of aftershocks sequences. We find that using a value of  $R$  independent of  $M$  leads to a slight underestimation of  $\alpha$ . On the other hand, using  $R$  proportional to the rupture length leads to a slight overestimation of  $\alpha$ . This explains the variability of  $\alpha$  obtained with the real seismicity data, when using different methods of aftershock selection. Based on our tests on synthetic catalogs, and our results for real seismicity data, we propose that  $\alpha$  is in the range  $0.8 \pm 0.05$  for the Southern California seismicity. This parameter is therefore significantly smaller than the value  $b = 0.95 \pm 0.05$  of the exponent of the magnitude distribution.

### 2.3 Model

We now propose a simple explanation for this non-trivial scaling of the number of aftershocks with the mainshock magnitude, and we suggest that  $\alpha$  can be related to the fractal structure of the spatial distribution of aftershocks. It is widely accepted that the aftershock zone scales with the rupture length [Utsu, 1961; Kagan, 2002]. Indeed, the aftershock zone is often taken as an estimate of the rupture length. This relationship can be rationalized by the expression of the stress change induced by the mainshock. While the area affected by the stress variation induced by an earthquake increases with the rupture length, the stress drop is independent of the main-

shock magnitude [Kanamori and Anderson, 1975]. The stress variation at a distance from the mainshock proportional to the fault length  $L$  is thus independent of the mainshock magnitude, neglecting the effect of the finite width of the crust and the visco-elastic deformation in the lower-crust. Therefore, assuming that aftershocks are triggered by the stress change induced by the mainshock, the density of aftershocks triggered at a distance  $R \sim L$  from the mainshock is independent of the mainshock magnitude. The increase of the number of aftershocks with the mainshock magnitude results only from the increase in the aftershock zone size with the rupture length.

The rupture length is related to the magnitude by [Kanamori and Anderson, 1975]

$$L \sim 10^{0.5M} . \quad (2.4)$$

The same relation thus holds between the aftershock zone size  $R$  and the mainshock magnitude.

In order to estimate the scaling of the number of aftershocks with the rupture length, we need to make an assumption about the spatial distribution of aftershocks around the mainshock. Assuming that aftershocks are uniformly distributed on the fault plane, and using (2.4), the number of aftershocks triggered by a mainshock of magnitude  $M$  is given by [Yamanaka and Shimazaki, 1990]

$$n_M \sim L^2 \sim 10^M \quad (2.5)$$

and thus leads to  $\alpha = 1$ . The value  $\alpha = 0.5$  obtained for a numerical model of seismicity suggests that in this model aftershocks are triggered mostly on the edge of the fracture area of the mainshock [Hainzl et al., 2000]. Our result  $\alpha = 0.8$  for the California seismicity implies that aftershocks are distributed neither uniformly on the rupture plane nor on the edge of the rupture, but rather on a fractal structure. Using the definition of the capacity fractal dimension, the number of aftershocks is

$$n_M \sim R^D , \quad (2.6)$$

where  $R$  is the characteristic length of the aftershock zone. Using (2.4) and (2.6), we obtain the scaling of the number of aftershocks with the mainshock magnitude

$$n_M \sim 10^{0.5DM} \quad (2.7)$$

which gives  $\alpha = 0.5D$ . Our estimation  $\alpha = 0.8$  for the California seismicity thus suggests  $D = 1.6$ . This value of the fractal dimension of aftershocks hypocenters has never been measured for the California seismicity. Our estimate of  $D$  is significantly smaller than the value measured in the range [2-2.8] for aftershock sequences in Japan [Guo and Ogata, 1997]. This fractal dimension of the spatial distribution of aftershocks results in part from the fractal structure of the fault system [Bonnet et al., 2001], but it may also reflect the non-uniformity of the distribution of the aftershocks on the fault due to the heterogeneity of stress or strength on the fault. The fractal dimension of the aftershock distribution may thus be smaller than the fractal distribution of the fault system.

## 2.4 Conclusion

While the energy release and the total slip on faults is controlled by the largest earthquakes, the finding that  $\alpha < b$  implies that small earthquakes are more important than large earthquakes in triggering aftershocks. Recent studies [Felzer et al., 2002; Helmstetter and Sornette, 2002a] have proposed that secondary aftershocks dominate an aftershock sequence, so that subsequent large aftershocks are more likely to be triggered indirectly by a previous aftershock of the mainshock. Our study further shows that the smallest aftershocks will dominate the triggering of following aftershocks. Therefore large aftershocks cannot be predicted, because they are likely to be triggered by the smallest aftershocks below the detection threshold of the seismic network. Small earthquakes taken individually have a very low probability of triggering an earthquake. But because they are much more numerous than larger earthquakes, collectively, they trigger more aftershocks. This result requires the existence of a small magnitude cut-off  $m_0$ , below which earthquakes may occur but cannot trigger aftershocks larger than  $m_0$ , or a change of the scaling of  $N(M)$  given by (2.3) for small earthquakes, otherwise the seismicity at all scales would be controlled by infinitely small earthquakes.

### Acknowledgments

I am very grateful to J.-R. Grasso, A. McGarr, D. Sornette, C. Voisin and L. Margerin for useful suggestions and discussions. I am also grateful for earthquake catalog data made available by the Southern California Earthquake Data Center.



## Chapitre 3

# Physical mechanisms for earthquake interactions and triggering

Aftershocks following large earthquakes are evidences that the stress change induced by an earthquake can trigger earthquakes. There is however no consensus on the underlying cause(s) of aftershocks and more generally of earthquake triggering. The rate of aftershocks usually decays with the time from the mainshock as Omori's law

$$N(t) \sim 1/(t + c)^p , \quad (3.1)$$

with  $p \approx 1$  [Omori, 1894]. This law is observed at all scales, from the dynamics of acoustic emissions in creep experiments [Scholz, 1968a], to the worldwide seismicity. We review here possible mechanisms of earthquake triggering that can reproduce Omori's law 3.1. Most of these mechanisms may describe both foreshock and aftershock sequences.

### 3.1 Stress-weakening processes

Sub-critical crack growth, stress corrosion, damage laws, and fatigue laws, are different laws describing the quasi-static growth of a crack or the creation of new cracks close to the crack tip. These mechanisms imply a time-dependent strength when subjected to a constant load. The rupture arises when the strength has decreased to the rupture level. These different laws, expressed either in terms of crack growth rate, slip velocity or stress, or assuming a distribution of time to failure, lead to the same Omori law decay of the seismicity following a large earthquake.

#### Sub-critical crack growth

Sub-critical crack growth has been observed in laboratory experiments [Atkinson, 1979]. This mechanism has been first proposed by Das and Scholz [1981] to explain the behavior of foreshocks and aftershocks.

The Griffith criterion states that a crack of length  $x$  becomes unstable when the stress intensity factor  $K$  given by

$$K \approx \sigma \sqrt{x} , \quad (3.2)$$

where  $\sigma$  is the stress, reaches a critical value  $K = K_c$ . However, before reaching the Griffith instability  $K = K_c$  a crack can grow sub-critically at velocity much less than the dynamic rupture velocity of the medium. This behavior results from stress corrosion or microplasticity at the crack tip. Laboratory experiments have shown that the velocity of crack lengthening  $\dot{x}$  increases with the stress intensity factor  $K$  as

$$\dot{x} \sim K^n , \quad (3.3)$$

where the stress-corrosion index  $n$  is a material constant, which varies between 10 and 100 [Atkinson, 1984]. An alternative exponential law has also been proposed [Wiederhorm and Bolz, 1970 ; Atkinson, 1984] :

$$\dot{x} \sim e^{CK} , \quad (3.4)$$

where  $C$  is a constant. Because the corrosion  $n$  exponent in (3.3) is very large, these two laws (3.3) and (3.4) are nearly indistinguishable.

Das and Scholz [1981] assume that aftershocks are due to small patches on the fault of the mainshock that have been loaded by the mainshock. They assume that following the mainshock these patches have a uniform distribution of stress-intensity factor  $K_0$  in the range  $[K_{min}, K_c]$ . They derived Omori's law with  $p = 1$  using the exponential form of the sub-critical crack growth law (3.4). Inserting (3.2) in (3.4) and integrating (3.4) gives the time to failure  $t_c$  as a function of the stress intensity factor  $K_0$  following the mainshock [Wiederhorm and Bolz, 1970]

$$t_c \sim \exp(-C'K_0) , \quad (3.5)$$

where  $C'$  is a constant. Assuming a uniform distribution of stress-intensity factor in the range  $[K_{min}, K_c]$ , the seismicity rate  $r(t_c)$  at time  $t_c$  following the mainshock can be evaluated as

$$r(t_c) = P(K_0) \frac{dK_0}{dt_c} \sim \frac{1}{t} , \quad (3.6)$$

where  $P(K_0)$  is the initial distribution of  $K$  after the mainshock.

An Omori law also arises when using equation (3.3), with an exponent  $p$  depending on the stress-corrosion index  $n$ . Shaw [1993] derives the Omori law decay of aftershocks from (3.3), assuming as in [Das and Scholz, 1981] an initial uniform distribution of stress intensity factor  $K_0$  following the mainshock. The sites that have the highest stress after the mainshock will fail before the others, while those at lower stress will take longer to rupture. The power-law decay of the rate of aftershocks following a mainshock occurs because a distribution uniform in stress gets stretched by the acceleration dynamics (3.3) into a non-uniform distribution in time.

Using (3.3) and (3.2), the stress intensity factor  $K$  evolves with time according to

$$\sigma^2 K^{n-1} = C\dot{K} , \quad (3.7)$$

where  $C$  is a constant. Integrating (3.7) and assuming a constant stress  $\sigma$ , we obtain

$$K(t) \sim \frac{1}{\left(t_c - t\right)^{\frac{1}{n-2}}}, \quad (3.8)$$

where the failure time  $t_c$  is given by

$$t_c = \frac{K_0^{2-n}}{C(n-2)}, \quad (3.9)$$

where  $K_0$  is the initial value of  $K$ .

The rate of aftershocks  $r(t_c)$  at time  $t_c$  following the mainshock can be evaluated as

$$r(t_c) = P(K_0) \frac{dK_0}{dt_c} \sim \frac{1}{t_c^{1+\frac{1}{n-2}}}. \quad (3.10)$$

This relation gives an Omori law decay of aftershocks with an exponent  $p = 1 + \frac{1}{n-2}$ , slightly larger than 1 for large  $n$ . This result retrieves as a special case for  $n = \infty$  the  $1/t$  Omori law decay derived by Das and Scholz [1981] using (3.4). Other choices of the initial state of the patches following the mainshock will lead to different forms of the rate of aftershocks and different values of the Omori exponent.

This law (3.3) has also been used by Yamashita and Knopoff [1987] and Reuschlé [1990] to model aftershocks behavior, and by Yamashita and Knopoff [1989] and Shaw [1993] to model foreshock sequences.

Yamashita and Knopoff [1987, 1992] also assume a power-law distribution of crack lengths. As a consequence, the Omori exponent  $p$  depends both on the corrosion exponent  $n$  and on the exponent of the crack length distribution.

### Stress corrosion, damage laws.

Stress corrosion cracking is a consequence of fluid-induced corrosion at crack tips. Laboratory experiments show that the presence of water in a rock sample alter the mechanical properties of the sample and decrease its strength. The stress corrosion is thought to be the main mechanism of sub-critical crack growth. The presence of fluid can also have a chemical effect on minerals directly, without the need for pre-existing cracks [see for a review Sornette, 1999a].

We study here a particular stress-corrosion law used by [Lee and Sornette, 2000] to model aftershocks. In contrast with the sub-critical crack growth law (3.3), this law is not derived from laboratory experiments. Lee and Sornette [2000] assume that the material strength  $B$  decreases with time when subjected to a stress  $\sigma$  as

$$\frac{dB}{dt} \sim -\sigma^n. \quad (3.11)$$

This law is justified by the fact that fluids subjected to a static stress can alter the mechanical properties of rocks at microscopic scales by hydrolytic weakening. This law describes damage and

stress-weakening induced by stress-corrosion at microscopic scales in the absence of fractures, while the law (3.3) describes the macroscopic effect of stress-corrosion on a pre-existing fault.

The stress-corrosion can be modeled either by a decreasing strength as in (3.11) or by an increasing damage or inelastic deformation.

Introducing the stress corrosion law (3.11) in the cellular automata model of Christensen and Olami [1992], Lee and Sornette [2000] reproduce a  $1/t$  power-law decay of aftershocks, decorated by log-periodic oscillations. Note that the model of Christensen and Olami [1992] without weakening process displays some temporal correlations, which are more important for larger dissipation. However, this simple model is not able to reproduce realistic aftershock sequences.

Lee and Sornette [2000] assume that the material strength  $B(t)$  evolves according to (in dimensionless units)

$$B(t) = B_0 - \frac{\sigma^n}{B_0}(t - t_0) , \quad (3.12)$$

where  $B_0$  is the strength at time  $t_0$ . A rupture occurs when the strength  $B$  decreases to the stress level. Using a mean-field approximation, replacing the stress in one point by the average stress, they derive an analytical solution for the seismicity rate that is in very good agreement with numerical simulations. Assuming that the strength  $B_0$  at time  $t_0$  is much larger than the stress, the time  $t_c$  needed for an isolated element to reach failure is given by

$$t_c \approx \frac{B_0^2}{\sigma^n} . \quad (3.13)$$

Over this interval  $t_c$ , essentially one event occurs on average per site and, as a consequence, the average stress goes from  $\sigma$  to  $(1 - \gamma)\sigma$ , corresponding to a stress drop  $\gamma\sigma$ . We can thus write

$$\frac{d\sigma}{dt} \sim -\frac{\gamma\sigma}{t_c} \approx \frac{\gamma\sigma^{1+n}}{B_0^2} , \quad (3.14)$$

whose solution is

$$\sigma(t) \sim (t + c)^{-1/n} , \quad (3.15)$$

where  $c$  is a constant determined from the initial state. The seismicity rate  $r(t)$  is proportional to  $1/t_c$  because  $t_c$  is the average time between two ruptures on each site. Inserting (3.15) in (3.13) gives Omori's law decay of aftershocks with  $p = 1$ . The fundamental difference between this model and the sub-critical growth law used by e.g. Das and Scholz [1981] or the rate-and-state model of Dieterich [1994] is that, in the model of Lee and Sornette [2000], the Omori law decay of aftershocks arises from the sum of the stress drops induced by all aftershocks, while in the models of [Das and Scholz, 1981 ; Dieterich, 1994] Omori's law is due only to the stress step induced by the mainshock, neglecting the interactions between earthquakes. The Omori law derived by Lee and Sornette [2000] is the "global" law taking into account all aftershocks triggered indirectly by the mainshock. Das and Scholz [1981] and Dieterich [1994] derived in their model the "local" Omori law which describes the number of aftershocks directly triggered by the mainshock, neglecting the secondary aftershocks triggered by other aftershocks.

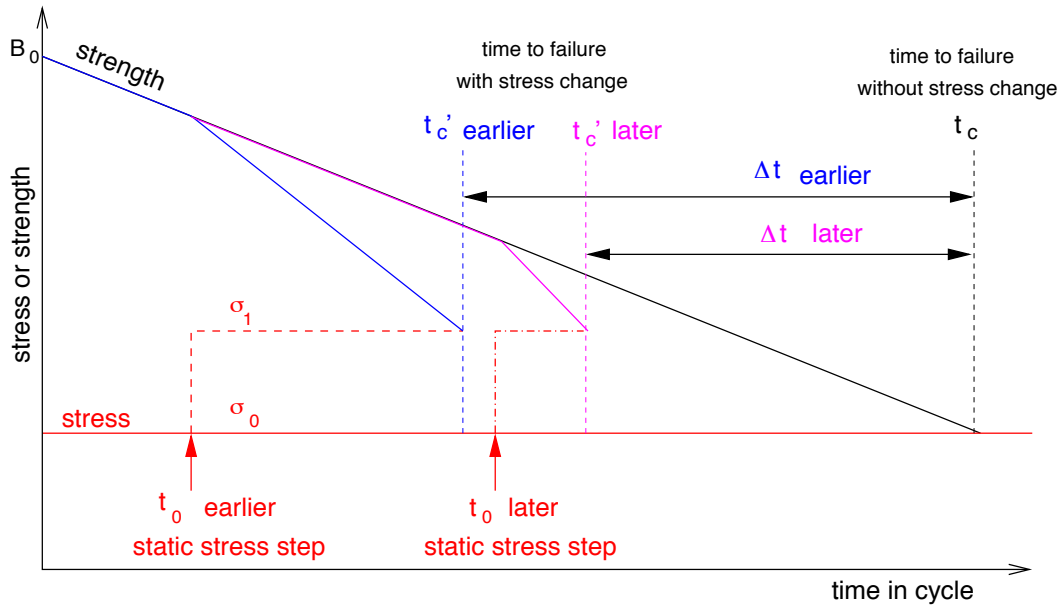


FIG. 3.1 – Time history of the stress and strength of an element subjected to static stress perturbations at two different times  $t_{0_{earlier}}$  and  $t_{0_{later}}$ . The crack length evolves according to the stress-corrosion law (equation 3.11). For the earlier perturbation the change in strength rate  $\Delta(dB/dt)$  is smaller than for the later perturbation because the strength  $B(t_0)$  at the time of the stress change is higher, and it takes more time to reach failure. However, the clock-advance time  $\Delta t$  is larger for the fault perturbed earlier in its cycle.

We can also use the stress-corrosion law (3.11) used by Lee and Sornette [2000] to derive the local Omori law in their model. Different choices of the initial conditions after the mainshock will give different forms of the aftershock decay rate.

First, the relation (3.13) between the time to failure and the stress is very close to the expression (3.9) of  $t_c$  derived using the sub-critical crack growth law (3.3). Therefore, if we assume that the effect of the mainshock is to redistribute uniformly the stress between a minimum value and the strength  $B$ , we obtain an Omori law decay of aftershocks with an exponent  $p = 1 + 1/n$ .

We can derive another form of the aftershock decay rate assuming a constant seismicity rate before the mainshock, instead of a uniform distribution of stress following the mainshock. We model here the effect of the mainshock by a uniform stress step. The effect of a stress step induced by the mainshock is to “clock-advance” the failure. Indeed, looking at equation (3.11) shows that the strength decreases faster for a higher applied stress, and therefore the failure time decreases with increasing stress. Figure 3.1 illustrates the effect of a stress step on a fault which evolves according to (3.12). The failure clock advance  $\Delta t$  is larger if the stress step is applied earlier in the loading cycle.

For a constant applied stress  $\sigma_0$ , the failure time  $t_c$  is given by

$$t_c = \frac{B_0(B_0 - \sigma_0)}{\sigma_0^n}, \tag{3.16}$$

where  $B_0$  is the strength at the beginning of the loading cycle at time  $t = 0$ .

If a stress step from  $\sigma_0$  to  $\sigma_1$  is applied at time  $t_0$ , the failure time is advanced from  $t_c$  to  $t'_c$

$$t'_c = t_0 + t \quad \text{if} \quad t > 0 \quad \text{else} \quad t'_c = t_0, \quad (3.17)$$

where the time  $t$  between the static stress change and the rupture is given by

$$t = \frac{(B_0 - \sigma_0^n t_0/B_0)(B_0 - \sigma_0^n t_0/B_0 - \sigma_1)}{\sigma_1^n}. \quad (3.18)$$

Assuming a population of faults with a uniform distribution of initial states  $P(t_0)$  in the interval  $[0, t_c]$  the seismicity rate following the stress step applied at time  $t = 0$  is given by

$$r(t) = P(t_0) \frac{dt_0}{dt}. \quad (3.19)$$

Using the relation (3.18) for  $t$ , we obtain

$$\begin{aligned} r(t) &\sim \frac{1}{\sqrt{c+t}} && \text{for} \quad t < t_{max}, \\ &= 0 && \text{for} \quad t > t_{max}, \end{aligned} \quad (3.20)$$

where the crossover time  $c$  is given by

$$c = \frac{\sigma_0^{n-1}}{4\sigma_1^{n-2}}, \quad (3.21)$$

and  $t_{max}$  is the duration of the aftershock sequence, given by the time to failure  $t'_c$  of a fault perturbed at time  $t_0 = 0$

$$t_{max} = t'_c(t_0 = 0) = \frac{(B_0 - \sigma_1)B_0}{\sigma_1^n}. \quad (3.22)$$

Expression (3.20) gives a crossover between a constant seismicity rate for times  $t < c$  and a power-law decay with an exponent  $p = 0.5$  at times  $c < t < t_{max}$ . Therefore, a stress step induced by a mainshock leads to a power law decay of aftershocks at large times  $t > c$  with an exponent  $p < 0.5$  smaller than the exponent  $p = 1$  of the global law taking into account the multiple interactions between aftershocks. The faster decay obtained when taking into account the stress changes induced by the aftershocks is due to the fact that aftershocks decrease the stress on average (because of the stress dissipation in the lattice and at the boundary of the lattice) and therefore decreases the rate of following aftershocks.

The damage law (3.11) can also be used to model an inverse Omori law acceleration of foreshock rate before a mainshock [Sornette et al., 1992].

## Fatigue laws, Arrhenius processes

Static fatigue laws describe the time dependent failure under a constant load of a broad variety of materials. The static fatigue of materials under uniaxial tension has been described by the law [Zhurkov, 1965]

$$t_c \sim \exp\left(\frac{U - \gamma\sigma}{RT}\right), \quad (3.23)$$

where  $t_c$  is the average time to failure,  $\sigma$  is the stress,  $T$  is the absolute temperature,  $R$  is the universal gas constant,  $U$  is an activation energy (proportional to the strength in absence of corrosion) and  $\gamma$  is a constant. This law has been shown to derive from a sub-critical crack growth law (3.4) by Wiederhorm and Bolz [1970].

Scholz [1968b] first suggested this mechanism to explain aftershocks. He derived Omori's law with  $p = 1$  using a static fatigue law and assuming that

- a uniform initial distribution of stress,
- all ruptures are independent,
- each element fails only once.

He also used the same model in [Scholz, 1968a] to reproduce the creep in brittle rocks.

Equation (3.23) corresponds to a probability of failure per unit time under a stress  $\sigma$  given by

$$\mu(\sigma) \sim \exp\left(\frac{\gamma\sigma}{RT}\right). \quad (3.24)$$

The fraction of elements subjected to a stress  $\sigma$  that fails between time  $t$  and  $t + dt$  is given by

$$n(\sigma, t)dt = \mu e^{-\mu(\sigma)t} dt. \quad (3.25)$$

To obtain the global rate of failure  $r(t)$  for the whole populations of elements, we integrate equation (3.25) over the population of initial stress  $P(\sigma)$ .

$$r(t) = \int \mu(\sigma) e^{-\mu(\sigma)t} P(\sigma) d\sigma \quad (3.26)$$

Scholz [1968b] assumes a uniform distribution of initial stress  $P(\sigma)$  in the interval  $[0, S]$ . In this case, the seismicity rate  $r(t)$  given by (3.26) is

$$r(t) \sim \frac{1}{t} [e^{-\mu(0)t} - e^{-\mu(S)t}], \quad (3.27)$$

which gives an Omori law decay of the rate of activity with  $p = 1$  for  $1/\mu(S) \ll t \ll 1/\mu(0)$ . Each element subjected to a stress  $\sigma$  has an exponential decay of the probability of failure given by (3.25), with a characteristic time depending of the stress (3.23). The power-law decay of the global seismic activity arises from the superposition of exponential decay rates with a power-law distribution of characteristic times  $P(t_c)$ . Indeed, a uniform distribution of stress gives a power-law distribution of times  $t_c$

$$P(t_c) = P(\sigma) \frac{d\sigma}{dt_c} \sim \frac{1}{t_c}. \quad (3.28)$$

We can generalize the model of Scholz [1968] to other choices of the distribution of initial stress  $P(\sigma)$ . We consider here the same model as in Scholz [1968] but with an exponential distribution of energies  $E = U - \gamma\sigma$  [Helmstetter and Sornette, in preparation]

$$P(E) \sim e^{-\frac{E}{E_0}}, \quad (3.29)$$

corresponding to an exponential distribution of stress barriers  $U/\gamma - \sigma$ . In order to evaluate the rate of activity  $r(t)$ , we transform (3.26) into

$$r(t) = \int \mu e^{-\mu t} P(\mu) d\mu . \quad (3.30)$$

where  $P(\mu)$  is given by

$$P(\mu) = P(E) \frac{dE}{d\mu} = \mu^{\theta-1} , \quad (3.31)$$

where  $\theta$  is given by  $\theta = \frac{RT}{E_0}$ . Putting (3.31) in (3.30) we obtain

$$r(t) \sim \frac{1}{t^{1+\theta}} , \quad (3.32)$$

which gives an Omori law decay of the rate of activity with  $p = 1 + \theta = 1 + \frac{RT}{E_0}$ . In this case, the power law decay comes from the competition between the exponential distribution of energies  $P(E)$  and the exponential relation between  $\mu$  and  $E$  (see chapter 14.2.2 in [Sornette, 2000a]). The model of Scholz [1968b] can be seen as a special case of our model for  $E_0 = \infty$ , corresponding to  $\theta = 0$  and thus  $p = 1$ .

Marcellini [1995, 1997] uses the same fatigue law (3.23) to describe aftershocks but with a very different model. He assumes that each aftershock decreases the stress in the fault zone. In this model, there is no disorder on the stress or strength field. The seismicity rate decreases with time due to the stress decrease induced by all aftershocks. He finds that the cumulative energy release increases as  $E \sim \log(t) + \text{constant}$ . This law corresponds to Omori's law decay of the seismicity rate with  $p = 1$  if the distribution of aftershock energies is independent of time. Assuming that all events have the same stress drop  $\Delta\sigma$ , and starting from a stress  $\sigma_0$  at the time of the mainshock, the time interval between two aftershocks  $i$  and  $i + 1$  is given by

$$t_{i+1} - t_i \sim e^{-\frac{\gamma\sigma_0 - (i+1)\gamma\Delta\sigma}{RT}} - e^{-\frac{\gamma\sigma_0 - i\gamma\Delta\sigma}{RT}} \sim e^{-\frac{i\gamma\Delta\sigma}{RT}} \sim t_i . \quad (3.33)$$

Therefore, the seismicity rate at time  $t_i$  is given by

$$r(t_i) = (t_{i+1} - t_i)^{-1} \sim \frac{1}{t_i} , \quad (3.34)$$

which decays with time according to Omori's law with  $p = 1$ . This analysis considers only stress decrease induced by all aftershocks and neglects the stress increase due to each aftershock.

The models of Scholz [1968b] and Marcellini [1995, 1997] use the same law (3.23) to reproduce Omori's law, but with very different mechanisms. In Scholz's model, the stress decreases with time because the weaker elements fail earlier, but this model neglects the stress changes induced by aftershocks. In Marcellini's model, the stress decreases with time due to the stress drop induced by all aftershocks.

Moreno et al. [2001] used another fatigue law proposed by [Coleman, 1957] to reproduce aftershock behavior in a cellular automata model [Christensen and Olami, 1992]. They assume that the characteristic time-to-failure  $t_c$  increases with the stress barrier  $\Delta\sigma$  as

$$t_c \sim (\Delta\sigma)^n , \quad (3.35)$$

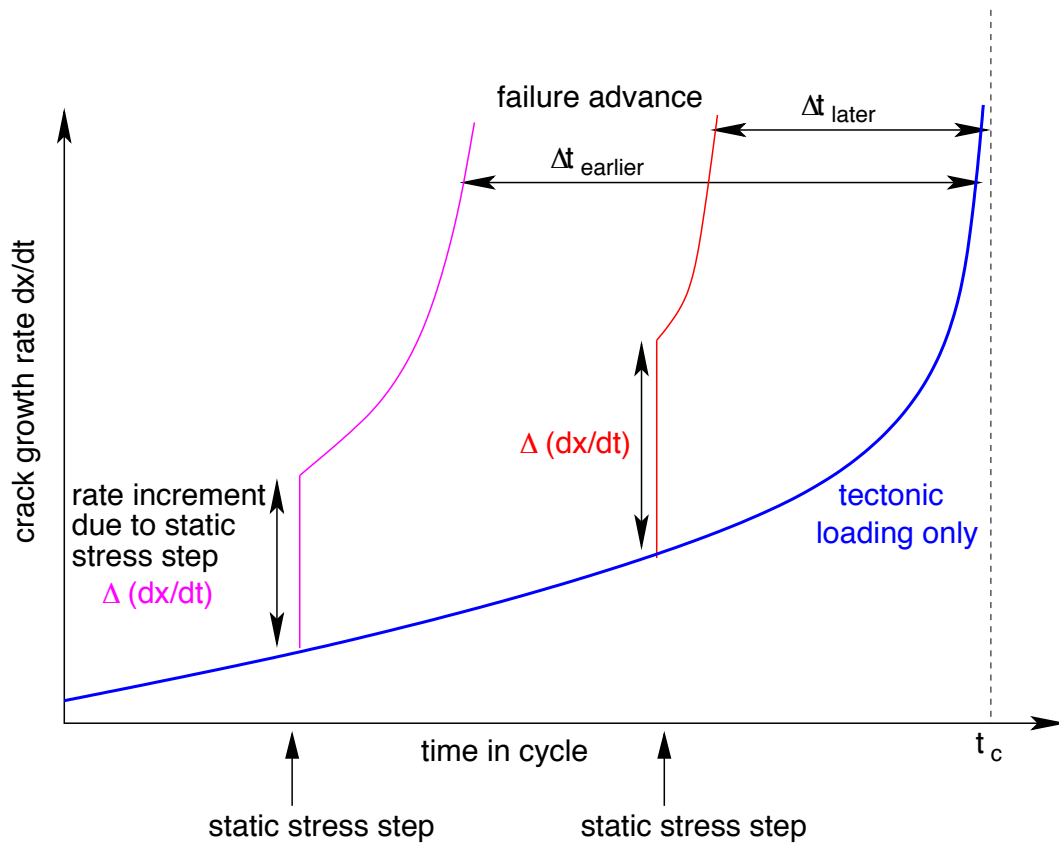


FIG. 3.2 – Time history of the growth rate of a crack subjected to static perturbations at two different times. The crack length evolves according to the rate and state friction law (equation 3.36). For the earlier perturbation the incremented growth rate  $\Delta(dx/dt)$  is smaller than for the later perturbation because  $dx(t_0)/dt$  is smaller, and it takes more time to reach failure. However, relative to the rate with no perturbation, the crack perturbed earlier spends a greater fraction of its total time to failure at an elevated rate and thus experiences a greater change in its failure time  $\Delta t$  (adapted from Figure 3 of [Gomberg, 2001]). Although this example is for Rate-and-state dependent friction law, the same negative correlation between  $\Delta t$  and the time of the stress perturbation applies to all accelerating failure models, such as the sub-critical crack growth.

where  $\Delta\sigma$  is the distance to the failure threshold, and the  $n$ -exponent is in the range  $[2 - 50]$ . For large  $n$  values, this law is very similar to the exponential law (3.23) used by [Scholz, 1968b; Marcellini, 1995, 1997]. They obtained aftershock sequences obeying Omori's law with  $p = 1$  (or close to 1) independently of the  $n$ -exponent and of the dissipation.

### 3.2 Rate-and-state dependent friction

Rate and state friction laws have been proposed by Dieterich [1994] to explain the clustering of seismicity and the pattern of aftershocks. The rate-and-state friction law is defined by [Ruina,

1983]

$$\tau = \sigma[\mu_0 + A \ln(v/v_0) + B(\theta/\theta_0)] , \quad (3.36)$$

where  $\tau$  and  $\sigma$  are shear and normal stress respectively,  $v$  is slip velocity, and  $\theta$  is a state variable.

The state variable  $\theta$  evolves according to

$$\frac{d\theta}{dt} = 1 - \frac{\theta v}{D_c} , \quad (3.37)$$

where  $D_c$  is the characteristic sliding distance for evolution of fault state. These laws lead to an unstable slip if  $B > A$ , because in this regime the steady-state friction coefficient decreases with increasing slip velocity. Preceding an earthquake, the slip velocity goes to infinity in finite time  $t_c$ . Close to the instability, the velocity evolves as [Dieterich, 1994]

$$v \sim \frac{1}{t_c - t} , \quad (3.38)$$

where  $t_c$  is determined by the initial conditions and the friction parameters.

The effect of a stress step induced by a mainshock on a fault will be to increase the slip rate on the fault and to advance the time to failure  $t_c$ , as illustrated in Figure 3.2. The effect of increasing the shear stress by  $\delta\tau$  is to increase the slip velocity from  $v$  to  $v'$  according to

$$v' = v \exp\left(\frac{\delta\tau}{A\sigma}\right) , \quad (3.39)$$

where  $A$  is a parameter of the friction law (3.36) and  $\sigma$  is the normal stress. Therefore, a stress step induced by a mainshock will trigger aftershocks by advancing their failure time. The new failure time  $t'_c$  following a stress step is given by  $t'_c = t_c - \Delta t$ . The advance of the failure time  $\Delta t$  is more important for faults which were far from the rupture before the stress step, as illustrated by Figure 3.2

Assuming an infinite population of faults with the same properties and with a uniform seismicity rate before the mainshock, the stress step induced by the mainshock triggers aftershocks with a rate given by Omori's law (3.1) with  $p = 1$ . This result has been derived analytically by Dieterich [1994] This analysis neglects the multiple interactions between aftershocks. The aftershocks are triggered by a single stress step induced by the mainshock, and subsequent stress changes induced by the aftershocks are neglected.

The duration of the aftershock sequence  $T_a$  is much smaller than the duration of the seismic cycle  $T_r$ . The aftershock duration for a mainshock stress  $\Delta\tau$  is given by

$$T_a = \frac{A\sigma T_r}{\Delta\tau} . \quad (3.40)$$

The assumption of a constant seismicity rate before the mainshock implies a uniform distribution of initial times  $0 < t_0 < t_c$  measured from the last rupture. The seismicity rate  $r(t)$  can be evaluated from the expression of the clock advance  $\Delta t$  as a function of the initial state  $t_0$  of

the fault. Following a stress step applied at time  $t = 0$ , the rate of failure at time  $t = t'_c - t_0$  is given by [Gomberg et al., 2000]

$$r(t) = -P(t_0) \frac{dt_0}{dt} \sim \frac{P(t_0)}{1 - \frac{d\Delta t}{dt_0}} . \quad (3.41)$$

The power-law distribution of aftershock times with  $p = 1$  derives from the non-linear dependence of  $\Delta t$  on the initial state  $t_0$ . Rather than fixing the state of the faults following the stress step as done by [Das and Scholz, 1981], we can use (3.41) to compute the seismicity rate  $r(t)$  depending on the initial state  $P(t_0)$  of the fault before the mainshock.

Introducing a spatial dependence of the stress released by the mainshock modifies the decay law of the aftershock rate, which decays as an apparent power-law with an exponent  $p \approx 0.8$  when considering only aftershocks at a fixed distance from the mainshock [Dieterich, 1994].

Ziv and Rubin [2002] use a numerical model of seismic activity on a fault, closely based on the numerical model of Dieterich [1995], which incorporates the rate and state friction law, in order to test the effect of multiple interactions between earthquakes on the decay of aftershocks. They obtained the same  $\frac{1}{t}$  decay law of aftershocks following a mainshock than Dieterich [1994] when taking into account the multiple interactions between aftershocks. The duration of the aftershock sequence is longer when taking into account these multiple interactions. They also derived analytical solutions for the seismicity rate following a mainshock and taking into account the stress changes induced by all aftershocks, which are in good agreement with the numerical simulations.

Dieterich and Kilgore [1996] suggest that the rate and state friction law may also reproduce foreshock sequences. In the rate and state friction model proposed by Dieterich [1994], foreshocks can be generated by two mechanisms :

- By the same mechanism leading to aftershock sequences following a stress step induced by a mainshock, this model can generate foreshocks if an aftershock becomes larger than its triggering event. An aftershock can be larger than the triggering event, but with a small probability, because all magnitudes are determined in the GR law independently of the magnitude of the triggering event.
- Foreshock may be triggered by the strain changes of the mainshock nucleation process. The accelerating slip due to the mainshock nucleation perturbs the stressing rate at a foreshock nucleation source and therefore increases the seismicity rate. They derive analytical solutions for the foreshock rate induced by this mechanism.

### 3.3 Visco-elastic relaxation of the lower crust

Viscous relaxation as been proposed by [Mikumo and Miyatake, 1979; Hainzl et al., 1999, 2000; Pelletier, 2000] to explain aftershock behavior.

Mikumo and Miyatake [1979] used a numerical model of a fault with a uniform distribution

of relaxation times. They also introduce a weakening and healing of the strength following an earthquake. They obtained an Omori law decay with  $1.1 < p < 1.4$  for the same time range than the distribution of relaxation times. The  $p$ -exponent is found to decrease with increasing heterogeneity of the frictional strength, and to increase if the healing time decreases.

Hainzl et al. [1999, 2000] used a cellular automata similar to the model of Christensen and Olami [1992]. They introduce post-seismic transient creep at the vicinity of the rupture. They assume that the stress dissipated during the rupture is then relaxed by the viscous crust. Following an earthquake, the visco-elastic relaxation of the crust leads to an exponential increase of the stress  $\Delta\sigma$  according to

$$\Delta\sigma \sim 1 - e^{-t/T} , \quad (3.42)$$

where  $T$  is the characteristic time of the viscous relaxation. The only heterogeneity in their model is the initial distribution of the stress. They obtain both foreshock and aftershock sequences, with the same  $p$ -exponent for foreshocks and aftershocks, but for very limited time intervals of the order of the relaxation time. The  $p$  value increases if the relaxation time  $T$  decreases. The  $p$ -value is also found to increase with the spatial coupling length of the viscous relaxation.

Pelletier [2000] has extended the previous model to include a distribution of static coefficient of friction in order to model structural heterogeneity, and obtained similar results.

Therefore, this mechanism cannot explain the Omori's law decay observed for very long time ranges, unless assuming a wide heterogeneity of the viscous relaxation time.

### 3.4 Pore fluid flow

Shallow earthquakes can induce changes in the fluid pore pressure that are comparable to stress drops on faults. The subsequent redistribution of pore pressure as a result of fluid flow slowly decreases the strength of rock and may result in delayed fracture. This mechanism has been proposed by Nur and Booker [1972] to reproduce aftershock behavior. Following an earthquake, pore fluid flows from regions of compression to regions of dilatation. This flow causes an increase of pore pressure and a consequent decrease in the strength in the regions of dilatation. Aftershocks occur if the strength drops to the level of the shear stress. The initial pore pressure  $P(\mathbf{r}, 0)$  is given by the hydrostatic stress  $\sigma(\mathbf{r})$  induced by the mainshock

$$P(\mathbf{r}, 0) \sim \sin \theta / r \quad (3.43)$$

in a coordinate system  $\mathbf{r}, \theta$  around the end of the crack. The initial pore pressure field (3.43) is characterized by a compression on one side of the fault tip and by a dilatation on the other side. After the mainshock, the fluid will flow from regions of compression toward those of dilatation.

The pore pressure  $P$  diffuses according to

$$\frac{\partial P(\mathbf{r}, t)}{\partial t} = c \nabla^2 P(\mathbf{r}, t) , \quad (3.44)$$

which gives

$$P(\mathbf{r}, t) \sim \frac{1 - e^{-\frac{r^2}{4ct}}}{r} \sin \theta, \quad (3.45)$$

where  $c$  is the hydraulic diffusivity. The peak of the fluid pressure diffuses with time as  $t^{1/2}$ . The pressure at the peak decays as  $t^{-1/2}$ . Nur and Booker [1972] suggests that the rate of aftershocks is proportional to the time-derivative of the pore pressure, integrated over the volume

$$r(t) \sim \int \frac{\partial P}{\partial t} dv \sim \frac{1}{t^{1/2}}. \quad (3.46)$$

This mechanism reproduces an Omori law decay of the aftershock rate but with an unrealistic exponent  $p = 0.5$  smaller than the usual value  $p \approx 1$ .

Moreover, the pore-fluid flow mechanism cannot be the sole explanation for aftershock triggering because aftershocks occur predominantly at the edge of the mainshock high-slip regions, while the fluid flow mechanism implies a diffusion of the aftershock activity with time that is not always observed in aftershock sequences [Mendoza and Hartzell, 1988; Scholz, 1990; and chapter 9 of this work].

### 3.5 Dynamics of stress redistribution on a hierarchical fault network

Many studies have proposed that the fault networks are scale-invariant (see for a review [Bonnet et al., 2001]). This fractal pattern may result from fragmentation models [e.g. Redner, 1990a, Cowie et al., 1993, 1995]. Some studies have proposed that the dynamics of stress distribution on pre-existing hierarchical structures of faults or tectonic block can reproduce foreshock and aftershock patterns [Blanter et al., 1997; Huang et al., 1998; Narteau et al., 2000; Gabrielov et al., 2000].

Huang et al. [1998] use a cellular automata model with a pre-existing fractal cell structure to model both foreshock and aftershock sequences. The loading and the redistribution of stress following an earthquake are controlled by the size of the fault. The system is loaded by adding particles at random sites, with a probability proportional to the cell area. The rupture threshold is also proportional to the cell area. The number of particles redistributed to an adjacent cell is proportional to the length of the cell. This model thus introduces coupling between cells of different sizes, mimicking the multi-scale interactions between faults. This system self-organizes in a stationary regime, with foreshock and aftershock sequences preceding and following characteristic earthquakes involving the largest cells. They obtained a  $p$ -value close to 0.9, with small fluctuations between 0.85 and 1.05. All mechanisms previously discussed involve a delay mechanism between a stress change and the rupture. In this model, this delay arises from the spatial heterogeneity of the loading rate and from the hierarchical structure.

Gabrielov et al. [2000] also reproduce foreshocks and aftershocks using a hierarchical model which incorporates

- a direct cascade of loading : the stress is applied to the largest elements and then redistributed to the smaller scales ;
- an inverse cascade of fracturing, which goes up the hierarchy, from the smaller to the larger elements.

Blanter et al. [1997] use a hierarchical model of blocks that reproduces aftershocks and foreshocks. Four blocks at a given level compose a block of the upper level. A memory effect is introduced at the smaller scale. Present states are determined by previous states of blocks at the same level. The perturbation then moves from the lower levels to the higher ones. This model reproduce Omori's law decay of aftershocks with  $0.8 < p < 1.2$  depending on the model parameters.

Narteau et al. [2000] consider a hierarchical system made of embedded cells of increasing levels. This model includes

- a direct cascade of stress redistribution after each event (from higher to lower levels). An event of scale  $k$  affects the stress in all the smallest-scale cells located in their neighborhood.
- a inverse cascade of fracturing (from lower to higher levels). An earthquake of a given scale  $k$  is associated with the moving state of a cell of level  $k$  and results from the coherent self-organization of fractures of lower scales.
- a constant healing rate following a rupture.

This model reproduces Omori's law decay of aftershocks with the exponent  $p$  in the range [1.1-1.5]. The power-law decay of aftershock rate is due to the heterogeneity of the stress field. An inverse Omori's law is also observed with a smaller exponent  $0.6 < p' < 0.9$ .

### 3.6 Are earthquakes triggered by static or dynamic stress changes ?

Most models of seismicity triggering assume that earthquakes are triggered by static stress changes. However, the dynamic stress change induced by the mainshock is larger than the static stress change, especially at large distances from the mainshock, because it decays more slowly than the static stress change. Static stress changes may trigger earthquakes both (i) by permanently incrementing the tectonic load acting on a fault and (ii) by altering properties of the fault. Dynamic stress changes can only trigger by the latter mechanism because they are transient.

Gomberg [2001] suggests that aftershock sequences cannot be triggered by the dynamic stress field for a large class of triggering mechanisms. All mechanisms, such as sub-critical crack growth or rate and state dependent friction, characterized by a non-linear acceleration of the sliding velocity under a constant stress rate, cannot explain the triggering of aftershocks by the dynamic stress at times significantly longer than the mainshock duration. Contrary to the case of a static stress step, the failure advance  $\Delta t$  induced by a dynamic stress perturbation is larger for the faults which were closer to the rupture before the perturbation (see Figure 3.3). Therefore, a

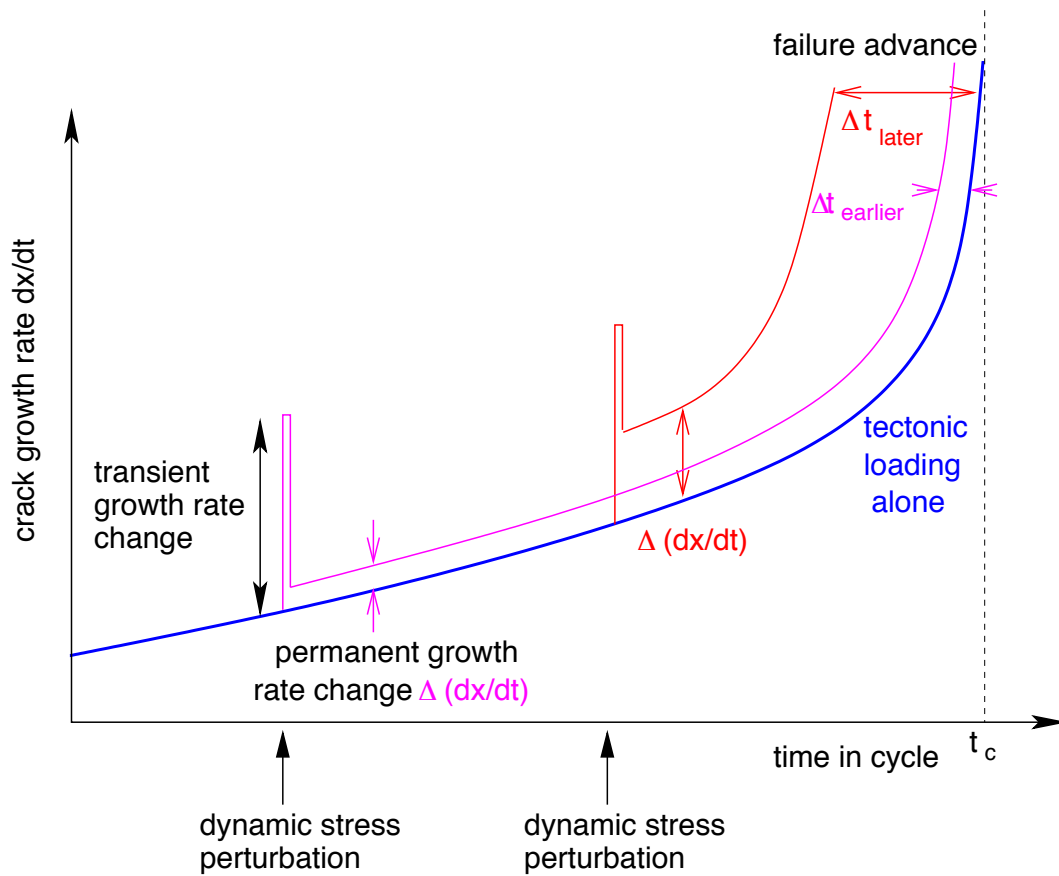


FIG. 3.3 – Time history of the growth rate of a crack subjected to dynamic perturbations at two different times. The crack length evolves according to the theory of sub-critical crack growth (equation 3.3). For the earlier perturbation the incremented growth rate  $\Delta(dx/dt)$  is smaller than for the later perturbation because  $dx(t_0)/dt$  is smaller. The dynamic stress step advances the failure time  $t_c$  by a time  $\Delta t$ . This clock-advance time  $\Delta t$  increases if the time when the stress step is applied increases (adapted from Figure 2 of [Gomberg, 2001]).

dynamic perturbation increases the seismicity rate only for a time equal to the duration of the transient, and then the seismicity rate becomes equal to or smaller than the background rate.

While there are some evidences that dynamic stress change may trigger aftershocks [Gomberg et al., 2001; Harris et al., 2002], the physical mechanisms are not yet understood. Possible mechanisms to explain dynamic triggering must induce a permanent decrease of the fault strength under a transient stress change, for example by cyclic fatigue.

### 3.7 Conclusion

Many physical mechanisms can reproduce Omori's law decay of aftershocks.

- These triggering mechanisms are either deterministic (almost all mechanisms) or stochastic (fatigue laws);

- These mechanisms either introduce explicitly a time delay between a static stress step and the failure (sub-critical crack-growth, pore fluid flow, damage laws, fatigue laws, viscous relaxation), or this delay arises from the multi-scale interactions between faults and the spatial heterogeneity of the loading rate [Huang et al., 1998].
- These mechanisms assume different initial conditions, either before or immediately after the mainshock. The effect of the mainshock is either to redistribute uniformly the stress between a minimum value and the rupture threshold [Scholz, 1968b ; Das and Scholz, 1981 ; Shaw, 1993], or to increment the stress by a static step [Nur and Booker, 1972 ; Dieterich, 1994]. In the last case, the initial conditions before the mainshock are fixed by assuming a constant seismicity rate before the mainshock [Dieterich, 1994] or a uniform stress [Nur and Booker, 1972].
- The Omori law decay of aftershock is either local, taking into account only the direct aftershocks triggered by the stress step induced by the mainshock [Scholz, 1968b ; Nur and Booker, 1972 ; Das and Scholz, 1981 ; Dieterich, 1994], or global, resulting from the multiple interactions between aftershocks [Lee and Sornette, 2000 ; Marcellini, 1995, 1997 ; Ziv and Rubin, 2002].

## Chapitre 4

# Possible mechanisms for the variability of the aftershock decay law

We have shown in section 3 that many mechanisms lead to Omori's law decay of aftershocks following a stress step induced by a mainshock.

Observations of aftershock decay suggest that the Omori exponent is not always equal to 1, but ranges between 0.3 and 2 [Davis and Frohlich, 1991a; Kisslinger and Jones, 1991; Guo and Ogata, 1995; Utsu et al., 1995]. What determines the variability of  $p$  value? Is  $p$  universal, as proposed by many physical models of aftershocks, or a function of the material properties of the crust, which are different from one location to another?

Most mechanisms discussed in section 3 give either  $p = 1$ , or an unrealistic small exponent  $p = 0.5$  [Nur and Booker, 1972]. A few models reproduce a variability of  $p$ -value. The  $p$  exponent is found to vary as a function of the corrosion index  $n$  when using the sub-critical growth law (3.3) to model aftershocks [Shaw, 1993]. However,  $p$  is very close to one in these models because the stress-corrosion index  $n$  is very large. Hainzl et al. [2002] propose that  $p$  value increases if the relaxation time  $T$  decreases. The  $p$ -value is also found to increase with the spatial coupling length of the viscous relaxation. However, their model fail to reproduce a power-law decay of the aftershock rate over more than one order of magnitude, and is therefore not able to account for observed aftershock sequences. Dieterich [1994] obtains an apparent exponent  $p \approx 0.8$  when including a decrease of the stress with the distance from the mainshock in his model of rate and state friction. A variability of  $p$ -value around 1 is observed by all models that impose a hierarchical fault structure [Yamashita and Knopoff, 1987; Blanter et al., 1997; Huang et al., 1998; Narteau et al., 2000]. In [Yamashita and Knopoff, 1987], the  $p$ -value is a function of the corrosion index  $n$  and of the exponent of the fault length distribution. The three other papers [Blanter et al., 1997; Huang et al., 1998; Narteau et al., 2000] do not explain the variability of  $p$

found in their numerical models. In the previous section, we have derived an analytical solution of the Arrhenius model of aftershocks coupled with an exponential distribution of stress. This analysis predicts an increase of  $p$  with the temperature  $T$ . In this model the deviation of  $p$  from 1 measures the ratio of the stress heterogeneity over the thermal agitation.

Are there others mechanisms that induce a variability of  $p$ -value ?

Lee [1999] claimed that his cellular automata model including stress-corrosion (3.11) was able to reproduce a realistic variability of  $p$  by two mechanisms :

- $p$ -value decreases below 1 for small values of the corrosion index  $n < 1$  ;
- $p$  can be smaller than 1 if only a fraction of the elements of the lattice is subjected to the stress-corrosion mechanism.

We have made numerical simulations using the same model as the one used by Lee [1999] and we have not been able to reproduce a variability of  $p$ -value with these mechanisms. In contrast, we found that either a small value of the corrosion index or a small fraction of elements subjected to stress corrosion leads to an increase in the crossover time  $c$  in (3.1) that can be interpreted as an apparent decrease of  $p$ -value at early times, due to the crossover between a constant seismicity rate at small times and the  $1/t$  power-law decrease of the seismicity rate at large times.

Marcellini [1995] claims that the  $p$ -value increases with the temperature in his Arrhenius model of aftershocks. This result is however incorrect. The correct analysis we derived in the previous section gives  $p = 1$  independently of the temperature.

We study below two mechanisms to explain the variability of  $p$ -value

- we show that a variability of  $p$ -value can be obtained in the model of Lee [1999] when introducing a disorder in the corrosion index  $n$  ;
- we obtain a variability of  $p$ -value with the temperature using a fatigue law (3.23). Using numerical simulations of a cellular automata model including the Arrhenius law (3.23) we obtain a decrease of  $p$  with the temperature  $T$ , in contrast with the increase of  $p$  with  $T$  obtained analytically when neglecting the interactions between aftershocks.

## 4.1 Stress-corrosion model

We consider the same model as in [Lee and Sornette, 2000]. This model is similar to the cellular automata of Christensen and Olami [1992] with an additional stress-corrosion process described by equation 3.12. As in [Lee and Sornette, 2000], the system is loaded by increasing uniformly the stress. When the system reaches the stationary state, we stop the external loading and study the relaxation of the system. An initial stress threshold  $B$  is assigned to each cell from a uniform distribution in the interval  $[1 - r, 1 + r]$ .

In this model, a element can fail by 3 mechanisms :

- when its stress  $\sigma$  reaches its threshold  $B$  due to the external loading  $\mu = \frac{d\sigma}{dt}$  ;
- when its stress  $\sigma$  reaches its threshold  $B$  because of the stress redistributed by a neighbor

during an avalanche ;

- by stress-corrosion when the strength decreases to the stress level.

When an element  $i, j$  fails, its stress  $\sigma_{i,j}$  is redistributed to the neighboring sites according to

$$\sigma'_{i,j} = (1 - \gamma) \sigma_{i,j} \quad (4.1)$$

$$\sigma'_{i,j\pm 1} = \sigma_{i,j\pm 1} + \frac{(1 - \beta)}{4} \gamma \sigma_{i,j} \quad (4.2)$$

$$\sigma'_{i\pm 1,j} = \sigma_{i\pm 1,j} + \frac{(1 - \beta)}{4} \gamma \sigma_{i,j} , \quad (4.3)$$

where  $\beta$  is the stress dissipation and  $\gamma$  is the relative stress drop. When an element fails, its threshold  $B$  is reassigned uniformly in the interval  $[1 - r, 1 + r]$ . Between two avalanches, the strengths  $B$  of all sites decay with time according to (3.12). When the external loading is stopped, the system relaxes to an equilibrium of zero stress due to the stress dissipation induced by the avalanches ("aftershocks").

Our preliminary results show that heterogeneities in strength, stress drop or stress dissipation still yield a universal  $p = 1$  exponent for Omori's law in agreement with the mean field analysis of Lee and Sornette [2000], while any disorder in the exponent  $n$  of the stress corrosion mechanism relating the damage rate  $dB/dt \propto \sigma^n$  to the local stress  $\sigma$  gives  $p < 1$  which becomes a continuous function of the heterogeneity of the corrosion index. If  $n$  is heterogeneous, the  $p$ -value also depends on the stress drop  $\gamma$  and on the dissipation  $\beta$ , while it is independent of  $\gamma$  and  $\beta$  if  $n$  is homogeneous.

Figure 4.1 compares different simulations with  $\beta = 0.1$ ,  $\gamma = 1$ ,  $r = 0.75$ , a lattice size  $L = 50$  and with  $n$  ranging between 0.1 and 10 without heterogeneity on  $n$ . In all cases, we obtain  $p = 1$  but the lower cut-off increases if  $n$  decreases. This may explain the decrease of  $p$  with  $n$  found by Lee [1999]. We have also tested that  $p$  is independent on the dissipation  $\beta$ , the stress drop  $\gamma$  and the heterogeneity of the strength field  $r$ .

If we introduce a disorder in the distribution of the stress corrosion index  $n$ ,  $p$  becomes a continuous function of the stress drop  $\gamma$ , of the heterogeneity of  $n$  and of the dissipation  $\beta$ . It is however independent of the heterogeneity  $r$  of the strength field. The heterogeneity of  $n$  also introduces a crossover in the decay of the average stress. Figure 4.2 shows the seismicity rate and the average stress for a numerical simulation with  $n$  uniformly distributed between 1 and 5.

The variability of  $p$  with the heterogeneity on  $n$  is shown on Figure 4.3a. The  $p$ -value also depends on the stress drop  $\gamma$  and in the dissipation  $\beta$  as shown in Figure 4.3b,c, while it is independent of  $\gamma$  and  $\beta$  if  $n$  is homogeneous.

We have also performed simulations with an external loading  $\mu = d\sigma/dt$ . In this case, following a transient Omori decay, the seismicity rate goes to a stationary regime characterized by a constant seismicity rate. The distribution of avalanches sizes is different from the power-law distribution of avalanches obtained without stress corrosion, as illustrated in Figure 4.4. By

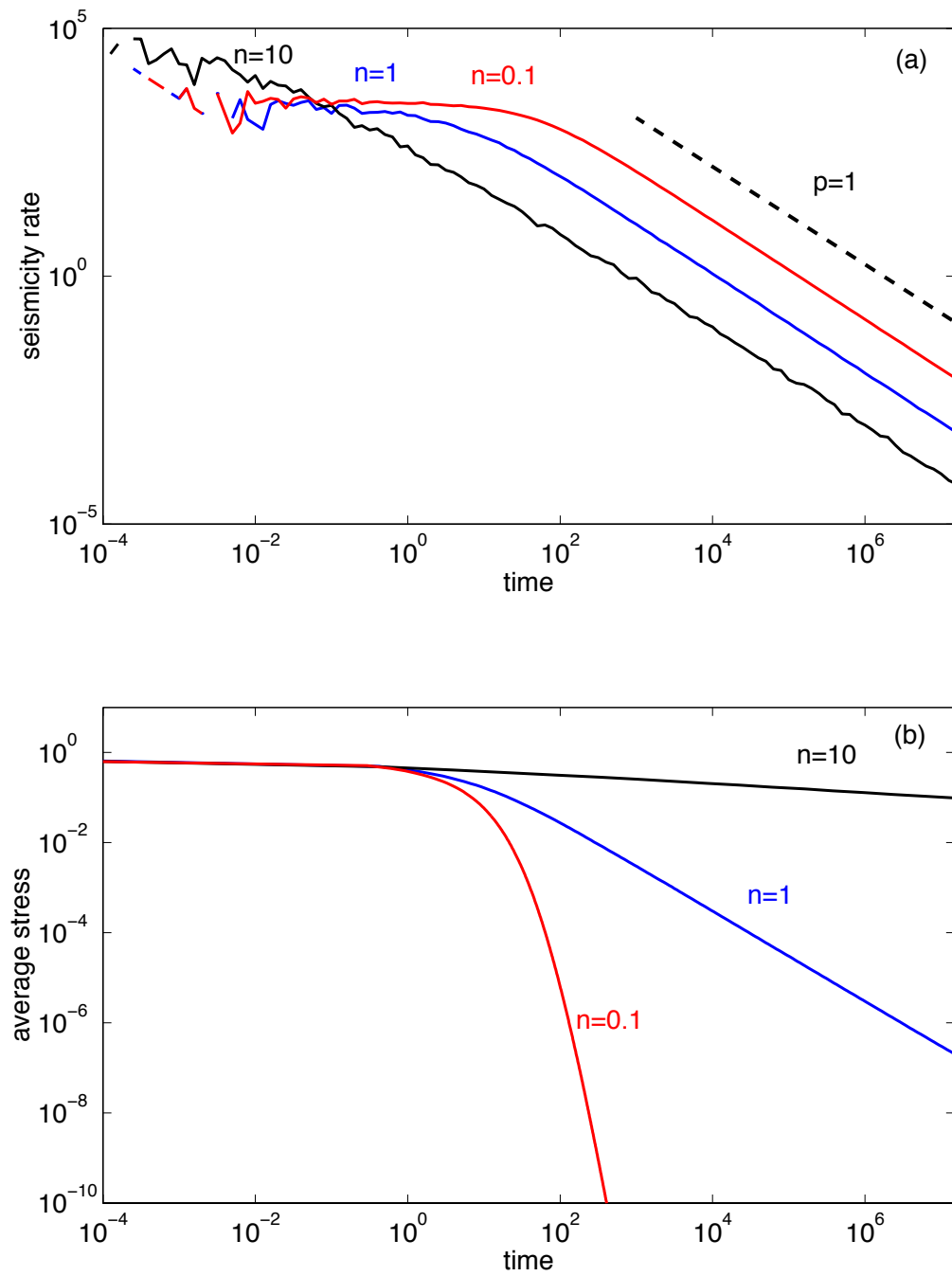


FIG. 4.1 – Rate of aftershocks for different simulations with  $\beta = 0.1$ ,  $\gamma = 1$ ,  $r = 0.75$ , a lattice size  $L = 50$  and with  $n$  ranging between 0.1 and 10 without heterogeneity on  $n$ . In all cases, we obtain  $p = 1$  but the lower cut-off increases if  $n$  decreases. The average stress (b) decays with time as  $t^{-1/n}$  in agreement with the mean-field analysis of Lee and Sornette [2000].

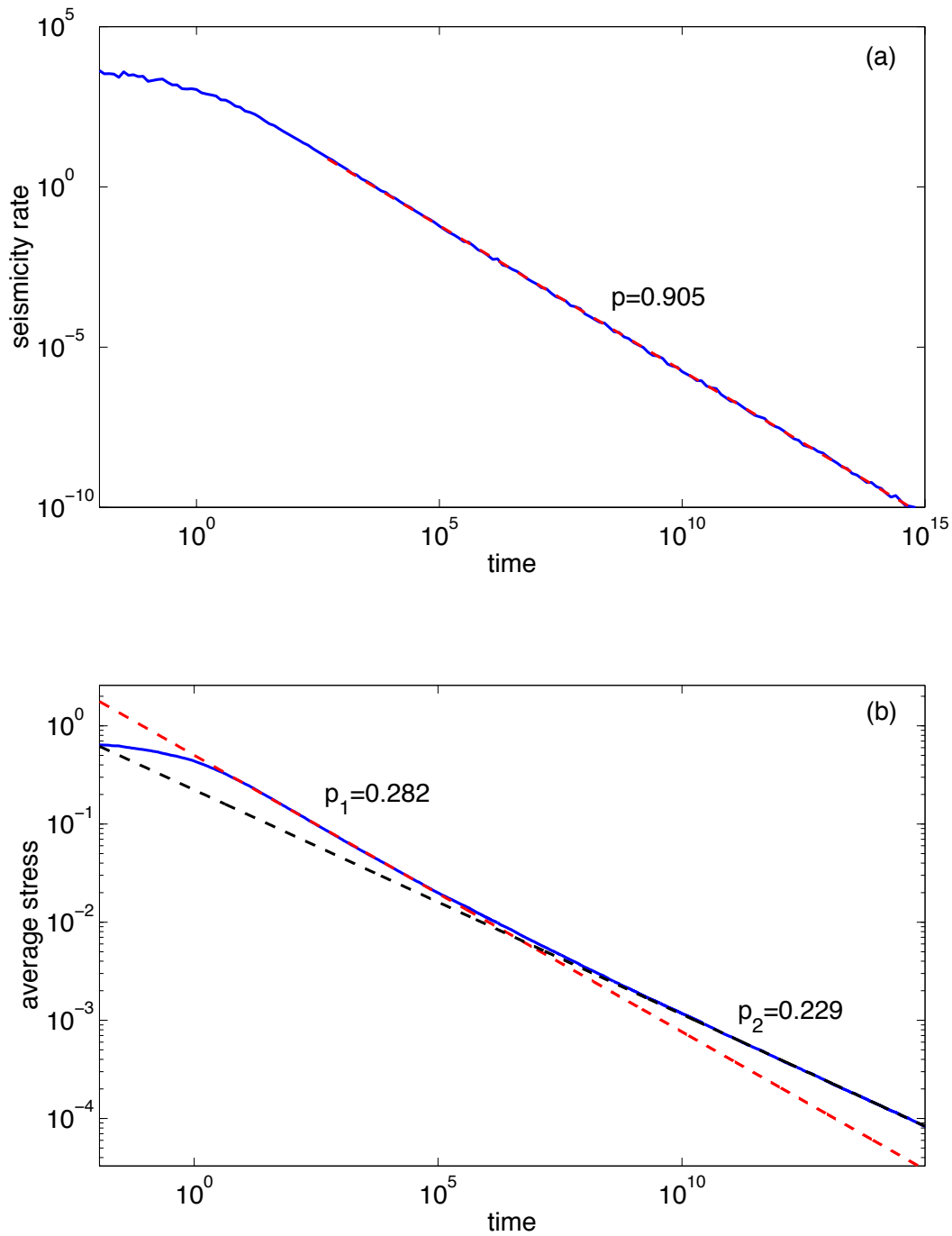


FIG. 4.2 – Rate of aftershocks (a) and average stress (b) for a simulation with  $\beta = 0.1$ ,  $\gamma = 1$ ,  $r = 0.75$ , a lattice size  $L = 50$  and with  $n$  uniformly distributed in the range  $[1, 5]$ . The seismicity rate decays as a power-law with an exponent  $p = 0.905$  without crossover. In contrast, the average stress presents a crossover at time  $t \approx 10^7$  between a power-law decay with exponent  $p_1 = 0.282$  for  $t < 10^5$  and a smaller exponent  $p_2 = 0.229$  for  $t > 10^{10}$ . The exponent of the stress decay is close to  $1/n_{max} = 0.2$ . The stress decay is mostly controlled by the sites which have the larger corrosion index  $n = n_{max} = 5$ .

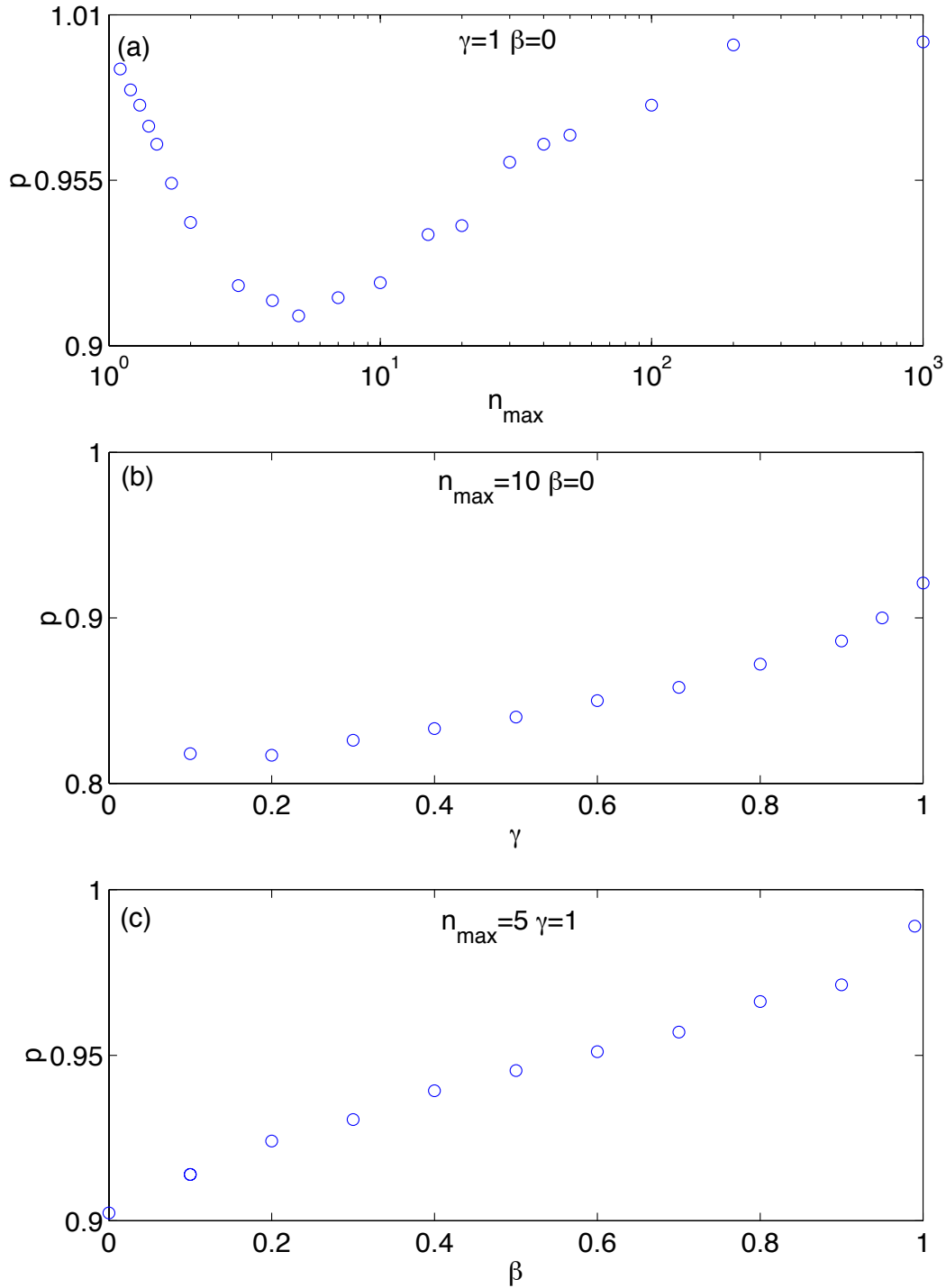


FIG. 4.3 – Variability of the Omori exponent for different simulations with  $r = 0.75$ , a lattice size  $L = 20$  and with  $n$  uniformly distributed in the range  $[1, n_{max}]$  (a) for different values of  $n_{max}$  with  $\gamma = 1$  and  $\beta = 0$ , (b) for different values of  $\gamma$  with  $n_{max} = 10$  and  $\beta = 0$ , (c) for different values of  $\beta$  with  $n_{max} = 5$  and  $\gamma = 1$ . We obtain a variability of  $p$  in the range  $[0.8, 1]$  depending on  $\gamma$ ,  $\beta$  and  $n_{max}$ .

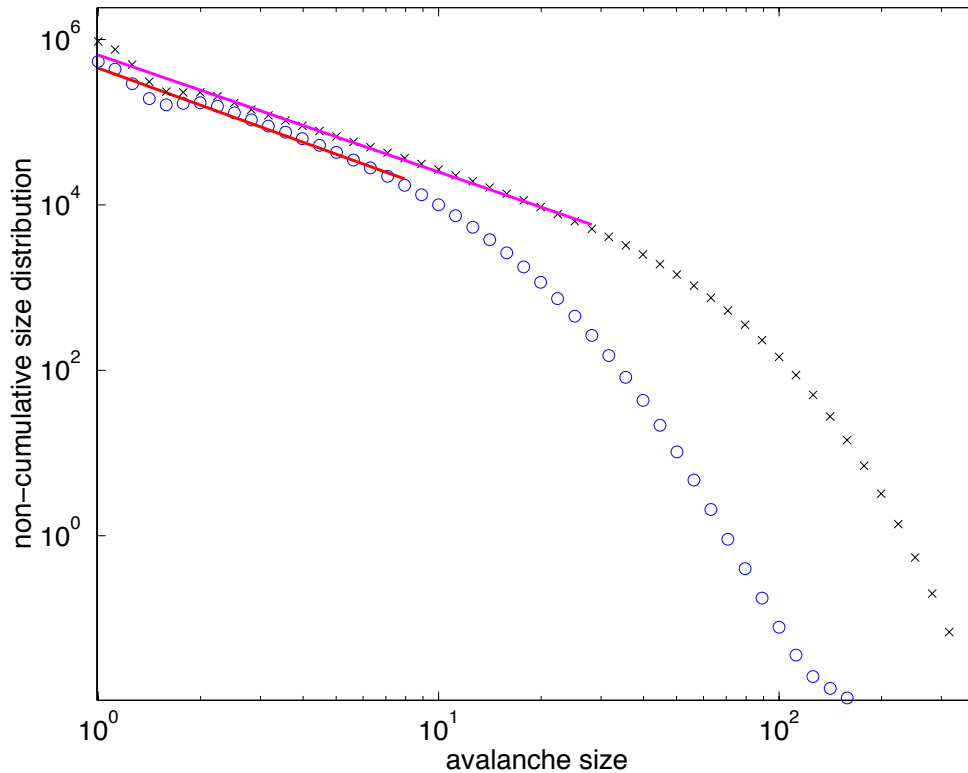


FIG. 4.4 – Avalanche size distribution in the stationary regime for numerical simulations with (circles) and without stress corrosion (crosses). The parameters for the 2 simulations are a matrix length  $L = 128$ , a stress drop  $\gamma = 1$ , a dissipation  $\beta = 0.1$ , an external loading  $\mu = 1$ , a strength heterogeneity  $r = 0.75$  and a corrosion index  $n = 10$ . For the two cases, the avalanche size follow a power-law distribution for small sizes with an exponent of the non-cumulative distribution close to 1.4, corresponding to a  $b$ -value of the magnitude distribution  $b = 0.4$ . This exponent increases with the dissipation  $\beta$ . The cut-off at large avalanches sizes is not a finite size effect but is controlled by the dissipation in absence of stress-corrosion. This cut-off is much smaller when a stress-corrosion process is added.

comparison with the size distribution without stress-corrosion, the proportion of large events is much smaller. The average stress obtained in the stress-corrosion model in the stationary state is also smaller than the average stress reached in the cellular automata without stress-corrosion. The stress-corrosion process destroys the self-organization of the system observed without stress-corrosion. Because there are no large avalanches in this model, there are no large fluctuations of the stress field which may trigger aftershocks.

## 4.2 Arrhenius model

Another possible model of the local Omori's law involves the activation of rupture over a local energy barrier by thermal or other sources of agitation (which we shall refer generically as the thermal agitation  $T$ ). This Arrhenius process has been involved by Scholz [1968b], Marcellini

[1995, 1997] and Moreno et al. [2001] to explain aftershock behavior. The model we study here is very similar to the cellular automata model used by Moreno et al. [2001] except that we use Arrhenius law (3.23) of failure rate instead of the power-law dependence between the stress and the failure rate (3.35) used by Moreno et al. [2001].

We consider the cellular automata of Christensen and Olami [1992] with the same rules of stress distribution (4.3) than described previously. We start with an initial uniform distribution of stress  $0 < \sigma_{i,j} < 1$  and we study the relaxation of the system without tectonic loading ( $\mu = 0$ ) due to aftershocks triggered by static fatigue. We take a constant strength  $B_{i,j} = 1$ . In this model, an element can fail either

- due to the stress redistribution during an avalanche if its stress  $\sigma_{i,j}$  reaches the failure threshold  $B_{i,j} = 1$ ;
- or by static fatigue.

The failure rate by static fatigue under a stress  $\sigma$  is given by

$$\lambda(\sigma) = K e^{\frac{1-\sigma}{T}}, \quad (4.4)$$

where  $T$  is the thermal agitation and  $K$  is a constant.

We obtain a power-law decay of the aftershocks rate with  $p$  decreasing if the temperature increases, between two crossover times  $t_{min} < t < t_{max}$ . The lower-cutoff  $t_{min}$  is close to 1 independently of the temperature, while the upper cut-off  $t_{max}$  decreases if  $T$  increases. Thus the duration of an aftershock sequence is longer if  $T$  is smaller. The Omori exponent  $p$  decreases from 1 to 0.2 as the temperature increases from 0.001 to 1 (Figure 4.6). The negative correlation between  $p$  and  $T$  obtained in the numerical simulations are in disagreement with the positive correlation predicted by the analytical results presented in section 3. This implies that the multiple interactions between aftershocks due to the stress changes induced by all aftershocks have a fundamental importance to control the rate of aftershock activity and cannot be neglected.

At large times  $t \gg t_{max}$ , the seismicity rate reaches a constant level without fluctuations. The average stress decreases exponentially for  $t \gg t_{max}$ , while it decays slower at early times  $t < t_{max}$  as seen in Figure 4.5e,f. In large times regime  $t \gg t_{max}$ , there are very few large avalanches (almost all avalanches involve a single site). Thus there are no aftershocks in this regime because there are no large fluctuations of the stress field.

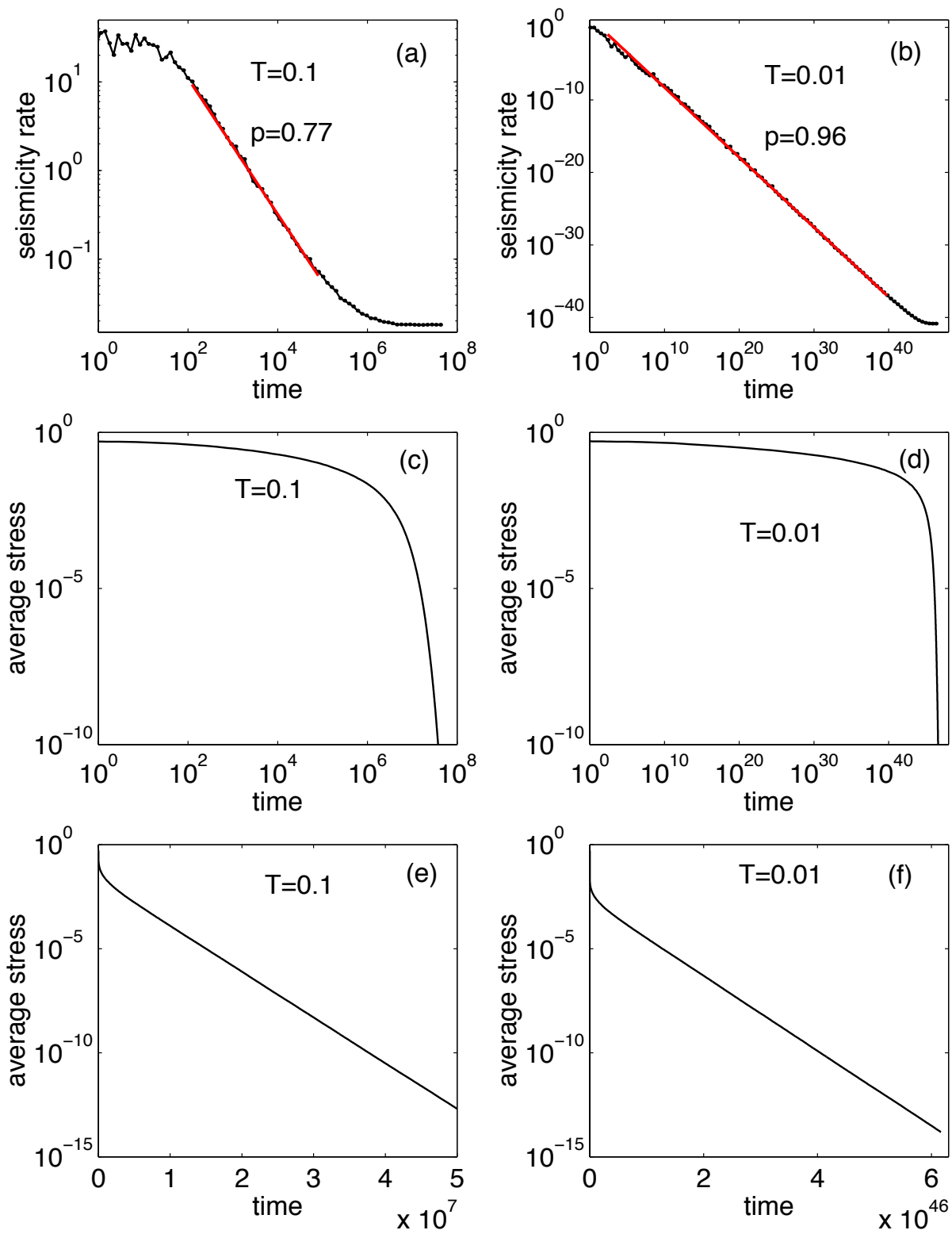


FIG. 4.5 – Rate of aftershocks and variation of the average stress with time for two simulations with  $\beta = 0$ ,  $\gamma = 1$ ,  $K = 1$ , a lattice size  $L = 20$  and for different values of the temperature (a,c,e)  $T = 0.1$  and (b,d,f)  $T = 0.01$ .

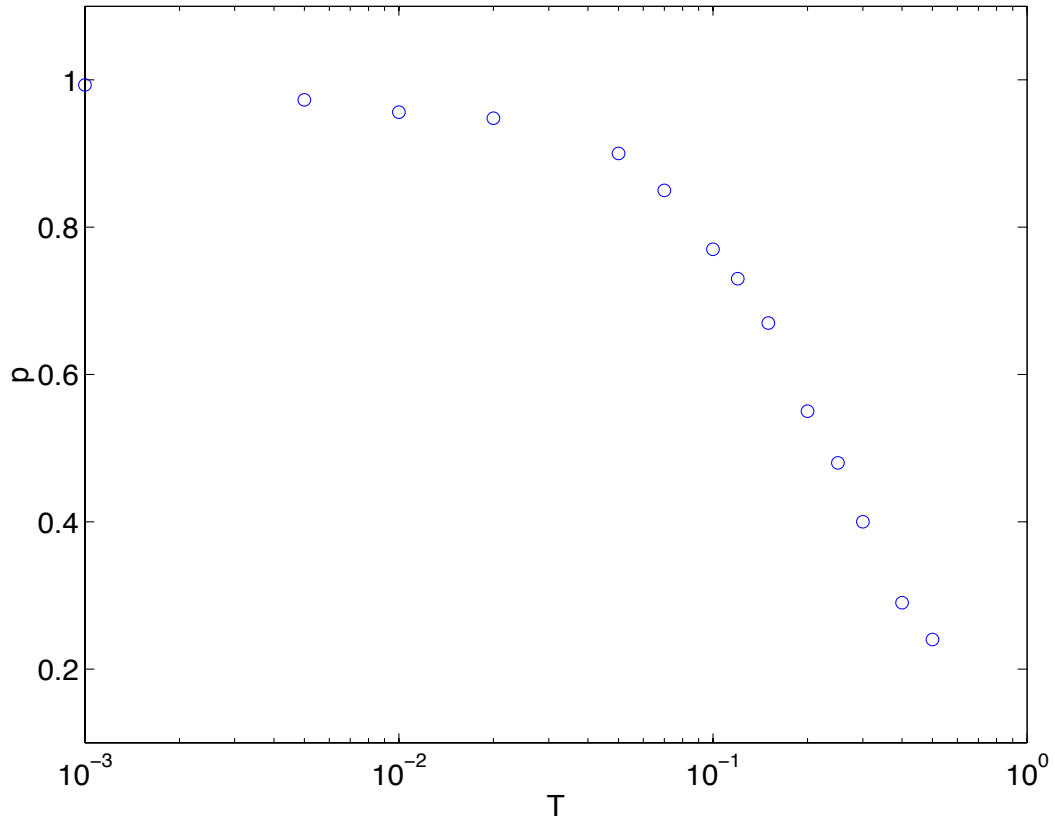


FIG. 4.6 – Variability of the Omori exponent  $p$  with the temperature  $T$  for different simulations with  $\beta = 0$ ,  $\gamma = 1$ ,  $K = 1$  and a lattice size  $L = 20$ .  $p$  decreases between 1 and 0.2 if the temperature increases between 0.001 and 0.5.

# Chapitre 5

## Sub-critical and super-critical regimes in epidemic models of earthquake triggering

Agnès Helmstetter

Laboratoire de Géophysique Interne et Tectonophysique,  
Université Joseph Fourier, BP 53X, 38041 Grenoble Cedex, France.

Didier Sornette

Laboratoire de Physique de la Matière Condensée, Université de Nice-Sophia Antipolis, and  
Department of Earth and Space Sciences and Institute of Geophysics and Planetary Physics,  
University of California, Los Angeles, California.

In press in *Journal of Geophysical Research*, 2002.

### Abstract

We present an analytical solution and numerical tests of the epidemic-type aftershock (ETAS) model for aftershocks, which describes foreshocks, aftershocks and mainshocks on the same footing. In this model, each earthquake of magnitude  $m$  triggers aftershocks with a rate proportional to  $10^{\alpha m}$ . The occurrence rate of direct aftershocks triggered by a single mainshock decreases with the time from the mainshock according to the “local” modified Omori law  $K/(t+c)^p$  with  $p = 1 + \theta$ . Contrary to the usual definition, the ETAS model does not impose an aftershock to have a magnitude smaller than the mainshock. Starting with a mainshock at time  $t = 0$  that triggers aftershocks according to the local Omori law, that in turn trigger their own aftershocks and so on, we study the seismicity rate of the global aftershock sequence composed of all the

secondary and subsequent aftershock sequences. The effective branching parameter  $n$ , defined as the mean aftershock number triggered per event, controls the transition between a sub-critical regime  $n < 1$  to a super-critical regime  $n > 1$ . A characteristic time  $t^*$ , function of all the ETAS parameters, marks the transition from the early time behavior to the large time behavior. In the sub-critical regime, we recover and document the crossover from an Omori exponent  $1 - \theta$  for  $t < t^*$  to  $1 + \theta$  for  $t > t^*$  found previously in [Sornette and Sornette, 1999a] for a special case of the ETAS model. In the super-critical regime  $n > 1$  and  $\theta > 0$ , we find a novel transition from an Omori decay law with exponent  $1 - \theta$  for  $t < t^*$  to an explosive exponential increase of the seismicity rate for  $t > t^*$ . The case  $\theta < 0$  yields an infinite  $n$ -value. In this case, we find another characteristic time  $\tau$  controlling the crossover from an Omori law with exponent  $1 - |\theta|$  for  $t < \tau$ , similar to the local law, to an exponential increase at large times. These results can rationalize many of the stylized facts reported for aftershock and foreshock sequences, such as (i) the suggestion [Liu, 1984; Bowman, 1997] that a small  $p$ -value may be a precursor of a large earthquake, (ii) the relative seismic quiescence sometimes observed before large aftershocks, (iii) the positive correlation between  $b$  and  $p$ -values, (iv) the observation that great earthquakes are sometimes preceded by a decrease of  $b$ -value and (v) the acceleration of the seismicity preceding great earthquakes.

## 5.1 Introduction

It is well known that the seismicity rate increases after a large earthquake, for time period up to one hundred years [Utsu *et al.*, 1995], and distances up to several hundred km [Tajima and Kanamori, 1985a; Steeples and Steeples, 1996; Kagan and Jackson, 1998; Meltzner and Wald, 1999; Dreger and Savage, 1999]. The rate of the triggered events usually decays in time as the modified Omori law  $n(t) = K/(t + c)^p$ , where the exponent  $p$  is found to vary between 0.3 and 2 [Davis and Frohlich, 1991; Kisslinger and Jones, 1991; Guo and Ogata, 1995; Utsu *et al.*, 1995] and is often close to 1 (see however [Kisslinger, 1993; Gross and Kisslinger, 1994] for alternative decay laws such as the stretched exponential).

These triggered events are called aftershocks if their magnitude is smaller than the first event. However, the definition of an aftershock contains unavoidably a degree of arbitrariness because the qualification of an earthquake as an aftershock requires the specification of time and space windows. In this spirit, several alternative algorithms for the definition of aftershocks have been proposed [Gardner and Knopoff, 1974; Reasenber, 1985; Molchan and Dmitrieva, 1992] and there is no consensus.

Aftershocks may result from several and not necessarily exclusive mechanisms (see [Harris, 2001] and references therein) : pore-pressure changes due to pore-fluid flows coupled with stress variations, slow redistribution of stress by aseismic creep, rate-and-state dependent friction within faults, coupling between the viscoelastic lower crust and the brittle upper crust,

stress-assisted micro-crack corrosion [Yamashita and Knopoff, 1987; Lee and Sornette, 2000], slow tectonic driving of a hierarchical geometry with avalanche relaxation dynamics [Huang *et al.*, 1998], dynamical hierarchical models with heterogeneity, feedbacks and healing [Blanter *et al.*, 1997], etc.

Since the underlying physical processes are not fully understood, the qualifying time and space windows are more based on common sense than on hard science. Particularly, there is no agreement about the duration of the aftershock sequence and the maximum distance between aftershock and mainshock. If one event occurs with a magnitude larger than the first event, it becomes the new mainshock and all preceding events are retrospectively called foreshocks. Thus, there is no way to identify foreshocks from usual aftershocks in real time. There is also no way to distinguish aftershocks from individual earthquakes [Hough and Jones, 1997]. The aftershock magnitude distribution follows the Gutenberg-Richter distribution with similar  $b$ -value as other earthquakes [Ranalli, 1969; Knopoff *et al.*, 1982]. They have also similar rupture process. Moreover, an event can be both an aftershock of a preceding large event, and a mainshock of a following earthquake. For example, the  $M=6.5$  Big Bear event is usually considered as an aftershock of the  $M=7.3$  Landers event, and has clearly triggered its own aftershock sequence. One can trace the difficulty of the problem from the long-range nature of the interactions between faults in space and time resulting in a complex self-organized crust.

In view of the difficulties in classifying sometimes an earthquake as a foreshock, a mainshock or an aftershock, it is natural to investigate models in which this distinction is removed and to study their possible observable consequences. In this spirit, the epidemic type aftershock (ETAS) model introduced by Kagan and Knopoff [1981, 1987] and Ogata [1988] provides a tool for understanding the temporal clustering of the seismic activity without distinguishing between aftershocks, foreshocks and mainshock events. The ETAS model is a generalization of the modified Omori law, which takes into account the secondary aftershock sequences triggered by all events. In this model, all earthquakes are simultaneously mainshocks, aftershocks and possibly foreshocks. An observed “aftershock” sequence is in the ETAS model the result of the activity of all events triggering events triggering themselves other events, and so on, taken together. The ETAS model aims at modeling complex aftershock sequences and global seismic activity. The seismicity rate is given by the superposition of aftershock sequences of all events. Each earthquake of magnitude  $m$  triggers aftershock with a rate proportional to  $10^{\alpha m}$  with the same coefficient  $\alpha$  for all earthquakes. The occurrence rate of aftershocks decreases with the time from the mainshock according to the modified Omori law  $K/(t+c)^p$ . The background seismicity rate is modeled by a stationary Poisson process with a constant occurrence rate  $\mu$ . Contrary to the usual definition, the ETAS model does not impose an aftershock to have a magnitude smaller than the mainshock. This way, the same law describes both foreshocks, aftershocks and mainshocks. This model has been used to give short-term probabilistic forecast of seismic activity [Kagan and Knopoff, 1987; Kagan and Jackson, 2000; Console and Murru, 2001], and

to describe the temporal and spatial clustering of seismic activity [Ogata, 1988, 1989, 1992, 1999, 2001; Kagan, 1991; Felzer et al, 2001]. Although the elementary results on the stability of the process have been known for many years [Kagan, 1991], no attempt has been made to study this model analytically in order to characterize its different regimes and obtain a deeper understanding of the combined interplay between the model parameters ( $b$ ,  $\alpha$ ,  $p$ ,  $K$ ,  $c$  and  $\mu$ ) on the seismic activity. We stress below the contrast between previous works in the mathematical statistical literature and our results.

It should be noted that the ETAS model suffers from an important defect : it is fundamentally a “branching” model [Harris, 1963; Vere-Jones, 1977], with no “loops”. What this means is that an event has a unique “mother-mainshock” and not several. In the real case, we can expect that some events may be triggered by the combined loading and action at distance in time and space of several previous earthquakes. Hence, events should have several “mothers” in general. This neglecting of “loops” is known in statistical physics as a “mean-field” approximation and allows us to simplify the analysis while still keeping the essential physics in a qualitative way, even if the details may not be precisely recovered quantitatively.

Sornette and Sornette [1999a] studied analytically a particular case of the ETAS model, in which the aftershock number does not depend on the mainshock magnitude, *i.e.*, for  $\alpha = 0$ . Starting with one event at time  $t = 0$  and considering that each earthquake generates an aftershock sequence with a “local” Omori exponent  $p = 1 + \theta$ , where  $\theta$  is a positive constant, they studied the decay law of the “global” aftershock sequence, composed of all secondary aftershock sequences. They found that the global aftershock rate decays according to an Omori law with an exponent  $p = 1 - \theta$ , smaller than the local one, up to a characteristic time  $t^*$ , and then recovers the local Omori exponent  $p = 1 + \theta$  for time larger than  $t^*$ .

Here, we generalize their analysis in the more general case  $\alpha > 0$  of the ETAS model, which includes a realistic magnitude distribution. We study the decay law of the global aftershock sequence as a function of the model parameters (local Omori law parameters and magnitude distribution). In addition to giving more complete analytical results, we present numerical simulations that test these predictions. We also generalize the investigation and analysis into the “super-critical” regime. Indeed, depending on the branching ratio  $n$ , defined as the mean aftershock number triggered per event, and on the sign of  $\theta$ , three different regimes for the seismic rate  $N(t)$  are found :

1. For  $n < 1$  (sub-critical regime), we recover the results of [Sornette and Sornette, 1999a], *i.e.* we find a crossover from an Omori exponent  $p = 1 - \theta$  for  $t < t^*$  to  $p = 1 + \theta$  for  $t > t^*$ .
2. For  $n > 1$  and  $\theta > 0$  (super-critical regime), we find a transition from an Omori decay law with exponent  $p = 1 - \theta$  to an explosive exponential increase of the seismicity rate.
3. In the case  $\theta < 0$ , we find a transition from an Omori law with exponent  $1 - |\theta|$  similar to the local law, to an exponential increase at large times, with a crossover time  $\tau$  different from the characteristic time  $t^*$  found in the case  $\theta > 0$ .

As we show below, these results can rationalize many properties of aftershock and foreshock sequences.

## 5.2 The model

We assume that a given event (the “mother”) of magnitude  $m_i \geq m_0$  occurring at time  $t_i$  gives birth to other events (“daughters”) in the time interval between  $t$  and  $t + dt$  at the rate

$$\phi_{m_i}(t - t_i) = \frac{K}{(t - t_i + c)^{1+\theta}} 10^{\alpha(m_i - m_0)} H(t - t_i) H(m_i - m_0), \quad (5.1)$$

where  $H$  is the Heaviside function :  $H(t - t_i) = 0$  for  $t < t_i$  and 1 otherwise,  $m_0$  is a lower bound magnitude below which no daughter is triggered.

This temporal power law decay follows the same mathematical law as Omori’s law for the rate of aftershocks following a mainshock, albeit with the modification that we do not specify that aftershocks (daughter earthquakes) have to be smaller than the triggering event (mother earthquake). The exponential term  $10^{\alpha(m - m_0)}$  describes the fact that the larger the magnitude  $m$  of the mother event, the larger is the number of daughters. The exponent  $p = 1 + \theta$  of the “local” Omori’s law, describing direct triggering of first generation daughters by a given mother, has no reason a priori to be the same as the one measured macroscopically which is usually found between 0.8 and 1.2 with an often quoted median value 1. This is in fact the question we address : assuming the form (5.1) for the “local” Omori’s law, is the global Omori’s law still a power law and, if yes, how does its exponent depend on  $p$ ? What are the possible regimes of aftershocks as a function of the parameters of the model?

This model can be extended to describe the spatio-temporal distribution of seismic activity. Following *Kagan and Knopoff* [1981], we can introduce a spatial dependence in (5.1) of the form

$$\phi_{m_i}(t - t_i, \vec{r} - \vec{r}_i) = \frac{K}{(t - t_i + c)^{1+\theta}} 10^{\alpha(m_i - m_0)} \rho(\vec{r} - \vec{r}_i) H(t - t_i) H(m_i - m_0), \quad (5.2)$$

where  $\rho(\vec{r} - \vec{r}_i)$  describes the probability distribution for an earthquake occurring at position  $\vec{r}_i$  to trigger an event at position  $\vec{r}$ . This term takes into account the spatial dependence of the stress induced by an earthquake, and enable us to model the spatial distribution of aftershocks clustered close to the mainshock. In this paper, we restrict our analysis to the temporal ETAS model without spatial dependence because we are mainly interested in describing the temporal evolution of seismic activity. The complete model with both spatial and temporal dependence (5.2) has been studied in [*Helmstetter and Sornette*, 2002] to derive the joint probability distribution of the times and locations of aftershocks including the whole cascade of secondary aftershocks. When integrating the rate of aftershocks calculated for the spatio-temporal ETAS model over the whole space, we recover the results given in this paper for the temporal ETAS model. Therefore, the results given here for the temporal ETAS model can be compared with real aftershock sequences when using all aftershocks whatever their distance from the mainshock.

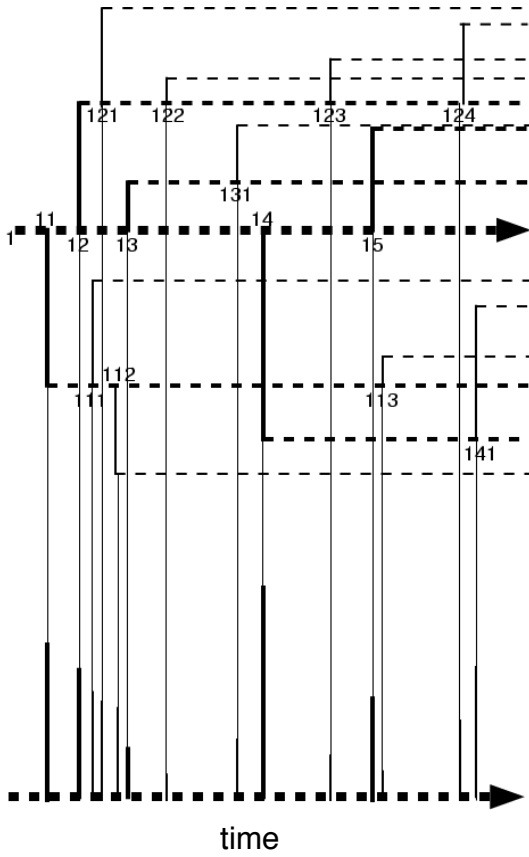


FIG. 5.1 – Schematic representation of the branching process associated with the ETAS model defined by (10.1) and (8.12). In this example, the thickest dashed line is the time arrow associated with the main shock indicated as ‘1’. This main shock triggered five direct aftershocks (of first generation) denoted ‘11’, ‘12’, ‘13’, ‘14’ and ‘15’ whose magnitudes are proportional to the length of their vertical lines (their position above or below the thickest dashed line is arbitrary and chosen to ensure a better visibility of the diagram). The aftershock ‘11’ triggered three (secondary) aftershocks denoted ‘111’, ‘112’ and ‘113’. The aftershock ‘12’ triggered four aftershocks denoted ‘121’, ‘122’, ‘123’ and ‘124’. The aftershock ‘13’ triggered a single aftershock denoted ‘131’. The aftershock ‘14’ also triggered a single aftershock denoted ‘141’. The aftershock ‘15’ did not trigger any aftershock. The observable catalog is the superposition of all these events which are projected on the thick dashed line at the bottom of the figure, keeping the thickness as a code for the generation number of each event.

The model (5.1) is a branching process because each daughter has only one mother and not several, as shown in Figure 5.1. As we said in the introduction, this “mean-field” assumption simplifies considerably the complexity of the process and allows for an analytical solution that we shall derive in the sequel. The key parameter is the average number  $n$  of daughter-earthquakes created per mother-event. Assuming that the distribution  $P(m)$  of earthquake sizes expressed in magnitudes  $m$  follows the Gutenberg-Richter distribution  $P(m) = b \ln(10) 10^{-b(m-m_0)}$ , the integral of  $\phi_m(t)$  over time and over all magnitudes  $m \geq m_0$  gives

$$n \equiv \int_0^{+\infty} dt \int_{m_0}^{+\infty} dm P(m) \phi_m(t) = n_0 \int_0^{\infty} \frac{dt}{(t+1)^{1+\theta}}, \quad (5.3)$$

where

$$n_0 \equiv \frac{K}{c^\theta} \frac{b}{b-\alpha}, \quad (5.4)$$

which is finite for  $b > \alpha$ . Three cases are analyzed below :  $n < 1$ ,  $n = 1$  and  $n > 1$ . The case  $n = 1$  corresponds to an average conservation of the number of events and can be associated with a brittle elastic crust without dissipation. The “dissipative” case  $n < 1$  can be interpreted as corresponding to a crust possessing a visco-elastic component and/or a partial coupling with a lower ductile layer, such that a part of the energy is released aseismically. The case  $n > 1$  corresponds to a process in which an earthquake sequence triggers an in-flow of energy from surrounding regions that may lead to a local self-exciting amplification. It can also correspond

to a coupling with other non-mechanical modes of energy storage, such as proposed in [Sornette, 2000b; Viljoen *et al.*, 2002] which can be triggered by an event and feed the ensuing earthquake sequence for a while. Of course, the super-critical process can only be transient and has to cross-over to another regime.

The case  $b < \alpha$  requires a special attention. In absence of truncation or cut-off, it leads to a finite-time singularity due to the interplay between long-memory and extreme fluctuations [Sornette and Helmstetter, 2002]. However, it is more common to introduce a truncation or roll-off of the Gutenberg-Richter law at an upper magnitude. We can for example use a Gamma distribution of energies, which is a power-law distribution tapered by an exponential tail. In this case, the branching ratio has been calculated by Kagan [1991] and is given by the approximate analytical expression valid for a corner magnitude  $m_c$  significantly larger than  $m_0$ ,

$$n_0 = \frac{K}{c^\theta} \frac{b}{b - \alpha} \frac{10^{b(m_c - m_0)} - 10^{\alpha(m_c - m_0)}}{10^{b(m_c - m_0)} - 1}. \quad (5.5)$$

For a corner magnitude  $m_c \gg m_0$ , and for  $\alpha < b$ , we recover the expression (5.4) for  $n_0$  obtained for the Gutenberg-Richter distribution without roll-off.

Note that  $n$  is defined as the average over all mainshock magnitudes of the mean number of events triggered by a mainshock. It is thus grossly misleading to think of the branching ratio as giving the number of daughters to a given earthquake, because this number is extremely sensitive to the specific value of its magnitude. Indeed, the number of aftershocks to a given mainshock increases exponentially with the mainshock magnitude as given by (5.1), so that large earthquakes will have many more aftershocks than small earthquakes. From (5.1) and (5.3), we can calculate the mean number of aftershocks  $N(M)$  triggered directly by a mainshock of magnitude  $M$

$$N(M) = n \frac{(b - \alpha)}{b} 10^{\alpha(M - m_0)}. \quad (5.6)$$

As an example, take  $\alpha = 0.8$ ,  $b = 1$ ,  $m_0 = 0$  and  $n = 1$ . Then, a mainshock of magnitude  $M = 7$  will have on average 80000 direct aftershocks, compared to only 2000 direct aftershocks for an earthquake of magnitude  $M = 5$  and less than 0.2 aftershocks for an earthquake of magnitude  $M = 0$ .

When  $\theta > 0$ ,  $\int_0^\infty \frac{dt}{(t+1)^{1+\theta}} = 1/\theta$  and the branching ratio  $n = n_0/\theta$  is finite. In this regime,  $n$  is an increasing function of the rate  $K$  and a decreasing function of  $\theta$ ,  $c$  and  $b - \alpha$ .

Even for  $b > \alpha$  and  $\theta > 0$ , the average number of daughters per mother can be larger than one :  $n > 1$ . This regime corresponds to the super-critical regime of branching processes [Harris, 1963; Sornette, 2000a] in which the total number of events grows on average exponentially with time. If  $n < 1$ , there is less than one earthquake triggered per earthquake on average. This is the sub-critical regime in which the number of events following the first main shock decays eventually to zero. The critical case  $n = 1$  is at the borderline between the two regimes. In this case, there is exactly one earthquake on average triggered per earthquake and the process is exactly at the critical point between death on the long run and exponential proliferation.

There is another scenario, occurring for  $\theta \leq 0$ , in which the seismicity blows up exponentially with time. In this case, the integral  $\int_0^\infty \frac{dt}{(t+1)^{1+\theta}}$  becomes unbounded. In principle,  $n$  becomes infinite : this does not invalidate the ETAS model per se. It only reflects the fact that the calculation of an average number of daughters per mother has become meaningless because of the anomalously slow decay of the kernel  $\phi(t)$ . This mechanism is reminiscent of that leading to anomalous diffusion and to aging in quenched random systems and spinglasses (see [Sornette, 2000a] for an introduction). As in these systems, any estimation of the averages depend on the time scale of study : due to the extremely slow decay of  $\phi(t)$ , the number of daughters created beyond any time  $t$  far exceeds the number of daughters created up to time  $t$ . Notwithstanding the decay, its cumulative effect creates this dominance of the far future. This regime is the opposite of the situation where  $\theta > 0$  where most of the daughters are created at relatively early times. Since the number of daughters born up to time  $t$  is an unbounded increasing function of  $t$ , it is intuitively appealing, as we show in the appendix, that this regime should be similar to the super-critical regime  $n > 1$  discussed above in the case  $\theta > 0$ .

Until now, we have discussed three issues related to the convergence of the ETAS sequences : (i) the condition  $\theta > 0$  ensures convergence at large times ; (ii) the convergence at short times is obtained by the introduction of the regularization constant  $c$  in the generalized Omori's law ; (iii) the condition  $\alpha < b$  is a necessary condition for the finiteness of the number of daughters. Finally, we should stress the role of the “ultra-violet” cut-off  $m_0$  on the magnitudes. In the ETAS model, only earthquakes of magnitude  $m \geq m_0$  are allowed to give birth to aftershocks, while events of smaller magnitudes are lost for the epidemic dynamics. If such a cut-off is not introduced and no cut-off is put on the Gutenberg-Richter toward small magnitudes, the dynamics becomes completely dominated by the swarms of very tiny earthquakes, which individually has very low probability to generate aftershocks but become so numerous that their collective effect becomes overwhelming in the dynamics. We would thus have the unphysical situation in which a magnitude 7 or 8 earthquake may be triggered by tiny earthquakes of magnitudes  $-2$  or less. We stress that the introduction of such a cut-off  $m_0$  is a simple way to prevent such a situation to occur, but it does not mean that small earthquakes of magnitude below  $m_0$  do not have their own aftershocks. It only means that such small earthquakes create aftershocks that can not participate in the epidemic process leading to significantly larger earthquakes ; these small earthquakes live their separate life. This is why they are not registered by the ETAS model. This formulation is of course only an end-member of many possible regularization procedures, which are well-known to be an ubiquitous requisite in mechanical models of rupture. An improvement of the ETAS model would be for instance to replace this abrupt cut-off  $m_0$  by introducing a roll-off in the Gutenberg-Richter law for the aftershocks with a characteristic corner magnitude decreasing with the magnitude of the mother earthquake. This and other schemes will not be explored here, as we want to analyze the simplest version possible.

We now describe briefly the connection with previous works in the mathematical statistics

literature. As we said above, the model (5.1) belongs to the general class of branching models [Moyal, 1962; Harris, 1963]. The elementary results on the stability of the process, such as the condition  $n < 1$ , have been known for many years, and go back to the origin of the ETAS model as a special case (for discrete magnitudes) or extension (for continuous magnitudes) of the class of “mutually exciting point processes” introduced in [Hawkes, 1971; 1972; Hawkes and Adamopoulos, 1973]. A convenient mathematical overview is in Chapter 5 of Daley and Vere-Jones [1988], especially Example 5.5(a) and associated exercises 5.5.2-5.5.6. For the ETAS model, the equations governing the probability generating functional, the probability of extinction within a given number of generations, the expectation measure for the total population, the second factorial moment (related to the covariance of the population) and their Fourier transform can be derived as special cases of results summarized there. In particular, the process initiated with a single event at the origin corresponds to the total progeny process for a general branching process model with time-magnitude state space and a single ancestor at time  $t = 0$ ; Exercise 5.5.6 gives the equations of the above cited variables for the case of fixed magnitudes (i.e.,  $\alpha = 0$ ). This direct probabilistic analysis in terms of generating functions effectively replaces the Wiener-Hopf theory in the present paper and mentioned also in [Hawkes, 1971; 1972; Hawkes and Oakes, 1974]. However, there is not explicit solutions given to these equations and there is no discussion of the change of regime from an effective Omori’s law  $1/t^{1-\theta}$  at early times to  $1/t^{1+\theta}$  at long times, nor mention of the interesting super-critical case, as done in the present work.

Hawkes [1971; 1972] and Hawkes and Adamopoulos [1973] use what is in effect an ETAS model with an exponential “bare” Omori’s law rather than the power law  $1/(t+c)^{1+\theta}$  defined in (5.1). Hawkes and Adamopoulos [1973] use it in an early study of earthquake data. The introduction of magnitudes is similar to the introduction of a marked process associated with a single point process [Hawkes, 1972]; however, the impact of magnitudes on the seismicity rate is assumed to be linear in [Hawkes, 1972] while it is multiplicative in the ETAS model. Our derivation presented in the appendix of the solution of the ETAS model for the mean rate of earthquakes in terms of its Laplace transform recovers previous results. For instance, equation (17) in [Hawkes and Oakes, 1974] is the same as our equation (5.29) in our Appendix (up to a factor  $\beta$  stemming from taking the cumulative number in [Hawkes and Oakes, 1974]). The key factor  $Q(\beta)$  in (5.30) corresponds to the quantity  $G_1(0)$  in equation (5) of [Hawkes, 1972]. The link between Hawkes’ “mutually exciting point processes” and branching processes was made explicit in [Hawkes and Oakes, 1974].

Some average properties of the ETAS model have been derived in the Master thesis of Ramselaar [1990]. Specifically, using the theory of Markov processes applied to branching processes, Ramselaar [1990] proves that, in the supercritical regime  $n > 1$  (where  $n$  is the average branching ratio defined in (5.5)), the average number of aftershocks stemming from a common ancestor grows exponentially as  $\sim e^{t/t^*}$  where  $t^*$  is the solution of  $nR(c/t^*) = 1$  and the function  $R$  is

defined in (5.32). The solution of this equation  $nR(c/t^*) = 1$  for  $t^*$  is the same as our  $t^*$  given by (5.12) and the exponential growth of *Ramselaar* is therefore the same as our result (5.17). We add on this asymptotic result, which is valid only at large times, by exhibiting the solution for the aftershock decay at early times. In addition, contrary to the incorrect claim of *Ramselaar* [1990] that “the Ogata earthquake process is critical or supercritical but is never subcritical,” we demonstrate that the subcritical regime exhibits a rich phenomenology.

### 5.3 Analytical solution

We analyze the case where there is an origin of time  $t = 0$  at which we start recording the rate of earthquakes, assuming that the largest earthquake of all has just occurred at  $t = 0$  and somehow reset the clock. In the following calculation, we will forget about the effect of events preceding the one at  $t = 0$  and count aftershocks that are created only by this main shock.

Let us call  $N_m(t)$  the rate of seismicity at time  $t$  and at magnitude  $m$ , that is,  $N_m(t)dt dm$  is the number of events in the time/magnitude interval  $dt \times dm$ . We define its expectation  $\lambda_m(t)dt dm \equiv E[N_m(t)dt dm]$ , as the mean number of earthquakes occurring between  $t$  and  $t + dt$  of magnitude between  $m$  and  $m + dm$ .  $\lambda_m(t)$  is the solution of a self-consistency equation that formalizes mathematically the following process : an earthquake may trigger aftershocks; these aftershocks may trigger their own aftershocks, and so on. The rate of seismicity at a given time  $t$  is the result of this cascade process. The self-consistency equation that sums up this cascade reads

$$\lambda_m(t) \equiv E[N_m(t)] = E \left[ \int_{m_0}^{\infty} dm' \int_{-\infty}^t d\tau \phi_{m'}(t - \tau) P(m) N_{m'}(\tau) \right] \quad (5.7)$$

$$= \int_{m_0}^{\infty} dm' \int_{-\infty}^t d\tau \phi_{m'}(t - \tau) P(m) E[N_{m'}(\tau)] \quad (5.8)$$

$$= \int_{m_0}^{\infty} dm' \int_{-\infty}^t d\tau \phi_{m'}(t - \tau) P(m) \lambda_{m'}(\tau). \quad (5.9)$$

If there is an external source  $S(t, m)$ , it should be added to the right-hand-side of (5.9).

The mean instantaneous rate  $\lambda_m(t)$  at time  $t$  is the sum over all induced rates from all earthquakes of all possible magnitudes that occurred at all previous times. The rate of events at time  $t$  induced per earthquake that occurred at an earlier time  $\tau$  with magnitude  $m'$  is equal to  $\phi_{m'}(t - \tau)$ . The term  $P(m)$  is the probability that an event triggered by an earthquake of magnitude  $m'$  is of magnitude  $m$ . We assume that this probability is independent of the magnitude of the mother-earthquake and is nothing but the Gutenberg-Richter law. This hypothesis can be easily relaxed if needed and  $P(m)$  can be generalized into  $P(m|m')$  giving the probability that a daughter-earthquake is of magnitude  $m$  conditioned on the value  $m'$  of the magnitude of the mother-earthquake. However, we do not pursue here this possibility as this hypothesis seems well-founded empirically [Ranalli, 1969; Knopoff et al., 1982]. The term  $S(t, m)$  is an external source which is determined by the physical process. We consider the case where a great earth-

quake occurs at the origin of time  $t = 0$  with magnitude  $M$ . In this case, the external source term is

$$S(t, m) = \delta(t) \delta(m - M) , \quad (5.10)$$

where  $\delta$  is the Dirac distribution. Other arbitrary source functions can be chosen.

By construction of the kernel (10.1), it is natural to search the solution for  $\lambda_m(t)$  as

$$\lambda_m(t) = P(m)\lambda(t) , \quad (5.11)$$

which makes explicit in the solution the hypothesis of a separation of the variables magnitude and time. *Helmstetter et al.* [2002] have shown that (5.11) is a correct ansatz for  $\alpha \leq b/2$ , which is the regime considered here. For  $\alpha \geq b/2$ , large fluctuations prevent the decoupling between time and magnitude to hold and lead to corrections to the predictions presented here, which, due to their complexity, will be described elsewhere. The ETAS model assumes that the time response and the magnitude response are independent at each generation. In reality and more generality, we can envision that the rate of activation of new earthquakes will depend on 1) the magnitude of the “mother” (which the ETAS model takes into account multiplicatively in (10.1)), 2) on the magnitude of the daughter (which is neglected in the ETAS model) and 3) on the time since the mother was born. Rather than having a very general kernel combining these three parameters nonlinearly, equations (10.1) is based on an hypothesis of independence between these different factors. In addition, assuming that the cascade of secondary aftershocks does not spoil this independence, this allows us to factorize them, leading to (5.11).

The problem is then to determine the functional form of  $\lambda(t)$ , assuming that  $\phi$  is given by (5.1). The integral equation (5.9) is a Wiener-Hopf integral equation [*Feller*, 1971]. It is well-known [*Feller*, 1971; *Morse and Feshbach*, 1953] that, if  $\phi(\tau)$  decays no slower than an exponential, then  $\lambda(t)$  has an exponential tail  $\lambda(t) \sim \exp[-rt]$  for large  $t$  with  $r$  solution of  $\int \phi(x) \exp[rx] dx = 1$ . This result implies that a global Omori’s law cannot be obtained by the epidemic ETAS branching model with, for instance, local exponential relaxation rates. In the present case,  $\phi(\tau)$  decays much slower than an exponential and a different analysis is called for that we now present. The solution of (5.9) is derived in the Appendix and is summarized in the following sections. For the sequel, it is useful to define the characteristic time

$$t^* \equiv c \left( \frac{n \Gamma(1 - \theta)}{|1 - n|} \right)^{\frac{1}{\theta}} , \quad (5.12)$$

where  $\Gamma(x)$  is the Gamma function :  $\Gamma(z) = \int_0^\infty du u^{z-1} e^{-u}$  which is nothing but  $(z - 1)!$  for positive integers  $z$ .

### The sub-critical regime $n < 1$ and $\theta > 0$

An approximation is made in the analytical solution so that the results presented below are only valid for  $t \gg c$ .

We define the parameter  $S_0$  that describes the external source term

$$S_0 = \frac{(b - \alpha)}{b} 10^{\alpha(M - m_0)} . \quad (5.13)$$

Two cases must be distinguished.

- For  $c \ll t \ll t^*$ , we get

$$\lambda_{t < t^*}(t) \sim \frac{S_0}{\Gamma(\theta)|1 - n|} \frac{t^{*-\theta}}{t^{1-\theta}} \quad \text{for } c \ll t \ll t^* . \quad (5.14)$$

- For  $t \gg t^*$ , we obtain

$$\lambda_{t > t^*}(t) \sim \frac{S_0}{\Gamma(\theta)(1 - n)} \frac{t^{*\theta}}{t^{1+\theta}} \quad \text{for } t \gg t^* . \quad (5.15)$$

We verify the self-consistency of the two solutions  $\lambda_{t > t^*}(t)$  and  $\lambda_{t < t^*}(t)$  by checking that  $\lambda_{t > t^*}(t^*) = \lambda_{t < t^*}(t^*)$ . In other words,  $t^*$  is indeed the transition time at which the “short-time” regime  $\lambda_{t < t^*}(t)$  crosses over to the “long-time” regime  $\lambda_{t > t^*}(t)$ .

The full expression of  $\lambda(t)$  valid at all times  $t \gg c$  is given by

$$\lambda(t) = \frac{S_0}{1 - n} \frac{t^{*-\theta}}{t^{1-\theta}} \sum_{k=0}^{\infty} (-1)^k \frac{(t/t^*)^{k\theta}}{\Gamma((k+1)\theta)} \quad (5.16)$$

Expression (5.16) provides the solution that describes the cross-over from the  $1/t^{1-\theta}$  Omori’s law (5.14) at early times to the  $1/t^{1+\theta}$  Omori’s law (5.15) at large times. The series  $\sum_{k=0}^{\infty} (-1)^k \frac{(t/t^*)^{k\theta}}{\Gamma((k+1)\theta)}$  is a series representation of a special Fox function [Glöckle and Nonnenmacher, 1993] (see the Appendix for details).

The ETAS model has been simulated numerically using the algorithm described in [Ogata, 1998, 1999]. Starting with a large event of magnitude  $M$  at time  $t = 0$ , events are then simulated sequentially. After each event, we calculate the conditional intensity  $\lambda(t)$  defined by

$$\lambda(t) = \sum_{t_i \leq t} \frac{K 10^{\alpha(m_i - m_0)}}{(t - t_i + c)^{1+\theta}}$$

where  $t$  is the time of the last event and  $t_i$  and  $m_i$  are the times and magnitudes of all preceding events that occurred at time  $t_i \leq t$ . The time of the following event is then determined according to the non-stationary Poisson process of conditional intensity  $\lambda(t)$ , and its magnitude is chosen in a Gutenberg-Richter distribution with parameter  $b$ . These simulations are compared to the theoretical predictions in Figure 5.2, which shows the aftershock seismic rate  $\lambda(t)$  in the sub-critical regime triggered by a main event of  $M = 6.8$ , for the parameters  $K = 0.024$  (constant in (5.1)), the threshold  $m_0 = 0$  for aftershock triggering,  $c = 0.001$ ,  $\alpha = 0.5$ , a  $b$ -value  $b = 1.0$  and  $\theta = 0.2$  (corresponding to a local Omori’s exponent  $p = 1.2$ ). These parameters lead to a branching ratio  $n = 0.95$  (equation (5.3)) and a characteristic cross-over time  $t^* = 4500$  (equation (5.12)). The noisy black line represents the seismicity rate obtained for the synthetic catalog. The local Omori law with exponent  $p = 1 + \theta = 1.2$  is shown for reference as the dotted line. The analytical solution (5.16) is shown as the thick line. The two dashed lines represent the approximation solutions (5.14) for  $t < t^*$  and (5.15) for  $t > t^*$ .

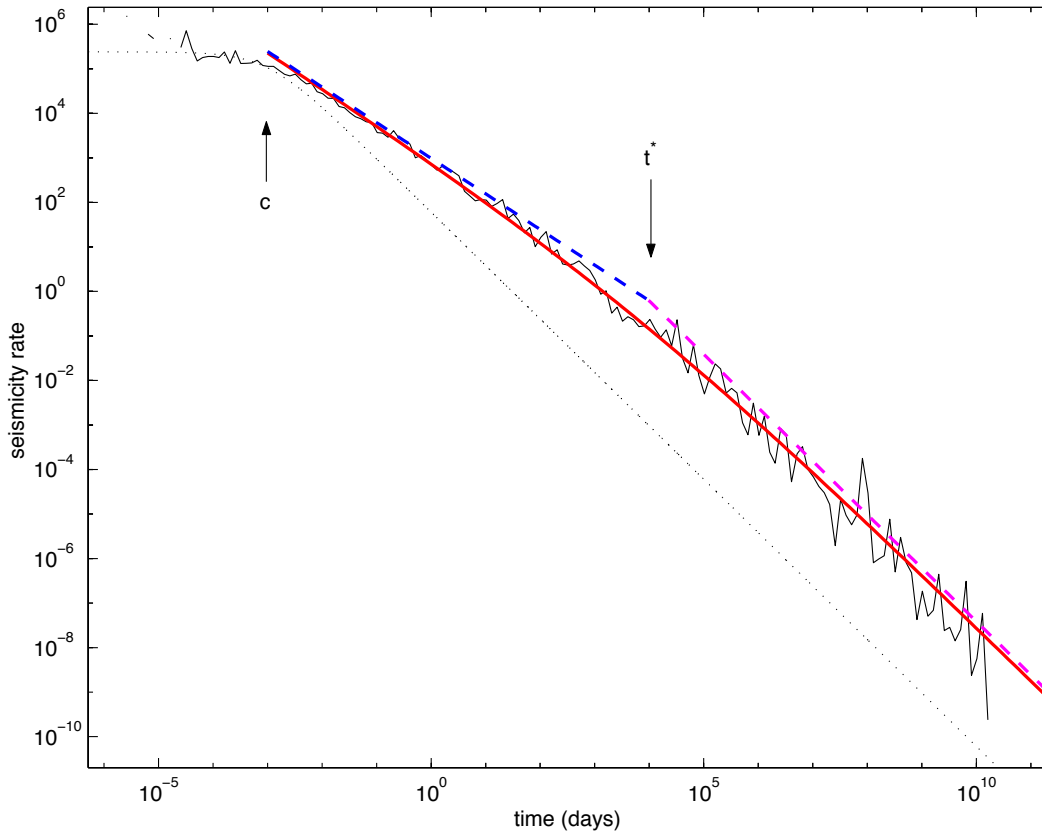


FIG. 5.2 – Seismicity rate  $N(t)$  in the sub-critical regime with  $n = 0.95$ . The noisy black line represents the seismicity rate obtained for a synthetic catalog generated using  $K = 0.024$ ,  $M = 6.8$ ,  $m_0 = 0$ ,  $c = 0.001$  day,  $\alpha = 0.5$ ,  $b = 1.0$  and  $\theta = 0.2$ , giving the characteristic time is  $t^* = 4500$  days. The local Omori law with exponent  $p = 1 + \theta = 1.2$  is shown for reference (dotted line). The analytical solution (5.16) is shown as the thick line. The two dashed lines represents the asymptotic solutions (5.14) for  $t < t^*$  and (5.15) for  $t > t^*$ .

### The super-critical regime $n > 1$ and $\theta > 0$

From the definition of the branching ETAS model for  $n > 1$ , it is clear that the number of events  $\lambda(t)$  blows up exponentially for large times as  $n - 1$  to a power proportional to the number  $t$  of generations. We shall show below that the rate of the exponential growth can be calculated explicitly, which yields  $\lambda(t) \sim e^{t/t^*}$ , where  $t^*$  has been defined in (5.12). However, there is an interesting early and intermediate time regime in the situation where a great event of magnitude  $M$  has just occurred at  $t = 0$ . In this case, the total seismicity is the result of two competing effects : (1) the total seismicity tends to decay according to the Omori's law governing the rate of daughter-earthquakes triggered by the great event ; (2) since each daughter may in turn trigger grand-daughters, grand-daughters may trigger grand-grand daughters and so on with a number  $n > 1$  of children per parent, the induced seismicity will eventually blow up exponentially. However, before blowing up, one can expect that seismicity will first decay

because it is mainly controlled by the large rate  $\sim 10^{\alpha(M-m_0)}$  directly induced by the great earthquake which decays according to its “local” Omori’s law. This decay will be progressively perturbed by the proliferation of daughters of daughters of ... and will cross-over to the explosive exponential regime.

At early times  $c \ll t \ll t^*$ , the early decay rate of aftershocks is the same  $\approx (S_0/\Gamma(\theta)(n-1)) (t^{*-\theta}/t^{1-\theta})$  as for the sub-critical regime (5.14) (see the Appendix). However, as time increases, the Appendix shows that the decay of aftershock activity can be represented as a power law with an effective apparent exponent  $\theta_{\text{app}} > \theta$  increasing progressively with time. The seismic rate will thus decay approximately as  $\sim 1/t^{1-\theta_{\text{app}}(t)}$ . Quantitatively, the large time behavior is (see the Appendix)

$$\lambda(t) \sim \frac{S_0}{(n-1)t^{*\theta}} e^{t/t^*} \quad (5.17)$$

exhibiting an exponential growth at large times. Expression (5.12) shows that  $1/t^* \sim |1-n|^{1/\theta}$ . Thus, as expected, the exponential growth disappears as  $n \rightarrow 1^+$ .

The full expression of  $\lambda(t)$  valid at times  $t \gg c$  is

$$\lambda(t) = \frac{S_0}{(n-1)} \frac{t^{*-\theta}}{t^{1-\theta}} \sum_{k=0}^{\infty} \frac{(t/t^*)^{k\theta}}{\Gamma((k+1)\theta)} \quad (5.18)$$

Expression (5.18) provides the solution that describes the cross-over from the  $1/t^{1-\theta}$  Omori’s law at early times (5.14) to the exponential growth (5.17) at large times.

Figure 5.3 tests these predictions by comparing them with direct numerical simulation of the ETAS model, in the case of a main shock of magnitude  $M = 6$ . The parameters of the synthetic catalog are  $K = 0.024$  (constant in (5.1)), the threshold  $m_0 = 0$  for aftershock triggering,  $c = 0.001$  day,  $\alpha = 0.5$ , a  $b$ -value  $b = 0.75$  and  $\theta = 0.2$  (corresponding to a local Omori’s exponent  $p = 1.2$ ). These parameters lead to a branching ratio  $n = 1.43$  (equation (5.3)) and a characteristic cross-over time  $t^* = 0.85$  day (equation (5.12)). The noisy black line represents the seismicity rate obtained for the synthetic catalog. The local Omori law with exponent  $p = 1 + \theta = 1.2$  is shown for reference as the dotted line. The analytical solution (5.18) is shown as the thick line. The two dashed lines correspond to the approximative analytical solutions (5.14) and (5.17). At early times  $c < t < t^*$ , the decay of  $N(t)$  is initially close to the prediction (5.14). For  $t > t^*$ , we observe that the analytical equation (5.18) is very close to the exponential solution (5.17), so as to be almost indistinguishable from it.

### Case $\theta < 0$ corresponding to a local Omori’s law exponent $p < 1$

We have already remarked that, in this case, the integral  $\int_0^\infty \frac{dt}{(t+1)^{1+\theta}}$  in the definition (5.3) of the branching ratio  $n$  becomes unbounded : the number of daughters created beyond any time  $t$  far exceeds the number of daughters created up to time  $t$ .

The appendix shows that the general equation (5.9) still holds and the general derivation starting with (5.24) up to (5.29) still applies.

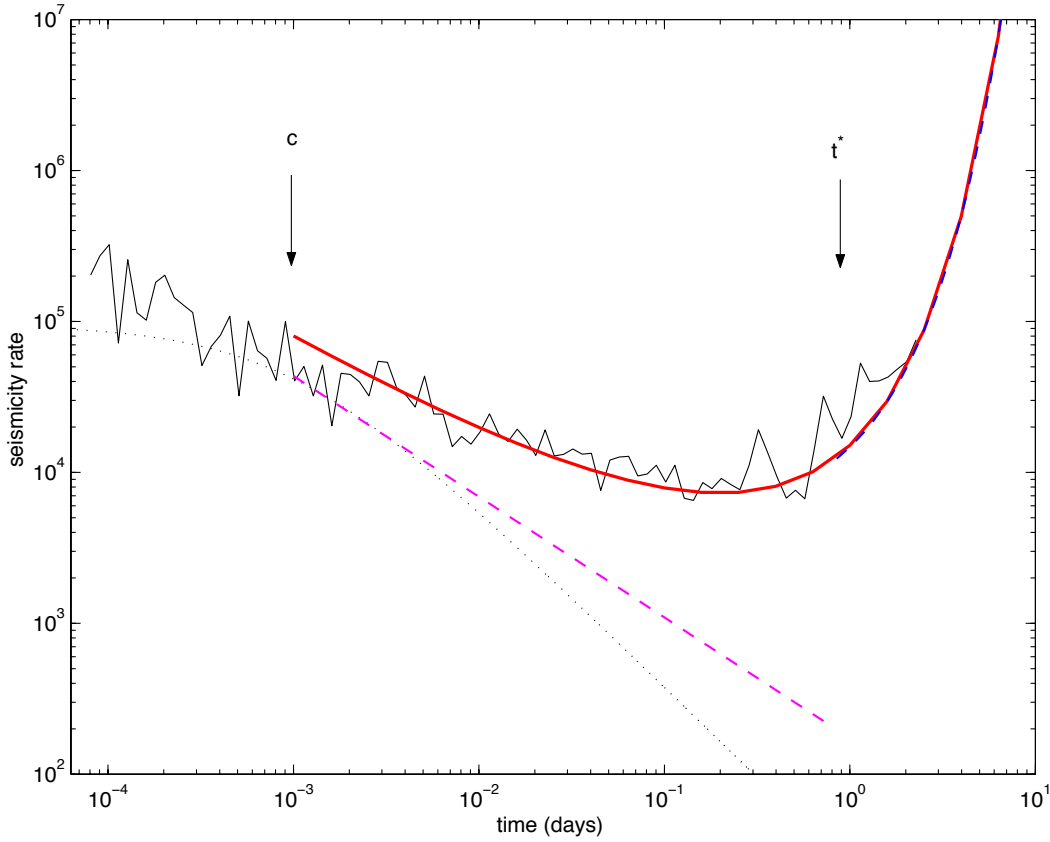


FIG. 5.3 – Seismicity rate  $N(t)$  in the super-critical regime. Same legend as in Figure 5.2. The synthetic catalog was generated using the same parameters as for Figure 5.2, except for a lowest  $b$ -value of  $b = 0.75$  and a smallest mainshock magnitude  $M = 6$ , leading to a branching number  $n = 1.43$  and a characteristic time  $t^* = 0.85$  day. The analytical solution (thick line) is calculated from equation (5.18). The two dashed lines correspond to the approximative analytical solutions (5.14) and (5.17).

Similarly to the super-critical case  $n > 1$  of the regime  $\theta > 0$ , we find a crossover from a power-law decay at early times to an exponential increase of the seismicity rate at large times. The characteristic time  $\tau$  that marks the transition between these two regimes is given by

$$\tau = c \left( \frac{n_0 \Gamma(|\theta|)}{1 + \frac{n_0}{|\theta|}} \right)^{-\frac{1}{|\theta|}}. \quad (5.19)$$

In contrast with the case  $\theta > 0$ , the early time behavior (*i.e.*,  $c \ll t \ll \tau$ ) of the global decay law in the case  $\theta < 0$  is similar to the local Omori law :

$$\lambda(t) = \frac{S_0}{(1 + \frac{n_0}{|\theta|}) \Gamma(|\theta|)} \frac{\tau^{-|\theta|}}{t^{1-|\theta|}} \quad (5.20)$$

Similarly to the super-critical case  $n > 1$  of the regime  $\theta > 0$ , the long time dependence of the regime  $\theta < 0$  is controlled by a simple pole  $1/\tau$  leading to a long-time seismicity growing exponentially

$$\lambda(t) = \frac{S_0}{(1 + \frac{n_0}{|\theta|}) \tau |\theta|} e^{t/\tau} \quad (5.21)$$

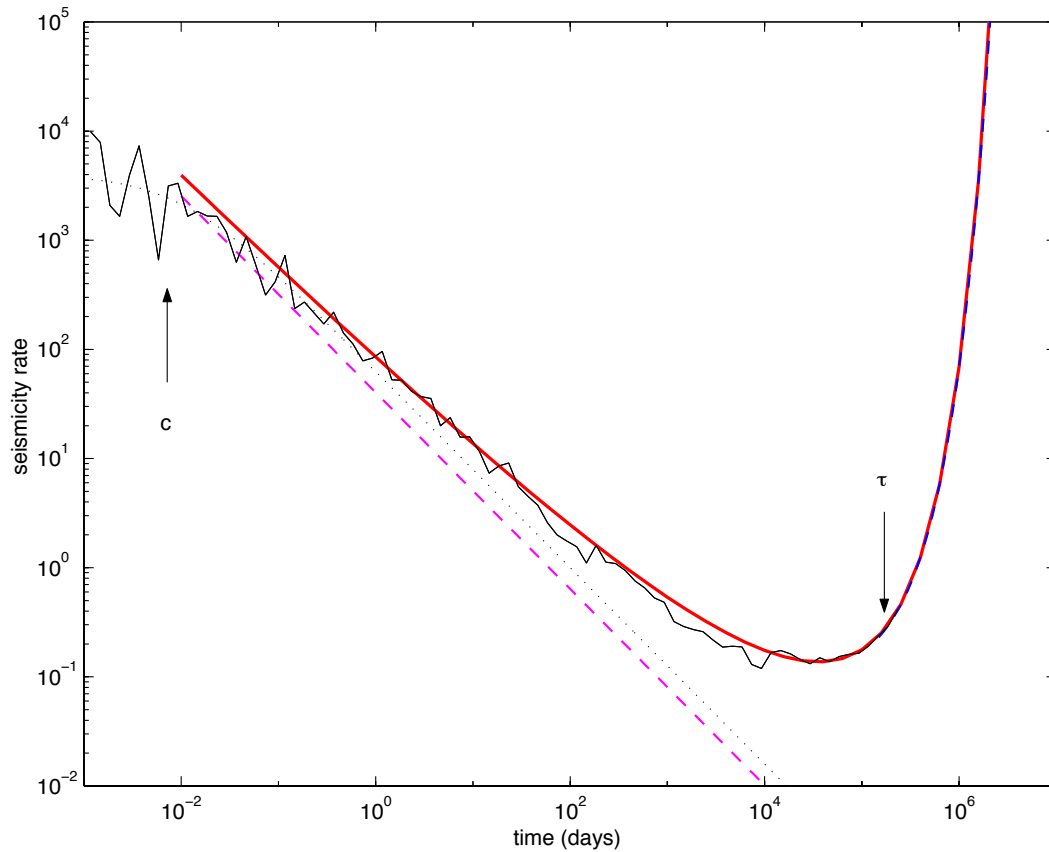


FIG. 5.4 – Seismicity rate  $N(t)$  in the case  $\theta < 0$  corresponding to a local Omori's law exponent  $p < 1$ . Same legend as in Figure 5.2. The synthetic catalog was generated using  $K = 0.02$ ,  $M = 7$ ,  $m_0 = 0$ ,  $c = 0.01$  day,  $\alpha = 0.5$ ,  $b = 1.0$  and  $\theta = -0.1$ , giving the characteristic time is  $\tau = 10^5$  days. The analytical solution (thick line) is calculated from equation (5.22). The two dashed lines correspond to the approximative analytical solutions (5.20) and (5.21).

This result is in agreement with the fact that the number of daughters born up to time  $t$  is an unbounded increasing function of  $t$ , and we should thus recover a regime similar to the super-critical case of  $\theta > 0$ .

The full expression of  $\lambda(t)$  valid at times  $t > c$  is

$$\lambda(t) = \frac{S_0}{(1 + \frac{m_0}{|\theta|})} \frac{1}{t} \sum_{k=1}^{\infty} \frac{(t/\tau)^{k|\theta|}}{\Gamma(k|\theta|)} \quad (5.22)$$

Expression (5.22) provides the solution that describes the cross-over from the local Omori law  $1/t^{1-|\theta|}$  at early times to the exponential growth at large times.

Figure 5.4 compares these predictions to a direct numerical simulation of the ETAS model, in the case of a main shock of magnitude  $M = 7$ . The parameters of the synthetic catalog are  $K = 0.02$ ,  $m_0 = 0$ ,  $c = 0.01$  day,  $\alpha = 0.5$ ,  $b = 1$  and  $\theta = -0.1$  (corresponding to a local Omori's exponent  $p = 0.9$ ). These parameters lead to a characteristic cross-over time  $\tau = 10^5$  day (equation (5.19)). The noisy black line represents the seismicity rate obtained for the synthetic

catalog. The local Omori law with exponent  $p = 1 + \theta = 0.9$  is shown for reference as the dotted line. The analytical solution (5.22) is shown as the thick line. The two dashed lines correspond to the approximative analytical solutions (5.20) and (5.21). At early times  $c < t < \tau$ , the decay of  $\lambda(t)$  is initially close to the prediction (5.20). For  $t > \tau$ , we observe that the analytical equation (5.22) is very close to the exponential solution (5.21), so as to be almost indistinguishable from it.

## 5.4 Discussion

Assuming that each event triggers aftershock sequences according to the local Omori law with exponent  $1 + \theta$ , we have shown that the decay law of the global aftershock sequence is different from the local one. Depending on the branching ratio  $n$ , which is a function of all ETAS parameters, we find two different regimes, the sub-critical regime for  $n < 1$  and the super-critical regime for  $n > 1$  and  $\theta > 0$ . For the two regimes in the case  $\theta > 0$ , a characteristic time  $t^*$ , function of  $c$ ,  $n$  and  $\theta$ , appears in the global decay law  $\lambda(t)$  and marks the transition between the early time behavior and the large time behavior. In the sub-critical regime ( $n < 1$ ), the global decay law is composed of two power laws. At early times ( $t < t^*$ ),  $\lambda(t)$  decays like  $t^{-1+\theta}$ . At large times ( $t > t^*$ ) the global decay law recovers the local law  $N(t) \sim t^{-1-\theta}$ . In the super-critical regime ( $n > 1$  and  $\theta > 0$ ), the early times decay law is similar to that of the sub-critical regime, and the seismicity rate increases exponentially for large times. The case  $\theta < 0$  leads to an infinite  $n$ -value, due to the slow decay with time of the local Omori law. In this case, we find a transition from an Omori law with exponent  $1 - |\theta|$  similar to the local law, to an exponential increase at large times, with a crossover time  $\tau$  different from the characteristic time  $t^*$  found in the case  $\theta > 0$ . Thus, the Omori law is only an approximation of the global decay law valid for some time periods and parameter values. The value of the local Omori exponent  $p = 1$  is the only one for which the local and the global decay rate are similar, and are both power-laws without any characteristic time. For small  $n$ ,  $t^*$  is very small so that in real data we should observe only the behavior  $t > t^*$  characteristic of large times. The global decay law then appears similar to the local Omori law. On the contrary, for  $n$  close to 1,  $t^*$  is very large by comparison with the time period available in real data, and we should observe only the power-law behavior  $\lambda(t) \sim t^{-1+\theta}$  characteristic of early times, with a global  $p$ -value smaller than the local one. Changing  $n$  thus provides an important source of variability of the exponent  $p$ .

### Estimation of $n$ and $t^*$ in earthquake data

In real earthquake data, it is possible to evaluate the branching value  $n$  in order to determine if the seismic activity is either in the sub- or the super-critical regime. The values of  $n$  and  $t^*$  can be evaluated from equations (5.3) and (5.12) as a function of the ETAS parameters  $b$ ,  $p = 1 + \theta$ ,  $c$ ,  $K$  and  $\alpha$ . The parameters of the ETAS model and their standard error can be

inverted from seismicity data (time and magnitudes of each event) using a maximum likelihood method [Ogata, 1988]. We now discuss the range of the different parameters obtained from such inversion procedure.

- The parameter  $\alpha$  is found to vary between 0.35 to 1.7, and is often close to 0.5 [Ogata, 1989, 1992; Guo and Ogata, 1997]. An  $\alpha$ -value of 0.5 means that a mainshock of magnitude  $M$  will have on average 10 times more aftershocks than a mainshock of magnitude  $M - 2$ , independently of  $M$ . Note that our definition of  $\alpha$  is slightly different from that used by Ogata and we have divided his  $\alpha$ -values by  $\ln(10)$  to compare with our definition.

For some seismicity sequences, Ogata [1989, 1992] and Guo and Ogata [1997] found  $\alpha > b$ . According to (5.3), this leads to an infinite  $n$ -value if we use a Gutenberg-Richter magnitude distribution. As we said, a truncation of the magnitude distribution is needed to obtain a physically meaningful finite  $n$ -value because the seismicity rate is controlled by the largest events.

A large  $\alpha$ -value can be associated with seismic activity called “swarms”, while a small  $\alpha$ -value is observed for aftershock sequences with a single mainshock and no significant secondary aftershock sequences [Ogata, 1992, 2001].

- The parameter  $c$  is usually found to be of the order of one hour [Utsu et al., 1995]. In practice, the evaluation of  $c$  is hindered by the incompleteness of earthquake catalogs just after the occurrence of the mainshock, due to overlapping aftershocks on the seismograms. A large  $c$  is often an artifact of a change of the detection threshold. Notwithstanding these limitations, well-determined non-zero  $c$ -value have been obtained for some aftershock sequences [Utsu et al., 1995]. Note that a non-zero  $c$  is required for the aftershocks rate to be finite just at the time of the mainshock.
- The “local”  $p$ -value, equal to  $1 + \theta$ , describes the decay law of the aftershock sequence triggered by a single earthquake. The local Omori law is the law  $\phi(t)$  obtained by inverting the ETAS model on the data. The “global”  $p$ -value describes the decay law of the whole aftershock sequence, composed of all secondary aftershocks triggered by each aftershock. We have shown that the Omori law is only an approximation of the global decay law, so that in the subcritical regime the global  $p$ -value will change from  $1 - \theta$  at early times to  $1 + \theta$  at large times. [Guo and Ogata, 1997] measured both the local and global  $p$ -values for 34 aftershock sequences in Japan, and found that the local  $p$ -value is usually slightly larger than the global  $p$ -value [Guo and Ogata, 1997]. This is in agreement with our prediction when identifying the local  $p$ -value with  $1 + \theta$  (recovered at large times) and the global  $p$ -value with  $1 - \theta$  found at early times. Guo and Ogata [1997] and Ogata [1992, 1998, 2001] found a local  $p$ -value smaller than one for some aftershocks sequences in Japan. Within the confine of the ETAS model, this corresponds to the case  $\theta < 0$  discussed above and in the appendix.
- The parameter  $K$  measures the rate of aftershocks triggered by each earthquake, inde-

pendently of its magnitude. Recall that the branching ratio  $n$  is proportional to  $K$ . It is usually found of the order of  $K \approx 0.02$  [Ogata, 1989, 1992; Guo and Ogata, 1997], but large variations of  $K$ -value from 0.001 to 5 are reported by Ogata [1992].

- The parameter  $\mu$  measures the background seismicity rate that is supposed to arise from the tectonic loading.  $\mu \simeq 0$  for an aftershock sequence triggered by a single mainshock. This parameter has no influence on the branching ratio  $n$ . In real catalogs, the background seismicity only accounts for a small part of the seismic activity.

We have computed the branching ratio  $n$  and the cross-over time  $t^*$  from the ETAS parameters measured by Ogata [1989, 1992] for several seismicity sequences in Japan and elsewhere. The ETAS parameters and the  $n$  and  $t^*$  values are given in Table 5.1. When the  $b$ -value is not given in the text, we have computed  $n$  and  $t^*$  assuming a  $b$ -value equal to 1. We find that the  $n$ -value is either smaller or larger than 1. This means that the seismicity can be interpreted to be either in the sub- or in the super-critical regime. An infinite  $n$ -value is found if the local  $p$ -value is smaller than one ( $\theta < 0$ ) or if the  $\alpha$ -value is larger than the  $b$ -value. For the same area, the ETAS parameters and the  $n$  and  $t^*$  values are found to vary in time, sometimes changing from the sub- to the super-critical regime. The characteristic time  $t^*$  shows large spatial and temporal variability, ranging from 0.4 days to  $10^{22}$  days. Large  $t^*$  values are related to a branching ratio  $n$  close to one, *i.e.*, close to the critical point  $n = 1$ . The ETAS model thus provides a picture of seismicity in which sub-critical and super-critical regimes are alternating in an intermittent fashion. As we shall argue, the determination of the regime may provide important clues and quantitative tools for prediction.

### Implications of the ETAS model in the sub-critical regime $n < 1$

In the sub-critical regime, the ETAS model can explain many of the departures of the global aftershock decay law from a pure Omori law.

The ETAS model contains by definition (and thus “explains”) the secondary aftershock sequences triggered by the largest aftershocks that are often observed [Correig *et al.*, 1997; Guo and Ogata, 1997; Simeonova and Solakov, 1999; Ogata, 2001]. In the ETAS model, the fact that secondary aftershock sequences of large aftershocks can stand out above the overall background aftershock seismicity results from the factor  $10^{\alpha(m_i - m_0)}$  in (5.1).

Our analytical results may rationalize why some alternative models of aftershock decay work better than the simple modified Omori law. In the sub-critical regime, we predict an increase of the apparent global  $p$ -value from  $1 - \theta$  at early times to  $1 + \theta$  at large times. To our knowledge, this change of exponent has never been observed. This change of power law may be approximated by the stretched exponential function proposed by [Kissinger, 1993; Gross and Kisslinger, 1994] to fit aftershock sequences. In the stretched exponential model, the rate of aftershocks  $\lambda(t)$  is defined by

$$\lambda(t) = K t^{q-1} e^{-(t/t_0)^q}, \quad (5.23)$$

TAB. 5.1 – ETAS parameters, branching ratio  $n$  and characteristic time  $t^*$  for the sequences studied by *Ogata* [1989, 1992]. We have computed  $n$  and  $t^*$  using equations (8.7) and (5.12) from the ETAS parameters  $K$ ,  $\alpha$ ,  $c$ ,  $p = 1 + \theta$  and  $\mu$  calculated by *Ogata* [1989, 1992] using a maximum likelihood method. For most sequences, we have assumed  $b = 1$  to evaluate  $n$  and  $t^*$  because  $b$ -value is not given in [Ogata, 1989, 1992]. Thus, there is a large uncertainty in the  $n$  and  $t^*$  values in the case where  $\alpha$  is close to 1.

Ref	seismicity data	$M_0$	$b$	$\mu$ day <sup>-1</sup>	$K$	$c$ day	$p$	$\alpha$	$n$	$t^*$ day
1	Japan, 1895-1980	6.0	1.0	0.005	0.087	0.02	1.0	0.7	Inf	<sup>a</sup>
1	Rat-Island 1963-1982	4.7	1.0	0.0	0.072	0.167	1.35	0.63	1.04	4600
1	Nagano, 1978-1986	2.5	0.9	0.021	0.008	0.017	0.85	0.94	Inf	<sup>b</sup>
1	Nagano aft., 1986	2.9	1.2	0.0	0.032	0.038	1.14	0.73	0.92	4.10 <sup>6</sup>
2	worldwide shallow eqs.	7.0	1.0	0.019	0.018	0.21	1.03	0.53	1.49	10 <sup>17</sup>
2	Aleutian, 10 yrs	4.7	1.0	0.008	0.042	0.03	1.13	0.62	1.34	2200
2	Tohoku, 95 years	6.0	1.0	0.0054	0.98	0.02	1.0	0.70	Inf <sup>a</sup>	
2	Tokachi-Oki aft., 1 yr	4.8	1.0	0.14	0.015	0.23	1.28	0.98	4.03	1.5
2	Niigata aft., 150 days	4.0	1.0	0.075	0.0005	0.15	1.37	1.26	Inf	<sup>b</sup>
2	Niigata aft., 150 days	2.5	1.0	0.47	0.0002	1.10	1.72	1.34	Inf	<sup>b</sup>
2	Izu Islands, 55 years	4.0	1.0	0.0038	0.062	0.012	1.14	0.16	0.96	10 <sup>8</sup>
2	Izu Peninsula, 7 years	2.5	1.0	0.022	0.035	0.003	1.35	0.17	0.91	7.3
2	Izu, 33 days	2.9	1.0	0.59	0.016	0.009	1.73	0.31	1.00	346.
2	Matsushiro, 20 yrs	3.9	1.0	0.0006	0.092	0.13	1.14	0.27	1.21	2200
2	Kanto, 1904-1916	5.4	1.0	0.028	0.010	0.010	1.00	0.62	Inf	<sup>a</sup>
2	Kanto, 1916-1923	5.4	1.0	0.025	0.001	0.010	1.02	1.31	Inf	<sup>b</sup>
2	Hachijo, 1938-1969	5.4	1.0	0.013	0.008	0.004	1.02	0.85	3.0	5.10 <sup>6</sup>
2	Hachijo, 1969-1973	5.4	1.0	0.016	0.001	0.013	1.00	1.11	Inf	<sup>a</sup>
2	Tonankai, 1933-1939	5.2	1.0	0.050	0.010	0.065	1.02	0.90	5.28	4.10 <sup>3</sup>
2	Tonankai, 1939-1944	5.2	1.0	0.031	0.009	0.011	1.01	0.83	5.54	10 <sup>7</sup>
2	Tokachi, 1926-1945	5.0	1.0	0.047	0.013	0.065	1.32	0.83	0.57	0.40
2	Tokachi, 1945-1952	5.0	1.0	0.041	5.20	11.6	3.50	1.37	Inf	<sup>b</sup>
2	Tokachi, 1952-1961	5.0	1.0	0.032	0.021	0.059	1.10	0.72	0.99	10 <sup>22</sup>
2	Tokachi, 1961-1968	5.0	1.0	0.014	0.014	0.005	0.86	0.43	Inf	7.10 <sup>5</sup> <sup>c</sup>

1 Ogata [1989] ; 2 Ogata [1992]

<sup>a</sup>  $t^*$  cannot be evaluated because  $p = 1$

<sup>b</sup>  $t^*$  cannot be evaluated because  $\alpha > b$

<sup>c</sup>  $\tau$  is given instead of  $t^*$  because  $\theta < 0$

where  $q$ ,  $K$  and  $t_0$  are constants. At early times, this function decays as a power law  $1/t^{1-q}$  with apparent Omori's exponent  $1 - q$ . For times larger than the relaxation time  $t_0$ , the seismicity rate decays exponentially in the argument  $(t/t_0)^q$ . For  $q < 1$ , this decay is much slower than exponential and can be accounted for by an apparent power law with larger exponent. Figure 5.5 compares the stretched exponential function with the analytical solution of the ETAS model (5.16) with parameters  $t^* = t_0$  and  $\theta = q$ , and with the Omori law of exponent  $p = 1 - q$ . These three laws have the same power-law behavior at early times, and then both the stretched exponential and the analytical solution (5.16) decay faster than the Omori law at large times. The fact that it is very difficult to distinguish the decay laws described by power laws and by stretched exponential has been illustrated in [Laherrère and Sornette, 1998] in many examples including earthquake size and fault length distributions. Kissinger [1993] and Gross and Kisslinger, 1994] compared this function to the modified Omori law  $\lambda(t) = K (t + c)^{-p}$  for several aftershock sequences in southern California. They found that the stretched exponential fit often works better for the sequences with a small  $p$ -value or a large  $q$ -value, indicative of a slow decay for small times. This is in agreement with our result that in the sub-critical regime a slowly decaying aftershock sequence (global  $p$ -value smaller than one) will then cross-over to a more rapid decay for time larger than  $t^*$ . The relaxation time  $t_0$  ranges between 2 days and 380 days for the sequences that are better fitted by the stretched exponential [Kissinger, 1993]. This parameter is analogous to  $t^*$  found in our model, because these two parameters define the transition from the early time power-law decay to another faster decaying behavior for large times. To further validate our results, these aftershock sequences should be fitted using equation (5.16) to compare our results with the stretched exponential function and determine if the transformation of the early time power law decay is better fitted by a stretched exponential fall-off or an increase in the apparent Omori exponent from  $1 - \theta$  to  $1 + \theta$  as predicted by our results.

The ETAS model can also rationalize some correlations found empirically between seismicity parameters. It may explain the rather large variability of the global empirical  $p$ -value. Guo and Ogata [1995] have reported a positive correlation between the Gutenberg-Richter  $b$ -value and the  $p$ -value (exponent of the global Omori law) for several aftershock sequences in Japan. A similar correlation has also been found by [Kisslinger and Jones, 1991] for several aftershock sequences in southern California, but this correlation was detectable only if the earthquake sequences were separated into thrust and strike slip events. This positive correlation between  $b$  and global  $p$  values is expected from our analysis. From equation (5.3), we see that a small  $b$ -value is associated with a large  $n$  value. For  $n \simeq 1$ , the characteristic time  $t^*$  is very large, so that the global aftershock rate decays as a power law with exponent  $1 - \theta$  over a large time interval. For  $n > 1$  and  $\theta > 0$ , we see an apparent global  $p$ -value smaller than  $1 - \theta$  which decreases with time. In contrast, for large  $b$ -values, the branching ratio  $n$  is small and the characteristic time  $t^*$  is very small. In this case, only the large time behavior is observed with a larger exponent  $1 + \theta$ . Consequently, in the subcritical regime, our results predict a change of the global  $p$ -value

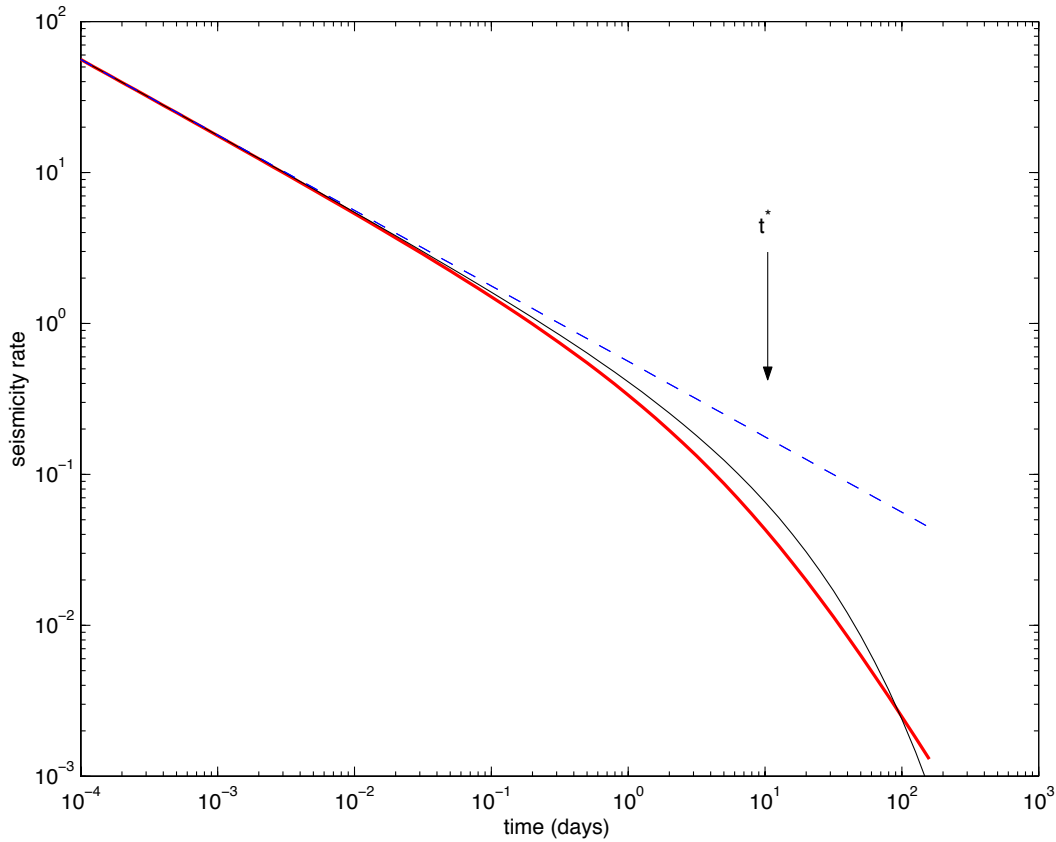


FIG. 5.5 – Comparison between the three decay laws of aftershock sequences : Omori law with  $p = 0.7$  (dashed line), stretched exponential with  $q = 0.3$  and  $t_0 = 10$  days (thin black line) and our analytical solution in the sub-critical regime (5.16) for  $\theta = q = 1 - p = 0.3$  and  $t^* = t_0 = 10$  days (solid gray line). At early times  $t \ll t^*$ , the three functions are similar and decay as  $t^{-0.7}$ . At large times, the stretched exponential function and the analytical solution of the ETAS model decay more rapidly than the Omori law. For times up to  $t = 10 t^*$ , the stretched exponential function is a good approximation of the ETAS model solution, and describes the transition from a power law decay at early times to a faster decay law.

from  $1 - \theta$  for small  $b$ -value and times  $t \ll t^*$  to  $1 + \theta$  for large  $b$ -values. There is also a positive correlation between  $p$ -value and  $b$ -value in the super-critical regime. For  $n > 1$  or  $\theta < 0$ , the global aftershock sequence is characterized by an apparent exponent  $p$  smaller than  $1 - |\theta|$  which decreases with time. Then, we expect the apparent exponent  $p$  to be all the smaller, the smaller is the  $b$ -value, because the characteristic times  $t^*$  for  $\theta > 0$  or  $\tau$  for  $\theta < 0$  decreases with  $b$ . The variability of the global  $p$  exponent reported by *Guo and Ogata* [1995] and *Kisslinger and Jones* [1991] may thus be explained by a change of  $b$ -value and a constant local  $p$  exponent. However, the results of *Guo and Ogata* [1997] contradict this interpretation. *Guo and Ogata* [1997] studied the same aftershock sequences than *Guo and Ogata* [1995] but they measured the local  $p$ -value of the ETAS model. They still found a large variability in the local  $p$ -value, and a positive correlation between this local  $p$ -value and the  $b$ -value.

## Implications of the ETAS model in the super-critical regime and in the case $\theta < 0$

In the regime where the mean number of aftershocks per mainshock is larger than one (*i.e.*,  $n > 1$ ), the mean rate of aftershocks increases exponentially for large times. However, because of the statistical fluctuations, the aftershock sequence has a finite probability to die. This probability of extinction can be evaluated for the simple branching model without time dependence [Harris, 1963]. Therefore, a branching ratio larger than 1 does not imply necessarily that the number of aftershocks will be infinite. If  $n$  is not too large, and if the number of aftershocks is small, there is a significant probability that the aftershock sequences will die, as observed in numerical simulations of the ETAS model. If the characteristic time  $t^*$  is very large, the aftershock sequence may not remain supercritical long enough for the exponential increase to be observed. Even if the large time exponential acceleration is rarely observed in real seismicity, it may explain the acceleration of the deformation before material failure. The early times behavior of the seismic activity preceding the exponential increase has also important possible implications for earthquake prediction, and can rationalize some empirically proposed seismic precursors, such as the low  $p$ -value [Liu, 1984; Bowman, 1997], or the relative seismic quiescence preceding large aftershocks [Matsu'ura, 1986; Drakatos, 2000].

It is widely accepted that about a third to a half of strong earthquakes are preceded by foreshocks [e.g., Jones and Molnar, 1979; Bowman and Kisslinger, 1984; Reasenberg, 1985, 1999; Reasenberg and Jones, 1989; Abercrombie and Mori, 1996], *i.e.*, are preceded by an unusual high seismicity rate for time periods of the order of days to years, and distance up to hundreds kilometers. However, there is no reliable method for distinguishing foreshocks from aftershocks. Indeed, the ETAS model makes no arbitrary distinctions between foreshocks, mainshocks and aftershocks and describes all earthquakes with the same laws. While this seems a priori paradoxical, our analysis of the ETAS model provides a useful tool for identifying foreshocks, *i.e.*, earthquakes that are likely to be followed by a larger event, from usual aftershocks that are seldom followed by a larger earthquake. The characterization of foreshocks will be performed in statistical terms rather than on a single-event basis. In other words, we will not be able to say whether any specific event is a precursor. It is the ensemble statistics that may betray a foreshock structure.

The crux of the method is that, when seismicity falls in the regime with a branching ratio  $n > 1$ , the corresponding earthquake sequences can be identified as foreshocks. This is because the super-critical regime corresponds to an exponentially accelerating seismicity for times larger than  $t^*$  : by a pure statistical effect, the larger number of earthquakes of any size will sample more and more the branch of the Gutenberg-Richter law toward large events. Thus by the sheer weight of numbers, larger and larger earthquakes will occur as time increases. Of course, we are not implying any precise deterministic growth law, but statistically, the largest events should indeed grow significantly, the more so, the more within the super-critical regime, the larger the

branching ratio  $n > 1$ . Conversely, this argument implies that, in the subcritical regime, the triggered events are usual aftershocks, because a mainshock is unlikely to be followed by a larger triggered event. Foreshock sequences can thus be identified by evaluating the branching ratio  $n$  from the inversion of seismic data (times and magnitudes of an earthquake sequence) for the ETAS parameters. There is however a finite probability that a triggered event in the subcritical regime be larger than the triggering event, and thus the triggering event will be a foreshock of the triggered event. Therefore, foreshocks can be observed even in the sub-critical regime, but they are less frequent than aftershocks.

A note of caution is in order : the direct estimation of  $n$  and  $t^*$  or  $\tau$  may be quite imprecise if the number of events is small. Based on our analysis and our results, the foreshock regime can be nevertheless identified with relatively good confidence if one assumes an upper bound for the local exponent  $p$ . Let us assume for instance that the local  $p$ -value is smaller than 1.3 (*i.e.*,  $\theta < 0.3$ ); according to our results, the global exponent  $p$  cannot become smaller than  $1 - \theta = 0.7$  in the sub-critical regime. In contrast, in the supercritical regime, we have shown that the apparent exponent is smaller than or at most equal to  $1 - \theta$ . Therefore, a measure of the global  $p$ -value yielding a value smaller than 0.7, is always associated with the super-critical regime. As we said above, *Guo and Ogata* [1997] and *Ogata* [1992, 1998, 2001] found a local  $p$ -value smaller than one for some aftershocks sequences in Japan corresponding to the case  $\theta < 0$ . A small global  $p$ -value can thus also result from a small local  $p$ -value. In sum, a small global  $p$ -value results either from a larger than one local  $p$ -value in the supercritical regime  $n > 1$  or from a small (smaller than 1) local  $p$ -value before the exponential growth regime.

Such a small  $p$ -value precursor was first proposed empirically by *Liu* [1984], who studied several aftershock sequences of moderate earthquakes that have been followed by a large earthquake. He proposed that a  $p$ -value smaller than 1 is a signature of a foreshock sequence, whereas  $p > 1$  is associated with normal aftershock sequences with a single mainshock in the past. He suggested that  $p$ -values close to one characterize double-mainshock sequences. These empirical rules are part of the earthquake prediction method used in China [*Liu*, 1984; *Zhang et al.*, 1999]. The small precursory  $p$ -value has been used with other precursors to predict the occurrence of a  $M = 6.4$  earthquake in China following another  $M = 6.4$  earthquake three months later [*Zhang et al.*, 1999]. A precursor associated with a small global  $p$ -value has also been observed by *Bowman* [1997] for a sequence in Australia. In 1987, several  $M = 4 - 5$  earthquakes occurred in a region that was not seismically active before, and triggered a large number of aftershocks characterized by an abnormally low  $p$ -value of 0.3. A sequence of three  $M \geq 6$  occurred one year later, followed by an aftershock sequence with a more standard  $p$ -value of 1.1. *Simeonova and Solakov* [1999] have also reported a very low  $p$ -value of 0.5, for one sequence of aftershocks in Bulgaria, that was followed one year latter by a larger earthquake. The first part of the aftershock sequence was well fitted by a modified Omori law, and then a significant deviation occurred with an abnormally high aftershock rate by comparison with the prior trend. This departure from an

Omori law is expected from our results for an aftershock sequence in the super-critical regime and the very low value of the exponent  $p$  can be interpreted as the apparent exponent within the cross-over from the  $1/t^{1-\theta}$  decay (5.14) at early times to the exponential explosion (5.17) at times  $t > t^*$  (see Figure 5.3).

In addition to the small precursory  $p$ -value predicted in the regime  $n > 1$ , we have shown that this regime is also characterized by a decrease of the apparent global  $p$ -value with time. Such a decrease of  $p$ -value has also been identified as a precursor by *Liu* [1984].

Other patterns may be a signature of the super-critical regime. The relative precursory quiescence suggested by *Drakatos* [2000] may also be explained by our results. In contrast to the “absolute” quiescence which detects changes in the background seismicity after removing the aftershocks from the catalog [e.g. *Wyss and Habermann*, 1988], the “relative” quiescence [*Matsu’ura*, 1986; *Drakatos*, 2000] takes into account the aftershocks and detects changes in seismic activity after a large mainshock by comparison with the usual Omori law decay of aftershocks. *Drakatos* [2000] studied several aftershock sequences in Greece which contains large aftershocks, *i.e.* aftershock with magnitude no smaller than  $M - 1.2$ , where  $M$  is the mainshock magnitude. For each sequence, he fitted the aftershock sequence by a modified Omori law up to the time of the large aftershock using a maximum likelihood method. He found that large aftershocks were often preceded by a relative quiescence by comparison with an Omori law, with an increase of the seismicity rate just before the large mainshock occurrence. Such a departure from an Omori law is predicted by our results in the super-critical regime. Indeed, in the super-critical regime, large aftershocks are likely to occur when the earthquake rate  $N(t)$  changes from an Omori law to the exponential explosion for times close to  $t^*$ .

To illustrate this concept, we have performed a simulation of the ETAS model in the super-critical regime and have applied the same procedure as used by *Drakatos* [2000] to fit the synthetic aftershock sequence by an Omori law up to the time of the first large aftershock. The parameters of the synthetic catalog are  $K = 0.024$ ,  $m_0 = 0$ ,  $c = 0.001$  day,  $\alpha = 0.5$ ,  $b = 0.8$  and  $\theta = 0.2$ , yielding  $n = 1.27$  and  $t^* = 4.6$  day. Figure 5.6 represents the cumulative aftershock number as a function of time for the synthetic catalog and the fit with a modified Omori law. From this figure, we see a clear relative seismic quiescence, as defined by a cumulative aftershock number smaller than that predicted by the fit. The aftershock activity recovers the level predicted by the fit at the time of the large aftershock. All these results are similar to those obtained by *Drakatos* [2000].

In the case  $n > 1$ , our results predict an exponential increase of the seismicity rate at large times. Because we assume that the magnitude distribution is independent of time, the same exponential acceleration is expected for both the cumulative energy release and the cumulative number of earthquakes. *Sykes and Jaumé* [1990] found that several large earthquakes in the San-Francisco Bay area were preceded by an acceleration of the cumulative energy release that can be fitted by an exponential function, as predicted by our results. In laboratory experiments

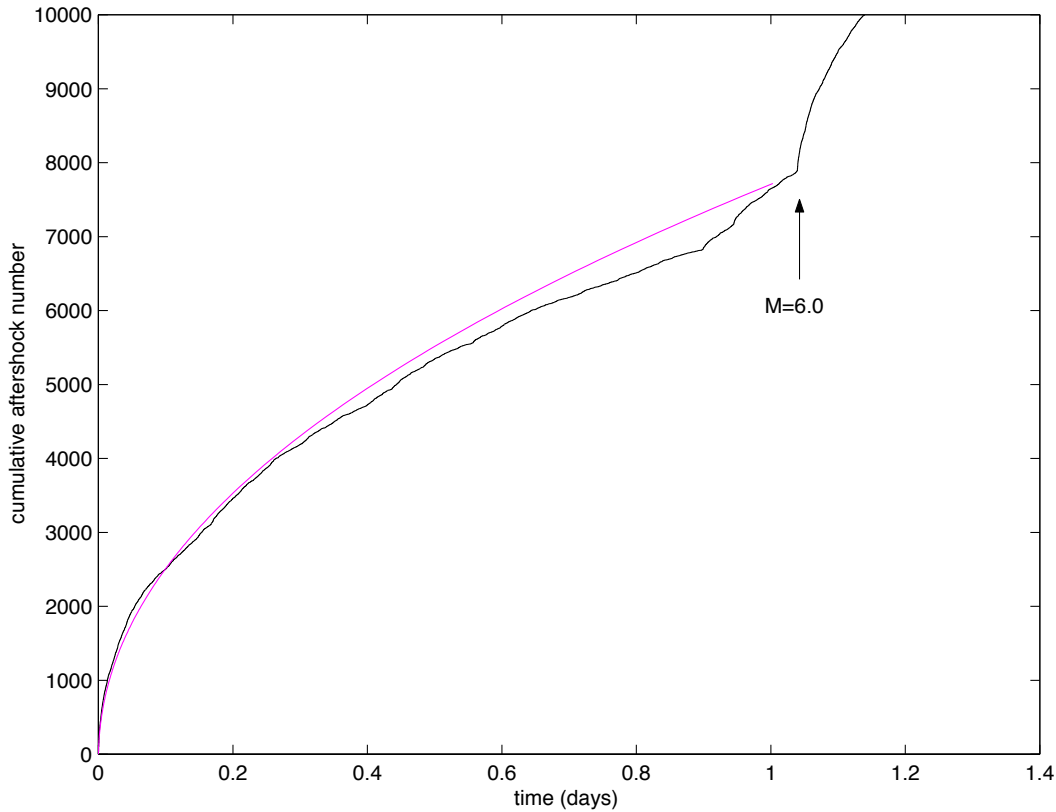


FIG. 5.6 – Cumulative aftershock number in the super-critical regime from a synthetic catalog generated using a branching ratio  $n = 1.27$ ,  $\theta = 0.2$  and  $t^* = 4.6$  days. The mainshock magnitude is  $M = 7.0$ . The thin line is a fit by an Omori law evaluated for time before the occurrence of the first  $M \geq 6.0$  aftershock. This fit gives an apparent global  $p$ -value of 0.58. Relative seismic quiescence (by comparison with an Omori law) is observed before the occurrence of the  $M = 6.0$  aftershock, due to the transition from an Omori law decay with exponent  $p = 1 - \theta = 0.8$  for time  $t \ll t^*$  to an exponential increase of the seismicity rate for time  $t \gg t^*$ .

of rupture, several studies have also observed an exponential acceleration of the seismic energy release before the macroscopic rupture [Scholz, 1968b; Meredith et al., 1990; Main et al., 1992].

More recently, many studies have reported an acceleration of seismicity prior to great events (see [Sammis and Sornette, 2002; Vere-Jones et al., 2001] for reviews) but they used a power-law instead of an exponential law to fit the acceleration of seismicity. A power-law increase of the seismicity before rupture is predicted by several statistical models of rupture in heterogeneous media, which consider the global rupture or the great earthquake as a critical point (see [Sornette, 2000a] for a review). Note that it is often difficult to distinguish in real data an exponential increase from a power-law increase, especially with a small number of points and for times far from the rupture time. No systematic study has been undertaken that compares these two laws to test if the acceleration of the seismicity is better fitted by a power-law rather than by an exponential law (see however [Johansen et al., 1996]).

We have stressed that the ETAS model is fundamentally a mean field approximation (branching process) which neglects “loops”, *i.e.*, multiple interactions. An important consequence of this approximation is that the super-critical regime cannot lead to a growth rate faster than exponential. Indeed, recall that an exponential growth is characterized by a time derivative of the number of events proportional to the number of events  $dN/dt = N/t^*$ , *i.e.*, is fundamentally a *linear* process. In a sequel to the present work [Sornette and Helmstetter, 2002], we show however that for  $b < \alpha$ , the impact of the largest earthquake induces an effective nonlinearity which leads to a faster-than-exponential growth rate, possibly leading to a finite-time singularity [Sammis and Sornette, 2002]. A faster-than-exponential growth rate may also be obtained by introducing multiple interactions between earthquakes and positive feedback : rather than the linear law  $dN/dt = N/t^*$  expressing the condition that each “daughter” has only one “mother”, we may expect an effective law  $dN/dt \sim N^\delta$ , with  $\delta > 1$  providing a measure of the effective number of ancestors impacting directly on the birth of a daughter. We may thus expect that an improvement of the ETAS model beyond the “mean-field” approximation would lead to power law acceleration of seismicity in some regions of the parameter space.

Other precursory patterns may also be related to the super-critical regime : they comprise the precursory earthquake swarm or burst of aftershocks [Evison, 1977 ; Keilis-Borok *et al.*, 1980a, 1980b ; Molchan *et al.*, 1990 ; Evison and Rhoades, 1999]. Swarms are earthquake sequences characterized by high clustering in space and time and the occurrence of several large events with magnitude larger than  $M - 1$ , where  $M$  is the magnitude of the largest event. A burst of aftershocks is a sequence of one or more mainshocks with abnormally large number of aftershocks at the beginning of their aftershock sequences [Keilis-Borok *et al.*, 1980a]. From our results, an abnormally high aftershock rate or a sequence with several large events are expected in the super-critical regime.

### Temporal change of $n$ -value and transition from one regime to the other one

It is often reported that the  $b$  and  $p$  values vary in space and time [e.g., Smith, 1981 ; Guo and Ogata, 1995, 1997 ; Wiemer and Katsumata, 1999]. We have documented that a part of the observed variation of the exponent  $p$  may not be genuine but result from an inadequate parameterization of a more complex reality. Because  $n$  and  $t^*$  are function of  $b$ ,  $p$  and the other ETAS parameters, we expect the fundamental parameters of the ETAS model, namely  $n$  and  $t^*$ , to vary significantly in space and time. The branching ratio  $n$  plays the role of a “control” parameter quantifying the distance from the critical point  $n = 1$  between the sub-critical and the super-critical regime ;  $t^*$  is a cross-over time and is sensitive to details of the systems. As a consequence, it is very reasonable to expect that the Earth’s crust will change from the sub-critical to the super-critical regime and vice-versa, as a function of time and location.

Equation (5.3) shows that the branching ratio  $n$  is a decreasing function of  $b$ . Accordingly, this may rationalize the observation that large earthquakes are sometimes preceded by a decrease

of the  $b$ -value [e.g. *Smith*, 1981]. A decrease of the  $b$ -value leads to an increase of the  $n$ -value, that can move the seismicity from the sub-critical to the super-critical regime, and thus increase the probability to observe a large earthquake. Other ETAS parameters ( $\alpha$ ,  $K$ ,  $p$  and  $c$ ) may also change in time and move the seismicity from one regime to the other one. *Ogata* [1989] measured the ETAS model parameters before and after the 1984 Western Nagano Prefecture earthquake ( $M = 6.8$ ). He found that the seismic activity preceding the mainshock was characterized by a lower  $b$ ,  $c$ ,  $K$  parameters and local  $p$  values than the seismicity following the mainshock. He also obtained a larger  $\alpha$ -value for the seismicity preceding the mainshock. All these changes of parameters, except the change in  $K$ , lead to a larger  $n$ -value before the mainshock than after. Before the mainshock,  $n$  is in principle infinite because the local  $p$ -value is smaller than one. As we already discussed, this corresponds to an explosive super-critical regime of growing seismicity. After the mainshock, we find  $n = 0.92$  and  $t^* = 10^6$  days, using the determination of the ETAS parameters. The seismicity has thus changed from a super-critical regime before the mainshock to a sub-critical regime after the mainshock.

## 5.5 Conclusion

We have provided analytical solutions of the ETAS model, which describes foreshocks, aftershocks and mainshocks on the same footing. Each event triggers an aftershock sequence with a rate that decays according to the local Omori law with an exponent  $p = 1 + \theta$ . The number of aftershocks per event increases with its magnitude. We suggest that the Earth's crust at a given time and location may be characterized by its branching ratio  $n$ , quantifying its regime. We propose that  $n$  is a fundamental parameter for understanding and characterizing the organization of the seismicity within the Earth's crust. In the sub-critical regime ( $n < 1$ ), the global rate of aftershocks (including secondary aftershocks) decays with the time from the mainshock with a decay law different from the local Omori law. We find a crossover from an Omori exponent  $1 - \theta$  for  $t < t^*$  to  $1 + \theta$  for  $t > t^*$ . The modified Omori law is thus only an approximation of the decay law of the global aftershock sequence. In the super-critical regime ( $n > 1$  and  $\theta > 0$ ), we find a novel transition from an Omori decay law with an exponent  $1 - \theta$  at early times to an explosive exponential increase of the seismicity rate at large times. The case  $\theta < 0$  leads to an infinite  $n$ -value, due to the slow decay with time of the local Omori law. In this case, we find a transition from an Omori law with exponent  $1 - |\theta|$  similar to the local law, to an exponential increase at large times, with a crossover time  $\tau$  different from the characteristic time  $t^*$  found in the case  $\theta > 0$ . These results can rationalize many of the stylized facts reported for foreshock and aftershock sequences, such as the suggestion that a small  $p$ -value may be a precursor of a large earthquake, the relative seismic quiescence preceding large aftershocks, the positive correlation between  $b$  and  $p$ -values, the observation that great earthquakes are sometimes preceded by a decrease of  $b$ -value and the acceleration of the seismicity preceding great earthquakes.

Finally, we would like to mention that our analysis can be generalized to various other choices of the local Omori law and of the magnitude distribution. The ETAS model can also be extended to describe the spatial distribution of the seismicity [*Helmstetter and Sornette, 2002*].

## 5.6 Appendix : technical derivation of the analytical solution

In this appendix, we provide the technical derivation of the results used in the main text for the sub-critical and super-critical regimes. We start from equation (5.9).

### General derivation for $\theta > 0$

The integral over  $\tau$  is the convolution of  $\lambda_{m'}$  with  $\phi_{m'}$ . Since there is an origin of time and we have a convolution operator, the natural tool is the Laplace transform  $\hat{f}(\beta) \equiv \int_0^{+\infty} f(t)e^{-\beta t} dt$ . Applying the Laplace transform to (5.9) yields

$$\hat{\lambda}_m(\beta) = \hat{S}(\beta, m) + P(m) \int_{m_0}^{\infty} dm' \hat{\phi}_{m'}(\beta) \hat{\lambda}_{m'}(\beta) . \quad (5.24)$$

where the r.h.s. has used the convolution theorem that the Laplace transform of a convolution of two functions is the product of the Laplace transform of the two functions. Let us now apply the integral operator  $\int_{m_0}^{\infty} dm \hat{\phi}_m(\beta)$  on both sides of (5.24) and define

$$\lambda(\beta) \equiv \int_{m_0}^{\infty} dm \hat{\phi}_m(\beta) \hat{\lambda}_m(\beta) , \quad (5.25)$$

$$Q(\beta) \equiv \int_{m_0}^{\infty} dm \hat{\phi}_m(\beta) P(m) , \quad (5.26)$$

and

$$\mathcal{S}(\beta) \equiv \int_{m_0}^{\infty} dm \hat{\phi}_m(\beta) \hat{S}(\beta, m) . \quad (5.27)$$

Then, expression (5.24) yields

$$\lambda(\beta) = \mathcal{S}(\beta) + Q(\beta)\lambda(\beta) , \quad (5.28)$$

whose solution is

$$\lambda(\beta) = \frac{\mathcal{S}(\beta)}{1 - Q(\beta)} . \quad (5.29)$$

This expression gives  $\lambda_m(t)$  after inversion of the integral operator  $\int_{m_0}^{\infty} dm \hat{\phi}_m(\beta)$  and of the Laplace transform.

The key quantity controlling the dependence of  $\lambda_m(t)$  is

$$Q(\beta) = \frac{K}{\theta c^\theta} \left( \int_{m_0}^{\infty} dm 10^{\alpha(m-m_0)} P(m) \right) \left( \theta \int_0^{\infty} dt \frac{e^{-\beta ct}}{(t+1)^{1+\theta}} \right) , \quad (5.30)$$

obtained by replacing the expression of  $\phi_m(t)$  defined in (5.1) and normalizing  $t/c \rightarrow t$ . Using  $P(m) = \ln(10) b 10^{-b(m-m_0)}$ , we obtain

$$Q(\beta) = n R(\beta c) , \quad (5.31)$$

where we have used the expression (5.3) of  $n$  and defined

$$R(\beta) \equiv \theta \int_0^{\infty} dt \frac{e^{-\beta t}}{(t+1)^{1+\theta}} = \theta e^{\beta} \beta^{\theta} \Gamma(-\theta, \beta) = 1 - e^{\beta} \beta^{\theta} \Gamma(1-\theta, \beta), \quad (5.32)$$

where

$$\Gamma(a, x) = \int_x^{\infty} dt e^{-t} t^{a-1} \quad (5.33)$$

is the (complementary) incomplete Gamma function [Abramowitz and Stegun, 1964] and we have used  $\Gamma(1+a, x) = a\Gamma(a, x) + x^a e^{-x}$  obtained by integration by part. Using the expansion of the incomplete Gamma function [Olver, 1974]

$$\Gamma(a, x) = \Gamma(a) - \sum_{k=0}^{+\infty} \frac{(-1)^k x^{a+k}}{k! (a+k)}, \quad \text{for } a > 0, \quad (5.34)$$

we obtain

$$R(\beta) = 1 - \Gamma(1-\theta) \beta^{\theta} + \frac{1}{1-\theta} \beta + \mathcal{O}(\beta^{1+\theta}, \beta^2, \beta^{2+\theta}, \beta^3, \dots). \quad (5.35)$$

It is possible, using the full expansion of the incomplete Gamma function, to estimate the value of  $\lambda(\beta)$  when the second term  $\frac{1}{1-\theta} \beta$  of the expansion cannot be neglected anymore compared with the term proportional to  $\beta^{\theta}$ . Thus, the expansion (5.35) using the first two terms only  $R(\beta) = 1 - \Gamma(1-\theta) \beta^{\theta}$  becomes invalid for  $\beta > [\Gamma(1-\theta)(1-\theta)]^{1/(1-\theta)}$ , *i.e.*, for times smaller than  $[\Gamma(2-\theta)]^{-1/(1-\theta)}$ . For all practical purpose, this is a small value and we can use safely the expansion (5.35) in the following calculations.

Let us now make explicit  $\lambda(\beta)$  :

$$\lambda(\beta) = \frac{K}{\theta c^{\theta}} R(\beta c) \int_{m_0}^{\infty} dm 10^{\alpha(m-m_0)} \int_0^{\infty} dt \lambda_m(t) e^{-\beta t}. \quad (5.36)$$

Using the definition of  $\lambda(t)$  given by (5.11) and the factorization of the times and magnitudes in (5.36), we obtain

$$\lambda(\beta) = nR(\beta c) \hat{\lambda}(\beta), \quad (5.37)$$

where

$$\hat{\lambda}(\beta) = \int_0^{\infty} dt \lambda(t) e^{-\beta t}. \quad (5.38)$$

Replacing (5.37) in (5.29) gives

$$\hat{\lambda}(\beta) = \frac{\mathcal{S}(\beta)}{nR(\beta c) (1 - nR(\beta c))}. \quad (5.39)$$

When a great earthquake occurs at the origin of time  $t = 0$  with magnitude  $M$ ,  $S(t, m) = \delta(t) \delta(m - M)$ , expression (5.27) gives

$$\mathcal{S}(\beta) = \frac{K}{\theta c^{\theta}} 10^{\alpha(M-m_0)} R(\beta c). \quad (5.40)$$

Thus, expression (5.39) becomes

$$\hat{\lambda}(\beta) = \frac{b - \alpha}{b} \frac{10^{\alpha(M-m_0)}}{(1 - nR(\beta c))}. \quad (5.41)$$

The dependence of  $\hat{\lambda}(\beta)$  on  $\beta$  is uniquely controlled by the denominator  $1 - nR(\beta c)$ .

## The sub-critical regime $n < 1$

The analysis proceeds exactly as in [Sornette and Sornette, 1999a]. For  $0 < \theta < 1$ , and for small  $\beta$  (large times),  $\hat{\lambda}(\beta)$  given by (5.41) is

$$\hat{\lambda}(\beta) = \frac{S_0}{1 - n[1 - d(\beta c)^\theta]} = \frac{S_0}{(1 - n)} \left( \frac{1}{1 + (\beta t^*)^\theta} \right), \quad (5.42)$$

where  $t^*$  is defined by (5.12) and the external source term  $S_0$  is defined by (5.13). We retrieve equation (13) of [Sornette and Sornette, 1999a] with the correspondence  $t_0 \rightarrow c$ .

Two cases must be distinguished.

- $\beta t^* < 1$  corresponds to  $t > t^*$  by identifying as usual the dual variable  $\beta$  to  $t$  in the Laplace transform with  $1/t$ . In this case, we can expand  $\frac{1}{1 + (\beta t^*)^\theta}$ , which leads to

$$\hat{\lambda}_{t > t^*}(\beta) \sim \frac{S_0}{1 - n} [1 - (\beta t^*)^\theta]. \quad (5.43)$$

We recognize the Laplace transform of a power law of exponent  $\theta$ , *i.e.*

$$\lambda_{t > t^*}(t) \sim \frac{S_0}{\Gamma(\theta)(1 - n)} \frac{t^{*\theta}}{t^{1+\theta}} \quad \text{for } t > t^* . \quad (5.44)$$

- For  $t < t^*$ ,  $\beta t^* > 1$  and (5.42) can be written with a good approximation as

$$\hat{\lambda}_{t < t^*}(\beta) = \frac{S_0}{(1 - n)(\beta t^*)^\theta} \sim \beta^{-\theta}. \quad (5.45)$$

Denoting  $\Gamma(z) \equiv \int_0^{+\infty} dt e^{-t} t^{z-1}$ , we see that  $\int_0^{+\infty} dt e^{-\beta t} t^{z-1} = \Gamma(z)\beta^{-z}$ . Comparing with (5.45), we thus get

$$\lambda_{t < t^*}(t) \sim \frac{S_0}{\Gamma(\theta)(1 - n)} \frac{t^{*\theta}}{t^{1-\theta}} \quad \text{for } t < t^* . \quad (5.46)$$

We verify the self-consistency of the two solutions  $\lambda_{t > t^*}(t)$  and  $\lambda_{t < t^*}(t)$  by checking that  $\lambda_{t > t^*}(t^*) = \lambda_{t < t^*}(t^*)$ . In other words,  $t^*$  is indeed the transition time at which the “short-time” regime  $\lambda_{t < t^*}(t)$  crosses over to the “long-time” regime  $\lambda_{t > t^*}(t)$ .

We now calculate the full expression of  $\lambda(t)$  valid at all times. We expand

$$\frac{1}{(\beta t^*)^\theta + 1} = \frac{1}{(\beta t^*)^\theta} \frac{1}{(\beta t^*)^{-\theta} + 1} = \frac{1}{(\beta t^*)^\theta} \sum_{k=0}^{\infty} (-1)^k (\beta t^*)^{-k\theta}, \quad (5.47)$$

Thus, by taking the inverse Laplace transform

$$\lambda(t) = \frac{S_0}{1 - n} \frac{1}{2\pi i} \int_{c-i\infty}^{c+i\infty} d\beta e^{\beta t} \sum_{k=0}^{\infty} (-1)^k (\beta t^*)^{-(k+1)\theta}. \quad (5.48)$$

The inverse Laplace transform of  $\beta^{-(k+1)\theta}$  is  $t^{(k+1)\theta-1}/\Gamma((k+1)\theta)$ . This allows us to write

$$\lambda(t) = \frac{S_0}{1 - n} \frac{t^{*\theta}}{t^{1-\theta}} \sum_{k=0}^{\infty} (-1)^k \frac{(t/t^*)^{k\theta}}{\Gamma((k+1)\theta)} \quad (5.49)$$

Expression (5.49) provides the solution that describes the cross-over from the  $1/t^{1-\theta}$  Omori's law (5.46) at early times to the  $1/t^{1+\theta}$  Omori's law (5.44) at large times. The series  $\sum_{k=0}^{\infty} (-1)^k \frac{(t/t^*)^{k\theta}}{\Gamma((k+1)\theta)}$  is a series representation of a special Fox function [Glöckle and Nonnenmacher, 1993] and it is also related to the generalized Mittag-Leffler function.

For large times  $t \gg t^*$ , a direct numerical evaluation of  $\lambda(t)$  from equation (5.49) is impossible due to the very slow convergence of the series. The padé summation method [Bender and Orzag, 1978] can be used to improve the convergence of this series and to evaluate numerically (5.49) for all times.

### The super-critical regime $n > 1$

We can analyze this regime by putting  $n > 1$  in (5.41) which can be written under a form similar to (5.42) :

$$\hat{\lambda}(\beta) = \frac{S_0}{(1 - nR(\beta c))} = \frac{S_0}{dn(\beta c)^\theta - (n-1)} = \frac{S_0}{(n-1)} \left( \frac{1}{(\beta t^*)^\theta - 1} \right), \quad (5.50)$$

In the second and third equalities of (5.50), we have used the small  $\beta$ -expansion (5.35) of  $R(\beta c)$  valid for  $0 < \theta < 1$ .

At early times  $c \ll t \ll t^*$ , *i.e.*,  $\beta t^* \gg 1$ ,  $\hat{\lambda}(\beta) \approx \frac{S_0}{(n-1)(\beta t^*)^\theta}$  which is the Laplace transform of (5.46) : thus, the early decay rate of aftershocks is the same  $\sim 1/t^{1-\theta}$  as for the sub-critical regime (5.46). However, as time increases, the dual  $\beta$  of  $t$  decreases and  $\hat{\lambda}(\beta)$  grows faster than  $\sim (\beta c)^{-\theta}$  due to the presence of the negative term  $-(n-1)$ . This can be seen as an apparent exponent  $\theta_{\text{app}} > \theta$  increasing progressively such that  $dn(\beta t^*)^\theta - 1 \approx C(\beta t^*)^{\theta_{\text{app}}}$ , where  $C$  is a constant. Note that  $\theta_{\text{app}} > \theta$  for the pure power law  $C(\beta c)^{\theta_{\text{app}}}$  to mimic the acceleration induced by the negative correction  $-(n-1)$ . The seismic rate will thus decay approximately as  $\sim 1/t^{1-\theta_{\text{app}}(t)}$ .

The large time behavior is controlled by the pole at  $\beta = 1/t^*$  of  $\hat{\lambda}(\beta)$ . Close to  $1/t^*$ ,

$$\hat{\lambda}(\beta) \approx \frac{S_0}{(n-1)\theta} \frac{1}{\beta t^* - 1}. \quad (5.51)$$

The inverse Laplace transform is thus

$$\lambda(t) = (2\pi i)^{-1} \int_{c-i\infty}^{c+i\infty} d\beta e^{\beta t} \hat{\lambda}(\beta) \sim \frac{S_0}{(n-1)t^*\theta} e^{t/t^*} \quad (5.52)$$

exhibiting the exponential growth at large times. Expression (5.12) shows that  $1/t^* \sim |1-n|^{1/\theta}$ . Thus, as expected, the exponential growth disappears as  $n \rightarrow 1^+$ .

We now calculate the full expression of  $\lambda(t)$  valid at all times. We expand

$$\frac{1}{(\beta t^*)^\theta - 1} = \frac{1}{(\beta t^*)^\theta} \frac{1}{1 - (\beta t^*)^{-\theta}} = \frac{1}{(\beta t^*)^\theta} \sum_{k=0}^{\infty} (\beta t^*)^{-k\theta}, \quad (5.53)$$

Thus

$$\lambda(t) = \frac{S_0}{(n-1)} \frac{1}{2\pi i} \int_{c-i\infty}^{c+i\infty} d\beta e^{\beta t} \sum_{k=0}^{\infty} (\beta t^*)^{-(k+1)\theta}. \quad (5.54)$$

The inverse Laplace transform of  $1/\beta^{(k+1)\theta}$  is  $t^{(k+1)\theta-1}/\Gamma((k+1)\theta)$ . This allows us to write

$$\lambda(t) = \frac{S_0}{(n-1)} \frac{t^{*-\theta}}{t^{1-\theta}} \sum_{k=0}^{\infty} \frac{(t/t^*)^{k\theta}}{\Gamma((k+1)\theta)} \quad (5.55)$$

Expression (5.55) provides the solution that describes the cross-over from the  $1/t^{1-\theta}$  Omori's law at early times to the exponential growth at large times. Note that the solution (5.55) can be obtained directly from (5.49) by removing the alternating sign  $(-1)^k$  in the sum. The solution (5.55) retrieves the two regimes discussed before.

1. For  $t < t^*$ , the sum in (5.55) is close to  $1/\Gamma(\theta)$ , which leads to

$$\lambda(t) \approx \frac{S_0}{\Gamma(\theta)(n-1)} \frac{t^{*-\theta}}{t^{1-\theta}}. \quad (5.56)$$

2. For  $t \geq t^*$ , the sum dominates. The sum is very similar to the series expansion of  $e^{t/t^*}$  and is actually proportional to  $e^{t/t^*}$  for large  $t$ . This result is obvious for  $\theta = 1$  since the series expansion becomes identical to that of  $e^{t/t^*}$ . This can be justified for other values of  $\theta$  as follows. For  $\theta \rightarrow 0$ , the discrete sum transforms into a continuous integral of the type

$$\int_0^{\infty} dx t^x / \Gamma(x). \quad (5.57)$$

A saddle-node approximation, performed using the Stirling approximation (which already gives a very good precision for small  $z$ )  $\Gamma(z) \approx \sqrt{2\pi} e^{-z} z^{z-\frac{1}{2}}$ , shows that the saddle-node of the integrand occurs for  $x \approx t/t^*$ , which then gives  $\lambda(t) \sim e^{t/t^*}$ . For arbitrary  $\theta$ , we can use the Poisson's summation rule

$$\sum_{r=-\infty}^{+\infty} f(r) = \int_{-\infty}^{+\infty} du f(u) + \sum_{q=1}^{+\infty} \int_{-\infty}^{+\infty} du f(u) \cos[2\pi qu], \quad (5.58)$$

on the function defined by

$$f(r) \equiv \frac{(t/t^*)^{r\theta}}{\Gamma(r\theta + \theta)}, \quad \text{for } r \geq 0 \quad (5.59)$$

and  $f(r) = 0$  for  $r < 0$ . The left-hand-side of (5.58) is nothing but the semi-infinite sum in (5.55). The first term in the right-hand-side retrieves the integral (5.57) encountered for the case  $\theta \rightarrow 0$ . This term thus contributes a term proportional to  $e^{t/t^*}$ . All the other terms contribute negative powers of  $t$  and are thus negligible compared to the exponential for  $t > t^*$ . This can be seen from the fact that each term with  $q \geq 1$  is similar to the sum in (5.49) for the subcritical case with alternating signs. The larger  $q$  is, the faster is the frequency of alternating signs and the smaller is the integral. The leading dependence  $\lambda(t) \sim e^{t/t^*}$  valid for any  $0 \leq \theta \leq 1$  retrieves the limiting behavior already given in (5.52) from a different approach for large times  $t \gg t^*$ . It has also been proved rigorously in [Ramselaar, 1990].

### Case $\theta < 0$ corresponding to a local Omori's law exponent $p < 1$

The general equation (5.9) still holds in this case and the general derivation starting with (5.24) up to (5.29) still applies. The key quantity controlling the dependence of  $\lambda_m(t)$  is still  $Q(\beta)$  defined by (5.30). Writing  $\theta = -|\theta|$ , we have

$$Q(\beta) = n_0 R'(\beta c), \quad (5.60)$$

where  $n_0$  is defined by (5.4) and

$$R'(\beta) \equiv \int_0^\infty dt \frac{e^{-\beta t}}{(t+1)^{1-|\theta|}} = e^\beta \beta^{-|\theta|} \Gamma(|\theta|, \beta) \quad (5.61)$$

where  $\Gamma(a, x)$  is the (complementary) incomplete Gamma function defined by (5.33). Using the exact expansion (5.34), we obtain

$$Q(\beta) = n_0 e^{\beta c} (\beta c)^{-|\theta|} \left( \Gamma(|\theta|) - \sum_{k=0}^{+\infty} \frac{(-1)^k (\beta c)^{|\theta|+k}}{k! (|\theta| + k)} \right). \quad (5.62)$$

For small  $\beta$ 's (*i.e.*, large times), expression (5.62) has the following leading behavior

$$Q(\beta) = n_0 \Gamma(|\theta|) (\beta c)^{-|\theta|} - \frac{n_0}{|\theta|} + n_0 \Gamma(|\theta|) (\beta c)^{1-|\theta|} + h.o.t. \quad (5.63)$$

where *h.o.t.* stands for higher-order terms in the expansion in increasing powers of  $\beta c$ .

The source term  $\mathcal{S}(\beta)$  in the denominator of  $\hat{\lambda}(\beta)$  given by (5.29) is now given by

$$\mathcal{S}(\beta) = K e^{|\theta|} 10^{\alpha(M-m_0)} R'(\beta c). \quad (5.64)$$

Expression (5.29) for  $\hat{\lambda}(\beta)$  then yields

$$\hat{\lambda}(\beta) = \frac{S_0}{1 - Q(\beta c)}, \quad (5.65)$$

where  $R'(\beta c)$  is given by (5.61),  $n_0$  is defined by (5.4) and  $S_0$  is defined by (5.13). The dependence of  $\hat{\lambda}(\beta)$  on  $\beta$  is uniquely controlled by the denominator  $1 - Q(\beta c) = 1 - n_0 R'(\beta c)$ .

Using (5.63), we get the leading behavior for small  $\beta c$

$$\begin{aligned} \hat{\lambda}(\beta) &= \frac{S_0}{1 + \frac{n_0}{|\theta|} - n_0 \Gamma(|\theta|) (\beta c)^{-|\theta|}} \\ &= \frac{S_0}{\left(1 + \frac{n_0}{|\theta|}\right) (1 - (\beta \tau)^{-|\theta|})} \end{aligned} \quad (5.66)$$

where the characteristic time  $\tau$  is given by (5.19).

At early times  $c < t < \tau$ ,  $(\beta \tau)^{-|\theta|} < 1$  so that

$$\hat{\lambda}(\beta) \approx \frac{S_0}{\left(1 + \frac{n_0}{|\theta|}\right)} \left(1 + (\tau \beta)^{-|\theta|}\right). \quad (5.67)$$

By applying the inverse Laplace transform, the constant term contributes a Dirac function  $\delta(t)$  which is irrelevant as the calculation is valid only for  $t > c$ . The other term  $(\tau\beta)^{-|\theta|}$  gives

$$\lambda(t) = \frac{S_0}{(1 + \frac{n_0}{|\theta|})\Gamma(|\theta|)} \frac{\tau^{-|\theta|}}{t^{1-|\theta|}} . \tag{5.68}$$

The early time behavior of  $\lambda(t)$  is thus similar to the local Omori law  $1/t^{1-|\theta|}$ .

Similarly to the super-critical case  $n > 1$  of the regime  $\theta > 0$ , the long time dependence of the regime  $\theta < 0$  is controlled by a simple pole  $\beta^* = \frac{1}{\tau}$ .

Thus, the long-time seismicity is given by

$$\lambda(t) = \frac{S_0}{(1 + \frac{n_0}{|\theta|})\tau|\theta|} e^{t/\tau} \tag{5.69}$$

We can also calculate the full expression of  $\lambda(t)$  valid at all times  $t > c$ . We expand

$$\frac{1}{1 - (\beta\tau)^{-|\theta|}} = \sum_{k=0}^{\infty} (\beta\tau)^{-k|\theta|} , \tag{5.70}$$

Removing the constant term, which by the inverse Laplace transform contributes a Dirac function  $\delta(t)$  which is irrelevant as the calculation is valid only for  $t \gg c$ , we get

$$\lambda(t) = \frac{S_0}{(1 + \frac{n_0}{|\theta|})} \frac{1}{2\pi i} \int_{c-i\infty}^{c+i\infty} d\beta e^{\beta t} \sum_{k=1}^{\infty} (\beta\tau)^{-k|\theta|} . \tag{5.71}$$

The inverse Laplace transform of  $1/\beta^{k|\theta|}$  is  $t^{k|\theta|-1}/\Gamma(k|\theta|)$ . This allows us to write

$$\lambda(t) = \frac{S_0}{(1 + \frac{n_0}{|\theta|})} \frac{1}{t} \sum_{k=1}^{\infty} \frac{(t/\tau)^{k|\theta|}}{\Gamma(k|\theta|)} \tag{5.72}$$

Expression (5.72) provides the solution that describes the cross-over from the local Omori law  $1/t^{1-|\theta|}$  at early times to the exponential growth at large times.

### Acknowledgments

We are very grateful to J.R. Grasso, G. Ouillon, V. Pisarenko, A. Sornette and D. Vere-Jones for useful suggestions and discussions and to D. Vere-Jones as a referee for his constructive remarks and for pointing out the relevant mathematical literature on “self-exciting” point processes. We thank Y. Ogata for kindly providing a copy of Ramselaar’s Master thesis. This work was partially supported by french INSU-Natural Hazard grant (A. H.) and by the James S. McDonnell Foundation 21st century scientist award/studying complex system (D. S.).



## Chapitre 6

# On the occurrence of finite-time singularities in epidemic models of rupture, earthquakes and starquakes

Didier Sornette

Laboratoire de Physique de la Matière Condensée, Université de Nice-Sophia Antipolis, and  
Department of Earth and Space Sciences and Institute of Geophysics and Planetary Physics,  
University of California, Los Angeles, California.

Agnès Helmstetter

Laboratoire de Géophysique Interne et Tectonophysique,  
Université Joseph Fourier, BP 53X, 38041 Grenoble Cedex, France.

Article publié sous la référence *Physica Review Letters*, 89, 158501, 2002.

### Abstract

We present a new kind of critical stochastic finite-time-singularity, relying on the interplay between long-memory and extreme fluctuations. We illustrate it on the well-established epidemic-type aftershock (ETAS) model for aftershocks, based solely on the most solidly documented stylized facts of seismicity (clustering in space and in time and power law Gutenberg-Richter distribution of earthquake energies). This theory accounts for the main observations (power law acceleration and discrete scale invariant structure) of critical rupture of heterogeneous materials, of the largest sequence of starquakes ever attributed to a neutron star as well as of earthquake sequences.

A large portion of the current work on rupture and earthquake prediction is based on the search for precursors to large events in the seismicity itself. Observations of the acceleration of seismic moment leading up to large events and “stress shadows” following them have been interpreted as evidence that seismic cycles represent the approach to and retreat from a critical state of a fault network [Sornette and Sammis, 1995; Saleur et al., 1996]. This “critical state” concept is fundamentally different from the long-time view of the crust as evolving spontaneously in a statistically stationary critical state, called self-organized criticality (SOC) [Bak and Tang, 1989; Sornette and Sornette, 1989]. In the SOC view, all events belong to the same global population and participate in shaping the self-organized critical state. Large earthquakes are inherently unpredictable because a big earthquake is simply a small earthquake that did not stop. By contrast, in the critical point view, a great earthquake plays a special role and signals the end of a cycle on its fault network. The dynamical organization is not statistically stationary but evolves as the great earthquake becomes more probable. Predictability might then become possible by monitoring the approach of the fault network towards the critical state. This hypothesis is proposed in [Sornette and Sammis, 1995; Saleur et al., 1996] is the theoretical induction of a series of observations of accelerated seismicity [Sykes and Jaumé, 1990; Bufe and Varnes, 1993] which has been later strengthened by several other observations [Harris and Simpson, 1996; Knopoff et al., 1996; Jones and Hauksson, 1997; Bowman et al., 1998; Brehm and Braile, 1998; Jaumé and Sykes, 1999; Ouillon and Sornette, 2000; Zoller et al., 2001; Yin, 2001]. Theoretical support has also come from simple computer models of critical rupture [Sornette and Vanneste, 1992; Vanneste and Sornette, 1992; Sornette et al., 1992; Sahimi and Arbabi, 1996; Andersen et al., 1997] and experiments of material rupture [Anifrani et al., 1999; Lamainière et al., 1996; Garcimartin et al., 1997; Johansen and Sornette, 2000], cellular automata, with [Anghel et al., 1999; Sà Martins et al., 2001] and without [Huang et al., 1998; Sammis and Smith, 1999] long-range interaction, and from granular simulators [Mora et al., 2000; Mora and Place, 2001]. Models of regional seismicity with more faithful fault geometry have been developed that also show accelerating seismicity before large model events [Heimpel, 1997; Bowman and King, 2001a; Ben-zion and Lyakhovskiy, 2001].

There are at least five different mechanisms that are known to lead to critical accelerated seismicity of the form

$$N(t) \propto 1/(t_c - t)^m \quad (6.1)$$

ending at the critical time  $t_c$ , where  $N(t)$  is the seismicity rate (or acoustic emission rate for material rupture). Such finite-time-singularities are quite common and have been found in many well-established models of natural systems, either at special points in space such as in the Euler equations of inviscid fluids, in vortex collapse of systems of point vortices, in the equations of General Relativity coupled to a mass field leading to the formation of black holes, in models

of micro-organisms aggregating to form fruiting bodies, or in the more prosaic rotating coin (Euler’s disk). They all involve some kind of positive feedback, which in the rupture context can be the following (see [Sammis and Sornette, 2002] for a review) : sub-critical crack growth [Das and Scholz, 1981], geometrical feedback in creep rupture [Krajcinovic, 1996], feedback of damage on the elastic coefficients with strain dependent damage rate [Ben-Zion and Lyahkovsky, 2001], feedback in a percolation model of regional seismicity [Sammis and Sornette, 2002], feedback in a stress-shadow model for regional seismicity [Bowman and King, 2001a ; Sammis and Sornette, 2002].

While these mechanisms are plausible, their relevance to the earth crust remains unproven. Here, we present a novel mechanism leading to a new kind of critical stochastic finite-time-singularity in the seismicity rate, using the well-established epidemic-type aftershock sequence (ETAS) model for aftershocks, introduced by [Kagan and Knopoff, 1981 ; 1987 ; Ogata, 1988], based solely on the most solidly documented stylized facts of seismicity mentioned above. The adjective “stochastic” emphasizes the fact that the critical time  $t_c$  is determined in large part by the specific sets of innovations of the random process. We show that, in a finite domain of its parameter space, the rate of seismic activity in the ETAS model diverges in finite time according to (6.1). The underlying mechanism relies on large deviations occurring in an explosive branching process. One of the advantage of this discovery is to be able to account for the observations of accelerated seismicity and acoustic emission in material failure, without invoking any new ingredient other than those already well-established empirically. We apply this insight to quantify the longest available starquake sequence of a neutron star soft  $\gamma$ -ray repeaters.

We shall use the example of earthquakes but the model applies similarly to microcracking in materials. The ETAS model is a generalization of the modified Omori law, in that it takes into account the secondary aftershock sequences triggered by all events. The modified Omori’s law states that the occurrence rate of the direct aftershock-daughters from an earthquake decreases with the time from the mainshock according to the “bare propagator”  $K/(t + c)^p$ . In the ETAS model, all earthquakes are simultaneously mainshocks, aftershocks and possibly foreshocks. Contrary to the usual definition of aftershocks, the ETAS model does not impose an aftershock to have an energy smaller than the mainshock. This way, the same law describes both foreshocks, aftershocks and mainshocks. An observed “aftershock” sequence of a given earthquake (starting the clock) is the result of the activity of all events triggering events triggering themselves other events, and so on, taken together. The corresponding seismicity rate (the “dressed propagator”), which is given by the superposition of the aftershock sequences of all events, is the quantity we derive here.

Each earthquake (the “mother”) of energy  $E_i \geq E_0$  occurring at time  $t_i$  gives birth to other events (“daughters”) of any possible energy, chosen with the Gutenberg-Richter density distribution  $P(E) = \mu/(E/E_0)^{1+\mu}$  with exponent  $\mu \simeq 2/3$ , at a later time between  $t$  and  $t + dt$

at the rate

$$\phi_{E_i}(t - t_i) = \rho(E_i) \Psi(t - t_i) . \quad (6.2)$$

$\rho(E_i) = K (E_i/E_0)^a$  gives the number of daughters born from a mother with energy  $E_i$ , with the same exponent  $a$  for all earthquakes. This term accounts for the fact that large mothers have many more daughters than small mothers because the larger spatial extension of their rupture triggers a larger domain.  $E_0$  is a lower bound energy below which no daughter is triggered.  $\Psi(t - t_i) = \frac{\theta c^\theta}{(t - t_i + c)^{1+\theta}}$  is the normalized waiting time distribution (local Omori's law or "bare propagator") giving the rate of daughters born a time  $t - t_i$  after the mother.

The ETAS model is fundamentally a "branching" model [Vere-Jones, 1977] with no "loops", i.e., each event has a unique "mother-mainshock" and not several. This "mean-field" or random phase approximation allows us to simplify the analysis while still keeping the essential physics in a qualitative way. The problem is to calculate the "dressed" or "renormalized" propagator (rate of seismic activity) that includes the whole cascade of secondary sequences [Sornette and Sornette, 1999a]. The key parameter is the average number  $n$  (or "branching ratio") of daughter-earthquakes created per mother-event, summed over all possible energies.  $n$  is equal to the integral of  $\phi_{E_i}(t - t_i)$  over all times after  $t_i$  and over all energies  $E_i \geq E_0$ . This integral converges to a finite value  $n < \infty$  for  $\theta > 0$  (local Omori's law decay faster than  $1/t$ ) and for  $a < \mu$  (not too large a growth of the number of daughters as a function of the energy of the mother). The resulting average rate  $N(t)$  of seismicity is the solution of the Master equation [Helmstetter and Sornette, 2002a]

$$N(t) = \int_0^t d\tau N(\tau) \int_{E_0}^{E_{\max}(t)} dE' P(E') \phi_{E'}(t - \tau) \quad (6.3)$$

giving the number  $N(t)dt$  of events occurring between  $t$  and  $t + dt$  of any possible energy. We have made explicit the upper bound  $E_{\max}(t)$  equal to the typical maximum earthquake energy sampled up to time  $t$ . For  $a < \mu$ , this upper bound has no impact on the results and can be replaced by  $+\infty$  [Helmstetter and Sornette, 2002a]. There may be a source term  $S(t)$  to add to the r.h.s. of (6.3), corresponding to either a constant background seismicity or to a large triggering earthquake. In this last case, the rate  $N(t)$  solution of (6.3) is the "dressed" propagator giving the renormalized Omori's law. A rich behavior, which has been fully classified by a complete analytical treatment [Helmstetter and Sornette, 2002a], has been found : sub-criticality  $n < 1$  [Sornette and Sornette, 1999a] and super-criticality  $n > 1$  [Helmstetter and Sornette, 2002a], where  $n$  depends on the control parameters  $\mu$ ,  $a$ ,  $\theta$ ,  $K$  and  $c$ . With a single value of the exponent  $1 + \theta$  of the "bare" propagator  $\Psi(t) \sim 1/t^{1+\theta}$ , we obtain a continuum of apparent exponents for the global rate of aftershocks [Helmstetter and Sornette, 2002] which may account for the observed variability of Omori's exponent  $p$  around  $p = 1$  reported by many workers.

Here, we explore the regime  $a \geq \mu$ , for which  $n$  is infinite. This signals the impact of large earthquake energies, suggesting the relevance of the upper bound  $E_{\max}(t)$  in (6.3). This case is actually observed in real seismicity by Drakatos et al. [2001] who obtained  $a > \mu$  for some

aftershock sequences in Greece, and by Guo and Ogata [1997] who found  $a > \mu$  for 13 out of 34 aftershock sequences in Japan. This case  $a > \mu$  also characterizes the seismic activity preceding the 1984  $M = 6.8$  Nagano Prefecture earthquake [Ogata, 1989]. After the mainshock, the seismicity returned in the sub-critical regime  $\theta > 0$ ,  $a < \mu$  and  $n < 1$ .

This case  $a \geq \mu$  is similar to that found underlying various situations of anomalous transport [Bouchaud and Georges, 1990 ; Sornette, 2000a] : in this regime of large fluctuations, the integral over earthquake energies is dominated by the upper bound. The maximum energy  $E_{\max}(t)$  sampled by  $N(t)\Delta t$  earthquakes is given by the standard condition  $N(t)\Delta t \int_{E_0}^{E_{\max}(t)} dE' P(E') \approx 1$ . This yields the robust median estimate  $E_{\max}(t) \sim [N(t)\Delta t]^{1/\mu}$ . Actually,  $E_{\max}(t)$  is itself distributed according to the Gutenberg-Richter distribution and thus exhibits large fluctuations from realization to realization, as we can see in Fig. 1. Putting this estimation of  $E_{\max}(t)$  in (6.3), we get

$$N(t) \propto \int_0^t d\tau \frac{N(\tau)}{(t - \tau + c)^{1+\theta}} [N(\tau)\Delta\tau]^{(a-\mu)/\mu} . \quad (6.4)$$

Let us note the appearance of the new term  $[N(\tau)\Delta\tau]^{(a-\mu)/\mu}$  resulting from the contribution of the upper bound in the integral  $\int dE' P(E')$ . This term replaces the constant found for the case  $a < \mu$ . Equation (6.4) shows that the exploration of larger and larger events in the tail in the Gutenberg-Richter distribution transforms the *linear* Master equation (6.3) into a *non-linear* equation : the non-linearity expresses a positive feedback according to which the larger is the rate  $N(t)$  of seismicity, the larger is the maximum sampled earthquake, and the larger is the number of daughters resulting from these extreme events. This process self-amplifies and leads to the announced finite-time singularity (6.1). However, to complete the derivation, we need to determine the yet unspecified time increment  $\Delta\tau$ . If  $N(\tau)$  obeys (6.1),  $\Delta\tau$  is not a constant that can be factorized away : it is determined by the condition that, over  $\Delta\tau$ ,  $N(\tau)$  does not change “significantly” in the interval  $[\tau, \tau + \Delta\tau]$ , i.e., no more than by a constant factor. Using the assumed power law solution (6.1), this gives  $\Delta\tau \propto t_c - \tau$ . Using this and inserting (6.1) into (6.4), we get,

$$\begin{aligned} m &= \frac{a/\mu}{(a/\mu) - 1} , & t_c - t \ll c \\ m &= \frac{(a/\mu) - 1 - \theta H(-\theta)}{(a/\mu) - 1} , & t_c - t \gg c , \end{aligned} \quad (6.5)$$

where  $H$  is the Heaviside function. Note that (6.5) predicts an exponent  $m > 1$  which is independent of  $\theta$  close to the critical time  $t_c$ . This is due to the fact that the time decay of the Omori’s kernel is not felt for  $t_c - t \leq c$ , where  $c$  acts as an ultraviolet cut-off. It is also interesting to find that  $m = 1$  independently of  $a$  and  $\theta$  in the regime  $\theta > 0$  (with of course  $a > \mu$ ) for which Omori’s kernel  $\sim 1/t^{1+\theta}$  decays sufficiently fast at long times that the predominant contributions to the present seismic rate come from events in the immediate past of the present time of observation. In contrast, the case  $\theta < 0$  is analogous to the anomalous long-time memory regime [Bouchaud and Georges, 1990 ; Sornette, 2000a] which keeps for ever the impact of past

events on future rates.

This prediction, based on the careful analysis of the integral in (6.4), has been verified by direct numerical evaluation of the equation (6.4). We have also checked that numerical Monte Carlo simulations of the ETAS model generates catalogs of events following this prediction, in an ensemble or median sense. Figure 6.1 shows the cumulative number  $\mathcal{N}(t) = \int_0^t d\tau N(\tau)$  of events for a typical realization of the ETAS model and compares it with  $E_{\max}(t)$  to illustrate that  $\mathcal{N}(t)$  is mostly controlled by the sampling of  $E_{\max}(t)$ , as discussed in the derivation of expression (6.4) leading to the finite-time-singularity (6.1). For the value  $\mu = 1$  chosen here,  $E_{\max}(t)$  follows the same power law as the cumulative number, as observed. The dashed line is the power law prediction (6.1) with (6.5) for  $a/\mu = 1.5$  and  $\theta = -0.2$  with slope  $m - 1 = 0.4$ . We have also generated 500 such catalogs and report in the inset the distribution  $p(m)$  of exponents  $m$  obtained by a best fit of  $\mathcal{N}(t)$  for each of the 500 catalogs to a power law  $1/(t_c - t)^{m-1}$ . The median of  $p(m)$  is exactly equal to the prediction shown by the vertical thin line while the mode is very close to it. Note however a rather large dispersion which is expected from the highly intermittent dynamics characteristic of this extreme-dominated dynamics. We now report a few comparisons between the prediction (6.5) and the median value of the exponent  $m$  obtained from 500 simulations for the following parameters :  $\theta = -0.2$ ,  $a = 1.1$ ,  $\mu = 1$ , predicted  $m = 3.$ , median  $m = 1.93$ ;  $\theta = -0.2$ ,  $a = 1.3$ ,  $\mu = 1$ , predicted  $m = 1.67$ , median  $m = 1.61$ ;  $\theta = -0.1$ ,  $a = 1.5$ ,  $\mu = 1$ , predicted  $m = 1.20$ , median  $m = 1.29$ ;  $\theta = -0.3$ ,  $a = 1.5$ ,  $\mu = 1$ , predicted  $m = 1.60$ , median  $m = 1.62$ .  $\theta = -0.2$ ,  $a = 1.7$ ,  $\mu = 1$ , predicted  $m = 1.29$ , median  $m = 1.37$ ; For  $a > 1.8\mu$  and for  $\theta > 0$ , the fluctuations are so large that a reliable determination of the  $m$  becomes questionable.

Figure 6.1 shows that the power law singularities are decorated by quite strong steps or oscillations, approximately equidistant in the variable  $\ln(t_c - t)$ . This log-periodicity has been previously proposed as a possibly important signature of rupture and earthquake sequences approaching a critical point [Sornette and Sammis, 1995; Saleur et al., 1996; Anifrani et al., 1999; Lamainère et al., 1996; Garcimartin et al., 1997; Johansen and Sornette, 2000]. Here, we present a simple novel mechanism for this observation, based on a refinement of the previous argument leading to  $E_{\max}(t) \sim [N(t)\Delta t]^{1/\mu}$ . Indeed, the most probable value for the energy  $E_n$  of the  $n$ -th largest earthquake ranked from the largest  $E_1 = E_{\max}$  to the smallest one is given by  $E_n(t) = \{[\mathcal{N}(t)\mu + 1]/[n\mu + 1]\}^{1/\mu}$  [Sornette et al., 1996], where  $\mathcal{N}(t) = \int_0^t N(t')dt'$ . Let us assume that the last new record was broken at time  $t_1$  leading to  $E_1(t_1) = \{[\mathcal{N}(t_1)\mu + 1]/[\mu + 1]\}^{1/\mu}$ . The next record will occur at a time  $t_2 > t_1$  whose typical value is such that  $E_2(t_2) = E_1(t_1)$  (the last record  $E_1(t_1)$  becomes the second largest event  $E_2(t_2)$  when a new record  $E_1(t_2)$  occurs). For large  $\mathcal{N}(t)$ , this gives  $\frac{\mathcal{N}(t_2)}{\mathcal{N}(t_1)} = (2\mu + 1)/(\mu + 1)$ . The preferred scaling ratio of the average log-periodicity is  $\lambda \equiv (t_c - t_1)/(t_c - t_2) = [(2\mu + 1)/(\mu + 1)]^{1/(m-1)}$ . For  $\mu = 1$ ,  $\theta = -0.2$ ,  $m = 1.4$  corresponding to figure 1, we obtain  $\lambda \approx 2.3$ , which is compatible with the data.

The prediction (6.5) rationalizes the “inverse” Omori’s law close to  $1/(t_c - t)$  that has been

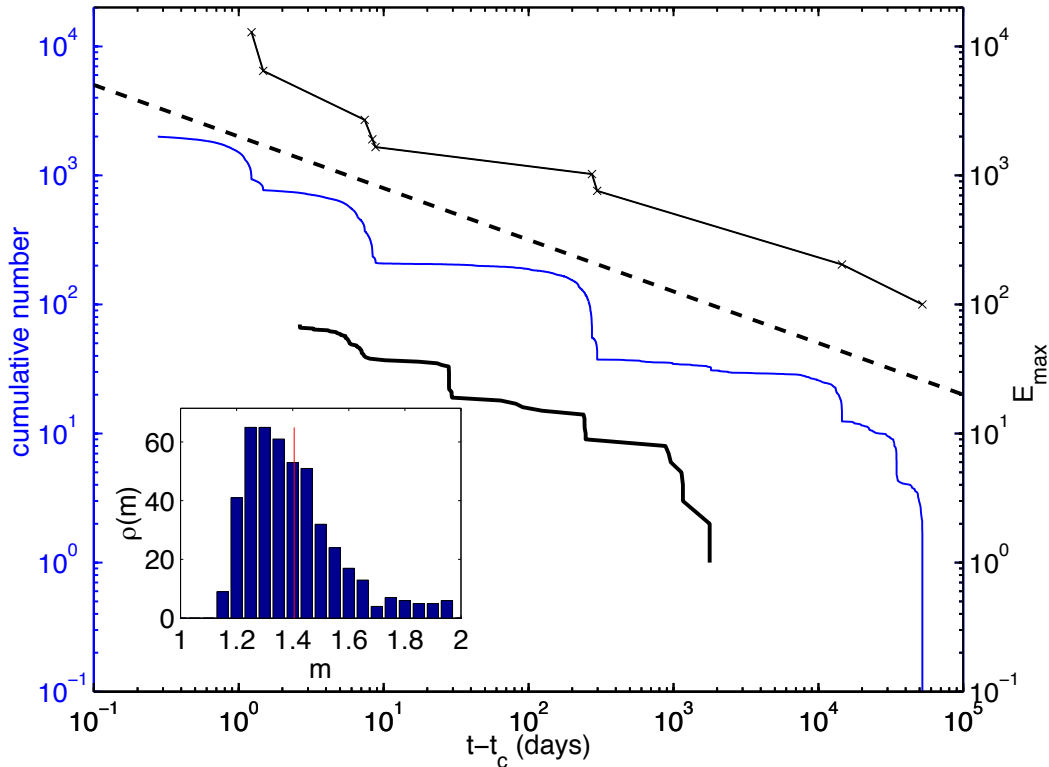


FIG. 6.1 – Cumulative number of events (scale on the left) as a function of the time from the critical point  $t_c$  for the starquake sequence (solid black line) and one typical simulation of the ETAS model (solid thin line) generated with  $\theta = -0.2$ ,  $a/\mu = 1.5$  and  $c = 0.001$  day. For the starquakes,  $t_c$  is the time of the strongest observed starquake in the sequence. The dashed line shows the theoretical exponent  $m - 1 = 0.4$  (6.5) for  $t_c - t > c$ . The crosses 'x' joined by straight segments give the time evolution of  $E_{\max}(t)$  (scale on the right). The inset gives the distribution of exponent measured for 500 numerical simulations. The median (vertical line) of the distribution of  $m$ -values is equal to the theoretical exponent  $m = 1.4$  (formula (6.5)).

documented for earthquake foreshocks [Jones and Molnar, 1976, 1979; Kagan and Knopoff, 1978]. The prediction (6.5) as well as the log-periodicity offers a general framework to rationalize several previous experimental reports of precursory acoustic emissions rates prior to global failures [Anifrani et al., 1999; Lamaignère et al., 1996; Garcimartin et al., 1997; Johansen and Sornette, 2000]. In this case, the energy release rate  $e(t)$  is found to follow a power law finite-time singularity. According to our theory,  $e(t) \propto N(t)E_{\max}(t) \propto 1/(t_c - t)^{m+(m-1)/\mu}$ .

Finally, we also show that this could explain starquakes catalogs. Starquakes are assumed to be ruptures of a super-dense 1-km thick crust made of heavy nuclei stressed by super-strong stellar magnetic field. They are observed through the associated flashes of soft  $\gamma$ -rays radiated during the rupture. Starquakes exhibit all the main stylized facts of their earthly siblings [Kosobokov et al., 2000]. The thick line in figure 6.1 shows the cumulative number of starquakes of the SGR1806-20 sequence, which is the longest sequence (of 111 events) ever attributed to the

same neutron star, as a function of the logarithm of the time  $t_c - t$  to failure. The starquake data is compatible with  $\mu = 1$  [Kossobokov et al., 2000],  $a = 1.5$  and  $\theta = -0.2$ , leading to  $m = 1.4$ .

### Acknowledgments

We are grateful to V. Keilis-Borok and V. Kossobokov for sharing the starquake data with us and W.-X. Zhou for discussions and help in a preliminary analysis of the data.

## Chapitre 7

# Predictability in the ETAS Model of Interacting Triggered Seismicity

Agnès Helmstetter

Laboratoire de Géophysique Interne et Tectonophysique,  
Université Joseph Fourier, BP 53X, 38041 Grenoble Cedex, France.

Didier Sornette

Laboratoire de Physique de la Matière Condensée, Université de Nice-Sophia Antipolis, and  
Department of Earth and Space Sciences and Institute of Geophysics and Planetary Physics,  
University of California, Los Angeles, California.

Submitted to *Journal of Geophysical Research*, 2002.

### Abstract

As part of an effort to develop a systematic methodology for earthquake forecasts, we use a simple model of seismicity based on interacting events which may trigger a cascade of earthquakes, well-known as the Epidemic-Type Aftershock Sequence model). The ETAS model is constructed on a (bare) Omori's law, the Gutenberg-Richter law and the idea that large events trigger more numerous aftershocks. We demonstrate the essential role played by the cascade of triggered seismicity in controlling the rate of aftershocks decay as well as the overall level of seismicity in the presence of a constant external seismicity source. The key parameter of this model, which controls the different regimes of the seismic activity, is the branching ratio, defined as the average number of triggered event per earthquake. This parameter is given two observable meanings as the ratio of triggered events over total seismicity and the ratio of secondary aftershocks over total aftershocks. We offer an analytical approach to account for the yet unobserved triggered seismicity adapted to the problem of forecasting future seismic rates at varying hori-

zons from the present. Tests presented on synthetic catalogs validate strongly the importance of taking into account all the cascades of still unobserved triggered events in order to predict correctly the future level of seismicity beyond a few minutes. We find a very strong predictability gain if one accepts to predict less than typically 25% of the large-magnitude targets. However, the probability gains degrade fast when one attempts to predict more than 30% of the targets. This results from the fact that a significant fraction of events remain uncorrelated from past seismicity. This delineates the fundamental limits underlying forecast skills, stemming from an intrinsic stochastic component in these interacting triggered seismicity models

## 7.1 Introduction

There are several solidly documented stylized facts in seismicity : (1) spatial clustering of earthquakes at many scales, (2) Gutenberg-Richter (GR) distribution of earthquake magnitudes and (3) clustering in time following large earthquakes, quantified by Omori's  $\approx 1/t^p$  law for aftershocks (with  $p \approx 1$ ). These “laws” are however only the beginning of a full model of seismic activity and earthquake triggering. In principle, if one could obtain a faithful representation (model) of the spatio-temporal organization of seismicity, one could use this model to develop algorithms for forecasting earthquakes. The ultimate quality of these forecasts would be limited by the quality of the model, the amount of data that can be used in the forecast and its reliability and precision, and the stochastic component of seismic activity. However, any earthquake prediction algorithm based on past seismicity explicitly or implicitly formulates assumptions on the physical mechanisms at the origin of the spatio-temporal organization of earthquakes. To simplify the discussion, two end-members can be considered. At one extreme, earthquakes are considered as “witnesses” of the organization of driving fields such as stress, fluid, underlying visco-elastic crust, and possibly others, driven themselves by tectonic forces and by their own internal dynamics. This view applies for instance to the simple textbook view of a single isolated fault loaded at a constant stress rate, in which characteristic earthquakes occur periodically by rupturing the whole fault, with a period equal to the ratio of the stress drop divided by the rate of stress loading. These earthquakes are “witnesses” or signatures of the tectonic loading. Then, successful earthquake forecasts can only be obtained by understanding and characterizing these fields and how they drive earthquakes. At the other extreme, earthquakes are the “actors,” which by their interactions and self-organization, transform a featureless (constant or white noise) tectonic driving force field into a complex structured seismicity. In this view, all the observed complexity can be understood from the interaction between earthquakes and their mutual triggering. For instance, the critical earthquake model belongs to this class as earthquakes progressively develop a long-range correlation in the stress field by smoothing it out to prepare the stage for a strong earthquake [Sornette and Sammis, 1995 ; Jaumé and Sykes, 1999].

Here, we analyze a simpler model of earthquake “actors”, and use it to test the fundamental

limits of predictability of this class of models. We restrict our analysis to the time domain, that is, we neglect the information provided by the spatial location of earthquakes which could be used to constrain the correlation between events and should be expected to improve the forecast skills. Our results should thus give lower bounds of the achievable predictive skills. This exercise can be considered as rather constrained but turns out to provide meaningful and useful insights.

Before presenting the model and developing the tools necessary for the prediction of future seismicity, we briefly summarize in the next section the evidence for triggered seismicity, that will help us justify and formulate the model. In section 3, we present and summarize the salient properties of the model of interacting triggered seismicity used in our analysis. Section 4 explains the two physical meanings of the average branching ratio  $n$ , that allows one to retrieve it from empirical catalogs. Section 5 develops and presents the formal solution of the problem of forecasting future seismicity rates conditioned on the knowledge of past seismicity quantified by a catalog of times of occurrences and of magnitudes of earthquakes. Section 6 gives the results of an intensive series of tests, which quantify in several alternative ways the quality of forecasts (regression of predicted versus realized seismicity rate, error diagrams, probability gains, information-based binomial scores). Comparisons with the Poisson null-hypothesis give a very significant success rate. However, only about 25% of the large-magnitude targets can be shown to be successfully predicted while the probability gain deteriorates rapidly when one attempts to predict more than 1/3 of the targets. We provide a detailed understanding of these results. Section 7 concludes.

## 7.2 Triggered seismicity and prediction

### Interactions between faults and earthquakes

A look at any geological map confirmed by sophisticated statistical tools (multifractal, wavelets, geostatistics) show that faults are complex structures organized into complex networks [Scholz and Mandelbrot, 1989; Sornette, 1991]. There are many evidences that such faults (and therefore earthquakes) interact, as suggested by calculations of stress redistribution [King *et al.*, 1994; Stein, 1999; Bowman and King, 2001; Sammis and Sornette, 2002], elastodynamic propagation of ruptures using laboratory-based friction law [Rice and Ben-Zion, 1996], simplified models of multiple faults [Sornette *et al.*, 1994; Robinson and Benites, 1995; Gorshkov *et al.*, 1997; Lee *et al.*, 1999; Ben-Zion *et al.*, 1999; Narteau *et al.*, 2000], as well as general constraints of kinematic and geometric compatibility of the deformations [Gabrielov *et al.*, 1996]. This dependence between earthquakes implies that any earthquake may have a (partial) role of triggering other earthquakes.

## Aftershocks ?

The existence of earthquake triggering is particularly obvious after large shallow earthquakes, for which the seismicity rate increases strikingly for time periods up to one hundred years [Utsu *et al.*, 1995; Ebel *et al.*, 2000], and distances up to several hundred km [Tajima and Kanamori, 1985; Steeples and Steeples, 1996; Kagan and Jackson, 1998; Meltzner and Wald, 1999; Dreger and Savage, 1999]. The rate of the triggered events usually decays in time as the modified Omori law  $n(t) = K/(t + c)^p$ , where the exponent  $p$  is found to vary between 0.3 and 2 [Davis and Frohlich, 1991; Kisslinger and Jones, 1991; Guo and Ogata, 1995; Utsu *et al.*, 1995; Huang *et al.*, 2000] and is often close to 1.

These triggered events are usually called aftershocks if their magnitude is smaller than the first event. However, the definition of an aftershock contains unavoidably a degree of arbitrariness because the qualification of an earthquake as an aftershock requires the specification of time and space windows. In this spirit, several alternative algorithms for the definition of aftershocks have been proposed [see for a review Molchan and Dmitrieva, 1992] and there is no consensus. Since the underlying physical processes are not fully understood, the qualifying time and space windows are more based on common sense than on hard science. Particularly, there is no agreement about the duration of the aftershock sequence and the maximum distance between aftershock and mainshock. If one event occurs with a magnitude larger than the first event, it becomes the new mainshock and all preceding events are retrospectively called foreshocks. Thus, there is no way to identify foreshocks from usual aftershocks in real time. There is also no way to distinguish aftershocks from individual earthquakes [Hough and Jones, 1997]. The aftershock magnitude distribution follows the Gutenberg-Richter (GR) distribution with similar  $b$ -value as other earthquakes [Ranalli, 1969; Knopoff *et al.*, 1982]. They have also similar rupture process. Moreover, an event can be both an aftershock of a preceding large event, a foreshock of a following large earthquake or even the mainshock of many other subsequent aftershocks. For example, the M=6.5 Big Bear event is usually considered as an aftershock of the M=7.3 Landers event, and has clearly triggered its own aftershock sequence. One can trace the difficulty of the problem from the long-range nature of the interactions between faults in space and time resulting in a complex self-organized crust.

## Proportion of aftershocks

These observations taken together are part of the growing evidence that a significant fraction of earthquakes in seismic catalogs are triggered events. The identification of aftershocks is often driven by the need to “decluster” catalogs. This obviously provides only a lower bound to the total fraction of triggered events. Gardner and Knopoff [1974] propose to detect aftershocks according to a windowing method. Applied to the Southern California catalog, they find that 2/3 of the events in the catalog are aftershocks. Reasenbergs [1985] analyzes the central California

catalog over the period 1969-1982, and identifies aftershocks from the constraint of obtaining a declustered catalog with a constant seismic rate. In this way, he finds that 48% of the events belong to a seismic cluster. *Davis and Frolich* [1991] use the ISC catalog and, out of 47500 earthquakes, find that 30% belong to a cluster, of which 76% are aftershocks and 24% are foreshocks. *Kagan* [1991] estimates the ratio of dependent events in various catalogs (California and worldwide) using an inversion by the maximum likelihood method of a simple cascade model of aftershock seismicity. The proportion of dependent earthquakes of the first generation that he estimates ranges between 0.1% for deep events to 90%, but is often close to 20%. *Kagan* [1991] also estimates the theoretical ratio of dependent events for the same catalogs, which is a function of the parameters of the cascade model. He finds that about 60% of the earthquakes are dependent events. *Knopoff* [2000] revisits a windowing method applied to the Southern California catalog over the period 1944-1990, for magnitudes  $M \geq 4$ . He finds again that clustered events constitute about 2/3 of the whole catalog.

### Proportion of secondary aftershocks

Among an aftershock sequence, a large proportion of aftershocks may be triggered indirectly by the mainshock, that is, they may be aftershocks of aftershocks triggered by the mainshock. Such secondary aftershock sequences are often observed following major aftershocks. For instance, the  $M = 6.5$  Big-Bear earthquake occurred a few hours following the Landers  $M = 7.3$  event and has clearly triggered its own aftershock sequence, as we already pointed out. Smaller aftershocks at any scale may also trigger their own aftershocks, but may be much more difficult to observe. Therefore, it is very difficult to distinguish between direct and secondary aftershocks and to quantify the proportion of secondary aftershocks.

*Correig et al.* [1997] analyze the secondary aftershocks of a  $M = 5.2$  mainshock in the eastern Pyrenees mountains between France and Spain. They separate aftershocks as being either leading aftershocks or cascades. Leading aftershocks represent only 10% of the aftershocks sequences. In their definition, cascade aftershocks are clusters of aftershocks following these leading aftershocks. If we identify leading aftershocks with direct aftershocks of the mainshock, the proportion of direct aftershocks equal to 10% allows us to give an estimation of the total fraction  $\approx 0.9$  of secondary aftershocks. *Felzer et al.* [2002] estimate the rate of secondary aftershocks, from a comparison of the Landers aftershock sequence with numerical simulations of a simple model of aftershock sequence. They find that about 85% of the aftershocks of the Landers event were secondary aftershocks. This implies that the 1999  $M_W$  7.1 Hector Mine earthquake was triggered, not by the 1992  $M_W$  7.3 Landers earthquake itself [*Felzer et al.*, 2002], but more likely by some of its aftershocks.

To sum up, aftershocks represent a large part, if not the majority, of catalogs of seismicity. Among an aftershock sequence, a large part of aftershocks are secondary aftershocks of the mainshock resulting from a cascade of aftershock triggering. There thus seems to be overwhelming

evidence that seismicity can only be understood by taking into account earthquake interactions at all scales and their mutual triggering.

## A rapid tour of methods of earthquake forecasts based on past seismicity

All the algorithms that have been developed for the prediction of future large earthquakes based on past seismicity rely on their characterization either as witnesses or as actors. In other words, these algorithms assume that their occurrence is related in some way to the approach of a large scale rupture.

### Pattern recognition (M8)

The use of premonitory patterns of seismic activity, such as a decrease of  $b$ -value, an increase in the rate of activity, an anomalous number of aftershocks, etc, has been codified mathematically by *Gelfand et al.* [1976] (see [*Keilis-Borok and Kossobokov*, 1990a,b] for useful reviews). In these algorithms, an alarm is defined when several precursory patterns are above a threshold calibrated in a training period. Predictions are updated each 6 months as new data becomes available. Most of the patterns used by this class of algorithms are reproduced by the model of triggered seismicity known as the ETAS (epidemic type aftershock seismicity) model [*Sornette and Sornette*, 1999; *Helmstetter and Sornette*, 2002a; *Helmstetter et al.*, 2002].

In the sequel, we shall use the term ETAS for the specific version studied here, which was formulated by [*Ogata*, 1988; 1989]. We stress that it is not just a model of aftershocks but of interacting triggered earthquakes. The prediction gain  $G$  of the M8 algorithm, defined as the ratio between the fraction of predicted events over the fraction of time occupied by alarms, is usually in the range 3 to 10 (recall that a random predictor would give  $G = 1$  by definition). A preliminary forward test of the algorithm for the time period July 1991 to June 1995 performed no better than the null hypothesis using a reshuffling of the alarm windows [*Kossobokov et al.*, 1997]. Later tests indicated however a statistical significance level of 92% for the prediction of  $M7.5+$  earthquakes by the algorithm M8-MSc for real-time intermediate-term predictions in the Circum Pacific seismic belt, 1992-1997, and above 99% for the prediction of  $M \geq 8$  earthquakes [*Kossobokov et al.*, 1999]. Our use of the statistical level must be understood as 1 minus the probability of observing a predictability at least as good as what was actually observed, under the null hypothesis that everything is due to chance alone. As of July 2002, the scores (counted from the formal start of the global test initiated by this team since July 1991) are as follows : For  $M8.0+$ , 8 events occurred, 7 predicted by M8, 5 predicted by M8-MSc; for  $M7.5+$ , 25 events occurred, 15 predicted by M8 and 7 predicted by M8-MSc.

### Short term forecast of aftershocks

*Reasenbergs and Jones* [1989] and *Wiemer* [2000] have developed algorithms to predict the rate

of aftershocks following major earthquakes. The rate of aftershocks of magnitude  $m$  following an earthquake of magnitude  $M$  is estimated by the expression

$$N_M(m) = \frac{k 10^{b(M-m)}}{(t+c)^p}, \quad (7.1)$$

where  $b$  is the  $b$ -value of the Gutenberg-Richter (GR) distribution. This approach neglects the contribution of seismicity prior to the mainshock, and does not take into account the specific times, locations and magnitudes of the aftershocks that have already occurred. In addition, this model (7.1) assumes arbitrarily that the rate of aftershocks increases with the magnitude  $M$  of the mainshock as  $\sim 10^{bM}$ , which may not be correct. A careful measure of this scaling for the southern California seismicity gives a different scaling  $\sim 10^{\alpha M}$  with  $\alpha = 0.8$  [Helmstetter, 2002]. Moreover, an analytical study of the ETAS model [Sornette and Helmstetter, 2002] shows that the case  $\alpha \geq b$  leads to an explosive seismicity rate, which is unrealistic to describe the seismic activity.

### Branching models

Simulation in branching models as a tool for predicting earthquake occurrence over large time horizons was proposed in [Kagan, 1973], and first implemented in [Kagan and Knopoff, 1977]. In a recent work, Kagan and Jackson [2000] use a variation of the ETAS model to estimate the rate of seismicity in the future but they neglect the seismicity that will be triggered between the present time and the horizon and which may dominate the future activity. Therefore, these predictions are only valid at very short terms, when very few earthquakes have occurred between the present and the horizon.

To solve this problem and to extend the predictions further in time, Kagan and Jackson [2000] propose to use Monte-Carlo simulations to generate many possible scenarios of the future seismic activity. However, they do not use this method in their forecasting procedure. These Monte-Carlo simulations will be implemented in our tests, as we describe below. This method has already been tested by Vere-Jones [1998] to predict a synthetic catalog generated using the ETAS model. Using a measure of the quality of seismicity forecasts in terms of a mean information gain per unit time, they obtain scores usually worse than the Poisson method. We use below the same class of model and implement a procedure taking into account the cascade of triggering. We find, in contrast with the claim of Vere-Jones [1998], a very strong probability gain. Notwithstanding serious attempts to understand Vere-Jones [1998]'s methodology (and numerous direct exchanges with the author), we confess that we do not understand the origin of the poor scores reported in [Vere-Jones, 1998] (see below).

In [Helmstetter et al., 2002], the forecast skills of algorithms based on three functions of the current and past seismicity (above a magnitude threshold) measured in a sliding window of 100 events have been compared. These functions are (i) the maximum magnitude  $M_{max}$  of the 100 events in that window, (ii) the apparent Gutenberg-Richter exponent  $\beta$  measured on these 100

events by the standard Hill maximum likelihood estimator and (iii) the seismicity rate  $r$  defined as the inverse of the duration of the window. For each function, an alarm was declared for the target of an earthquake of magnitude larger than 6 when the function is either larger (for  $M_{max}$  and  $r$ ) or smaller (for  $\beta$ ) than a threshold. These functions  $M_{max}$ ,  $\beta$  and  $r$  are similar and in some cases identical to precursors and predictors that have been studied by other authors. *Helmstetter et al.* [2002] found that these three predictors are considerably better than those obtained for a random prediction, with the prediction based on the seismicity rate  $r$  being by far the best. This is a logical consequence of the model of interacting triggered seismicity used in [*Helmstetter et al.*, 2002] and also in the present work, in which any relevant physical observable is slaved to the seismicity rate. At least in the class of interacting triggered seismicity, the largest possible amount of information is recovered by targeting the seismicity rate. All other targets are derived from it as linear or non-linear transformations of it. Our present study refines and extend the preliminary tests of [*Helmstetter et al.*, 2002] by using the full model of seismicity rather than the coarse-grained measure  $r$ . We note also that the forecasting methods of *Rundle et al.* [2001; 2002] are based on a calculation of the coarse-grained seismicity above a small magnitude threshold, which is then simply projected to the future.

### 7.3 The model of triggered seismicity

In this first investigation, we limit ourselves to the time domain, studying time series of past seismicity summed over an overall spatial region, without taking account of the information on earthquake positions. It is easy to check that this approach will always lead to underestimating the predictive skills that could be achieved with a full spatio-temporal treatment. However, the problem is sufficiently complex that we find it useful to go through this first step and develop the relevant concepts and first tests using only information on seismic time sequences. We shall present elsewhere the corresponding results for the general spatio-temporal problem.

The present parametric form that defines the ETAS model used in this paper was formulated in [*Ogata*, 1985, 1987, 1988]. See [*Ogata*, 1999] and [*Helmstetter and Sornette*, 2002a] for reviews of its origins, a description of the different versions of the model and of its applications to model or predict seismic activity. It is important to stress that the ETAS model is not only a model of aftershock sequences as the acronym ETAS (Epidemic-Type Aftershock Sequence) would make one to believe but is fundamentally a model of triggered interacting seismicity.

In addition to the strict definition of the ETAS model used by *Ogata* [1985, 1987, 1988, 1989, 1999], there were and still are a variety of alternative parametric forms of the extended “mutually exciting point processes” with marks (that is, magnitudes) introduced by *Hawkes* [1971, 1972], which have been applied to earthquakes, including [*Kagan and Knopoff*, 1987; *Kagan*, 1991] and [*Lomnitz*, 1974]. [*Kagan and Knopoff*, 1987] differs from [*Ogata*, 1985, 1987, 1988] in replacing the role played by the parameter  $c$  in the modified Omori law (7.1) by an

abrupt cut-off which models the duration of the mainshock. They think that a non-zero value of  $c$  is merely the artifact of the missing events immediately after the mainshock. In contrast, based on the observation of the records of seismic waves, *Utsu* [1970, 1992] considers that the parameter  $c$  is not merely due to such artifact but also possesses some physical meaning. The analysis of [*Helmstetter and Sornette*, 2002a] shows that the choice of a non-zero  $c$  value [*Ogata*, 1988] or an abrupt cut-off [*Kagan and Knopoff*, 1987] does not lead to any detectable differences in simulated catalogs at time scales beyond  $c$  (which is usually very small). Thus, from the point of view of the collective behavior of the model, both formulations lead to essentially indistinguishable catalogs and statistical properties. [*Lomnitz*, 1974]’s model (that he called the “Klondike model”) was also directly inspired by [*Hawkes*, 1971] and is similar to the ETAS model, but assumes different parametric forms : in particular, the number of triggered events is taken proportional to the magnitude, and not to the exponential of the magnitude. *Kagan and Jackson* [2000] use also a formulation of the same class but with again another more complex specification of the time, space and magnitude dependence of the triggering process and propagator.

## Definitions

The ETAS model of triggered seismicity is defined as follows [*Ogata*, 1985 ; 1987 ; 1988 ; 1989 ; 1992 ; 1999]. We assume that a given event (the “mother”) of magnitude  $m_i \geq m_0$  occurring at time  $t_i$  gives birth to other events (“daughters”) in the time interval between  $t$  and  $t + dt$  at the rate

$$\phi_{m_i}(t - t_i) = \Phi(t - t_i) \rho(m_i) , \quad (7.2)$$

where  $\Phi(t)$  is the direct Omori’s law normalized to 1

$$\Phi(t) = \frac{\theta c^\theta}{(t + c)^{1+\theta}} H(t) , \quad (7.3)$$

where  $\theta > 0$ ,  $H(t)$  is the Heaviside function, and  $c$  is a regularizing time scale that ensures that the seismicity rate remains finite close to the mainshock.  $\rho(m)$  gives the total number of aftershocks triggered directly by an event of magnitude  $m$

$$\rho(m) = k 10^{\alpha(m-m_0)} , \quad (7.4)$$

where  $m_0$  is a lower bound magnitude below which no daughter is triggered. The adjective “direct” refers to the events of the first generation triggered in first-order lineage from the mother event. The combination of (7.3) and (7.4) is originally due to *Utsu* [1970].

The model is complemented by the Gutenberg-Richter (GR) law which states that each earthquake has a magnitude chosen according to the density distribution

$$P(m) = b \ln(10) 10^{-b(m-m_0)} . \quad (7.5)$$

$P(m)$  is normalized :  $\int_{m_0}^{\infty} dm P(m) = 1$ . When magnitudes are translated into energies, the GR law becomes the (power law) Pareto law.

## Definition of the average branching ratio $n$

The key parameter of model (7.2) is the average number (or “branching ratio”)  $n$  of daughter-earthquakes created per mother-event. This average is performed over time and over all possible mother magnitudes. This average branching ratio  $n$  is a finite value for  $\theta > 0$  and for  $\alpha < b$  for which it is equal to

$$n \equiv \int_0^\infty dt \int_{m_0}^\infty dm P(m) \rho(m) \Phi(t) = \frac{kb}{b-\alpha} . \quad (7.6)$$

The normal regime corresponds to the subcritical case  $n < 1$  for which the seismicity rate decays after a mainshock to a constant background (in the case of a steady-state source) decorated by fluctuations in the seismic rate.

Since  $n$  is defined as the average over all mainshock magnitudes of the mean number of events triggered by a mainshock, it is thus grossly misleading to think of the branching ratio as giving the number of daughters to a given earthquake, because this number is extremely sensitive to the specific value of its magnitude as shown by (7.4). As an example, take  $\alpha = 0.8$ ,  $b = 1$ ,  $m_0 = 0$  and  $n = 1$ . Then, a mainshock of magnitude  $M = 7$  will have on average 80000 direct aftershocks, compared to only 2000 direct aftershocks for an earthquake of magnitude  $M = 5$  and less than 0.2 aftershocks for an earthquake of magnitude  $M = 0$ .

## Formulation of the global seismicity and renormalized Omori’s law

We define the “bare propagator”  $\phi(t)$  of the seismicity as the integral of (7.2) over all magnitudes

$$\phi(t) = \int_{m_0}^\infty dm P(m) \rho(m) \phi_m(t) = n\Phi(t) , \quad (7.7)$$

which is normalized to  $n$  since  $\Phi(t)$  is normalized to 1. The meaning of the adjective “bare” will become clear below, when we explain that cascades of triggered events renormalize  $\phi(t)$  into an effective (that we call “renormalized” or “dressed”) propagator  $K(t)$ . This terminology is borrowed from statistical and condensed-matter physics which deal with physical phenomena occurring at multiple scales in which similar cascades of fluctuations lead to a renormalization of “bare” into “dressed” properties when going from small to large scales. It seems natural to us to use the same terminology in order to capture the fundamental effect of cascades of triggered seismicity that modify/decorate/dress/renormalize the initial (bare) laws put in the model at the level of individual events. See also [Sornette and Sornette, 1999; Helmstetter and Sornette, 2002a] where this terminology was introduced in the present context.

The total seismicity rate  $\lambda(t)$  at time  $t$  is given by the sum of an “external” source  $s(t)$  and the aftershocks triggered by all previous events

$$\lambda(t) = s(t) + \sum_{i|t_i \leq t} \phi_{m_i}(t - t_i) , \quad (7.8)$$

where  $\phi_{m_i}(t - t_i)$  is defined by (7.2). Here, “external” source refers to the concept that  $s(t)$  is

the rate of earthquakes *not* triggered by other previous earthquakes. This rate acts as a driving force ensuring that the seismicity does not vanish and models the effect of the tectonic forcing.

Taking the ensemble average of (7.8) over many possible realizations of the seismicity (or equivalently taking the mathematical expectation), we obtain the following equation for the first moment or statistical average  $N(t)$  of  $\lambda(t)$  [Sornette and Sornette, 1999; Helmstetter and Sornette, 2002a]

$$N(t) = s(t) + \int_{-\infty}^t d\tau \phi(t - \tau) N(\tau) . \tag{7.9}$$

The average seismicity rate is the solution of this self-consistent integral equation, which embodies the fact that each event may start a sequence of events which can themselves trigger secondary events and so on. The cumulative effect of all the possible branching paths of activity gives rise to the net seismic activity  $N(t)$ . In words, expression (7.9) means that the seismic activity at time  $t$  may be due to a possible external source  $s(t)$  plus the sum over all past times  $\tau$  of the total previous activities  $N(\tau)$  that may trigger an event at time  $t$  according to the bare Omori's law  $\phi(t - \tau)$ .

The global rate of aftershocks including secondary aftershocks triggered by a mainshock of magnitude  $M$  occurring at  $t = 0$  is given by  $\rho(M)K(t)/n$ , where the renormalized Omori's law  $K(t)$  is obtained as a solution of (7.9) with the general source term  $s(t)$  replaced by the Dirac function  $\delta(t)$  :

$$K(t) = \delta(t) + \int_0^t \phi(t - \tau) K(\tau) d\tau . \tag{7.10}$$

The solution for  $K(t)$  can be obtained as the following series [Helmstetter and Sornette, 2002a]

$$K(t) = \delta(t) + \frac{1}{1-n} \frac{t^{*-\theta}}{t^{1-\theta}} \sum_{k=0}^{k=\infty} (-1)^k \frac{(t/t^*)^{k\theta}}{\Gamma((k+1)\theta)} . \tag{7.11}$$

The infinite sum expansion is valid for  $t > c$ , and  $t^*$  is a characteristic time measuring the distance to the critical point  $n = 1$  defined by

$$t^* = c \left( \frac{n\Gamma(1-\theta)}{|1-n|} \right)^{1/\theta} . \tag{7.12}$$

$t^*$  is infinite for  $n = 1$  and becomes very small for  $n \ll 1$ . The leading behavior of  $K(t)$  at short times reads

$$K(t) = \frac{1}{1-n} \frac{1}{\Gamma(\theta)} \frac{t^{*-\theta}}{t^{1-\theta}} , \quad \text{for } c < t < t^* , \tag{7.13}$$

showing that the effect of the cascade of secondary aftershocks renormalizes the bare Omori's law  $\Phi(t) \sim 1/t^{1+\theta}$  given by (7.3) into  $K(t) \sim 1/t^{1-\theta}$ , as illustrated by Figure 7.1.

Once the seismic response  $K(t)$  to a single event is known, the complete average seismicity rate  $N(t)$  triggered by an arbitrary source  $s(t)$  can be obtained using the theorem of Green functions for linear equations with source terms [Morse and Feshbach, 1953]

$$N(t) = \int_{-\infty}^t d\tau s(\tau) K(t - \tau) . \tag{7.14}$$

Expression (7.14) provides the general solution of (7.9).

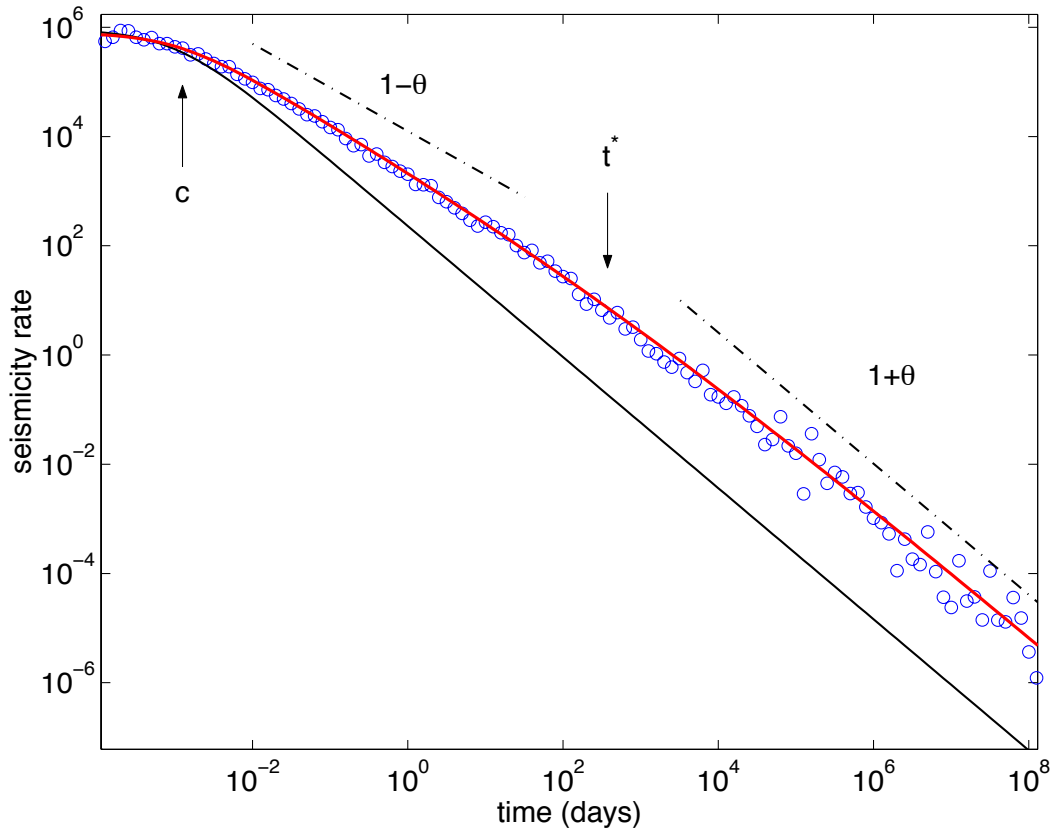


FIG. 7.1 – A realization of the HKKO-ETAS model shows the seismicity rate (open circles) as a function of time after a large earthquake. This illustrates the differences between the observed seismicity rate  $\lambda(t)$  (open circle), the average renormalized (or dressed) propagator  $K(t)$  (solid line), and the local propagator  $\Phi_m(t)$  (thin line). This aftershock sequence has been generated using the HKKO-ETAS model with parameters  $n = 0.91$ ,  $\alpha = 0.5$ ,  $b = 1$ ,  $\theta = 0.2$ ,  $m_0 = 0$  and  $c = 0.001$  day, starting from a mainshock of magnitude  $M = 8$  at time  $t = 0$ . The global aftershock rate is significantly higher than the direct (or first generation) aftershock rate, described by the local propagator  $\Phi_m(t)$ . The value of the branching ratio  $n = 0.915$  implies that about 91.5% of aftershocks are triggered indirectly by the mainshock. The global aftershock rate  $N(t)$  decreases on average according to the dressed propagator  $K(t) \sim 1/t^{1-\theta}$  for  $t < t^*$ , which is significantly slower than the local propagator  $\phi(t) \sim 1/t^{1+\theta}$ .

#### 7.4 Physical meaning of the average branching ratio $n$

The branching ratio defined by (7.6) is the key parameter of this model, which controls the different regimes of seismic activity. We give below two observable meanings for this parameter as the ratio of triggered events over total seismicity and the ratio of secondary aftershocks over total aftershocks.

## Response of the seismicity to a constant source rate

Let us consider the situation in which  $s(t)$  corresponds to a constant Poisson source process with intensity  $\mu$ , representing the effect of tectonic loading. Then, the observed seismicity results both from this constant background seismicity source rate and from the direct and indirect aftershocks triggered by this background seismicity. In the regime  $n < 1$ , the global seismicity is stationary, with large fluctuations following large earthquakes due to the triggered aftershock sequences. Taking the background seismicity rate to be equal to  $\mu$ , the rate of aftershocks  $r_0$  triggered directly by the background seismicity is on average  $r_0 = \mu n$  because each single background event triggers on average  $n$  events, when averaging over all magnitudes. The rate of second generation aftershocks, triggered by aftershocks of the background events, is  $r_1 = nr_0 = \mu n^2$ . At the  $i^{\text{th}}$  generation, the rate of aftershocks triggered indirectly by the background seismicity rate  $\mu$  is given by  $r_i = \mu n^i$ . Summing over all generations, the global rate  $R_{aft}$  of direct and indirect aftershocks of the background seismicity in the sub-critical regime  $n < 1$  is given by

$$R_{aft.} = \sum_{i=0}^{i=\infty} r_i = \mu \sum_{i=1}^{i=\infty} n^i = \frac{\mu n}{1-n} . \quad (7.15)$$

The global seismicity rate  $R$  is given by the sum of the background seismicity rate  $\mu$  and of the rate of aftershocks  $R_{aft.}$  :

$$R = \mu + R_{aft.} = \mu + \frac{\mu n}{1-n} = \frac{\mu}{1-n} . \quad (7.16)$$

This result (7.16) shows that the effect of the cascade of aftershocks of aftershocks and so on is to renormalize the average background seismicity  $\mu$  to a significant higher level, the closer  $n$  is to the critical value 1. This result is well-known in branching process literature [*Harris*, 1963; *Daley and Vere-Jones*, 1988] and has also been derived by *Kagan* [1991] for the slightly modified version of the ETAS model using  $c = 0$  and replacing it by an abrupt cut-off at early times. This concept is illustrated in Figure (7.2).

The proportion of aftershocks (of any generation) is thus equal to

$$r_{aft.} = \frac{R_{aft.}}{R} = n . \quad (7.17)$$

This expression (7.17) shows that the average branching ratio  $n$  can be directly observed from a suitable analysis of seismicity catalogs. Indeed, clustering algorithms for detecting and counting aftershocks provide a direct estimation (and in general a lower bound) of  $n$  as discussed above in the section of the proportion of aftershocks.

The result (7.17) can be derived directly from the master equation (7.9). Inserting  $s(t) = \mu$  in (7.9) and taking the expectation  $R = \langle N(t) \rangle$  gives the global average seismicity rate

$$R = \mu + R \int_{-\infty}^t \phi(t-\tau) d\tau = \mu + nR , \quad (7.18)$$

which recovers expression (7.16).

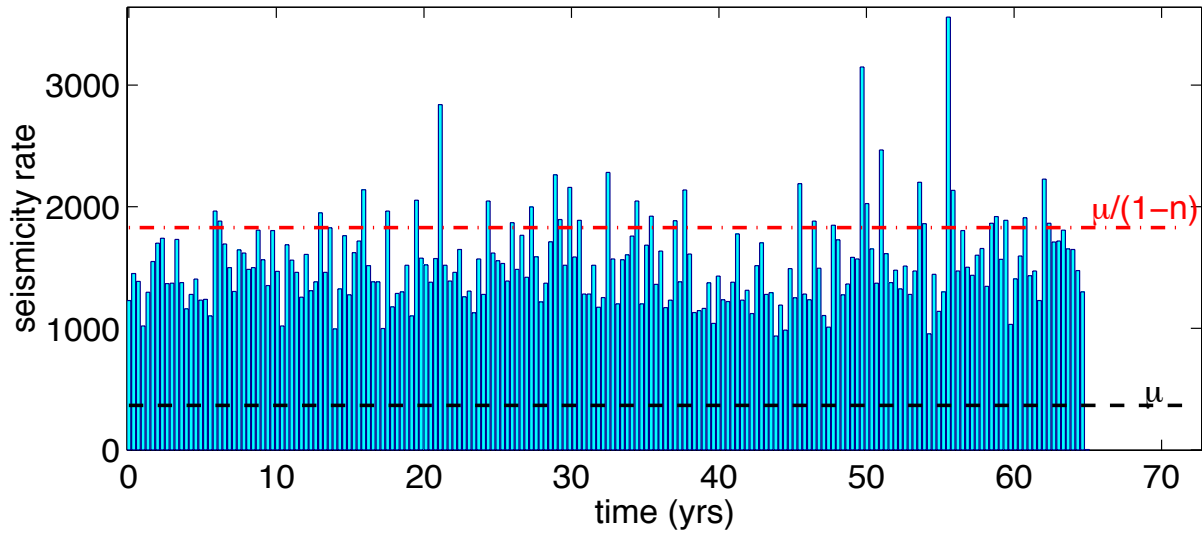


FIG. 7.2 – Rate of seismic activity for a synthetic catalog generated using the HKKO-ETAS model with parameters  $\mu = 1$  source events per day,  $c = 0.001$  day,  $n = 0.8$ ,  $\theta = 0.2$ ,  $b = 1$  and  $\alpha = 0.5$ . The average seismicity rate is close to the expected value  $\mu^* = \mu/(n - 1)$  predicted by (7.16) shown as a thin dashed line. The seismicity rate is always significantly larger than the background rate  $\mu$  shown as the thick dashed line, due to the direct and indirect aftershocks triggered by the external source, which represent here 80% of the catalog for the value  $n = 0.8$ .

### Proportion of secondary aftershocks

Let us now give another meaning for  $n$  as well as an additional empirical tool to estimate it. For this, we calculate the total number of aftershocks  $n_t$  triggered by a mainshock of magnitude  $M$ , including all the generations of secondary aftershocks, as follows. The number of direct aftershocks is given by  $n_0 = \rho(M)$  using the definition (7.2). The average number of second generation aftershocks  $n_1$  is given by the product of  $n_0$  with the average number of aftershocks per earthquake defined by  $n$ . Therefore  $n_1 = \rho(M)n$ . The number of grand-grand-daughters of the mainshock is  $n_2 = \rho(M)n^2$ . The number of aftershocks for the  $i^{\text{th}}$  generation is  $n_i = \rho(M)n^i$ . The total number of aftershocks triggered by a mainshock of magnitude  $M$  is thus given by

$$S = \sum_{i=0}^{\infty} n_i = \rho(M) \sum_{i=0}^{\infty} n^i = \frac{\rho(M)}{1-n}. \quad (7.19)$$

For  $n \ll 1$ ,  $S \approx \rho(M)$ , i.e., most aftershocks are directly triggered by the mainshock. For  $n \approx 1$ ,  $S \gg \rho(M)$ , i.e., most aftershocks are secondary aftershocks of the mainshock. The proportion of secondary aftershocks is given by

$$r_{sec.aft.} = \frac{S - n_0}{S} = \frac{\frac{\rho(M)}{1-n} - \rho(M)}{\frac{\rho(M)}{1-n}} = n. \quad (7.20)$$

This result (7.20) shows that the average branching ratio  $n$  is nothing but the fraction among all aftershocks of the aftershocks triggered indirectly by the mainshock. This fraction of indirectly

triggered aftershocks is therefore known as soon as  $n$  can be calculated from the knowledge of the ETAS parameters  $\alpha$ ,  $b$ ,  $k$ ,  $c$  and  $\theta$  using for instance a maximum likelihood method [Ogata, 1988; Kagan, 1991].

We can also derive the result (7.20) from the master equation (7.9). Inserting  $s(t) = \delta(t)\rho(M)$  in (7.9) and taking the integral of (7.9) gives the global number of direct and indirect aftershocks

$$\begin{aligned}
 S &= \int_0^\infty N(t) dt \\
 &= \rho(M) + \int_0^\infty dt \int_0^t N(\tau) \phi(t - \tau) d\tau \\
 &= \rho(M) + \int_0^\infty d\tau N(\tau) \int_\tau^\infty \phi(t - \tau) dt \\
 &= \rho(M) + n \int_0^\infty N(\tau) d\tau \\
 &= \rho(M) + n S,
 \end{aligned} \tag{7.21}$$

which recovers expression (7.19) for  $S$ .

## 7.5 Formal solution of the earthquake prediction problem

Having stressed the importance of the indirect triggered seismicity in determining both the overall level (7.15) of seismicity and its decay law (7.11,7.13), we now formulate the task of earthquake prediction within this model of triggered seismicity restricted to the time domain. In this paper, we do not address the delicate issue related to the fact that not all earthquakes are observable or observed. Indeed, calibrations of the ETAS parameters using the magnitude cut-offs dictated by the requirement of seismic catalogs completeness rather than by the physics of triggered seismicity may lead to misleading results, as unobserved events may play a significant role (in their sheer number) in triggering observable seismicity. To our knowledge, all previous calibrations of real seismic catalogs have bypassed this problem, which will be studied using a technique derived from our renormalized Omori's law in a subsequent paper.

We thus assume that seismicity that occurred in the past until the “present” time  $u$  and which does trigger future events is observable. The seismic catalog is constituted of a list of entries  $\{(t_i, m_i), t_i < u\}$  giving the times  $t_i$  of occurrence of the earthquakes and their magnitude  $m_i$ . Our goal is to set up the best possible predictor for the seismicity rate for the future from time  $u$  to time  $t > u$ , based on the knowledge of this catalog  $\{(t_i, m_i), t_i < u\}$ . The time difference  $t - u$  is called the horizon. In the ETAS model studied here, magnitudes are determined independently of the seismic rate, according to the GR distribution. Therefore, the sole meaningful target for predictions is the seismic rate. Once its forecast is issued, the prediction of strong earthquakes is obtained by combining the GR law with the forecasted seismic rate.

The average seismicity rate  $N(t)$  at time  $t > u$  in the future is made of two contributions :

- the background source of seismicity of intensity  $\mu$  at time  $t$  plus the background events

- that occurred between  $u$  and  $t$  and their following aftershocks that may trigger an event at time  $t$  ;
- the earthquakes that have occurred in the past at times  $t_i < u$  and all the events they triggered between  $u$  and  $t$  and their following aftershocks that may trigger an event at time  $t$ .

We now examine each contribution in turn.

### Seismicity at times $t > u$ triggered by a constant source $\mu$ active from $u$ to $t$

Using the background seismicity source  $\mu$  to predict the seismicity in the future would underestimate the seismicity rate because it does not take into account the aftershocks of the background seismicity. On the contrary, using the “renormalized” seismicity rate  $\mu/(1-n)$  derived in (7.15) would overestimate the seismicity rate because the earthquakes that were triggered before time  $u$  by the background seismicity would be counted twice, since they are registered in the catalog up to time  $u$ . The correct procedure is therefore to evaluate the rate of seismicity triggered by a constant source  $\mu$  starting at time  $u$  to remove the influence of earthquakes that have been recorded at times less than  $u$ , whose influence for times larger than  $u$  is examined later.

The response  $K_\mu(t)$  of the seismicity to a constant source term  $\mu$  starting at time  $u$  is obtained using (7.14) as

$$K_{\mu,u}(t) = \mu \int_{u^+}^t d\tau [K(t-\tau) - \delta(t-\tau)] = \mu \mathcal{K}(t-u) , \quad (7.22)$$

where  $\mathcal{K}(t)$  is the integral of  $K(t) - \delta(t)$  given by (7.11) :

$$\mathcal{K}(t) = \frac{1}{1-n} \left(\frac{t}{t^*}\right)^\theta \sum_{k=0}^{k=\infty} (-1)^k \frac{(t/t^*)^{k\theta}}{\Gamma((k+1)\theta+1)} . \quad (7.23)$$

For times larger that  $t \gg t^*$ ,  $K_\mu(t)$  reaches its asymptotic value  $K_\mu = \frac{\mu}{1-n}$ , derived in (7.16). Expression (7.22) takes care of both the background source seismicity of intensity  $\mu$  at time  $t$  and of its aftershocks and their following aftershocks from time  $u$  to  $t$  that may trigger events at time  $t$ .

### Hypermetropic renormalized propagator

We now turn to the effect of the past known events prior to time  $u$  on future  $t > u$  seismicity, taking into account the direct and secondary aftershocks of each earthquakes that have occurred in the past at times  $t_i < u$  counted from time  $u$ . Since the ETAS model is linear in the rate variable, we consider first the problem of a single past earthquake at time  $t_i < u$  and will then sum over all past earthquakes.

A first approach for estimating the seismicity at  $t > u$  due to event  $i$  that occurred at time  $t_i < u$  is to use the bare propagators  $\Phi(t-t_i)$ , as done e.g. by *Kagan and Jackson* [2000]. This

extrapolation leads to an underestimation of the seismicity rate in the future because it does not take into account the secondary aftershocks. This is a quite bad approximation when  $n$  is not very small, and especially for  $n > 0.5$ , since the secondary aftershocks are then more numerous than direct aftershocks.

An alternative would be to express the seismicity at  $t > u$  due to an earthquake that occurred at  $t_i < u$  by the global propagator  $K(t - t_i)$ . However, this approach would overestimate the seismicity rate at time  $t$  because of double counting. Indeed,  $K(t - t_i)$  takes into account the effect of all events triggered by event  $i$ , including those denoted  $j$ 's that occurred at times  $t_i < t_j < u$  and which are directly observable and counted in the catalog. Thus, using  $K(t - t_i)$  takes into account these events  $j$ , that are themselves part of the sum of contributions over all events in the catalog.

The correct procedure is to calculate the seismicity at  $t > u$  due to event  $i$  by including all the seismicity that it triggered only after time  $u$ . This defines what we term the ‘‘Hypermetropic renormalized propagator’’  $K_u^*(t - t_i)$ . It is ‘‘renormalized’’ because it takes into account secondary and all subsequent aftershocks. It is ‘‘Hypermetropic’’ because this counting of triggered seismicity starts only after time  $u$  such that this propagator is oblivious to all the seismicity triggered by event  $i$  at short times from  $t_i$  to  $u$ .

We now apply these concepts to estimate the seismicity triggered directly or indirectly by a mainshock with magnitude  $M$  that occurred in the past at time  $t_i$  while removing the influence of the triggered events  $j$  occurring between  $t_i$  and  $u$ . This gives the rate

$$S_M(t) = \frac{\rho(M)}{n} K_u^*(t - t_i) , \quad (7.24)$$

where the Hypermetropic renormalized propagator  $K_u^*$  is given by

$$K_u^*(t) = \int_u^t \phi(\tau) K(t - \tau) d\tau . \quad (7.25)$$

$K_u^*(t)$  defined by (7.25) recovers the bare propagator  $\Phi(t)$  for  $t \approx u$ , i.e., when the rate of direct aftershocks dominates the rate of secondary aftershocks triggered at time  $t > u$ . Indeed, taking the limit of (7.25) for  $u \rightarrow t$  gives

$$\begin{aligned} K_{u \rightarrow t}^*(t) &= \int_{u \rightarrow t}^t d\tau \phi(\tau) K(t - \tau) \\ &= \int_{u \rightarrow t}^t d\tau \phi(\tau) \delta(t - \tau) = \phi(t) . \end{aligned} \quad (7.26)$$

This result simply means that the prediction of future seismicity in the near future is mostly dominated by the sum of the direct Omori’s laws of all past events. This limit recovers procedures used by [Kagan and Jackson, 2000].

In the other limit,  $u \approx t_i$ , i.e., for an event that occurred at a time  $t_i$  just before the present  $u$ ,  $K_u^*(t)$  recovers the dressed propagator  $K(t)$  (up to a Dirac function) since there are no other

registered events between  $t_i$  and  $t$  and all the seismicity triggered by event  $i$  must be counted. Using equation (7.10), this gives

$$K_{u \rightarrow 0}^*(t) = \int_{u \rightarrow 0}^t d\tau \phi(\tau) K(t - \tau) = K(t) - \delta(t) . \quad (7.27)$$

Using again (7.10), we can rewrite (7.25) as

$$K_u^*(t) = K(t) - \int_0^u K(t - \tau) \phi(\tau) d\tau . \quad (7.28)$$

Putting (7.11) in (7.25) we obtain for  $t \geq c$

$$K_u^*(t) = \frac{\theta}{\Gamma(\theta) \Gamma(1 - \theta)} \int_0^{t-u} \frac{1}{(t - x + c)^{1+\theta}} \frac{1}{x^{1-\theta}} \sum_{k=0}^{\infty} (-1)^k \frac{(x/t^*)^{k\theta}}{\Gamma((k+1)\theta)} dx , \quad (7.29)$$

where  $x = t - \tau$ . Appendix A presents useful asymptotics and approximations of  $K_u^*(t)$ .

We have performed numerical simulations of the ETAS model to test our predictions on the Hypermetropic renormalized propagator  $K_u^*(t)$  (7.25,7.29). We first consider the unrealistic case where  $\alpha = 0$ , i.e., all events trigger the same number of aftershocks whatever their magnitude. Figure 7.3 shows the result of a simulation using a synthetic catalog generated by a large event that happened at time  $t = 0$ , using the parameters  $n = 0.1$ ,  $c = 0.001$  day,  $\alpha = 0$ ,  $\theta = 0.1$  and  $\mu = 0$ . The seismic activity  $K_u^*(t)$  is obtained by removing, the influence of aftershocks that were triggered in the past  $0 < t_i < u$  where the present is taken equal to  $u = 10$  days. The simulation shows a very good agreement between the results obtained by averaging over 1000 synthetic catalogs and the theoretical prediction (7.25,7.29). The Hypermetropic renormalized propagator  $K_u^*(t)$  is significantly larger than the bare Omori's law  $\Phi(t)$  but smaller than the renormalized propagator  $K(t)$  as expected. Note that  $K_u^*(t)$  first increases with the horizon  $t - u$  up to horizons of the order of  $u$  and then crosses over to a decay law  $K_u^*(t) \sim 1/t^{1-\theta}$  parallel to the dressed propagator  $K(t)$ . Figure 7.4 is similar to Figure 7.3, but uses more realistic parameters :  $n = 1$ ,  $\theta = 0.2$  and  $\alpha = 0.5$ . At early times  $t \approx u$ , the measured seismicity rate is in good agreement with the Hypermetropic renormalized propagator  $K^*(t)$  defined by (7.25). At large times however, the observed seismicity rate decays significantly faster than the predictions.

In the averaging performed in all previous calculations and which allowed us to derive the Master equation for  $K(t)$ , we made the assumption that one can neglect the coupling between the fluctuations of the local rates and the realized magnitudes of earthquakes. This assumption turns out to be unwarranted for  $\alpha > 1/2$  in the case of  $K(t)$  [Helmstetter *et al.*, 2002]. For  $K^*(t)$ , the effect seems to be even stronger and is observed for smaller  $\alpha$ 's as shown in Figure 7.4. The full analytical quantification of this effect can be obtained using the exact mapping to CTRW (continuous-time random walks) developed in [Helmstetter and Sornette, 2000b] and will be reported elsewhere. In the mean time, in order to test the skills of forecasts based on

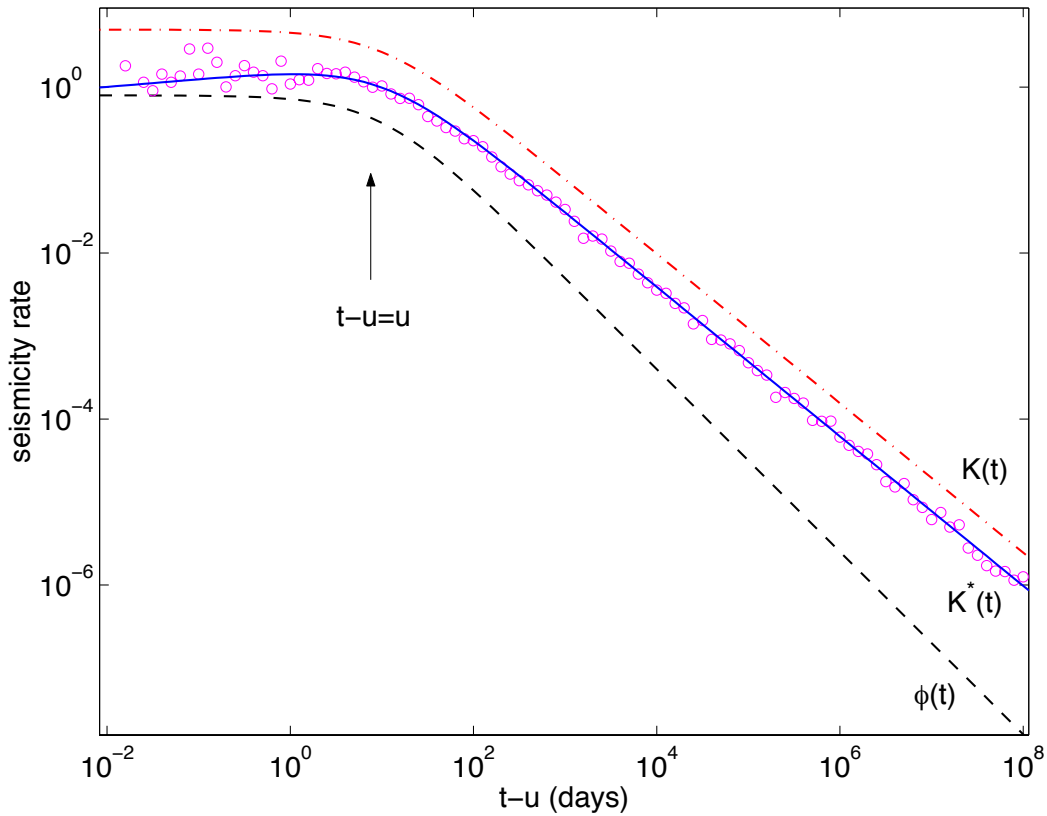


FIG. 7.3 – Seismicity rate (blinded renormalized propagator) following a large event that happened at time  $t = 0$ , removing the influence of aftershocks that were triggered in the past  $0 < t_i < u$  with  $u = 10$  days. We have averaged over 1000 simulations starting at time  $u = 10$  days after a large event of magnitude  $m = 6$ , using the parameters  $n = 0.9992$ ,  $c = 0.001$  day,  $\alpha = 0$ ,  $\theta = 0.2$  and  $m_0 = 0$ . There is a very good agreement between the observed blind seismicity rate (open circles) and the predicted  $K^*(t)$  shown as the continuous line. The dashed (respectively dotted-dashed) line represents the bare Omori's propagator  $\phi(t)$  (respectively the renormalized propagator  $K(t)$ ).

cascades of triggered seismicity over a finite time horizon, we shall resort below to what amounts to numerical calculations of  $K(t)$  and  $K_u^*(t)$  obtained by generating many seismic catalogs based on the known seismicity up to time  $u$ . Each such catalog synthesized for times  $t > u$  constitutes a possible scenario for the future seismicity. Averaging over many such scenarios provides the expected mean seismicity. As a bonus, this will allow us to define confidence intervals.

## 7.6 Prediction tests

Knowing the times  $t_i$  and magnitude  $m_i$  of all events that occurred in the past up to the present  $u$ , the mean seismicity rate  $N_u(t)$  predicted for the future  $t > u$  by taking into account

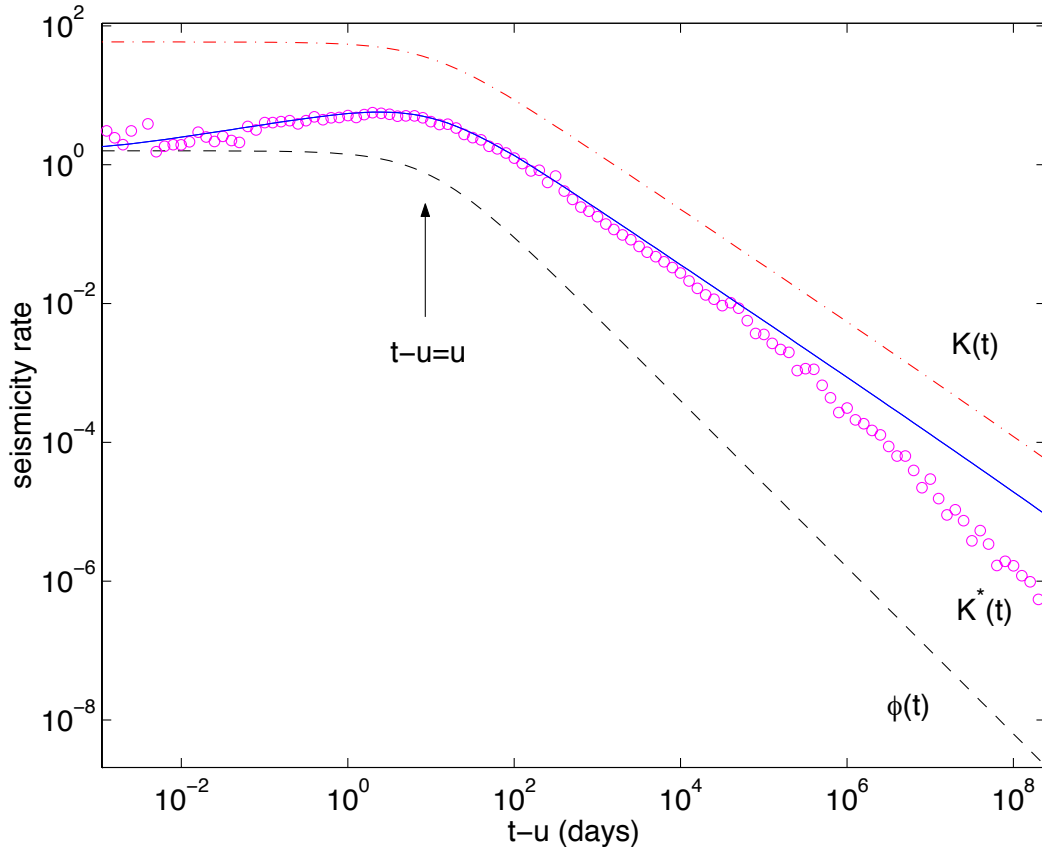


FIG. 7.4 – Same as Figure 7.3 for  $n = 1$ ,  $\theta = 0.1$  and  $\alpha = 0.5$ . At early times  $t \approx u$ , the measured blind seismicity rate is in good agreement with the blinded renormalized propagator  $K^*(t)$  defined by (7.25). At large times however, the observed seismicity rate decays significantly faster than the predictions, due to the coupling between the fluctuations of the times and magnitudes of triggered events that are not taken into account by the master equation (7.9) used to estimate  $K^*(t)$ .

all triggered events and the seismicity background  $\mu$  is given formally by

$$N_u(t) = \mu \mathcal{K}(t - u) + \sum_{i|t_i < u} \frac{\rho(m_i)}{n} K_u^*(t - t_i), \quad (7.30)$$

where  $K_u^*(t - t_i)$  is given by (7.25) and  $\mathcal{K}(t)$  is given by (7.23). In the language of the statistics of point processes, expression (7.30) amounts to using the conditional intensity function. The conditional intensity function indeed gives an unequivocal answer to the question of what is the best predictor of the process. All future behaviors of the process, starting from the present time  $u$  and conditioned by the history up to time  $u$ , can be simulated exactly once the form of the conditional intensity is known. To see this, we note that the conditional intensity function, if projected forward on the assumption that no additional events are observed (and assuming no external variables intervene), gives the hazard function of the time to the next occurring event past  $u$ . So if the simulation proceeds by using this form of hazard function, then by recording the time of the next event when it does occur, and so on, ensures that one is always working

with the exact formula for the conditional distributions of the inter-event times. The simulations then truly represent the future of the process, and any functional can be taken from them in whatever form is suitable for the purpose at hand.

In practice, we thus use the catalog of known earthquakes up to time  $u$  and generate many different possible scenarios for the seismicity trajectory that each take into account all the relevant past triggered seismicity up to the present  $u$ . For this, we use the thinning simulation method, as explained by *Ogata* [1999]. We then define averages over these scenarios to obtain the forecasted seismicity  $N_u(t)$ .

### Fixed present and variable forecast horizon

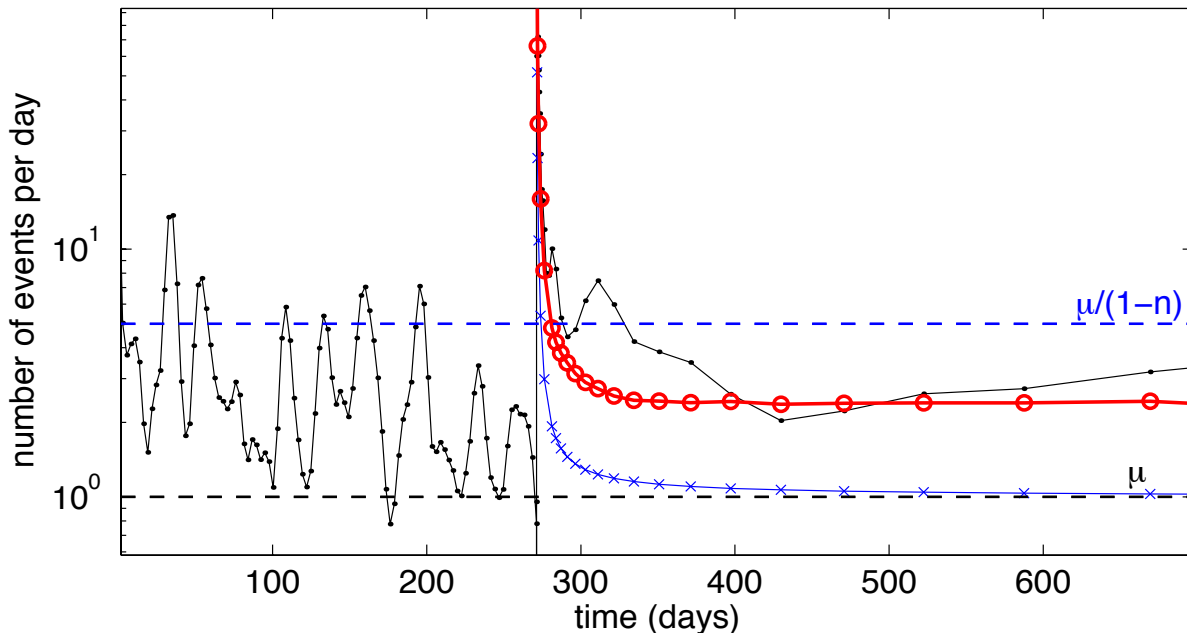


FIG. 7.5 – Rate of seismic activity for a synthetic catalog (black dots) generated with the parameters  $n = 0.8$ ,  $\theta = 0.2$ ,  $\alpha = 0.8$ ,  $b = 1$ ,  $c = 0.001$  day,  $m_0 = 3$  and  $\mu = 1$  event per day. We compare different methods of prediction of the seismicity rate following a large event  $M = 7$  that has occurred at the time of the large peak shown in the figure. Using the data up to the present time  $t_i \leq u$ , where  $u$  is the “present” taken fixed just after the the  $M = 7$  earthquake, we try to predict the future activity up to 1 year in the future. We use two predictions algorithms : the sum of the bare propagators of all past events  $t_i \leq u$  (crosses), and the median of the seismicity rate obtained over 500 scenarios generated with the HKKO-ETAS model, using the same parameters as for the synthetic catalog we want to predict, and taking into account the specific realization of the synthetic catalog up to the present.

Figure 7.5 illustrates the problem of forecasting the aftershock seismicity following a large  $M = 7$  event. Imagine that we have just witnessed the  $M = 7$  event and want to predict the seismic activity afterward over a varying horizon from days to years in the future. In this

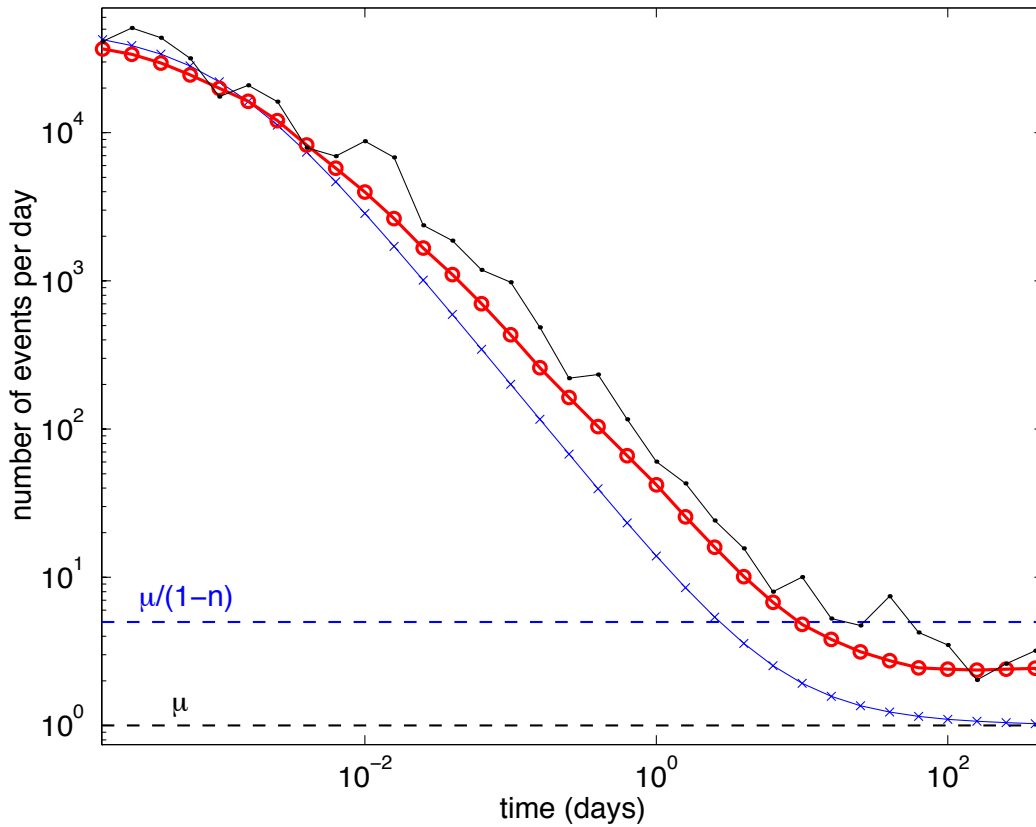


FIG. 7.6 – Same as Figure 7.5 but as a function of the logarithm of the time after the mainshock. At early time  $t - u < 10^{-2}$  days, the predicted seismicity rate is correctly predicted by the naive bare Omori's law shown by the crosses which is indistinguishable from the more elaborate scheme involving all cascades of triggered events. At larger times, the cascade of triggered seismicity renormalizes the seismicity rate to a significantly higher level, which is correctly forecasted by the mean over the 500 scenarios.

simulation,  $u$  is kept fixed at the time just after the  $M = 7$  event and  $t$  is varied. A realization of the instantaneous rate of seismic activity (number of events per day) of a synthetic catalog is shown by the black dots. This simulation has been performed with the parameters  $n = 0.8$ ,  $\alpha = 0.8$ ,  $b = 1$ ,  $c = 0.001$  day,  $m_0 = 3$  and  $\mu = 1$  event per day. This single realization is compared with two prediction algorithms : the sum of the bare propagators of all past events  $t_i \leq u$  (crosses), and the median of the seismicity rate obtained over 500 scenarios generated with the ETAS model, using the same parameters as used for generating the synthetic catalog we want to predict, and taking into account the specific realization of events in each scenario up to the present. Figure 7.6 is the same as Figure 7.5 but shows the seismic activity as a function of the logarithm of the time after the mainshock. These two figures illustrate clearly the importance of taking into account all the cascades of still unobserved triggered events in order to predict correctly the future rate of seismicity beyond a few minutes. The aftershock activity forecast gives a very reasonable estimation of the future activity rate, while the extrapolation of the bare Omori's law of the strong  $M = 7$  event together with the past seismicity under-estimates very

badly the future seismicity beyond half-an-hour after the strong event.

### Varying “present” with fixed forecast horizon

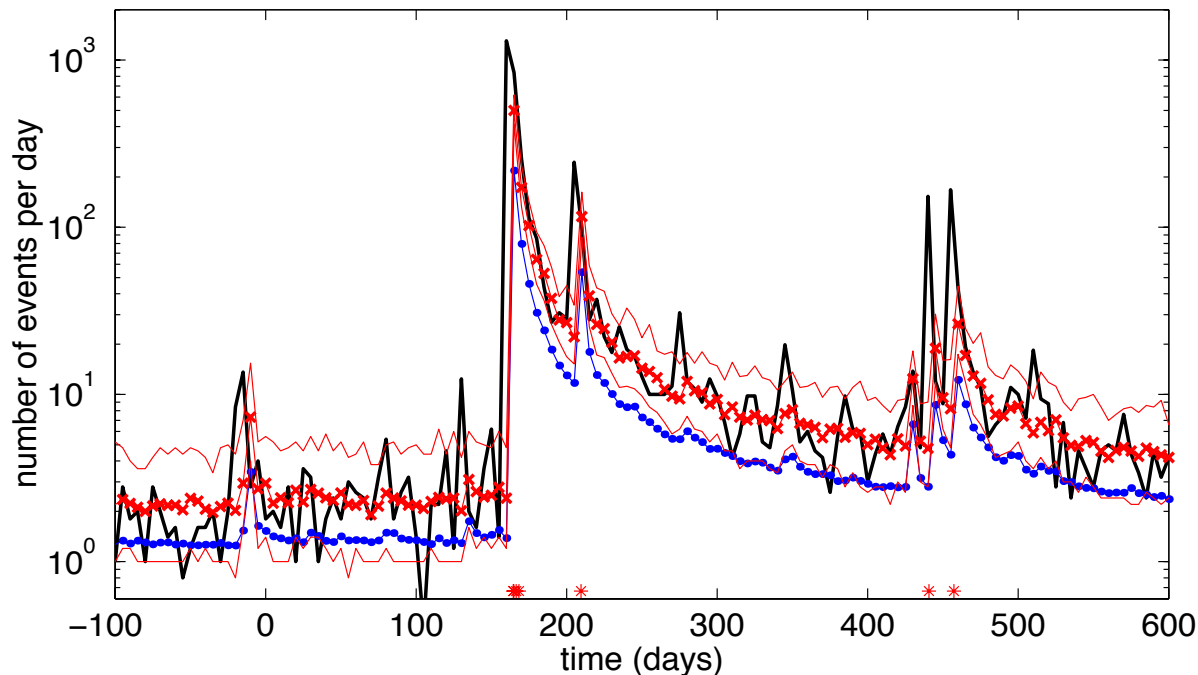


FIG. 7.7 – Comparison between the seismicity rate (solid black line) observed for a 5 days time period, with the predicted seismicity rate using either the sum of the bare propagators of the past seismicity (dots) or using the median of 100 scenarios (crosses) generated with the same parameters as for the synthetic catalog we want to predict,  $n = 0.8$ ,  $\theta = 0.2$ ,  $c = 0.001$  day,  $\mu = 1$  event per day,  $M_0 = 3$ ,  $b = 1$  and  $\alpha = 0.8$ . The thin solid lines indicate the first and 9<sup>th</sup> deciles of the set of 100 scenarios : there is 80% probability that the predicted seismicity over the next 5 days falls within these two lines. Stars indicate the occurrence of a large  $M \geq 7$  earthquake. Forecasts are updated every 5 days.

Figure 7.7 compares a single realization of the seismicity rate (solid black line) observed and summed over a 5 days period and divided by 5 so that it is expressed as a daily rate, with the predicted seismicity rate using either the sum of the bare propagators of the past seismicity (dots) or using the median of 100 scenarios (crosses) generated with the same parameters as for the synthetic catalog we want to predict :  $n = 0.8$ ,  $c = 0.001$  day,  $\mu = 1$  event per day,  $m_0 = 3$ ,  $b = 1$  and  $\alpha = 0.8$ . The predictions calculate the total number of events over each 5 day period lying ahead of the present, taking into account all past realized seismicity up to the present including the still unobserved triggered seismicity. This total number of forecasted events is again divided by 5 to express the prediction as daily rates. The thin solid lines indicate the first and 9<sup>th</sup> deciles of the distributions of the number of events observed in the pool of 100 scenarios. Stars indicate the occurrence of large  $M \geq 7$  earthquakes. Only a small part of the

whole time period used for the prediction is shown, including the largest  $M = 8.5$  earthquake of the catalog, in order to illustrate the difference between the observed seismicity rate and the different methods of predictions.

The observed seismicity rate is always larger than the seismicity rate predicted using the sum of the bare propagators of the past activity. This reflects the fact that the seismicity, that will occur up to 5 days in the future, is dominated by the seismicity that will be triggered in the near future that is still unobserved but must be taken into account. The observed seismicity rate is close to the median of the scenarios (crosses), and the fluctuations of the observed seismicity rate are in good agreement with the expected fluctuations measured by the deciles of the distributions of the seismicity rate over all generated scenarios.

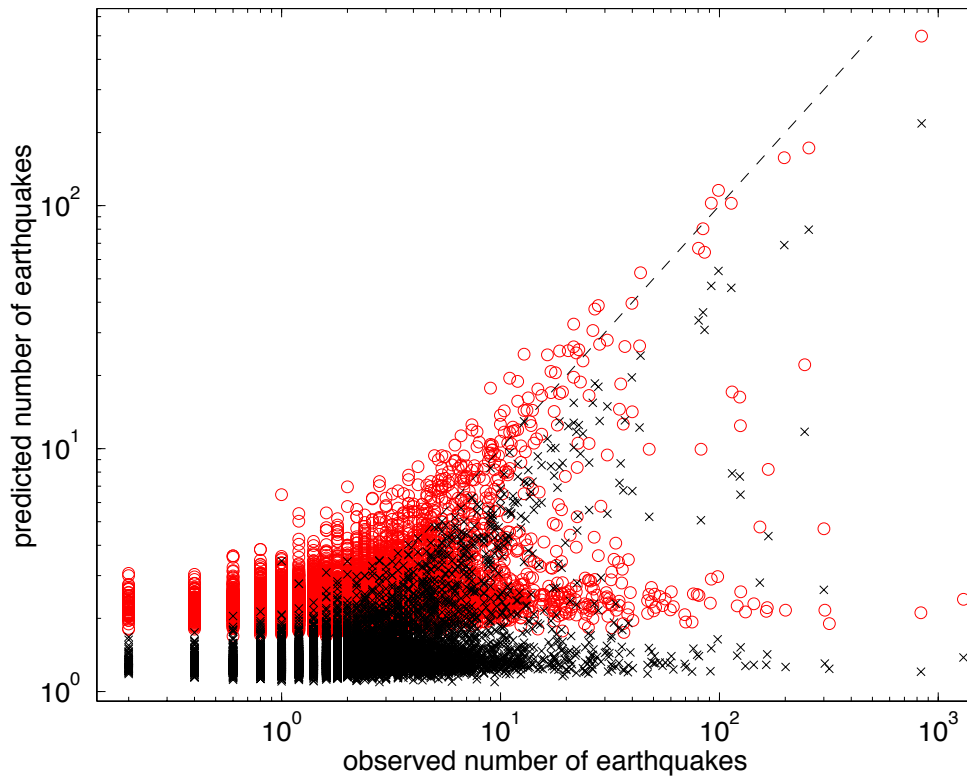


FIG. 7.8 – Comparison between the seismicity rate observed for a 5 days time period from the present with the predicted seismicity rate over the same 5 days period using either the sum of the bare propagators of the past seismicity (crosses) or using the median of 100 scenarios (circles), corresponding to the same data shown in Figure 7.7 but using a long synthetic catalog of  $N = 200000$  events over a time period of 150 yrs. The dashed line corresponds to the perfect prediction when the predicted seismicity rate is equal to the observed seismicity rate. This figure shows that the best predictions are obtained using the median of the scenarios rather than using the bare propagator, which always underestimates the observed seismicity rate. The meaning of two clusters (along the diagonal and lying horizontally at small predicted seismicity) are discussed in the text. Forecasts are updated every 5 days. A faster rate of updating does not change the fraction of predictable events lying close to the diagonal.

Figure 7.8 compares the predictions of the seismicity rate over a 5 day horizon with the

realized seismicity of a typical synthetic catalog, of which a small fraction of the history has been shown in Figure 7.7. This comparison is performed by plotting the predicted number of events in each 5 day horizon window as a function of the corresponding realized number of events. The open circles (respectively crosses) correspond to the forecasts using the median of 100 scenarios (respectively the sum of the bare Omori's propagators of the past seismicity). This Figure uses a synthetic catalog of  $N = 200000$  events of magnitude larger than  $m_0 = 3$  covering a time period of 150 yrs. The dashed line corresponds to the perfect prediction when the predicted seismicity rate is equal to the observed seismicity rate. This Figure shows that the best predictions are obtained using the median of the scenarios rather than using the bare propagator, which always underestimates the observed seismicity rate, as we have already shown.

The most striking feature of Figure 7.8 is the existence of several clusters, reflecting two mechanisms underlying the observed seismicity.

1. cluster LL with large predicted seismicity and large observed seismicity ;
2. cluster SL with small predicted seismicity and large observed seismicity ;
3. cluster SS with small predicted seismicity and small observed seismicity ;

Cluster LL along the diagonal reflects the predictive skill of the triggered seismicity algorithm : this is when future seismicity is triggered by past seismicity. Cluster SL lies horizontally at low predicted seismicity rates and reflect the fact that large realized seismicity rates can also be triggered by an unforecasted strong earthquake, which occurs by chance, even when the seismicity background is rather low. This mechanism expresses a fundamental limit of predictability since the ETAS model allows for strong events even with low prior seismicity, as the earthquake magnitudes are drawn from the GR, independently of any process. The occurrence of large events in periods of low seismicity is a rather improbable event but is not excluded as we observe in the simulations and as outlined by the second horizontal cluster in Figure 7.8. About 20% of the large values of the observed seismicity rate above 10 events per day fall in the LL cluster, corresponding to a good predictability of about 20% of the large peaks of observed seismic activity. The cluster SS is consistent with a predictive skill but small seismicity is not usually an interesting target. Note that there are no cluster of large predicted seismicity associated with small observed seismicity.

Figure 7.9 is the same as Figure 7.7 for a longer time window of 50 days, which stresses the importance of taking into account the yet unobserved future seismicity in order to accurately predict the level of future seismicity. Figure 7.10 is the same as Figure 7.8 for the prediction time window of 50 days with forecasts updated each 50 days. Increasing the time window  $T$  of the prediction from 5 to 50 days leads to a smaller variability of the predicted seismicity rate. However, fluctuations of the seismicity rate of one order of magnitude can still be predicted with this model. The ETAS model therefore performs much better than a Poisson process for large horizons of 50 days.

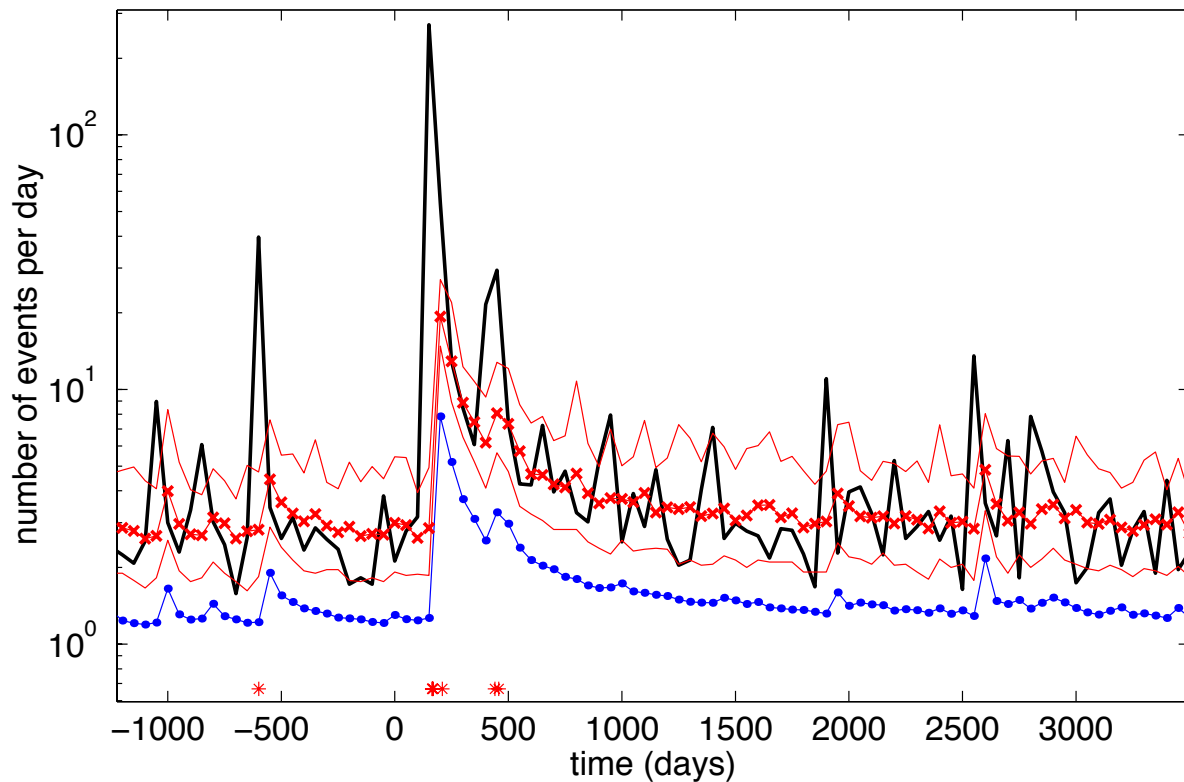


FIG. 7.9 – Same as Figure 7.7 but for a larger horizon  $t = 50$  days.

### Error diagrams and prediction gains

In order to quantify the predictive skills of different prediction algorithms for the seismicity of the next five days, we use the error diagram [Molchan, 1991; 1997; Molchan and Kagan, 1992]. The predictions are made from the present to 5 days in the future and are updated each 0.5 day. Using a shorter time between each prediction, or updating the prediction after each major earthquake, will obviously improve the predictions, because large aftershocks occur often just after the mainshock. But in practice the forecasting procedure is limited by the time needed to estimate the location and magnitude of an earthquake. Moreover, predictions made at very short term in advance (a few minutes) are not very useful.

An error diagram requires the definition of a target, here  $M \geq 6$  earthquakes, and plots the fraction of targets that were not predicted as a function of the fraction of time occupied by the alarms (total durations of the alarms normalized by the duration of the catalog). We define an alarm when the predicted seismic rate is above a threshold. Recall that the seismic rate is the physical quantity that embodies completely all the available information on past events. All targets one might be interested in derive from the seismic rate.

Figure 7.11 presents the error diagram for  $M \geq 6$  targets, using a time window  $T = 5$  days to estimate the seismicity rate, and a time  $dT = 0.5$  days between two updates of the predictions.

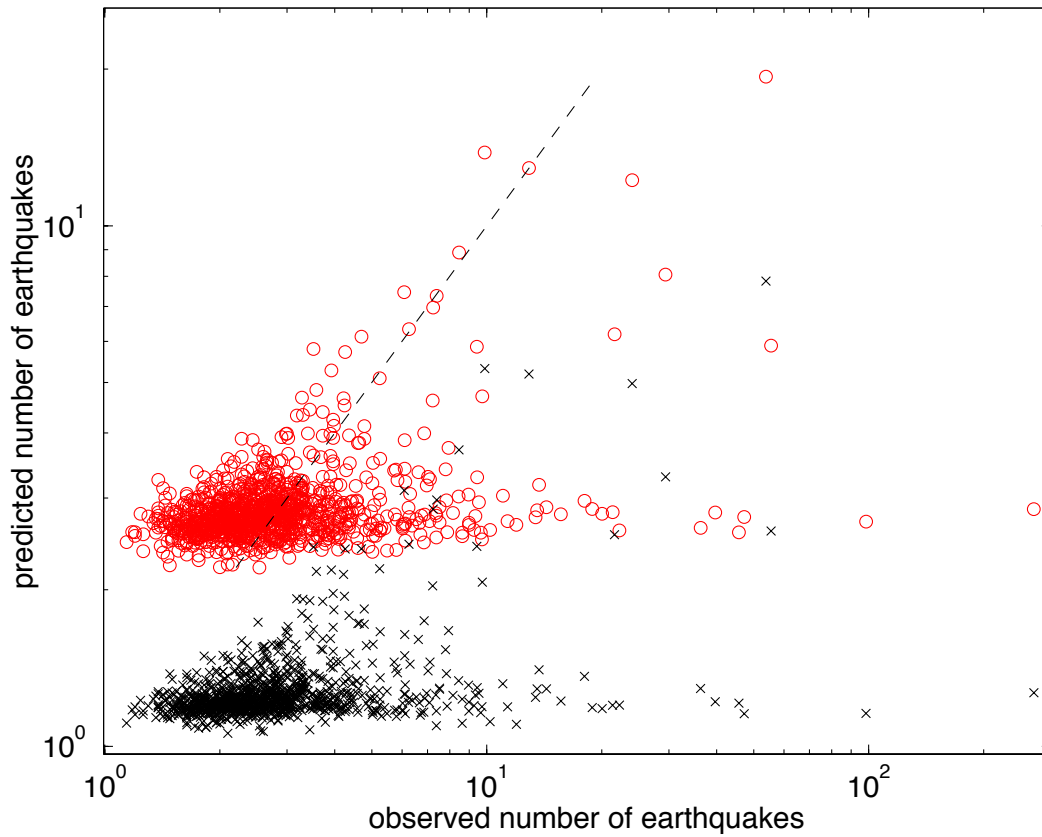


FIG. 7.10 – Same as Figure 7.8 but for a larger horizon  $t = 50$  days. For such large horizons, taking into account the cascade of triggered seismicity makes a huge difference on the performance of the predicted seismicity rate.

We use different prediction algorithms, either the bare propagator (dots), the median (circles) or the mean (triangles) number of events obtained for the 100 scenarios already generated to obtain Figures 7.7 and 7.8. Each point of each curve corresponds to a different threshold ranging from 0.1 to 1000 events per day. The results for these three prediction algorithms are considerably better than those obtained for a random prediction, shown as a dashed line for reference.

Ideally, one would like the minimum numbers of failures and the smallest possible alarm duration. Hence, a perfect prediction corresponds to points close to the origin. In practice, the fraction of failure to predict is 100% without alarms and the gain of the prediction algorithm is quantified by how fast the fraction of failure to predict decreases from 100% as the fraction of alarm duration increases. Formally, the gain  $G$  reported below is defined as the ratio of the fraction of predicted targets ( $= 1 - \text{number of failures to predict}$ ) divided by the fraction of time occupied by alarms. A completely random prediction corresponds to  $G = 1$ .

We observe that about 50% of the  $M \geq 6$  earthquakes can be predicted with a small fraction of alarm duration of about 20%, leading to a gain of 2.5 for this value of the alarm duration. The gain is actually significantly stronger for shorter fractions of alarm duration : as shown in panel

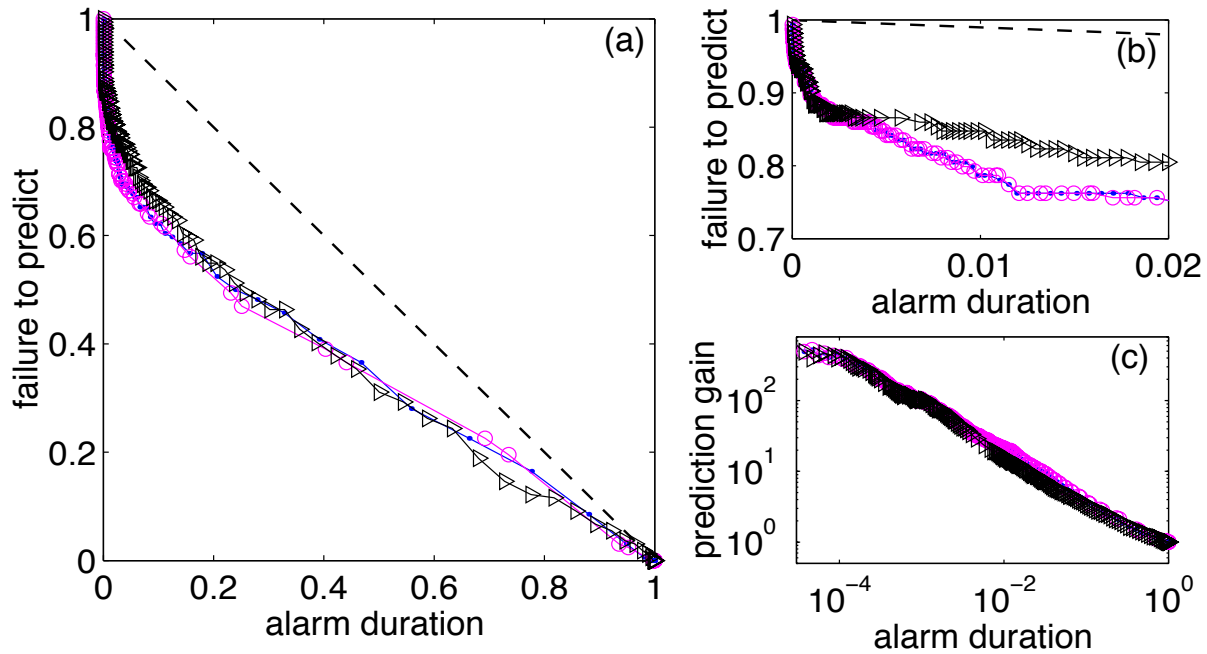


FIG. 7.11 – Error diagram of different prediction algorithms, using either the bare propagator (dots), the median (circles) or the mean (triangles) number of events obtained for the scenarios. The synthetic catalog and the prediction methods are the same as for Figures 7.7 and 7.8. We use a time horizon (window size) of  $T = 5$  days to estimate the seismicity rate but we update the predictions each 0.5 day. Target events are  $M \geq 6$  earthquakes. An alarm is defined when the predicted seismicity rate is above a threshold. Each point of the curve corresponds to a different threshold ranging from 0.1 to 1000 events per day. The quality of the predictions is measured by plotting the ratio of failures to predict as a function of the total durations of the alarms normalized by the duration of the catalog. The results for these three algorithms are considerably better than those obtained for a random prediction, shown as a dashed line for reference. This Figure shows that about 20% of large peaks of seismic activity can be predicted with a very small alarm duration of about 1%. Panel (b) is a magnification of panel (a) close to the origin of the alarm duration showing the very fast increase of the success fraction ( $= 1 - \text{failure to predict}$ ) as the alarm duration increases from 0. Panel (c) shows that the predicted gain, defined as the ratio of the success fraction over the alarm duration, is approximately an inverse power law with exponent slightly larger than  $1/2$  as a function of the alarm duration.

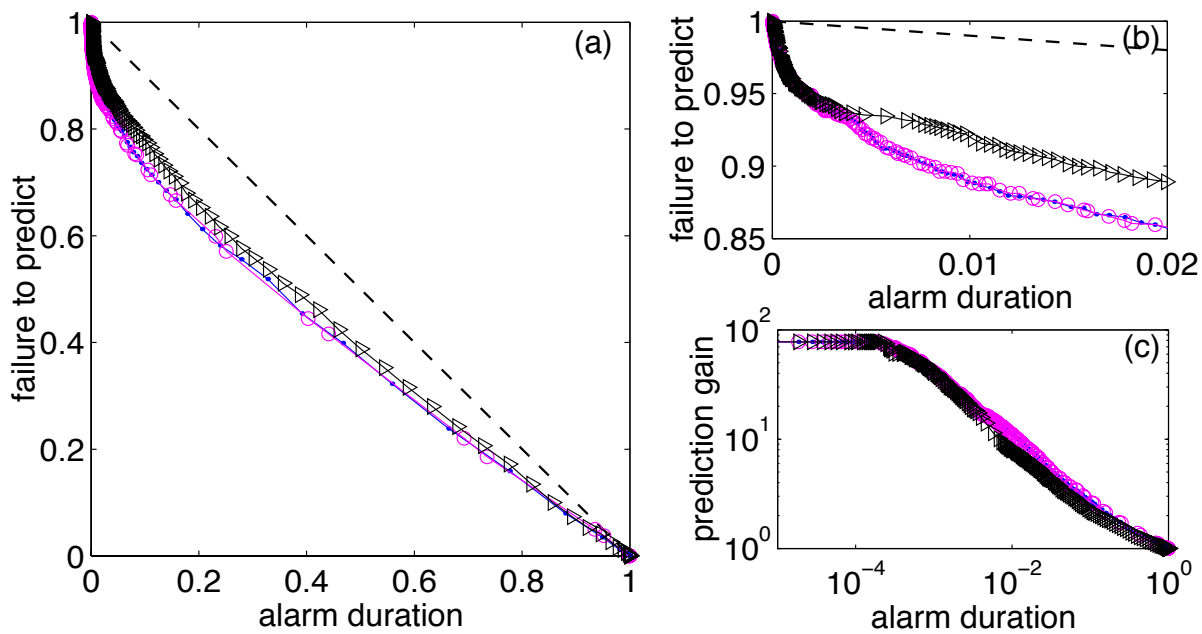


FIG. 7.12 – Same as Figure 7.11 but for targets with lower magnitudes  $M \geq 5$ . Panel (c) shows that the predicted gain is again approximately an inverse power law with exponent close to  $1/2$  as a function of the alarm duration.

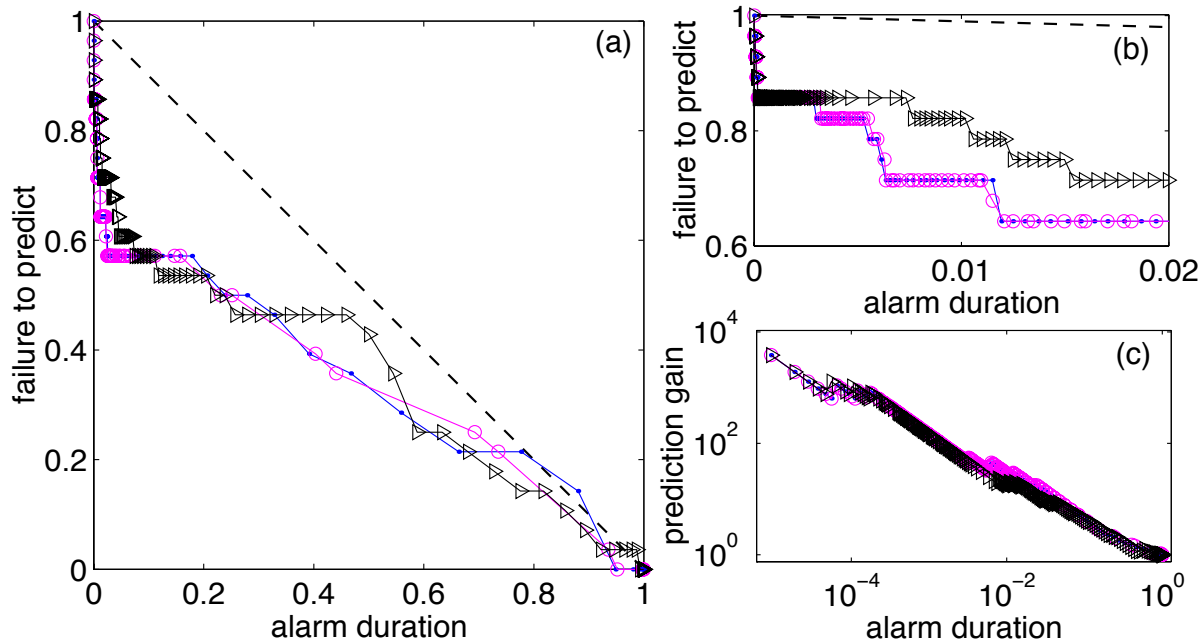


FIG. 7.13 – Same as Figure 7.11 but for targets with larger magnitudes  $M \geq 7$ . Panel (c) shows that the predicted gain is again approximately an inverse power law with exponent slightly smaller than 1 as a function of the alarm duration. Comparing this figure with Figures 7.11 and 7.12 suggests that the exponent defined in panel (c) is slowly increasing with the magnitude of the targets.

(b) of Figure 7.11, 25% of the  $M \geq 6$  earthquakes can be predicted with a small fraction of alarm duration of about 2%, leading to a gain of 12.5. The origin of this good skill for only a fraction of the targets has been discussed in relation with Figure 7.8, and is associated with those events that occur in times of large seismic rate (cluster along the diagonal in Figure 7.8). Panel (c) of Figure 7.11 shows the dependence of the prediction gain  $G$  as a function of the alarm duration : the three prediction schemes give essentially the same approximately power law increase with exponent close to 1/2 of the gain as the duration of alarm decreases. For small alarm duration, the gain reaches values of several hundreds. This saturation at very small values of the alarm duration is due to the finite-size effect that only a few targets are sampled ultimately. Figures 7.12 and 7.13 are similar to Figure 7.11, respectively for smaller targets of magnitudes larger than 5 and larger targets of magnitudes larger than 7.

Table 7.1 presents the results for the prediction gain and for the number of successes using different choices of the time window  $T$  and of the update time  $dT$  between two predictions, and for different values of the target magnitude between 5 and 7. The prediction gain decreases if the time between two updates of the prediction increases, because most large earthquakes occur at very short times after a previous large earthquake. In contrast, the prediction gains do not depend on the time window  $T$  for the same value of the update time  $dT$ .

The prediction gain is observed to increase significantly with the target magnitude, especially in the range of small fraction of alarm durations (see Table 7.1 and Figures 7.11-7.13). However,

TAB. 7.1 – Prediction gain for different choices of the alarm duration, and/or different values of the time interval  $T$ , of the update time  $dT$ , and of the target magnitude  $M_t$ .  $N_1$  is the number of targets  $M \geq M_t$ ;  $N_2$  is the number of intervals with at least one target.  $G_{max}$  is the maximum prediction gain, which is realized for an alarm duration  $A$  (in proportion of the total duration of the catalog), which is also given in the table. All three prediction algorithms used here provide the same gain as a function of the alarm duration, corresponding to different choices of the alarm threshold on the predicted seismicity rate.  $N_s$  is the number of successful predictions, using the alarm threshold that provides the maximum predictions gain  $G_{max}$  for an alarm duration  $A$  (we count only one success when two events occur in the same interval). This number  $N_s$  is always very small, but a much larger number of successes can be obtained with a larger alarm duration.  $N_{1\%}$ ,  $N_{10\%}$ ,  $N_{50\%}$  are the number of successes corresponding to an alarm duration (in proportion of the total duration of the catalog) of 1%, 10% and 50% respectively, corresponding to the prediction gains  $G_{1\%}$ ,  $G_{10\%}$  and  $G_{50\%}$ . The values of  $G_{50\%}$  show a saturation in the predictive power when increasing the fraction of alarm time, reflecting the fundamental limitation stemming from the fraction of large earthquakes not associated with a large seismic rate. Reading for instance of the last line of this table, we observe that, out of 26 time windows of 50 days that contained a  $M \geq 7$  earthquake, we are able to predict 7 of them with only 1% of the time occupied by alarms. Only two additional ones are predicted when using 10% of the time occupied by alarms. And only another four are predicted by increasing the time of alarms to half the total duration of the catalog. We use non-overlapping time intervals for the predictions of length  $T$ , with a time  $dT \leq T$  between two predictions. The catalog spans 150 years corresponding to a little more than  $10^5$  half-day periods.

T	dT	$M_t$	$N_1$	$N_2$	$G_{max}$	$A$	$N_s$	$N_{1\%}$	$N_{10\%}$	$N_{50\%}$	$G_{1\%}$	$G_{10\%}$	$G_{50\%}$
1.0	1.0	5.0	2003	1332	40.4	$3.2 \times 10^{-4}$	17	120	332	806	9.01	2.49	1.21
1.0	1.0	5.5	637	461	117.	$7.4 \times 10^{-5}$	4	58	136	303	12.6	2.95	1.31
1.0	1.0	6.0	198	159	339.	$3.7 \times 10^{-5}$	2	30	56	94	18.9	3.52	1.18
1.0	1.0	6.5	66	55	979.	$1.9 \times 10^{-5}$	1	10	15	28	18.2	2.73	1.02
1.0	1.0	7.0	29	27	665.	$5.6 \times 10^{-5}$	1	7	11	14	25.9	4.07	1.04
5.0	0.5	5.0	2003	1389	77.5	$1.1 \times 10^{-4}$	12	155	382	853	11.2	2.75	1.23
5.0	0.5	5.5	637	483	223.	$7.4 \times 10^{-5}$	8	72	155	320	14.9	3.21	1.33
5.0	0.5	6.0	198	164	656.	$1.9 \times 10^{-5}$	2	35	64	106	21.3	3.90	1.29
5.0	0.5	6.5	66	57	1889.	$9.3 \times 10^{-6}$	1	12	18	32	21.0	3.16	1.12
5.0	0.5	7.0	29	28	3847.	$9.3 \times 10^{-6}$	1	8	12	17	28.6	4.29	1.21
5.0	5.0	5.0	2003	1172	9.2	$6.5 \times 10^{-4}$	7	53	222	652	4.52	1.89	1.11
5.0	5.0	5.5	637	420	25.6	$3.7 \times 10^{-4}$	4	30	93	253	7.14	2.21	1.20
5.0	5.0	6.0	198	145	74.3	$2.8 \times 10^{-4}$	3	16	38	85	11.0	2.62	1.17
5.0	5.0	6.5	66	53	203.	$1.9 \times 10^{-4}$	2	7	12	30	13.2	2.26	1.13
5.0	5.0	7.0	29	26	414.	$1.9 \times 10^{-4}$	1	6	9	14	23.1	3.46	1.08
10.	10.	5.0	2003	1067	5.1	$5.6 \times 10^{-4}$	3	32	167	584	3.00	1.57	1.09
10.	10.	5.5	637	400	13.5	$3.7 \times 10^{-4}$	2	19	77	229	4.75	1.93	1.15
10.	10.	6.0	198	137	39.3	$1.9 \times 10^{-4}$	1	10	30	78	7.30	2.19	1.14
10.	10.	6.5	66	50	107.	$1.9 \times 10^{-4}$	1	5	8	26	10.0	1.60	1.04
10.	10.	7.0	29	24	224.	$1.9 \times 10^{-4}$	1	5	7	13	20.8	2.92	1.08
50.	50.	5.0	2003	701	1.5	0.016	17	11	84	370	1.57	1.20	1.06
50.	50.	5.5	637	329	3.3	$9.3 \times 10^{-4}$	1	8	43	181	2.43	1.31	1.10
50.	50.	6.0	198	123	8.8	$9.3 \times 10^{-4}$	1	5	20	62	4.07	1.63	1.01
50.	50.	6.5	66	48	22.4	$9.3 \times 10^{-4}$	1	4	7	32	8.33	1.46	1.33
50.	50.	7.0	29	22	48.9	$9.3 \times 10^{-4}$	1	4	5	16	18.2	2.27	1.45
50.	5.	5.0	2003	1172	9.2	$6.5 \times 10^{-4}$	7	53	209	657	3.37	1.78	1.12
50.	5.	5.5	637	420	25.6	$3.7 \times 10^{-4}$	4	27	89	251	4.76	2.12	1.20
50.	5.	6.0	198	145	74.3	$2.8 \times 10^{-4}$	3	13	37	82	7.24	2.55	1.13
50.	5.	6.5	66	53	203.	$1.9 \times 10^{-4}$	2	7	11	24	8.49	2.08	0.91
50.	5.	7.0	29	26	414.	$1.9 \times 10^{-4}$	2	7	9	13	15.4	3.46	1.00

this increase of the prediction gain does not mean that large earthquakes are more predictable than smaller ones, in contrast with for instance the critical earthquake theory [Sornette and Sammis, 1995; Jaumé and Sykes, 1999; Sammis and Sornette, 2002]. In the ETAS model, the increase of the prediction gain with the target magnitude is solely the result of decreasing statistics, i.e., is due to the decrease of the number of target events with the target magnitude. Indeed, choosing  $N$  events at random in the catalog independently of their magnitude gives on average the same prediction gain as for the  $N$  largest events. This demonstrates that the larger predictability of large earthquakes is solely a size effect. We now clarify the statistical origin of this size effect.

Let us consider a catalog of total duration  $D$  with a total number  $N$  of events analyzed with  $D/T$  time windows with horizon  $T$ . These  $D/T$  windows can be sorted out by decreasing seismicity  $r_1 > r_2 > \dots > r_n > \dots$ , where  $r_i$  is the  $i$ -th largest number of events in a window of size  $T$ . There are  $n_1, n_2, \dots, n_i, \dots$  windows of type  $1, 2, \dots, i, \dots$  respectively, such that  $\sum_i r_i n_i = N$ . Then, the frequency-probability that an earthquake drawn at random from the catalog falls within a window of type  $i$  is

$$p_i = \frac{r_i n_i}{N} . \quad (7.31)$$

We have found that, over more than three decades spanning from 1 event to  $10^3 - 10^4$  events per window, the cumulative distribution of these  $p_i$ 's is a power law with exponent approximately equal to  $\kappa = 0.4$ . This power law is found for the observable realized seismicity as well as for the seismicity predicted by the different methods discussed above. Such a small exponent  $\kappa$  implies that the few windows that happen to have the largest number of events contain a significant fraction of the total seismicity. It can be shown [Feller, 1971] that, in absence of any constraint, the single window with the largest number of events contains on average  $1 - \kappa = 60\%$  of the total seismicity. This would imply that there is a 60% probability that an earthquake drawn at random within the catalog (of 150 years) belongs to this single window of 5 days. Actually this effect of extreme values is smaller because the random variables  $p_i$  have to sum up to 1 by definition. This can be shown to entail a roll-off of the cumulative distribution depleting the largest values of  $p_i$ . Empirically, we find that the most active window out of the approximately 54,000 daily windows of our 150 years long catalog contains only 3% of the total number of events. While this value of 3% is smaller than the prediction of 60% in absence of normalization, it is considerably larger than the “democratic” result which would predict a fraction of about 0.002% of the seismicity in each window. Since a high seismicity rate implies strong interactions and triggering between earthquakes and is usually associated with recent past high seismicity, the events in such a window are highly predictable. When the number of targets increases, one starts to sample statistically other windows with smaller seismicity which have therefore a weaker relation with triggered seismicity and thus present less predictive power.

In our previous discussion, we have not distinguished the skills of the three algorithms, because they perform essentially the same with respect to the assigned targets. This is very

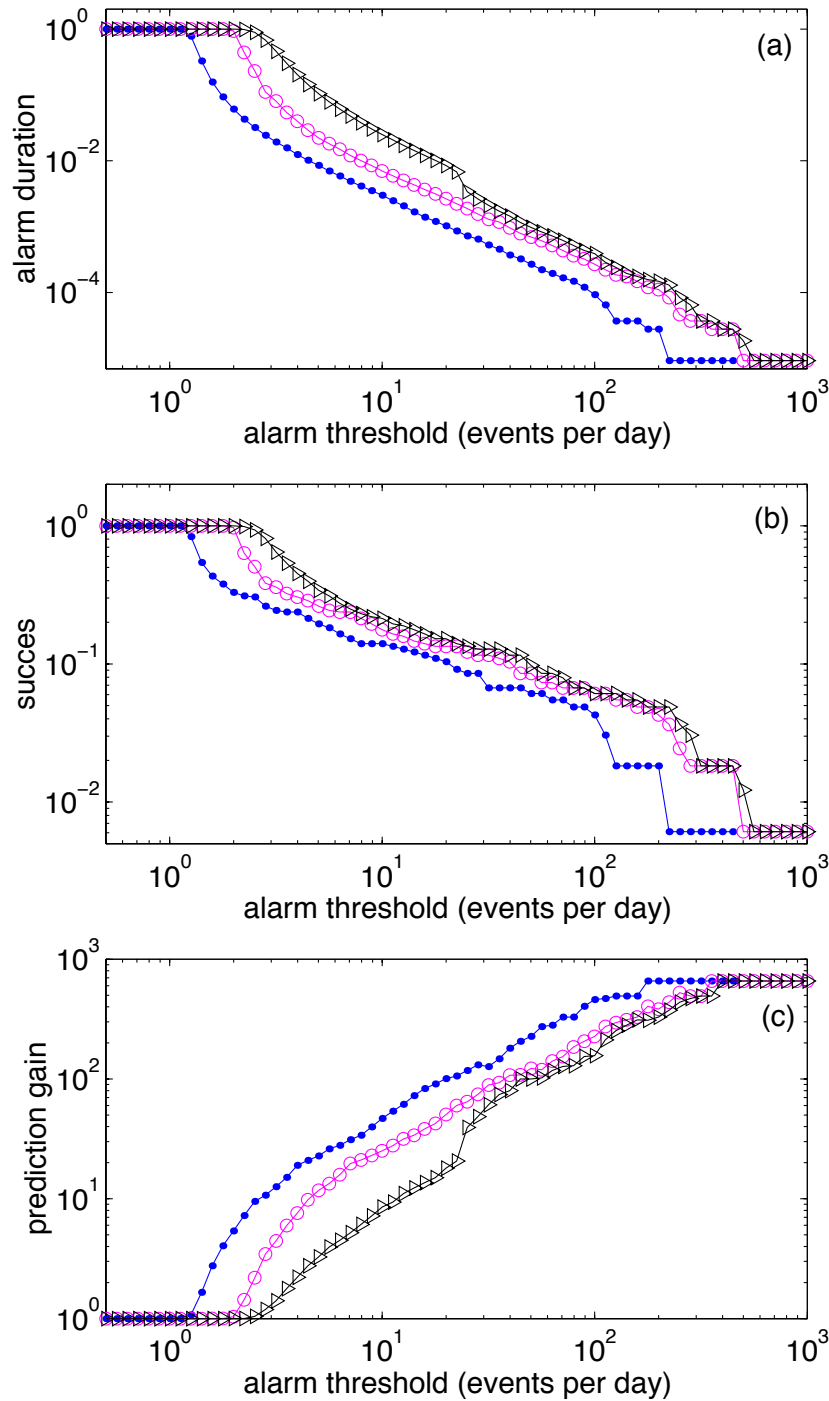


FIG. 7.14 – Analysis of the prediction methods, using the same synthetic catalog and predictions methods as for Figures 7.7-7.13. We use a time window  $T = 5$  days to estimate the predicted seismicity rate, and a time  $dT = 0.5$  days between two updates of the prediction. Target events are  $M \geq 6$  earthquakes. The duration of alarms normalized by the total duration of the catalog is shown in panel (a) as a function of the alarm threshold for the three predictions methods : bare propagator (dots), the median (circles) and the mean (triangles) number of events obtained for the scenarios. The proportion of successes is shown in panel (b). The prediction gain shown in panel (c) is defined by the ratio of the proportion of successes (b) over the duration of alarms (a). The prediction gain for large values of the alarm threshold is significantly higher than the random prediction gain equal to 1.

surprising from the perspective offered by all our previous analysis showing that the naive use of the direct Omori's law without taking into account the effect of any indirect triggered seismicity strongly underestimate the future seismicity. We should thus expect a priori that this prediction scheme should be significantly worse than the two others based on a correct counting of all unobserved triggered seismicity. The explanation for this paradox is given by examining Figure 7.14, which presents further insight in the prediction methods applied to the synthetic catalogs used in Figures 7.5-7.13. Figure 7.14 shows three quantities as a function of the threshold in seismicity rate used to define an alarm, for each of the three algorithms. These quantities are respectively the duration of alarms normalized by the total duration of the catalog shown in panel (a), the fraction of successes ( $= 1 - \text{failure to predict}$ ) shown in panel (b) and the prediction gain shown in panel (c). These three panels tell us that the incorrect level of seismic activity predicted by the bare Omori's law approach can be compensated by the use of a lower alarm threshold. In other words, even if the seismicity rate predicted by the bare Omori's law approach is very wrong in absolute values, its time evolution in relative terms contains basically the same information as the full-fledged method taking into account all unobserved triggered seismicity. Therefore, an algorithm that can adjust the alarm threshold to the incorrect level of seismicity and detect a relative change of seismicity can perform as well as the complete approach for the forecast of the assigned targets. This example is a remarkable illustration of the fact that predictions of different targets can have very different skills which depend on the targets. Here, there is no doubt that using the full-fledged renormalized approach is the correct and only method to get the best possible predictor of future seismicity rate. However, other simpler and more naive methods can perform almost as well for more restricted targets, such as the prediction of only strong earthquakes.

## Information gain

We now follow *Kagan and Knopoff* [1977] who introduced the entropy/information concept linking the likelihood gain to the entropy per event and hence to the predictive power of the fitted model and *Vere-Jones* [1998] who suggests to use information gain to compare different models and to estimate the predictability of a process.

Our forecast algorithm provides the average seismicity rate  $\lambda_i$  above  $m_0$  in the time interval  $(t_i, t_i + T)$ . Assuming a constant magnitude distribution given by (7.5), the probability  $p_i$  to have at least an event above the target magnitude  $M_t$  in the time interval  $(t_i, t_i + T)$  can be evaluated from the average seismicity rate  $\lambda_i$  by

$$p_i = 1 - \exp\left(-\lambda_i 10^{-b(M_t - m_0)}\right). \quad (7.32)$$

Figure 7.15 shows the probability  $p_i$  obtained for different choices of the target magnitude  $M_t$ , for the same sequence as in Figure 7.7.

The binomial score  $B$  compares the prediction  $p_i$  with the realization  $X_i$ , with  $X_i = 1$  if a

TAB. 7.2 – Binomial scores  $B$  for several prediction algorithms and different choices of the time interval  $T$  and the target magnitude  $M_t$ .  $B_{med}$  is evaluated from the median of the seismicity rate of the scenarios;  $B_{mean}$  from the average seismicity rate;  $B_{meanl}$  using the exponential  $\lambda = \exp(\log \langle n \rangle)$  of the average of the logarithm of the seismicity rate;  $B_\phi$  is measured using the bare propagator to estimate the seismicity rate;  $B_{pois}$  using a Poisson process with a seismicity rate equal to the average value of the catalog.  $N_1$  is the number of target events  $M \geq M_t$ ;  $N_2$  is the number of intervals with at least one target event. Note that  $B_{med}$  seems to be often the best for the smaller magnitudes while  $B_{mean}$  is often the best for the largest magnitudes.

T (days)	$M_t$	$N_1$	$N_2$	$B_{med}$	$B_{meanl}$	$B_{mean}$	$B_\phi$	$B_{pois}$
1.	5.0	2003	1332	-5997.7	-5995.1	-6341.0	-6057.3	-6361.8
1.	5.5	637	461	-2512.4	-2511.7	-2614.6	-2545.0	-2678.7
1.	6.0	198	159	-1007.8	-1006.9	-1042.2	-1023.2	-1089.4
1.	6.5	66	55	-409.9	-409.3	-420.5	-416.8	-434.3
1.	7.0	29	27	-217.8	-216.6	-218.1	-224.0	-233.3
5.	5.0	2003	1172	-3626.3	-3632.5	-3851.7	-3717.8	-3862.8
5.	5.5	637	420	-1720.0	-1719.1	-1774.8	-1765.4	-1810.7
5.	6.0	198	145	-732.1	-731.9	-748.9	-752.8	-776.7
5.	6.5	66	53	-321.2	-320.5	-322.0	-331.3	-335.4
5.	7.0	29	26	-171.3	-170.5	-168.1	-179.3	-183.5
10.	5.0	2003	1067	-2651.0	-2662.7	-2822.4	-2736.0	-2852.4
10.	5.5	637	400	-1391.3	-1393.0	-1438.9	-1439.9	-1465.4
10.	6.0	198	137	-621.1	-621.2	-637.3	-640.3	-648.6
10.	6.5	66	50	-276.6	-276.2	-280.1	-286.1	-285.2
10.	7.0	29	24	-147.2	-146.4	-145.3	-155.3	-154.3
50.	5.0	2003	701	-699.0	-717.3	-787.3	-758.7	-817.2
50.	5.5	637	329	-658.9	-666.0	-698.8	-702.7	-706.2
50.	6.0	198	123	-379.6	-381.1	-392.5	-398.5	-395.5
50.	6.5	66	48	-192.2	-191.5	-192.5	-204.3	-197.9
50.	7.0	29	22	-104.5	-103.5	-102.3	-113.3	-107.5

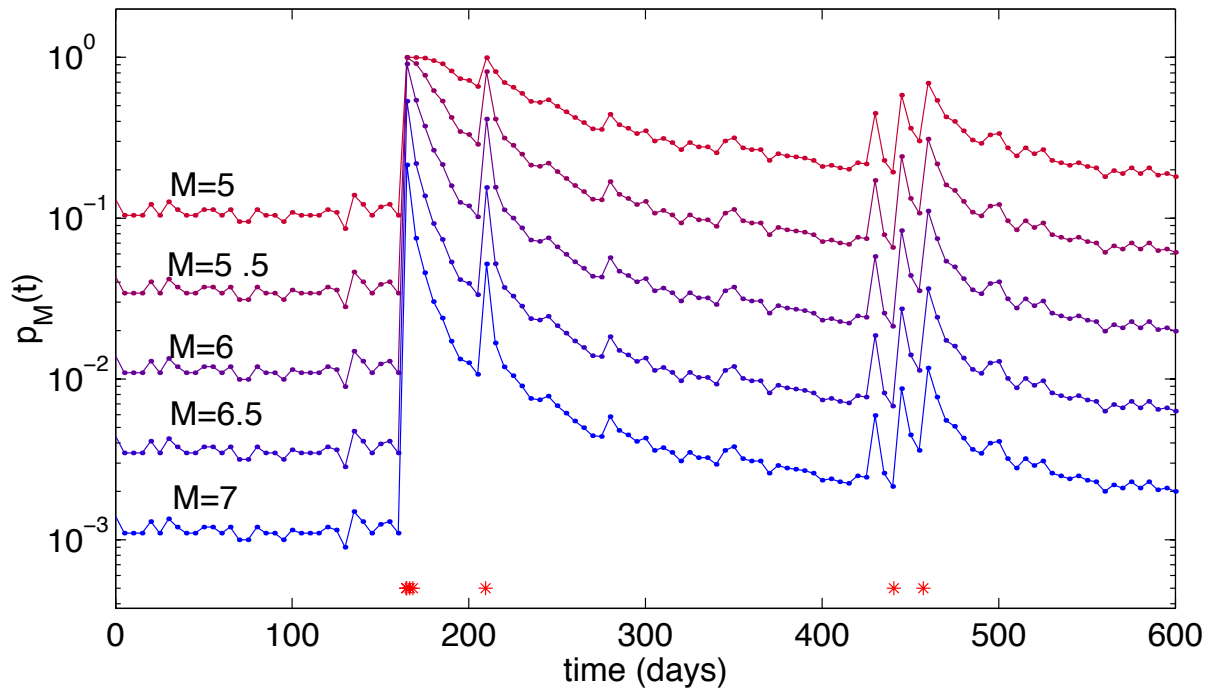


FIG. 7.15 – Probability  $p_M(t)$  of having at least an event of magnitude larger than  $M$  in the time interval  $(t, t+T)$  with  $T=5$  days. We have evaluated  $p_M$  for  $M$  between 5 and 7, from the seismicity rate predicted by the median of 100 scenarios, and using equation (7.32) to estimate the probability  $p_M(t)$  from the average seismicity rate  $\lambda(t)$  in the time interval  $(t, t+T)$ .  $p_M(t)$  is plotted for the sequence shown in Figure 7.7. Stars indicate the occurrence of a large  $M \geq 7$  earthquake. The largest  $M = 8.55$  event of the sequence occurs at time  $t = 164$  days when the seismicity rate is close to the average value. Thus, this event cannot be predicted. Six large  $M > 7$  earthquakes occur in the following 500 days when the seismicity rate is still above its average value, including three  $M > 7$  events in the 5 days immediately following the great event.

target event occurred in the interval  $(t_i, t_i + T)$  and  $X_i = 0$  otherwise. For the whole sequence of intervals  $(t_i, t_i + T)$ , the binomial score is defined by

$$B = \sum_i X_i \log(p_i) + (1 - X_i) \log(1 - p_i) , \quad (7.33)$$

where the sum is performed over all (non-overlapping) time windows covering the whole duration of the catalog. The first term represents the contribution to the score from those intervals which contain an event, and the second term the contribution to the score from those intervals which contain no event. In order to test the performance of a forecast algorithm, we compare the binomial score  $B$  of the forecast with the binomial score of a Poisson process. The results for different choices of the time interval  $T$  and of the target magnitude  $M_t$  are listed in Table 2. We evaluate the binomial score  $B$  for different prediction algorithms (i) the average of the seismicity rate over all scenarios, (ii) the exponential of the average of the logarithm of the mean of the

seismicity rate, (iii) the median of the seismicity rate and (iv) the sum of the bare propagators of the past seismicity. The results for all forecasting methods are in general better than the Poisson process, i.e., the binomial score for the forecasting algorithms are larger than the score obtained with a Poisson process. The scores of the forecasting methods which take into account the cascade of secondary aftershocks ( $B_{med}$ ,  $B_{mean}$  and  $B_{meanl}$  in Table 2 are significantly better than the score  $B_\phi$  obtained with the bare propagator, even for short time intervals  $T$ . For large times intervals  $T \geq 10$  days, and for large target magnitudes, the results for the bare propagator are even worse than the results obtained with a Poisson process.

Our tests show that the prediction skills depend strongly on all the parameters  $\alpha, b, n, \theta$  and  $\mu$ . The larger  $\alpha$  is, the better the predictability is as the triggered seismicity is very active in this case because strong and large aftershock time series occur. The impact of the  $b$ -value is felt relative to  $\alpha$  through its influence in the branching ratio  $n$  : the larger  $n$  is (i.e., closest to the critical value 1), the better is the predictability as the triggered seismicity is the strongest. The larger  $\theta$  is, the faster is the decay of the bare Omori's propagator. If  $n < 1$ , the larger  $\theta$  is, the shorter is  $t^*$  and the faster is also the decay of the renormalized Omori's propagator  $K(t)$ , hence the weaker is the cascade of secondary aftershocks, and the worse is the predictability. Lastly, the background rate of seismicity  $\mu$  controls the "noise" level and the time over which a triggered sequence of events is above it and can thus be identified as a useful signal for predicting the future seismicity rate : thus, the larger  $\mu$  is, the poorer is the predictive skill.

Our results are in complete disagreement with those reported in [Vere-Jones, 1998] on the same ETAS model : we conclude that the ETAS model has a significantly higher predictive power than the Poisson process while Vere-Jones [1998] concludes that the forecasting performance of the ETAS model is worse than the Poisson. Vere-Jones and Zhuang confirm (private communication) that their simulations reported in [Vere-Jones, 1998] does take into account the seismicity triggered from the present  $u$  till the advent of the large earthquake target. This is particularly important as the real seismicity is much higher than predicted in absence of the cascade of triggering events as we have shown here. Its neglect is expected to have serious consequences in the scores. But, as far we can understand from [Vere-Jones, 1998] and private communications, Vere-Jones and Zhuang's procedure and ours are very similar, if not indistinguishable and the discrepancy cannot be accounted in this way. The tests of [Vere-Jones, 1998] have been performed using a  $\alpha/b$  ratio of  $0.57/1.14 = 0.5$  smaller than the value  $\alpha/b = 0.8$  used in our simulations. This discrepancy may lead to a smaller predictability for the simulations of [Vere-Jones, 1998] because there are fewer large aftershock sequences. The branching ratio  $n = 0.78$  used by [Vere-Jones, 1998] is very close to our value  $n = 0.8$ . However, the difference in the ETAS parameters cannot explain why Vere-Jones [1998] obtains a better predictability for a Poisson process than for the ETAS model.

Figures 7.8 and 7.10 and our tests show unambiguously that the ETAS model has a significant degree of predictability above the Poisson process. We thus caution that a suitable assessment of

the forecasting skills of a model requires several complementary quantitative measures, such as the predicted versus observed seismicity rates, the error diagram and predictability gain and the entropy-information gains, and a large number of target events. We hope that the present work will stimulate a quantitative reassessment of [Vere-Jones, 1998]’s results by the New-Zealand group in the goal of assessing the ultimate limit of the ETAS model as a good model of genuine seismicity.

## 7.7 Conclusions

Using a simple model of triggered seismicity, the ETAS model, based on the (bare) Omori’s law, the Gutenberg-Richter law and the idea that large events trigger more numerous aftershocks, we have demonstrated the essential role played by the cascade of triggered seismicity in controlling the rate of aftershock decay as well as the overall level of seismicity in the presence of a constant external seismicity source. We have developed an analytical approach to account for the triggered seismicity adapted to the problem of forecasting future seismic rates at varying horizons from the present. Tests presented on synthetic catalogs have validated the use of interacting triggered seismicity to forecast large earthquakes in these models. This work provides what we believe is a useful benchmark from which to develop real prediction tests of real catalogs. These tests have also delineated the fundamental limits underlying forecast skills, stemming from an intrinsic stochastic component in the seismicity models. Our results offer a rationale for the fact that pattern recognition algorithms may perform better for strong earthquakes than for weaker events. Although the predictability of an earthquake is independent of its magnitude in the ETAS model, the prediction gain is better for the largest events because they are less numerous and it is thus more probable that they are associated with periods of large seismicity rates, which are themselves more predictable.

We have shown in [Helmstetter *et al.*, 2002] that most precursory patterns used in prediction algorithms, such as a decrease of  $b$ -value or an increase of seismic activity can be reproduced by the ETAS model. If the physics of triggering is fully characterized by the class of models discussed here, this suggests that detection of patterns and precursory indicators are sub-optimal compared with the prediction based on a full modeling of the seismicity. The calibration of the ETAS model or some of its variants on real catalogs as done in [Kagan and Knopoff, 1987; Kagan and Jackson, 2000; Console and Murru, 2001]; Ogata, 1988, 1989, 1992, 1999, 2001; Kagan, 1991; Felzer *et al.*, 2001] represent important steps in this direction. However, in practical terms, the issue of the model errors associated with the use of an incorrect model calibrated on an incomplete data set with not fully known parameters may make this statement weaker or even turn it on its head. This needs to be seriously investigated in the future.

## 7.8 Appendix A : Hypermetropic renormalized propagator $K_u^*(t)$ in various limits

### Hypermetropic renormalized propagator for $t \ll t^*$

Putting the asymptotic expansion of  $K(t)$  for  $t < t^*$  (7.13) in (7.25) we obtain for  $t \gg c$  and  $t > u$

$$K_{u < t < t^*}^*(t) = \frac{1}{\Gamma(\theta) \Gamma(1-\theta)} \frac{(t+c-u)^\theta}{(u+c)^\theta (t+c)}, \quad (7.34)$$

which recovers  $K(t)$  for  $u = 0$ .

### Hypermetropic renormalized propagator for $t \gg u$

In the regime  $t \gg u$ , we can rewrite (7.28) as

$$\begin{aligned} K_u^*(t) &\approx K(t) - K(t) \int_0^u \phi(\tau) d\tau \\ &\approx K(t) \left( 1 - n \left( 1 - \frac{c^\theta}{(u+c)^\theta} \right) \right) \end{aligned} \quad (7.35)$$

### Hypermetropic renormalized propagator for $t \approx u$

In the regime  $t \approx u$  and  $t - u \gg c$ , we can rewrite (7.25) as

$$\begin{aligned} K_u^*(t) &\approx \phi(t) \int_u^t K(t-\tau) d\tau \\ &\approx \phi(t) (\mathcal{K}(t-u) + 1), \end{aligned} \quad (7.36)$$

where  $\mathcal{K}(t)$  is the integral of  $K(t) - \delta(t)$  given by (7.23). The second term in (7.36) comes from the Dirac  $\delta(t)$  in the expression (7.10) of  $K(t)$ .

### Acknowledgments

We are very grateful to D. Harte, Y.Y. Kagan, Y. Ogata and D. Vere-Jones for useful exchanges.



## Chapitre 8

# Diffusion of epicenters of earthquake aftershock, Omori law and generalized continuous-time random walk model

Agnès Helmstetter

Laboratoire de Géophysique Interne et Tectonophysique,  
Université Joseph Fourier, BP 53X, 38041 Grenoble Cedex, France.

Didier Sornette

Laboratoire de Physique de la Matière Condensée, Université de Nice-Sophia Antipolis, and  
Department of Earth and Space Sciences and Institute of Geophysics and Planetary Physics,  
University of California, Los Angeles, California.

In press in *Physical Review E*, 2002.

### Abstract

The epidemic-type aftershock sequence model (ETAS) is a simple stochastic process modeling seismicity, based on the two best-established empirical laws, the Omori law (power law decay  $\sim 1/t^{1+\theta}$  of seismicity after an earthquake) and Gutenberg-Richter law (power law distribution of earthquake energies). In order to describe also the space distribution of seismicity, we use in addition a power law distribution  $\sim 1/r^{1+\mu}$  of distances between triggered and triggering earthquakes. The ETAS model has been studied for the last two decades to model real seismicity catalogs and to obtain short-term probabilistic forecasts. Here, we present an exact mapping

between the ETAS model and a class of CTRW (continuous time random walk) models, based on the identification of their corresponding Master equations. This mapping allows us to use the wealth of results previously obtained on anomalous diffusion of CTRW. After translating into the relevant variable for the ETAS model, we provide a classification of the different regimes of diffusion of seismic activity triggered by a mainshock. Specifically, we derive the relation between the average distance between aftershocks and the mainshock as a function of the time from the mainshock and of the joint probability distribution of the times and locations of the aftershocks. The different regimes are fully characterized by the two exponents  $\theta$  and  $\mu$ . Our predictions are checked by careful numerical simulations. We stress the distinction between the “bare” Omori law describing the seismic rate activated directly by a mainshock and the “renormalized” Omori law taking into account all possible cascades from mainshocks to aftershocks of aftershock of aftershock, and so on. In particular, we predict that seismic diffusion or sub-diffusion occurs and should be observable only when the observed Omori exponent is less than 1, because this signals the operation of the renormalization of the bare Omori law, also at the origin of seismic diffusion in the ETAS model. We present new predictions and insights provided by the ETAS to CTRW mapping that suggest novel ways for studying seismic catalogs. Finally, we discuss the present evidence for our predicted sub-diffusion of seismicity triggered by a main shock, stressing the caveats and limitations of previous empirical works.

## 8.1 Introduction

The spatio-temporal complexity of earthquakes is often invoked as an illustration of the phenomenon of critical self-organization with scale-invariant properties [Sornette, 1991; Rundle and Klein, 1995; Main, 1996; Sornette, 1999a; Turcotte, 1999]. This concept points to the importance of developing a system approach in which large scale properties can emerge from the repeating interactions occurring at smaller scales. Such ideas are implemented in models proposing links between the physics of earthquakes and concepts of statistical physics, such as critical points, self-organized criticality, spinodal decomposition, critical depinning, etc., in order to explain the most solidly established facts in the phenomenology of earthquakes, of which we cite the three most important.

- LAW 1 : The Gutenberg-Richter law [Gutenberg and Richter, 1944] states that the cumulative distribution of earthquake magnitudes  $m$  sampled over broad regions and large time intervals is proportional to  $10^{-bm}$ , with a  $b$ -value  $b \approx 1$ . Translating into energies  $E$  with the correspondence  $m = (2/3) \log_{10} E + \text{constant}$  leads to a power law  $\sim 1/E^B$  with  $B \approx 2/3$ .
- LAW 2 : Omori law for aftershocks [Omori, 1894] states that the rate of earthquakes triggered by a mainshock decays with time according to an inverse power  $1/t^p$  of time with an exponent  $p \approx 1$ .

- LAW 3 : The earthquakes are clustered in space along hierarchical fault structures [Ouillon et al., 1996] and their spatial distribution over long times can be approximately described by a fractal dimension close to 2.2 (in three dimensions) [Kagan and Knopoff, 1980].

There are many other empirical “laws” but these three characterize the very fundamentals of seismicity in size, time and space.

We should immediately point out that these three laws come with significant caveats.

1. There have been on-going controversies on the universality of the exponent  $B$  or  $b$ -value of the Gutenberg-Richter law [Pisarenko and Sornette, 2002; Kagan, 1999b].
2. The exponent  $p$  of Omori law exhibits a large variability from one aftershock sequence to another aftershock sequence and is found typically in the range from 0.3 to 2. We note however that not all these values, especially the extreme ones, automatically reflect a bona-fide power law decay and one should exert caution in attributing too much confidence to them.
3. The view that geological faults and earthquake hypocenters are fractal objects is now recognized to be a naive description of a much more complex reality in which a hierarchy of scales occur with possibly different organizations at different scales [Ouillon et al., 1996].

In addition, a major difficulty for making progress in modeling and predicting earthquakes is that these three and other laws may be “explained” by a large variety of models, with many different mechanisms. For instance, with respect to the first two laws, we observe the following.

- There are many mechanisms that create a power law distribution of earthquake sizes (see for instance the list of mechanisms described in Chapter 14 of [Sornette, 2000a]).
- Omori law is essentially a slowly decaying “propagator” describing a long-time memory of past events impacting on the future seismic activity. Such slow power law time decay of the Omori propagator may result from several and not necessarily exclusive mechanisms (see [Harris, 2000] and references therein) : pore-pressure changes due to pore-fluid flows coupled with stress variations, slow redistribution of stress by aseismic creep, rate-and-state dependent friction within faults, coupling between the viscoelastic lower crust and the brittle upper crust, stress-assisted micro-crack corrosion [Yamashita and Knopoff, 1987; Lee and Sornette, 2000], slow tectonic driving of a hierarchical geometry with avalanche relaxation dynamics [Huang et al., 1998], etc.

The zeroth order description of earthquakes is to consider a single isolated homogeneous fault on which earthquakes are recurrent to accommodate the long-term slow tectonic loading. But faults are not isolated and the most conspicuous observation is that earthquakes interact and influence each other on complex fault structures. Understanding these interactions is essential for understanding earthquakes and fault self-organization. However, the full impact of interactions between earthquakes is still far from being well understood. The simplest and clearest observation of earthquake interaction is provided by aftershocks whose phenomenology is captured by Omori law (LAW 2). Indeed, aftershocks are the most obvious and striking signature of the clustering

of the seismicity in time and space, and are observed after all large shallow earthquakes. Most aftershocks are triggered a few hours or days after the mainshock. However, due to the very slow power law decay of the rate of aftershock, known as the Omori law [Omori, 1894], aftershocks can be triggered up to a hundred years after the mainshock [Utsu et al., 1995]. Aftershocks often occur near the rupture zone of the mainshock with a variety of focal mechanisms suggesting that they are actually on separate structures [Bath and Richter, 1958; Beroza and Zoback, 1993]. They are also sometimes triggered at very large distances from the mainshock [Hill et al., 1993; Steeples and Steeples, 1996; Kagan and Jackson, 1998; Meltzner and Wald, 1999; Dreger and Savage, 1999]. As an example, Hill et al. [1993] observed aftershocks of the Landers earthquake as far as 1250 km from the epicenter. Similarly to the temporal distribution of aftershocks, a power-law distribution seems to describe well the distribution of distances between pairs of events [Kagan and Jackson, 1998]. Since a power-law decays slowly, it describes a slow decay of the probability of observing aftershocks at large distances to the mainshock.

Thus, Omori law can be considered as the simplest and best established description of earthquake interactions of a certain kind. The question we investigate is whether it can be used fruitfully to explain a larger variety of earthquake interactions beyond the class of observations that were used to establish it. In a series of papers [Sornette and Sornette, 1999a; Helmstetter and Sornette, 2002a; Sornette and Helmstetter, 2002], we find that Omori law for aftershocks plus the constrain that aftershocks are distributed according to the Gutenberg-Richter power law for earthquake size distribution *independently* of the magnitude of their progenitor is enough to derive many of the other empirical “laws,” as well the variability of the  $p$ -exponent. Here, we test the potential of this approach to account for and to quantify observations on aftershock diffusion.

Aftershock diffusion refers to the phenomenon of expansion or migration of aftershock zone with time [Mogi, 1968; Imoto, 1981; Chatelain et al., 1983; Tajima and Kanamori, 1985a,b; Wesson, 1987; Ouchi and Uakawa, 1986; Noir et al., 1997; Jacques et al., 1999]. Immediately after the mainshock occurrence, most aftershocks are located close to the rupture plane of the mainshock, then aftershocks seem to migrate away from the mainshock, at velocity ranging from 1 km/h to 1 km/year [Jacques et al., 1999; Rydelek and Sacks, 2001]. Note that this expansion is not universally observed, but is more important in some areas than in others [Tajima and Kanamori, 1985a,b].

The diffusion of aftershocks is usually interpreted as a diffusion of the stress induced by the mainshock, either by a viscous relaxation process [Rydelek and Sacks, 2001], or due to fluid transfer in the crust [Nur and Booker, 1972; Hudnut et al., 1989; Noir et al., 1997]. Another interpretation of the expansion of aftershocks is given by Dieterich [1994], who reproduces the Omori law decay of aftershocks and the expansion of the aftershock zone with time, using a rate and state friction law and assuming that the rate of aftershocks is proportional to the stress rate. In his model, the expansion of aftershock zone arises from the non-uniform stress induced

by the mainshock. Another alternative explanation is that the diffusion of aftershocks is mainly due to the occurrence of large aftershocks, and to the localization of secondary aftershock close to the largest aftershocks, as observed by Ouchi and Uakawa [1986]. The apparent diffusion of the seismicity may thus result from a cascade process; the mainshock triggers aftershocks that in turn trigger their own aftershocks, and thus lead to an expansion of the aftershock zone.

In the present paper, we investigate the epidemic time aftershock sequence model (ETAS), and show that the cascade of secondary aftershocks can indeed explain the reported diffusion of aftershocks. The ETAS model was introduced by Kagan and Knopoff [1987] and Ogata [1988] to describe the temporal and spatial clustering of seismicity. This model provides a tool for understanding the clustering of the seismic activity, without arbitrary distinction between aftershocks, foreshocks and mainshocks. In this model, all earthquakes are assumed to be simultaneously mainshocks, aftershocks and possibly foreshocks. Each earthquake generates aftershocks that decay with time according to Omori law, which will in turn generate their own aftershocks. The seismicity rate at any given time and location is given by the superposition of aftershock sequences of all events impacting that region at that time according to space-time “propagators.” The additional ingredient in the version of the ETAS model that we study is that the number of aftershock per earthquake increases exponentially  $\propto 10^{\alpha m}$  with the magnitude  $m$  of the mainshock (i.e., as a power law  $\propto E^{2\alpha/3}$  of the energy released by the mainshock), in agreement with the observations [Yamanaka and Shimazaki, 1990; Drakatos et al., 2001]. Since the energy of an earthquake is a power law of its rupture length, this law expresses the very reasonable idea that the number of events related to a given earthquake is proportional to a power of its volume of influence. The value of the exponent  $\alpha$  controls the nature of the seismic activity, that is, the relative role of small compared to large earthquakes. Few studies have measured  $\alpha$  in seismicity data [Yamanaka and Shimazaki, 1990; Guo and Ogata, 1997; Helmstetter, 2002]. This parameter  $\alpha$  is often found close to  $b$  [Yamanaka and Shimazaki, 1990] or fixed arbitrarily equal to  $b$  [Kagan and Knopoff, 1987; Felzer et al., 2002]. In the case where  $\alpha$  is close to the Gutenberg-Richter  $b$ -value, this law also reproduces [Felzer et al., 2002] the self-similar empirical Bath’s law [Bath, 1965], which states that the average difference  $m_M - m_A$  in size between a mainshock and its largest aftershock is 1.2 magnitude units, regardless of the mainshock magnitude:  $m_A = m_M - 1.2$ . If  $\alpha < b$ , small earthquakes, taken together, trigger more aftershocks than larger earthquakes. In contrast, large earthquakes dominate earthquake triggering if  $\alpha \geq b$ . This case  $\alpha \geq b$  has been studied analytically in the framework of the ETAS model by Sornette and Helmstetter [2002] and has been shown to eventually lead to a finite time singularity of the seismicity rate. This explosive regime cannot however describe a stationary seismic activity.

A natural way to tame this singular behavior is to introduce an upper cut-off for the magnitude distribution at large magnitudes, mirroring the cut-off  $m_0$  used for the low-magnitude range. The physical argument for introducing this cut-off is based on the finiteness of the maximum earthquake that the earth is capable of carrying. The specific way of introducing such

a cut-off (abrupt or smooth with a transition to a power law with larger exponent or to an exponential taper) is not very important qualitatively because all these laws will regularize the singular behavior and make the average branching ratio  $n$  finite. Such regularization with a maximum upper magnitude then allows  $\alpha \geq b$ . The special case  $\alpha = b$  required for Bath's law to hold exactly can not therefore be excluded.

However, based on a recent re-analysis of seismic catalogs using the powerful collapse technique, one of us [Helmstetter, 2002] has presented strong evidence that  $\alpha$  is strictly smaller than  $b$ . In this paper, we will therefore consider only the case  $\alpha < b$  and take  $\alpha = 0.5$  specifically in our numerical simulations. In this regime  $\alpha < b$ , Bath's law cannot be reproduced because the average difference in size between a mainshock and its largest aftershock increases with the mainshock magnitude. For  $\alpha < b$ , it is easy to show that Bath's law is replaced by  $m_A = (\alpha/b)m_M - \text{constant}$ , where  $m_M$  and  $m_A$  are the magnitudes of the mainshock and of the largest aftershock. Tests of this prediction will be reported in a future publication but we expect that distinguishing this modified Bath's law from Bath's law will be a difficult task due to the limited range of the studied magnitudes as well as the dependence of the distribution of  $m_M - m_A$  on the magnitude thresholds chosen for the mainshocks and for the aftershocks [Console et al., 2002].

We assume that the distribution of all earthquakes follow the Gutenberg-Richter distribution and take this distribution of aftershock sizes to be independent of the magnitude of the mainshock. Therefore, an earthquake can trigger a larger earthquake, albeit with a small probability. This model can thus describe a priori both aftershock and foreshock sequences. The ETAS model has been calibrated to real seismicity catalogs to retrieve its parameters [Ogata, 1988, 1989, 1992, 1999, 2001, Kagan, 1991a; Guo and Ogata, 1997; Felzer et al., 2002] and to give short-term probabilistic forecast of seismic activity by extrapolating past seismicity into the future via the use of its space-time propagator [Kagan and Knopoff, 1987; Kagan and Jackson, 2000; Console and Murru, 2001].

The ETAS model is a branching model which exhibits different regimes [Helmstetter and Sornette, 2002a] depending upon the value of the branching ratio  $n$ , defined by the average number of primary aftershocks per earthquake. The critical case  $n = 1$  corresponds to exactly one primary aftershock per earthquake, when averaging over all mainshock magnitudes larger than a threshold  $m_0$ . Let us stress that  $n$  is an average quantity which does not reflect adequately the large variability of the number of aftershocks per main shock, as a function of its magnitude. Indeed, the number of aftershocks per mainshock increases exponentially fast as a function of the mainshock magnitude, so that large mainshocks will have significantly more than  $n$  aftershocks. For  $\alpha = 0.5$ , a magnitude 7-earthquake gives typically 10 times more direct aftershocks than a magnitude 5, and 100 times more direct aftershocks than a magnitude 3-earthquake. The increase in triggered seismic activity with the magnitude of the mainshock is obviously stronger for a larger value of  $\alpha$ . Note that these numbers refer to aftershocks of the first generation ; the total

number of triggered events is larger by the factor  $1/(1-n) \sim 10$  (for  $n \approx 0.9$  which is typical), due to the cascades of secondary aftershocks. Notwithstanding this large variability, the average number  $n$  of primary aftershocks per earthquake controls the global regime. For  $n$  exactly equal to 1, seismicity is at the border between death and growth. In the sub-critical regime  $n < 1$ , since each earthquake triggers on average less than one aftershock, starting from a large event, the seismicity will decrease with time and finally die out. The super-critical  $n > 1$  corresponds to more than one primary aftershock per earthquake on average. Starting from a large earthquake, after a transient regime, the average seismicity will finally increase exponentially with time [Helmstetter and Sornette, 2002a], but there is still a finite probability for aftershock sequences to die out.

The numerical simulations reported below have been performed with  $\alpha = 0.5$ . It is probable that a good fit to seismic data is obtained by using a value of  $\alpha \approx 0.8$  larger than the value 0.5, as reviewed and documented recently by one of us [Helmstetter, 2002]. We have checked that results similar to those presented below hold true qualitatively for larger values  $0.5 < \alpha < 1$ . Such larger values of  $\alpha$  lead however to stronger fluctuations which are more difficult to handle numerically because the variance of the number  $\rho(m)$  of direct triggered aftershocks defined below in (8.3) becomes undefined for  $\alpha > 0.5$ . A full understanding of this regime requires a special treatment that will be reported elsewhere.

Sornette and Sornette [1999a] studied analytically a particular case of this model, without magnitude and spatial dependence, and they considered only the subcritical regime  $n < 1$ . Starting with one event at time  $t = 0$  and considering that each earthquake generates an aftershock sequence with a “local” Omori exponent  $p = 1 + \theta$ , where  $\theta > 0$ , they studied the decay law of the “global” aftershock sequence, composed of all secondary aftershock sequences, i.e., by taking into account that the primary aftershocks can create secondary aftershocks which themselves may trigger tertiary aftershocks and so on. They found that the global aftershock rate decays according to an Omori law with an exponent  $p = 1 - \theta < 1$ , up to a characteristic time [Sornette and Sornette, 1999a; Helmstetter and Sornette, 2002a]

$$t^* = c \left( \frac{n \Gamma(1 - \theta)}{|1 - n|} \right)^{1/\theta}, \quad (8.1)$$

and then recovers the local Omori exponent  $p = 1 + \theta$  for time larger than  $t^*$ . Helmstetter and Sornette [2002a] extended their analysis to the general ETAS model with magnitude dependence, and considered both the sub- and the super-critical regime, but still restricted the analysis to the temporal distribution of the seismicity, without spatial dependence. In the sub-critical regime, they recovered the crossover found by Sornette and Sornette [1999a]. In addition, Helmstetter and Sornette [2002a] give the explicit mathematical formula for the gradual transition between the Omori law with exponent  $p = 1 - \theta$  for  $t \ll t^*$  to the Omori law with exponent  $p = 1 + \theta$  for  $t \gg t^*$ . This smooth transition can be observed in Figure 8.1 on the line calculated for  $t^* = 10^9$  with  $n < 1$ .  $t^*$  can thus be viewed as the time where the apparent exponent  $p$  of the Omori

law is approximately in between the two asymptotic values  $1 - \theta$  and  $1 + \theta$ . A more rigorous mathematical definition [Helmstetter and Sornette, 2002a] is that  $t^*$  is the characteristic time scale such that  $\beta t^*$  is the dimensionless variable of the Laplace transform (with variable  $\beta$ ) of the seismicity rate.

In the super-critical regime, Helmstetter and Sornette [2002a] found a novel transition between a power-law decay with exponent  $p = 1 - \theta$  at early times, similar to the sub-critical regime, to an exponential increase of the seismicity at large times. The regime where  $\alpha > b$  or equivalently  $2\alpha/3 > B$  has been found to lead to a new kind of critical stochastic finite-time-singularity [Sornette and Helmstetter, 2002], relying on the interplay between long-memory and extreme fluctuations. Recall that the number of aftershocks per earthquake increases as a power law  $\propto E^{2\alpha/3}$  of the energy released by the mainshock whereas the number of earthquakes of energy  $E$  decreases as the Gutenberg-Richter law  $\propto 1/E^{1+B}$ . Intuitively, when  $2\alpha/3 > B$ , the increase in the rate of creation of aftershocks with the mainshock energy more than compensate the decrease of the probability to get a large mainshock when the mainshock energy increases. This theory based solely on the ETAS model has been found to account for the main observations (power law acceleration and discrete scale invariant structure) of critical rupture of heterogeneous materials, of the largest sequence of starquakes ever attributed to a neutron star as well as of some earthquake sequences [Sornette and Helmstetter, 2002].

In the sequel, we extend the analytical study of the temporal ETAS model [Sornette and Sornette, 1999a; Helmstetter and Sornette, 2002a; Sornette and Helmstetter, 2002] to the spatio-temporal domain. To model the spatial distribution of aftershocks, we assume that the distance between a mainshock and each of its direct aftershock is drawn from a given distribution, independently of the magnitude of the mainshock and of the delay between the mainshock and its aftershocks. For illustration but without loss of generality for the mapping to the continuous time random walks model (CTRW) discussed later, we shall take a power law distribution of distances between earthquakes. We take the simplest and most parsimonious hypothesis that space, time and magnitude are decoupled in the earthquake propagator. Our first result is to establish a correspondence between the ETAS model and the CTRW, first introduced by Montroll and Weiss [1965] and used to model many physical processes. We then build on this analogy to derive the joint probability distribution of the times and locations of aftershocks. We show analytically that, for sufficiently short times  $t < t^*$ , the average distance between a mainshock and its aftershock increases subdiffusively as  $R \sim t^H$ , where the exponent  $H$  depends on the local Omori exponent  $1 + \theta$  and on the distribution of the distances between an earthquake and its aftershocks. We also demonstrate that the local Omori law is not universal, but varies as a function of the distance from the mainshock. Due to the diffusion of aftershocks with time, the decay of aftershock is faster close to the mainshock than at large distances. These non-trivial space-time couplings occur notwithstanding the decoupling between space, time and magnitude in the “bare” propagator, and is due to the existence of cascades of aftershocks.

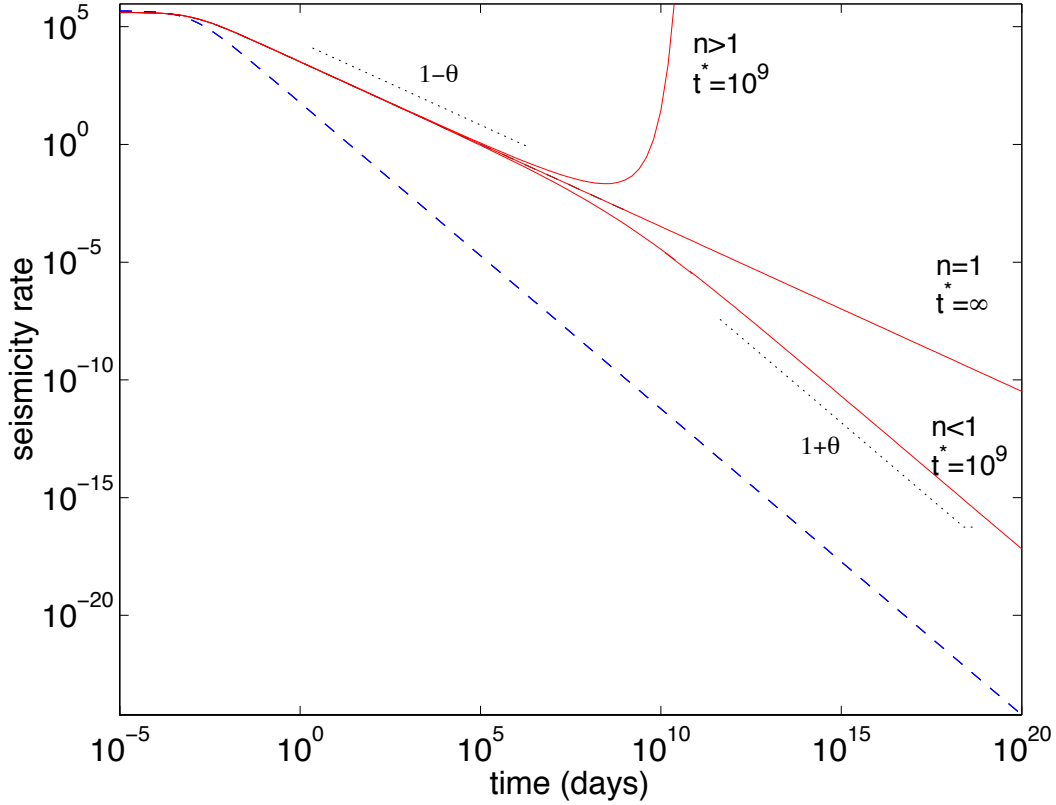


FIG. 8.1 – Seismicity rate  $N(t)$  for the temporal ETAS model calculated for  $\theta = 0.3$  and  $c = 0.001$  day. The local law  $\phi(t) \propto 1/t^{1+\theta}$ , which gives the probability distribution of times between an event and its (first-generation) aftershocks is shown as a dashed line. The global law  $N(t)$ , which includes all secondary and successive aftershocks generated by all the aftershocks of the first event, is shown as a solid line for the three regimes,  $n < 1$ ,  $n = 1$  and  $n > 1$ . In the critical regime  $n = 1$ , the seismicity rate follows a renormalized or dressed Omori law  $\propto 1/t^p$  for  $t > c$  with an exponent  $p = 1 - \theta$ , smaller than the exponent of the local law  $1 + \theta$ . In the sub-critical regime ( $n < 1$ ), there is a crossover from an Omori law  $1/t^{1-\theta}$  for  $t < t^*$  to  $1/t^{1+\theta}$  for  $t > t^*$ . In the super critical regime ( $n > 1$ ), there is a crossover from an Omori law  $1/t^{1-\theta}$  for  $t < t^*$  to an exponential increase  $N(t) \sim \exp(t/t^*)$  for  $t > t^*$ . We have chosen on purpose values of  $n = 0.9997 < 1$  and  $n = 1.0003 > 1$  very close to 1 such that the crossover time  $t^* = 10^9$  days given by (8.1) is very large. In real data, such large  $t^*$  would be undistinguishable from an infinite value corresponding to the critical regime  $n = 1$ . This representation is chosen for pedagogical purpose to make clear the different regimes occurring at times smaller and larger than  $t^*$ . In reality, we can expect  $n$  to be significantly smaller or larger than 1, such that  $t^*$  becomes maybe of the order of months, years to decades and the observed Omori law will thus lie in the cross-over regime, given an apparent Omori exponent anywhere from  $1 - \theta$  to  $1 + \theta$ .

A recent work of Krishnamurthy et al. [2000] substantiates the general modeling strategy used here of representing the space-time dynamics of earthquakes by an effective stochastic process (the ETAS model) entirely defined by two exponents (corresponding to our  $\mu$  and  $H(\theta, \mu)$  defined below), where  $\mu$  is the exponent of the power law distribution of jumps between successive active sites and  $H$  is the (sub-)diffusion exponent. Indeed, Krishnamurthy et al. [2000] show that the Bak and Sneppen model and the Sneppen model of extremal dynamics (corresponding to a certain class of self-organized critical behavior [Sornette, 2000a]) can be completely characterized by a suitable stochastic process called “Linear fractional stable motion.” Beyond recovering the scaling exponents of this model, the stochastic process strategy predicts the conditional probabilities of successive activations at different sites and thus offers novel insights. We note that this approach with the Linear fractional stable motion is extremely close in spirit as well as in form to our approach mapping the ETAS model to the CTRW model. The ETAS model can thus be taken to represent an effective stochastic process of the complex self-organization of seismicity.

## 8.2 The epidemic-type aftershock (ETAS) model

### Definitions and specific parameterization of the ETAS model

We assume that a given event (the “mother”) of magnitude  $m_i$  occurring at time  $t_i$  and position  $\vec{r}_i$  gives birth to other events (“daughters”) of any possible magnitude chosen with some independent Gutenberg-Richter distribution at a later time between  $t$  and  $t + dt$  and at point  $\vec{r} \pm d\vec{r}$  to within  $d\vec{r}$  at the rate

$$\phi_{m_i}(t - t_i, \vec{r} - \vec{r}_i) = \rho(m_i) \Psi(t - t_i) \Phi(\vec{r} - \vec{r}_i) . \quad (8.2)$$

We will refer to  $\phi_{m_i}(t - t_i, \vec{r} - \vec{r}_i)$  both as the seismic rate induced by a single mother or as the “bare propagator”. It is the product of three independent contributions :

1.  $\rho(m_i)$  gives the number of daughters born from a mother with magnitude  $m_i$ . This term will in general be chosen to account for the fact that large mearthquakes have many more triggered events than small earthquakes. Specifically, we take

$$\rho(m_i) = K 10^{\alpha(m_i - m_0)} , \quad (8.3)$$

which, as we said earlier, is justified by the power law dependence of the volume of stress perturbation as a function of the earthquake size.  $\alpha$  quantifies how fast the average number of daughters per mother increases with the magnitude of the mother.

2.  $\Psi(t - t_i)$  is a normalized waiting time distribution giving the rate of daughters born at time  $t - t_i$  after the mother. The normalization condition reads  $\int_0^{+\infty} dt \Psi(t) = 1$ .  $\Psi(t - t_i)dt$  can thus be interpreted as the probability for a daughter to be born between  $t$  and  $t + dt$

from the mother that was born at time  $t_i$ .  $\Psi(t - t_i)$  embodies Omori law : it is the “bare” or “direct” Omori law

$$\Psi(t) = \frac{\theta c^\theta}{(t + c)^{1+\theta}} H(t) , \quad (8.4)$$

where  $\theta > 0$  and  $H(t)$  is the Heaviside function.

3.  $\Phi(\vec{r} - \vec{r}_i)$  is a normalized spatial “jump” distribution from the mother to each of her daughter, quantifying the probability for a daughter to be triggered at a distance  $|\vec{r} - \vec{r}_i|$  from the mother. Specifically, we take

$$\Phi(\vec{r}) = \frac{\mu}{d(\frac{|\vec{r}|}{d} + 1)^{1+\mu}} , \quad (8.5)$$

which has the form of an (isotropic) elastic Green function dependence describing the stress transfer in an elastic upper crust. The exponent  $\mu$  is left adjustable to account for heterogeneity and the possible complex modes of stress transfers. The normalization condition reads  $\int d\vec{r} \Phi(\vec{r}) = 1$  where the integral is carried out over the whole space.

The physical justification for this decoupled model (8.2) in which  $\phi_{m_i}(t - t_i, \vec{r} - \vec{r}_i)$  is the product of three independent distributions is that elastic waves propagate at kilometers per second and thus almost instantaneously reset the stress field after a large main shock. In other words, there is a well-defined separation of time scales between the time of propagation of seismic waves (seconds to minutes) which control the convergence to a new mechanical equilibrium after the main shock and the time scales involved in aftershock sequences (hours, days, months to many years). The spatial dependence in (8.2) reflects the stress redistribution. This new stress field then relaxes slowly and more or less independently from point to point leading to the local Omori law  $\Psi(t - t_i)$ . Notwithstanding this argument, the decoupling in (8.2) between the local responses in magnitudes, space and time is mostly performed because of its simplicity. It constitutes an approximation that should be checked and relaxed in future studies.

We assume a distribution  $P(m)$  of earthquake sizes expressed in magnitudes  $m$  which follows the Gutenberg-Richter distribution

$$P(m) = b \ln(10) 10^{-b(m-m_0)} , \quad (8.6)$$

with a  $b$ -value usually close to 1.  $m_0$  is a lower bound magnitude below which no daughter is triggered.

### The branching ratio $n$

A key parameter of the ETAS is the average number  $n$  of daughter-earthquakes created per mother-event, summed over all possible magnitudes. As we shall see, it is also natural to call it the “branching ratio”. To see this, consider the integral of the seismic rate  $\phi_{m_i}(t - t_i, \vec{r} - \vec{r}_i)$  induced by one earthquake over all times after  $t_i$ , over all spatial positions and over all magnitudes

$m_i \geq m_0$ , which must give by definition the average number  $n$  of direct (or primary) daughter-earthquakes created per mother-event independently of its magnitude. For  $\alpha < b$  and using (8.2), (8.3) and (8.6), it is exactly given by

$$\begin{aligned} n &\equiv \int d\vec{r} \int_{t_i}^{+\infty} dt \int_{m_0}^{+\infty} dm_i P(m_i) \phi_{m_i}(t - t_i, \vec{r} - \vec{r}_i) \\ &= \int_{m_0}^{+\infty} dm_i P(m_i) \rho(m_i) = \frac{K b}{b - \alpha}, \end{aligned} \quad (8.7)$$

since the two integrals over time and space contribute each a factor 1 by the normalization of  $\Psi$  and  $\Phi$ . This result (8.7) is identical to that found in absence of spatial dependence of  $\phi_{m_i}(t - t_i)$  with respect to  $\vec{r} - \vec{r}_i$  due to the factorization of the rate  $\rho$ , time  $\Psi$  and space  $\Phi$  dependences [Helmstetter and Sornette, 2002a]. The branching ratio has also been evaluated in the case where the magnitude distribution follows a gamma distribution [Kagan, 1991a].

We stress again that  $n$  is an *average* quantity which does not reflect the large fluctuations in the number of aftershocks from events to events. Indeed, large events with magnitudes  $M$  produce in general many more aftershocks than small events with magnitude  $m < M$ , simply because  $\rho(M) \gg \rho(m)$  if  $M > m$  (see the exponential dependence (8.3) of  $\rho(m)$  on the magnitude  $m$ ).

## Numerical simulation of the spatial ETAS model

The ETAS model has been simulated numerically using the algorithm described in [Ogata, 1998, 1999]. Starting with a large event of magnitude  $M$  at time  $t = 0$ , events are then simulated sequentially. At any given time  $t$ , we calculate the conditional seismic rate  $\lambda(t)$  defined by

$$\lambda(t) = \sum_{t_i \leq t} K 10^{\alpha(m_i - m_0)} \frac{\theta c^\theta}{(t - t_i + c)^{1+\theta}} \quad (8.8)$$

where  $K = n(b - \alpha)/b$ , and  $t_i$  and  $m_i$  are the times and magnitudes of all preceding events that occurred at time  $t_i \leq t$ . Note that we use the bare propagator because the sum in (8.8) is performed exhaustively on the complete catalog of past events. The time of the following event is then determined according to the non-stationary Poisson process of conditional intensity  $\lambda(t)$ , and its magnitude is chosen according to the Gutenberg-Richter distribution with parameter  $b$ . To determine the position in space of this new event, we first choose its mother randomly among all preceding events with a probability proportional to their rate of aftershocks  $\phi_{m_i}(t - t_i)$  evaluated at the time of the new event. Once the mother has been chosen, we generate the distance  $r$  between the new earthquake and its mother according to the power-law distribution  $\Phi(\vec{r})$  given by (8.5). The location of the new event is determined by assuming an isotropic distribution of aftershocks. By this rule, it is clear that new events tend to be close in general to the last large earthquakes, leading to space clustering.

Note that this two-steps procedure is equivalent to but more convenient for a numerical implementation than the one-step method, consisting of calculating at each point on a fine

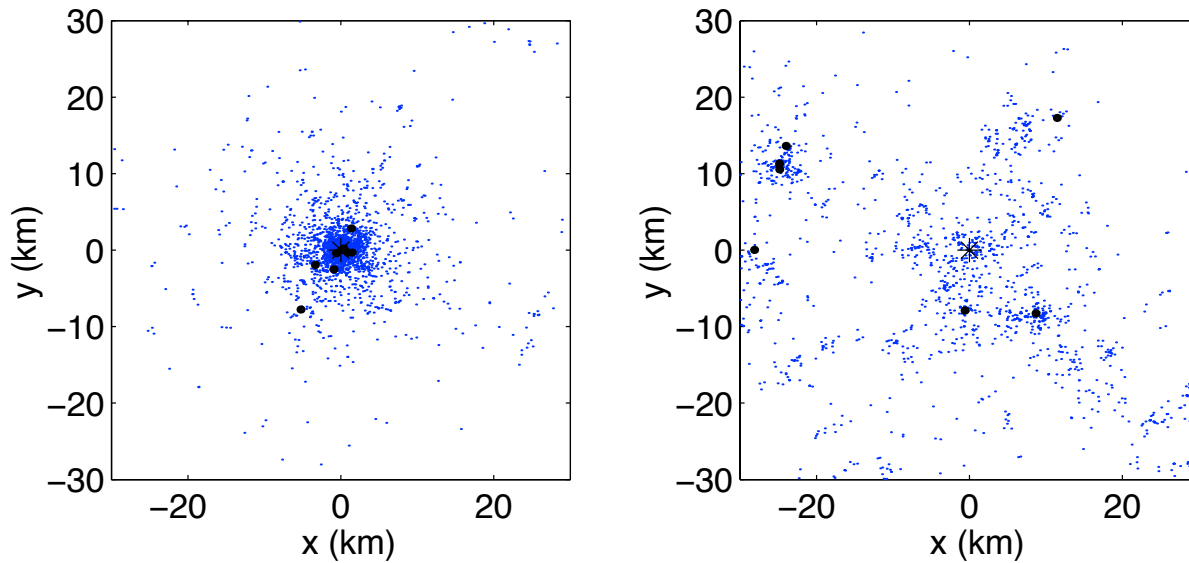


FIG. 8.2 – Maps of seismicity generated by the ETAS model with parameters  $b = 1$ ,  $\theta = 0.2$ ,  $\mu = 1$ ,  $d = 1$  km,  $\alpha = 0.5$ ,  $c = 0.001$  day and a branching ratio  $n = 1$ . The mainshock occurs at the origin of space with magnitude  $M = 7$ . The minimum magnitude is fixed at  $m_0 = 0$ . The distances between mainshock and aftershocks follow a power-law with parameter  $\mu = 1$  and the local (or bare) Omori law is  $\propto 1/t^{1+\theta}$ . According to the theory developed in the text, the average distance between the first mainshock and the aftershocks is thus expected to grow as  $R \sim t^{0.2}$  (equation (8.53)). The two plots are for different time periods of the same numerical simulation, such that the same number of earthquakes  $N = 3000$  is obtained for each graph : (a) time between 0 and 0.3 days; (b) time between 30 and 70 yrs. Real aftershock sequences are indeed observed to last decades up to a century. Large black dots indicate large aftershocks around which other secondary aftershocks cluster. The mainshock is shown by a black star. At early times, aftershocks are localized close to the mainshock, and then diffuse and cluster around the largest aftershocks.

space-covering grid the seismic rate, equal to the sum over all preceding mothers weighted by the bare space  $\Phi(\vec{r})$  and time  $\Psi(t)$  propagators given by (8.5) and (8.4); after normalizing, these rates then provide to each grid point a probability for the event to occur on that point. The equivalence between our two-step procedure and the direct calculation of the seismic rates is based on the law of conditional probabilities : probability of next event ( $A$ ) = probability of next event conditioned on its mother (event  $B$ )  $\times$  probability of choosing the mother, i.e.,  $P(A, B) = P(A|B) \times P(B)$ .

Figure 8.2 shows the result of a numerical simulation of the ETAS model which exhibits a diffusion of the seismic activity. We simulate a sequence of aftershocks and secondary aftershocks starting from a mainshock of magnitude  $M = 7$ , with the following parameters :  $\theta = 0.2$ ,  $b = 1$ ,  $\alpha = 0.5$ ,  $n = 1$  and  $\mu = 1$ . At early times, aftershocks are localized close to the mainshock, and then diffuse and cluster close to the largest aftershocks. This (sub-)diffusion is extremely slow, as we shall quantify in the sequel. Our purpose is to provide a theory for this process based on

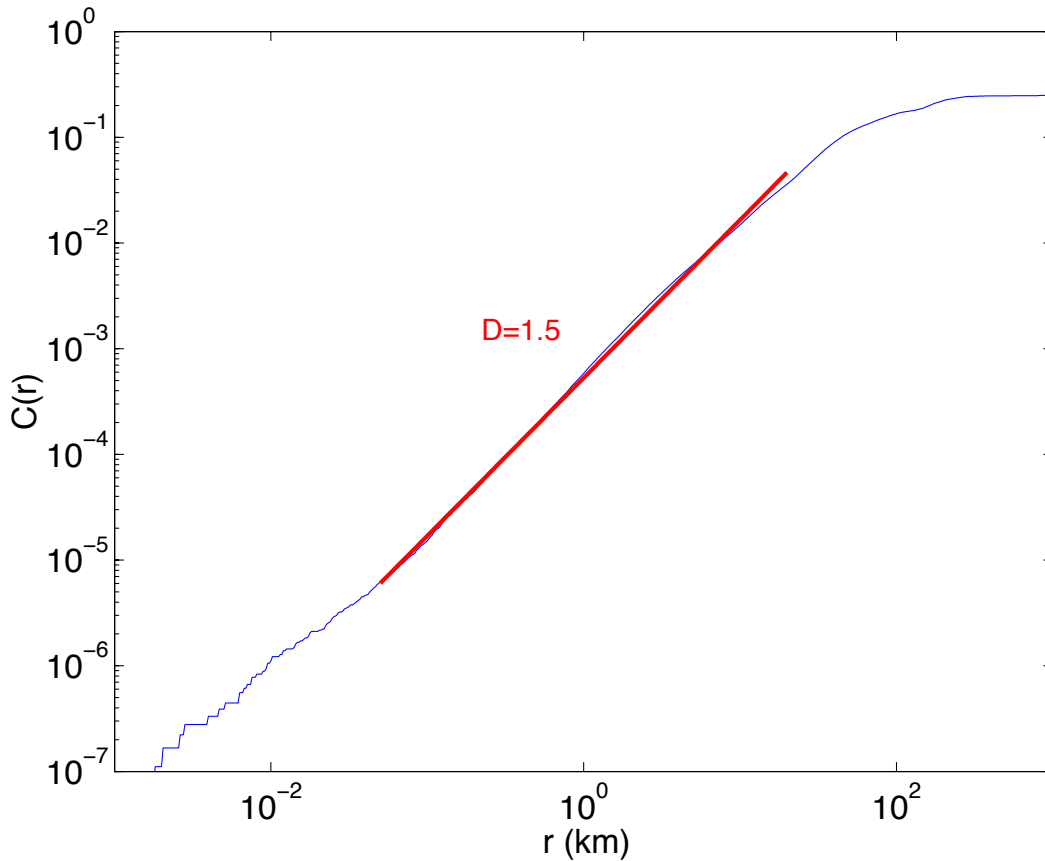


FIG. 8.3 – Plot of the correlation function of the 3.000 epicenters generated in the time interval [30, 70] yrs and shown in the right panel of figure 8.2, calculated following Grassberger-Procaccia’s algorithm [18], as a function of scale  $r$ , in double-logarithmic scales.

the ETAS model. This theory will be tested by numerical simulations.

The different regimes are illustrated by Figure 8.1 which shows the seismicity rate  $N(t)$  for the temporal ETAS model studied by [Sornette and Sornette, 1999a; Helmstetter and Sornette, 2002a] obtained by summing the seismic activity over all space, for the 3 cases  $n < 1$  (sub-critical),  $n = 1$  (critical) and  $n > 1$  (super-critical). The sub-critical regime is characterized by the existence of the time scale  $t^*$  given by (8.1). There is no difference between the critical case  $n = 1$  and the sub-critical case for  $t < t^*$  (see Figure 8.1). Indeed, the difference between the sub-critical regime and the critical regime can be observed only for  $t > t^*$ . A simple way to see this is to realize that the critical regime  $n = 1$  gives  $t^* = +\infty$ , meaning that, in the critical regime, one is always in the situation  $t < t^*$ .

It is interesting to note that the spatial distribution of epicenters shown in the right panel of Figure 8.2 has the visual appearance of a fractal set of points. This is confirmed by the calculation of the correlation dimension of this set of  $N = 3000$  points generated in the time interval [30, 70] yrs, which is found approximately equal to  $D_2 = 1.5 \pm 0.05$  over more than two decades in spatial scales, as shown in Figure 8.3. If we use instead all 30,000 events of the simulation performed up

to time  $t = 70$  yrs, we find  $D_2 = 1.85 \pm 0.05$  while the correlation dimension of the geometrical set made of the epicenters of the 10,000 last events (time interval  $[7, 70]$  yrs) is  $D = 1.7 \pm 0.05$ , also over more than two decades in scale. These values are similar to those reported for 2D maps of active fault systems [Scholz and Mandelbrot, 1989; Sornette et al., 1993; Barton and Lapointe, 1995; Ouillon et al., 1996], and are in good agreement with  $D_2$  values in the range  $[1.65, 1.95]$  measured for aftershocks epicenters [Nanjo et al., 2000]. The fractal clustering of the earthquake epicenters, according to the ETAS model, occurs because of a self-similar process taking place on many different scales. However, the description of this multi-scale process solely in terms of a single fractal dimension fails to fully embody the complex spatial superposition of local “singularities” associated with each aftershock on the one hand and finite-size effects (stemming from the finite lifetime of each aftershock sequence) on the other hand. Each event indeed creates its cloud of direct aftershocks which can be characterized by its singular exponent  $1-\mu$  for  $\mu \leq 1$  and 0 for  $\mu > 1$ , defined by the scaling  $\propto \int_0^R r dr / r^{1+\mu} \propto R^{1-\mu}$  of the “mass” of the cloud with its radius  $R$ . Finite-size effects and randomness have been documented to generate realistic but sometimes spurious fractal signatures [Ouillon and Sornette, 1996; Hamburger et al., 1996; Eneva, 1996; Malcai et al., 1997]. This problem requires a special study which is left for another work.

## Relationship with the space-independent ETAS model

The spatial ETAS model reduces to the space-independent ETAS model solved in [Helmstetter and Sornette, 2002a] by integrating the dressed propagator obtained below over all space. In the Fourier representation (see expression (8.21)), this corresponds to putting the wavenumber  $k$  to zero. Indeed, for  $k = 0$ , the Fourier transform amounts to perform a simple integration over all space. Since  $\hat{\Phi}(\vec{k} = \vec{0}) = 1$ , expression (8.21) derived below reduces to the form studied at length in [Helmstetter and Sornette, 2002a]. Therefore, all results reported previously hold also for the version of the space-dependent ETAS model studied here, when averaging over the whole space. This is an important property that all the solutions discussed below must obey.

## 8.3 Mapping of the ETAS model on the CTRW model

In order to study the space-time properties of the ETAS model, it is very useful to use a correspondence between the ETAS model and the continuous time random walk (CTRW) that we establish here. In this way, we can adapt and use the wealth of results previously derived for the CTRW. But first, let us demonstrate the correspondence between the ETAS and CTRW models. For this, our strategy is to derive the Master equation for both models and show that they are identical.

## The Master equation of the ETAS model

The ETAS model can be rephrased by defining the rate  $\phi_{m_i \rightarrow m}(t - t_i, \vec{r} - \vec{r}_i)$  at which a given event (the ‘‘mother’’) of magnitude  $m_i \geq m_0$  occurring at time  $t_i$  and position  $\vec{r}_i$  gives birth to other events (‘‘daughters’’) of specified magnitude  $m$  at a later time between  $t$  and  $t + dt$  and at point  $\vec{r}$  to within an infinitesimal volume  $|d\vec{r}|$ . Note that the only difference with respect to the previous definition (8.2) is that we now specify also the magnitude  $m$  of the daughter.  $\phi_{m_i \rightarrow m}(t - t_i, \vec{r} - \vec{r}_i)$  is given by

$$\phi_{m_i \rightarrow m}(t - t_i, \vec{r} - \vec{r}_i) = \rho(m_i \rightarrow m) \Psi(t - t_i) \Phi(\vec{r} - \vec{r}_i) , \quad (8.9)$$

where  $\Psi(t - t_i)$  and  $\Phi(\vec{r} - \vec{r}_i)$  are the same as previously while

$$\rho(m_i \rightarrow m) = P(m) \rho(m_i) . \quad (8.10)$$

With the parameterization (8.3) and (8.6), this reads

$$\rho(m_i \rightarrow m) = n \ln(10) (b - \alpha) 10^{\alpha(m_i - m_0)} 10^{-b(m - m_0)} . \quad (8.11)$$

Let us consider the case where there is an origin of time  $t = 0$  at which we start recording the rate of earthquakes, assuming that a large earthquake has just occurred at  $t = 0$  and somehow reset the clock. In the following calculation, we will forget about the effect of events at times prior to  $t = 0$  and count all aftershocks that are created only by this main shock.

Let us call  $N_m(t, \vec{r}) dt dm d\vec{r}$  the number of earthquakes occurring between  $t$  and  $t + dt$  of magnitude between  $m$  and  $m + dm$  inside of box of volume  $|d\vec{r}|$  centered at point  $\vec{r}$ .  $N_m(t, \vec{r})$  is the solution of a self-consistency equation that formalizes mathematically the following process : an earthquake may trigger aftershocks ; these aftershocks may trigger their own aftershocks, and so on. The rate of seismicity at a given time  $t$  and position  $\vec{r}$  is the result of this cascade process. The self-consistency equation that sums up this cascade reads

$$N_m(t, \vec{r}) = S(t, \vec{r}, m) + \int d\vec{r}' \int_{m_0}^{\infty} dm' \int_0^t d\tau \phi_{m' \rightarrow m}(t - \tau, \vec{r} - \vec{r}') N_{m'}(\tau, \vec{r}') . \quad (8.12)$$

The rate  $N_m(t, \vec{r})$  at time  $t$  and position  $\vec{r}$  is the sum over all induced rates from all earthquakes of all possible magnitudes that occurred at all previous times and locations propagated to the present time  $t$  and to the position  $\vec{r}$  of observation by the corresponding bare propagator. The induced rate of events per earthquake that occurred at an earlier time  $\tau$  and position  $\vec{r}'$  is equal to  $\phi_{m' \rightarrow m}(t - \tau, \vec{r} - \vec{r}')$ . The source term  $S(t, \vec{r})$  is the main shock plus the background seismicity, if any. In absence of background seismicity, a main earthquake which occurs at the origin of time  $t = 0$  at position  $\vec{r} = \vec{0}$  with magnitude  $M$  gives

$$S(t, \vec{r}, m) = \delta(t) \delta(m - M) \delta(\vec{r}) \quad (8.13)$$

where  $\delta$  is the Dirac distribution. Other arbitrary source functions can be chosen.

The source term corresponding to a single mainshock is indeed the delta function (8.13) rather than the direct Omori law created by this mainshock in direct lineage. To see this, notice that the direct Omori law is recovered from (8.12) by replacing  $N_{m'}(\tau, \vec{r}')$  in the integral by  $S(t, \vec{r}, m)$  given by (8.13). This shows that the difference between the renormalized and the direct Omori laws comes from taking into account the secondary, tertiary, etc., cascade of aftershocks.

As we have seen, a key assumption of the ETAS model is that the daughters born from a given mother have their magnitude drawn independently of the magnitude of the mother and of the process that give them birth, with a probability given by the Gutenberg-Richter distribution (8.6). The consequences resulting from relaxing this hypothesis will be reported elsewhere. Keeping this assumption, it can be shown [Helmstetter et al., 2002] that, for  $\alpha \geq b/2$ , an ensemble of realizations will obey

$$N_m(t, \vec{r}) = P(m) N(t, \vec{r}) , \quad \text{for } t > 0 , \tag{8.14}$$

which makes explicit the separation of the magnitude from the time and space variables.  $N(t, \vec{r})$  is the number of events at position  $\vec{r}$  at time  $t$  of any possible magnitude. Expression (8.14) means that the Gutenberg-Richter distribution is preserved at all times. That (8.14) holds exactly for the ETAS model stems from the fact that the waiting time  $\Psi(t)$  distribution (8.4) and jump size  $\Phi(\vec{r})$  distribution (8.5) are independent of the magnitudes, and that fluctuations in the seismicity rate are not too strong for  $\alpha \leq b/2$ . Note that, in a more complex model in which time, space and magnitudes are interdependent, expression (8.14) would become a mean-field approximation, in which the fluctuations of the rates induced by the fluctuations of the realized magnitudes of the daughters factorize from the process.

Putting (8.14) in (8.12), for  $t > 0$  when the source term  $S(t, \vec{r}, m)$  is identically zero, one can simplify by  $P(m)$  and obtain

$$N(t, \vec{r}) = \int d\vec{r}' \int_0^t d\tau \phi(t - \tau, \vec{r} - \vec{r}') N(\tau, \vec{r}') , \quad t > 0 , \tag{8.15}$$

where

$$\phi(t - \tau, \vec{r} - \vec{r}') = \int_{m_0}^{\infty} dm' P(m') \phi_{m'}(t - \tau, \vec{r} - \vec{r}') . \tag{8.16}$$

Equation (8.15) is nothing but the expectation (or statistical average, i.e., average over an ensemble of realizations) of expression (8.8), with the definition  $N(t, \vec{r}) \equiv \mathbb{E}[\lambda(t) \Phi(\vec{r})]$ . Therefore, the Master equation obtained here gives us only the first moment of the space-time dynamics of seismicity. It is not difficult to derive the equations for the variance and covariance of the seismic rate as well as higher moments.

The value of the source term at  $t = 0$  that should be incorporated in (8.15) requires more care. Indeed, a naive treatment would give a source term  $\delta(t)\delta(m - M)\delta(\vec{r})/P(M)$  obtained by simply dividing by  $P(m)$ , expressed at  $m = M$  due to the Dirac distribution  $\delta(m - M)$ . However, this source term still depends on  $m$  via the Dirac distribution  $\delta(m - M)$  and is thus unsuitable

as a source term of the equation (8.15) which is independent of  $m$ . In order to circumvent this difficulty, one has to get rid of the Dirac distribution  $\delta(m - M)$ . The corresponding procedure has been described in details in [Helmstetter and Sornette, 2002a] and consists in applying the integral operator  $\int_{m_0}^{\infty} dm \hat{\phi}(\beta, \vec{r})$  to (8.12), where  $\hat{\phi}(\beta, \vec{r})$  is the Laplace transform with respect to the time variable of  $\phi(t, \vec{r})$ . In this way, the Dirac distribution  $\delta(m - M)$  is regularized. Identifying with the results of [Helmstetter and Sornette, 2002a], we obtain that  $N(t, \vec{r})$  is solution of (8.15) with a source term

$$S_M(t, \vec{r}) = \delta(r)\delta(t)\rho(M)/n , \quad (8.17)$$

where  $\rho(M)$  is defined in (8.3) and  $n$  is given by (8.7). Thus, the complete Master equation for the number  $N(t, \vec{r})$  of events at position  $\vec{r}$  at time  $t$  of any possible magnitude is solution of

$$N(t, \vec{r}) = S_M(t, \vec{r}) + \int d\vec{r}' \int_0^t d\tau \phi(t - \tau, \vec{r} - \vec{r}') N(\tau, \vec{r}') , \quad t > 0 , \quad (8.18)$$

$N(t, \vec{r})$  is the “dressed” or “renormalized” propagator, obtained by summing the bare Omori propagator over all possible aftershock cascades.  $N(t, \vec{r})$  can also be called the renormalized Omori law [Sornette and Sornette, 1999a].

The essential assumption used to derive (8.12) is that the fluctuations of the earthquake magnitudes in a given sequence can be considered to be decoupled from those of the seismic rate. This approximation can be shown to be valid for  $\alpha \leq b/2$  [Helmstetter et al., 2002], for which the random variable  $\rho(m_i)$  has a finite variance. In this case, any coupling between the fluctuations of the earthquake energies and the instantaneous seismic rate provides only subdominant corrections to the equation (8.12). For  $\alpha > b/2$ , the variance of  $\rho(m_i)$  is mathematically infinite or undefined as  $\rho(m_i)$  is distributed according to a power law with exponent  $b/\alpha < 2$ . In this case, the Master equation (8.12) is not completely correct as an additional term must be included to account for the effect of the dependence between the fluctuations of earthquake magnitudes and the instantaneous seismic rate. Our results are presented below for  $\alpha = 0.5$  which belongs to the first regime  $\alpha \leq b/2$ . For  $\alpha > b/2$ , Helmstetter et al. [2002] have shown that the renormalization of the bare propagator into the dressed propagator is weaker than for  $\alpha \leq b/2$ , all the more so as  $\alpha \rightarrow b$ . Preliminary numerical simulations for  $\alpha > b/2$  shows that our results presented below hold qualitatively but with a reduction of the observed spatial diffusion exponent compared to the value predicted from the Master equation approach developed here. This regime  $\alpha > b/2$  is probably relevant to the real seismicity [Yamanaka and Shimazaki, 1990; Guo and Ogata, 1997; Helmstetter, 2002], even if a precise estimation of  $\alpha$  is very difficult.

## A Master equation of the CTRW model

We now demonstrate that the self-consistent mean field equation (8.18) is identical to the Master equation of a continuous-time random walk (CTRW). Random walks underlie many physical processes and are often the basis of first-order description of natural processes. The

CTRW model, which is a generalization of the naive model of a random walker which jumps by  $\pm 1$  spatial step on a discrete lattice at each time step, was introduced by [Montroll and Weiss, 1965] and investigated by many other workers [Montroll and Scher, 1973; Sher and Montroll, 1975; Kenkre et al., 1973; Shlesinger, 1974; Weiss, 1994]. The CTRW considers a continuous distribution of spatial steps as well as time steps (which can be seen either as waiting times between steps or as durations of the steps). The CTRW model is thus based on the idea that the length of a given jump, as well as the waiting time  $\tau_i = t_i - t_{i-1}$  elapsing between two successive jumps are drawn from a joint probability density function (pdf)  $\phi(\vec{r}, t)$ , which is usually referred to as the jump pdf. From a mathematical point of view, a CTRW is a process subordinated to random walks under the operational time defined by the process  $\{t_i\}$ .

From  $\phi(\vec{r}, t)$ , the jump length pdf  $\Phi(\vec{r}) = \int_0^{+\infty} dt \phi(\vec{r}, t)$  and the waiting time pdf  $\Psi(t) = \int d\vec{r} \phi(\vec{r}, t)$  can be deduced. Thus,  $\Phi(\vec{r})d\vec{r}$  produces the probability for a jump length in the interval  $(\vec{r}, \vec{r} + d\vec{r})$  and  $\Psi(t)dt$  the probability for a waiting time in the interval  $(t, t + dt)$ . When the jump length and waiting time are independent random variables, this corresponds to the decoupled form  $\phi(\vec{r}, t) = \Psi(t) \Phi(\vec{r})$ . If both are coupled, a jump of a certain length involves a time cost or, vice versa in a given time span the walker can only travel a maximum distance. With these definitions, a CTRW process can be described through a Master equation (see [Weiss, 1994; Hughes, 1995; Meltzner et al., 2000] for a review and references therein) which turns out to be given by an equation which is identical to (8.18).

This connection between the ETAS model of earthquakes and a model of random walks provides an important advance for the understanding of spatio-temporal earthquake processes, as it allows one to borrow for the deep knowledge accumulated in past decades on random walks. In the same spirit, polymer physics acquired its status as a fundamental physical problem from its previous status of an applied field of research in chemistry when Flory, Edwards, de Gennes, des Cloizeaux and others showed how to formulate problems in polymer physics in the language of random walks and how to extract novel results. In the sequel of this article, we use this analogy to provide a wealth of new predictions as well as new questions for earthquake aftershocks.

In the context of the CTRW, we have the following correspondence.

- $N(t, \vec{r})$  is the pdf for the random walker to just arrive at position  $\vec{r}$  at time  $t$ .
- The source term  $S_M(t, \vec{r})$  given by (8.17) denotes the initial condition of the random walk, here chosen to be at the origin of space at time  $t = 0$ . The constant  $\rho(M)/n$  adds the possibility via the parameter  $M$  to have more than one initial walker at the origin.
- In the CTRW context, the Master equation (8.18) states that the pdf  $N(t, \vec{r})$  of just having arrived at position  $\vec{r}$  at time  $t$  comes from all possible paths in number  $N(\tau, \vec{r}')$  having crossed a position  $\vec{r}'$  at an earlier time  $\tau$ , weighted by a transfer or propagator function  $\phi(t - \tau, \vec{r} - \vec{r}')$  describing all the possible steps of the random walker from  $(\tau, \vec{r}')$  to  $(t, \vec{r})$ .

It is important to stress that  $N(t, \vec{r})$  defined above is different from the standard quantity  $W(t, \vec{r})$  usually studied in random walk problems, defined as the probability to find the random

walk at position  $\vec{r}$  at time  $t$ . The relationship between  $N(t, \vec{r})$  and  $W(t, \vec{r})$  is

$$W(t, \vec{r}) = \int_0^t dt' \left[ 1 - \int_0^{t-t'} dt'' \Psi(t'') \right] N(t', \vec{r}) . \quad (8.19)$$

The term  $1 - \int_0^{t-t'} dt'' \Psi(t'')$  in bracket is the probability for the walker not to jump in the time interval  $[t', t]$  and the integral in the right-hand-side of (8.19) means that the probability  $W(t, \vec{r})$  for the random walker to be at position  $\vec{r}$  at time  $t$  is the sum over all possible scenarios in which the walker just arrives at  $\vec{r}$  at an earlier time  $t'$  and then does not jump until time  $t$ . In the context of earthquake aftershocks,  $W(t, \vec{r})$  is the probability that an event at  $\vec{r}$  has occurred at a time  $t' \leq t$  and that the whole system has remained quiescent from  $t'$  to  $t$ .

In the Fourier-Laplace domain (see below), expression (8.19) reads

$$\hat{W}(\beta, \vec{k}) = \frac{1 - \hat{\Psi}(\beta)}{\beta} \hat{N}(\beta, \vec{k}) . \quad (8.20)$$

In general, the CTRW models transport phenomena in any heterogeneous media. It has for instance been used successfully for describing the behavior of chemical species as they migrate through porous media [Margolin et al., 2000; Berkowitz and Scher, 2001]. In insight, it is rather natural that it can be applied to the “transport of stress” through the heterogeneous crust and thus to the description of the anomalous diffusion of seismic activity. Table 8.1 synthesizes the correspondence between the ETAS and CTRW models and then draws its consequences.

## Experimental verifications of the cross-over between the two power law Omori decays

The crossover from an Omori law  $1/t^{1-\theta}$  for  $t < t^*$  to  $1/t^{1+\theta}$  for  $t > t^*$  found in [Sornette and Sornette, 1999a; Helmstetter and Sornette, 2002a] with  $t^*$  given by (8.1) has actually a counterpart in the CTRW. This behavior was first studied by Scher and Montroll [1975] in a CTRW with absorbing boundary condition to model photoconductivity in amorphous semiconductors  $\text{As}_2\text{Se}_3$  and an organic compound TNF-PVK finding  $\theta \approx 0.5$  and  $\theta = 0.8$  respectively. In a semiconductor experiment, electric holes are injected near a positive electrode and then transported to a negative electrode where they are absorbed. The transient current follows exactly the transition  $1/t^{1-\theta}$  for  $t < t^*$  to  $1/t^{1+\theta}$  for  $t > t^*$  found for Omori law for earthquake aftershocks in the ETAS model. In the semiconductor context, the finiteness of  $t^*$  results from the existence of a force applied to the holes while in the ETAS model it results from a finite distance  $1 - n$  to the critical point  $n = 1$  in the subcritical regime. When the force goes to zero or  $n \rightarrow 1$ ,  $t^* \rightarrow +\infty$ .

A similar transition has been recently proposed to model long-term time series measurements of chloride, a natural passive tracer, in rainfall and runoff in catchments [Sher et al., 2002]. The quantity analogous to the dressed Omori propagator is the effective travel time distribution  $h(t)$  which governs the global lag time between injection of the tracer through rainfall and outflow to

TAB. 8.1 – Correspondence between the ETAS (Epidemic-type aftershock sequence) and CTRW (continuous-time random walk) models. ‘pdf’ stands for probability density function.

	ETAS	CTRW
$\Psi(t)$	pdf for a “daughter” to be born at time $t$ from the mother that was born at time 0	pdf of waiting times
$\Phi(\vec{r})$	pdf for a daughter to be triggered at a distance $\vec{r}$ from its mother	pdf of jump sizes
$m$	earthquake magnitude	tag associated with each jump
$\rho(m)$	number of daughters per mother of magnitude $m$	local branching ratio
$n$	average number of daughters created per mother summed over all possible magnitudes	control parameter of the random walk survival (branching ratio)
$n < 1$	subcritical aftershock regime	subcritical “birth and death”
$n = 1$	critical aftershock regime	the standard CTRW
$n > 1$	supercritical exponentially growing regime	explosive regime of the “birth and death” CTRW
$N(t, \vec{r})$	number of events of any possible magnitude at $\vec{r}$ at time $t$	pdf of just having arrived at $\vec{r}$ at time $t$
$W(t, \vec{r})$	pdf that an event at $\vec{r}$ has occurred at a time $t' \leq t$ and that no event occurred anywhere from $t'$ to $t$	pdf of being at $\vec{r}$ at time $t$

the stream.  $h(t)$  has been shown to have a power-law form  $h(t) \sim 1/t^{1-m}$  with  $m$  between -0.3 and 0.2 for different time series [Kirchner and Weil, 1998]. This variability may be due to the transition between an exponent  $1 - \theta$  at short times to  $1 + \theta$  at long times [Sher et al., 2002], where  $\theta$  is the exponent of the bare distribution of individual transition times.

## General and formal solution of the spatial ETAS model

Let us solve (8.18) for the number  $N(t, \vec{r})$  of events at position  $\vec{r}$  at time  $t$  of any possible magnitude. Recall that  $N(t, \vec{r})$  can also be interpreted as the dressed Omori propagator. Extending [Helmstetter and Sornette, 2002a] to the spatial domain and also in analogy with the standard approach to solve the CTRW, the Laplace-in-time Fourier-in-space transform  $\hat{N}(\beta, \vec{k})$  of  $N(t, \vec{r})$  is given by

$$\hat{N}(\beta, \vec{k}) = \frac{\hat{S}_M(\beta, \vec{k})}{1 - n\hat{\Psi}(\beta)\hat{\Phi}(\vec{k})}, \quad (8.21)$$

where  $\hat{S}_M(\beta, \vec{k})$  is the Laplace Fourier transform of the source  $S_M(t, \vec{r})$  given by (8.17) and  $\hat{\Psi}(\beta)$  (respectively  $\hat{\Phi}(\vec{k})$ ) is the Laplace (respectively Fourier) transforms of  $\Psi(t)$  (respectively  $\Phi(\vec{r})$ ). For a mainshock of magnitude  $M$  occurring at time  $t = 0$  and position  $\vec{r} = 0$ , the source term is thus  $\hat{S}_M(\beta, \vec{k}) = \rho(M)/n$ . The only difference between expression (8.21) and the Laplace-Fourier transform of the pdf of the CTRW of just having arrived at  $\vec{r}$  at time  $t$  occurs when the branching ratio  $n$  is different from 1. In general, solutions of CTRW models are expressed for  $n = 1$  and for the variable  $W(t, \vec{r})$  which is simply related to  $N(t, \vec{r})$  according to (8.19). Using (8.19) and (8.21) leads to

$$\hat{W}(\beta, \vec{k}) = \frac{1 - \hat{\Psi}(\beta)}{\beta} \frac{\hat{S}_M(\beta, \vec{k})}{1 - n\hat{\Psi}(\beta)\hat{\Phi}(\vec{k})}, \quad (8.22)$$

In the following, we exploit (8.22) to obtain analytical solutions of the spatial ETAS model in different regimes, that provide specific predictions on the conditions necessary for observing aftershock diffusion. In addition, we provide specific predictions on the exponent  $H$  of the diffusion law  $R \sim t^{HH}$  that are tested by numerical simulations.

## 8.4 Critical regime $n = 1$

### Classification of the different regimes

Numerous works on the CTRW have investigated many possible forms for  $\Psi(t)$  and  $\Phi(\vec{r})$  and have provided the asymptotic long time and large scale dependence of  $W(t, \vec{r})$  (see [Weiss, 1994; Hughes, 1995; Meltzner et al., 2000; Berkowitz and Scher, 2001] and references therein). Here, we restrict our discussion to the cases where both  $\Psi(t)$  and  $\Phi(\vec{r})$  have power law tails as given by (8.4) and (8.5). The long-time and large scale behavior of the ETAS and CTRW are controlled by the behavior of the Laplace-Fourier transforms for small  $\beta$  and small  $|\vec{k}|$ .

Two cases must be distinguished depending on the exponent  $\mu$  controlling the weight of the tail of  $\Phi(\vec{r})$ .

- For  $\mu > 2$ , the variance  $\langle (\vec{r})^2 \rangle = \sigma^2$  of the jump size distribution exists. To leading order in  $k = |\vec{k}|$ ,  $\hat{\Phi}(\vec{k})$  can be expanded as

$$\hat{\Phi}(\vec{k}) = 1 - \sigma^2 k^2 + \mathcal{O}(k^o), \quad \text{with } o > 2. \quad (8.23)$$

- For  $\mu \leq 2$ , the variance  $\langle (\vec{r})^2 \rangle$  is infinite. This regime of “long jumps” leads to so-called Lévy flights. In this case, to leading order in  $k = |\vec{k}|$ ,  $\hat{\Phi}(\vec{k})$  can be expanded as

$$\hat{\Phi}(\vec{k}) = 1 - \sigma^\mu k^\mu + \mathcal{O}(k^o), \quad \text{where } 0 < \mu \leq 2, \quad \text{with } o > \mu, \quad (8.24)$$

where  $\sigma$  is a characteristic distance defined by

$$\sigma = \begin{cases} d [\Gamma(1 - \mu)]^{1/\mu}, & 0 < \mu < 1, \\ \frac{d \pi}{\mu \Gamma(\mu-1) \sin(\pi\mu/2)}, & 1 < \mu < 2. \end{cases} \quad (8.25)$$

For a distribution  $\Psi(t)$  of waiting times of the form of a local Omori law (8.4) with exponent  $\theta < 1$ ,  $\hat{\Psi}(\beta)$  can be expanded for small  $\beta$  as

$$\hat{\Psi}(\beta) = 1 - (\beta c')^\theta + \mathcal{O}(\beta^\omega), \quad \text{with } \omega \geq 1. \quad (8.26)$$

where  $c'$  is proportional to  $c$  up to a numerical constant  $c' = c(\Gamma(1 - \theta))^{1/\theta}$  in the case  $\theta < 1$ .

Putting the leading terms of the expansions of  $\hat{\Phi}(\vec{k})$  for small  $|\vec{k}|$  and of  $\hat{\Psi}(\beta)$  for small  $\beta$  in (8.21) gives

$$\hat{N}(\beta, \vec{k}) = \frac{\hat{S}_M(\beta, \vec{k})}{1 - n + n(\beta c')^\theta + n\sigma^\mu k^\mu}. \quad (8.27)$$

The corresponding  $\hat{W}(\beta, \vec{k})$  is obtained from (8.22) by

$$\hat{W}(\beta, \vec{k}) = \hat{S}_M(\beta, \vec{k}) \frac{(\beta)^{\theta-1} c'^\theta}{1 - n + n(\beta c')^\theta + n\sigma^\mu k^\mu}. \quad (8.28)$$

The critical regime  $n = 1$  gets rid of the constant term  $1 - n$  in the denominator of (8.27) and (8.28). This case is analyzed in details below.

The regime  $n \neq 1$  introduces a characteristic time  $t^*$  given by (8.1). In the sub-critical regime, equation (8.27) can be rewritten as

$$\hat{N}(\beta, \vec{k}) = \frac{\hat{S}_M(\beta, \vec{k})}{(1 - n)} \frac{1}{1 + (\beta t^*)^\theta + (kr^*)^\mu}. \quad (8.29)$$

where  $r^*$  is defined by

$$r^* = \sigma \left( \frac{n}{1 - n} \right)^{1/\mu}. \quad (8.30)$$

For  $t < t^*$  and  $r < r^*$ , the dressed propagator is given by the same expression as for the critical case and all our results below hold. For large times  $t > t^*$  and large distances  $r > r^*$ , we can factorize (8.29) as a product of a function of time and a function of space

$$\hat{N}(\beta, \vec{k}) \simeq \frac{\hat{S}_M(\beta, \vec{k})}{(1 - n)} \frac{1}{(1 + (\beta t^*)^\theta)} \frac{1}{(1 + (kr^*)^\mu)}. \quad (8.31)$$

Thus, there is no diffusion in the sub-critical regime for  $t > t^*$  and  $r > r^*$ . We shall not analyze further this trivial regime  $n < 1$  and  $t > t^*$  and will only analyze the case  $t < t^*$ . If there is the need, the cross-over can be calculated explicitly using (8.27).

In order to get the leading behavior of  $N(t, \vec{r})$  from that of  $W(t, \vec{r})$ , we see from (8.21) and (8.22) that  $\hat{N}(\beta, \vec{k}) = \frac{\beta}{1-\Psi(\beta)} \hat{W}(\beta, \vec{k}) \approx \beta^{1-\theta} c'^{-\theta} \hat{W}(\beta, \vec{k})$ . The inverse Laplace transform of  $1/\beta^\theta$  is  $1/[\Gamma(\theta) t^{1-\theta}]$ . Using the fact that the Laplace transform of  $df/dt$  is  $\beta$  times the Laplace transform of  $f(t)$  minus  $f(0)$ , we get  $N(t, \vec{r})$  as the derivative of a convolution

$$N(t, \vec{r}) = \frac{c'^{-\theta}}{\Gamma(\theta)} \frac{d}{dt} \int_0^t dt' \frac{W(t', \vec{r})}{(t-t')^{1-\theta}} = c'^{-\theta} {}_0D_t^{1-\theta} W(t, \vec{r}) . \quad (8.32)$$

In (8.32), we have dropped the Dirac function coming from the inverse Laplace transform of the constant term  $f(0)$ , which provides a contribution only at the origin of time  $t = 0$ . Note that the operator  $\frac{1}{\Gamma(\theta)} \frac{d}{dt} \int_0^t dt' \frac{W(t', \vec{r})}{(t-t')^{1-\theta}}$  is nothing but the so-called fractional Riemann-Liouville derivative operator of order  $1-\theta$  applied to the function  $W(t, \vec{r})$  of time  $t$  and is usually denoted  ${}_0D_t^{1-\theta} W(t, \vec{r})$ .

### The standard diffusion case $\theta > 1$ and $\mu > 2$

The standard diffusion process is recovered for  $\theta \geq 1$  (for which the average waiting time is finite) and for  $\mu \geq 2$  (for which the variance of the jump length is finite). In this case,  $\hat{N}(\beta, \vec{k}) = \frac{\hat{S}_M(\beta, \vec{k})}{\beta c' + \sigma^2 k^2}$ . For an impulsive source leading to  $\hat{S}_M(\beta, \vec{k}) = \text{constant}$ , this is the Laplace-Fourier transform of the standard diffusion propagator

$$N(t, \vec{r}) \propto \frac{1}{(Dt)^{d/2}} \exp[-(\vec{r})^2/Dt] , \quad \text{where } D = \sigma^2/c' , \quad (8.33)$$

where  $d$  is the space dimension. This solution is valid for  $|\vec{r}|/\sqrt{Dt}$  not too large. For larger values, large deviations lead to corrections with the power law tail of the input jump distribution  $\Phi(\vec{r}) \sim 1/|\vec{r}|^{1+\mu}$  defined in (8.5), along the lines presented for instance in [Sornette, 2000a (section 3.5)]. This regime is not relevant to the aftershock problem for which usually  $0 < \theta < 1$ .

### Long waiting times ( $\theta < 1$ ) and finite variance of the jump sizes ( $\mu > 2$ )

Putting the leading terms of the expansions of  $\hat{\Phi}(\vec{k})$  (8.23) and of  $\hat{\Psi}(\beta)$  (8.26) in (8.21) gives

$$\hat{N}(\beta, \vec{k}) = \frac{1}{(\beta c')^\theta + (\sigma k)^2} \quad (8.34)$$

The expression (8.34) can be inverted with respect to the Fourier transform, and then inverted with respect to the Laplace transform using Fox functions [Meltzner et al., 2000; Barkai et al., 2000]. The solution for  $W(t, \vec{r})$  in one dimension is given for instance in [Meltzner et al., 2000] in terms of an infinite sum

$$W(t, \vec{r}) = \frac{1}{2D} \frac{1}{t^{\frac{\theta}{2}}} \sum_{k=0}^{\infty} \frac{(-1)^k z^{-k}}{k! \Gamma(1 - \theta(k+1)/2)} \quad (8.35)$$

where

$$z = \frac{D t^{\theta/2}}{|\vec{r}|} \quad (8.36)$$

and  $D = \sigma/c^{\theta/2}$ .

Expression (8.35) and many others below involve the Gamma function of negative arguments. We recall that the Gamma function  $\Gamma(u)$  can be analytically continued to the whole complex plane, except for the simple poles  $u = 0, -1, -2, -3, \dots$ . Thus,  $\Gamma(u)$  is defined everywhere but at these poles. In order to get the expression of the Gamma function for negative arguments, one can use two formulae :  $\Gamma(1-u) \times \Gamma(u) = \pi/\sin(\pi u)$  and  $\Gamma(1+u) = u\Gamma(u)$ . Both these formulae are valid for all points with the possible exception of the arguments at poles  $0, -1, -2, \dots$ . For instance,  $\Gamma(-\theta) = \Gamma(1-\theta)/(-\theta) = -[\pi/\theta \sin(\pi\theta)]/\Gamma(\theta)$ , for  $0 < \theta < 1$ .

Expression (8.35) can be rewritten as a Fox-function [Mathai and Saxena, 1978]

$$W(t, z) = \frac{1}{2D} \frac{1}{t^{\frac{\theta}{2}}} H_{1,1}^{1,0} \left[ \frac{1}{z} \left| \begin{matrix} (1-\theta/2, \theta/2) \\ (0, 1) \end{matrix} \right. \right] \quad (8.37)$$

whose asymptotic dependence for large  $z$ , obtained from a standard theorem of the Fox function (equation (1.6.3) of [Mathai and Saxena, 1978]),

$$W(t, z) \sim \frac{1}{D} \frac{1}{t^{\frac{\theta}{2}}} \frac{1}{z^{\frac{2-\theta}{2-\theta}}} \exp \left( - \left( 1 - \frac{\theta}{2} \right) \left( \frac{\theta}{2} \right)^{\frac{\theta}{2-\theta}} z^{\frac{2}{2-\theta}} \right) \quad (8.38)$$

is in agreement with the result of Roman and Alemany [1994] and Barkai et al. [2000] for a space dimension  $d_f = 1$ , including the dependence in the power law prefactor to the exponential. The exponential dependence  $W(t, r) \sim \exp \left( -\text{const} (r/Dt^{\theta/2})^{\frac{2}{2-\theta}} \right)$  in (8.38) holds in arbitrary dimensions  $d_f$ , the only modification occurring in the prefactor whose power of  $z$  change with the space dimension  $d_f$  as [Roman and Alemany, 1994; Barkai et al., 2000]

$$W_{d_f}(t, z) \sim \frac{1}{D} \frac{1}{t^{\frac{\theta}{2}}} \frac{1}{z^{\frac{d_f(1-\theta)}{2-\theta}}} \exp \left( - \left( 1 - \frac{\theta}{2} \right) \left( \frac{\theta}{2} \right)^{\frac{\theta}{2-\theta}} z^{\frac{2}{2-\theta}} \right). \quad (8.39)$$

The expression of  $N(t, \vec{r})$  can be obtained from  $W(t, \vec{r})$  using the fractional Riemann-Liouville derivation (8.32) of order  $1-\theta$ . Inserting expression (8.35) in (8.32) and using the expression of the fractional Riemann-Liouville derivative operator  ${}_0D_t^\alpha$  applied to an arbitrary power  $t^\mu$ , i.e.,  ${}_0D_t^\alpha t^\mu = \frac{\Gamma(1+\mu)}{\Gamma(1+\mu-\alpha)} t^{\mu-\alpha}$ , we obtain

$$N(t, \vec{r}) = \frac{c^{1-\theta}}{2Dt^{1-\frac{\theta}{2}}} \sum_{k=0}^{\infty} \frac{(-1)^k z^k}{k! \Gamma((1-k)\theta/2)}. \quad (8.40)$$

Expression (8.40) can be used to evaluate  $N(t, \vec{r})$  for small  $z$ , but the numerical evaluation of (8.40) is impossible for large  $z$ . In order to obtain the asymptotic behavior of  $N(t, \vec{r})$ , expression (8.40) can be rewritten as a Fox-function [Mathai and Saxena, 1978]

$$N(t, \vec{r}) = \frac{c^{1-\theta}}{2Dt^{1-\frac{\theta}{2}}} H_{1,1}^{1,0} \left[ \frac{1}{z} \left| \begin{matrix} (\theta/2, \theta/2) \\ (0, 1) \end{matrix} \right. \right]. \quad (8.41)$$

Employing again the standard theorem of the Fox function (equation (1.6.3) of [Mathai and Saxena, 1978]), the asymptotic behavior of  $N(t, r)$  for large distances  $r$  such that  $r > Dt^{\theta/2}$  is given by

$$N(t, r) \sim \frac{c'^{-\theta}}{Dt^{1-\frac{\theta}{2}}} \left( \frac{|\vec{r}|}{Dt^{\theta/2}} \right)^{\frac{1-\theta}{2-\theta}} \exp \left( - \left( 1 - \frac{\theta}{2} \right) \left( \frac{\theta}{2} \right)^{\frac{\theta}{2-\theta}} \left( \frac{|\vec{r}|}{Dt^{\theta/2}} \right)^{\frac{2}{2-\theta}} \right). \quad (8.42)$$

The exponential dependence  $N(t, r) \sim \exp \left( -\text{const} (r/Dt^{\theta/2})^{\frac{2}{2-\theta}} \right)$  in (8.42) holds in arbitrary dimensions.

This expression becomes incorrect for very large distances because it would predict an exponential or slightly super-exponential decay with  $r$ . This cannot be true as the global law cannot decay faster than the local law (8.5). The reason for (8.42) to become incorrect at large distances is that the expansion of  $\hat{N}(\beta, \vec{k})$  for small  $|\vec{k}|$  (large distances) given by (8.34) has been truncated at the order  $k^2$ . There is however a subdominant term  $\propto k^\mu$  that describes the power law tail of the local law (8.5) and also of the global law asymptotically. A similar situation occurs in the application of the central limit theorem for sums of  $N$  random variables with power law distributions with exponents  $\mu > 2$  [Sornette, 2000a] : the distribution of the sum  $S$  is a Gaussian in its bulk for  $|S| < \sqrt{N \ln N}$  and crosses over to a power law with tail exponent  $\mu$  for larger  $S$ . In a similar way, the cross-over of  $N(t, r)$  to the asymptotic local power law (8.5) can be recovered by an analysis including the subleading correction  $\propto k^\mu$  to the expansion (8.34).

Expression (8.40) shows that the global rate of seismicity cannot be factorized as a product of a distribution of times and a distribution of distances. This space-time coupling implies that the seismic activity diffuses with time, and that the decay of the rate of aftershocks depends on the distance from the first mainshock. This coupling of space and time stems from the cascade of aftershocks, from the primary aftershocks to the secondary aftershocks to the tertiary aftershocks and so on.

Figure 8.4 presents the decay of the seismic activity  $N(r, t)$  obtained using expression (8.40) for small  $z$  and expression (8.42) for large  $z$ , as a function of the time from the mainshock and as a function of the distances  $r$ . Close to the mainshock epicenter, expression (8.40) predicts that the global seismicity rate decays with time as the renormalized Omori law

$$N(t, 0) \sim \frac{1}{t^{1-\theta/2}}. \quad (8.43)$$

The same decay is found at any fixed point  $\vec{r}$  for times  $t > (|\vec{r}|/D)^{2/\theta}$ . At all times, the same decay  $1/t^{1-\theta/2}$  is also obtained by measuring the aftershock seismicity in a local box at a distance from the main shock origin increasing with time as  $r \sim t^{\frac{\theta}{2}}$  (this is nothing but putting  $z = \text{constant}$  in (8.40)). At large distances  $r > Dt^{\theta/2}$ , the global decay law is different from a power-law decay. Figure 8.4 shows that the rate of aftershocks presents a truncation at early times, which increases as the distance  $r$  increases. At large times, the rate of aftershocks recovers the  $1/t^{1-\theta/2}$  power-law decay (8.43). We stress that a fit of the global law  $N(r, t)$  over the whole time interval by an Omori law would yield an apparent exponent  $p < 1 - \theta/2$  that decreases with  $r$ .

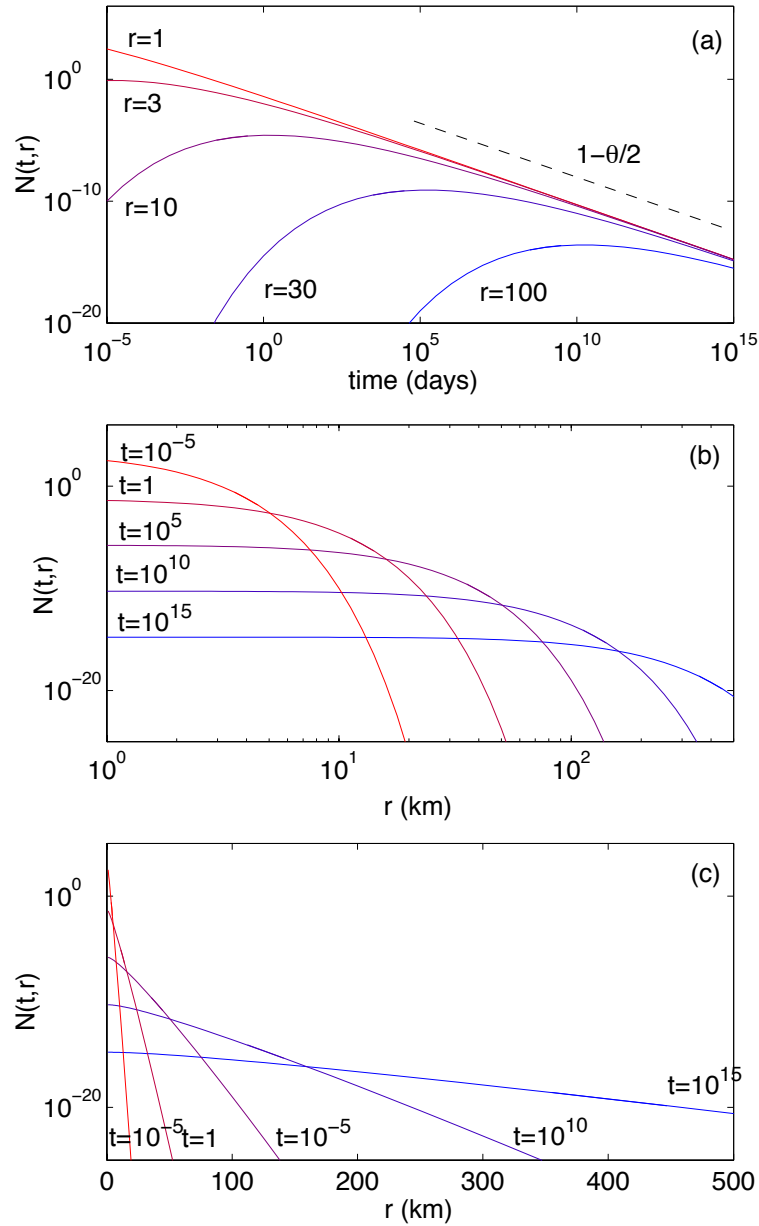


FIG. 8.4 – Rate of seismicity  $N(t, r)$  in the critical regime  $n = 1$  for  $\theta = 0.2$ ,  $\mu > 2$ ,  $c' = 1$  day and  $\sigma = 1$  km, evaluated from expressions (8.40) and (8.42), plotted as a function of the time (a) for different values of the distance  $r$  between the mainshock and its aftershocks, and (b,c) as a function of  $r$  (logarithmic scale for  $r$  in (b) and linear scale for  $r$  in (c)) for different values of the time between the mainshock and its aftershocks. The temporal decay of seismicity with time is characterized by a power-law decay  $N(r, t) \sim 1/t^{1-\theta/2}$  close to the mainshock epicenter or at large times for  $r \ll Dt^{\theta/2}$ . For large distances  $r \gg Dt^{\theta/2}$ , there is a truncation of the power-law decay at early times  $t^{\theta/2} \ll r/D$ , because the seismicity has not yet diffused up to the distance  $r$ . Although the distribution of distances between a mainshock and its direct aftershocks  $\Phi(r)$  follows a power-law distribution with exponent  $1 + \mu$ , the log-linear graph (c) shows that the global rate of aftershocks  $N(\vec{r}, t)$  decreases approximately exponentially as a function of the distance from the mainshock, with a characteristic distance that increases with time. This is in agreement with expression (8.42) which predicts  $N(t, r) \sim \exp\left[-\left(|\vec{r}|/Dt^{\theta/2}\right)^{\frac{2}{2-\theta}}\right]$ , i.e.,  $N(t, r) \sim \exp(C(t)|\vec{r}|^q)$  with an exponent  $q = 2/(2 - \theta)$  close to 1 within the exponential.

Integrating (8.40) over the whole one-dimensional space, we recover the global Omori law

$$N(t) = \int dr N(t, r) \sim \frac{1}{t^{1-\theta}} \quad (8.44)$$

found in [Sornette and Sornette, 1999a; Helmstetter and Sornette, 2002a]. Thus, we have found an additional source of variability of the exponent  $p$  of the Omori law : if measured over the whole catalog, we should measure  $p = 1 - \theta$  in the critical regime  $n = 1$  while  $p = 1 - \theta/2$  is slightly larger when measured in certain time- and space-windows, as described above. Thus, in this regime, pruning of catalogs may lead to continuous change from the value  $1 - \theta$  to  $1 - \theta/2$ . In addition, as we have mentioned, the cross-over in time may lead to still smaller apparent exponents, thus enhancing the impression of variability of the exponent  $p$ . In reality, this range of  $p$ -values are seen to result from the complex spatio-temporal organization of the aftershock seismicity of the ETAS model. These results should lead us to be cautious when analyzing real catalogs with respect to the conditions and regimes under which the analysis is performed.

There is another observable that characterizes how an aftershock sequence invades space as a function of time. Expression (8.40) indeed predicts a sub-diffusion process quantified by

$$\langle |\vec{r}|^2 \rangle \sim t^{2H} , \quad (8.45)$$

with  $H = \theta/2$  since the natural variable is  $z$  given by (8.36). Indeed, expression (8.40) tells us that, up to a global rescaling function of time, the rate of aftershocks is identical for a fixed value of  $z$ . Thus, any aftershock structure diffuses according to (8.45).

This prediction is checked in Figure 8.5 by numerical simulations. 1000 synthetic catalogs have been generated with  $\mu = 3$ ,  $\theta = 0.2$  and  $n = 1$ . The average distance between the first mainshock and its aftershocks as a function of the time from the mainshock has been averaged over these 1000 simulations. The theoretical diffusion exponent is  $H = \theta/2 = 0.1$ , in good agreement with the asymptotic behavior observed in the numerical simulation. In practice, in order to minimize the effect of fluctuations and optimize the speed of convergence, we estimate numerically  $\exp[\langle \ln |\vec{r}| \rangle]$  which is also expected to scale as  $\exp[\langle \ln |\vec{r}| \rangle] \sim t^{\theta/2}$  due to the simple scaling form of (8.41).

This problem has also been solved exactly in [Barkai, 2001a] in the context of the so-called fractional Fokker-Planck equation, which amounts to replace the distribution  $\Phi(\vec{r})$  of jumps (8.5) by a Gaussian function. This fractional Fokker-Planck equation allows one to introduce the possibility of bias or drift in the CTRW and therefore in the aftershock sequence.

## Exponential waiting time distribution and long jump size Lévy distribution ( $\mu < 2$ )

This case with an exponential distribution

$$\Psi(t) = \lambda e^{-\lambda t} \quad (8.46)$$

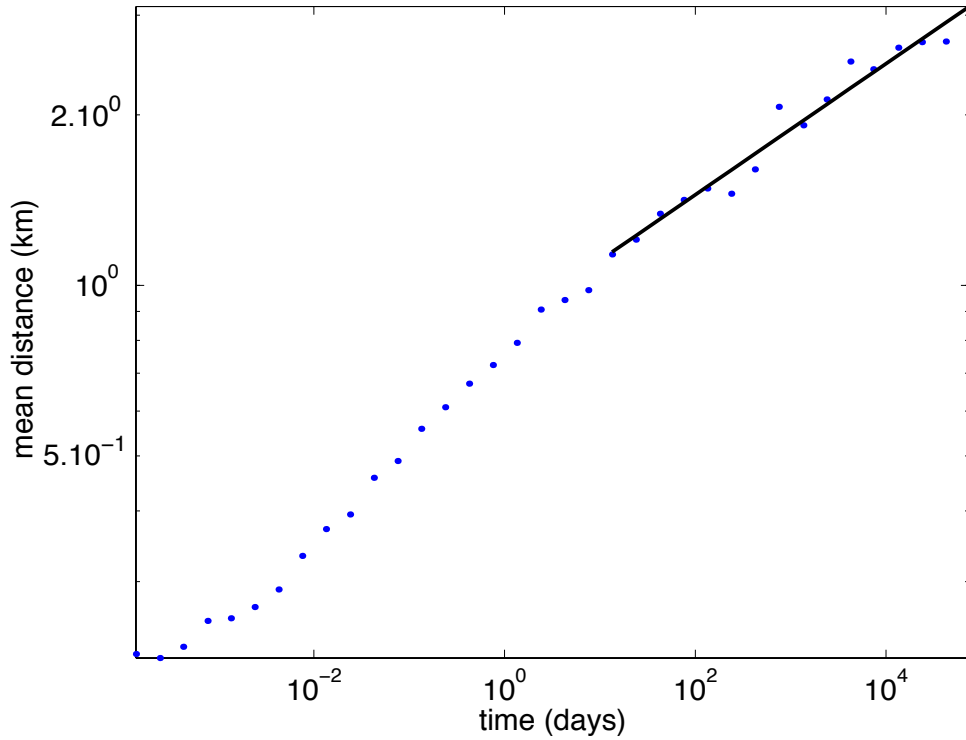


FIG. 8.5 – Average distance between the first mainshock and its aftershocks as a function of the time from the mainshock, for numerical simulations of the ETAS model in the critical regime  $n = 1$ , generated with the parameters  $\theta = 0.2$ ,  $d = 1$  km,  $\mu = 3$  and  $c = 10^{-3}$  day. The theoretical prediction for the diffusion exponent is thus  $H = \theta/2 = 0.1$ . We observe a crossover from a larger exponent at early times when the mean distance is close to the characteristic scale  $d = 1$  km of the distribution of distances between an aftershock and its progenitor, to a sub-diffusion with an exponent close to the theoretical prediction at large times. The solid line is a fit of the numerical data for times  $t > 10$  days, which gives an exponent  $H = 0.12$  slightly larger than the predicted value  $H = 0.1$ .

of waiting times with a Lévy distribution  $\Phi(\vec{r}) = L_\mu(|\vec{r}|)$  of jump sizes with tail exponent  $\mu < 2$  has been investigated by Budde et al. [Bude et al., 2001]. One finds

$$\langle |\vec{r}|^2 \rangle^{1/2} \sim t^{1/\mu}, \quad (8.47)$$

corresponding to a superdiffusion regime with Hurst exponent  $H = 1/\mu > 1/2$ . The full distribution function  $W(t, \vec{r})$  corresponding to the critical regime  $n = 1$  is known for  $\lambda t \gg 1$  :

$$W(t, \vec{r}) \propto \frac{1}{(\lambda t)^{1/\mu}} L_\mu \left( \frac{|\vec{r}|}{(\lambda t)^{1/\mu}} \right). \quad (8.48)$$

The corresponding  $N(t, \vec{r})$  is obtained from (8.20). The Laplace transform of the exponential distribution (8.46) is  $\hat{\Psi}(\beta) = \lambda/(\beta + \lambda)$ . We thus get

$$\hat{N}(\beta, \vec{k}) = (\beta + \lambda) \hat{W}(\beta, \vec{k}), \quad (8.49)$$

and thus

$$N(t, \vec{r}) = \frac{\partial W(t, \vec{r})}{\partial t} + \lambda W(t, \vec{r}). \quad (8.50)$$

Expression (8.50) together with (8.48) predicts a diffusion law  $r \sim t^H$  with  $H = 1/\mu$  which is in good agreement with our simulations. At large times  $|\vec{r}| \ll (\lambda t)^{1/\mu}$ ,  $N(t, \vec{r}) \approx \lambda W(t, \vec{r}) \sim 1/t^{1/\mu}$ , given an apparent local Omori exponent  $\theta = 1 - 1/\mu$ . This offers a new mechanism for generating Omori law for aftershocks from purely exponential local relaxation but with a heavy distribution of jump sizes. This power-law decay should be observed only at a fixed distance  $r$  or over a limited domain from the mainshock in the regime of large times.

Integrating over the whole space,  $\int d\vec{r} W(t, \vec{r}) = 1$  which gives  $N(t) = \delta(t) + \lambda$  equal to a constant seismic rate. This results from an initial mainshock at  $t = 0$  leading to the cascade of aftershocks adjusting delicately to this constant rate for the critical value  $n = 1$  of the branching parameter. In the sub-critical regime  $n < 1$ , the Omori law integrated over space gives instead  $N(t) \propto \exp[-(1-n)\lambda t]$ , showing that the characteristic decay time  $1/(1-n)\lambda$  of the dressed Omori propagator  $N(t)$  becomes much larger (much longer memory) than the decay time  $1/\lambda$  of the bare Omori propagator.

For  $\mu > 2$ , we recover the standard diffusion corresponding to  $\theta > 1$  and  $\mu > 2$  discussed in section 8.4.

### Long waiting times ( $\theta < 1$ ) and long jump sizes (Lévy flight regime for $\mu \leq 2$ )

Putting the leading terms of the expansions of  $\hat{\Phi}(\vec{k})$  and of  $\hat{\Psi}(\beta)$  in (8.21) gives

$$\hat{N}(\beta, \vec{k}) = \hat{S}_M(\beta, \vec{k}) \frac{1}{(\beta c')^\theta + (\sigma k)^\mu} . \quad (8.51)$$

The corresponding  $\hat{W}(\beta, \vec{k})$  is given by

$$\hat{W}(\beta, \vec{k}) = \hat{S}_M(\beta, \vec{k}) \frac{(\beta)^{\theta-1} c'^\theta}{(\beta c')^\theta + (\sigma k)^\mu} . \quad (8.52)$$

Equation (8.52) has been studied extensively in the context of the CTRW model as a long wavelength  $|\vec{k}| \rightarrow 0$  and long time  $\beta \rightarrow 0$  approximation to investigate the long time behavior of the CTRW. Kotulski [1995a] has developed a rigorous approach, based on limit theorems, to classify the asymptotic behaviors of different type of CTRWs and justifies the approximation (8.52) for the long time behavior. Barkai [2001b] has studied the quality of the long wavelength  $|\vec{k}| \rightarrow 0$  and long time  $\beta \rightarrow 0$  approximation (8.52) by solving the exact CTRW problem for the case when the waiting time distribution  $\Psi(t)$  is a one-sided stable Lévy law of index  $\theta$  with the same tail as (8.4) and the distribution  $\Phi(\vec{r})$  of jumps is a symmetric stable Lévy of index  $\mu$  with the same tail as (8.5). Their Laplace and Fourier transforms, that appear in the denominator of (8.22), are respectively  $\hat{\Psi}(\beta) = \exp[-\beta^\theta]$  and  $\hat{\Phi}(\vec{k}) = \exp[-|\vec{k}|^\mu/2]$ . Note that the long wavelength  $|\vec{k}| \rightarrow 0$  and long time  $\beta \rightarrow 0$  approximation gives  $1 - \exp[-(c'\beta)^\theta] \exp[-|\sigma\vec{k}|^\mu] = (c'\beta)^\theta + |\sigma\vec{k}|^\mu$ , which recovers (8.51). By comparing the exact solution of (8.21) for  $\Psi(t)$  and  $\Phi(\vec{r})$  of the above Lévy form with that of the long wavelength  $|\vec{k}| \rightarrow 0$  and long time  $\beta \rightarrow 0$  approximation (8.52), Barkai [2001b] finds that certain solutions of (8.52) diverge on the origin,

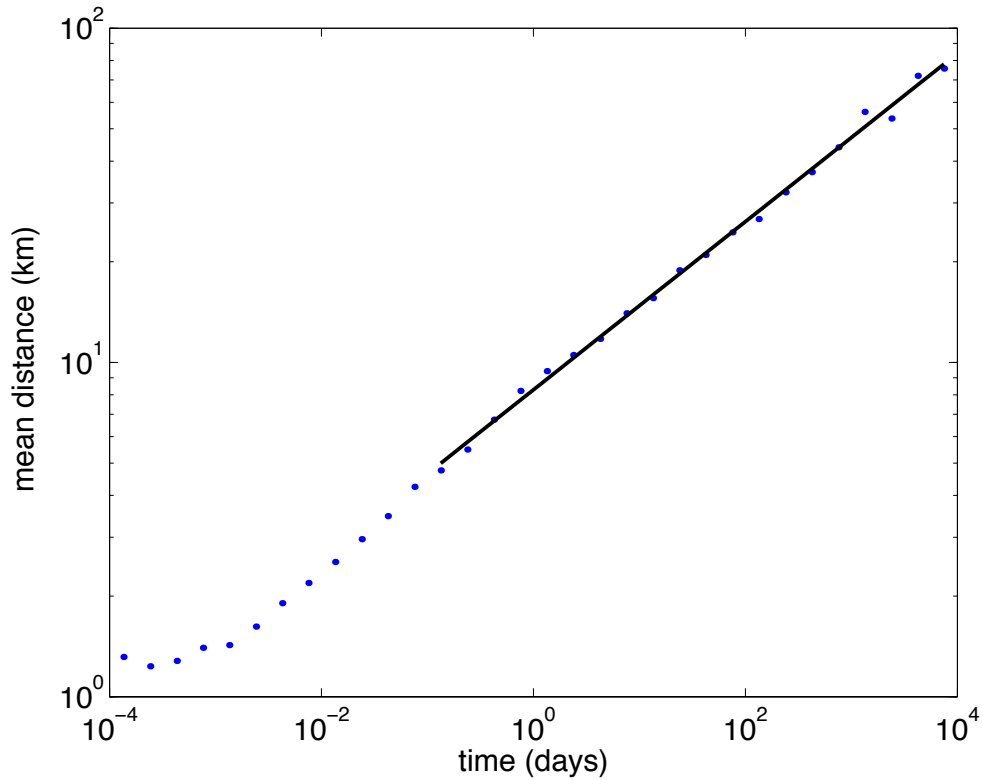


FIG. 8.6 – Average distance between the first mainshock and its aftershocks as a function of the time from the mainshock, for a numerical simulation of the ETAS model in the critical regime  $n = 1$ , with  $\theta = 0.2$ ,  $\mu = 0.9$ ,  $c' = 1$  day and  $\sigma = 1$  km. The solid line is a fit of the data which gives an exponent  $H = 0.25$  in good agreement with the predicted value  $H = 0.22$ .

a behavior not found for the corresponding solutions of (8.21). In addition, certain solutions of the full equation (8.21) converge only very slowly for  $\mu < 1$  to the solutions of the long-time approximation (8.52). These results validate our use of the asymptotic long time behavior with respect to the scaling laws but provide a note of caution if one needs more precise non-asymptotic information. In this case, such information can be obtained by a suitable analysis of the full equation (8.21).

Using power counting, expression (8.52) predicts a diffusion process (8.45) with exponent

$$H = \frac{\theta}{\mu} . \quad (8.53)$$

This prediction is checked by numerical simulation of the ETAS model in the critical regime  $n = 1$ , with  $\theta = 0.2$ ,  $\mu = 0.9$ , shown in Figure 8.6. The average distance between the first mainshock and its aftershocks as a function of the time from the mainshock indeed increases according to (8.45) with an exponent  $H$  in very good agreement with the prediction  $H = \theta/\mu = 0.22$ . As the form of the denominator in (8.52) is independent of the space dimension, the prediction (8.53) is valid in any space dimension.

The natural variable for the expansions given below allowing to compute  $N(t, \vec{r})$  is

$$z = \frac{D t^{\theta/\mu}}{|\vec{r}|}, \quad (8.54)$$

where  $D = \sigma/c^{\theta/\mu}$  and  $c' = c(\Gamma(1-\theta))^{1/\theta}$ .

### $z$ -expansion of the solution

$W(t, \vec{r})$  can be obtained as the following sum (equation (5.10) of [Saichev and Zaslavsky, 1997])

$$W(t, \vec{r}) = \frac{1}{\pi |\vec{r}|} \sum_{m=0}^{+\infty} (-1)^m z^{m\mu} \frac{\Gamma(m\mu + 1)}{\Gamma(m\theta + 1)} \cos \left[ \frac{\pi}{2} (m\mu + 1) \right]. \quad (8.55)$$

Applying (8.32) to (8.55) term by term in the sum, we get

$$N(t, \vec{r}) = \frac{c'^{-\theta}}{D\pi t^{1-\theta+\theta/\mu}} \sum_{m=0}^{+\infty} (-1)^m z^{1+m\mu} \frac{\Gamma(m\mu + 1)}{\Gamma((m+1)\theta)} \cos \left[ \frac{\pi}{2} (m\mu + 1) \right], \quad (8.56)$$

The asymptotics

$$\frac{\Gamma(m\mu + \mu + 1) \Gamma(m\theta + 1)}{\Gamma(m\theta + \theta + 1) \Gamma(m\mu + 1)} \sim \frac{\Gamma(m\mu + \mu + 1) \Gamma((m+1)\theta)}{\Gamma((m+2)\theta) \Gamma(m\mu + 1)} \sim m^{\mu-\theta} \quad (8.57)$$

show that the series (8.55) and (8.56) exist only for  $\mu < \theta$ . It can be shown that these series exist for all  $z$  in this case. This series converges very slowly for large  $z$  but the Padé summation method [Bender and Orzag, 1978] can be used to improve the convergence of (8.56) in the case  $\mu < \theta$ , and can also be used to estimate (8.56) in the case  $\mu > \theta$  for which the series diverges.

The space integral  $\int dr N(t, r)$  over the whole one-dimensional volume  $V$ , with  $N(t, r)$  given by (8.56), recovers the global Omori law

$$\int_V dr N(t, r) \sim \frac{1}{t^{1-\theta}}. \quad (8.58)$$

Note the non-trivial phenomenon in which the superposition of all aftershock activities transforms the local Omori law or “bare propagator” (8.4)  $\Psi(t) \sim \frac{1}{t^{1+\theta}}$  into the global Omori law or “dressed propagator”  $\frac{1}{t^{1-\theta}}$ . This effects was predicted in [Sornette and Sornette, 1999a; Helmstetter and Sornette, 2002a] in the version of the ETAS model without space dependence. These results are consistent with the claim of section 8.2 according to which all results reported previously for the version of the ETAS model without space dependence hold also for the version of the space-dependent ETAS model studied here, when averaging over the whole space.

The asymptotic behavior for  $|\vec{r}| \gg D t^{\frac{\theta}{\mu}}$  (i.e.,  $z \ll 1$ ) and  $\mu < \theta$  is obtained by keeping only the first non-zero term ( $m = 1$ ) in (8.56) which is convergent for all  $z$  in the case  $\mu < \theta$

$$N(t, \vec{r}) = \frac{\sin\left(\frac{\pi\mu}{2}\right)}{\sigma c' \pi} \frac{\Gamma(1+\mu)}{\Gamma(2\theta)} \left(\frac{c'}{t}\right)^{1-2\theta} \left(\frac{\sigma}{|\vec{r}|}\right)^{1+\mu}, \quad \text{for } |\vec{r}| \gg D t^{\frac{\theta}{\mu}}. \quad (8.59)$$

At fixed large  $|\vec{r}|$  and for  $t < |\vec{r}|/D|^{\frac{\mu}{\theta}}$ , this predicts a local Omori law with exponent  $p = 1 - 2\theta$ .

### 1/z-expansion of the solution

We use the theory of Fox functions [Mathai and Saxena, 1978] to obtain  $N(t, \vec{r})$  as an infinite series in  $1/z$ . For this, we first rewrite expression (8.56) as a Fox function [Mathai and Saxena, 1978]

$$N(t, \vec{r}) = \frac{c^{1-\theta}}{D \mu \pi t^{1-\theta+\theta/\mu}} R \left( H_{2,2}^{1,2} \left[ z e^{i\pi/2} \left| \begin{array}{l} (1/\mu, 1/\mu), (1, 1) \\ (1/\mu, 1/\mu), (\theta/\mu - \theta + 1, \theta/\mu) \end{array} \right. \right] \right), \quad (8.60)$$

where  $R(z)$  indicates the real part of  $z$ .

The  $1/z$  expansion of  $N(t, \vec{r})$  can be obtained using the dual expansion of the Fox function (8.60) (expression (3.7.2) of [Mathai and Saxena, 1978])

$$N(t, \vec{r}) = \frac{c^{-\theta}}{D \pi \mu t^{1-\theta+\theta/\mu}} \sum_{m=0}^{+\infty} (-1)^m \left[ \mu z^{1-\mu-m\mu} \frac{\Gamma(1-(m+1)\mu) \sin((m+1)\mu\pi/2)}{\Gamma(-m\theta)} + \frac{z^{-m}}{m!} \frac{\pi \cos(m\pi/2)}{\sin((m+1)\pi/\mu) \Gamma(\theta - (m+1)\theta/\mu)} \right]. \quad (8.61)$$

This expansion exists only for  $\mu > \theta$  (conditions of page 71 below eq. (3.7.2) of [Mathai and Saxena, 1978]). This is easily checked by the behavior of an asymptotics similar to (8.57). Note that the series (8.61) is not defined in the special case  $\mu = 1$  due to the presence of the ill-defined ratio  $\Gamma(0)/\Gamma(0)$  and a different approach is required, such as the integral representation of  $W(t, \vec{r})$  developed in [Saichev and Zaslavsky, 1997]. The global Omori law obtained by integrating over the whole space (8.61) is again  $N(t) \sim 1/t^{1-\theta}$  as expected from the analysis of the ETAS model without space dependence [Helmstetter and Sornette, 2002a].

Keeping only the largest term of (8.61) for large  $z$ , we obtain the asymptotic behavior for small distances  $r < D t^{\theta/\mu}$

$$N(t, r) \simeq \frac{\Gamma(1-2\mu) \Gamma(1+\theta) \sin(\pi\mu) \sin(\pi\theta)}{c' \sigma \pi^2 (r/\sigma)^{1-2\mu} (t/c')^{1+\theta}} \quad \text{for } \mu < 0.5$$

$$N(t, r) \simeq \frac{c^{1-\theta}}{c' \sigma \mu \Gamma(\theta - \theta/\mu) \sin(\pi/\mu)} \frac{1}{(t/c')^{1-\theta+\theta/\mu}} \quad \text{for } 0.5 < \mu < 2. \quad (8.62)$$

Note that for  $r < D t^{\theta/\mu}$  and  $0.5 < \mu < 2$ , the leading behavior of  $N(t, r)$  is independent of  $r$ .

Equation (8.62) thus predicts an apparent exponent

$$\begin{aligned} p &= 1 + \theta & \text{for } \mu < 0.5 \\ p &= 1 - \theta + \theta/\mu & \text{for } 0.5 < \mu < 2 \end{aligned} \quad (8.63)$$

for small distances  $r < D t^{\theta/\mu}$ . This prediction is valid only in the case  $\mu > \theta$  for which the series (8.61) is convergent. However, the same asymptotic results are also obtained by different methods in the case  $\mu < \theta$ , for instance expression (8.63) is recovered for all  $\mu < 2$  using the integral representation of [Saichev and Zaslavsky, 1997] [A. Saichev, private communication]. The numerical evaluation of (8.56), which converges for  $\mu < \theta$ , also recovers the asymptotic

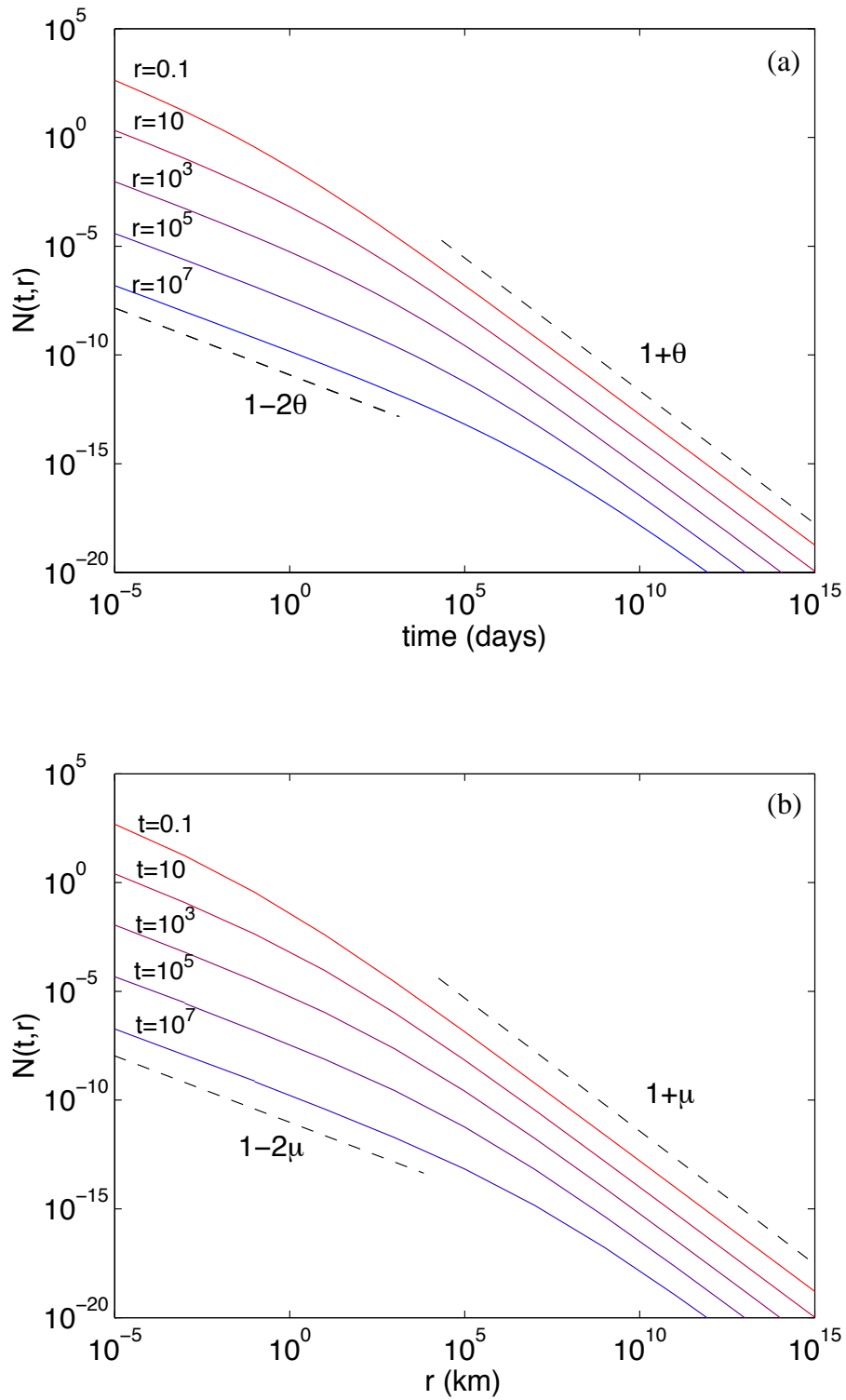


FIG. 8.7 – Rate of seismicity  $N(t,r)$  for  $\theta = 0.2$ ,  $\mu = 0.2$ ,  $c' = 1$  day and  $\sigma = 1$  km, evaluated from expressions (8.56) and (8.62), plotted as a function of the time (a) for different values of the distance  $r$  between the mainshock and its aftershocks, and (b) as a function of  $r$  for different values of the time between the mainshock and its aftershocks. We stress again that the time scales shown here do not necessarily correspond to real observable time scales but are presented to demonstrate clearly the existence of the two regimes. The dashed lines give the predicted asymptotic dependence in each regime.

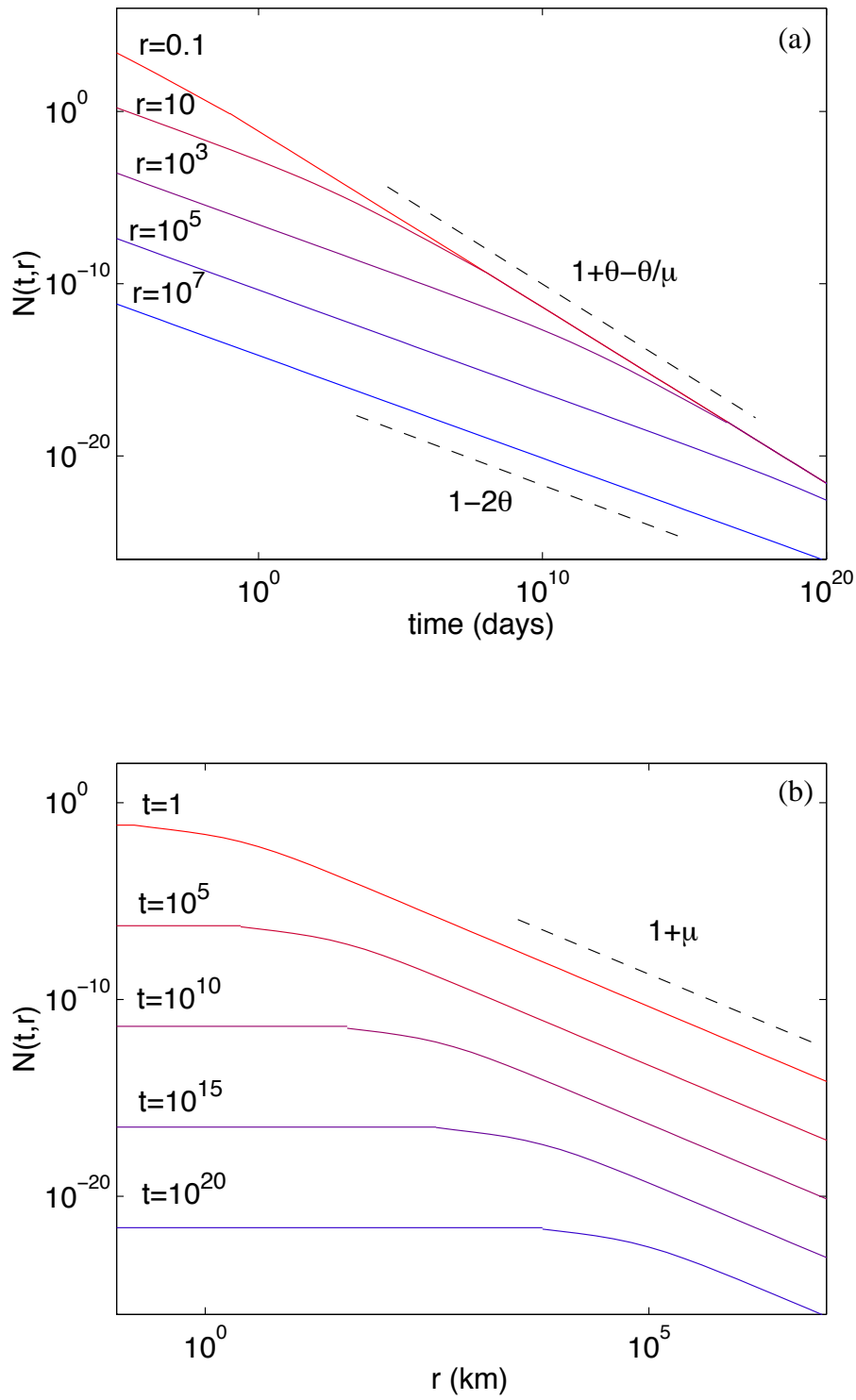


FIG. 8.8 – Rate of seismicity  $N(t, r)$  for  $\theta = 0.2$ ,  $\mu = 0.9$ ,  $c' = 1$  day and  $\sigma = 1$  km, evaluated from expressions (8.56) and (8.62), plotted as a function of the time (a) for different values of the distance  $r$  between the mainshock and its aftershocks, and (b) as a function of  $r$  for different values of the time between the mainshock and its aftershocks. The dashed lines give the predicted asymptotic dependence in each regime.

results (8.62). The two regimes  $\mu < 0.5$  and  $0.5 < \mu < 2$  are illustrated in Figures 8.7 and 8.8 respectively. The seismicity rate  $N(t, \vec{r})$  is evaluated from expression (8.56) for small  $z$  and from expression (8.61) for large  $z$ .

We also performed numerical simulations of the ETAS and CTRW models and the results are in good agreement with expression (8.56) and (8.61) for  $N(\vec{r}, t)$  for  $t \gg c$  and  $r \gg d$ . For very small times  $t \ll c$ , or for very small distances  $r \ll d$ , expressions (8.56) and (8.61) are not valid because they are based on a long wavelength  $|\vec{k}| \rightarrow 0$  and long time  $\beta \rightarrow 0$  approximation. Numerical simulations of the ETAS model in the case  $\theta = 0.2$  and  $\mu = 0.9$  are presented in Figure 8.9, and are in good agreement with the analytical solutions (8.56) and (8.61) shown in Figure 8.8 for the same parameters, except from the truncation of  $N(t, r)$  for times  $t \ll c$  and distances  $r \ll d$  that are not reproduced by the analytical solution.

### A simple non-separable joint distribution of waiting times and jump sizes : coupled spatial diffusion and long waiting time distribution

Consider the choice for  $\phi_{m_i}(t - t_i, \vec{r} - \vec{r}_i)$  replacing (8.2) by

$$\phi_{m_i}(t - t_i, \vec{r} - \vec{r}_i) = \rho(m_i) \Psi(t - t_i) \Phi(|\vec{r} - \vec{r}_i|/\sqrt{Dt}) , \quad (8.64)$$

where  $\rho(m_i)$  and  $\Psi(t)$  are again given by (8.3) and (8.4) while (8.5) is changed into

$$\Phi(|\vec{r} - \vec{r}_i|/\sqrt{Dt}) = \frac{1}{\sqrt{2Dt}} \exp(-|\vec{r} - \vec{r}_i|^2/Dt) . \quad (8.65)$$

The spatial diffusion of seismic activity is now coupled to the waiting time distribution. Expression (8.65) captures the effect that, in order for aftershocks to spread over large distances by the underlying physical process, they need time. In fact, returning to the discussion in the introduction on the various proposed mechanisms for aftershocks, expression (8.65) embodies a microscopic diffusion process.

In this case, (8.21) must be replaced by

$$\hat{N}(\beta, \vec{k}) = \frac{\hat{S}_M(\beta, \vec{k})}{1 - n\hat{\phi}(\beta, \vec{k})} , \quad (8.66)$$

where  $\hat{\phi}(\beta, \vec{k})$  is the Laplace-Fourier transform of the product  $\Psi(t) \Phi(|\vec{r}|/\sqrt{Dt})$ . For large times and long distances for which the first terms in the expansion in  $\beta$  and  $k$  are sufficient, and for  $n = 1$ , we obtain

$$\hat{\phi}(\beta, \vec{k}) \propto \frac{\hat{S}_M(\beta, \vec{k})}{(\beta + Dk^2)^\theta} . \quad (8.67)$$

The inverse Laplace-Fourier transform of (8.66) is

$$N(t, \vec{r}) \sim \frac{1}{t^{1-\theta}} \frac{1}{\sqrt{2\pi Dt}} \exp(-|\vec{r}|^2/Dt) . \quad (8.68)$$

As expected, expression (8.68) recovers the dressed Omori propagator in the case of absence of space dependence [Helmstetter and Sornette, 2002a]. At finite  $r$  and long times, the dressed

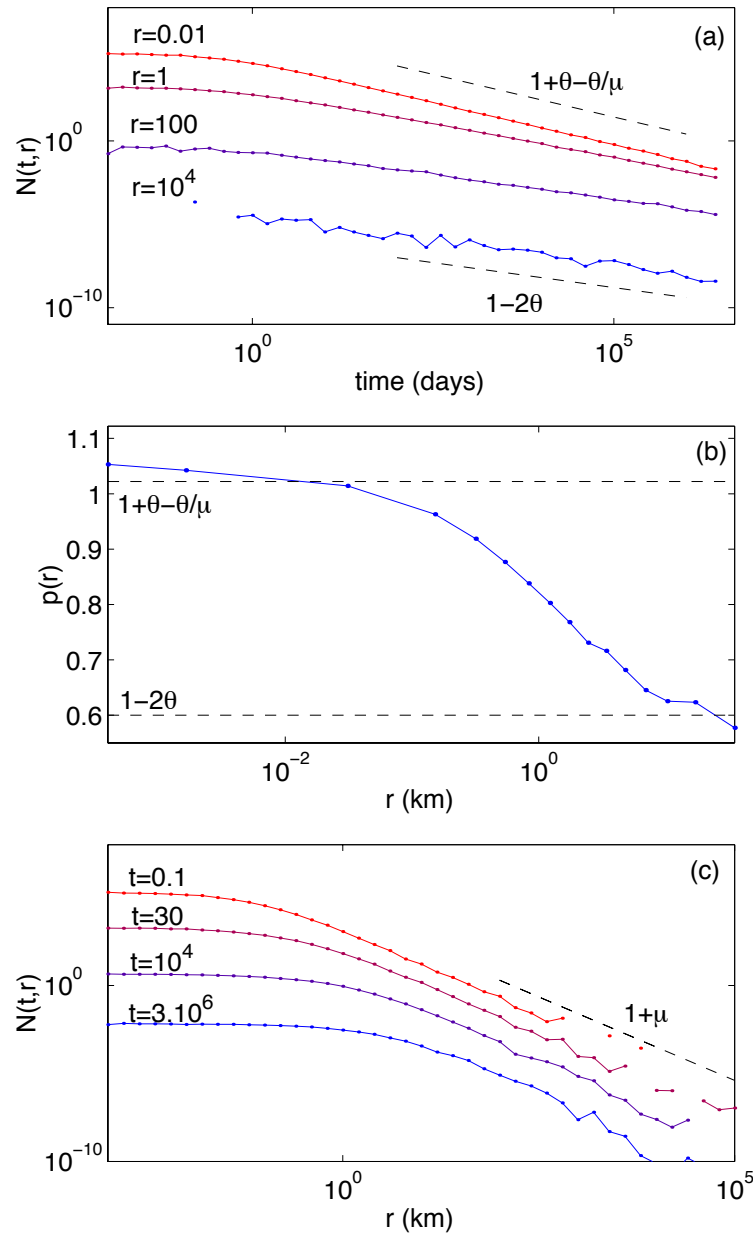


FIG. 8.9 – Rate of seismicity  $N(t, r)$  obtained from numerical simulations of the ETAS model generated with the same parameters as in Figure 8.8 ( $\theta = 0.2$ ,  $\mu = 0.9$ ,  $c' = 1$  day and  $d = 1$  km).  $N(r, t)$  is computed by averaging over 500 numerical realizations of the ETAS model. (a) aftershock rate as a function of the time from the mainshock for several distances  $|\vec{r}|$  ranging from 0.01 to  $10^4$  km. (b) Apparent Omori exponent measured for times  $t > 10$  as a function of the distance from the mainshock. The aftershock decay rate (with time) is larger close to the mainshock epicenter than at large distances from the mainshock. The asymptotic values for small and large distances are in agreement with the predictions (8.63) for  $r \ll Dt^{\theta/\mu}$  and (8.59) for  $r \gg Dt^{\theta/\mu}$ , which are shown as the horizontal dashed lines. (c) Rate of seismicity  $N(t, r)$  as a function of the distance between aftershocks and mainshock for various times. The theoretical prediction for large distances is shown as the dashed line with slope  $-(1 + \mu)$ .

Omori law also decay as  $1/t^{1-\theta}$ . The diffusion of aftershocks is normal with the standard diffusion exponent  $H = 1/2$ .

## 8.5 Discussion

Using the analogy between the ETAS model and the CTRW model established here, we have derived the relation between the average distance between aftershocks and the mainshock as a function of the time from the mainshock, and the joint probability distribution of the times and locations of aftershocks.

We have assumed that each earthquake triggers aftershocks at a distance  $r$  and time  $t$  according to the bare propagator  $\phi(r, t)$ , which can be factorized as  $\Psi(t)\Phi(r)$ . This means that the distribution  $\Phi(r)$  of the distances between an event and its direct aftershocks is decoupled from the distribution  $\Psi(t)$  of waiting time. Hence, the direct aftershocks triggered by a single mainshock do not diffuse in space with time. Notwithstanding this decoupling in space and time of the bare propagator  $\phi(r, t)$ , we have shown that the global law or dressed propagator  $N(t, \vec{r})$  defined as the global rate of events at time  $t$  and at position  $\vec{r}$ , cannot be factorized into two distributions of waiting times and space jumps. This joint distribution of waiting times and positions of the whole sequence of aftershocks cascading from a mainshock is different from the product of the bare time and space propagators.

The mean distance between the mainshock and its aftershocks, including secondary aftershocks, increases with the time from the mainshock, due to the cascade process of aftershocks triggering aftershocks triggering aftershocks, and so on. In the critical case  $n = 1$ , this diffusion takes the form of a power-law relation  $R \sim t^H$  of the average distance  $R$  between aftershocks and the mainshock, as a function of the time  $t$  from the mainshock. If the local Omori law is characterized by an exponent  $0 < \theta < 1$ , and if the space jumps follow a power law  $\Phi(r) \sim 1/(r+d)^{1+\mu}$ , the diffusion exponent is given by  $H = \theta/\mu$  in the case  $\mu < 2$  and  $H = \theta/2$  in the case  $\mu > 2$ . Depending on the  $\theta$  and  $\mu$  values, we can thus observe either sub-diffusion ( $H < 1/2$ ) or super-diffusion ( $H > 1/2$ ), as summarized in Figure 8.10. In the sub-critical ( $n < 1$ ) and super-critical ( $n > 1$ ) regimes, this relation is still valid up to the characteristic time  $t^*$  given by (8.1) and for distances smaller than  $r^* \propto Dt^{*H}$  given by (8.30). For  $t > t^*$  and  $r > r^*$  in the sub-critical regime, the global distributions of times and distances between the mainshock and its aftershocks are decoupled and there is therefore no diffusion. In the super-critical regime, the aftershock rate increases exponentially for  $t > t^*$  and the aftershocks diffuses more rapidly than before  $t^*$ .

In the critical regime, the cascade of secondary aftershocks introduces a variation of the apparent Omori exponent as a function of the distance from the mainshock. The asymptotic values of the Omori exponent in the different regimes are summarized in Table 8.2. In the regime  $\mu < 2$ , we observe a transition from an Omori law decay with an exponent  $p = 1 - 2\theta$  at early times  $t^H \ll r/D$  to a larger exponent at large times. This provides another mechanism to explain

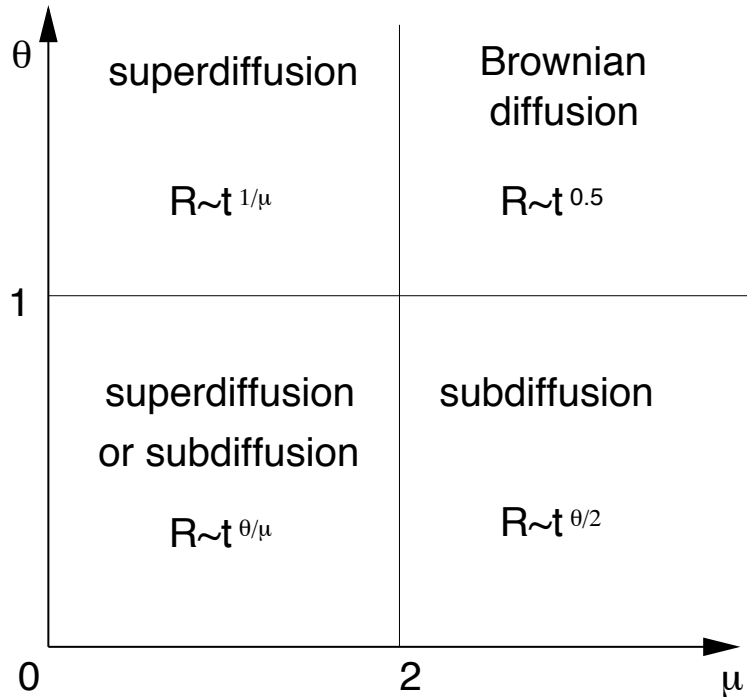


FIG. 8.10 – Classification of the different regime of the diffusion of aftershocks in space as a function of time from the main shock. The bare Omori law for aftershocks decay with time as  $1/t^{1+\theta}$ . The jump size distribution between the earthquake “mother” and its “daughters” is proportional to  $1/r^{1+\mu}$ .  $R(t)$  is the average distance between all aftershocks triggered up to time  $t$  after the mainshock.

the observed variability of the Omori exponent. In the regime  $\mu > 2$ , a power-law decay of the seismicity with time is observed only at large times  $t^H \gg r/D$ . At early times, or at large distances  $r \gg Dt^H$ , the seismicity rate is very small, because the seismicity as not yet diffused up to the distance  $r$ .

We should emphasize that our theoretical analysis of aftershock diffusion predicts the behavior of the ensemble average of aftershock sequences. Individual sequences may depart from this ensemble average, especially for sequences with few earthquakes and limited durations. For long sequences (20,000 events say), we have verified that the exponent  $H$  measured on individual sequences does not deviate from the ensemble average value by more than about 20%. As already discussed, the impact of fluctuations becomes however more effective as the parameter  $\alpha$  increases above  $b/2$ .

The diffusion of the seismicity also renormalizes the spatial distribution of the seismicity, which is very different from the local distribution  $\Phi(r)$  of distances between a triggering event and its direct aftershocks. In the regime  $\mu > 2$ , the global seismicity rate  $N(t, \vec{r})$  decays exponentially with the distance from the mainshock, whereas the local distribution of distances  $\Phi(r)$  is a power-law distribution. In the regime  $\mu < 2$ , the local law  $\Phi(r) \sim r^{-1-\mu}$  is recovered at large distances, but a slower decay for  $0.5 < \mu < 2$  or a constant rate for  $\mu < 0.5$  is observed at small distances

TAB. 8.2 – Asymptotic values of the (renormalized) Omori exponent (of the dressed propagator) in the different regimes for  $z \ll 1$  and  $z \gg 1$  where  $z \equiv \frac{D t^{HH}}{r}$ .

	large $z$ $r \ll D t^H$	small $z$ $r \gg D t^H$
$\mu < 0.5$	$p = 1 + \theta$	$p = 1 - 2\theta$
$0.5 \leq \mu < 2$	$p = 1 - \theta + \theta/\mu$	$p = 1 - 2\theta$
$2 \leq \mu$	$p = 1 - \theta/2$	not defined <sup>1</sup>

<sup>1</sup> The Omori exponent is not defined in this case because the dependence of  $N(t, \vec{r})$  with respect to time given by expression (8.42) and represented in Figure 8.4 has a contribution from the exponential asymptotics which is different from a power-law for large distances  $r \gg D t^H$ .

$r \ll D t^H$ .

These predictions on the decrease of the Omori exponent with  $r$  have not yet been observed in earthquake catalogs, but an expansion of the aftershock zone has been reported in many studies [Mogi, 1968; Imoto, 1981; Chatelain et al., 1983; Tajima and Kanamori, 1985a,b; Wesson, 1987; Ouchi and Uakawa, 1986; Noir et al., 1997; Jacques et al., 1999]. However, very few studies have quantified the diffusion law. Noir et al. [1997] show that the earthquake Dobi sequence (central Afar, August 1989) composed of 22  $M > 4.6$  earthquakes presented a migration that was in agreement with a diffusion process due to fluid transfer in the crust, characterized by a normal diffusion process with exponent  $H = 0.5$ . Tajima and Kanamori [1985a,b] studied several aftershock sequences in subduction zone and observed a much slower logarithmic diffusion, which is compatible with a low exponent  $H$  close to 0.1. In some cases, the aftershock sequence displays no expansion with time. For instance, Shaw [1993] studied several aftershock sequences in California and concluded that the distribution of distances between the mainshock and its aftershocks is independent of time. This can be explained by the fact that the Omori exponent measured in [Shaw, 1993] is very close to 1, thus  $\theta$  is very small and our prediction is that the exponent  $H$  should be very small.

In fact, the ETAS model predicts that diffusion should be observed only for aftershock sequences with a measured Omori exponent  $p$  significantly smaller than 1, which can only occur according to our model when the bare Omori propagator with exponent  $1 + \theta$  is renormalized into the dressed propagator with global exponent  $1 - \theta$ . We have shown that this renormalization of the exponent only occurs at times less than  $t^*$ , while for longer times in the sub-critical regime  $n < 1$  the dressed Omori propagator recovers the value of the bare exponent  $1 + \theta > 1$  (see Figure 8.1). Therefore, identifying an empirical observation of  $p < 1$  with our prediction  $p = 1 - \theta$  indicates that the aftershock sequence falls in the “good” time window  $t < t^*$  in which the renormalization operates. We have also shown that the dressed propagator gives a diffusion

only for  $t < t^*$ . We can thus conclude that, according to the ETAS model, the observation of an empirical Omori exponent larger than 1 is indicative of the large time  $t > t^*$  behavior in the sub-critical regime  $n < 1$ , for which there is no diffusion. This provides a possible explanation for why many sequences studied by [Tajima and Kanamori, 1985a,b; Shaw, 1993] do not show a diffusion of the aftershock epicenters. Reciprocally, a prerequisite for observing diffusion in a given aftershock sequence is that the empirical  $p$ -value be less than 1 in order to qualify the regime  $t < t^*$ .

An alternative model has been discussed by Dieterich [1994] who showed that the spatial variability of the stress induced by a mainshock, coupled with a rate and state friction law, results in an expansion of the aftershock zone with time. This expansion does not take the form of a diffusion law as observed in the ETAS model, the relation between the characteristic size of the aftershock zone does not grow as a power law of the time from the mainshock (equation (22) and Figure 6 of [Dieterich, 1994]).

Marsan et al. [1999, 2000] and Marsan and Bean [2001] studied several catalogs at different scales, from the scale of a deep mine to the world-wide seismicity, and observed that the average distance between two earthquakes increases as a power-law of the time between them, with an exponent often close to 0.2, indicative of a sub-diffusion process. They interpreted their results as a mechanism of stress diffusion, that may be due to fluid transfer with heterogeneous permeability leading to sub-diffusion. Their analysis is quite different from those used in other studies, because they consider all pairs of events, without distinction between aftershocks and mainshocks. This analysis can however lead to spurious diffusion, and in some cases this method does not detect diffusion in synthetic data set with genuine diffusion. We have tested their analysis on a synthetic catalog generated by superposing a background seismicity with uniform spatial and temporal distribution, and 10 mainshocks with poissonian distribution in time and space, and with a power-law distribution of energies. Each of these mainshocks generates only *direct* aftershocks, without secondary cascades of aftershocks, and the number of aftershocks increases exponentially with the magnitude of the mainshock. This way, we generate a synthetic catalog without any physical process of diffusion, and which includes all the other well-established characteristics of real seismicity : clustering in space and time superposed to a seismicity background. Applying the analysis of [Marsan et al., 1999, 2000; Marsan and bean, 2001] to this synthetic data set leads to an apparent diffusion process with a well-defined exponent  $H = 0.5$ . However, this apparent diffusion does not reflect a genuine diffusion but simply describes the crossover from the characteristic size of an aftershock zone at early times to the larger average distance between uncorrelated events at large times. In plain words, the apparent power law  $R \propto t^H$  is nothing but a cross-over and is not real. Furthermore, applying this analysis to a synthetic catalog generated using the ETAS model, without seismicity background, and with a theoretical diffusion exponent  $H = 0.2$ , the method yields  $H = 0.01$  if we use all the events of the catalog. If we select only events up to a maximum distance  $r_{max}$  to apply the same proce-

ture as in [Marsan et al., 1999, 2000; Marsan and bean, 2001], we obtain larger values of  $H$  which are more in agreement with the theoretical exponent  $H = 0.2$  but with large fluctuations that are function of  $r_{max}$ . Therefore, it is probable that the diffusion reported in [Marsan et al., 1999, 2000; Marsan and bean, 2001] is not real and results from a cross-over between two characteristic scales of the spatial earthquake distribution. It may be attributed to the analyzing methodology which mixes up uncorrelated events. We are thus reluctant to compare the results of [Marsan et al., 1999, 2000; Marsan and bean, 2001] with the predictions obtained with the ETAS model.

One can similarly question the results on anomalous diffusion of seismicity obtained by Sotolongo-Costa et al. [2000], who considered 7500 micro-earthquakes recorded by a local spanish network from 1985 to 1995. They interpret the sequence of earthquakes as a random walk process, in which the walker jumps from an earthquake epicenter to the next in sequential order. The time between two successive events is seen as a waiting time between two jumps and the distance between these events is taken to correspond to the jump size. Since the distributions of time intervals and of distances between successive earthquakes are both heavy-tailed (approximately power laws), their model is a CTRW. We cannot stress enough that their CTRW model of seismicity has nothing to do with our results on the mapping of the ETAS model onto a CTRW. Their procedure is ad-hoc and their results depend obviously strongly on the space domain of the analysis since distant earthquakes that are completely unrelated can be almost simultaneous! We also stress that our mapping of the ETAS model onto the CTRW model does not correspond to identifying an earthquake sequence as a *single* realization of a CTRW, as assumed arbitrarily by Sotolongo-Costa et al. [2000].

Our predictions obtained here are thus difficult to test on seismicity data, due to the small number of events available and the restricted time periods and distance ranges, and because the seismicity background can strongly affect the results. New methods should hence be developed to investigate if there is a real physical process of diffusion in seismic activity and to compare the observations of real seismicity with the quantitative predictions of the ETAS model. Preliminary study of aftershock sequences in California leads to the conclusion that most aftershock sequences are characterized by an Omori exponent  $p > 1$ , indicative of the sub-critical regime with  $t > t^*$ . As expected from our predictions in this regime, we do not observe an expansion of the aftershock zone. However, a few sequences give a value  $p < 1$  and also exhibit an increase of the average distance between the mainshock and its aftershocks consistent with our predictions. A detailed report of this analysis will be reported elsewhere.

## 8.6 Conclusion

We have studied analytically and numerically the ETAS (epidemic-type aftershock) model, which is a simple stochastic process modeling seismicity, based on the two best-established

empirical laws for earthquakes, the power law decay of seismicity after an earthquake and a power law distribution of earthquake energies. This model assumes that each earthquake can trigger aftershocks, with a rate increasing with its magnitude. In this model, the seismicity rate is the result of the whole cascade of direct and secondary aftershocks.

We have first established an exact correspondence between the ETAS model and the CTRW (continuous-time random walk) model. We have then used this analogy to derive the joint probability of times and distances of the seismicity following a large earthquake and we have characterized the different regimes of diffusion.

We have shown that the diffusion of the seismicity should be observed only for times  $t < t^*$ , where  $t^*$  is a characteristic time depending on the model parameters, corresponding to an observed Omori exponent smaller than one. Most aftershock sequences have an observed Omori exponent larger than one, corresponding to the subcritical regime of the ETAS model, for which there is no diffusion. The diffusion of the seismicity produces a decrease of the Omori exponent as a function of the distance from the mainshock, the decay of aftershocks being faster close to the mainshock than at large distances. The spatial distribution of seismicity is also renormalized by the cascade process, so that the observed distribution of distances between the mainshock and its aftershocks can be fundamentally different from the bare propagator  $\Phi(r)$  which gives the distribution of the distances between triggered and triggering earthquakes. We have also noted that the ETAS model generates apparent but realistical fractal spatial patterns.

Assuming that the distances between triggering and triggered events are independent of the time between them, this model generates a diffusion of the whole sequence of aftershocks with the time from the mainshock, which is induced by the cascade of aftershocks triggering aftershocks, and so on. Our results thus provides a simple explanation of the diffusion of aftershock sequences reported by several studies, which was often interpreted as a mechanism of anomalous stress diffusion. We see that no such “anomalous stress diffusion” is needed and our theory provides a parsimonious account of aftershock diffusion resulting from the minimum physical ingredients of the ETAS model.

## Acknowledgments

We are very grateful to B. Berkowitz, S. Gluzman, J.-R. Grasso, Y. Klafter, L. Margerin, A. Saichev and G. Zaslavsky for useful suggestions and discussions.



## Chapitre 9

# Observations of diffusion of aftershocks epicenters

We present here preliminary results on an analysis of aftershock sequences in California and a comparison with the predictions of the diffusion of seismic activity in the ETAS model derived in the precedent chapter. We want to characterize the temporal and spatial distribution of aftershocks triggered directly or indirectly by a large earthquake, and the coupling between the spatial and temporal distributions.

The analysis of real data is much more difficult than the study of synthetic sequences, due to the smaller number of earthquakes available, the presence of background activity, and problems of catalog completeness especially just after large mainshocks.

In addition, real seismicity is much more complicated than the ETAS model. Several properties of seismicity and aftershock sequences are not taken into account in the ETAS model. We first present the limitations of the ETAS model and of the analytical analysis presented in the previous section. Due to the limitations of the seismicity data and of the analytical analysis, it is difficult to obtain reliable quantitative results on the diffusion exponent. However, some qualitative predictions of the ETAS model should be observed in real data :

- only sequences in the early time regime  $t < t^*$  characterized by an Omori exponent  $p < 1$  should diffuse ;
- the diffusion of seismic activity should be related to a decrease of the  $p$  Omori exponent as the distance  $r$  from the mainshock increases ;
- the characteristic size of the cluster is expected to grow as  $R \sim t^H$ , with the diffusion exponent  $H$  positively correlated with the  $\theta$ -value.

We present the method of analysis of real sequences, and point out the problems of previous analysis of diffusion in real data. We present the results for several aftershock sequences in California and compare these results with the predictions of the ETAS model.

## 9.1 Limits of the analytical study

### One dimensional analysis.

We have derived analytical results for the one dimensional ETAS model, which is not realistic to describe real aftershock sequences. Real seismicity is localized on a fractal structure, intermediate between a two dimensional space (the fault plane of the mainshock) and a three dimensional space. However, the main characteristic of diffusion, the scaling of the characteristic size  $R$  with time as  $R \sim t^H$ , is correct in any dimension with the same expression for  $H$ . Other results concerning the full spatio-temporal distribution of aftershocks will be slightly dependent on the dimension of the model. In particular, we have performed numerical simulations of the ETAS model in 2 dimensions which give the same scaling  $R \sim t^H$ , and the same form of the spatio-temporal distribution (exponential distribution of distances  $r$  for  $\mu > 2$  and power-law distribution if  $\mu < 2$ ) but the value of the Omori exponent for  $r = 0$  depends on the dimension of the system. Moreover, the ETAS model does not take into account the spatial extension of an earthquake and its finite duration, but consider an earthquake as a point in space and time at the location of the hypocenter.

### The analytical solutions are correct only for $\alpha < b/2$ .

The essential assumption used in the analytical study is that the fluctuations of the earthquake magnitudes in a given sequence can be considered to be decoupled from those of the seismic rate. This approximation can be shown to be valid for  $\alpha \leq b/2$  [Helmstetter et al., 2002], for which the random variable  $\rho(m_i)$  has a finite variance. This regime is maybe not adapted to real aftershock sequences, as shown in chapter 2 where we have measured  $\alpha = 0.8$  for the southern California seismicity, using a superposed epoch analysis. For  $\alpha > b/2$ , the variance of  $\rho(m_i)$  is mathematically infinite or undefined as  $\rho(m_i)$  is distributed according to a power law with exponent  $b/\alpha < 2$ . In this case, an additional term must be included to account for the effect of the dependence between the fluctuations of earthquake magnitudes and the instantaneous seismic rate. For  $\alpha > b/2$ , we show in section 10 that the renormalization of the bare propagator into the dressed propagator is weaker than for  $\alpha \leq b/2$ , all the more so as  $\alpha \rightarrow b$ . Numerical simulations for  $\alpha > b/2$  show that our results presented in the previous section hold qualitatively but with a reduction of the observed spatial diffusion exponent compared to the value predicted from the master equation. Numerical simulations performed with  $\theta = 0.2$ ,  $n = 1$ ,  $b = 1$ ,  $\mu = 1$  and  $\alpha = 0.8$  yield an Omori exponent of the global sequence  $p = 1$  instead of  $p = 1 - \theta = 0.8$  predicted by the analytical solution of the master equation, and a diffusion exponent  $H = 0.11$  instead of the value  $H = 0.2$  expected for  $\alpha < b/2$ .

## Independence between the mainshock size and the aftershock cluster size.

Another limitation of our analytical approach is that we assume the distribution of distances between a mainshock and its aftershocks to be independent of the mainshock magnitude. However, it is a well established property of aftershock sequences [Utsu, 1961 ; Kagan, 2002] that the size of the aftershock area is proportional to the mainshock rupture length. This property can be included in the ETAS model, by assuming that the characteristic distance  $d$  of the mainshock-aftershock distance distribution (8.5) is proportional to the rupture length. This model can be studied using Monte-Carlo simulations of the ETAS model, but is much more difficult to study analytically than the decoupled model. Using numerical simulations of the coupled model, with  $d$  related to the magnitude  $M$  of the mainshock by  $d \sim 10^{0.5M}$ , we obtain a slower diffusion than in the decoupled model. The diffusion exponent of the coupled model is about half the exponent of the decoupled model at early times. The two models give similar results with the same diffusion exponent at large times, when the characteristic size  $R$  of the cluster is larger than the mainshock rupture length. The difference between the two models is more important for large mainshock magnitudes, because it takes more time for the aftershock cluster to reach a size larger than the mainshock length.

## 9.2 Method

The major problem when analyzing real seismicity data comes from the background seismicity. It can significantly alter the evaluation of the characteristic distance of the aftershock, even for a very small proportion of background events. To illustrate this problem, we analyze in Figure 9.1 a synthetic catalog generated by superposing an aftershock sequence with a constant seismicity background. The background seismicity induces an increase of the characteristic distance with time, that is very similar to a real diffusion when using limited time and space scales.

Marsan et al. [1999, 2000, 2001] have proposed a method to remove the influence of the background seismicity. A major difference between their analysis and this work is that they consider all pairs of events, independently of their magnitude. They study the average distance between all points as a function of the time between them. Therefore, there is no causal relation between the events they consider. In order to remove the influence of the uncorrelated seismicity, they use the global catalog to estimate the average distance between two points, and they remove the contribution of the average seismicity to estimate the spatio-temporal distribution of the correlated seismicity. The major assumption they make it to consider that the average seismicity is dominated by the uncorrelated seismicity. This assumption is however not reasonable for real seismicity which is dominated by the triggered seismicity (see section 7 for a discussion of the proportion of aftershocks in seismicity catalogs). Marsan et al. [1999, 2000, 2001] studied several catalogs at different scales, from the scale of a mine to the world-wide seismicity, and observed that the average distance between two earthquakes increases as a power-law of the time

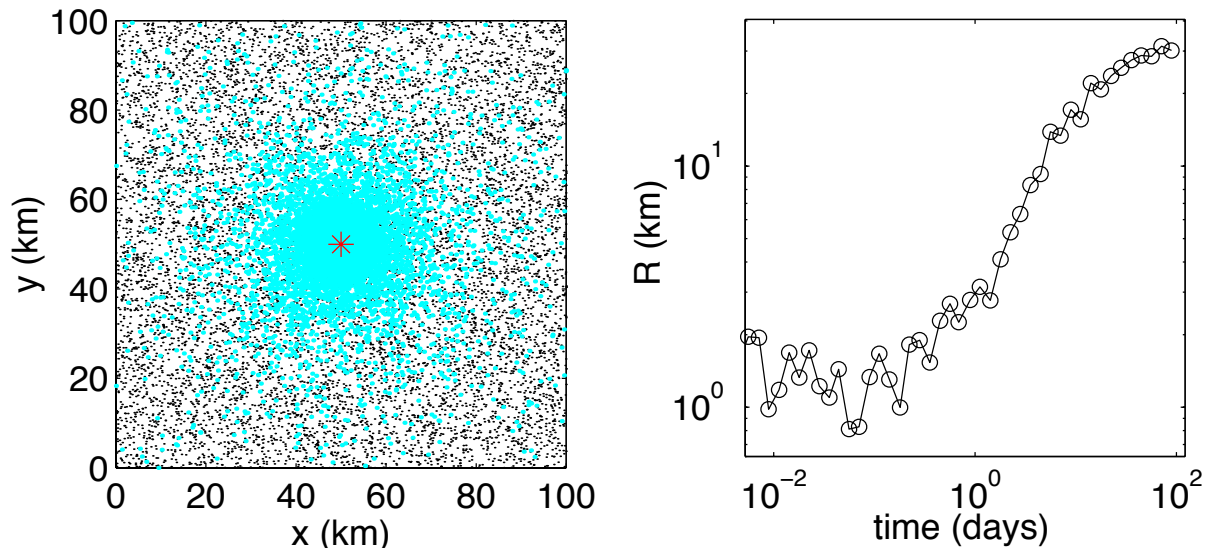


FIG. 9.1 – Analysis of a synthetic aftershock sequence. We have superposed a synthetic aftershock sequence with a uniform and constant seismicity background. This sequence has been generated without secondary aftershocks and without diffusion : all aftershocks are determined according to a power-law distribution of times with exponent  $p = 1$ . The spatial distribution of aftershocks is isotropic, with a power-law distribution of distances from the mainshock with an exponent  $\mu = 0.5$ . Panel (a) shows a map of seismicity with the background events shown as small black dots and the aftershocks shown as large gray dots. The mainshock is shown as a star at the center. Panel (b) shows the characteristic distance  $R$  of the cluster measured by  $R = \exp(\langle \log(r) \rangle)$  for a moving time window. The increase of  $R$  with time is due to the transition between the aftershock sequence at early times and the background seismicity at large times.

between them, with an exponent often close to 0.2, indicative of a sub-diffusion process. They interpreted their results as a mechanism of stress diffusion, that may be due to fluid transfer with heterogeneous permeability leading to sub-diffusion.

We believe that their results are strongly affected by the background seismicity. Because they do not take correctly into account the background seismicity, the diffusion they observe may reflect the transition between the correlated seismicity at early times and the uncorrelated seismicity at large times. As already discussed in the previous section, we have tested their method on synthetic catalogs and we found that their analysis can lead to spurious diffusion, and in some cases this method does not detect diffusion in synthetic data set with genuine diffusion. The spurious diffusion observed with their analysis is due to the background seismicity. The failure of their analysis to detect diffusion on synthetics catalogs generated with the ETAS model is due to their methods of estimation of the characteristic size between two events. They use the mean distance between all points, while the mean distance between two points was infinite in the catalog ( $\mu = 1$  in (8.5)). A more stable estimate of the characteristic distance

when using power-law distribution of distances is to use the exponential  $R = \exp(\langle \log(r) \rangle)$  of the mean of the logarithm of the distance, as done in this work, or the median of the distance distribution. When truncating the catalog at a maximum distance  $r_{max}$  as done in real data, their analysis detects a diffusion of aftershocks with a reasonable exponent, but their method displays much larger fluctuations than our method, and is very sensitive to the choice of  $r_{max}$ .

In this study, we analyze individual aftershock sequences, and we consider the diffusion of the seismicity triggered directly or indirectly by the mainshock. We adjust the values of the time  $T$  and the space  $D$  windows used to select aftershocks so that the rate of background activity is negligible in comparison with the aftershock rate. The background seismicity rate is estimated by the average seismicity before the mainshock. We also adjust the minimum magnitude  $m_0$  and the minimum time  $t_{min}$  used in the analysis in order to obtain a catalog that is complete for  $t_{min} < t < T$  and  $m > m_0$ . We estimate the average size of the aftershocks area as a function of the time from the mainshock in order to estimate the diffusion exponent  $H$ . We measure the Omori exponent by plotting the rate of activity as a function of time in a log-log plot, and by measuring the slope  $p$  by a linear regression for  $t_{min} < t < T$ . We have also used a maximum likelihood method to estimate both the Omori exponent  $p$  and the  $c$ -value in (3.1). In most cases, the two methods provide similar values of  $p$ . We also estimate the variation of  $p$  with the distance  $r$  between the mainshock and its aftershocks by selecting aftershocks at different distances between the mainshock. Another prediction of the ETAS model is the modification of the distribution of distances  $r$  with time. We plot the distribution of distances  $r$  between the mainshock and its aftershock for several time windows to test if there is an expansion of the aftershock area with time. We have tested this method using synthetic catalogs generated with the ETAS model, including a constant seismicity background. We have checked that our method provides a reliable estimate of the diffusion exponent and is almost not affected by the background activity.

### 9.3 Seismicity data

We study two different catalogs, (i) the catalog of Southern California seismicity provided by the Southern California Seismic Network for the period 1932-2000, and (ii) the catalog of Northern California seismicity provided by the Northern California Seismic Network since 1968. The minimum magnitude for completeness ranges from  $M = 4$  in 1932 to  $M < 2$  for the two catalogs since 1980. The average error on earthquake location is about 1 km for epicenters, but is larger for hypocenters. Therefore we consider only the spatial distribution of epicenters.

## 9.4 Results

We have analyzed 20 aftershock sequences of major earthquakes in California with a number of aftershocks larger than 500. The results for all sequences are listed in Table 9.1.

The results for the largest aftershock sequence following the 1992  $M = 7.3$  Landers event are shown in Figure 9.2. For this sequence we obtain an Omori exponent  $p = 1.1$ , which is stable

TAB. 9.1 – Analysis of aftershock sequences of California.  $M$  is the mainshock magnitude,  $T$  and  $R$  are the temporal and spatial windows used to select aftershocks,  $M_0$  is the minimum magnitude of aftershocks,  $p$  is the Omori exponent measured for  $t_{min} < t < T$ ,  $N$  is the number of aftershocks,  $H$  is the diffusion exponent,  $p_1$  and  $p_2$  are the Omori exponent measured for small distance and larges distances respectively.

earthquake	date	$M$	$T$	$R$	$M_0$	$t_{min}$	$N$	$p$	$H$	$p_1$	$p_2$
	dd/mm/yy		days	km		days					
Kern-County	21/07/52	7.5	5478	70	2.5	300	1300	1.12	0.04	1.25	1.13
	01/08/75	5.7	1826	15	2.0	1.0	785	1.09	-0.00	1.13	1.09
Imperial Valley	15/10/79	6.4	36	80	2.5	0.2	677	1.44	-0.04	0.71	1.58
Westmorland	26/04/81	5.7	73	20	1.7	0.2	587	1.41	0.15	2.30	0.82
Coalinga	02/05/83	6.7	1826	22	2.0	1.0	3133	1.03	0.03	1.12	0.94
Morgan-Hill	24/04/84	6.2	182	30	1.5	1.0	633	0.59	0.00	0.61	0.74
Round-Valley	23/11/84	6.1	182	15	2.0	0.1	1398	0.93	0.04	0.95	0.89
North Palm Springs	8/07/86	5.6	365	15	1.5	1.0	2331	1.11	0.05	1.19	0.92
Oceanside	13/07/86	5.4	3650	20	2.0	0.5	1926	0.80	0.03	0.88	0.69
Chalfant Valley	21/07/86	6.4	1826	20	2.0	1.0	2985	1.16	0.03	1.12	0.98
Superstition-Hill	24/11/87	6.6	18	50	1.8	0.4	794	1.22	0.11	1.47	0.90
Loma-Prieta	18/10/89	7.0	36	50	2.0	0.1	728	1.06	0.06	1.09	0.69
Joshua-Tree	23/04/92	6.1	36	30	1.6	3.0	3658	1.11	0.11	1.20	0.73
Cape Mendocino	25/04/92	6.5	36	70	2.0	0.6	1197	1.20	-0.04	1.11	1.31
Landers	28/06/92	7.3	365	60	2.2	3.0	7278	1.09	0.00	1.07	1.02
Big Pine	17/05/93	6.2	365	25	1.5	2.0	780	1.25	0.02	1.29	1.31
Northridge	17/01/94	6.7	1826	30	2.0	2.0	3254	1.13	0.01	1.11	0.97
Nevada	12/09/94	5.5	365	25	2.5	5.0	502	1.10	-0.03	0.90	0.97
	15/05/99	5.6	735	10	1.5	0.2	1570	0.85	0.05	1.05	0.78
Hector-Mine	16/10/99	7.1	1826	35	2.5	1.0	1812	1.14	0.01	1.18	1.13

when looking at different distances  $r$ . The characteristic cluster size is also stable over more than two orders of magnitude in time ( $H \approx 0$ ). The analysis of the distance distribution at different times also confirms that there is no diffusion of seismic activity. This sequence is interpreted according to our results as belonging to the sub-critical regime  $n < 1$  with  $t > t^*$ . Therefore, the results are in agreement with the predictions of the ETAS model that no diffusion should be observed if the Omori exponent is larger than 1. Many other sequences yield results similar to the Landers sequence, with  $p > 1$  and almost no diffusion ( $H \approx 0$ ) (see Table 9.1).

A few aftershock sequences are characterized by a small  $p < 1$  exponent, but do not show a significant diffusion ( $H < 0.05$ ), in disagreement with our analysis of the ETAS model. For example, the aftershock sequence of the  $M = 5.4$  July 13, 1986 Oceanside earthquake has a low  $p = 0.8$  Omori exponent, which decreases as a function of the distance from the mainshock, but the diffusion exponent  $H = 0.03$  is much smaller than expected by the theory (see Figure 9.3). A global  $p$ -value of 0.8 implies that the  $\theta$ -value is equal to or larger than 0.2. Therefore, the diffusion exponent should not be smaller than  $H = 0.1$  from our results (see Figure 8.10). However, these are several limitations of the analytical study discussed previously that may explain the  $H$ -value smaller than expected. Both the fact that  $\alpha > b/2$  and the dependence of the aftershock area with the mainshock magnitude tend to decrease the diffusion exponent by comparison to the analytical predictions based on the master equation (8.12).

In contrast with our predictions, the largest value of the diffusion exponent  $H = 0.15$  (see Table 9.1 and Figure 9.4) is obtained for the April 26, 1981 Westmorland earthquake which has the largest value of the Omori exponent  $p = 1.4$ . For this sequence, we clearly see an expansion of the aftershock area when comparing the distance distribution at different times, and a decrease of  $p$  with  $r$ . A significant diffusion exponent  $H > 0$  with  $p > 1$  may be observed in the ETAS model in the crossover regime for  $t \approx t^*$  where  $p$  is already larger than 1, but where a diffusion of seismic activity is still observed. Indeed, when looking at numerical aftershock sequences in the sub-critical regime, a diffusion of seismic activity persists up to  $t \approx 100 t^*$  even if the Omori exponent is larger 1. But the diffusion exponent in the crossover regime for  $t \approx t^*$  should be smaller than in the early time  $t < t^*$  regime when  $p$  is smaller than 1.

Figure 9.5 summarizes the results for  $p$  and  $H$  listed in Table 9.1. All values of the diffusion exponent  $H$  are very small when compared to previous studies [Marsan et al., 1999, 2000 ; Marsan and Bean, 2001]. This suggests that their results were affected by the background seismic activity, and were not due to a real diffusion process. We do not obtain a negative correlation between the diffusion exponent and the Omori exponent, as expected by the theory.

## 9.5 Conclusion

We have analyzed 20 aftershock sequences of California and we found that the diffusion of seismic activity is very weak, when compared to previous studies. The finding that most

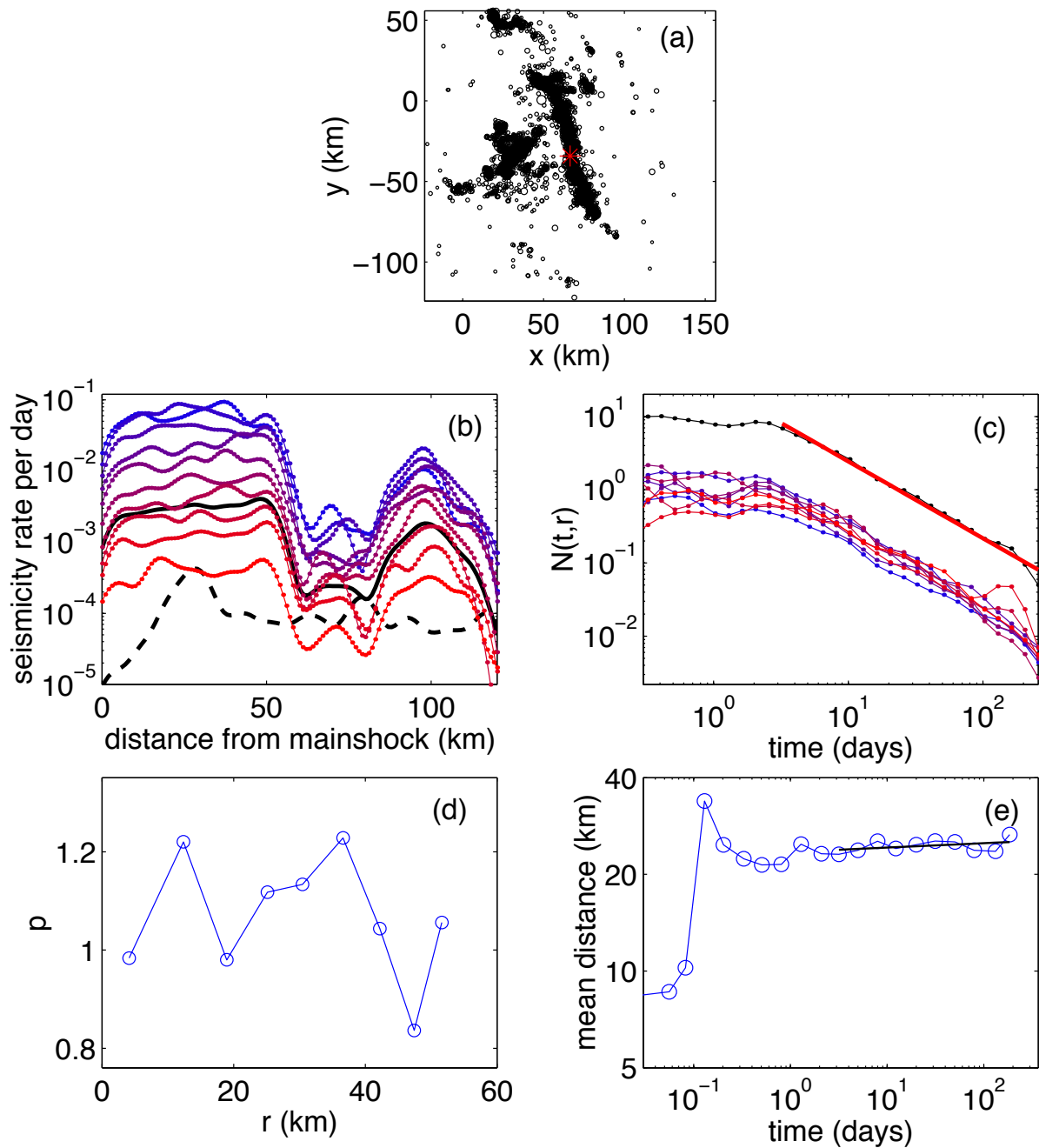


FIG. 9.2 – Analysis of the June, 28, 1992,  $M = 7.3$  Landers aftershock sequence. (a) map of aftershocks, the mainshock is shown by a star; (b) rate of seismic activity as a function of the distance from the mainshock for different times after the mainshock (increasing time from top to bottom (blue to red)). The background activity preceding the mainshock is shown as a dashed line. The whole aftershock sequence is shown as a solid black line; (c) rate of aftershocks for the whole sequence (black line at the top), and for different distances from the mainshock (increasing distance from blue to red); (d) variation of the Omori exponent with the distance from the mainshock; (e) characteristic size of the aftershock cluster as a function of the time from the mainshock.

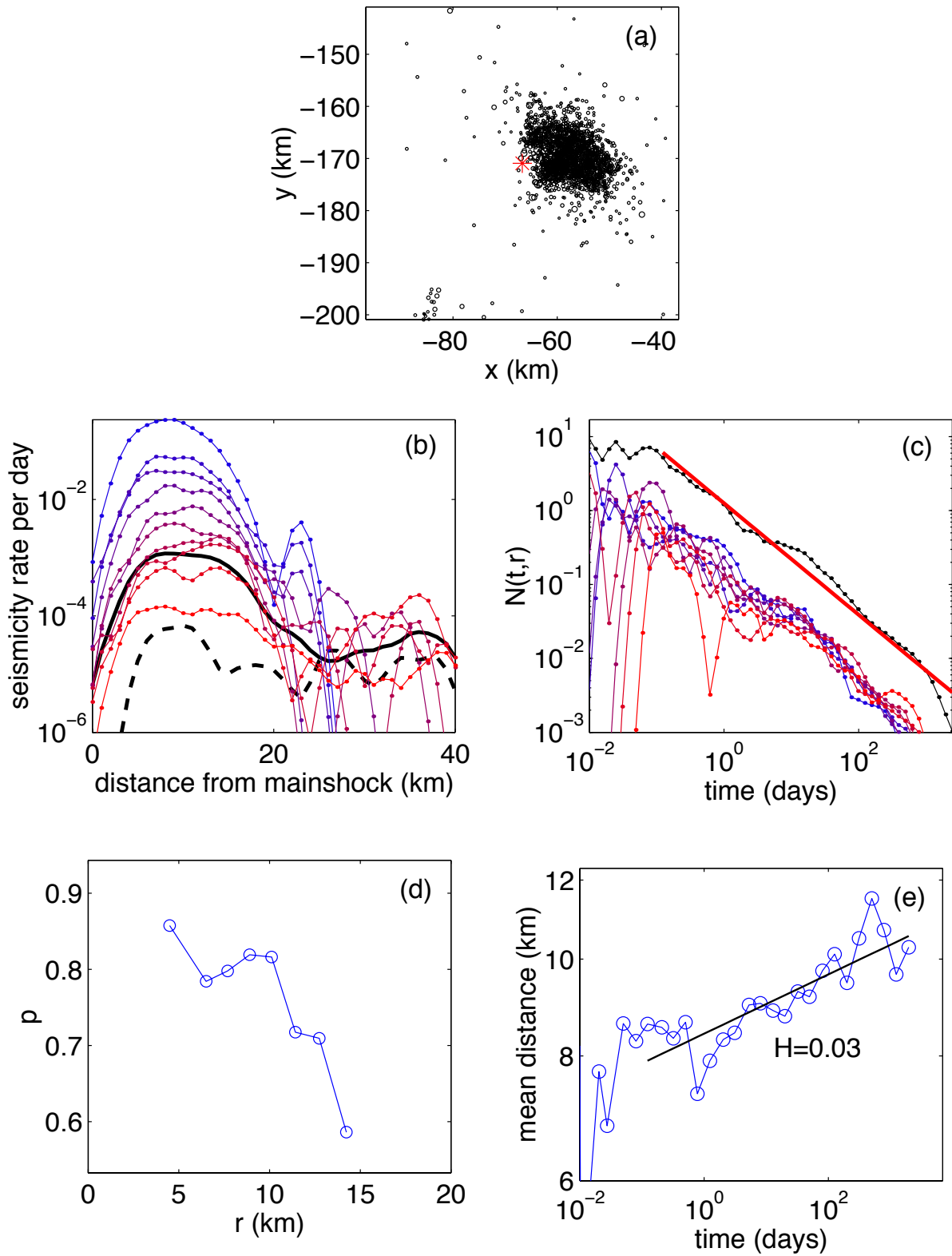


FIG. 9.3 – Analysis of the July 13, 1986,  $M = 5.4$  Oceanside earthquake. Same legend as in Figure 9.2.

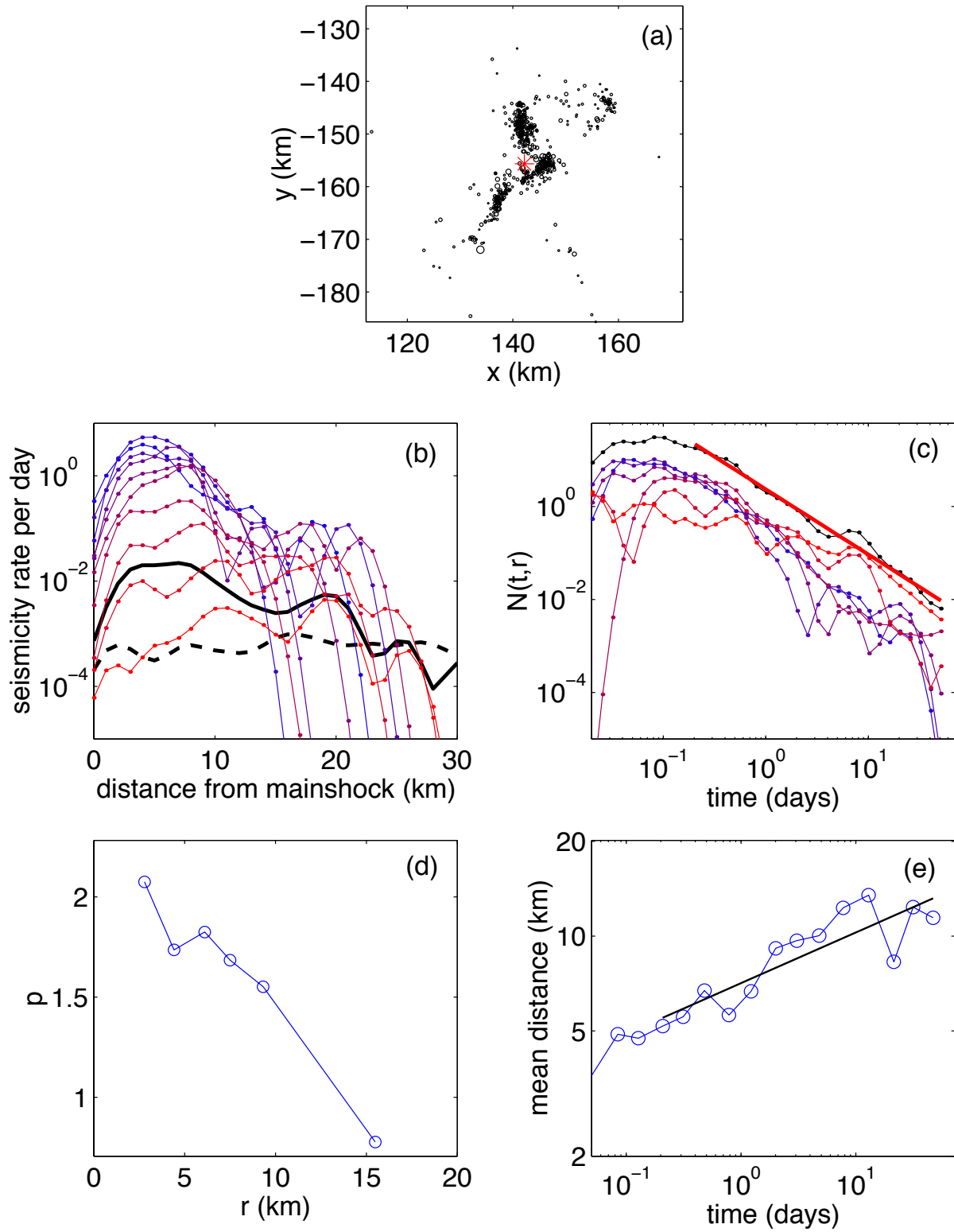


FIG. 9.4 – Analysis of the April 26, 1981,  $M = 5.7$  Westmorland earthquake. Same legend as in Figure 9.2.

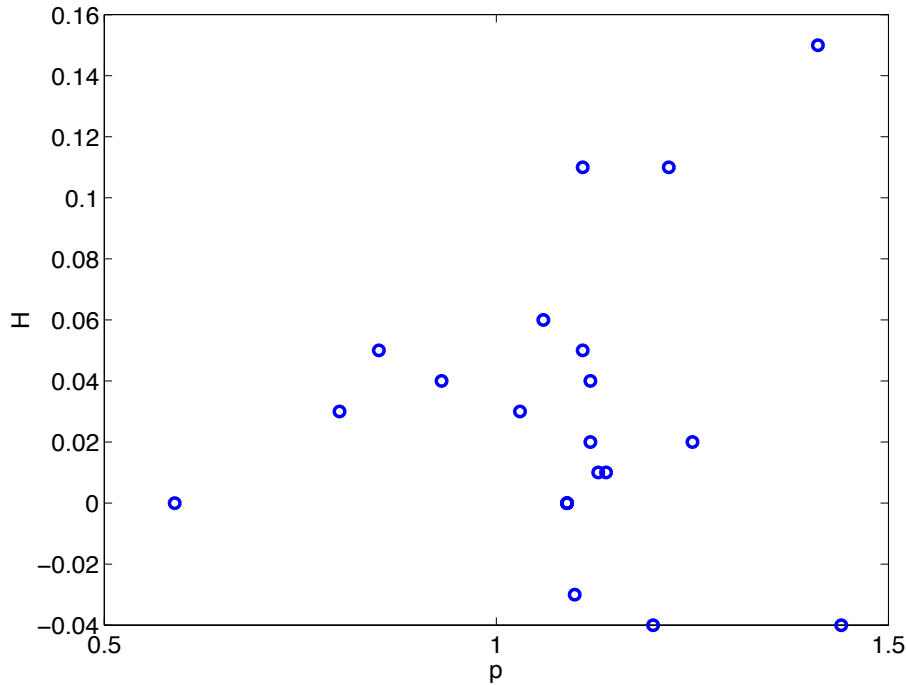


FIG. 9.5 – Diffusion exponent  $H$  as a function of the Omori exponent  $p$  for the aftershock sequences described in Table 9.1.

aftershock sequences do not diffuse, but that a few other sequences display a significant diffusion, suggests that the diffusion of seismic activity is not due to a mechanism of stress transfer as suggested previously [Noir et al., 1997; Marsan et al., 1999; Marsan et al., 2000; Marsan and Bean, 2001], but can be explained by the cascade of secondary aftershocks. This process is very sensitive to small changes in the parameters of the seismic activity such as the branching ratio  $n$  and the local Omori exponent  $\theta$ . This variability of  $n$  and  $\theta$  may thus explain the variability of the diffusion exponent from one sequence to another one. The expected variability of the diffusion exponent with the Omori exponent (see Figure 9.5) is however not in agreement with the observations : some aftershock sequences with  $p < 1$  do not show a significant diffusion, as expected by the theory, while a sequence with a very high  $p$ -value of 1.4 displays a large value of the diffusion exponent equal to 0.15. These discrepancies between the theory and the observations may be due to the small number of events available in each sequence, which can induce high statistical fluctuations of the measured diffusion exponent. The estimation of  $H$  is also difficult due to the limited range of time and space scales available, by comparison to the synthetic data studied in chapter 8. The presence of background activity may also significantly bias the estimation of  $H$ . Moreover, we have assumed in the ETAS model that the mainshock can be represented by a point. This is obviously incorrect at small distances from the mainshock epicenter by comparison with the mainshock rupture length. But the results at large distances from the mainshock epicenter should be in agreement with the ETAS model. If there was a significant diffusion of aftershock with time, we should observe an expansion of the aftershock

area, which should be much larger than the mainshock rupture length at large times after the mainshock. This is not what we observe in the aftershock sequences studied here, except maybe for the Westmorland sequence which shows a significant expansion of the aftershock area with time. For most sequences, the spatial distribution of aftershocks is mostly limited to the mainshock rupture area. The rate of aftershocks is very small at distances larger than the rupture length, even at large times after the mainshock.

# Chapitre 10

## Mainshocks are aftershocks of conditional foreshocks : how do foreshock statistical properties emerge from aftershock laws

Agnès Helmstetter<sup>1</sup>, Didier Sornette<sup>2</sup> and Jean-Robert Grasso<sup>1</sup>

<sup>1</sup> Laboratoire de Géophysique Interne et Tectonophysique, Université Joseph Fourier, BP 53X, 38041 Grenoble Cedex, France.

<sup>2</sup> Laboratoire de Physique de la Matière Condensée, Université de Nice-Sophia Antipolis, and Department of Earth and Space Sciences and Institute of Geophysics and Planetary Physics, University of California, Los Angeles, California.

In press in *Journal of Geophysical Research*, 2002.

### Abstract

The inverse Omori law for foreshocks discovered in the 1970s states that the rate of earthquakes prior to a mainshock increases on average as a power law  $\propto 1/(t_c - t)^{p'}$  of the time to the mainshock occurring at  $t_c$ . Here, we show that this law results from the direct Omori law for aftershocks describing the power law decay  $\sim 1/(t - t_c)^p$  of seismicity after an earthquake, provided that any earthquake can trigger its suit of aftershocks. In this picture, the seismic activity at any time is the sum of the spontaneous tectonic loading and of the activity triggered by all preceding events weighted by their corresponding Omori law. The inverse Omori law then emerges as the

expected (in a statistical sense) trajectory of seismicity, conditioned on the fact that it leads to the burst of seismic activity accompanying the mainshock. In particular, we predict and verify by numerical simulations on the Epidemic-Type Aftershock Sequence (ETAS) model that  $p'$  is always smaller than or equal to  $p$  and a function of  $p$ , of the  $b$ -value of the Gutenberg-Richter law (GR) and of a parameter quantifying the number of direct aftershocks as a function of the magnitude of the mainshock. The often documented apparent decrease of the  $b$ -value of the GR law at the approach to the main shock results straightforwardly from the conditioning of the path of seismic activity culminating at the mainshock. However, we predict that the GR law is not modified simply by a change of  $b$ -value but that a more accurate statement is that the GR law gets an additive (or deviatoric) power law contribution with exponent smaller than  $b$  and with an amplitude growing as a power law of the time to the mainshock. In the space domain, we predict that the phenomenon of aftershock diffusion must have its mirror process reflected into an inward migration of foreshocks towards the mainshock. Using this model, we show that foreshock sequences are special aftershock sequences which are modified by the condition to end up in a burst of seismicity associated with the mainshock. Foreshocks are not just statistical creatures, they are genuine forerunners of large shocks as shown by the large prediction gains obtained using several of their qualifiers.

## 10.1 Introduction

Large shallow earthquakes are always followed by an increase in seismic activity, defined as an aftershock sequence. It is also well-known that large earthquakes are sometimes preceded by an unusually large activity rate, defined as a foreshock sequence. Omori law describing the power law decay  $\sim 1/(t - t_c)^p$  of aftershock rate with time from a mainshock that occurred at  $t_c$  has been proposed more than one century ago [*Omori*, 1894], and has since been verified by many studies [*Kagan and Knopoff*, 1978; *Davis and Frohlich*, 1991; *Kisslinger and Jones*, 1991; *Utsu et al.*, 1995]. See however [*Kisslinger*, 1993; *Gross and Kisslinger*, 1994] for alternative decay laws such as the stretched exponential and its possible explanation [*Helmstetter and Sornette*, 2002a].

Whereas the Omori law describing the aftershock decay rate is one of the few well-established empirical laws in seismology, the increase of foreshock rate before an earthquake does not follow such a well-defined empirical law. There are huge fluctuations of the foreshock seismicity rate, if any, from one sequence of earthquakes to another one preceding a mainshock. Moreover, the number of foreshocks per mainshock is usually quite smaller than the number of aftershocks. It is thus essentially impossible to establish a deterministic empirical law that describes the intermittent increase of seismic activity prior to a mainshock when looking at a single foreshock sequence which contains at best a few events. Although well-developed individual foreshock sequences are rare and mostly irregular, a well-defined acceleration of foreshock rate prior to a

mainshock emerges when using a superposed epoch analysis, in other words, by synchronizing several foreshock sequences to a common origin of time defined as the time of their mainshocks and by stacking these synchronized foreshock sequences. In this case, the acceleration of the seismicity preceding the mainshock clearly follows an inverse Omori law of the form  $N(t) \sim 1/(t_c - t)^{p'}$ , where  $t_c$  is the time of the mainshock. This law has been first proposed by *Papazachos* [1973], and has been established more firmly by [*Kagan and Knopoff*, 1978; *Jones and Molnar*, 1979].

A clear identification of foreshocks, aftershocks and mainshocks is hindered by the difficulties in associating an unambiguous and unique space-time-magnitude domain to any earthquake sequence. Identifying aftershocks and foreshocks requires the definition of a space-time window. All events in the same space-time domain define a sequence. The largest earthquake in the sequence is called the mainshock. The following events are identified as aftershocks, and the preceding events are called foreshocks.

Large aftershocks show the existence of secondary aftershock activities, that is, the fact that aftershocks may have their own aftershocks, such as the  $M = 6.5$  Big Bear event, which is considered as an aftershock of the  $M = 7.2$  Landers Californian earthquake, and which clearly triggered its own aftershocks. Of course, aftershocks of aftershocks can be clearly identified without further insight and analysis as obvious bursts of transient seismic activity above the background seismicity level, only for the largest aftershocks. But because aftershocks exist on all scales, from the laboratory scale e.g. [*Mogi*, 1967; *Scholz*, 1968], to the worldwide seismicity, we may expect that all earthquakes, whatever their magnitude, trigger their own aftershocks, but with a rate increasing with the mainshock magnitude, so that only aftershocks of the largest earthquakes are identifiable unambiguously.

The properties of aftershock and foreshock sequences depend on the choice of these space-time windows, and on the specific definition of foreshocks [e.g. *Ogata et al.*, 1996], which can sometimes be rather arbitrary. In the sequel, we shall consider two definitions of foreshocks for a given space and time window :

1. we shall call “foreshock” of type I any event of magnitude smaller than or equal to the magnitude of the following event, then identified as a “main shock”. This definition implies the choice of a space-time window  $R, T$  used to define both foreshocks and mainshocks. Mainshocks are large earthquakes that were not preceded by a larger event in this space-time window. The same window is used to select foreshocks before mainshocks ;
2. we shall also consider “foreshock” of type II, as any earthquake preceding a large earthquake, independently of the relative magnitude of the foreshock compared to that of the mainshock. This second definition will thus incorporate seismic sequences in which a foreshock could have a magnitude larger than the mainshock, a situation which can alternatively be interpreted as a mainshock followed by a large aftershock.

The advantage of this second definition is that foreshocks of type II are automatically defined

as soon as one has identified the mainshocks, for instance, by calling mainshocks all events of magnitudes larger than some threshold of interest which can be 6, 7 or 8. Foreshocks of type II are thus all events preceding these large magnitude mainshocks. In contrast, foreshocks of type I need to obey a constraint on their magnitude, which may be artificial, as suggested from the previous discussion. All studies published in the literature deal with foreshocks of type I. Using a very simple model of seismicity, the so-called ETAS (epidemic-type aftershock) model, we shall show that the definition of foreshocks of type II is also quite meaningful and provides new insights for classifying earthquake phenomenology and understanding earthquake clustering in time and space.

The exponent  $p'$  of the inverse Omori law is usually found to be smaller than or close to 1 [Papazachos *et al.*, 1967; Papazachos *et al.*, 1975b; Kagan and Knopoff, 1978; Jones and Molnar, 1979; Davis and Frohlich, 1991; Shaw, 1993; Ogata *et al.*, 1995; Maeda, 1999; Reasenberg, 1999], and is always found smaller than or equal to the direct Omori exponent  $p$  when the 2 exponents  $p$  and  $p'$  are measured simultaneously on the same mainshocks [Kagan and Knopoff, 1978; Davis and Frohlich, 1991; Shaw, 1993; Maeda, 1999; Reasenberg, 1999]. Shaw [1993] suggested in a peculiar case the relationship  $p' = 2p - 1$ , based on a clever but slightly incorrect reasoning (see below). We shall recover below this relationship only in a certain regime of the ETAS model from an exact treatment of the foreshocks of type II within the framework of the ETAS model.

Other studies tried to fit a power law increase of seismicity to individual foreshock sequences. Rather than the number of foreshocks, these studies usually fit the cumulative Benioff strain release  $\epsilon$  by a power-law  $\epsilon(t) = \epsilon_c - B(t_c - t)^z$  with an exponent  $z$  that is often found close to 0.3 (see [Jaumé and Sykes, 1999; Sammis and Sornette, 2002] for reviews). Assuming a constant Gutenberg Richter  $b$ -value through time, so that the acceleration of the cumulative Benioff strain before the mainshock is due only to the increase in the seismicity rate, this would argue for a  $p'$ -value close to 0.7. These studies were often motivated by the critical point theory [Sornette and Sammis, 1995], which predicts a power-law increase of seismic activity before major earthquakes (see e.g. [Sammis and Sornette, 2002] for a review). However, the statistical significance of such a power-acceleration of energy before individual mainshock is still controversial [Zöller and Hainzl, 2002].

The frequency-size distribution of foreshocks has also been observed either to be different from that of aftershocks,  $b' < b$ , e.g. [Suyehiro, 1966; Papazachos *et al.*, 1967; Ikegami, 1967; Berg, 1968], or to change as the mainshock is approached. This change of magnitude distribution is often interpreted as a decrease of  $b$ -value, first reported by [Kagan and Knopoff, 1978; Li *et al.*, 1978; Wu *et al.*, 1978]. Others studies suggest that the modification of the magnitude distribution is due only to moderate or large events, whereas the distribution of small magnitude events is not modified [Rotwain *et al.*, 1997; Jaumé and Sykes, 1999]. Knopoff *et al.* [1982] state that only in the rare cases of catalogs of great length, statistically significant smaller  $b$ -value for foreshocks than for aftershocks are found. Nevertheless they believe the effect is likely to be real

in most catalogs, but at a very low level of difference.

On the theoretical front, there have been several models developed to account for foreshocks. Because foreshocks are rare and seem the forerunners of large events, a natural approach is to search for physical mechanisms that may explain their specificity. And, if there is a specificity, this might lead to the use of foreshocks as precursory patterns for earthquake prediction. Foreshocks may result from a slow sub-critical weakening by stress corrosion [Yamashita and Knopoff, 1989, 1992; Shaw, 1993] or from a general damage process [Sornette *et al.*, 1992]. The same mechanism can also reproduce aftershock behavior [Yamashita and Knopoff, 1987; Shaw, 1993]. Foreshocks and aftershocks may result also from the dynamics of stress distribution on pre-existing hierarchical structures of faults or tectonic blocks [Huang *et al.*, 1998; Gabrielov *et al.*, 2000a,b; Narteau *et al.*, 2000], when assuming that the scale over which stress redistribution occurs is controlled by the level of the hierarchy (cell size in a hierarchical cellular automaton model). Dodge *et al.* [1996] argue that foreshocks are a byproduct of an aseismic nucleation process of a mainshock. Other possible mechanisms for both aftershocks and foreshocks are based on the visco-elastic response of the crust and on delayed transfer of fluids in and out of fault structures [Hainzl *et al.*, 1999; Pelletier, 2000].

Therefore, most of these models suggests a link between aftershocks and foreshocks. In the present work, we explore this question further by asking the following question : is it possible to derive most if not all of the observed phenomenology of foreshocks from the knowledge of only the most basic and robust facts of earthquake phenomenology, namely the Gutenberg-Richter and Omori laws ? To address this question, we use what is maybe the simplest statistical model of seismicity, the so-called ETAS (epidemic-type aftershock) model, based only on the Gutenberg-Richter and Omori laws. This model assumes that each earthquake can trigger aftershocks, with a rate increasing as a power law  $E^a$  with the mainshock energy  $E$ , and which decays with the time from the mainshock according to the “local” Omori law  $\sim 1/(t - t_c)^{1+\theta}$ , with  $\theta \geq 0$ . We stress that the exponent  $1 + \theta$  is in general different from the observable  $p$ -value, as we shall explain below. In this model, the seismicity rate is the result of the whole cascade of direct and secondary aftershocks, that is, aftershocks of aftershocks, aftershocks of aftershocks of aftershocks, and so on.

In two previous studies of this model, we have analyzed the super-critical regime [Helmstetter and Sornette, 2002a] and the singular regime [Sornette and Helmstetter, 2002] of the ETAS model and have shown that these regimes can produce respectively an exponential or a power law acceleration of the seismicity rate. These results can reproduce an individual accelerating foreshock sequence, but they cannot model the stationary seismicity with alternative increasing and decreasing seismicity rate before and after a large earthquake. In this study, we analyze the stationary sub-critical regime of this branching model and we show that foreshock sequences are special aftershock sequences which are modified by the condition to end up in a burst of seismicity associated with the mainshock. Using only the physics of aftershocks, all the foreshock

phenomenology is derived analytically and verified accurately by our numerical simulations. This is related to but fundamentally different from the proposal by *Jones et al.* [1999] that foreshocks are mainshocks whose aftershocks happen to be big.

Our analytical and numerical investigation of the ETAS model reveals many of the properties of real foreshocks sequences.

- The rate of foreshocks increases before the mainshock according to the inverse Omori law  $N(t) \sim 1/(t_c - t)^{p'}$  with an exponent  $p'$  smaller than the exponent  $p$  of the direct Omori law. The exponent  $p'$  depends on the local Omori exponent  $1 + \theta$ , on the exponent  $\beta$  of the energy distribution, and on the exponent  $a$  which describes the increase in the number of aftershocks with the mainshock energy. In contrast with the direct Omori law, which is clearly observed after all large earthquakes, the inverse Omori law is a statistical law, which is observed only when stacking many foreshock sequences.
- While the number of aftershocks increases as the power  $E^a$  of the mainshock energy  $E$ , the number of foreshocks of type II is independent of  $E$ . Thus, the seismicity increases on average according to the inverse Omori law before any earthquake, whatever its magnitude. For foreshocks of type I, the same results hold for large mainshocks while the conditioning on foreshocks of type I to be smaller than their mainshock makes their number increase with  $E$  for small and intermediate values of the mainshock size.
- Conditioned on the fact that a foreshock sequence leads to a burst of seismic activity accompanying the mainshock, we find that the foreshock energy distribution is modified upon the approach of the mainshock, and develops a bump in its tail. This result may explain both the often reported decrease in measured  $b$ -value before large earthquakes and the smaller  $b$ -value obtained for foreshocks compared with other earthquakes.
- The modification of the Gutenberg-Richter distribution for foreshocks is shown analytically to take the shape of an additive correction to the standard power law, in which the new term is another power law with exponent  $\beta - a$ . The amplitude of this additive power law term also exhibits a kind of inverse Omori law acceleration upon the approach to the mainshock, with a different exponent. These predictions are accurately substantiated by our numerical simulations.
- When looking at the spatial distribution of foreshocks, we find that the foreshocks migrate towards the mainshock as the time increases. This migration is driven by the same mechanism underlying the aftershock diffusion [*Helmstetter and Sornette, 2002b*].

Our presentation is organized as follows. In the next section, we define the ETAS model, recall how the average rate of seismicity can be obtained formally from a Master equation and describe how to deal with fluctuations decorating the average rate. Section 10.3 provides the full derivation of the inverse Omori law, first starting with an intuitive presentation followed by a more technical description. Section 10.4 contains the derivation of the modification of the distribution of foreshock energies. Section 10.5 describes the migration of foreshock activity.

Section 10.6 is a discussion of how our analytical and numerical results allows us to rationalize previous empirical observations. In particular, we show that foreshocks are not just statistical creatures but are genuine forerunners of large shocks that can be used to obtain significant prediction gains. Section 10.7 concludes.

## 10.2 Definition of the ETAS model and its master equation for the renormalized Omori law

### Definitions

The ETAS model was introduced by *Kagan and Knopoff* [1981, 1987] and *Ogata* [1988] to describe the temporal and spatial clustering of seismicity and has since been used by many other workers with success to describe real seismicity. Its value stems from the remarkable simplicity of its premises and the small number of assumptions.

Contrary to the usual definition of aftershocks, the ETAS model does not impose an aftershock to have an energy smaller than the mainshock. This way, the same underlying physical mechanism is assumed to describe both foreshocks, aftershocks and mainshocks. The abandon of the ingrained concept (in many seismologists' mind) of the distinction between foreshocks, aftershocks and mainshocks is an important step towards a simplification and towards an understanding of the mechanism underlying earthquake sequences. Ultimately, this parsimonious assumption will be validated or falsified by the comparison of its prediction with empirical data. In particular, the deviations from the predictions derived from this assumption will provide guidelines to enrich the physics.

In order to avoid problems arising from divergences associated with the proliferation of small earthquakes, the ETAS model assumes the existence of a magnitude cut-off  $m_0$ , or equivalently an energy cut-off  $E_0$ , such that only earthquakes of magnitude  $m \geq m_0$  are allowed to give birth to aftershocks larger than  $m_0$ , while events of smaller magnitudes are lost for the epidemic dynamics. We refer to [*Helmstetter and Sornette*, 2002a] for a justification of this hypothesis and a discussion of ways to improve this description.

The ETAS model assumes that the seismicity rate (or “bare Omori propagator”) at a time between  $t$  and  $t + dt$ , resulting in direct “lineage” (without intermediate events) from an earthquake  $i$  that occurred at time  $t_i$ , is given by

$$\phi_{E_i}(t - t_i) = \rho(E_i) \Psi(t - t_i) , \quad (10.1)$$

where  $\Psi(t)$  is the normalized waiting time distribution (that we shall take later given by (10.4) and  $\rho(E_i)$  is defined by

$$\rho(E_i) = k (E_i/E_0)^a \quad (10.2)$$

gives the average number of daughters born from a mother with energy  $E_i \geq E_0$ . This term

$\rho(E_i)$  accounts for the fact that large mothers have many more daughters than small mothers because the larger spatial extension of their rupture triggers a larger domain. Expression (10.2) results in a natural way from the assumption that aftershocks are events influenced by stress transfer mechanisms extending over a space domain proportional to the size of the mainshock rupture [Helmstetter, 2002]. Indeed, using the well-established scaling law relating the size of rupture and the domain extension of aftershocks [Kagan, 2002] to the release energy (or seismic moment), and assuming a uniform spatial distribution of aftershocks in their domain, expression (10.2) immediately follows (it still holds if the density of aftershocks is slowly varying or power law decaying with the distance from the mainshock).

The value of the exponent  $a$  controls the nature of the seismic activity, that is, the relative role of small compared to large earthquakes. Few studies have measured  $a$  in seismicity data [Yamanaka and Shimazaki, 1990; Guo and Ogata, 1997; Helmstetter, 2002]. This parameter  $a$  is often found close to the  $\beta$  exponent of the energy distribution [e.g., Yamanaka and K. Shimazaki, 1990] or fixed arbitrarily equal to  $\beta$  [e.g., Kagan and Knopoff, 1987; Reasenberg and Jones, 1989; Felzer et al., 2001]. For a large range of mainshock magnitudes and using a more sophisticated scaling approach, Helmstetter [2002] found  $a = 0.8\beta$  for the Southern California seismicity. If  $a < \beta$ , small earthquakes, taken together, trigger more aftershocks than larger earthquakes. In contrast, large earthquakes dominate earthquake triggering if  $a \geq \beta$ . This case  $a \geq \beta$  has been studied analytically in the framework of the ETAS model by Sornette and Helmstetter [2002] and has been shown to eventually lead to a finite time singularity of the seismicity rate. Previous studies performed in this regime  $a \geq \beta$  have not found this result because of their focus on limited time series restricted to end prior to the predicted singularity. This explosive regime cannot however describe a stationary seismic activity. In this paper, we will therefore consider only the case  $a < \beta$ .

An additional space-dependence can be added to  $\phi_{E_i}(t - t_i)$  [Helmstetter and Sornette, 2002b]: when integrated over all space, the prediction of the space-time model retrieves those of the pure time-dependent model. Since we are interested in the inverse Omori law for foreshocks, which is a statement describing only the time-dependence, it is sufficient to use the time-only version of the ETAS model for the theory.

The model is complemented by the Gutenberg-Richter law which states that each aftershock  $i$  has an energy  $E_i \geq E_0$  chosen according to the density distribution

$$P(E) = \frac{\beta E_0^\beta}{E^{1+\beta}}, \quad \text{with } \beta \simeq 2/3. \quad (10.3)$$

$P(E)$  is normalized  $\int_{E_0}^{\infty} dE P(E) = 1$ .

In view of the empirical observations that the observed rate of aftershocks decays as a power law of the time since the mainshock, it is natural to choose the “bare” modified Omori law (or the normalized waiting time distribution between events)  $\Psi(t - t_i)$  in (10.1) also as a power law

$$\Psi(t - t_i) = \frac{\theta c^\theta}{(t - t_i + c)^{1+\theta}}. \quad (10.4)$$

$\Psi(t - t_i)$  is the rate of daughters of the first generation born at time  $t - t_i$  from the mother-mainshock. Here,  $c$  provides an “ultra-violet” cut-off which ensures the finiteness of the number of aftershocks at early times. It is important to recognize that the observed aftershock decay rate may be different from  $\Psi(t - t_i)$  due to the effect of aftershocks of aftershocks, and so on [Sornette and Sornette, 1999a; Helmstetter and Sornette, 2002a]

The ETAS model is a “branching” point-process [Harris, 1963; Daley and Vere-Jones, 1988] controlled by the key parameter  $n$  defined as the average number (or “branching ratio”) of daughter-earthquakes created per mother-event, summed over all times and averaged over all possible energies. This branching ratio  $n$  converges to a finite value for  $\theta > 0$  and for  $a < \beta$  for which it is equal to

$$n \equiv \int_0^\infty dt \int_{E_0}^\infty dE P(E) \phi_E(t) = \frac{k\beta}{\beta - a}. \quad (10.5)$$

The normal regime corresponds to the subcritical case  $n < 1$  for which the seismicity rate decays after a mainshock to a constant background (in the case of a steady-state source) decorated by fluctuations in the seismic rate.

The total rate of seismicity  $\lambda(t)$  at time  $t$  is given by

$$\lambda(t) = s(t) + \sum_{i | t_i \leq t} \phi_{E_i}(t - t_i) \quad (10.6)$$

where  $\phi_{E_i}(t - t_i)$  is defined by (10.1). The sum  $\sum_{i | t_i \leq t}$  is performed over all events that occurred at time  $t_i \leq t$ , where  $E_i$  is the energy of the earthquake that occurred at  $t_i$ .  $s(t)$  is a stationary Poisson background stemming from plate tectonics and provides a driving source to the process. The second term in the right-hand-side of expression (10.6) is nothing but the sum of (10.1) over all events preceding time  $t$ .

Note that there are three sources of stochasticity underlying the dynamics of  $\lambda(t)$  : (i) the source term  $s(t)$  often taken as Poissonian, (ii) the random occurrences of preceding earthquakes defining the time sequence  $\{t_i\}$  and (iii) the draw of the energy of each event according to the distribution  $P(E)$  given by (10.3). Knowing the seismic rate  $\lambda(t)$  at time  $t$ , the time of the following event is then determined according to a non-stationary Poisson process of conditional intensity  $\lambda(t)$ , and its magnitude is chosen according to the Gutenberg-Richter distribution (10.3).

## The Master equation for the average seismicity rate

It is useful to rewrite expression (10.6) formally as

$$\lambda(t) = s(t) + \int_{-\infty}^t d\tau \int_{E_0}^{+\infty} dE \phi_E(t - \tau) \sum_{i | t_i \leq t} \delta(E - E_i) \delta(\tau - t_i), \quad (10.7)$$

where  $\delta(u)$  is the Dirac distribution. Taking the expectation of (10.7) over all possible statistical scenarios (so-called ensemble average), we obtain the following Master equation for the first moment or statistical average  $N(t)$  of  $\lambda(t)$  [Helmstetter and Sornette, 2002a]

$$N(t) = s(t) + \int_{-\infty}^t d\tau \phi(t - \tau) N(\tau) , \quad (10.8)$$

where

$$\phi(t) \equiv \int_{E_0}^{\infty} dE' P(E') \phi_{E'}(t) . \quad (10.9)$$

By virtue of (10.5),  $\int_0^{\infty} \phi(t) dt = n$ . We have used the definitions

$$N(t) = \langle \lambda(t) \rangle = \left\langle \sum_{t_i \leq t} \delta(t - t_i) \right\rangle , \quad (10.10)$$

and

$$P(E) = \langle \delta(E - E_i) \rangle , \quad (10.11)$$

where the brackets  $\langle \cdot \rangle$  denotes the ensemble average. The average is performed over different statistical responses to the same source term  $s(t)$ , where  $s(t)$  can be arbitrary.  $N(t)dt$  is the average number of events occurring between  $t$  and  $t + dt$  of any possible energy.

The essential approximation used to derive (10.8) is that

$$\langle \rho(E_i) \delta(E - E_i) \delta(\tau - t_i) \rangle = \langle \rho(E_i) \delta(E - E_i) \rangle \langle \delta(\tau - t_i) \rangle \quad (10.12)$$

in (10.7). In words, the fluctuations of the earthquake energies can be considered to be decoupled from those of the seismic rate. This approximation is valid for  $a < \beta/2$ , for which the random variable  $\rho(E_i)$  has a finite variance. In this case, any coupling between the fluctuations of the earthquake energies and the instantaneous seismic rate provide only sub-dominant corrections to the equation (10.8). For  $a > \beta/2$ , the variance of  $\rho(E_i)$  is mathematically infinite or undefined as  $\rho(E_i)$  is distributed according to a power law with exponent  $\beta/a < 2$  (see chapter 4.4 of [Sornette, 2000]). In this case, the Master equation (10.8) is not completely correct as an additional term must be included to account for the dominating effect of the dependence between the fluctuations of earthquake energies and the instantaneous seismic rate.

Equation (10.8) is a linear self-consistent integral equation. In the presence of a stationary source of average level  $\langle s \rangle$ , the average seismicity in the sub-critical regime is therefore

$$\langle N \rangle = \frac{\langle s \rangle}{1 - n} . \quad (10.13)$$

This result (10.13) shows that the effect of the cascade of aftershocks of aftershocks and so on is to renormalize the average background seismicity  $\langle s \rangle$  to a significantly higher level, the closer  $n$  is to the critical value 1.

In order to solve for  $N(t)$  in the general case, it is convenient to introduce the Green function or “dressed propagator”  $K(t)$  defined as the solution of (10.8) for the case where the source term

is a delta function centered at time  $t = 0$  corresponding to a single mainshock :

$$K(t) = \delta(t) + \int_0^t d\tau \phi(t - \tau) K(\tau) . \quad (10.14)$$

Physically,  $K(t)$  is nothing but the “renormalized” Omori law quantifying the fact that the event at  $t = 0$  started a sequence of aftershocks which can themselves trigger secondary aftershocks and so on. The cumulative effect of all the possible branching paths of activity gives rise to the net seismic activity  $K(t)$  triggered by the initial event at  $t = 0$ . Thus, the decay rate of aftershocks following a mainshock recorded in a given earthquake catalog is described by  $K(t)$ , while  $\Psi(t)$  defined by (10.4) is a priori unobservable (see however [Helmstetter and Sornette, 2002a]).

This remark is important because it turns out that the renormalized Omori law  $K(t)$  may be very different from the bare Omori law  $\Psi(t - t_i)$ , because of the effect of the cascade of secondary, tertiary, ..., events triggered by any single event. The behavior of the average renormalized Omori law  $K(t)$  has been fully classified in [Helmstetter and Sornette, 2002a] (see also [Sornette and Sornette, 1999a]) : with a single value of the exponent  $1 + \theta$  of the “bare” propagator  $\Psi(t) \sim 1/t^{1+\theta}$  defined in (10.4), one obtains a continuum of apparent exponents for the global rate of aftershocks. This result may account for the observed variability of Omori exponent  $p$  in the range  $0.5 - 1.5$  or beyond, as reported by many workers [Utsu *et al.*, 1995]. Indeed, the general solution of (10.14) in the subcritical regime  $n < 1$  is

$$\begin{aligned} K(t) &\sim 1/t^{1-\theta} , \text{ for } c < t < t^* , \\ K(t) &\sim 1/t^{1+\theta} , \text{ for } t > t^* , \end{aligned} \quad (10.15)$$

where

$$t^* \approx c(1 - n)^{-1/\theta} . \quad (10.16)$$

Thus, in practice, the apparent  $p$  exponent can be found anywhere between  $1 - \theta$  and  $1 + \theta$ . This behavior (10.15) is valid for  $a < \beta/2$  for which, as we explained already, the fluctuations of the earthquake energies can be considered to be decoupled from those of the seismic rate.

In the case  $a > \beta/2$ , this approximation is no more valid and the problem is considerably more difficult due to the coupling between the fluctuations in the sequence of earthquake energies and the seismic rate. We have not been able to derive the detailed solution of the problem in this regime but nevertheless can predict that the apparent exponent for the dressed propagator  $K(t)$  should change continuously from  $1 - \theta$  to  $1 + \theta$  as  $a$  increases towards  $\beta$  from below. The argument goes as follows. Starting from (10.7), it is clear that the larger  $a$  is, the larger is the dependence between the times of occurrences contributing to the sum over  $\delta(\tau - t_i)$  and the realizations of corresponding earthquake energies contributing to the sum over  $\delta(E - E_i)$ . This is due to the fact that very large earthquakes trigger many more aftershocks for large  $a$ , whose energies influence subsequently the time of occurrences of following earthquakes, and so on. The larger is the number of triggered events per shock, the more intricately intertwined are the times

of occurrence and energies of subsequent earthquakes. This dependence can be captured by the following ansatz, which corrects (10.12) :

$$\begin{aligned} \langle \rho(E_i) \delta(E - E_i) \delta(\tau - t_i) \rangle &\approx \\ \langle \rho(E_i) \delta(E - E_i) \rangle \langle \delta(\tau - t_i) \rangle + f(a) [\delta(\tau - t_i)]^2, \end{aligned} \quad (10.17)$$

where  $f(a) = 0$  for  $a < \beta/2$  and increases with  $a > \beta/2$ . The quadratic term just expresses the dependence between  $\rho(E_i) \delta(E - E_i)$  and  $\delta(\tau - t_i)$ , i.e.,  $\rho(E_i) \delta(E - E_i)$  has a contribution proportional to  $\delta(\tau - t_i)$ . Indeed, recall that if two random variables  $X$  and  $Y$  are (linearly) correlated, this means that one can regress one with respect to the other and write  $Y = fX + x$ , where  $f$  is simply related to the correlation coefficient between  $X$  and  $Y$  and  $x$  is an idiosyncratic noise uncorrelated with  $X$ . Then,

$$\langle XY \rangle = f \langle X^2 \rangle + \langle X \rangle \langle x \rangle. \quad (10.18)$$

The mechanism leading to the quadratic term  $\langle X^2 \rangle$  is at the source of  $[\delta(\tau - t_i)]^2$  in (10.17). This new contribution leads to a modification of (10.14) according to

$$K(t) \sim \int_0^t d\tau \phi(t - \tau) K(\tau) + f(a) \int_0^t d\tau \phi(t - \tau) [K(\tau)]^2. \quad (10.19)$$

Dropping the second term in the right-hand-side of (10.19) recovers (10.14). Dropping the first term in the right-hand-side of (10.19) yields the announced result  $K(t) \propto 1/t^{1+\theta}$  even in the regime  $t < t^*$ . We should thus expect a cross-over from  $K(t) \propto 1/t^{1-\theta}$  to  $K(t) \propto 1/t^{1+\theta}$  as  $a$  increases from  $\beta/2$  to  $\beta$ . This prediction is verified accurately by our numerical simulations.

Once we know the full (ensemble average) seismic response  $K(t)$  from a single event, the complete solution of (10.8) for the average seismic rate  $N(t)$  under the action of the general source term  $s(t)$  is

$$N(t) = \int_{-\infty}^t d\tau s(\tau) K(t - \tau). \quad (10.20)$$

Expression (10.20) is nothing but the theorem of Green functions for linear equations with source terms [*Morse and Feshbach*, 1953]. Expression (10.20) reflects the intuitive fact that the total seismic activity at time  $t$  is the sum of the contributions of all the external sources at all earlier times  $\tau$  which convey their influence up to time  $t$  via the “dressed propagator” (or renormalized Omori law)  $K(t - \tau)$ .  $K(t - \tau)$  is the relevant kernel quantifying the influence of each source  $s(\tau)$  because it takes into account all possible paths of seismicity from  $\tau$  to  $t$  triggered by each specific source.

## Deviations from the average seismicity rate

Similarly to the definition (10.14) of the average renormalized propagator  $K(t)$ , let us introduce the stochastic propagator  $\kappa(t)$ , defined as the solution of (10.6) or (10.7) for the source

term  $s(t) = \delta(t)$ . The propagator  $\kappa(t)$  is thus the seismicity rate initiated by a single earthquake at the origin of times, which takes into account the specific sequence of generated earthquakes. Since the earthquakes are generated according to a probabilistic (generalized Poisson) process, repeating the history leads in general to different realizations.  $\kappa(t)$  is thus fundamentally realization specific and there are as many different  $\kappa(t)$ 's as there are different earthquake sequences. In other words,  $\kappa(t)$  is a stochastic function. Obviously,  $\langle \kappa(t) \rangle \equiv K(t)$ , that is, its ensemble average retrieves the average renormalized propagator.

From the structure of (10.6) or (10.7) which are linear sums over events, an expression similar to (10.20) can be written for the non-average seismic rate with an arbitrary source term  $s(t)$  :

$$\lambda(t) = \int_{-\infty}^t d\tau s(\tau) \kappa_{\{\tau\}}(t - \tau) , \quad (10.21)$$

where the subscript  $\{\tau\}$  in the stochastic kernel  $\kappa_{\{\tau\}}(t - \tau)$  captures the fact that there is a different stochastic realization of  $\kappa$  for each successive source. Taking the ensemble average of (10.21) recovers (10.20). The difference between the stochastic kernel  $\kappa_{\{\tau\}}(t - \tau)$ , the local propagator  $\phi_E(\tau)$  and the renormalized propagator  $K(\tau)$  is illustrated on Figure 10.1 for a numerical simulation of the ETAS model.

We show in the Appendix A that  $\lambda(t)$  can be expressed as

$$\lambda(t) = N(t) + \int_{-\infty}^t d\tau \eta(\tau) K(t - \tau) , \quad (10.22)$$

where  $\eta(\tau)$  is a stationary noise which can be suitably defined. This is the case because the fluctuations  $\delta P(E)$  of the Gutenberg-Richter law and of the source  $s(t)$  are stationary processes, and because the fluctuations of  $\delta\kappa$  are proportional to  $K(t)$ . The expression of  $\eta(\tau)$  can be determined explicitly in the case where the fluctuations of the energy distribution  $P(E)$  dominate the fluctuations of the seismicity rate  $\kappa(\tau)$  (see Appendix A).

### 10.3 Derivation of the inverse Omori law and consequences

#### Synthesis of the results

The normal regime in the ETAS model corresponds to the subcritical case  $n < 1$  for which the seismicity rate decays on average after a mainshock to a constant background (in the case of a steady-state source) decorated by fluctuations. How is it then possible in this framework to get an accelerating seismicity preceding a large event? Conceptually, the answer lies in the fact that when one defines a mainshock and its foreshocks, one introduces automatically a conditioning (in the sense of the theory of probability) in the earthquake statistics. As we shall see, this conditioning means that specific precursors and aftershocks must precede and follow a large event. In other words, conditioned on the observation of a large event, the sequence of events preceding it cannot be arbitrary. We show below that it in fact follows the inverse Omori

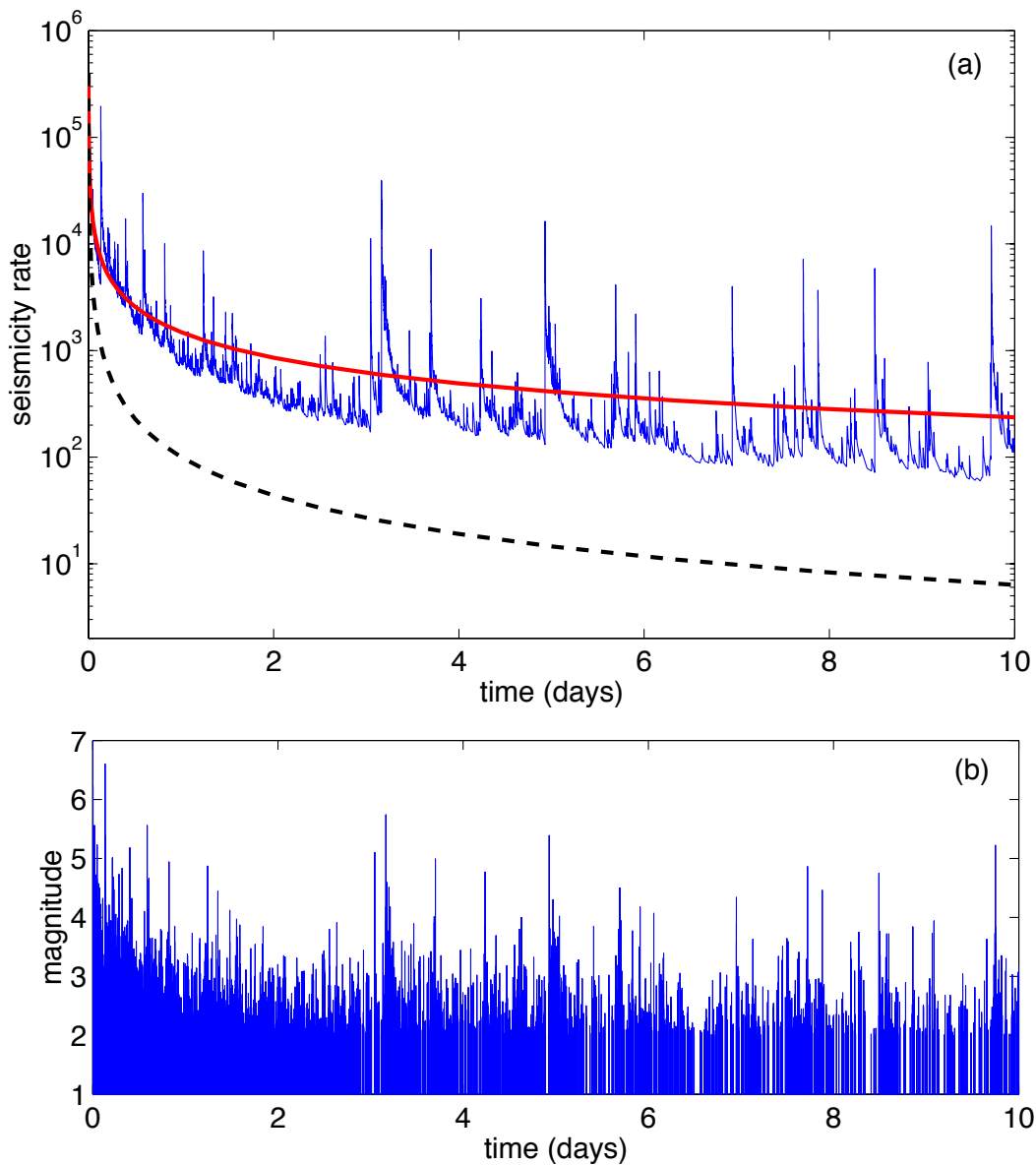


FIG. 10.1 – An example of a realization of the ETAS model, which illustrates the differences between the observed seismicity rate  $\kappa(t)$  (noisy solid line), the average renormalized (or dressed) propagator  $K(t)$  (solid line), and the local propagator  $\phi_E(t)$  (dashed line). The magnitude of each earthquake are shown in panel (b). This aftershock sequence has been generated using the ETAS model with parameters  $n = 1$ ,  $a = 0.8\beta$ ,  $\theta = 0.2$ ,  $m_0 = 2$  and  $c = 0.001$  day, starting from a mainshock of magnitude  $M = 7$  at time  $t = 0$ . The global aftershock rate  $\kappa(t)$  is significantly higher than the direct (or first generation) aftershock rate, described by the local propagator  $\phi_E(t)$ . The global aftershock rate  $\kappa(t)$  decreases on average according to the dressed propagator  $K(t) \sim 1/t^{1-\theta}$ , which is significantly slower than the local propagator  $\phi(t) \sim 1/t^{1+\theta}$ . The best fit to the observed seismicity rate  $\kappa(t)$  is indistinguishable from the average dressed propagator  $K(t)$ . Large fluctuations of the seismicity rate corresponds to the occurrence of large aftershocks, which trigger their own aftershock sequence. Third-generation aftershocks can be easily observed.

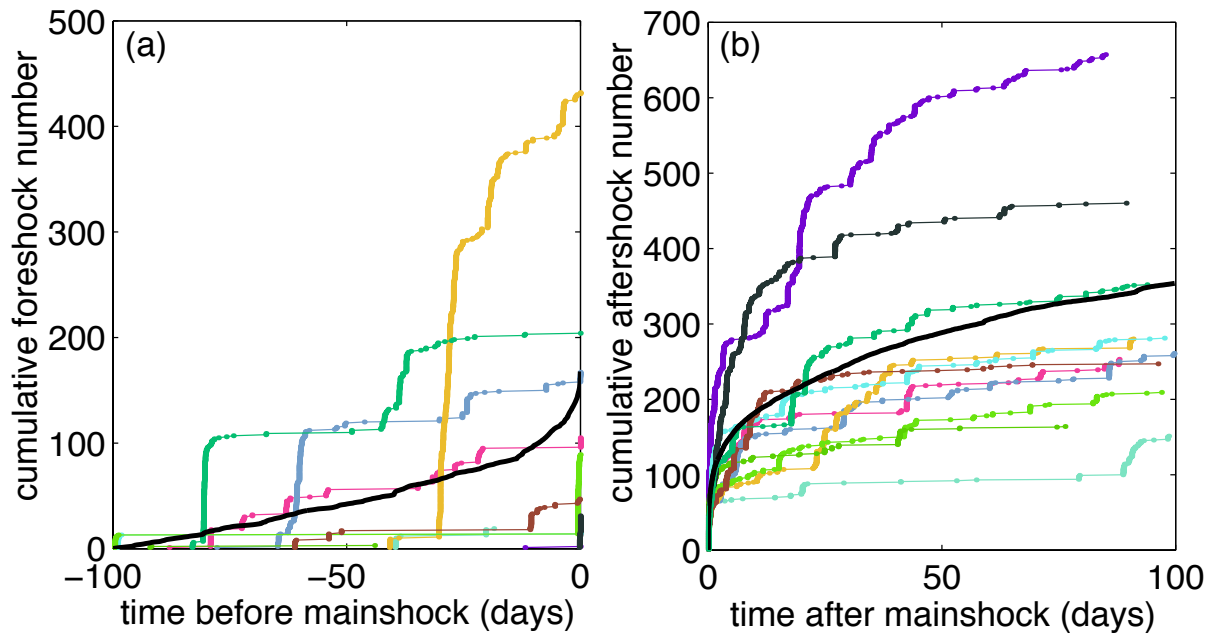


FIG. 10.2 – Typical foreshock (a) and aftershock (b) sequences generated by the ETAS model, for mainshocks of magnitude  $M = 5.5$ . We show 11 individual sequences in each panel. The solid black line represents the mean seismicity rate before and after a mainshock of magnitude  $M = 5.5$ , estimated by averaging over 250 sequences. The synthetic catalogs have been generated using the parameters  $n = 1$ ,  $\theta = 0.2$ , and  $a = 0.5\beta$ , with a minimum magnitude threshold  $m_0 = 2$ . In contrast with the direct Omori law, which is clearly observed after any large mainshock, there are large fluctuations from one foreshock sequence to another one, and the inverse Omori law (with accelerating seismicity) is only observed when averaging over a large number of foreshock sequences.

law in an average statistical sense. Figure 10.2 presents typical realizations of foreshock and aftershock sequences in the ETAS model as well as the direct and inverse Omori law evaluated by averaging over many realizations. The deceleration of the aftershock activity is clearly observed for each individual sequence as well as in their average. Going to backward time to compare with foreshocks, the acceleration of aftershock seismicity when approaching the main event is clearly visible for each sequence. In contrast, the acceleration of foreshock activity (in forward time) is only observable for the ensemble average while each realization exhibits large fluctuations with no clearly visible acceleration. This stresses the fact that the inverse Omori law is a statistical statement, which has a low probability to be observed in any specific sequence.

Intuitively, it is clear that within the ETAS model, in order for an event to occur, one needs a relatively large increase both in seismicity rate and in magnitudes of the earthquakes, so that this increase of seismicity can trigger an event with a non-negligible probability. Indeed, within the ETAS model, all events are the result of the sum of the background seismicity (due to tectonic forces) and of all other earthquakes that can trigger their aftershocks.

How does the condition that an earthquake sequence ends at a mainshock impact on the

seismicity prior to that mainshock? How does this condition create the inverse Omori law? Since earthquake magnitudes are independently drawn from the Gutenberg-Richter law, the statistical qualification of a mainshock, that we place without loss of generality at the origin of time, corresponds to imposing an anomalous burst of seismic activity  $\lambda(0) = \langle N \rangle + \lambda_0$  at  $t = 0$  above its average level  $\langle N \rangle$  given by (10.13).

The question then translates into what is the path taken by the noise  $\eta(\tau)$  in (10.22) for  $-\infty < \tau < 0$  that may give rise to this burst  $\lambda_0$  of activity. The solution is obtained from the key concept that the set of  $\eta(\tau)$ 's for  $-\infty < \tau < 0$  is biased by the existence of the conditioning, i.e., by the large value of  $\lambda(0) = \langle N \rangle + \lambda_0$  at  $t = 0$ . This does not mean that there is an unconditional bias. Rather, the existence of a mainshock requires that a specific sequence of noise realizations must have taken place to ensure its existence. This idea is similar to the well-known result that an unbiased random walk  $W(t)$  with unconditional Gaussian increments with zero means sees its position take a non-zero expectation

$$\langle W(\tau) \rangle|_c = [W(t) - W(0)] \frac{\tau}{t}, \quad (10.23)$$

if one knows the beginning  $W(0)$  and the end  $W(t)$  position of the random walk, while the unconditional expectation  $\langle W(\tau) \rangle$  is identically zero. Similarly, the conditional increment from  $\tau$  to  $\tau + d\tau$  of this random walk become not non-zero and equal to (in non-rigorous notation)

$$d\tau \frac{W(t) - W(0)}{t}, \quad (10.24)$$

in contrast with the zero value of the unconditional increments.

In the ETAS model which is a marked point process, the main source of the noise on  $\lambda(t)$  is coming from the ‘‘marks’’, that is, the energies drawn for each earthquake from the Gutenberg-Richter power law distribution (10.3). Expression (10.2) shows that the amplitude  $\eta_\tau$  of the fluctuations in the seismic rate is proportional to  $E_\tau^a$ , where  $E_\tau$  is the energy of a mother-earthquake occurring at time  $\tau$ . Since the energies are distributed according to the power law (10.3) with exponent  $\beta$ ,  $\eta_\tau \propto E_\tau^a$  is distributed according to a power law with exponent  $m = \beta/a$  (see for instance chapter 4.4 of [Sornette, 2000]).

We first study the subcritical regime  $n < 1$  for times  $t_c - t < t^*$ , where  $t^*$  is defined by (10.16). Two cases must then be considered.

- For  $a < \beta/2$ ,  $m > 2$ , the variance and covariance of the noise  $\eta_\tau$  exist and one can use conditional covariances to calculate conditional expectations. We show below that the inverse Omori law takes the form

$$E[\lambda(t)|\lambda_0] \propto \frac{\lambda_0}{(t_c - t)^{1-2\theta}}, \quad (10.25)$$

that is,  $p' = 1 - 2\theta$ .

- for  $a \geq \beta/2$ ,  $m = \beta/a \leq 2$  and the variance and covariance of  $\eta_\tau$  do not exist : one needs a special treatment based on stable distributions. In this case, neglecting the coupling

between the fluctuations in the earthquake energies and the seismic rate, we find that the inverse Omori law takes the form

$$E[\lambda(t)|\lambda_0] \propto \frac{\lambda_0}{(t_c - t)^{1-m\theta}} . \quad (10.26)$$

Taking into account the dependence between the fluctuations in the earthquake energies and the seismic rate, the exponent  $p'$  progressively increases from  $1 - 2\theta$  towards the value  $1 + \theta$  of the bare propagator as  $a$  goes from  $\beta/2$  to  $\beta$  (see figure 10.6). The increase of  $p'$  is thus faster than the dependence  $1 - m\theta$  predicted by (10.26).

In the large times limit  $t_c - t > t^*$  (far from the mainshock) of the subcritical regime, we also obtain an inverse Omori law which takes the form

$$E[\lambda(t)|\lambda_0] \propto \frac{\lambda_0}{(t_c - t)^{1+\theta}} , \quad \text{for } a < \beta/2 \quad (10.27)$$

and

$$E[\lambda(t)|\lambda_0] \propto \frac{\lambda_0}{(t_c - t)^{1+(m-1)\theta}} , \quad \text{for } \beta/2 \leq a \leq \beta . \quad (10.28)$$

The direct and inverse Omori laws are clearly observed in numerical simulations of the ETAS model, when stacking many sequences of foreshocks and aftershocks, for various mainshock magnitudes (Figures 10.3 and 10.4). Our main result shown in Figure 10.3 is that, due to conditioning, the inverse Omori law is *different* from the direct Omori law, in that the exponent  $p'$  of the inverse Omori law is in general smaller than the exponent  $p$  of the direct Omori law. Another fundamental difference between aftershocks and foreshocks found in the ETAS model is that the number of aftershocks increases as a power  $E^a$  of the mainshock energy  $E$  as given by (10.2), whereas the number of foreshocks of type II is independent of the mainshock energy (see Figures 10.3 and 10.4). Because in the ETAS model the magnitude of each event is independent of the magnitude of the triggering events, and of the previous seismicity, the rate of seismicity increases on average according to the inverse Omori law before any earthquake, whatever its magnitude. beginfigure

The number of foreshocks of type I increases with the mainshock magnitude, for small and intermediate mainshock magnitudes and saturates to the level of foreshocks of type II for large mainshocks because the selection/condition acting of those defined foreshocks becomes less and less severe as the magnitude of the mainshock increases (see Figure 10.5). The conditioning that foreshocks of type I must be smaller than their mainshock induces an apparent increase of the Omori exponent  $p'$  as the mainshock magnitude decreases. The predictions (10.15) and (10.25) on the  $p$  and  $p'$ -value of type II foreshocks are well-verified by numerical simulations of the ETAS model up to  $a/\beta \leq 0.5$ , as presented on Figure 10.6. However, for  $a/\beta > 0.5$ , both  $p$  and  $p'$  are found larger than predicted by (10.15) and (10.26) respectively, due to the coupling between the fluctuations in the earthquake energies and those of the seismic rate. This coupling occurs because the variance of the number  $\rho(E)$  of direct aftershocks of an earthquake of energy  $E$  is unbounded for  $a > \beta/2$ , leading to strong burst of seismic activity coupled with strong

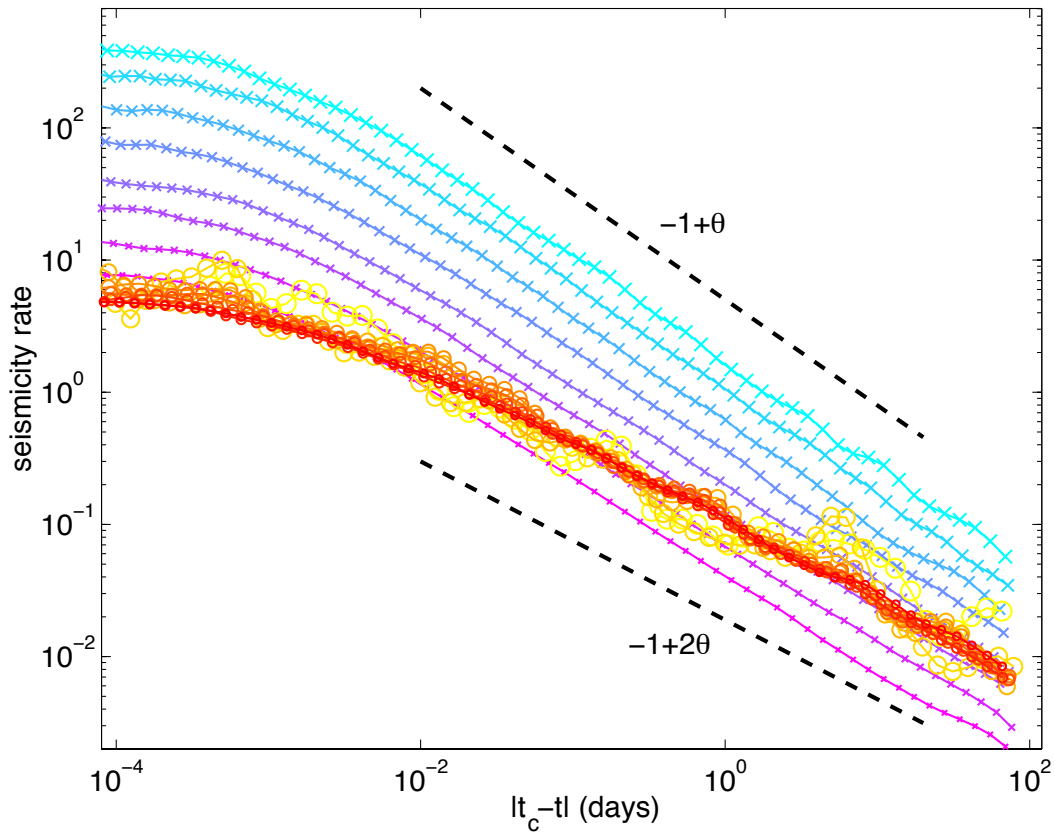


FIG. 10.3 – Direct and inverse Omori law for a numerical simulation with  $a = 0.5\beta$  and  $\theta = 0.2$  showing the two exponents  $p = 1 - \theta$  for aftershocks and  $p' = 1 - 2\theta$  for foreshocks of type II. The rate of aftershocks (crosses) and foreshocks (circles) per mainshock, averaged over a large number of sequences, is shown as a function of the time  $|t_c - t|$  to the mainshock, for different values of the mainshock magnitude between 1.5 and 5, with a step of 0.5. The symbol size increases with the mainshock magnitude. The truncation of the seismicity rate for small times  $|t_c - t| \simeq 0.001$  is due to the characteristic time  $c = 0.001$  in the bare Omori propagator  $\Psi(t)$ , and is the same for foreshocks and aftershocks. The number of aftershocks increases with the mainshock energy as  $N \simeq E^a$ , whereas the number of foreshocks of type II is independent of the mainshock energy.

fluctuations of the earthquake energies. In this regime, expression (10.19) shows that  $p$  changes continuously between  $1 - \theta$  for  $a/\beta = 0.5$  to  $1 + \theta$  for  $a = \beta$  in good agreement with the results of the numerical simulations. In this case  $a \geq \beta/2$ , the exponent  $p'$  is also observed to increase between  $p' = 1 - 2\theta$  for  $a = \beta/2$  to  $p' = 1 + \theta$  for  $a = \beta$ , as predicted below.

The dissymmetry between the inverse Omori law for foreshocks and the direct Omori law (10.15) for aftershocks stems from the fact that, for foreshocks, one observes a seismic rate conditional on a large rate at the time  $t_c$  of the mainshock while, for the aftershocks, one observes the direct response  $K(t)$  to a single large shock. The later effect stems from the term  $\rho(E)$  given by (10.2) in the bare Omori propagator which ensures that a mainshock with a large magnitude triggers aftershocks which dominates overwhelmingly the seismic activity. In

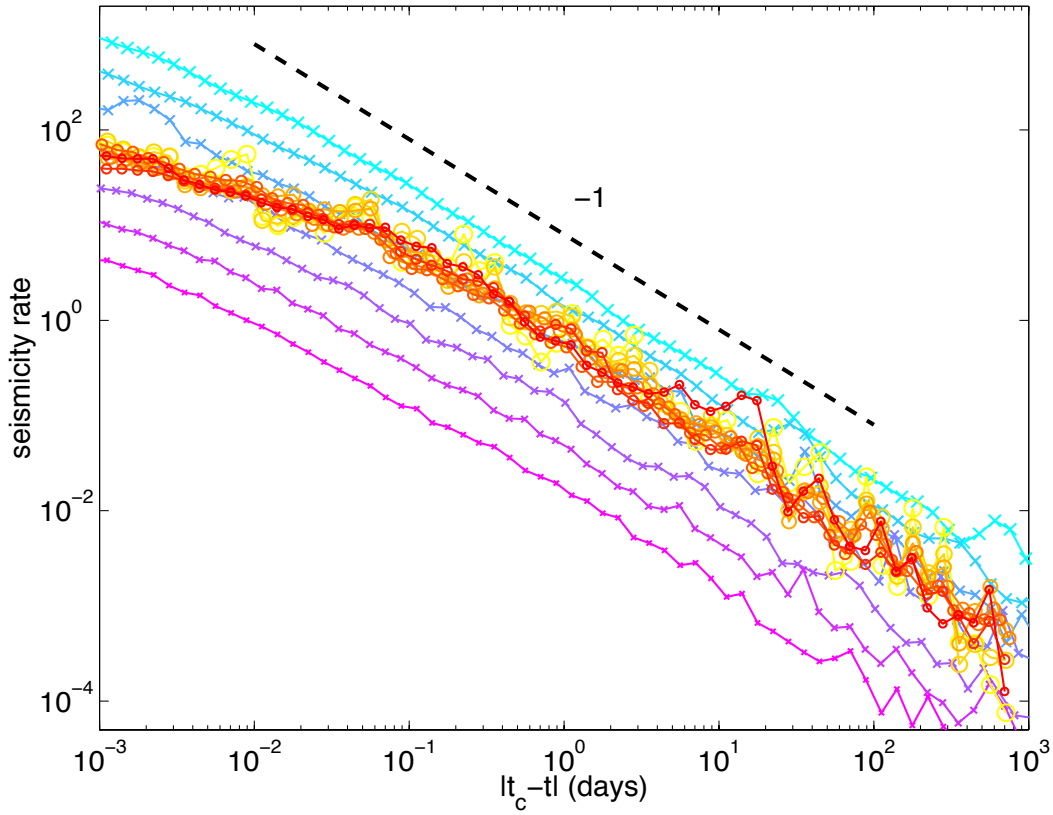


FIG. 10.4 – Same as Figure 10.3 for  $a = 0.8\beta$ , showing the larger relative ratio of foreshocks to aftershocks compared to the case  $a = 0.5\beta$ .

the special case where one take the exponent  $a = 0$  in (10.2), a mainshock of large magnitude has no more daughters than any other earthquake. As a consequence, the observed Omori law stems from the same mechanism as for the foreshock and the increasing foreshock activity (10.25) gives the same parametric form for the aftershock decay, with  $t_c - t$  replaced by  $t - t_c$  (this is for instance obtained through the Laplace transform of the seismic rate). This gives the exponent  $p = p' = 1 - 2\theta$  for  $a = 0$  as for the foreshocks, but the number of aftershocks is still larger than the number of foreshocks. This result is born out by our numerical simulations (not shown).

These results and the derivations of the inverse Omori law make clear that mainshocks are more than just the aftershocks of their foreshocks, as sometimes suggested [Shaw, 1993; Jones *et al.*, 1999]. The key concept is that all earthquakes are preceded by some seismic activity and may be seen as the result of this seismic activity. However, on average, this seismic activity must increase to be compatible statistically with the occurrence of the main shock : this is an unavoidable statistical certainty with the ETAS model, that we derive below. The inverse Omori law is fundamentally a conditional statistical law which derives from a double renormalization process : (1) the renormalization from the bare Omori propagator  $\Psi(t)$  defined by (10.4) into the renormalized or dressed propagator  $K(t)$  and (2) the conditioning of the fluctuations in seismic activity upon a large seismic activity associated with the mainshock. In summary, we can state

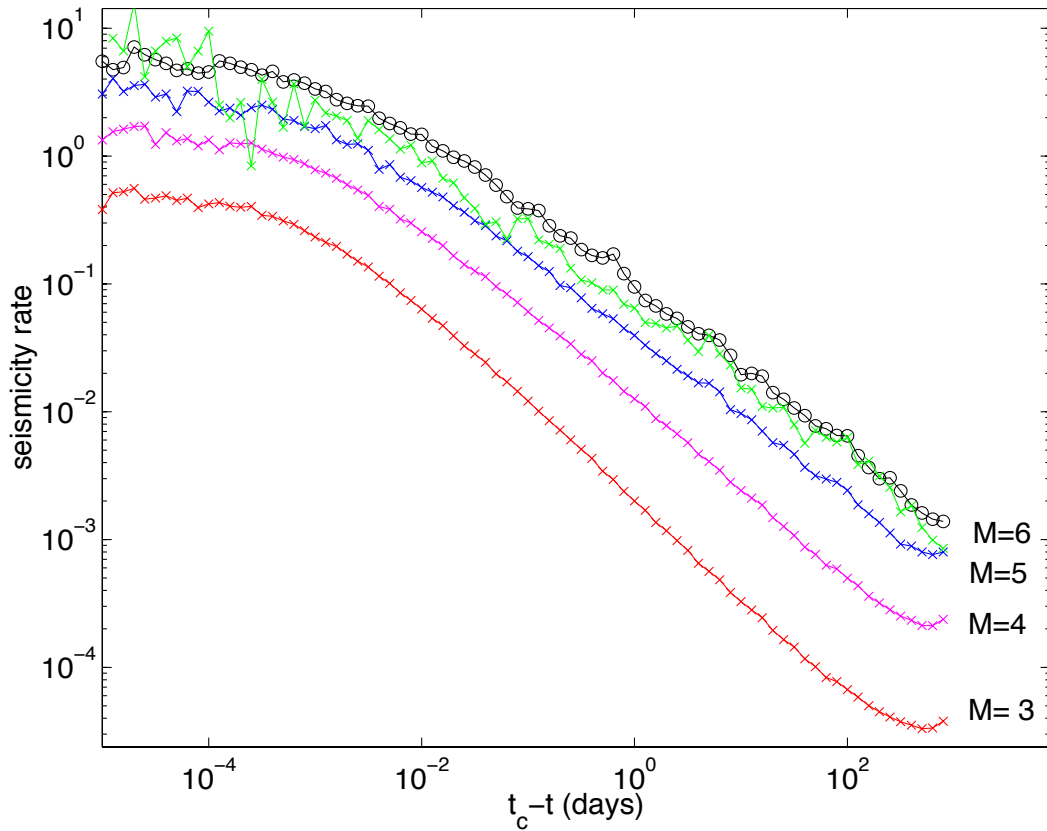


FIG. 10.5 – Foreshock seismicity rate per mainshock for foreshocks of type II (circles) and foreshocks of type I (crosses), for a numerical simulation with  $n = 1$ ,  $c = 0.001$ ,  $\theta = 0.2$ ,  $a = 0.5\beta$  and  $m_0 = 2$ . For foreshocks of type I, we have considered mainshock magnitudes  $M$  ranging from 3 to 6. We have rejected from the analysis of foreshocks of type I all mainshocks which have been preceded by a larger event in a time interval extending up to  $t = 1000$  days preceding the mainshock. The rate of foreshocks of type II is independent on the mainshock magnitude  $M$ , while the rate of foreshocks of type I increases with  $M$ . For large mainshock magnitudes, the rate of foreshocks of type I is very close to that of foreshocks of type II. The conditioning that foreshocks of type I must be smaller than their mainshock induces an apparent increase of the Omori exponent  $p'$  as the mainshock magnitude decreases. It induces also an upward bending of the seismicity rate at times  $t \approx 1000$ , especially for the small magnitudes.

that mainshocks are aftershocks of conditional foreshocks. We stress again that the statistical nature of foreshocks does not imply that there is no information in foreshocks on future large earthquakes. As discussed below, foreshocks are genuine forerunners of large shocks.

### The inverse Omori law $\sim 1/t^{1-2\theta}$ for $a < \beta/2$

Let us call  $X(t) = \lambda(t) - N(t)$  given by (10.22) and  $Y = \lambda(0) - N(0)$ . It is a standard result of stochastic processes with finite variance and covariance that the expectation of  $X(t)$  conditioned on  $Y = \lambda_0$  is given by [Jacod and Shiryaev, 1987]

$$E[X(t)|Y = \lambda_0] = \lambda_0 \frac{\text{Cov}(X(t), Y)}{E[Y^2]}, \quad (10.29)$$

where  $E[Y^2]$  denotes the expectation of  $Y^2$  and  $\text{Cov}(X(t), Y)$  is the covariance of  $X$  and  $Y$ . Expression (10.29) recovers the obvious result that  $E[X(t)|Y = \lambda_0] = 0$  if  $X$  and  $Y$  are uncorrelated.

Using the continuous limit in which the noise  $\eta(\tau)$  converges to a centered Gaussian noise

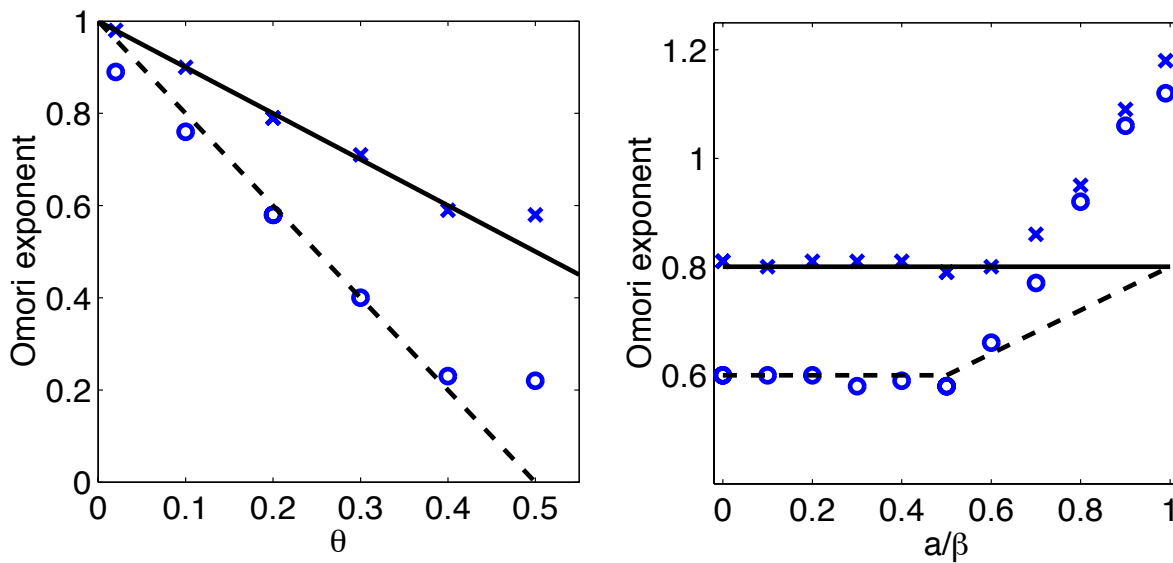


FIG. 10.6 – Exponents  $p'$  and  $p$  of the inverse and direct Omori laws obtained from numerical simulations of the ETAS model. The estimated values of  $p'$  (circles) for foreshocks and  $p$  (crosses) for aftershocks are shown as a function of  $\theta$  in the case  $\alpha = 0.5$  (a), and as a function of  $a/\beta$  in the case  $\theta = 0.2$  (b). For  $a/\beta$  not too large, the values of  $p'$  for foreshocks are in good agreement with the predictions  $p' = 1 - 2\theta$  for  $a/\beta < 0.5$  (10.32) and  $p' = 1 - \beta \theta/a$  for  $a/\beta > 0.5$  (10.41). The theoretical values of  $p'$  are represented with dashed lines in each plot, and the theoretical prediction for  $p$  is shown as solid lines. For  $a/\beta$  not too large, the measured exponent for aftershocks is in good agreement with the prediction  $p = 1 - \theta$  (10.15). For  $a/\beta > 0.5$ , both  $p$  and  $p'$ -values are larger than the predictions (10.15) and (10.41). For  $a/\beta$  close to 1, both  $p$  and  $p'$  are found close to the exponent  $1 + \theta = 1.2$  of the bare propagator  $\psi(t)$ . See text for an explanation.

by the virtue of the central limit theorem, we obtain

$$\text{Cov}(X(t), Y) = \int_{-\infty}^t d\tau K(t - \tau) K(-\tau) , \quad (10.30)$$

and

$$\text{E}[Y^2] = \int_{-\infty}^0 d\tau [K(-\tau)]^2 . \quad (10.31)$$

$\text{E}[Y^2]$  is thus a constant while, for  $|t| < t^*$  where  $t^*$  is defined in (10.16),  $\text{Cov}(X(t), Y) \sim 1/|t|^{1-2\theta}$ . Generalizing to a mainshock occurring at an arbitrary time  $t_c$ , this yields the inverse Omori law

$$\text{E}[\lambda(t)|\lambda(t_c) = \langle N \rangle + \lambda_0] = \langle N \rangle + C \frac{\lambda_0}{(t_c - t)^{1-2\theta}} , \quad (10.32)$$

where  $C$  is a positive numerical constant.

Expression (10.32) predicts an inverse Omori law for foreshocks in the form of an average acceleration of seismicity proportional to  $1/(t_c - t)^{p'}$  with the inverse Omori exponent  $p' = 1 - 2\theta$ , prior to a mainshock. This exponent  $p'$  is smaller than the exponent  $p = 1 - \theta$  of the renormalized propagator  $K(t)$  describing the direct Omori law for aftershocks. This prediction is well-verified by numerical simulations of the ETAS model shown in Figure 10.3.

As we pointed out in the introduction, *Shaw* [1993] derived the relationship  $p' = 2p - 1$ , which yields  $p' = 1 - 2\theta$  for  $p = 1 - \theta$ , based on a clever interestingly incorrect reasoning that we now clarify. Actually, there are two ways of viewing his argument. The most straightforward one used by Shaw himself consists in considering a single aftershock sequence starting at time 0 from a large mainshock. Let us consider two aftershocks at time  $t - \tau$  and  $t$ . Forgetting any constraint on the energies, the earthquake at time  $t - \tau$  can be viewed as a foreshock of the earthquake at time  $t$ . Summing over all possible positions of these two earthquakes at fixed time separation  $\tau$  then amounts to constructing a kind of foreshock count which obeys the equation

$$\int_0^{+\infty} dt K(t - \tau) K(t) , \quad (10.33)$$

where  $K(t)$  is the number of aftershocks at time  $t$ . This integral (10.33) recovers equation (12) of [*Shaw*, 1993]. If  $K(t) \sim 1/t^p$ , this integral predicts a dependence  $1/\tau^{2p-1}$  for the effective foreshock activity. This derivation shows that the prediction  $p' = 2p - 1$  results solely from the counting of pairs at fixed time intervals in an aftershock sequence. It is a pure product of the counting process.

We can also view this result from the point of view of the ETAS model. In the language of the ETAS model, Shaw formula (12) uses the concept that a mainshock is an aftershock of a cascade of aftershocks, themselves deriving from an initial event. To implement this idea, he uses (what corresponds to) the dressed propagator  $K(t)$  for the probability of an aftershock resulting from the initial event and also for the rate of mainshocks deriving from an aftershock of the initial event. From our previous studies [*Sornette and Sornette*, 1999a; *Helmstetter and Sornette*, 2002a], one can see that this corresponds to an illicit double counting or double renormalization.

This danger of double counting is illustrated by comparing the formulas (10.8, 10.14) with (10.20) : either the direct tectonic source of seismicity  $s(t)$  impacts in future seismicity via the renormalized or dressed propagator as in (10.20), or we can count all past seismic activity as in (10.8, 10.14), but then they must be accounted for in the future seismicity only through the bare propagator. What is then the reason for the correct value derived by *Shaw* [1993] ? It turns out that his double counting recovers the mathematical form resulting from the effect of the conditioning on the source term leading to  $s(t) \sim K(t)$  valid for  $a \leq \beta/2$  as derived below in (10.37). This proportionality  $s(t) \sim K(t)$  is physically at the origin of (10.30) leading to our formula (10.30) at the origin itself of the inverse Omori law, which takes the same form as the expression (12) in [*Shaw*, 1993]. The limited value of this derivation (10.33) is also made clear by its failure for  $a > \beta/2$ , as already explained.

### The inverse Omori law $\sim 1/t^{1-\theta\beta/a}$ for $a \geq \beta/2$

Expression (10.22) defines the fluctuating part  $X(t) = \lambda(t) - N(t)$  of the seismic rate as a sum of random variables  $\eta(\tau)$  with power law distributions weighted by the kernel  $K(t - \tau)$ . These random variables  $\eta(\tau)$ , which are mainly dominated by the fluctuations in event magnitudes but also receive contributions from the intermittent seismic rate, are conditioned by the realization of a large seismicity rate

$$X(0) = \lambda_0 = \int_{-\infty}^0 d\tau \eta(\tau) K(-\tau) , \quad (10.34)$$

which is the correct statistical implementation of the condition of the existence of a large shock at  $t = 0$ . Since the conditioning is performed on  $X(0)$ , that is, upon the full set of noise realizations acting up to time  $t = 0$ , the corresponding conditional noises up to time  $t < 0$  contribute all to  $E[X(t)|X(0) = \lambda_0]_{t < 0}$  by their conditional expectations as

$$E[X(t)|X(0) = \lambda_0]_{t < 0} = \int_{-\infty}^t d\tau E[\eta(\tau)|X(0)] K(t - \tau) . \quad (10.35)$$

In Appendix B, it is shown that, for identically independently distributed random variables  $x_i$  distributed according to a power law with exponent  $m = \beta/a \leq 2$  and entering the sum

$$S_N = \sum_{i=1}^N K_i x_i \quad (10.36)$$

where the  $K_i$  are arbitrary positive weights, the expectation  $E[x_i|S_N]$  of  $x_i$  conditioned on the existence of a large realization of  $S_N$  is given by

$$E[x_i|S_N] \propto S_N K_i^{m-1} . \quad (10.37)$$

To apply this result to (10.35), it is convenient to discretize it. Some care should however be exercised in this discretization (1) to account for the expected power law acceleration of

$E[X(t)|X(0) = \lambda_0]$  up to  $t = 0$  and (2) to discretize correctly the random noise. We thus write

$$\begin{aligned} \int_{-\infty}^0 d\tau \eta(\tau) K(-\tau) &\approx \sum_{\tau_i < 0} \int_{\tau_i}^{\tau_{i+1}} d\tau \eta(\tau) K(-\tau) \\ &\sim \sum_{\tau_i < 0} (\tau_{i+1} - \tau_i) K(-\tau_i) x_i, \end{aligned} \quad (10.38)$$

where  $x_i \sim \eta_i(\tau_{i+1} - \tau_i)$  is the stationary discrete noise distributed according to a power law distribution with exponent  $m = \beta/a$ . The factor  $(\tau_{i+1} - \tau_i) \propto |\tau_i|$  in front of the kernel  $K(-\tau_i)$  is needed to regularize the discretization in the presence of the power law acceleration up to time 0. In the notation of Appendix B,  $(\tau_{i+1} - \tau_i) K(-\tau_i) \propto |\tau_i| K(-\tau_i) \sim 1/|\tau_i|^{-\theta}$  plays the role of  $K_i$ . We also need an additional factor  $(\tau_{i+1} - \tau_i)$  to obtain a regularized noise term : thus,  $\eta_i(\tau_{i+1} - \tau_i) \propto \eta_i |\tau_i|$  plays the role of  $x_i$ . This discretization procedure recovers the results obtained by using (10.29) and the variance and covariance of the continuous integrals for the case  $a < \beta/2$  where they are defined. Note that the last expression in equation (10.38) does not keep track of the dimensions as we are only able to obtain the leading scaling behavior in the discretization scheme.

Using (10.37), we thus obtain  $E[\eta_i|\tau_i| |X(0) = \lambda_0] \propto \frac{\lambda_0}{|\tau_i|^{-\theta(m-1)}}$  and thus

$$E[\eta_i|X(0) = \lambda_0] \propto \frac{\lambda_0}{|\tau_i|^{1-\theta(m-1)}}. \quad (10.39)$$

Similarly to (10.38), the discrete equivalent to (10.35) reads

$$\begin{aligned} E[X(t)|X(0) = \lambda_0]_{t < 0} & \\ &\approx \sum_{\tau_i < t} (\tau_{i+1} - \tau_i) K(t - \tau_i) E[\eta_i|\tau_i| |X(0) = \lambda_0] \\ &\sim \int_{-\infty}^t d\tau \frac{1}{|t - \tau|^{1-\theta}} \frac{\lambda_0}{|\tau|^{1-\theta(m-1)}} \sim \frac{\lambda_0}{|t|^{1-m\theta}}, \end{aligned} \quad (10.40)$$

where we have re-introduced factors  $\tau_{i+1} - \tau_i$  to reverse to the continuous integral formulation and have use the definition  $m = \beta/a$ . Expression (10.40) gives the inverse Omori law

$$E[X(t)|X(t_c) = \lambda_0]_{t < 0} \propto \frac{\lambda_0}{(t_c - t)^{1-\theta\beta/a}} \quad (10.41)$$

for foreshock activity prior to a mainshock occurring at time  $t_c$ . Note that the border case  $m = \beta/a = 2$  recovers our previous result (10.32) as it should.

The problem is that this derivation does not take into account the dependence between the fluctuations in the earthquake energies and the seismic rate, which become prominent precisely in this regime  $\beta/2 \leq a \leq \beta$ . We have not been able yet to fully solve this problem for arbitrary values  $a$  but can nevertheless predict that (10.41) must be replaced by

$$E[X(t)|X(0) = \lambda_0]_{t < 0} \propto \frac{\lambda_0}{|t|^{1+\theta}}, \quad \text{for } a \rightarrow \beta. \quad (10.42)$$

We follow step by step the reasoning from expression (10.35) to (10.40), with the following modifications imposed by the regime  $\beta/2 \leq a \leq \beta$ .

1. The conditional expectations given by (10.37) must be progressively changed into  $E[x_i|S_N] \propto S_N K_i$  as  $a \rightarrow \beta$ , due to the coupling between energy and seismic rate fluctuations (leading to (10.17) via the mechanism (10.18)). Indeed, the coupling between energy and seismic rate fluctuations gives rise to the dependence  $E[x_i|S_N] \propto K_i$  which becomes dominant over the conditional expectations given by (10.37) for  $m < 2$ .
2. As shown with (10.19), the dependence between the fluctuations in the earthquake energies and the seismic rate leads to change  $K(t) \propto 1/t^{1-\theta}$  into  $K(t) \propto 1/t^{1+\theta}$  as  $a \rightarrow \beta$  even in the regime  $t < t^*$ .

This leads finally to changing expressing (10.40) into

$$E[X(t)|X(0)] \sim \int_{-\infty}^t d\tau \frac{1}{|t-\tau+c|^{1+\theta}} \frac{\lambda_0}{|\tau|^{1+\theta}}, \quad (10.43)$$

where we have re-introduced the regularization constant  $c$  to ensure convergence for  $\tau \rightarrow t$ . Taking into account the contribution  $\propto t^\theta$  at this upper bound  $t$  of the integrand  $\propto 1/|t-\tau+c|^{1+\theta}$ , we finally get (10.42). This result is verified numerically in Figure 10.6.

### The inverse Omori law in the regime $t_c - t > t^*$

The inverse Omori laws derived in the two preceding sections are valid for  $t_c - t < t^*$ , that is, sufficiently close to the mainshock. A similar inverse Omori law is also obtained for  $t_c - t > t^*$ . In this goal, we use (10.15) showing that the propagator  $K(t-\tau) \propto 1/(t-\tau)^{1-\theta}$  must be replaced by  $K(t-\tau) \propto 1/(t-\tau)^{1+\theta}$  for time difference larger than  $t^*$ . It would however be incorrect to deduce that we just have to change  $-\theta$  into  $+\theta$  in expressions (10.32) and (10.41), because the integrals leading to these results behave differently : as in (10.43), one has to re-introduced the regularization constant  $c$  to ensure convergence for  $\tau \rightarrow t$  of  $1/|t-\tau+c|^{1+\theta}$ . The final results are thus given by (10.32) and (10.41) by changing  $-\theta$  into  $+\theta$  and by multiplying these expressions by the factor  $t^\theta$  stemming from the regularization  $c$ . Thus, in the large time limit  $t_c - t > t^*$  (far from the mainshock) of the subcritical regime, we also obtain an inverse Omori law which takes the form (10.27) for  $a < \beta/2$  and the form (10.28) for  $\beta/2 \leq a \leq \beta$ . These predictions are in good agreement with our numerical simulations.

## 10.4 Prediction for the Gutenberg-Richter distribution of foreshocks

We have just shown that the stochastic component of the seismic rate can be formulated as a sum of the form (10.36) of variables  $x_i$  distributed according to a power law with exponent  $m = \beta/a$  and weight  $K_i$ . It is possible to go beyond the derivation of the conditional expectation  $E[x_i|S_N]$  given by (10.37) and obtain the conditional distribution  $p(x_i|S_N)$  conditioned on a large value of the realization of  $S_N$ .

For this, we use the definition of conditional probabilities

$$p(x_i|S_N) = \frac{p(S_N|x_i)p(x_i)}{P_N(S_N)}, \quad (10.44)$$

where  $P_N(S_N)$  is the probability density function of the sum  $S_N$ . Since  $p(S_N|x_i)$  is simply given by

$$p(S_N|x_i) = P_{N-1}(S_N - K_i x_i), \quad (10.45)$$

we obtain

$$p(x_i|S_N) = p(x_i) \frac{P_{N-1}(S_N - K_i x_i)}{P_N(S_N)}. \quad (10.46)$$

This shows that the conditional Gutenberg-Richter distribution  $p(x_i|S_N)$  is modified by the conditioning according to the multiplicative correcting factor  $P_{N-1}(S_N - K_i x_i)/P_N(S_N)$ . For Large  $N$ ,  $P_N$  and  $P_{N-1}$  tend to stable Lévy distributions with the same index  $m$  but different scale factors equal respectively to  $\sum_j K_j^m$  and  $\sum_{j \neq i} K_j^m$ . The tail of  $p(x_i|S_N)$  is thus

$$p(x_i|S_N) \sim \left(1 - \frac{K_i^m}{\sum_j K_j^m}\right) \frac{1}{x_i^{1+m}} \frac{1}{(1 - (K_i x_i/S_N))^{1+m}}. \quad (10.47)$$

Since  $K_i x_i \ll S_N$ , we can expand the last term in the right-hand-side of (10.47) and obtain

$$p(x_i|S_N) \sim \left(1 - \frac{K_i^m}{\sum_j K_j^m}\right) \left[ \frac{1}{x_i^{1+m}} + (1+m)(K_i/S_N) \frac{1}{x_i^m} \right]. \quad (10.48)$$

Since  $x_i \sim E_i^a$ , we use the transformation property on distribution functions  $p(x_i)dX_i = p(E_i)dE_i$  to obtain the pdf of foreshock energies  $E_i$ . Going back to the continuous limit in which  $K_i/S_N \sim (t_c - t)^{-(1-\theta)}/(t_c - t)^{-(1-\beta\theta)} = 1/(t_c - t)^{(\beta-1)\theta}$ , we obtain the conditional Gutenberg-Richter distribution for foreshocks

$$P(E|\lambda_0) \sim \frac{E_0^\beta}{E^{1+\beta}} + \frac{C}{(t_c - t)^{\theta(\beta-a)/a}} \frac{E_0^{\beta'}}{E^{1+\beta'}} \quad (10.49)$$

where

$$\beta' = \beta - a, \quad (10.50)$$

and  $C$  is a numerical constant. The remarkable prediction (10.49) with (10.50) is that the Gutenberg-Richter distribution is modified upon the approach of a mainshock by developing a bump in its tail. This modification takes the form of an additive power law contribution with a new “ $b$ -value” renormalized/amplified by the exponent  $a$  quantifying the dependence of the number of daughters as a function of the energy of the mother. Our prediction is validated very clearly by numerical simulations reported in Figures 10.7 and 10.8.

## 10.5 Migration of foreshocks towards the mainshock

By the same mechanism leading to (10.32) via (10.29) and (10.30), conditioning the foreshock seismicity to culminate at a mainshock at time  $t_c$  at some point  $\vec{r}$  taken as the origin of space

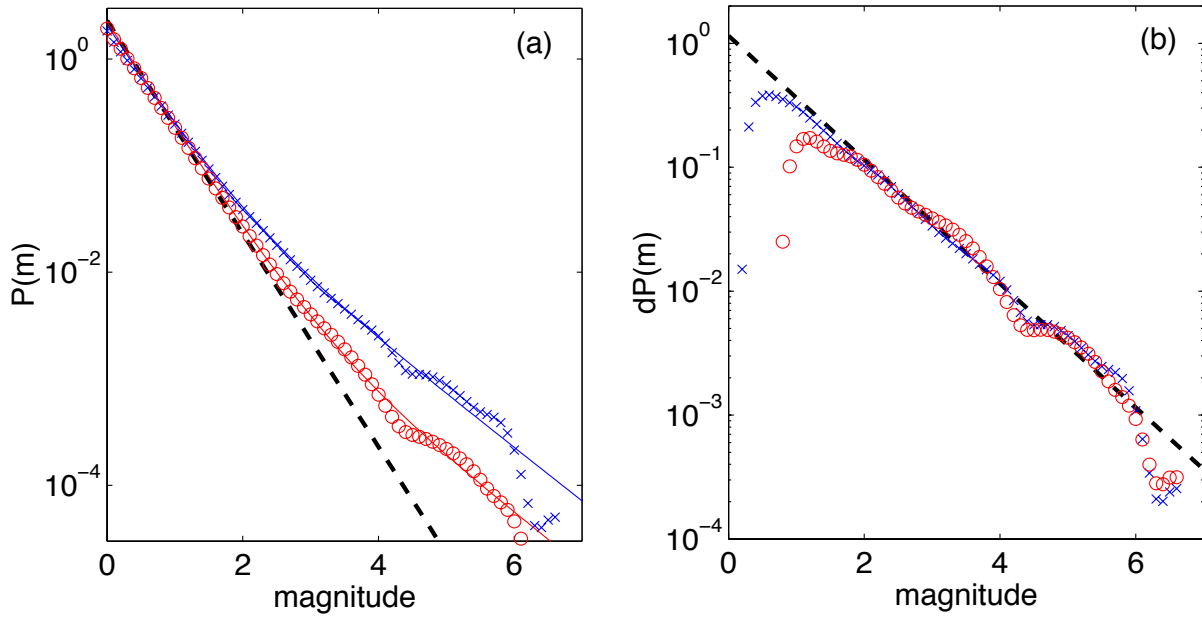


FIG. 10.7 – Magnitude distribution of foreshocks for two time periods :  $t_c - t < 0.1$  (crosses) and  $1 < t_c - t < 10$  (circles), for a numerical simulation of the ETAS model with parameters  $\theta = 0.2$ ,  $\beta = 2/3$ ,  $c = 10^{-3}$ ,  $m_0 = 2$  and  $a = \beta/2 = 1/3$ . The magnitude distribution  $P(m)$  shown on the first plot (a) has been built by stacking many foreshock sequences of magnitudes  $M > 2.5$  mainshocks. The observed magnitude distribution is in very good agreement with the prediction (10.49), shown as a solid line for each time period, that the magnitude distribution is the sum of the unconditional Gutenberg-Richter law with an exponent  $b = 1.5\beta = 1$ , shown as a dashed black line, and a deviatoric Gutenberg-Richter law  $dP(m)$  with an exponent  $b' = b - \alpha = 0.5$  with  $\alpha = 1.5a = 0.5$ . The amplitude of the perturbation increases if  $t_c - t$  decreases as expected from (10.49). The observed deviatoric magnitude distribution  $dP(m)$  is shown on plot (b) for the same time periods, and is in very good agreement with the prediction shown as a dashed black line. We must stress that the energy distribution is *no more* a pure power law close to the mainshock, but the sum of two power laws. The panel on the right exhibits the second power law which is created by the conditioning mechanism underlying the appearance of foreshocks. See text.

must lead to a migration towards the mainshock. The seismic rate  $\lambda(\vec{r}, t)$  at position  $\vec{r}$  at time  $t < t_c$  conditioned on the existence of the mainshock at position  $\vec{0}$  at time  $t_c$  is given by

$$E[\lambda(\vec{r}, t) | \lambda(\vec{0}, t_c)] \sim \int_{-\infty}^t d\tau \int d\vec{\rho} K(\vec{r} - \vec{\rho}, t - \tau) K(\vec{\rho}, t_c - \tau). \quad (10.51)$$

$K(\vec{r} - \vec{\rho}, t - \tau)$  is the dressed spatio-temporal propagator giving the seismic activity at position  $\vec{r}$  and time  $t$  resulting from a triggering earthquake that occurred at position  $\vec{\rho}$  at a time  $\tau$  in the past. Its expression is given in [Helmstetter and Sornette, 2002b] in a variety of situations. Assuming that the probability distribution for an earthquake to trigger an aftershock at a distance  $r$  is of the form

$$\rho(r) \sim 1/(r + d)^{1+\mu}, \quad (10.52)$$

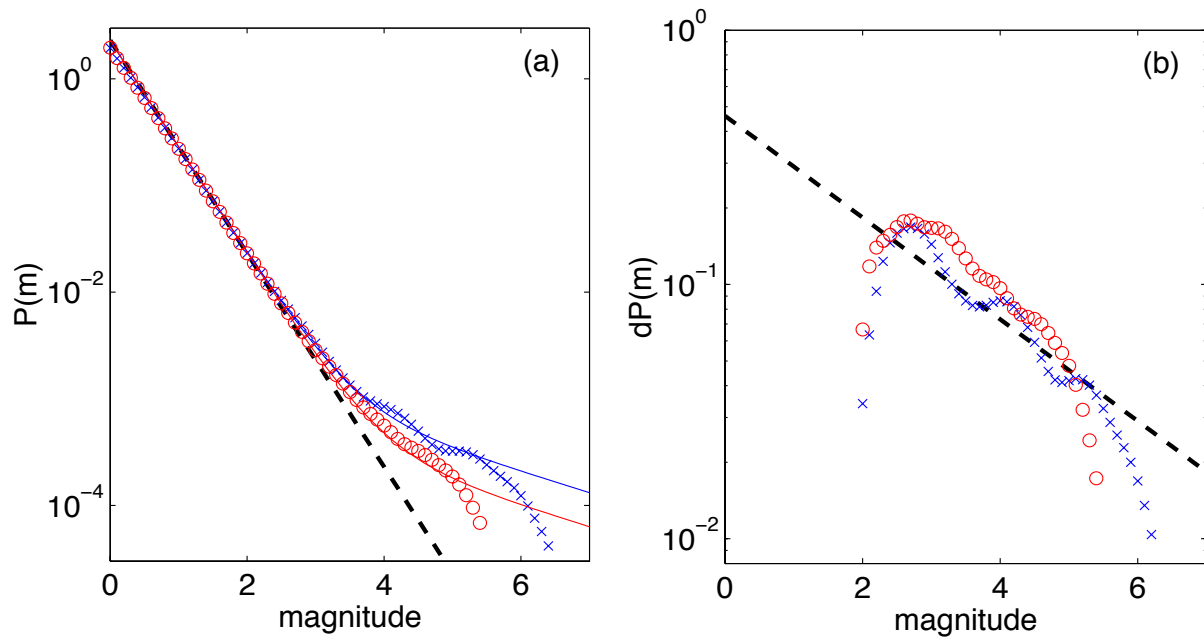


FIG. 10.8 – Same as Figure 10.7 but for  $a = 0.8\beta$ . In this case, the deviatoric Gutenberg-Richter contribution is observed only for the largest magnitudes, for which the statistics is the poorest, hence the relatively large fluctuations around the exact theoretical predictions.

[Helmstetter and Sornette, 2002b] have shown that the characteristic size of the aftershock area slowly diffuses according to  $R \sim t^H$ , where the time  $t$  is counted from the time of the mainshock. For simplicity,  $d$  is taken independent of the mainshock energy.  $H$  is the Hurst exponent characterizing the diffusion given by

$$H = \frac{\theta}{\mu} \quad \text{for } \mu < 2, \quad H = \frac{\theta}{2} \quad \text{for } \mu > 2. \quad (10.53)$$

This diffusion is captured by the fact that  $K(\vec{r} - \vec{\rho}, t - \tau)$  depends on  $\vec{r} - \vec{\rho}$  and  $t - \tau$  essentially through the reduced variable  $|\vec{r} - \vec{\rho}| / (t - \tau)^H$ . Then, expression (10.51) predicts that this diffusion must be reflected into an inward migration of foreshock seismicity towards the mainshock with the same exponent  $H$ .

These results are verified by numerical simulations of the ETAS model. Figure 10.9 presents the migration of foreshock activity for two numerical simulations of the ETAS model, with different parameters. As for the inverse Omori law, we have superposed many sequences of foreshock activity to observe the migration of foreshocks. For a numerical simulation with parameters  $n = 1$ ,  $\theta = 0.2$ ,  $\mu = 1$ ,  $d = 1$ ,  $c = 0.001$ ,  $a = 0.5\beta$  and  $m_0 = 2$ , we see clearly the localization of the seismicity as the mainshock approaches. We obtain an effective migration exponent  $H = 0.18$ , describing how the effective size  $R$  of the cloud of foreshocks shrinks as time  $t$  approaches the time  $t_c$  of the main shock :  $R \sim (t_c - t)^H$  (see Figure 10.9a,c). This result is in good agreement with the prediction  $H = 0.2$  given by (10.53). The spatial distribution of foreshocks around the mainshock is similar to the distribution of aftershocks around the main-

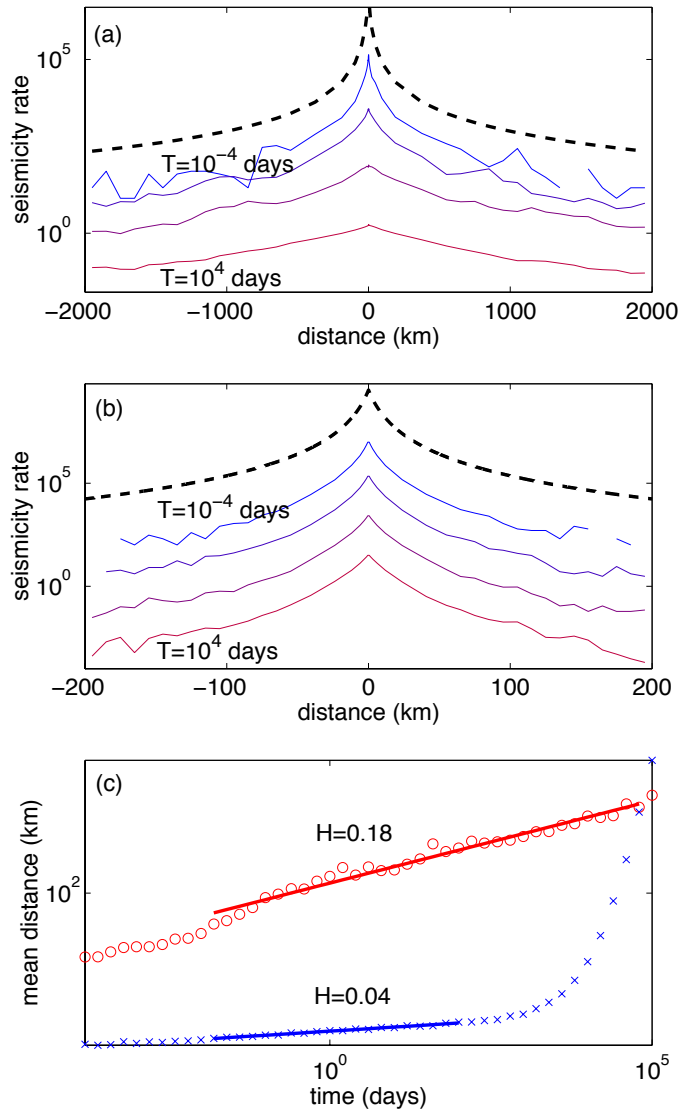


FIG. 10.9 – Migration of foreshocks, for superposed foreshock sequences generated with the ETAS model for two choices of parameters, (a)  $n = 1$ ,  $\theta = 0.2$ ,  $a = 0.5\beta$ ,  $\mu = 1$ ,  $d = 10$ ,  $c = 0.001$ ,  $m_0 = 2$  and (b)  $n = 1$ ,  $\theta = 0.02$ ,  $a = 0.5\beta$ ,  $\mu = 3$ ,  $d = 1$ ,  $c = 0.001$ ,  $m_0 = 2$ . The distribution of foreshock-mainshock distances is shown on panel (a) and (b) for the two simulations, for different time periods ranging between  $10^{-4}$  to  $10^4$  days. The distribution of mainshock-aftershock distances given by (10.52) describing direct lineage is shown as a dashed line for reference. On panel (a), we see clearly a migration of the seismicity towards the mainshock, as expected by the significant diffusion exponent  $H = 0.2$  predicted by (10.53). In contrast, the distribution of the foreshock-mainshock distances shown in panel (b) is independent of the time from the mainshock, as expected by the much smaller exponent diffusion  $H = 0.01$  predicted by (10.53). The characteristic size of the foreshock cluster is shown as a function of the time to the mainshock on panel (c) for the two numerical simulations. Circles correspond to the simulation shown in panel (a) and crosses correspond to the simulation shown in panel (b). The solid line is a fit of the characteristic size of the foreshock cluster by  $R \sim t^H$ . For the simulation generated with  $\theta = 0.2$  and  $\mu = 1$  (circles), we obtain  $H = 0.18 \pm 0.02$  in very good agreement with the prediction  $H = \theta/\mu = 0.2$  (10.53). The simulation generated with  $\theta = 0.02$  and  $\mu = 3$  (crosses) has a much smaller exponent  $H = 0.04 \pm 0.02$ , in good agreement with the expected value  $H = \theta/2 = 0.01$  (10.53). A faster apparent migration is observed at large times for this simulation, due to the transition from the uniform background distribution for large times preceding the mainshock to the clustered seismicity prior to the mainshock.

shock. Figure 10.9b,c presents the migration of foreshock activity for a numerical simulation with  $\theta = 0.01$ ,  $\mu = 1$ ,  $d = 1$ ,  $c = 0.001$  leading to a very small diffusion exponent  $H = 0.01$ . The analysis of this foreshock sequence gives an effective migration exponent  $H = 0.04$  for short times, and a faster apparent migration at longer times due to the influence of the background activity. See [Helmstetter and Sornette, 2002b] for a discussion of artifacts leading to apparent diffusions of seismicity resulting from various cross-over phenomena.

## 10.6 Discussion

It has been proposed for decades that many large earthquakes were preceded by an unusually high seismicity rate, for times of the order of weeks to months before the mainshock [Omori, 1908; Richter, 1958; Mogi, 1963]. Although there are large fluctuations in the foreshock patterns from one sequence to another one, some recurrent properties are observed.

- (i) The rate of foreshocks increases as  $1/(t_c - t)^{p'}$  as a function of the time to the main shock at  $t_c$ , with an exponent  $p'$  smaller than or equal to the exponent  $p$  of direct Omori law ;
- (ii) the Gutenberg-Richter distribution of magnitudes is modified as the mainshock approaches, and is usually modeled by a decrease in  $b$ -value ;
- (iii) The epicenters of the foreshocks seem to migrate towards the mainshock.

We must acknowledge that the robustness of these three laws decreases from (i) to (iii). In previous sections, we have shown that these properties of foreshocks derive simply from the two most robust empirical laws of earthquake occurrence, namely the Gutenberg-Richter and Omori laws, which define the ETAS model. In this ETAS framework, foreshock sequences emerge on average by conditioning seismicity to lead to a burst of seismicity at the time of the mainshock. This analysis differs from two others analytical studies of the ETAS model [Helmstetter and Sornette, 2002b; Sornette and Helmstetter, 2002], who proposed that accelerating foreshock sequences may be related either to the super-critical regime  $n > 1$  or to the singular regime  $a > \beta$  (leading formally to  $n \rightarrow \infty$ ) of the ETAS model. In these two regimes, an accelerating seismicity sequence arises from the cascade of aftershocks that trigger on average more than one aftershock per earthquake. Here we show that foreshock sequences emerge in the stationary sub-critical regime ( $n < 1$ ) of the ETAS model, when an event triggers on average less than one aftershock. In this regime, aftershock have a low probability of triggering a larger earthquake. Nonetheless, conditioning on a high seismicity rate at the time of the mainshock, we observe, averaging over many mainshocks, an increase of the seismicity rate following the inverse Omori law. In addition, as we shall show below, this increase of seismicity has a genuine and significant predictive power.

## Difference between type I and type II foreshocks

Our results applies to foreshocks of type II, defined as earthquakes preceding a mainshock in a space-time window preceding a mainshock, independently of their magnitude. This definition is different from the usual definition of foreshocks, which imposes a mainshock to be larger than the foreshocks (foreshocks of type I in our terminology). Using the usual definition of foreshocks in our numerical simulations of the ETAS model, our results remain robust but there are quantitative differences introduced by the somewhat arbitrary constraint entering into the definition of foreshocks of type I :

1. a roll-off in the inverse Omori-law,
2. a dependence of the apparent exponent  $p'$  on the time window used to define foreshocks and mainshocks and
3. a dependence of the rate of foreshocks and of  $p'$  on the mainshock magnitude.

As seen in Figure 10.5, these variations between foreshocks of type I and type II are observed only for small mainshocks. Such foreshocks are less likely the foreshocks of a mainshock and are more likely to be preceded by a larger earthquake, that is, to be the aftershocks of a large preceding mainshock. These subtle distinctions should attract the attention of the reader on the arbitrariness underlying the definition of foreshocks of type I and suggest, together with our results, that foreshocks of type II are more natural objects to define and study in real catalogs. This will be reported in a separate presentation.

## Inverse Omori law

Conditioned on the fact that a mainshock is associated with a burst of seismicity, the inverse Omori law arises from the expected fluctuations of the seismicity rate leading to this burst of seismicity. Depending on the branching ratio  $n$  and on the ratio  $a/\beta$ , the exponent  $p'$  is found to vary between  $1 - 2\theta$  and  $1 + \theta$ , but is always found to be smaller than the exponent  $p$  of the direct Omori law. Our results thus reproduce both the variability of  $p'$  and the lower value measured for  $p'$  than for  $p$  reported by [Papazachos, 1973, 1975b; Page, 1986; Kagan and Knopoff, 1978; Jones and Molnar, 1979; Davis and Frohlich, 1991; Shaw, 1993; Utsu et al., 1995; Ogata et al., 1995; Maeda, 1999]. In their synthesis of all  $p$  and  $p'$  values Utsu et al. [1995] report  $p'$ -value in the range 0.7-1.3, while  $p$  of aftershocks ranges from 0.9 to 1.5. The few studies that have measured simultaneously  $p$  and  $p'$  using a superposed epoch analysis have obtained  $p'$  either roughly equal to  $p$  [Kagan and Knopoff, 1978; Shaw, 1993] or smaller than  $p$  [Davis and Frohlich, 1991; Ogata et al., 1995; Maeda, 1999]. The finding that  $p \approx p' \approx 1$  suggested by [Shaw, 1993; Reasenber, 1999] for the California seismicity can be interpreted in our framework as either due to a very small value  $\theta$ , or due to a large  $a/\beta$  ratio close to 0.8, as shown in Figures 10.4 and 10.6. The result  $p' < p$  reported by [Maeda, 1999] for the Japanese seismicity and by [Davis and Frohlich, 1991] for the worldwide seismicity can be related to a rather small  $a/\beta$  ratio, as also illustrated

in Figures 10.3 and 10.6.

In contrast with the direct Omori law, which is clearly observed after all large shallow earthquakes, the inverse Omori law is an average statistical law, which is observed only when stacking many foreshock sequences. Simulations reported in Figure 10.2 illustrate that, for individual foreshock sequences, the inverse Omori law is difficult to capture. Similarly to what was done for real data [*Kagan and Knopoff*, 1978; *Jones and Molnar*, 1979; *Davis and Frohlich*, 1991; *Shaw*, 1993; *Ogata et al.*, 1995; *Maeda*, 1999; *Reasenberg*, 1999], the inverse Omori law emerges clearly in our model only when using a superposed epoch analysis to average the seismicity rate over a large number of sequences. Our results are thus fundamentally different from the critical point theory [*Sammis and Sornette*, 2002] which leads to a power-law increase of seismic activity preceding each single large earthquake over what is probably a larger space-time domain [*Keilis-Borok and Malinovskaya*, 1964; *Bowman et al.*, 1998]. Our results can thus be considered as providing a null-hypothesis against which to test the critical point theory.

### Foreshock occurrence rate

In term of occurrence rate, foreshocks are less frequent than aftershocks (e.g. [*Kagan and Knopoff*, 1976, 1978; *Jones and Molnar*, 1979]). The ratio of foreshock to aftershock numbers is close to 2-4 for  $M = 5 - 7$  mainshocks, when selecting foreshocks and aftershocks at a distance  $R = 50 - 500$  km from the mainshock and for a times  $T = 10 - 100$  days before or after the mainshock [*Kagan and Knopoff* 1976; 1978; *Jones and Molnar*, 1979; *von Seggern et al.*, 1981; *Shaw*, 1993]. In our simulations, large mainshocks have significantly more aftershocks than foreshocks, in agreement with observations, while small earthquakes have roughly the same number of foreshocks (of type II) and of aftershocks. The ratio of aftershocks to foreshock of type II increases if the ratio  $a/\beta$  decreases, as observed when comparing the case  $a = 0.5\beta$  shown in Figure 10.3 with the results obtained in the case  $a = 0.8\beta$  represented in Figure 10.4. This may be explained by the relatively larger weights of the largest earthquakes which increase with increasing  $a$ , and by our definition of aftershocks and foreshocks : recall that aftershock sequences are conditioned on not being preceded by an event larger than the mainshock, whereas a foreshock of type II can be larger than the mainshock. Thus, for large  $a/\beta < 1$ , most “mainshocks”, according to our definition, are aftershocks of a preceding large earthquake, whereas aftershock sequences cannot be preceded by an earthquake larger than the mainshock.

The retrospective foreshock frequency, that is, the fraction of mainshocks that are preceded by a foreshock, is reported to range from 10% to 40% using either regional or worldwide catalogs [*Jones and Molnar*, 1979; *von Seggern et al.*, 1981; *Yamashina*, 1981; *Console et al.*, 1983; *Jones*, 1984; *Agnew and Jones*, 1991; *Lindh and Lim*, 1995; *Abercrombie and Mori*, 1996; *Michael and Jones*, 1998; *Reasenberg*, 1999]. The variability of the foreshock rate is closely related to the catalog threshold for the magnitude completeness for the small events [*Reasenberg*, 1999]. These results are in line with our simulations.

The observed number of foreshocks per mainshock slowly increases with the mainshock magnitude [e.g. data from *Kagan and Knopoff, 1978; Shaw, 1993; Reasenberg, 1999*]. In our model, the number of foreshocks of type II is independent of the mainshock magnitude, because the magnitude of each earthquake is independent of the previous seismicity history. An increase of the number of foreshocks of type I as a function of the mainshock magnitude is observed in our numerical simulations (see Figure 10.5) because, as we explained before, the constraint on the foreshock magnitudes to be smaller than the mainshock magnitude is less severe for larger earthquakes and thus filter out less foreshocks. Therefore, our results can explain the increase in the foreshock frequency with the mainshock magnitude reported using foreshocks of type I. The slow increase of the number of foreshocks with the mainshock magnitude, if any, is different from the predictions of both the nucleation model [*Dodge et al., 1996*] and of the critical point theory [*Sammis and Sornette, 2002*] which predict an increase of the foreshocks rate and of the foreshock zone with the mainshock size.

### Magnitude distribution of foreshocks

Many studies have found that the apparent  $b$ -value of the magnitude distribution of foreshocks is smaller than that of the magnitude distribution of the background seismicity and of aftershocks. Case histories analyze individual foreshock sequences, most of them being chosen a posteriori to suggest that foreshock patterns observed in acoustic emissions preceding rupture in the laboratory could apply to earthquakes [*Mogi, 1963; 1967*]. A few statistical tests validate the significance of reported anomalies on  $b$ -value of foreshocks. A few others studies use a stacking method to average over many sequences in order to increase the number of events.

A  $b$ -value anomaly, usually a change in the mean  $b$ -value, for earthquakes preceding a mainshock has been proposed as a possible precursor on many retrospective case studies [*Suyehiro, 1966; Papazachos et al., 1967; Ikegami, 1967; Berg, 1968; Bufe, 1970; Fedotov et al., 1972; Wyss and Lee, 1973; Papazachos, 1975a,b; Ma, 1978; Li et al., 1978; Wu et al. 1978; Cagnetti and Pasquale, 1979; Stephens et al., 1980; Smith, 1981, 1986; Imoto 1991; Enescu and Kito, 2001*]. Most case histories argue for a decrease of  $b$ -value, but this decrease, if any, is sometimes preceded by an increase of  $b$ -value [*Ma, 1978; Smith, 1981, 1986; Imoto 1991*]. In a couple of cases, temporal decreases in  $b$ -value before Chinese earthquakes were used to issue successful predictions [*Wu et al., 1978; Zhang et al., 1999*].

Because of the paucity of the foreshock numbers, most of the study of individual sequences does not allow to estimate a robust temporal change of  $b$ -values before mainshocks, nor to characterize the shape of the magnitude distribution. A few studies have demonstrated the statistical significance of decreases of  $b$ -value when the time to the mainshock decreases using a superposed epoch analysis [*Kagan and Knopoff, 1978; Molchan and Dmitrieva, 1990; Molchan et al., 1999*]. Using 200 foreshocks sequences of regional and worldwide seismicity, *Molchan et al.* [1999] found that the  $b$ -value is divided by a factor approximately equal to 2 a few days or

hours before the mainshock. *Knopoff et al.* [1982] found no significant differences between the  $b$ -value of aftershocks and foreshocks when investigating 12 individual sequences of California catalogs. When all the aftershocks and foreshocks in a given catalog are superposed, the same study showed for catalogs of large durations (e.g. ISC, 1964-1977 ; NOAA, 1965-1977) that the  $b$ -value for foreshocks is significantly smaller than the  $b$ -value for aftershocks [*Knopoff et al.*, 1982]. The same pattern being simulated by a branching model for seismicity, *Knopoff et al.* [1982] surmise that the observed and simulated changes in magnitude distribution value arises intrinsically from the conditioning of aftershocks and foreshocks and from the smaller numbers of foreshocks relatively to aftershocks numbers when counted from the mainshock time. The result of [*Knopoff et al.*, 1982] is often cited as disproving the reality of a change of  $b$ -value. Our results find that a change in  $b$ -value in the ETAS branching model of seismicity is a physical phenomenon with real precursory content. This shall be stressed further below in association with Figure 10.10. Therefore, the fact that a change in  $b$ -value can be reproduced by a branching model of seismicity cannot discredit the strong empirical evidence of a change of  $b$ -value [*Knopoff et al.*, 1982] and its genuine physical content capturing the interactions between and triggering of earthquakes.

The observed modification of the magnitude distribution of foreshocks is usually interpreted as a decrease of  $b$ -value as the mainshock approaches. However, some studies argue that the Gutenberg-Richter distribution before a mainshock is no more a pure power-law distribution, due to an apparent increase of the number of large events relatively to the Gutenberg-Richter law, while the rate of small earthquakes remains constant. Such pattern is suggested by *Rotwain et al.* [1997] for both acoustic emission preceding material failure, and possibly for Californian seismicity preceding large earthquakes. Analysis of seismicity before recent large shocks also argue for an increase in the rate of moderate and large earthquakes before a mainshock [*Jaumé and Sykes*, 1999]. *Knopoff et al.* [1982] also suspected a deviation from a linear Gutenberg-Richter distribution for foreshocks. Our study of the ETAS model confirms that such a modification of the magnitude distribution before a mainshock must be expected when averaging over many foreshock sequences.

Intuitively, the modification of the magnitude distribution arises in our model from the increase of the aftershock rate with the mainshock magnitude. Any event has thus a higher probability to occur just after a large event, because this large event induces an increase of the seismicity rate. The novel properties that we demonstrate is that, before a mainshock, the energy distribution is no more a pure power-law, but it is the sum of the unconditional distribution with exponent  $\beta$  and an additional deviatoric power-law distribution with a smaller exponent  $\beta' = \beta - a$  as seen from expression (10.49). In addition, we predict and verify numerically in figures 10.7 and 10.8 that the amplitude of the deviatoric term increases as a power-law of the time to the mainshock. A similar behavior has been proposed as a precursory pattern termed “pattern upward bend” [*Keilis-Borok et al.*, 2001] or alternatively providing “pattern

$\gamma$ ” measured as the difference between the slope of the Gutenberg-Richter for low and for large magnitudes. According to our results, pattern  $\gamma$  should increase from 0 to the value  $a$ .

According to the ETAS model, the modification of the magnitude distribution is independent of the mainshock magnitude, as observed by [Kagan and Knopoff, 1978; Knopoff et al. 1982; Molchan and Dmitrieva, 1990; Molchan et al., 1999]. Therefore, all earthquakes, whatever their magnitude, are preceded on average by an increase of the rate of large events. Although the foreshock magnitude distribution is no more strictly speaking a pure power-law but rather the sum of two power laws, a single power-law distribution with a decreasing  $b$ -value as the time of the mainshock is approached is a simple and robust way to quantify the increasing importance of the tail of the distribution, especially for the short foreshock sequences usually available. This rationalizes the suggestion found in many works that a decrease in  $b$ -value is a (retrospective) signature of an impending mainshock. The novel insight provided by our analysis of the ETAS model is that a better characterization of the magnitude distribution before mainshocks may be provided by the sum of two power law distributions expressed by equation (10.49) and tested in synthetic catalogs in Figures 10.7 and 10.8. This rationalizes both the observed relatively small  $b$ -values reported for foreshocks and the apparent decrease of  $b$ -value when the mainshock approaches. Similarly to the inverse Omori law, the modification of the magnitude distribution prior the mainshock is a statistical property which yields a unambiguous signal, only when stacking many foreshock sequences. This may explain the variability of the patterns of  $b$ -value observed for individual foreshock sequences.

A modification of the magnitude distribution before large earthquakes is also expected from the critical point theory [Sammis and Sornette, 2002]. The energy distribution far from a critical point is characterized by a power-law distribution with an exponential roll-off. As the seismicity evolves towards the critical point, the truncation of the energy distribution increases. At the critical point, the average energy becomes infinite (in an infinite system) and the energy distribution follows a pure power-law distribution. This modification of the seismicity predicted by the critical point theory is different from the one reported in this study, but the two models yield an apparent decrease of  $b$ -value with the time from the mainshock. Therefore, it is difficult to distinguish the two models in real seismicity data. However, the difference between the two models is that a modification of the energy distribution should only be observed before major earthquakes according to the critical point theory. Of course, one can not exclude that both mechanisms occur and are mixed up in reality.

## Implications for earthquake prediction

The inverse Omori law and the apparent decrease of  $b$ -value have been derived in this study as statistical laws describing the average fluctuations of seismicity conditioned on leading to a burst of seismicity at the time of the mainshock. This does not mean that there is not a genuine physical content in these laws. We now demonstrate that they may actually embody an

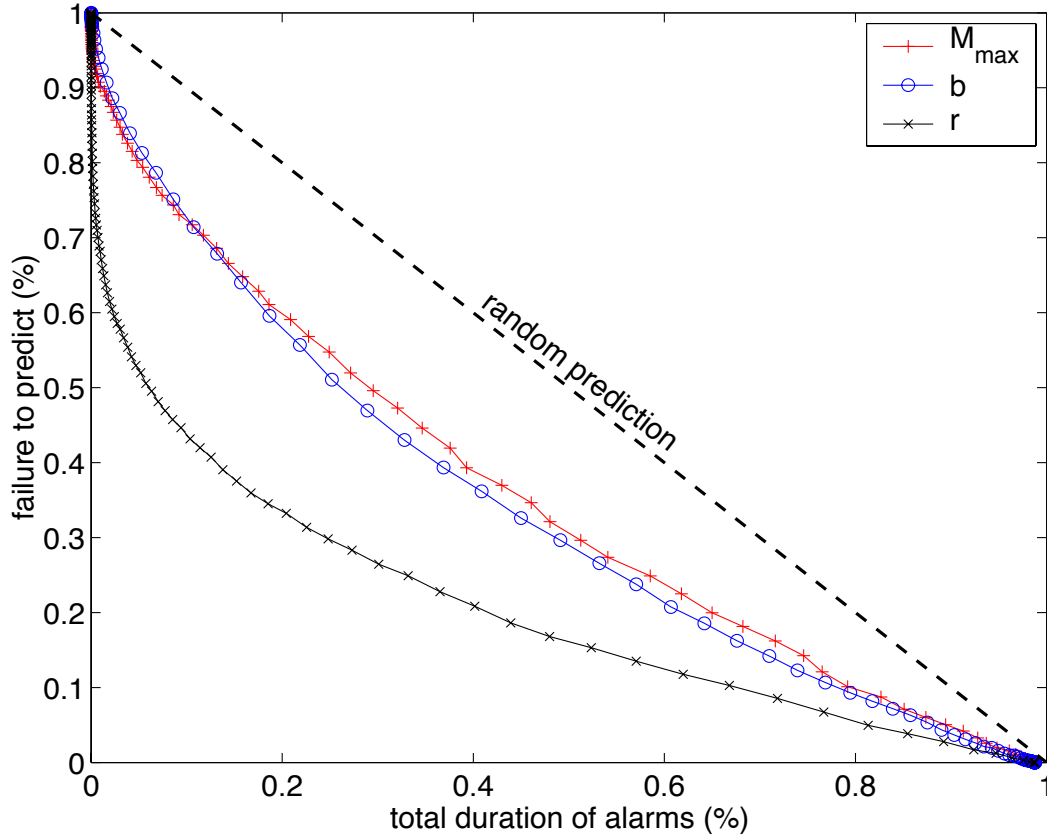


FIG. 10.10 – Results of prediction tests for synthetic catalogs generated with the parameters  $a = 0.5\beta$ ,  $n = 1$ ,  $\beta = 2/3$ ,  $\theta = 0.2$  and a constant source  $\mu = 0.001$ . The minimum magnitude is  $m_0 = 3$  and the target events are  $M \geq 6$  mainshocks. We have generated 500 synthetic catalogs of 10000 events each, leading to a total of 4735  $M \geq 6$  mainshocks. We use three functions measured in a sliding window of 100 events : (i) the maximum magnitude  $M_{max}$  of the 100 events in that window, (ii) the apparent Gutenberg-Richter exponent  $\beta$  measured on these 100 events by the standard Hill maximum likelihood estimator and (iii) the seismicity rate  $r$  defined as the inverse of the duration of the window. For each function, we declare an alarm when the function is either larger (for  $M_{max}$  and  $r$ ) or smaller (for  $\beta$ ) than a threshold. Once triggered, each alarm remains active as long as the function remains larger (for  $M_{max}$  and  $r$ ) or smaller (for  $\beta$ ) than the threshold. Scanning all possible thresholds constructs the continuous curves shown in the error diagram. The quality of the predictions is measured by plotting the ratio of failures to predict as a function of the total durations of the alarms normalized by the duration of the catalog. The results for these three functions are considerably better than those obtained for a random prediction, shown as a dashed line for reference. The best results are obtained using the seismicity rate. Predictions based on the Gutenberg-Richter  $\beta$  and on the maximum magnitude observed within the running window provide similar results.

important part of the physics of earthquakes and describe the process of interactions between and triggering of earthquakes by other earthquakes. For this purpose, we use the modification of the magnitude frequency and the increase of the seismicity rate as predicting tools of future individual mainshocks. In the present work, we restrict our tests to the ETAS branching model used as a playing ground for our ideas.

Using numerical simulations of the ETAS model generated with  $b = 1$ ,  $a = 0.5\beta$ ,  $n = 1$ ,  $m_0 = 3$  and  $\theta = 0.2$ , we find that large earthquakes occur more frequently following a small locally estimated  $b$ -value. We have measured the  $b$ -value using a maximum likelihood method for a sliding window of 100 events. For instance, we find that 29% of the large  $M > 6$  mainshocks occur in a 11% time period where  $\beta$  is less than 95% of the actual  $b$ -value (that is  $b < 0.95$ ). This leads a significant prediction gain of  $g = 2.7$ , defined as the ratio of the successful prediction (29%) over the duration of the alarms (11%) [Aki, 1981]. A random prediction would lead  $g = 1$ .

A much larger gain can be obtained using other precursory indicators related to the inverse Omori law. First, a large earthquake is likely to occur following another large earthquake. For the same simulation, fixing an alarm if the largest event within the 100 preceding earthquakes is larger than  $M = 6$  yields a probability gain  $g = 10$  for the prediction of a mainshock of magnitude equal to or larger than  $M = 6$ . Second, a large seismicity rate observed at a given “present” time will lead on average to a large seismicity rate in the future, and thus it increases the probability of having a large earthquake. Measuring the seismicity rate over a sliding window with flexible length imposed to contain exactly 100 events and fixing the alarm threshold at 0.05 events per day, we are able to predict 20% of the  $M \geq 6$  events with just 0.16% of the time period covered by the alarms. This gives a prediction gain  $g = 129$ .

Figure 10.10 synthesizes and extends these results by showing the so-called error diagram [Molchan, 1991 ; 1997] for each of three functions measured in a sliding window of 100 events : (i) the maximum magnitude  $M_{max}$  of the 100 events in that window, (ii) the apparent Gutenberg-Richter exponent  $\beta$  measured on these 100 events by the standard Hill maximum likelihood estimator and (iii) the seismicity rate  $r$  defined as the inverse of the duration of the window. For each function, an alarm is declared for the next event when the function is either larger (for  $M_{max}$  and  $r$ ) or smaller (for  $\beta$ ) than a threshold. Scanning all possible thresholds constructs the continuous curves shown in the figure. The results on the prediction obtained by using these three precursory functions are considerably better than those obtained for a random prediction, shown as a dashed line for reference. We have not tried at all to optimize any facet of these prediction tests, which are offered for the sole purpose of stressing the physical reality of the precursory information contained in the foreshocks.

## Migration of foreshocks

Among the proposed patterns of foreshocks, the migration of foreshocks towards the mainshocks is much more difficult to observe than either the inverse Omori law or the change in

$b$ -value. This is due to the limited number of foreshocks and to the location errors. Similarly to other foreshock patterns, a few case-histories have shown seismicity migration before a mainshock. When reviewing 9  $M > 7$  shallow earthquakes in China, *Ma et al.* [1990] report a migration of  $M > 3 - 4$  earthquakes towards the mainshock over a few years before the mainshock and at a distance of a few hundreds of kilometers. Less than 20 events are used for each case study. While the case for the diffusion of aftershocks is relatively strong [*Kagan and Knopoff*, 1976, 1978; *von Seggern et al.*, 1981; *Tajima and Kanamori*, 1985] but still controversial, the migration of foreshocks towards the mainshock area, suggested using a stacking method [e.g., *Kagan and Knopoff*, 1976, 1978; *von Seggern et al.*, 1981; *Reasenber*, 1985] is even less clearly observed.

Using the ETAS model, *Helmstetter and Sornette* [2002b] have shown that the cluster of aftershocks diffuses on average from the mainshock according to the diffusion law  $R \sim t^H$ , where  $R$  is the typical size of the cluster and  $H$  is the so-called Hurst exponent which can be smaller or larger than  $1/2$ . In the present study, we have shown analytically and numerically that this diffusion of aftershocks must be reflected into a (reverse) migration of seismicity towards the mainshock, with the same diffusion exponent  $H$  (defined in (10.53)). We should however point out that this predicted migration of foreshocks, as well as the diffusion of aftershocks, is significant only over a finite domain of the parameter space over which the ETAS model is defined. Specifically, a significant spatio-temporal coupling of the seismicity leading to diffusion and migration is expected and observed in our simulations only for sufficiently large  $\theta$ 's and for short times  $|t_c - t| < t^*$  from the mainshock, associated with a direct Omori exponent  $p$  smaller than 1. This may explain why the diffusion of aftershocks and the migration of foreshocks is often difficult to observe in real data.

An additional difficulty in real data arises from the background seismicity, which can induce a spurious diffusion of aftershocks or migration of foreshocks (see Figure 10.9c). As for the other foreshock patterns derived in this study, the migration of foreshocks towards the mainshock and the spatial distribution of foreshocks are independent of the mainshock magnitude. These results disagree with the observations of [*Keilis-Borok and Malinovskaya*, 1964; *Bowman et al.*, 1998] who suggest that the area of accelerating seismicity prior a mainshock increases with the mainshock size. An increase of the foreshock zone with the mainshock size may however be observed in the ETAS model when using foreshocks of type I (conditioned on being smaller than the mainshock) and introducing a characteristic size of the aftershock zone  $d$  in (10.52) increasing with the mainshock size.

## 10.7 Conclusion

We have shown that the ETAS (epidemic-type aftershock) branching model of seismicity, based on the two best established empirical Omori and Gutenberg-Richter laws, contains es-

essentially all the phenomenology of foreshocks. Using this model, decades of empirical studies on foreshocks are rationalized, including the inverse Omori law, the  $b$ -value change and seismicity migration. For each case, we have derived analytical solutions that relates the foreshock distributions in the time, space and energy domain to the properties of a simple earthquake triggering process embodied by aftershocks. We find that all previously reported properties of foreshocks arises from the Omori and Gutenberg-Richter law when conditioning the spontaneous fluctuations of the rate of seismicity to end with a burst of activity, which defines the time of the mainshock. The foreshocks laws are seen as statistical laws which are clearly observable when averaging over a large number of sequences and should not be observed systematically when looking at individual foreshock sequences. Nevertheless, we have found that foreshocks contain genuine important physical information of the triggering process and may be used successfully to predict earthquakes with very significant probability gains. Taking these results all together, this suggests that the physics of aftershocks is sufficient to explain the properties of foreshocks, and that there is no essential physical difference between foreshocks, aftershocks and mainshocks.

## 10.8 Appendix A : Deviations from the average seismicity rate

Using the definition of  $\lambda(t)$  (10.7), in the case where the external  $s(t)$  source term is a Dirac  $\delta(t)$ , we obtain the following expression for the stochastic propagator

$$\kappa(t) = \delta(t) + \int_{-\infty}^t d\tau \int_{E_0}^{+\infty} dE \phi_E(t - \tau) \sum_{i | t_i \leq t} \delta(E - E_i) \delta(\tau - t_i) , \quad (10.54)$$

We now express the deviation of  $\kappa(t)$  from its ensemble average  $K(t)$ . This can be done by using (10.11), which means that the distribution density of earthquake energies is constructed by recording all earthquakes and by counting the frequency of their energies. Thus,  $\delta(E - E_\tau)$  can be seen as the sum of its average plus a fluctuation part, namely, it can be formally expressed as  $\delta(E - E_\tau) = P(E) + \delta P(E)$ , where  $\delta P(E)$  denotes the fluctuation of  $\delta(E - E_\tau)$  around its ensemble average  $P(E)$ . Similarly,  $\kappa(t) = \sum_{t_i \leq t} \delta(t - t_i) = K(t) + \delta\kappa(t)$ , where  $\delta\kappa(t)$  is the fluctuating part of the seismic rate around its ensemble average  $K(t)$ .

We can thus express the sum of products of Dirac functions in (10.54) as follows :

$$\sum_{i | t_i \leq t} \delta(E - E_i) \delta(t - t_i) = P(E)K(t) + \delta(P\kappa)(E, t) . \quad (10.55)$$

As a first illustration, we can use the approximation that the fluctuations of the product  $\delta(E - E_\tau) \sum_{t_i \leq t} \delta(t - t_i)$  can be factorized to write

$$\begin{aligned} \delta(E - E_t) \sum_{t_i \leq t} \delta(t - t_i) &= (P(E) + \delta P(E)) (K(t) + \delta\kappa(t)) \\ &\approx P(E)K(t) + P(E) \delta\kappa(t) + K(t) \delta P(E) . \end{aligned} \quad (10.56)$$

Using expression (10.54) for  $\kappa(t)$  and expression (10.14) for  $K(t)$ , and putting (10.56) in (10.54), we then obtain

$$\kappa(t) = K(t) + \int_0^t d\tau \int_{E_0}^{+\infty} dE \phi_E(t - \tau) \delta(P\kappa)(E, \tau) , \quad (10.57)$$

where

$$\delta(P\kappa)(E, \tau) \equiv \delta P(E)K(\tau) + P(E)\delta\kappa(t) . \quad (10.58)$$

By construction, the average of the double integral in the r.h.s. of (10.57) is zero. The double integral thus represents the fluctuating part of the realization specific seismic response  $\kappa(t)$  to a triggering event. Inserting (10.57) in (10.21), we obtain

$$\begin{aligned} \lambda(t) = N(t) + \\ \int_{-\infty}^t d\tau s(\tau) \int_0^{t-\tau} du \int_{E_0}^{+\infty} dE \phi_E(t - \tau - u) \delta(P\kappa)(E, u) . \end{aligned} \quad (10.59)$$

Using  $\int_{-\infty}^t d\tau \int_0^{t-\tau} du = \int_0^{+\infty} du \int_{-\infty}^{t-u} d\tau$ , expression (10.59) reads

$$\begin{aligned} \lambda(t) = N(t) + \\ \int_{E_0}^{+\infty} dE \int_0^{+\infty} du \delta(P\kappa)(E, u) \int_{-\infty}^{t-u} d\tau s(\tau) \phi_E(t - \tau - u) . \end{aligned} \quad (10.60)$$

For instance, let us consider the first contribution  $\delta P(E)K(\tau)$  of  $\delta(P\kappa)(E, \tau)$  given by (10.58). Denoting

$$\epsilon \equiv \int_{E_0}^{+\infty} dE \rho(E) \delta P(E) , \quad (10.61)$$

$\lambda(t)$  given by (10.60) is of the form (10.22) with

$$\eta(\tau) = \epsilon \int_0^{+\infty} dx s(\tau - x) \Psi(x) , \quad (10.62)$$

where  $\Psi(x)$  is the bare Omori propagator defined in (10.4).

The only property needed below is that the stochastic process  $\eta(\tau)$  be stationary. This is the case because the fluctuations of  $\delta P(E)$  and of the source  $s(t)$  are stationary processes. Similarly, the second contribution  $P(E)\delta\kappa(\tau)$  of  $\delta(P\kappa)(E, \tau)$  given by (10.58) takes the form (10.22) if  $\delta\kappa(\tau)$  is a noise proportional to  $K(t)$ . At present, we cannot prove it but this seems a natural assumption. More generally, one could avoid the decomposition of  $\delta(P\kappa)(E, \tau)$  given by (10.58) and get the same result as long as  $\delta(P\kappa)(E, t)$  is equal to a stationary noise multiplying  $K(t)$ .

## 10.9 Appendix B : Conditioning weighted power law variables on the realization of their sum

Consider i.i.d. (identically independently distributed) random variables  $x_i$  distributed according to a power law  $p(x_i)$  with exponent  $m \leq 2$ . Let us define the sum

$$S_N = \sum_{i=1}^N K_i x_i , \quad (10.63)$$

where the  $K_i$ 's are arbitrary positive weights. Here, we derive that the expectation  $E[x_i|S_N]$  of  $x_i$  conditioned on the existence of a large realization of  $S_N$  is given by (10.37).

By definition,  $E[x_i|S_N] = N/D$  where

$$N = \int dx_1 \dots \int dx_N x_i p(x_1)\dots p(x_N) \delta \left( S_N - \sum_{j=1}^N K_j x_j \right), \quad (10.64)$$

and  $D$  is the same expression without the factor  $x_i$ . The Fourier transform of (10.64) with respect to  $S_N$  yields

$$\hat{N}(k) = \left[ \prod_{j \neq i} \hat{p}(kK_j) \right] \frac{1}{ik} \frac{d\hat{p}(kK_i)}{dK_i} = \frac{1}{ik} \frac{d}{dK_i} \left[ \prod_{j=1}^N \hat{p}(kK_j) \right]. \quad (10.65)$$

We have used the identity  $\int dx_i x_i p(x_i) e^{ikK_i x_i} = \frac{1}{ik} \frac{d\hat{p}(kK_i)}{dK_i}$  and  $\hat{p}(k)$  is the Fourier transform of  $p(x)$ . Note that  $\prod_{j=1}^N \hat{p}(kK_j)$  is nothing but the Fourier transform  $\hat{P}_S(k)$  of the distribution  $P_N(S_N)$ . Using the elementary identities of derivatives of Fourier transforms and by taking the inverse Fourier transform, we thus get

$$N = \frac{d}{dK_i} \int_{S_N}^{+\infty} dX P_N(X). \quad (10.66)$$

By definition, the denominator  $D$  is identically equal to  $P_N(S_N)$ . This yields the general result

$$E[x_i|S_N] = \frac{1}{P_N(S_N)} \frac{d}{dK_i} \int_{S_N}^{+\infty} dX P_N(X). \quad (10.67)$$

In the special case where all  $K_i$ 's are equal, this gives the ‘‘democratic’’ result  $E[x_i|S_N] = S_N/N$ .

For power law variables with distribution  $p(x) \sim 1/x^{1+m}$  with  $m < 2$ , we can use the generalized central limit theorem to obtain that  $P_N(X)$  converges for large  $N$  to a stable Lévy law  $L_m$  with index equal to the exponent  $m$  and scale factor  $\sum_{j=1}^N K_j^m$  [Gnedenko and Kolmogorov, 1954; Sornette, 2000] :

$$P_N(S_N) \rightarrow_{N \rightarrow \infty} L_m \left( \frac{S_N}{\left( \sum_{j=1}^N K_j^m \right)^{1/m}} \right). \quad (10.68)$$

The only dependence of  $P_N(S_N)$  in  $K_i$  is found in the scale factor. Putting the expression (10.68) into (10.67) yields the announced result (10.37). In particular, for  $m = 2$ , this recovers the standard result for Gaussian variables that  $E[x_i|S_N] \sim S_N K_i$ , because the stable Lévy law of index  $m = 2$  is the Gaussian distribution.

## Acknowledgments

We are very grateful to Y.Y. Kagan, G. Ouillon and V. Pisarenko for useful suggestions and discussions. This work was partially supported by french INSU-Natural Hazard grant (AH and JRG) and by the James S. Mc Donnell Foundation 21st century scientist award/studying complex system (DS).



# Chapitre 11

## Observations of the inverse Omori's law for foreshocks

In the previous chapter we have shown that a simple stochastic model including only the properties of aftershocks, (i) the direct Omori law, (ii) the Gutenberg-Richter distribution of magnitudes with a constant  $b$  for all events and (iii) an increase of the number of triggered events with the mainshock magnitude, reproduces most properties of foreshocks sequences : (i) the inverse Omori law for foreshocks, (ii) an apparent decrease of  $b$ -value before a mainshock and (iii) a migration of seismicity toward the mainshock. These precursory patterns are observed only when averaging over a large number of sequences, and are independent of the mainshock magnitude.

We present here a preliminary analysis of real seismicity data and a comparison with the predictions of the model presented in chapter 10.

### 11.1 Seismicity data

We use the catalog of the Southern California Data Center over the period 1932-2000, which is almost complete above  $M = 3$  for this time period. More than 22000  $M \geq 3$  earthquakes have been recorded over this period. The largest event of the catalog is the  $M = 7.5$  1952 Kern-County earthquake.

### 11.2 Selection of foreshocks and aftershocks

We have used several methodologies to construct foreshock and aftershock sequences. We consider both type I and type II foreshocks, as defined in chapter 10.

## Aftershocks

We use the same procedure as in chapter 2 to select aftershocks after a mainshock. For each magnitude interval  $(M, M + \Delta M)$ , a mainshock is defined as an earthquake in the magnitude range  $(M, M + \Delta M)$  that was not preceded by a larger event in a space-time window  $R_2, T$  before the mainshock. The distance  $R_2$  is chosen as the maximum size of the clusters in the catalog, i.e. close to 50 km for the California seismicity, in order to remove the influence of large earthquakes that occurred before the mainshock. We then select as aftershocks all events which occurred in a space-time window  $R, T$  after each mainshock.

## Foreshocks of type II

We first select those earthquakes that have a recorded magnitude in the interval between  $M$  and  $M + \Delta M$ . These events are called “mainshocks” of magnitude  $M$ . In contrast with the previous definition of mainshocks used to select aftershocks, we consider here all events with magnitude in the interval between  $(M, M + \Delta M)$  as mainshocks, even if they were preceded by larger events. For each of these mainshocks, we define as foreshocks of type II all events that occurred over a time  $T$  before the mainshock and at a distance smaller than  $R$  from the mainshock.

## Foreshocks of type I

We use the same restrictions in the definition of mainshocks for the selection of type I foreshocks as for the selection of aftershocks, i.e., we consider as mainshocks all events in the magnitude range  $(M, M + \Delta M)$  that were not preceded by a larger event in a space-time window  $R_2, T$ . The foreshocks are then selected in a space-time window  $R, T$  before each mainshock. In contrast with type II foreshocks defined above, the selection of type I foreshocks is rather arbitrary and is very sensitive to the choice of the space-window  $R_2, T$  used to select mainshocks.

## 11.3 Inverse Omori’s law

We use a superposed epoch analysis to stack all foreshock and aftershock sequences synchronized at the time of the “mainshocks” in different mainshock magnitude intervals, and for different choices of the space-time window  $R, T$  used to define foreshocks and aftershocks. We use larger magnitude intervals  $\Delta M$  for larger mainshock magnitudes, because there is not enough data for large mainshock magnitudes. Previous studies of foreshocks using superposed epoch analysis [Papazachos, 1975a,b ; Jones and Molnar, 1976, 1979 ; Kagan and Knopoff, 1978 ; Shaw, 1993 ; Reasenber, 1999] have considered type I foreshocks. We have shown in the previous chapter that the analysis of type II foreshocks may be also quite meaningful and less arbitrary than the study of type I foreshocks. These two definitions of foreshocks should lead to the same

results for large mainshocks.

## Type II foreshocks

Figure 11.1 shows the results obtained for type II foreshocks selected using a space-time window  $T = 1$  yr and  $R = 50$  km. The results are very similar to the results shown in Figure 10.4 for numerical simulations of the ETAS model generated with  $n = 1$ ,  $\alpha = 0.8$ ,  $\theta = 0.2$ ,  $b = 1$  and  $c = 0.001$ . We see clearly a power-law acceleration of the seismicity rate before a mainshock with a similar exponent  $p \approx 0.8$  as for the decrease of the rate of aftershocks following a mainshock. The exponent  $p'$  for foreshocks is roughly equal to the  $p$ -exponent of aftershocks, in agreement with the results obtained with numerical simulations with  $\alpha = 0.8$  (see Figure 10.4 and 10.6). A significantly smaller exponent for foreshocks than for aftershocks is expected from our results only for large  $\theta$  and small  $\alpha < b/2$  (see section 10.3).

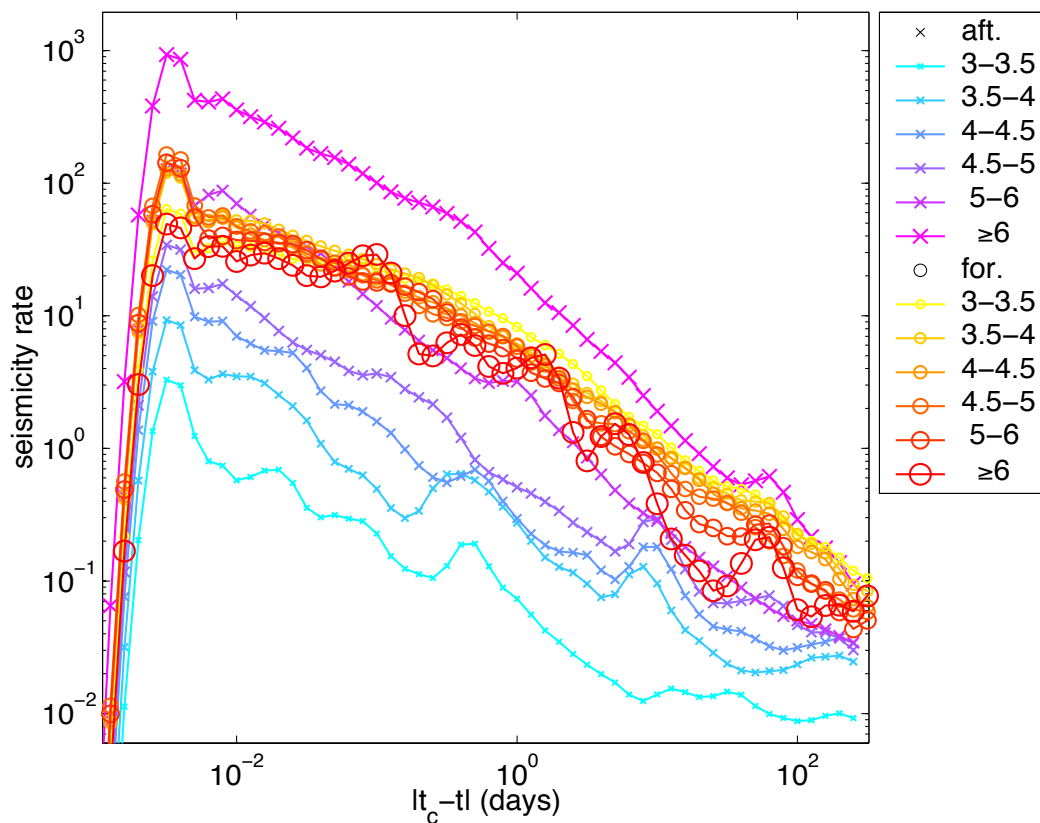


FIG. 11.1 – Rate of seismic activity per mainshock before (type II foreshocks, circles) and after a mainshock (aftershocks, crosses) occurring at time  $t_c$ , obtained by stacking many earthquake sequences for different mainshock magnitude intervals between 3 and 7. The foreshock rates have thus been folded back onto the aftershock sequences for better comparison. Foreshocks and aftershocks have been selected using a space-time window  $T = 1$  yr and  $R = 50$  km. The rate of aftershocks per mainshock increases with the mainshock magnitude as  $N(M) \approx 10^{0.8M}$  while the rate of type II foreshocks is independent of the mainshock magnitude.

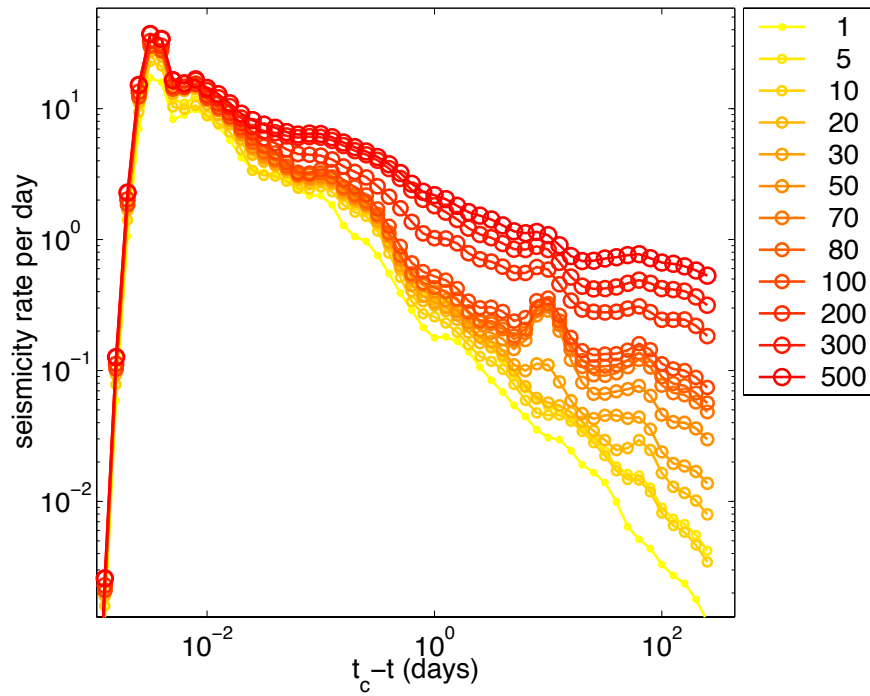


FIG. 11.2 – Rate of aftershocks for mainshock magnitudes in the range (4.5, 5), and for different choices of the distance  $R$  used to select aftershocks around the mainshock. We use a distance  $R_2 = 50$  km and a time window  $T = 1$  yr to select as mainshocks earthquakes in the magnitude range (4.5, 5) that were not preceded by a larger earthquake in the space-time window  $T, R_2$ .

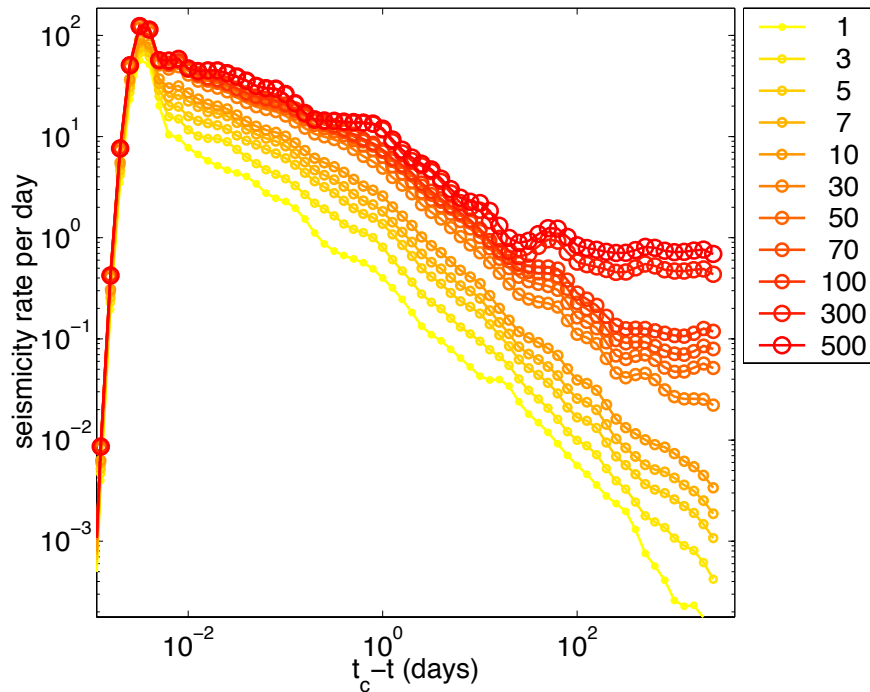


FIG. 11.3 – Rate of type II foreshocks for mainshock magnitudes in the range (4, 4.5), and for different choices of the distance  $R$  used to select foreshocks around the mainshock.

The large fluctuations obtained for real data when comparing to synthetic catalogs (Figures 10.3 and 10.4) are due to the smaller number of events, 23000 events in the catalog of California seismicity compared to  $5 \times 10^6$  events generated for the synthetic catalogs. The number of foreshocks is smaller than the number of aftershocks, except for small mainshock magnitudes and large times from the mainshock. The rate of aftershocks per mainshock increases with the mainshock magnitude as  $N(M) \approx 10^{0.8M}$  while the rate of type II foreshocks is independent of the mainshock magnitude, as predicted by the ETAS model.

The truncation of the seismicity rate for small times  $|t_c - t| < 1$  day, especially for aftershocks of large  $M > 7$  mainshocks and for foreshocks, is due to the incompleteness of the catalog at very short times. The catalog is incomplete at early times following large  $M > 6$  mainshocks due to the saturation of the seismic network. The truncation is also observed for foreshocks because a large fraction of type II foreshocks occur at early times after a large earthquake, when the seismicity rate is very high and the seismic network is saturated. At large times from the mainshock the seismicity rate decreases to the level of the background seismicity, as seen clearly in Figure 11.1 for the rate of aftershocks following small  $M = 3$  mainshocks. Large fluctuations are observed for the rate of foreshocks of  $M > 7$  mainshocks due to the small number of sequences in the catalog.

Both the direct and the inverse Omori laws can be observed up to 10 yrs after and before the mainshock, when using a small distance  $R$  to select foreshock and aftershocks around the mainshock. Figures 11.2 and 11.3 show the rate of aftershocks and foreshocks respectively, for mainshock magnitudes between 4 and 4.5, and for different values of the distance  $R$  used to select aftershocks and foreshocks. For the selection of aftershocks, mainshocks have been selected with  $R_2 = 50$  km. The direct and the inverse Omori laws are observed up to the largest distance  $R = 500$  km, but the duration of the foreshock and aftershock sequences decreases if  $R$  increases due to the increase of the effect of the background seismicity.

## Type I foreshocks

The results for type I foreshocks are presented in Figure 11.4. There are much larger fluctuations for the rate of type I foreshocks than for type II foreshocks (Figure 11.1) due to the smaller number of type I foreshocks. A large fraction of type II foreshocks are usual “aftershocks” of large  $M > 6$  earthquakes and are therefore rejected from the analysis of type I foreshocks, which are constrained to be smaller than their mainshock. However, we see clearly a power-law acceleration of the seismicity before a mainshock for type I foreshocks. This result implies that large mainshocks can be triggered by smaller earthquakes. The exponent  $p'$  of the inverse Omori law is roughly equal to the Omori exponent of type II foreshocks and to the exponent  $p$  of the direct Omori law of aftershocks. The rate of type I foreshocks increases slowly with the mainshock magnitude. This increase is however not due to a larger predictability of larger earthquakes, as expected for example in the critical point theory [Sammis and Sornette, 2002] and as observed

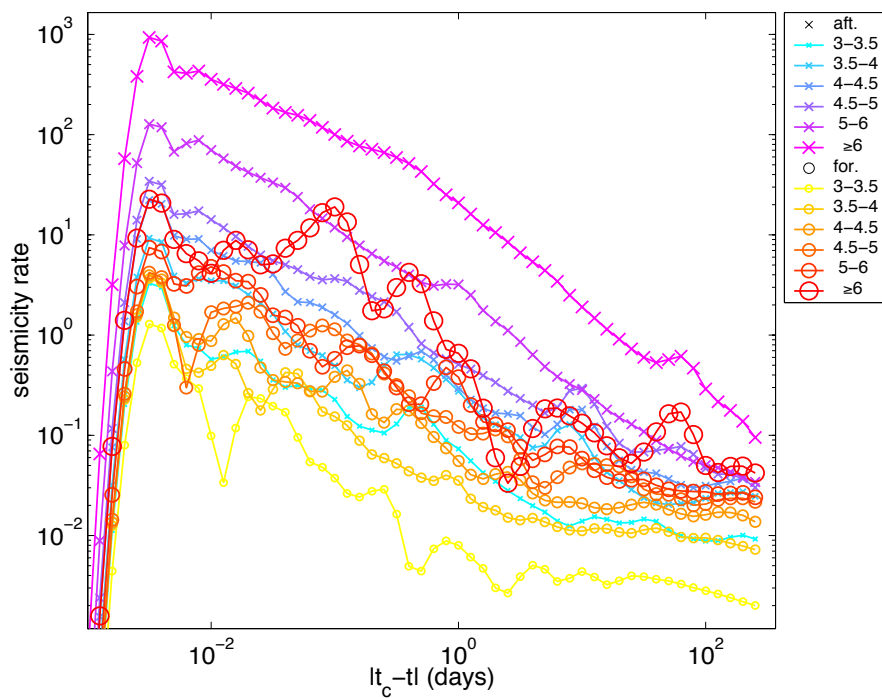


FIG. 11.4 – Same as Figure 11.1 for type I foreshocks, which have been selected using a space-time window  $R_1 = R_2 = 50$  km and  $T = 1$  yr. The rate of type I foreshocks increases slowly with the mainshock magnitude, due to the rules used to define type I foreshocks, which lead to a more drastic selection and pruning for smaller mainshock magnitudes. For large mainshock magnitudes  $M$ , the inverse Omori's law is independent of  $M$ , as for type II foreshocks.

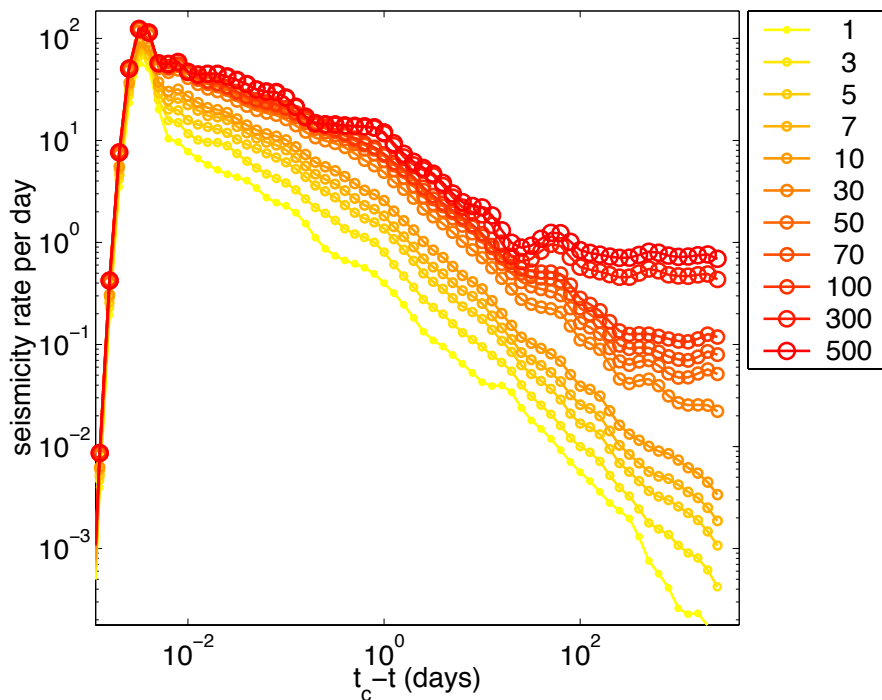


FIG. 11.5 – Same as Figure 11.3 for type I foreshocks selected using a space-time window  $R_2=50$  km and  $T = 1$  yr.

in a numerical model of seismicity [Huang et al., 1998]. The increase of the number of type I foreshocks with the mainshock magnitude is similar to the results obtained for the numerical simulations of the ETAS model shown in Figure 10.5, and can be explained by the rules used to define type I foreshocks, which lead to a more drastic selection and pruning for smaller mainshock magnitudes. As expected by our study of the triggering model, the inverse Omori's law becomes independent of the mainshock magnitudes  $M$  for large  $M$ .

The results for different values of the distance  $R$  used to select foreshocks are shown in Figure 11.5. The apparent exponent  $p'$  of the inverse Omori law decreases if the distance  $R$  increases, due to the increase of the background seismic activity with  $R$ . This variation of the Omori exponent  $p'$  with  $R$  may also result in part from the migration of the seismic activity towards the mainshock discussed in section 11.5.

## 11.4 Modification of the magnitude distribution before a mainshock

In section 10.4 we have shown that the conditioning of a seismicity sequence to lead to a mainshock results in a modification of the magnitude distribution. We predict that the foreshock magnitude distribution  $P(m)$  gets an additive (or deviatoric) power law contribution  $dP(m)$  with an exponent smaller than  $b$  and with an amplitude growing as a power law of the time to the mainshock.

The magnitude distribution at time  $t_c - t$  before the mainshock is given by (10.49)

$$P(m) = (1 - q)P_0(m) + q dP(m) , \quad (11.1)$$

where  $P_0(m)$  is the average magnitude distribution  $P_0(m) \sim 10^{-bm}$  and  $dP(m)$  is another GR law with a smaller exponent  $b' = b - \alpha$ . The amplitude  $q$  of the deviatoric distribution in (11.1) increases as a power-law of the time from the mainshock according to

$$q \sim (t_c - t)^{-\theta \frac{(b-\alpha)}{\alpha}} . \quad (11.2)$$

This analytical result is in very good agreement with the numerical simulations (Figure 10.7 and 10.8). There are however large statistical fluctuations of the foreshock magnitude distribution, even for the large number  $5 \times 10^6$  of events used in the synthetic catalog. We test here the predictions of the model using the SCEC catalog, with only 22000 events, and with additional difficulties coming from the incompleteness of the catalog for small magnitudes at early times after a large earthquake.

We have considered type II foreshocks of  $M > 3$  “mainshocks” selected using  $R = 20$  km and  $T = 1$  yr. We have evaluated the magnitude distribution at different times from the mainshock and we have fitted this distribution to our prediction (11.1). For each time window we have estimated the exponent  $b'$  of the deviatoric GR distribution  $dP(m)$  and the amplitude  $q$  of the

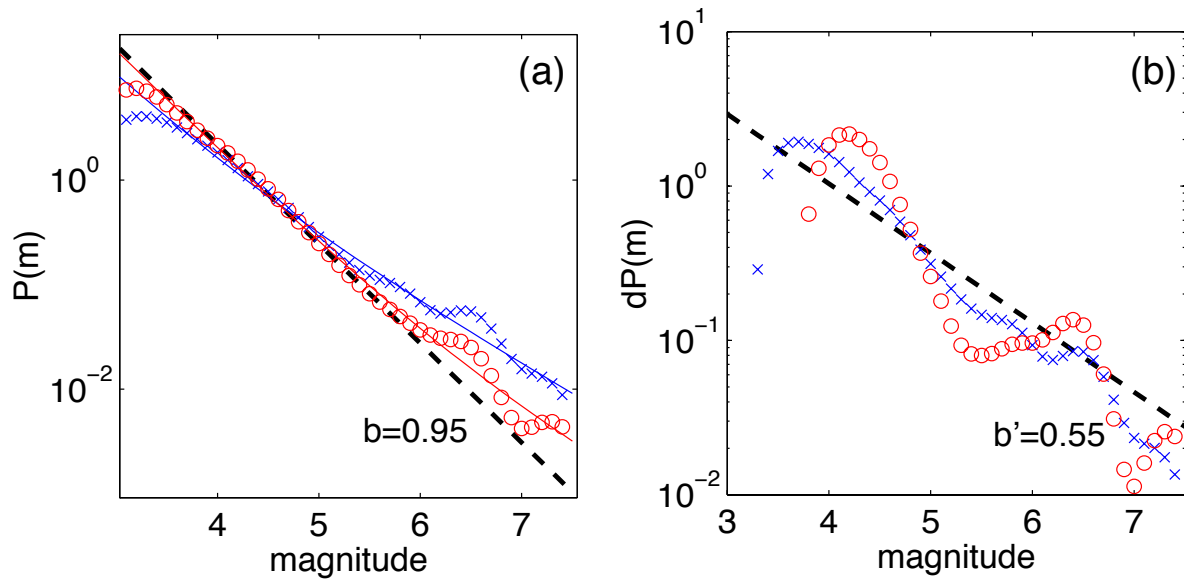


FIG. 11.6 – Magnitude distribution (a) of type II foreshocks, for “mainshocks” of magnitude  $M \geq 3$ , using a space-time window  $R = 20$  km and  $T = 1$  yr and deviatoric distribution (b) for two time periods : for times less than 1 day before the mainshock (crosses) and between 10 days and 1 yr before the mainshock (circles). The dashed line in panel (a) is the reference Gutenberg-Richter distribution  $P_0(m)$  with  $b = 0.95$  measured for the whole catalog. The dashed line in panel (b) is the deviatoric distribution  $dP(m)$  obtained by fitting  $P(m)$  in panel (a) for the two time periods by  $P(m) = qP(m) + (1 - q)dP(m)$  where  $dP(m) \sim 10^{-b'm}$  with  $b' \approx 0.55$  for the two time periods.

deviatoric component. The exponent  $b$  of the average distribution  $P_0(m)$  is fixed to  $b = 0.95$  estimated using the whole catalog.

The results presented in Figures 11.6 and 11.7 are in rather good agreement with our predictions. The foreshock magnitude distribution is well fitted in the magnitude range  $4 \leq M \leq 7$  by the sum of two power-laws (11.1), with an exponent  $b' \approx 0.6$  independently of the time from the mainshock (see Figure 11.7d). However, the  $b'$ -exponent of the deviatoric distribution is significantly larger than the prediction  $b' = b - \alpha$  with  $b = 0.95$  measured for the whole catalog, and  $\alpha = 0.8$  obtained in chapter 2. The truncation for small magnitudes  $m < 4$  is due to the incompleteness of the catalog just after large earthquakes. The amplitude  $q$  of the deviatoric distribution increases when the mainshock approaches, in rather good agreement with a power law increase (11.2) with an exponent of 0.3 (see Figure 11.7b). The quantitative value of this exponent is however very poorly constrained.

## 11.5 Migration of foreshocks

We study the space-time distribution of type II foreshocks, in order to investigate how the spatial distribution of the seismicity evolves before a mainshock. We use a superposed epoch

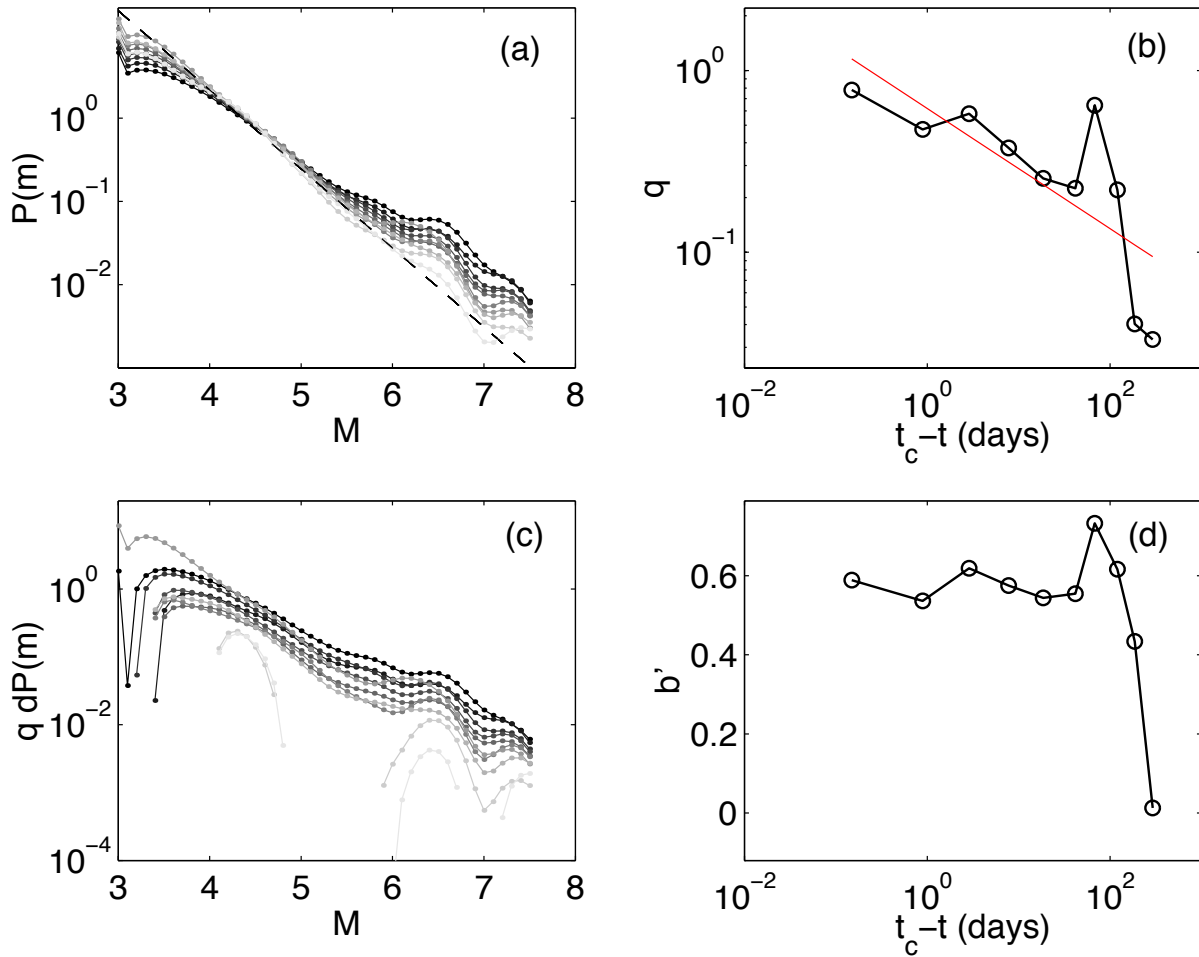


FIG. 11.7 – Magnitude distribution  $P(m)$  (a) and deviatoric distribution  $dP(m)$  (c) measured for 10 times windows of equal number of events. The color of each curve in (a) and (c) ranges from gray to black as the time from the mainshock  $t_c - t$  decreases from 1 yr to 0.01 day. We consider as mainshocks all events whatever their magnitude  $M > 3$ . The type II foreshocks are selected using a space-time window  $R = 20$  km and  $T = 1$  yr before each earthquake. The exponent  $b'$  of the deviatoric distribution  $dP(m)$  is shown in panel (d), and is rather constant around 0.6 for all times periods, excepted at very long times before the mainshock. The amplitude  $q$  of the deviatoric distribution is shown in panel (b). The solid line in (b) is a fit of  $q(t_c - t)$  by a power-law of exponent 0.3.

analysis to stack all foreshock sequences synchronized at the time of the mainshock and with a common origin of space at the location of each mainshock. Our results obtained with the ETAS model (section 10.5) predict an inverse diffusion of the seismic activity toward the mainshock similar to the diffusion of aftershocks presented in chapter 8. The characteristic size  $R$  of the foreshock cluster is expected to decrease before the mainshock according to

$$R \sim (t_c - t)^{\theta/\mu}, \quad (11.3)$$

where  $\mu$  is the exponent of the distribution of distances between triggering and triggered earthquakes (8.5) and  $\theta$  is a parameter of the bare Omori's law  $\Psi(t) \sim 1/(t+c)^{1+\theta}$  (8.4). This law (11.3) describes the localization of the seismicity as the mainshock approaches. The analysis of the California seismicity presented in Figure 11.8 shows clearly a migration of the seismicity towards the mainshock, as confirmed by the significant diffusion exponent  $H = 0.27$  shown in Figure 11.9. It is however difficult to state if the inverse diffusion of foreshock activity shown in Figures 11.8 and 11.9 reflects a real process of diffusion described by (11.3) or if this migration is an artifact of the background seismicity. Indeed, the transition between the foreshock activity clustered around the mainshock at early times before the mainshock and the background activity at large times may induce an apparent inverse diffusion of the seismicity rate similar to the observations. This problem has already been discussed in section 9.2 in the case of aftershock diffusion.

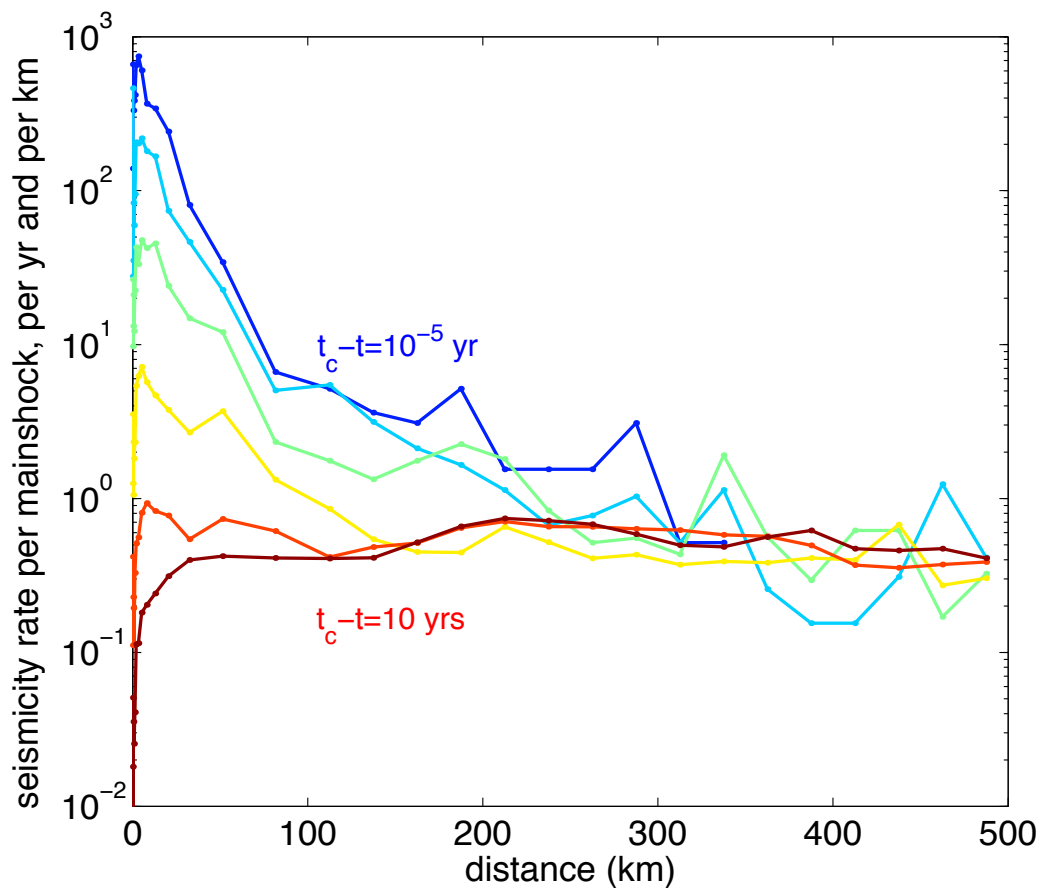


FIG. 11.8 – Rate of type II foreshocks before  $M \geq 4.5$  mainshocks as a function of the distance from the mainshock for different values of the time before the mainshock. We use logarithmic bins for the time windows. We evaluate the seismicity rate for different distances from the mainshock by counting the number of events in each interval  $(r, r + \Delta r)$ . The seismicity rate is normalized by the number of mainshocks, the duration of the time window and the width of the space window  $\Delta r$  used to estimate the seismicity rate.

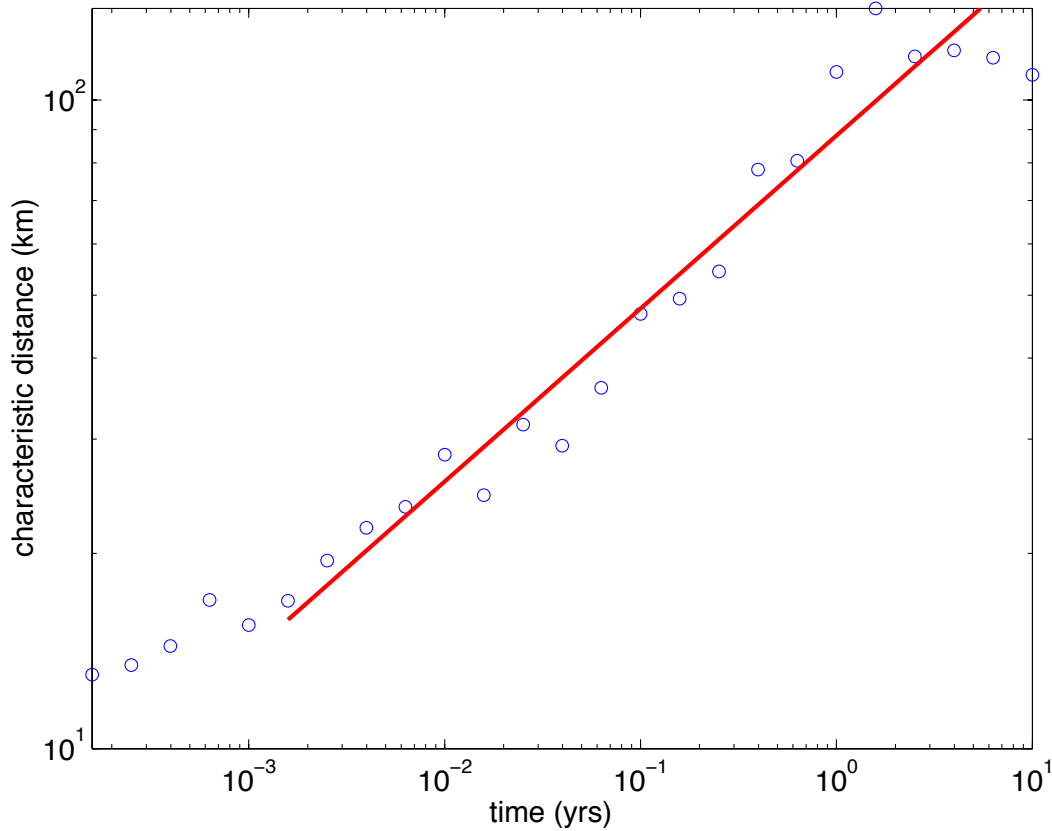


FIG. 11.9 – Characteristic size of the foreshock cluster preceding  $M \geq 4$  earthquakes, measured by the median of the distance between all foreshock-mainshock pairs, as a function of the time before the mainshock. Foreshocks have been selected at a distance less than 200 km around the mainshock. The solid line is a fit by a power-law  $R \sim t^H$  with  $H = 0.27$ .

The spurious diffusion observed in Figure 9.1 when superposing a constant and uniform background seismicity with an aftershock sequence is not however able to reproduce a clear power-law diffusion as given by (11.3) over more than three orders of magnitude in time, as observed for foreshock data (Figure 11.9). But the case of real seismicity is more complicated than the simple synthetic catalog generated in section 9.2, because the background seismicity is neither uniform in time nor in space. The superposition of foreshock sequences with a non-uniform background distribution may induce a spurious diffusion over a larger time interval than shown in Figure 9.1.

Interactions between foreshocks and mainshocks are very long range both in time and in space. At short distances from the mainshock  $r < 5$  km, we see an increase of the seismicity rate up to 10 yrs before the mainshock. Foreshocks are triggered at distances as large as 200 km from the mainshock at very short times  $t_c - t < 1$  day before the mainshock.

## 11.6 Conclusion

Most properties of the foreshock sequences analyzed here are in very good agreement with the predictions of the triggering model. It is however difficult to obtain reliable quantitative measurements of the parameters of the inverse Omori's law and of the GR law of foreshocks due to the small number of events in the catalog and due to the incompleteness of the catalog at early times after large earthquakes. A power-law acceleration of the seismicity is clearly observed both for type I and type II foreshocks. We obtain a significant modification of the magnitude distribution before a mainshock. This modification of the magnitude distribution is well predicted by our result (11.1), but the quantitative value of the exponent  $b'$  of the deviatoric distribution is larger than expected by the model. We also clearly see a localization of the seismicity close to the mainshock, but this inverse diffusion of the seismic activity may be an artifact of the background seismic activity.

The main result of this analysis is that the precursory modification of the seismic activity before a mainshock is independent of the mainshock magnitude, as expected by the triggering model. Therefore large earthquakes are not more predictable than smaller earthquakes on the basis of the power-law acceleration of the seismicity before a mainshock or using the modification of the magnitude distribution. The increase of the number of type I foreshocks with the mainshock magnitude can be explained by the rules used to select type I foreshocks, which are more drastic for smaller mainshocks.

## Chapitre 12

# Endogenous versus exogenous shocks in systems with memory

Didier Sornette

Laboratoire de Physique de la Matière Condensée, Université de Nice-Sophia Antipolis, and  
Department of Earth and Space Sciences and Institute of Geophysics and Planetary Physics,  
University of California, Los Angeles, California.

Agnès Helmstetter

Laboratoire de Géophysique Interne et Tectonophysique,  
Université Joseph Fourier, BP 53X, 38041 Grenoble Cedex, France.

In press in *Physica A*, 2002.

### Abstract

Systems with long-range persistence and memory are shown to exhibit different precursory as well as recovery patterns in response to shocks of exogenous versus endogenous origins. By endogenous, we envision either fluctuations resulting from an underlying chaotic dynamics or from a stochastic forcing origin which may be external or be an effective coarse-grained description of the microscopic fluctuations. In this scenario, endogenous shocks result from a kind of constructive interference of accumulated fluctuations whose impacts survive longer than the large shocks themselves. As a consequence, the recovery after an endogenous shock is in general slower at early times and can be at long times either slower or faster than after an exogenous perturbation. This offers the tantalizing possibility of distinguishing between an endogenous versus exogenous cause of a given shock, even when there is no “smoking gun”. This could help in investigating the exogenous versus self-organized origins in problems such as the causes of major biological extinctions, of change of weather regimes and of the climate, in tracing the source of

social upheaval and wars, and so on. Sornette et al. [2002] have already shown how this concept can be applied concretely to differentiate the effects on financial markets of the Sept. 11, 2001 attack or of the coup against Gorbachev on Aug., 19, 1991 (exogenous) from financial crashes such as Oct. 1987 (endogenous).

## 12.1 Introduction

Most complex systems around us exhibit rare and sudden transitions, that occur over time intervals that are short compared to the characteristic time scales of their posterior evolution. Such extreme events express more than anything else the underlying “forces” usually hidden by almost perfect balance and thus provide the potential for a better scientific understanding of complex systems. These crises have fundamental societal impacts and range from large natural catastrophes such as earthquakes, volcanic eruptions, hurricanes and tornadoes, landslides, avalanches, lightning strikes, meteorite/asteroid impacts, catastrophic events of environmental degradation, to the failure of engineering structures, crashes in the stock market, social unrest leading to large-scale strikes and upheaval, economic drawdowns on national and global scales, regional power blackouts, traffic gridlock, diseases and epidemics, and so on. It is essential to realize that the long-term behavior of these complex systems is often controlled in large part by these rare catastrophic events [Sornette, 1999b]. The outstanding scientific question is how such large-scale patterns of catastrophic nature might evolve from a series of interactions on the smallest and increasingly larger scales [Sornette, 2002], or whether their origin should be searched from exogenous sources.

Starting with Hurst’s study of 690 time series records of 75 geophysical phenomena, in particular river flow statistics, documenting the so-called “Hurst effect” of long term persistence [Hurst, 1951], many studies in the last decades have investigated the existence of long memory effects in a large variety of systems, including meteorology (wind velocity, moisture transfer in the atmosphere, precipitation), oceanography (for instance wave-height), plasma turbulence, solar activity, stratosphere chemistry, seismic activity, internet traffic, financial price volatility, cardiac activity, immune response, and so on.

The question addressed here is whether the existence of long memory processes may lead to specific signatures in the precursory and in the relaxation/recovery/adaptation of a system after a large fluctuation of its activity, after a profound shock or even after a catastrophic event, that may allow one to distinguish an internal origin from an exogenous source. Let us put this question in perspective with regards to the extinction of biological species as documented in the fossil record. During the past 550 million years, there have been purportedly five global mass extinctions, each of which had a profound effect on life on Earth. The last end-Cretaceous mass extinction (with the disappearance of 39–47% of fossilizable genera and perhaps 75% of species) marking the Cretaceous/Tertiary (K/T) boundary about 65 millions ago is often attributed to

the impact of a huge meteor in the Yucatan peninsula [Kyte, 1998]. Another scenario is that a burst of active volcanism was the real origin of the extinction [Courillot, 1990; Courillot, 1999]. It has been suggested that this extinction was actually driven by longer-term climatic changes, as evidence by the fact that certain species in the Late Maastrichtian disappeared a distinctive time before the K/T boundary [Marshall, 1998; Marshall and Ward, 1996]. A completely endogenous origin has also been proposed, based on the concepts of nonlinear feedbacks between species [Milton and Belair, 1990; Allen et al., 1993] illustrated by self-organized criticality and punctuated equilibrium [Bak, 1996; Sole et al., 1997] (see [Kirchner and Weil, 1998] for a rebuttal). The situation is even murkier for the extinctions going further in the past, for which the smoking guns, if any, are not observable (see however the strong correlation between extinctions and volcanic traps presented in [Courillot, 1999]). How can we distinguish between an exogenous origin (meteorite, volcanism, abrupt climate change) and endogenous dynamics, here defined as the progressive self-organizing response of the network of interacting species that may generate its own demise by nonlinear intermittent negative feedbacks or in response to the accumulation of slowly varying perturbations in the environment? Is it possible to distinguish two different exogenous origins, one occurring over a very short time interval (meteorite) and the other extending over a long period of time (volcanism), based on the observations of the recovery and future evolution of diversity?

The aviation industry provides another vivid illustration of the question on the endogenous versus exogenous origin of a crisis. Recently, airlines became the prime industry victim of the September 11, 2001 terrorist attacks. The impact of the downturn in air travel has been severe not just on the airlines but also on lessors and aircraft manufacturers. The unprecedented drop in air travel and airline performance prompted the US government to provide \$5 billion in compensation and to make available \$10 billion in loan guarantees. This seems a clear-cut case for an exogenous shock. However, the industry was deteriorating before the shock of September 11. In the first eight months of 2001, passenger traffic for US carriers rose by an anemic 0.7 percent, a sharp fall from annual growth of nearly 4 percent over the previous decade [Costa et al., 2002], illustrated by the record levels of the earned profits of \$39 billion and of delivery of more than 4,700 jetliners from 1995 to 2000. The US airlines' net profits dropped from margins of nearly 4 percent during 1998-2000 to losses of greater than 3 percent during the first half of 2001, despite aggressive price cuts as airlines tried to fill seats and profits vanished.

Many other examples are available. We propose to address this general question of exogenous versus endogenous origins of shocks by quantifying how the dynamics of the system may differ in its response to an exogenous versus endogenous shock. We start with a simple "mean field" model of the activity  $A(t)$  of a system at time  $t$ , viewed as the effective response to all past perturbations embodied by some noisy function  $\eta(\tau)$ ,

$$A(t) = \int_{-\infty}^t d\tau \eta(\tau) K(t - \tau) , \quad (12.1)$$

where  $K(t - \tau)$  can be called the memory kernel, propagator, Green function, or response function of the system at a later time  $t$  to a perturbation  $\eta(\tau)$  that occurred at an earlier time  $\tau$ . Notwithstanding the linear structure of (12.1), we do not restrict our description to linear systems but take (12.1) as an effective coarse-grained description of possible complex nonlinear dynamics. For instance, it has been shown [Krishnamurth et al., 2000] that the extremal nonlinear dynamics of the Bak and Sneppen model and of the Sneppen model of extremal evolution of species, which exhibit a certain class of self-organized critical behavior [Sornette, 2000a], can be accurately characterized by the stochastic process called “Linear fractional stable motion”, which has exactly the form (12.1) for the activity dynamics.

Expression (12.1) contains for instance the fractional Brownian motion (fBm) model introduced by Mandelbrot and Van Ness [Mandelbrot and Ness, 1968] as a simple extension of the memoryless random walk to account for the Hurst effect. From an initial value  $B_H(0)$ , we recall that the fBm is defined by

$$B_H(t) - B_H(0) = \frac{1}{\Gamma(H + (1/2))} \int_{-\infty}^t d\tau \eta(\tau) K(t - \tau), \quad (12.2)$$

where  $d\tau \eta(\tau) = dW_\tau$  is usually taken as the increment of the standard random walk with white noise spectrum and Gaussian distribution with variance  $E[dW_\tau] = d\tau$  and the memory kernel  $K(t - \tau)$  is given by

$$K(t - \tau) = (t - \tau)^{H - \frac{1}{2}}, \quad \text{for } 0 \leq \tau \leq t \quad (12.3)$$

$$= (t - \tau)^{H - \frac{1}{2}} - (-\tau)^{H - \frac{1}{2}}, \quad \text{for } \tau < 0. \quad (12.4)$$

For  $H > 1/2$ , the fBm  $B_H(t)$  exhibits long term persistence and memory, since the effect of past innovations of  $dW_\tau$  is felt in the future with a slowly decaying power law weight  $K(t - \tau)$ . For our purpose, the fBm is non-stationary and it is more relevant to consider globally statistically stationary processes.

Here, we consider processes which can be described by an integral equation of the form (12.1) and (12.2) but with possibly different forms for the noise innovations  $\eta$  and for the memory kernel  $K$ . Simple viscous systems correspond to  $K(t - \tau) \propto \exp[-(t - \tau)/T]$ , where  $T$  is a characteristic relaxation time. Complex fluids, glasses, porous media, semiconductors, and so on, are characterized by a memory kernel  $K(t - \tau) \propto e^{-a(t - \tau)^\beta}$ , with  $0 < \beta < 1$ , a law known under the name Kohlrausch–Williams–Watts law [Phillips, 1996]. It is also interesting to consider fractional noise motion (fNm) defined as the time derivative of  $B_H(t)$ , which does possess the property of statistical stationarity. A fNm is defined by (12.1) with

$$K_{\text{fNm}}(t - \tau) = \frac{1}{(t - \tau)^{\frac{3}{2} - H}} = \frac{1}{(t - \tau)^{1 - \theta}}, \quad (12.5)$$

for  $H = 1/2 + \theta$ . Persistence  $1/2 < H < 1$  (respectively antipersistence  $0 < H < 1/2$ ) corresponds to  $0 < \theta < 1/2$  (respectively  $-1/2 < \theta < 0$ ). Such a memory kernel describes also the renormalized Omori’s law for earthquake aftershocks [Sornette and Sornette, 1999a; Helmstetter and Sornette, 2002a].

## 12.2 Exogenous versus endogenous shock

In the following, we consider systems described by a long memory integral (12.1) with kernel  $K(t)$  decaying faster than  $1/\sqrt{t}$  at large times, so as to ensure the condition of statistical stationarity. This excludes the fBm which are non-stationary processes but includes the fNm.

### Exogenous shock

An external shock occurring at  $t = 0$  can be modeled in this framework by an innovation which takes the form of a jump  $A_0 \delta(\tau)$ . The response of the system for  $t > 0$  is then

$$A(t) = A_0 K(t) + \int_{-\infty}^t d\tau \eta(\tau) K(t - \tau). \quad (12.6)$$

The expectation of the response to an exogenous shock is thus

$$\mathbb{E}_{\text{exp}}[A(t)] = A_0 K(t) + n \langle \eta \rangle, \quad (12.7)$$

where  $\langle \eta \rangle$  is the average noise level and  $n = \int_0^{+\infty} d\tau K(\tau)$  is the average impact of a perturbation which is usually smaller than 1 to ensure stationarity (this corresponds to the sub-critical regime of branching processes [Harris, 1963]).

The time evolution of the system after the shock is thus the sum of the process it would have followed in absence of shock and of the kernel  $K(t)$ . The response  $A_0 K(t)$  to the jump  $A_0 \delta(\tau)$  exemplifies that  $K(t)$  is the Green function or propagator of the coarse-grained equation of motions of the system. Expression (12.6) simply expresses that the recovery of the system to an external shock is entirely controlled by its relaxation kernel.

### Endogenous shock

#### Conditional response function

Let us consider the natural evolution of the system, without any large external shock, which nevertheless exhibits a large burst  $A(t = 0) = A_0$  at  $t = 0$ . From definition (12.1), it is clear that a large “endogenous” shock requires a special set of realization of the innovations  $\{\eta(t)\}$ . To quantify the response in such case, we recall a standard result of stochastic processes with finite variance and covariance that the expectation of some process  $X(t)$  conditioned on some variable  $Y$  taking a specific value  $Y_0$  is given by [Jacod and Shiryaev, 1987]

$$\mathbb{E}[X(t)|Y = A_0] - \mathbb{E}[X(t)] = (A_0 - \mathbb{E}[Y]) \frac{\text{Cov}(X(t), Y)}{\mathbb{E}[Y^2]}, \quad (12.8)$$

where  $\mathbb{E}[Y^2]$  denotes the expectation of  $Y^2$ ,  $\text{Cov}(X(t), Y)$  is the covariance of  $X$  and  $Y$ ,  $\mathbb{E}[X(t)]$  and  $\mathbb{E}[Y]$  are the (unconditional) average of  $X(t)$  and of  $Y$ . Expression (12.8) recovers the obvious result that  $\mathbb{E}[X(t)|Y = A_0] = \mathbb{E}[X(t)]$  if  $X$  and  $Y$  are uncorrelated. A result generalizing (12.8)

holds when  $\eta(\tau)$  has an infinite variance corresponding to a distribution with a power law tail with exponent smaller than 2 [Helmstetter et al., 2002].

Let us assume that the process  $A(t)$  and the innovations  $\eta$ 's have been defined with zero mean, which is always possible without loss of generality by a translation. Let us call  $X(t > 0) = A(t)$  and  $Y = A(0)$ . Under the assumption that the noise  $\eta(\tau)$  has a finite variance, we obtain from (12.1)

$$\text{Cov}(A(t), A(0)) = \int_{-\infty}^0 d\tau K(t - \tau) K(-\tau) , \quad (12.9)$$

and

$$\text{E}[A(0)^2] = \int_{-\infty}^0 d\tau [K(-\tau)]^2 . \quad (12.10)$$

For stationary processes such that  $K(t)$  decays faster than  $1/\sqrt{t}$  so as to make the integral in (12.10) convergent,  $\text{E}[A(0)^2]$  is a constant. We thus obtain the posterior ( $t > 0$ ) response (above the stationary average) to an endogenous shock occurring at time  $t = 0$  under the form of a conditional expectation of  $A(t)$ , conditioned by the existence of this shock :

$$\text{E}_{\text{endo}}[A(t)|A(0) = A_0] \propto A_0 \int_0^{+\infty} du K(t + u) K(u) , \quad (12.11)$$

for large  $A_0$ . This relaxation of the activity after an endogenous shock is in general significantly different from that given by (12.7) following an exogenous shock.

### Conditional noise trajectory

What is the source of endogenous shocks characterized by the response function (12.11)? To answer, let us consider the process  $W(t) \equiv \int_{-\infty}^t d\tau \hat{\eta}(\tau)$ , where  $\hat{\eta}(t) = \eta(t) - \langle \eta \rangle$  defines the centered innovations forcing the system (12.1). Using property (12.8), we find that for  $t < 0$

$$\text{E}_{\text{endo}}[W(t)|A(0) = A_0] = \frac{\text{Cov}[W(t), A(0)]}{\text{Var}[A(0)]} \cdot (A_0 - \text{E}[A]) \propto (A_0 - \text{E}[A]) \int_{-\infty}^t d\tau K(-\tau) , \quad (12.12)$$

where  $\text{E}_{\text{endo}}[W(t)|A(0) = A_0] = 0$  for  $t > 0$  since the conditioning does not act after the shock. Expression (12.12) predicts that the expected path of the continuous innovation flow prior to the endogenous shock (i.e., for  $t < 0$ ) grows like  $\Delta W(t) = \hat{\eta}(t)\Delta t \sim K(-t)\Delta t$  upon the approach to the time  $t = 0$  of the large endogenous shock. In other words, conditioned on the observation of a large endogenous shock, there is specific set of trajectories of the innovation flow  $\eta(t)$  that led to it. These conditional innovation flows have an expectation given by (12.12).

Inserting expression (12.12) for the average conditional noise in definition (12.1) of the process, we obtain an expression proportional to (12.11). This shows that the precursory activity preceding and announcing the endogenous shock follows the same time dependence as relaxation (12.11) following the shock, with the only modification that  $t$  (for  $t > 0$  counting time after the shock at  $t = 0$ ) is changed into  $-t$  (for  $t < 0$  counting time before the shock at  $t = 0$ ). We can also use (12.12) into (12.1) and calculate the activity after the endogenous shock to recover

(12.11). These are two equivalent ways of arriving at the same result, the one using (12.12) illuminating the fundamental physical origin of the endogenous response.

These results allow us to understand the distinctive features of an endogenous shock compared to an external shock. The later is a single very strong instantaneous perturbation that is sufficient in itself to move the system significantly according to (12.6). In contrast, an “endogenous” shock is the result of the cumulative effect of many small perturbations, each one looking relatively benign taken alone but, when taken all together collectively along the full path of innovations, can add up coherently due to the long-range memory of the dynamical process. In summing, the term “endogenous” is used here to refer to the sum of the contribution of many “small” innovations adding up according to a specific most probable trajectory, as opposed to the effect of a single massive external perturbation.

### Numerical simulation of an epidemic branching process with long-range memory

To illustrate our predictions (12.7) and (12.11), we use a simple epidemic branching model defined as follows. The model describes the time evolution of the rate of occurrence of events as a function of all past history. What is called “event” can be the creation of a new species or a new family of organisms as in [Courtilot and Gaudemer, 1996], the occurrence of an earthquake as in [Sornette and Sornette, 1999a; Helmstetter and Sornette, 2002a], the amplitude of the so-called financial volatility as in [Sornette et al., 2002] or of aviation traffic, a change of weather regime, a climate shift and so on. The rate  $\lambda(t)$  of events at time  $t$  is assumed to be a function of all past events according to

$$\lambda(t) = \sum_{i | t_i < t} \phi(t - t_i), \quad (12.13)$$

where the sum is carried over all past events that occurred at times  $t_i$  prior to the present  $t$ . The influence of such an event at a previous time  $t_i$  is felt at time  $t$  through the bare propagator  $\phi(t - t_i)$ . In our present illustration, we consider a process equivalent to a fNm with Hurst exponent  $H = 1/2 + \theta$ , which can be shown to correspond to the choice  $\phi(t) = \theta c^\theta / (t + c)^{1+\theta}$ , where  $c$  is an ultra-violet regularization time embodying a delay process at early times in the activity response after an event. Indeed, the Master equation corresponding to the process (12.13) can be shown [Sornette and Sornette, 1999a; Helmstetter and Sornette, 2002a] to be nothing but (12.1) with the renormalized or dressed propagator  $K(t) \propto 1/(t + c)^{1-\theta}$ .

Numerical simulations of the epidemic branching process are performed by drawing events in succession according to a non-stationary Poisson process with instantaneous rate (12.13). Figures 12.1 and 12.2 show successive magnifications of time series of the activity rate after an exogenous shock and around an endogenous shock, respectively, in order to visualize the precursory and relaxation activities. In figure 12.2, an external source of activity necessary for seeding has been added as a Poisson process of rate  $\mu = 10^{-3}$  corresponding on average to one

external event over a time interval of 1000. The most striking visual difference is the existence of the precursory signal occurring at many time scales for the endogenous shock.

Figure 12.3 quantifies the precursory and relaxation rates associated with activity shocks. The top panel shows the relaxation of the activity (rate of events) following an external shock compared to that after an endogenous shock, for a single realization.  $t_c$  is the time of the shock. The horizontal axis is  $t - t_c$  for the relaxation of the activity after the shock. The precursory activity prior to the shock is also shown for the endogenous shock as a function of  $t_c - t$ . The bottom panel shows the same three activity functions after averaging over many realizations, translating time in the averaging so that all shocks occur at the same time denoted  $t_c$ . The prediction (12.7) states that the relaxation of the activity after an exogenous shock should decay as  $K(t) \propto 1/(t - t_c + c)^{1-\theta}$  while the decay after an endogenous shock should be given by (12.11) which predicts the law  $\propto 1/(t - t_c + c)^{1-2\theta}$ , that is, a significantly smaller exponent for  $\theta > 0$ . Similarly, we predict that the precursory activity prior to an endogenous shock should increase as  $\propto 1/(t_c - t + c)^{1-2\theta}$ . These predictions are verified with very good accuracy, as seen in figure 12.3.

These simulations confirm that there is a distinctive difference in the relaxation after an endogenous shock compared to an exogenous shock, if the memory kernel is sufficiently long-ranged. For a single realization, there are unavoidable fluctuations that may blur out this difference. However, we see a quite visible precursory signal (foreshock activity) that is symmetric to that relaxation process in the case of an endogenous shock. This follows from the model used here which obeys the time-reversal symmetry. This may be used as a distinguishing signature of an endogenous shock.

### 12.3 Classification of the distinctive responses for different classes of memory kernels

The family of power law kernels used in the simulations presented in figures 12.1, 12.2 and 12.3 are only one possibility among many. Our formalism allows us to classify the distinctive properties of the relaxation and precursory behaviors that can be expected for an arbitrary memory kernel. We now provide this classification by studying (12.7) and (12.11).

#### Short-time response

We compare the initial slopes of the relaxations after the occurrence of the shock at  $t = 0$ . Thus, by short-time, we mean the asymptotic decay law just after the shock. For this, we expand (12.7) to get

$$E_{\text{exo}}[A(t)] = A_0 K(0) \left[ 1 + \frac{K'(0)}{K(0)} t + \mathcal{O}(t^2) \right] = A_0 K(0) \left[ 1 + \frac{d \ln K}{dt} \Big|_{t=0} t + \mathcal{O}(t^2) \right], \quad (12.14)$$

where  $K'(t)$  denotes the derivative of  $K(t)$  with respect to time.

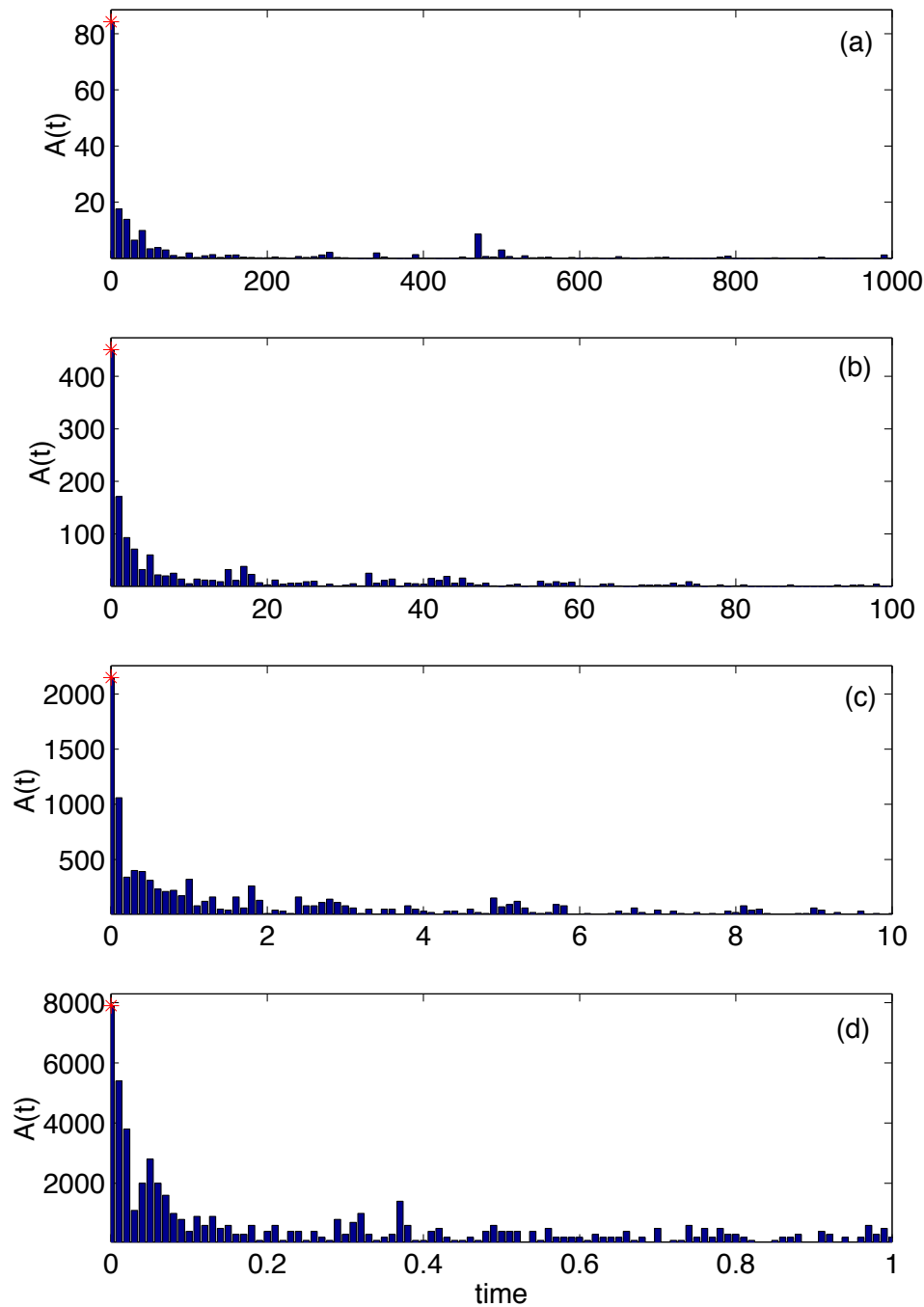


FIG. 12.1 – Rate of activity following an exogenous shock in a numerical simulation of the epidemic branching model (12.13) generated with a memory kernel decaying as a power law  $\phi(t) \sim 1/(t+c)^{1+\theta}$  with parameters  $\theta = 0.1$  and  $c = 0.001$  without a constant source term ( $\mu = 0$ ). The rate of activity following an exogenous shock that occurred at  $t = 0$  is shown at increasing magnification from top to bottom. It is evaluated using a bin size decreasing by factors of 10 from  $\delta t = 10$  (a) to  $\delta t = 0.01$  (d). Averaging over many such realizations would yield the average power law decay  $K(t) \sim 1/(t+c)^{1-\theta}$  predicted by (12.7).

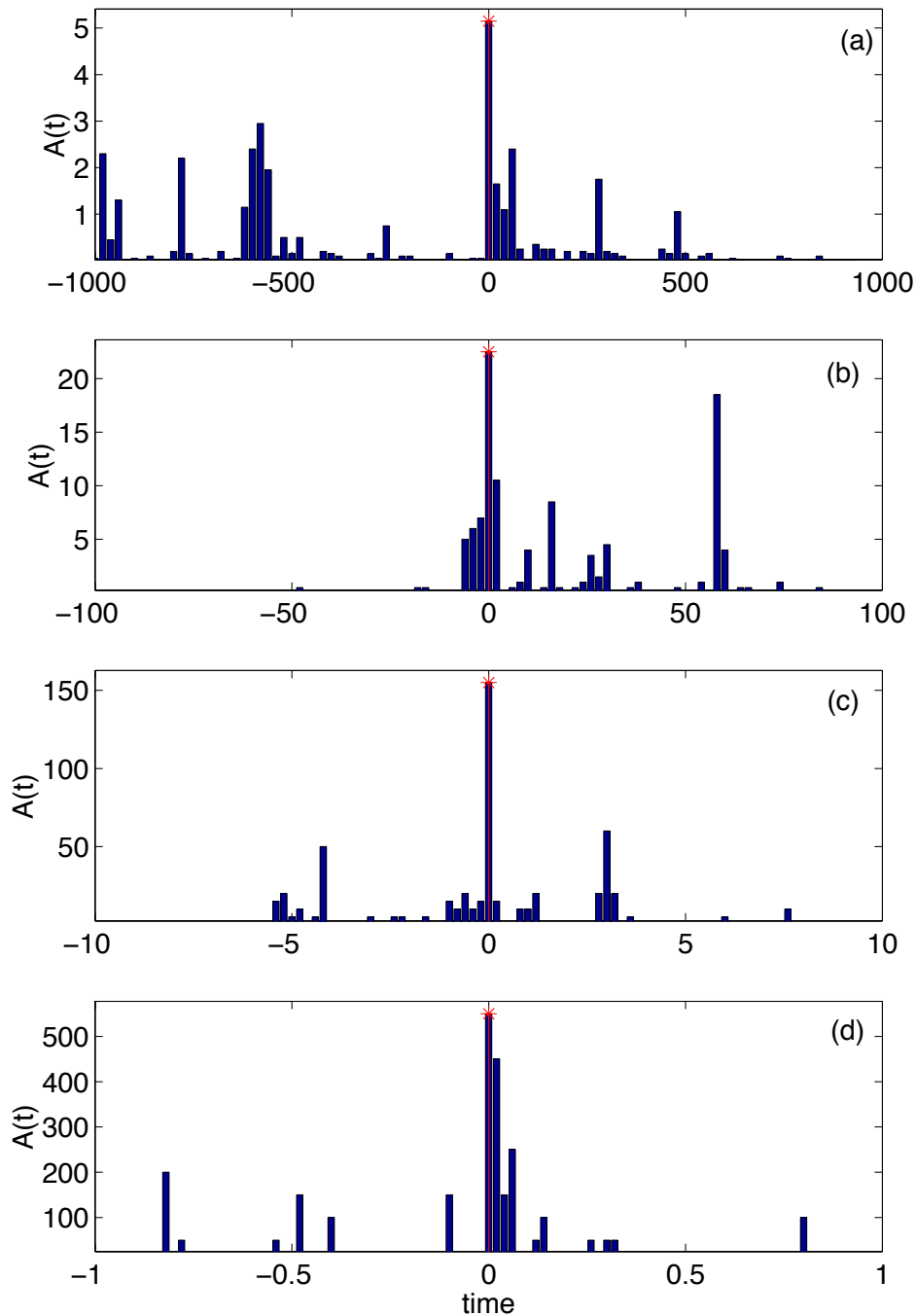


FIG. 12.2 – Rate of activity prior to and after an endogenously generated major burst of activity generated by a numerical simulation of the epidemic branching model (12.13) with a power law kernel with the same parameters  $\theta = 0.1$  and  $c = 0.001$  as in figure 12.1 with in addition a constant Poisson source term with rate  $\mu = 0.001$  corresponding, on average, to one event added from an external source per 1000 time units. Most of the observed activity is thus the result of interactions between events. The rate of activity close to the largest peak of activity is shown at increasing magnifications from top to bottom and is evaluated as in figure 12.1. Both precursory and relaxational processes can be observed at many time scales.

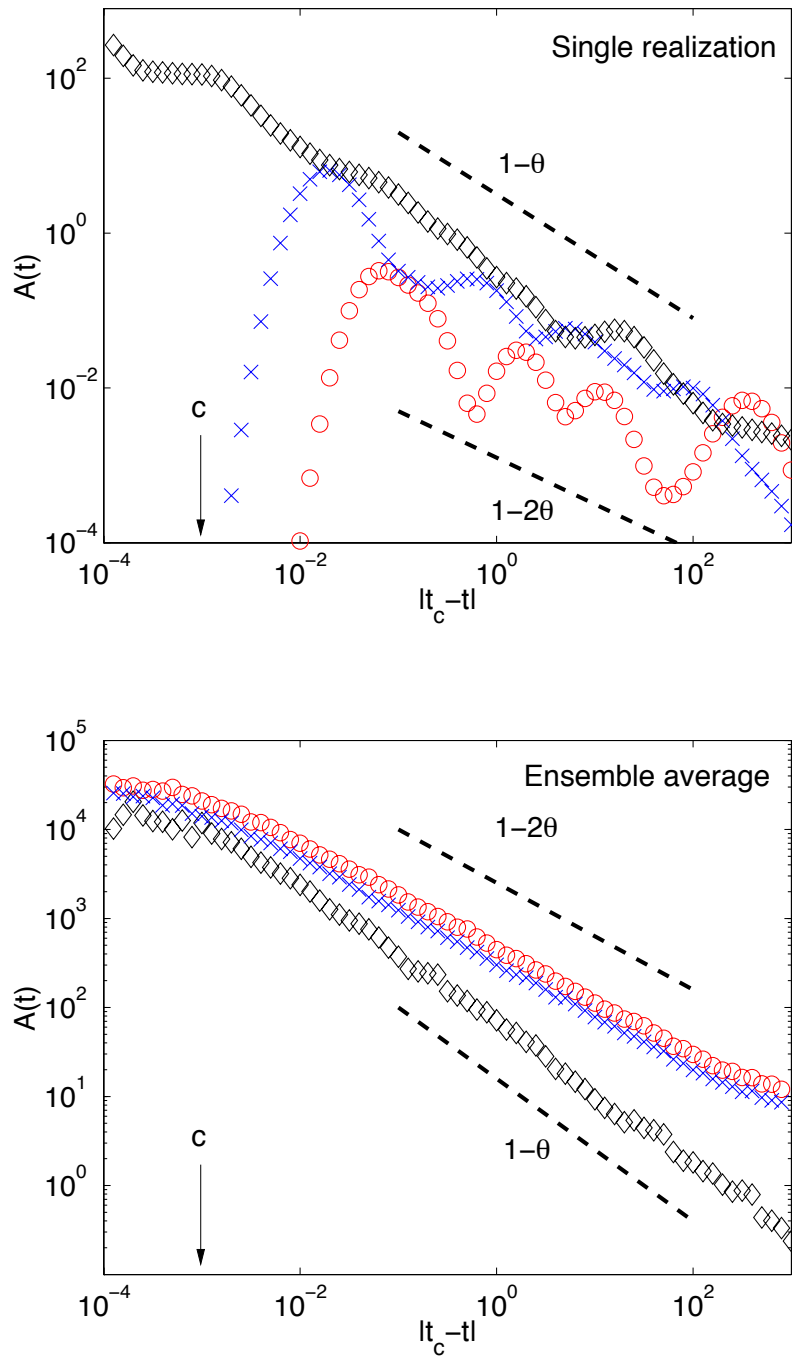


FIG. 12.3 – Rate of activity for a single sequence (a) of the epidemic branching model defined by (12.13) generated with a memory kernel decaying as a power law of time with the parameters  $\theta = 0.2$  and  $c = 10^{-3}$  and averaged over many sequences (b). The exogenous relaxation is shown with diamonds, the endogenous relaxation is shown as crosses and circles are for the precursory activity in the endogenous case. Large fluctuations are observed in the precursory activity and in the endogenous relaxation when looking at a single sequence, due to the small number  $\approx 100$  of observed events. Averaging over 50 realizations, we see clearly the faster decay rate  $\sim 1/t^{1-\theta}$  for the exogenous relaxation predicted by (12.7) compared with the endogenous one predicted by (12.11). The same decay rate  $\sim 1/t^{1-2\theta}$  predicted by (12.11) is observed for both the endogenous precursory and post-event relaxation.

Similarly, expanding the integral in (12.11) for short times, we obtain

$$E_{\text{endo}}[A(t)|A(0) = A_0] \propto A_0 F(0) \left[ 1 + \frac{1}{2} \frac{d \ln F}{dt} \Big|_{t=0} t + \mathcal{O}(t^2) \right], \quad (12.15)$$

where

$$F(t) \equiv \int_t^{+\infty} du [K(u)]^2 \quad (12.16)$$

is a monotonically decreasing function of time.

It is convenient to use the parameterization

$$F(t) = e^{-g(t)}, \quad (12.17)$$

where  $g(t)$  is an monotonously increasing function of time. Inserting (12.17) in (12.14) and (12.15) leads to

$$E_{\text{exo}}[A(t)] = A_0 K(0) \left[ 1 - \left( \frac{1}{2} g'(0) - \frac{1}{2} \frac{g''(0)}{g'(0)} \right) t + \mathcal{O}(t^2) \right], \quad (12.18)$$

and

$$E_{\text{endo}}[A(t)|A(0) = A_0] \propto A_0 F(0) \left[ 1 - \frac{1}{2} g'(0) t + \mathcal{O}(t^2) \right]. \quad (12.19)$$

1. For  $g''(0) = 0$ , that is,  $g(t) = 2\alpha t$  corresponding to a pure exponential relaxation  $K(t) \propto \exp[-\alpha t]$ , the velocities of the responses to an exogenous and to endogenous shock are identical;
2. for  $g''(0) > 0$  corresponding to a super-exponential relaxation  $K(t) \propto \exp[-\alpha t^c]$  with  $c > 1$ , the exogenous relaxation is slower than the endogenous one;
3. for  $g''(0) < 0$  corresponding to a sub-exponential relaxation such as a stretched exponential  $K(t) \propto \exp[-\alpha t^c]$  with  $c < 1$  or to the family of regularly varying functions such as power laws, the exogenous relaxation is faster than the endogenous one.

The exponential relaxation thus marks the boundary between two opposite regimes. As is intuitive, a sub-exponential relaxation betraying a long memory process leads to a slower short-time recovery after an endogenous shock, because it results from a long preparation process (12.12).

### Asymptotic long-time response

Since  $K(t)$  is a monotonously decaying function,  $K(t+u) \leq K(t)$  for any  $u \geq 0$ . This leads to the following inequality

$$E_{\text{endo}}[A(t)|A(0) = A_0] \leq A_0 K(t) \int_0^{+\infty} du K(u), \quad (12.20)$$

which is valid if the integral  $\int_0^{+\infty} du K(u)$  exists, that is, if  $K(t)$  decays faster than  $1/t$  at large times. This shows that, as soon as  $K(t) \ll C/t$  for any positive constant  $C$ ,  $E_{\text{endo}}[A(t)|A(0) = A_0] < E_{\text{exo}}[A(t)]$ . But the difference may be small and unobservable. For instance, for  $K(t) \propto$

$1/t^{1+\theta}$  with  $\theta > 0$ , a careful examination of the integral in (12.11) shows that, due to the contribution of the conditional noise close to the shock, we have

$$E_{\text{endo}}[A(t)|A(0) = A_0] \propto \frac{A_0}{t^{1+\theta}} \sim E_{\text{exo}}[A(t)] . \quad (12.21)$$

Thus, there is no qualitative difference in the relaxation rates of an endogenous shock and exogenous shock in this case : the contributions of all the conditional activity prior to the endogenous shock is equivalent to that of the shock itself. A more elaborate analysis specific to the problem at hand must be performed to predict the prefactors that will be different in the endogenous and exogenous cases.

In contrast, for memory kernels  $K(t) \propto 1/t^{1-\theta}$  with  $\theta > 0$  decaying slower than  $1/t$ , as for a stationary fNm of the form (12.5), we obtain

$$E_{\text{endo}}[A(t)|A(0) = A_0] \propto \frac{A_0}{t^{1-2\theta}} \gg E_{\text{exo}}[A(t)] \propto \frac{A_0}{t^{1-\theta}} . \quad (12.22)$$

In this case, the relaxation following an endogenous shock decays significantly more slowly than for an exogenous shock. This case is exemplified in figure 12.3. In the long time limit, the decay law  $1/t$  thus marks the boundary between two opposite regimes.

## Illustration

An illustration of this critical behavior is provided by the response of the price volatility  $\sigma_{\Delta t}$  at scale  $\Delta t$  defined as the amplitude (absolute value) of the return  $r_{Dt}(t) \equiv \ln[p(t)/p(t - \Delta t)] = \epsilon(t) \cdot \sigma_{\Delta t}(t) = \epsilon(t) \cdot e^{\omega_{\Delta t}(t)}$  of a financial asset.  $\epsilon(t)$  is a random sign. Indeed, financial price time series have been shown to exhibit a long-range correlation of their log-volatility  $\omega_{\Delta t}$ , described by a model [Muzy et al., 2000; Sornette et al., 2002] in which  $\omega_{\Delta t}(t)$  follows the process (12.1) with

$$K_{\Delta t}(t) \sim K_0 \sqrt{\frac{\lambda^2 T}{t}} \quad \text{for } \Delta t \ll t \ll T , \quad (12.23)$$

where  $T \approx 1$  year is a so-called integral time scale. This form (12.23) corresponds to parameterization (12.5) with  $\theta = 1/2$ . Sornette et al. [2002] have shown that there is a clear distinction between the relaxation of stock market volatility after an exogenous event such as the September 11, 2001 attack or the Aug., 19, 1991 coup against Gorbachev and that after an endogenous event such as the October 19, 1987 crash. In this model, the long-range memory acting on the logarithm of the volatility induces an additional effect, namely the exponent of the power law relaxation after an endogenous shock is a linear function of the amplitude of the shock.

## Synthesis of the asymptotic short and long time regimes

We have found two special functional forms for the response kernel  $K(t) \propto 1/t$  and  $K(t) \propto \exp[-\alpha t]$ , which are “invariant” or indifferent with respect to the endogenous versus exogenous

origin of a shock. Thus, for normal exponential relaxation processes as well as for power relaxation  $\propto 1/t$ , the functional form of the recovery does not allow one to distinguish between an endogenous and an exogenous shock.

These two invariants  $K(t) \propto \exp[-\alpha t]$  and  $K(t) \propto 1/t$  delineate two opposite regimes, the first one for short time scales and the second one for long-time scales :

1. for  $K(t) \propto 1/t^{1-\theta}$  with  $\theta > 0$ , the endogenous response decays more slowly than the exogenous response, at all time scales ;
2. for  $\exp[-\alpha t] \ll K(t) \ll 1/t$  for any positive  $\alpha$ , the endogenous response decays more slowly than the exogenous response at short time scales and has the same dependence as the exogenous response at long time scales ; this regime describes for instance the stretched exponential relaxation of complex fluids alluded to above ;
3. for  $K(t) \ll \exp[-\alpha t]$  for any positive  $\alpha$ , the endogenous response decay faster than the exogenous response at all time scales.

More complicated behaviors can occur when the memory kernel  $K(t)$  exhibits a change of regime, crossing the exponential and/or  $1/t$  boundaries at certain time scales. Each situation requires a specific analysis which yields sometimes surprising non-intuitive results [Helmstetter et al., 2002].

## 12.4 Conclusion

We think that the conceptual framework presented here may be applied to a large variety of situations, beyond those alluded to in the introduction. For instance, the result (12.12) has been shown to explain the so-called inverse Omori's law for earthquake foreshock activity before a mainshock, in a simple model of earthquake triggering [Helmstetter et al., 2002]. The same mechanism may explain the premonitory seismicity pattern known as "burst of aftershocks" [Keilis-Borok et al., 1978] : a mainshock with an abnormally large number of aftershocks has been found to be a statistically significant precursor to strong earthquakes [Molchan et al., 1990].

Many dynamical systems in Nature, such as geophysical and biological systems (immune network, memory processes in the brain, etc.), or created by man such as social structures and networks (Internet), States and so on, exhibit long-memory effects due to a wealth of possible mechanisms. For instance, Krishan Khurana at UCLA has suggested to us that the concept proposed here could explain that endogenous civil wars have long-lasting effects with slow reconstruction compared with the fast recovery after exogenous wars (that is, imposed or coming from the outside). The increasing emphasis on the concepts of emergence and complexity has emphasized an endogenous origin of the complicated dynamical behavior of complex systems. In reality, most (so-called) complex systems are the result of their internal dynamics/adaptation in response to a flow of external perturbations, but some of these external perturbations are rare extreme shocks. What is the role of these exogenous shocks in the self-organization of a complex

system? Can one distinguish the impact of extreme exogenous shocks from an endogenous organization at different time scales? Our present analysis has just scratched the surface of these important and deep questions by suggesting an angle of attack based on the conditional historical process at the basis of strong endogenous fluctuations. Extensions of the present simplified framework involve the generalization to multidimensional coupled processes such as in [Jefferies et al., 2002] and to nonlinear spatio-temporal processes.

We are grateful to A.B. Davis, V. Keilis-Borok and V.F. Pisarenko for useful exchanges.



# Chapitre 13

## Conclusions

We now summarize our main results :

- We have measured the scaling of the number of aftershocks with the mainshock size, and showed that seismicity triggering is driven by the smallest earthquakes.
- We have investigated several physical mechanisms underlying the local Omori's law to explain its observed variability.
- We have classified the different regimes of triggered seismicity in the ETAS model.
- We have proposed an improvement of the prediction methods based on point processes, by taking into account the secondary cascades of aftershocks.
- We have shown how these cascades of triggered seismicity may lead to aftershock diffusion and foreshock migration and compared our numerical and analytical results with observations of real seismicity.
- We have discovered that the inverse Omori's law for foreshocks may derive from the direct Omori's law for aftershocks as the most probable trajectory of seismicity, conditioned on the fact that it leads to a burst of seismic activity accompanying the mainshock. Observations of real seismicity are in good agreement with the results derived for the ETAS model.
- We have shown that the often documented apparent decrease of the  $b$ -value of the GR law at the approach to the mainshock results straightforwardly from the conditioning of the path of seismic activity culminating at the mainshock. In the ETAS model, the magnitude distribution is not modified by a decrease of  $b$ -value, but by a deviatoric distribution with a constant exponent  $b' < b$  and with an amplitude growing as a power-law of the time to the mainshock. Analysis of seismicity data using a superposed epoch analysis are in good agreement with the results obtained with the ETAS model.

The ETAS model discussed here can be improved to take into account the following features

- The possible dependence between the magnitude of a mainshock and its aftershocks. Is the magnitude of an aftershock limited by the size of the mainshock? Or can any small event trigger a larger earthquake?

- The anisotropy of the seismic activity. We can for example introduce a dependence of the aftershock rate on the focal mechanism of the mainshock to reproduce the anisotropy of the Coulomb stress.
- The possible decrease of seismic activity following a large event, in the regions where the stress change induced by the mainshock is negative. This decrease of seismic activity in “stress shadows” is however still controversial.
- The localization of the seismicity on faults. The seismicity can be constrained by existing fault geometry, when the fault network is known. Alternatively, we can include a non-uniform seismicity background, deduced from the past seismicity, to obtain a realistic spatial distribution of seismicity.

Is the physics of triggering fully characterized by the class of models discussed here? Or are there other processes that lead to large earthquakes? If yes, this would imply that earthquakes are not only actors speaking to and influencing each other. Some of them may be also witnesses of “forces” beyond their realm. It is thus particularly interesting to develop a methodology to test the limits of the triggered-seismicity models, specifically to identify what processes and patterns can not be reproduced and/or explained.

A possible alternative, still controversial, is the critical earthquake concept that requires interactions or rather influences beyond what seems reasonable within the strict confine of elastic stress redistribution. In this context, observations of the acceleration of seismic moment leading up to large events and “stress shadows” following them have been interpreted as evidence that seismic cycles represent the approach to and retreat from a critical state of a fault network (see [Sammis and Sornette, 2002] for a review). Predictability might then become possible by monitoring the approach of the fault network toward the critical state.

The outstanding question is thus the following : are the often reported precursory patterns of seismic activity ( $b$ -value decrease, power-law acceleration of the seismic activity, ...) completely explained by the ETAS model used in this work? In this case, the ETAS model would provide a significant predictability of earthquake activity, as shown in chapter 7, but the accurate prediction of a single event (in time, space and magnitude) would be impossible because of the inherent stochasticity of the model. If some precursory patterns are not completely reproduced by the ETAS model, these precursors may provide a higher predictability of large earthquakes. The ETAS model should therefore be used as a null hypothesis to test precursory patterns and prediction algorithms, and may be improved to take into account some seismicity patterns that are not yet reproduced by the simple ETAS model used in this work.

Deuxième partie

**Instabilités gravitaires**



## Chapitre 14

# Statistical analysis of rockfall volumes : implication for rockfall dynamics

Carine Dussauge<sup>1</sup>, Jean-Robert Grasso<sup>2</sup> and Agnès Helmstetter<sup>2</sup>

<sup>1</sup> Laboratoire Interdisciplinaire de Géologie et de mécanique, Université Joseph Fourier, Grenoble, France.

<sup>2</sup> Laboratoire de Géophysique Interne et Tectonophysique, Université Joseph Fourier, Grenoble, France.

Accepted in *Journal of Geophysical Research*, 2002.

### Abstract

We analyse the volume distribution of natural rock falls on different geological settings, i.e. calcareous cliffs in the French Alps, Grenoble area, and granite Yosemite cliffs, California sierra, and different volume ranges, i.e. regional and world wide catalogs. Contrary to previous studies that included several types of landslides, we restrict our analysis to rock fall sources which originated on sub vertical cliffs. For the three data sets, we find that the rock fall volumes follow a power law distribution with a similar exponent value, within error bars. This power-law distribution was also proposed for rock fall volumes that occurred along road cuts. All these results argue for a recurrent power law distribution of rock fall volumes on sub vertical cliffs, for a large range of rock fall sizes ( $10^2 - 10^{10} \text{ m}^3$ ), regardless of the geological settings and of the pre-existing geometry of fracture patterns that are drastically different on the three studied

areas. The power law distribution for rock fall volumes could emerge from two types of processes. First, the observed power law distribution of rock fall volumes is similar to the one reported for both fragmentation experiments and fragmentation models. This argues for the geometry of rock mass fragment sizes to possibly control the rock fall volumes. This way neither cascade nor avalanche processes would influence the rock fall volume distribution. Second, without any requirement of scale invariant quenched heterogeneity patterns, the rock mass dynamics can arise from avalanche processes driven by fluctuations of the rock mass properties, e.g. cohesion or friction angle. This model may also explain the power-law distribution reported for landslides involving unconsolidated materials. We find that the exponent values of rock fall volume on sub vertical cliffs,  $0.5 \pm 0.2$ , is significantly smaller than the  $1.2 \pm 0.3$  value reported for mixed landslide types. This change of exponents can be driven by the material strength, that controls the in-situ topographic slope values, as simulated in numerical models of landslides [*Densmore et al.*, 1998; *Champel et al.*, 2002].

## 14.1 Introduction

Rock falls, rockslides and rock avalanches are defined as rapid movements of rocks driven by global gravity forces, having their origin on steep rock slopes, including sub vertical cliffs. These phenomena are a subset of the more general landslide phenomena, which can include falls, slumps and slides in all kind of ground material from stiff rock mass to unconsolidated or poorly cemented materials [*Varnes*, 1978; *Keefers*, 1999]. The word rock fall is usually used to describe small phenomena, ranging in size from block falls of a few  $\text{dm}^3$  up to  $10^4 \text{ m}^3$  events. Rockslides sometimes involve more than  $10^5 \text{ m}^3$  and rock avalanches can reach several million cubic meters [*Varnes*, 1978; *Keefers*, 1984; 1999]. In this study we will use the rock fall label without any volume distinction, nor distinction in the failure mechanism.

As for floods, earthquakes or volcanic eruptions, evaluating rock fall dynamics means analysing the location, size and time patterns of rock fall events. Here we focus on the distribution of rock fall volumes. For some natural phenomena, including floods and earthquakes, statistical analysis are used to derive the recurrence rate of an event of a given size. The flood sizes are proposed to follow an exponential distribution [e.g. *Guillot and Duband*, 1967; *U.S. Water Resources Council*, 1982], whereas the earthquake sizes are best fitted by a power law distribution [*Gutenberg and Richter*, 1949]. On the first hand, the size distribution can be used for hazard assessment, if we hypothesize the distribution to be stationary over time. On the other hand, the type of distribution can provide routes to further investigate the underlying physical processes.

Power law distributions have been suggested to characterize rock fall distributions triggered along road-cuts [*Noever*, 1993; *Hungr et al.*, 1999], or natural cliffs [*Gardner*, 1970; *Wieczorek et al.*, 1995]. In this study we analyse the volume distributions of rock falls from natural cliffs, in different geological settings, different volume ranges and different time scales. Contrary to

earthquakes, rainfalls, or floods, few if any natural slopes or cliffs are continuously monitored in order to provide the exact time of occurrence, location and size of rock fall events. Due to the lack of instrumental monitoring of rock falls, the available inventories are weak compared to some other natural phenomena, with several possible biases induced by non homogeneous sampling in time, space and size domains. We test how reports of rock fall activity can be used to investigate rock fall volume distribution, the way other scientists used historical catalogs to further constrain contemporary, short time, instrumental catalogs e.g. [*Wesnowsky et al.*, 1983; 1984].

We compare volume distributions of natural rock falls that occurred on Grenoble cliffs, French Alps [*RTM*, 1996], Yosemite cliffs, Sierra Nevada, California [*Wieczorek et al.*, 1992] and a worldwide inventory of large rockslides [*Couture*, 1998]. The first two case studies investigate the same temporal scale, about one century, and the same spatial scale, roughly 100 km of cliff length. The main difference between these 2 case studies is the involved rock masses, layered calcareous cliffs and massive granite rock cliffs, for Grenoble and Yosemite catalogs respectively. For each area, we validate statistically the power law distribution function as an estimate for the observed rock fall volume distribution. Exponent values are similar, within error bars, for the three data sets. This suggests that the distribution law for rock fall volume does not depend on either the geological setting or the scale of observation. These results are similar to analysis of rock falls that occurred along road cuts [*Noever*, 1993; *Hungr et al.*, 1999]. We show how this distribution law can be used for rock fall hazard assessment, by analysing the validity domains and limits of this approach. We investigate the possible mechanical models that can reproduce this power law distribution of rock fall volumes.

## 14.2 Data

### Measurement techniques for rock fall inventories

Concerning the study of earthquakes, rainfalls or floods, instrumental monitoring provides direct or indirect estimates of events occurrence in size, time, and space domains. Few instrumental measurements exist for the study of the rock fall activity, especially concerning natural cliffs. One study uses a continuous seismic monitoring to detect rock fall events and to size up rock fall volumes on a single, well defined cliff [*Rousseau*, 1999]. *Rousseau* [1999] uses a seismic model to derive the volume of a rock fall event from the amplitude of the recorded seismic signals. Generally, data about rock falls are mainly reported by forest guards or road surveyors without the help of any quantifying tool. Due to this lack of instrumental monitoring, the rock fall volumes inventories suffer several possible biases.

First, the sampling in time domain is driven by the visit rate of the field survey observer, this survey being usually part of a forestry or road survey (not specific to rock fall observation). For some events, the field evidences can disappear within the laps time of two visits. For other

events, the visit rate can induce a cumulative effect on rock fall volumes estimates, i.e. all the rock falls which occurred at the same place are estimated as one single event at the sampling rate resolution.

Second, in size domain, rock fall events are reported mainly when they induce damages to natural or anthropic entities. Impacts on forest trees, trails, roads and housing are the main criteria to report the occurrence of a rock fall event. Therefore the rock falls which did not induce damages are seldom reported. This induces a censoring effect for the so-called small events. Small volumes are also under sampled because of the screening effect due to man made protective structures, such as rock fences or forests. As a consequence, non-instrumental inventories are obviously incomplete for the small events.

Another possible bias emerges from the inaccuracy of volume estimates, which are based on the observation of the deposit area, sometimes coupled with the observation of the visible scar on the slope. Error bars for volumes are thus large and difficult to quantify. For large rock fall volumes, i.e. volumes greater than a few hundreds of cubic meters, the volume estimate comes from the area covered with new rock material and its thickness. For smaller rock falls the sum of the volumes of the largest blocks is usually used as a volume estimate. When visible, the surface of the cliff scar that is induced by the rock fall is further used, its thickness being more difficult to assess.

### **The Grenoble rock fall inventory, French Alps**

The first data set reports rock falls that occurred on subvertical cliffs surrounding the urban area of Grenoble city, French Alps [RTM, 1996]. These cliffs are part of the Chartreuse and Vercors subalpine massifs, made of sedimentary rocks from upper Jurassic and lower Cretaceous age (limestone and marls). Initial bedding is folded and faulted due to alpine horizontal compressive stresses, resulting mostly in subvertical fractures across gently inward dipping stratification (Figure 14.1). The cliffs dimensions are 50 m to 400 m in height, 120 km in length, as cumulative values on two successive rocky walls (Figure 14.1). The cliffs elevation ranges from 800 m to 2000 m. For such an altitude, in the French Alps, the climatic conditions correspond to wet springs and falls seasons and frozen conditions in wintertime. The area is suggested to have a slow tectonic deformation rate, i.e. less than a few mm/yr either for horizontal or for vertical displacements [Martinod *et al.*, 1996]. Historical and instrumental seismicity rates are low, with a few  $M=4$  earthquakes reported in the area during the last 5 centuries [Fréchet, 1978; Grasso *et al.*, 1992]. There is no report on rock falls possibly triggered by earthquakes. One possible change in loading conditions is the last glacial unloading (Würm, dated  $10^4$  yrs before present).

Rock fall activity that occurred in the Grenoble calcareous Alps from 1248 to 1995 was reported by the Restauration des Terrains de Montagnes Office (RTM), a forestry office in charge of natural risks in the French Alps, since 1870 [RTM, 1996]. As the RTM office was created in 1870, the 1870-1890 period is the threshold between archive reports for rock fall events

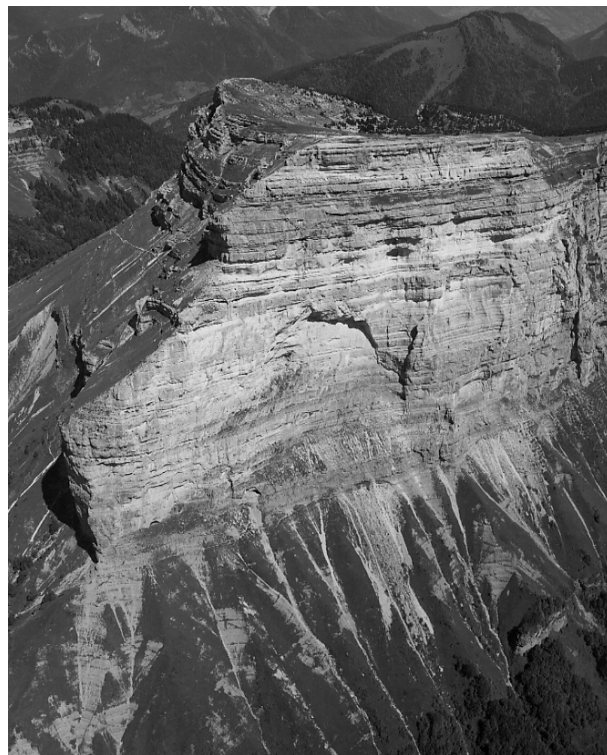
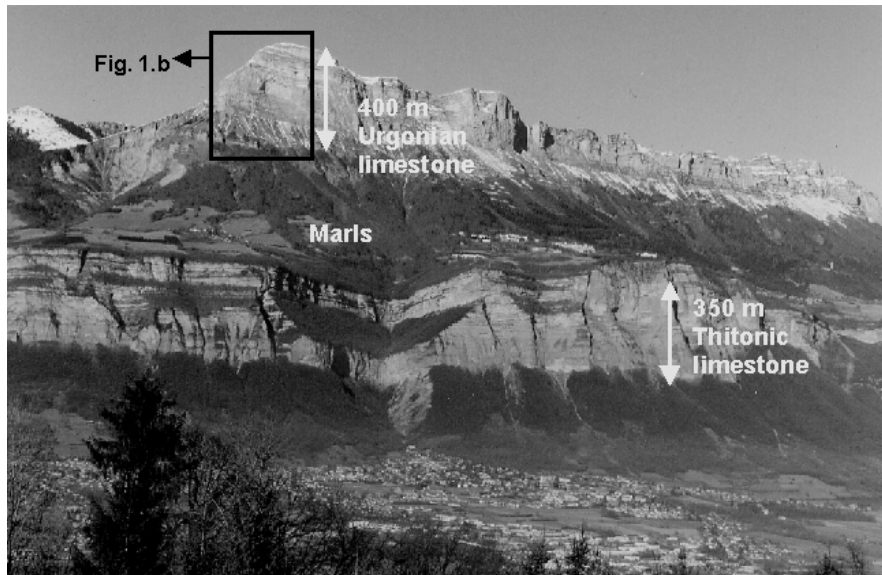


FIG. 14.1 – East face of the Chartreuse massif, Grenoble, France. (a) Subvertical calcareous cliffs are separated into two levels; the intermediate, less steep, slope is associated to marly levels. The maximum height of each level is 350-400 m and the total length of cliffs is 120 km. Note the sub-urban area of Grenoble at the bottom of the cliffs. The photograph, by *J.M. Vengeon*, is roughly 5% of the total area covered by the Grenoble rock fall inventory [ *RTM*, 1996]. (b) Geometry of the fracture pattern, as detailed from top of the cliff on (a). It is roughly characterized by a subhorizontal bedding and subvertical orthogonal joints.

and the specific survey of mountain slopes. For each event the available data from the Grenoble catalog are (i) the location of the rock fall, (ii) the date of occurrence, (iii) the volume and the induced damages. Most of this information has been reported by forest guards as described in the previous section, with a sampling rate of once every a few weeks. For some roughly estimated volumes, we provide new volume estimates on the basis of in-situ observation and re-analysis of reports. Reported volumes range from  $3.10^{-2} \text{ m}^3$ , i.e. typical of a slight damage on a single house, to  $5.10^8 \text{ m}^3$ . The largest event of this data set is the 1248 Mt Granier rock avalanche, 40 km north of Grenoble, with a volume of  $5.10^8 \text{ m}^3$  [*Goguel and Pachoud, 1972*].

For this data set, we know that rock fall volumes smaller than a few tens of  $\text{m}^3$  are not always reported because of the sampling procedure. On the other hand, volumes greater than  $500 \text{ m}^3$  are always damaging events by their impact either on infrastructures or on forests and they induce changes in the cliff pattern (scars, change in colour, geometry), that are rarely invisible. We thus assume the Grenoble inventory to be complete for volumes greater than  $500 \text{ m}^3$ . Because of the non-uniform temporal sampling (Figure 14.2), one large event in 1248 and just a few ones reported in the 17th - 19th centuries period, we select events within the 1935-1995 time window only. This period is a trade off between a minimum number of available events and a period for which the sampling can be considered as uniform. On such a basis, the Grenoble catalog we used involves 87 events.

### The Yosemite Valley rock fall inventory, California

The second data set we use gathers rock falls that occurred in the Yosemite Valley, Sierra Nevada, California [*Wieczorek, 1992*]. It concerns cliffs of massive granite from Cretaceous age. The total area covers almost 100 km of cliff length. Cliffs have a maximum height of 1000 m, with a mean value of 300 m, and an elevation ranging from 1000 to 2300 m (Figure 14.3). The climatic setting is roughly a dry and warm spring and summer, and cold wet falls and winter. Rock falls result partly from exfoliation and sheeting processes that are induced by the release of pressure of previously buried rocks (Figure 14.3). The resulting sheets tend to be mainly parallel to the topography [*Huber, 1987*]. This area is subjected to a moderate to strong tectonic loading, induced by the subduction of the Pacific plate beneath the North American plate. Resulting tectonic deformations are of the order of 5 mm/yr for uplift rate and 5 mm/yr for horizontal compression. Roughly, 5% of the rock falls are reported as triggered by earthquakes [*Wieczorek, 1992*]. Last glacial unloading corresponds to the end of the Tioga epoch, 15000 years BP at relatively low elevation [*Huber, 1987*].

The historical Yosemite rock fall inventory reports 395 events in the 1850-1992 period [*Wieczorek, 1992*]. Most of them are reported by either National Park Rangers or USGS geologists. As for the Grenoble inventory, there are large uncertainties on reported volumes, and a non-uniform sampling of small volume rock falls over time. The sampling rate is globally shorter than one month, observed data being collected in the Superintendent Monthly report. This sampling rate

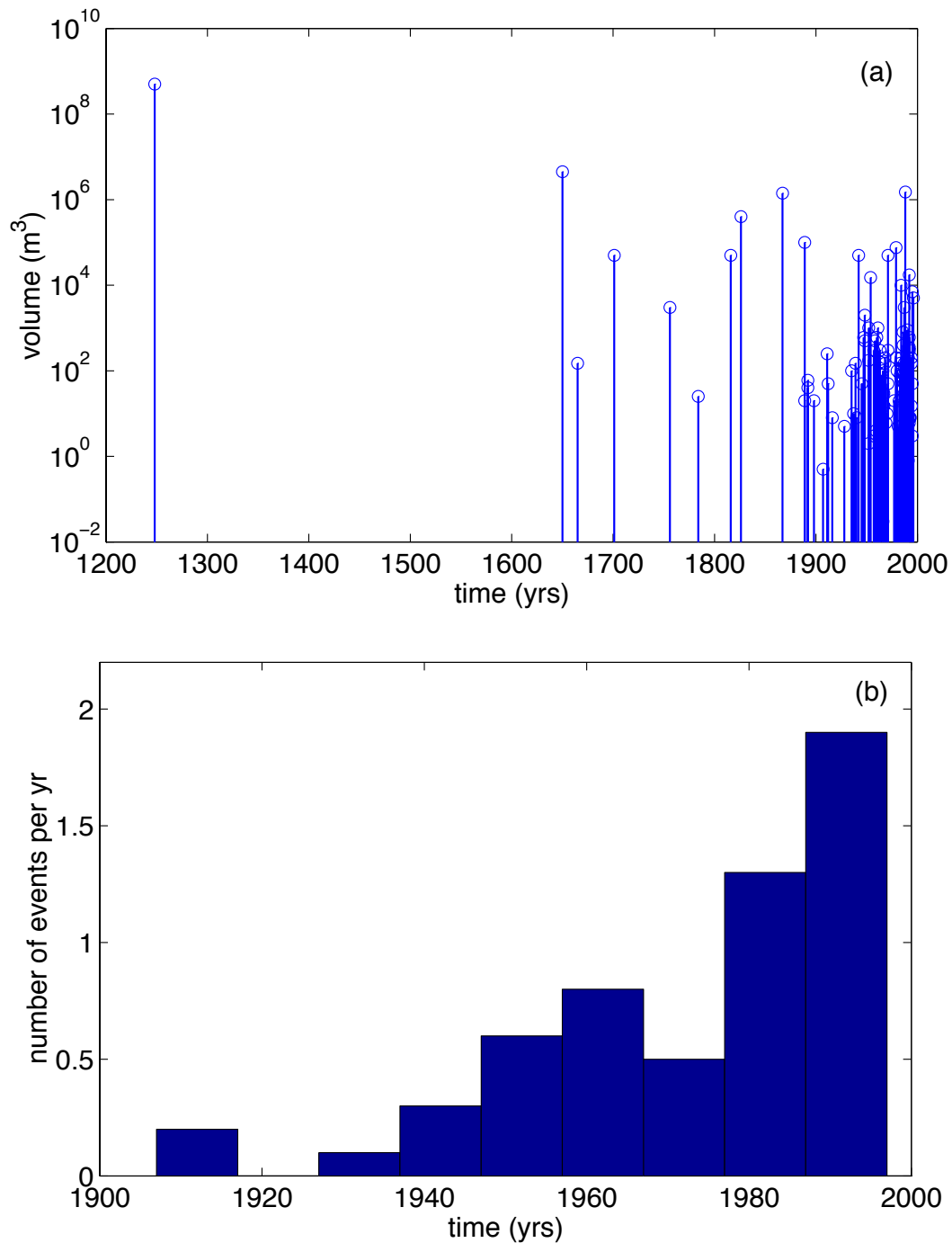


FIG. 14.2 – Occurrence rate for rock falls for Grenoble area, *RTM* inventory [1996]. a) volumes and time of occurrence in the 1200-1995 period. b) Occurrence rate in the 1935-1995 period for volume larger than  $50 \text{ m}^3$ . Due to the non uniform temporal and volume samplings, the studied catalog is restricted to the 1935-1995 period, involving 87 events with volumes ranging from  $10^{-2}$  to  $10^6 \text{ m}^3$ .



FIG. 14.3 – Cliffs surrounding the Yosemite Valley, California Sierra. (a) Subvertical granitic cliffs, maximum height 800-1000 m, total length 100 km ; photograph by *G. Wiczorek*. (b) Detailed view of the Fairview dome : the fracture pattern is roughly characterized by a sheeting process giving joints parallel to the topography, and spaced subvertical joints ; photograph by *J.R. Grasso*.

has been much shorter in the last ten years [*Wieczorek*, personal communication]. The threshold for the inventory completeness for the small events is not estimated.

There are two classes of volume estimates in the Yosemite inventory. For one class of rock falls, roughly one quarter of the inventory, the reports allow a quantitative estimate of volumes. For the second class, only qualitative estimates are given. Following the same criterion as for the Grenoble catalog, we select events with quantitative volume estimates in the 1915-1992 period (Figure 14.4). We obtain 101 events, with volumes ranging from 1 to  $6.10^5 \text{ m}^3$ . Because qualitative volume estimates exist in the inventory for volumes as large as a few thousands cubic meters, this volume catalog is not complete up to large volumes. We will consider this volume inventory as a subset of the genuine volumes of the Yosemite rock fall population, for the 1915-1992 period.

## A worldwide rock falls inventory

The last data set we use is a worldwide collection of large rockslides and rock avalanches, as old as the last glacial epoch [*Couture*, 1998]. Contrary to the two previous data sets of rock falls that occurred within homogeneous geological setting, e.g. calcareous and granite cliffs respectively, *Couture* [1998] is an overview of the phenomenology of rock avalanches on Earth and other planets. Therefore the geological setting of these events is obviously heterogeneous, and the sampling method just comes out from a bibliographic study.

From the Couture inventory, we selected 142 Earth events. Estimated volumes are provided by historical reports, based on observations of cliff scars and deposits or on geomorphological patterns for the oldest events. The collection is not supposed to be exhaustive [*Couture*, 1998]. The sampling is neither uniform in time, recent events being more often reported than older ones, nor in space domain. Also, the sampling is not uniform in size, the largest events being preferentially reported in historical reports. Like the Yosemite inventory, this data set is one subset of the complete worldwide catalog.

## 14.3 Statistical analysis of volume distribution

For the three data sets, we test which distribution function best describes the rock fall volume data. For each catalog, the selected events correspond to the time window for which the catalog is supposed to be homogeneous in the time domain. Because of the censoring effect, there is an under sampling of small volume events. For the largest observed volumes, with a size comparable to the cliff height, the distribution may be truncated because of finite size effects. Accordingly, we select only rock fall events above a given volume. This minimum volume is a-priori unknown, and will be estimated from the adjustment of distribution laws to the data. First we search which distribution functions may describe our data. Second, using the  $\chi^2$  criterion, we test if the rock fall volume distribution is consistent with the hypothesized distribution functions.

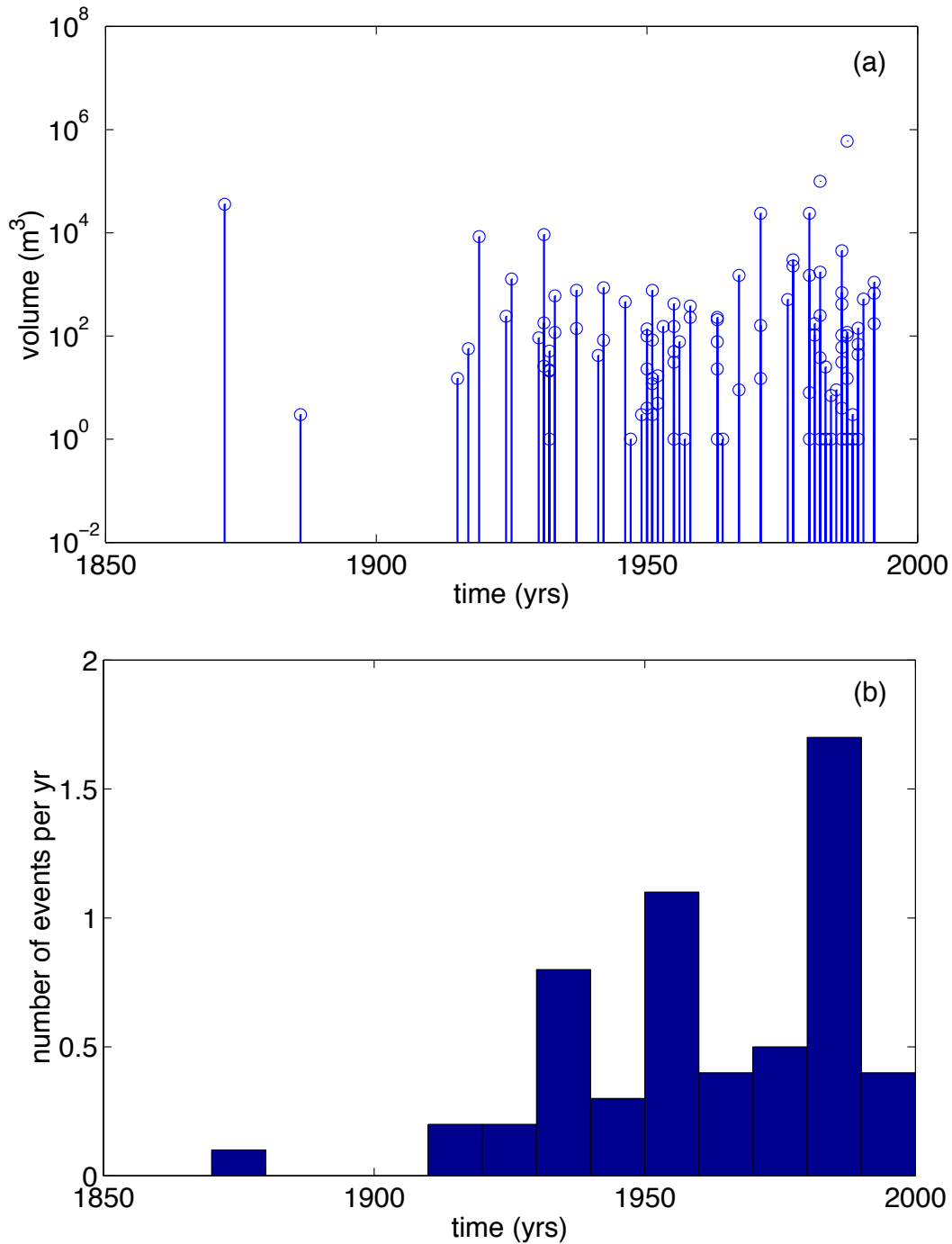


FIG. 14.4 – Occurrence rate for rock falls from the Yosemite Valley data set [Wieczorek, 1992]. a) Volume and occurrence for the 1850-1992 period. b) Occurrence rate in the the 1915-1992 period for volume larger than  $50 \text{ m}^3$ . Due to the non uniform temporal sampling shown on the 1850-1992 period, the time window selected for the study is 1915-1995, involving 101 events with volumes ranging from 1 to  $10^6 \text{ m}^3$ .

TAB. 14.1 – Characteristics of rock fall volume distributions for the 3 studied data sets.  $N$  is the total number of events in the catalog,  $N_{fit}$  is the number of events with volume above  $V_0$  used for the fit.

data	time	$N$	$V_{obs}$ m <sup>3</sup>	$V_0$ m <sup>3</sup>	$N_{fit}$	$b_{lr}$	$b_{ml}$	$\chi_r^2$
RTM	1935-1995	87	$10^{-2} - 10^6$	40	55	0.40	$0.41 \pm 0.06$	0.58
Yosemite	1915-1992	101	$1 - 10^6$	50	55	0.46	$0.45 \pm 0.06$	0.72
Worldwide	10 000 yrs	142	$10^3 - 2 \times 10^{10}$	$3.1 \times 10^7$	54	0.58	$0.51 \pm 0.07$	1.07

## Grenoble inventory

The observed cumulative distribution for the Grenoble cliffs is evaluated for the 87 rock fall events in the 1935-1995 period (Figure 14.5). The distribution is almost linear in a log-log plot for volumes larger than 40 m<sup>3</sup>. For volumes smaller than 40 m<sup>3</sup>, we observe a downward departure from the linear behavior that is typical of a censoring effect. Accordingly, we test how the observed cumulative volume distribution may be adjusted by a power-law distribution for the 55 events of volume above 40 m<sup>3</sup>, i. e.,

$$N(V) \sim V^{-b}, \quad (14.1)$$

with  $V$  the rock fall volume,  $N(V)$  the number of events greater than  $V$  and  $b$  a constant parameter. First we use the maximum likelihood method [Aki, 1965] and linear regression to estimate the  $b$ -value. The maximum likelihood estimate for  $b$  is

$$b = \frac{1}{\ln(10) \langle \log(V) \rangle - \log(V_0)}, \quad (14.2)$$

in the case of a pure power law distribution, with a standard deviation determined by,

$$\sigma = \frac{b}{\sqrt{N_1}}, \quad (14.3)$$

where  $V_0$  is the minimum volume used in the power law fit,  $\langle \log(V) \rangle$  is the average of  $\log(V)$  for events larger than  $V_0$  and  $N_1$  the number of events with volume larger than  $V_0$ . A more complex equation is necessary when the distribution is bounded to a given  $V_{max}$  value. This is not the case of the data we fit, i.e. we have no a-priori bound on the maximum volume size.

For the Grenoble inventory, these two techniques provide similar values,  $b \sim 0.40$  (Table 14.1). The standard deviation of  $b$  given by (14.3) is 0.06, as estimated from the maximum likelihood method. These values are not sensitive to either a  $V_0$  value increase above 40 m<sup>3</sup> or a change in the analysed time period. Second, we use the  $\chi^2$  test to validate the hypothesis that the observed volume distribution follows a power law distribution for volumes larger than 40 m<sup>3</sup>. The  $\chi^2$  test compares an observed histogram to a histogram obtained by sampling the hypothesized distribution function [e.g. Press et al., 1992; Taylor, 1997]. The  $\chi^2$  value measures

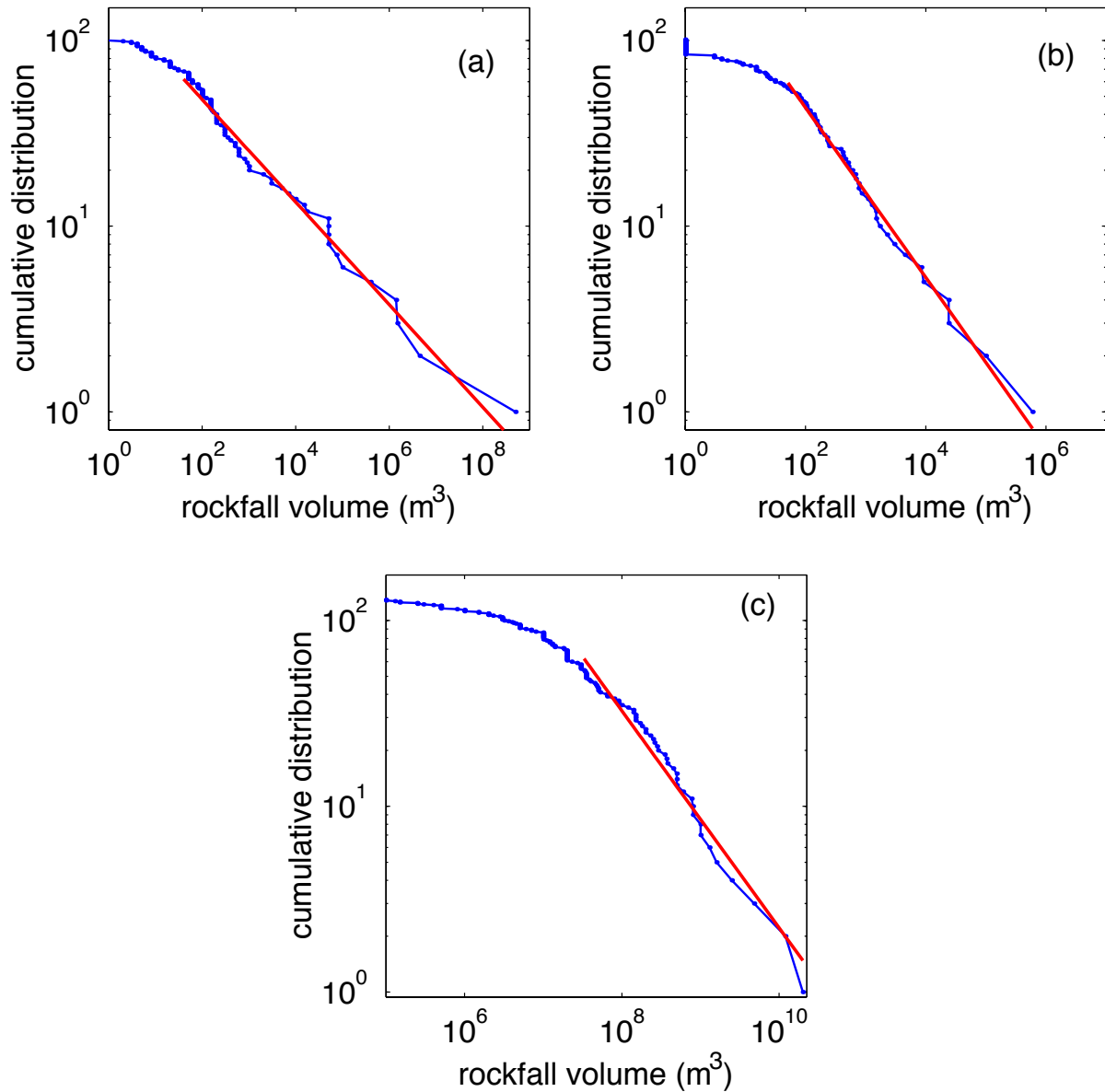


FIG. 14.5 – Cumulative volume distributions for rock falls. (a) Grenoble area. Rock falls occur on a calcareous cliffs of 120 km of length. We used the 87 events of the 1935-1995 time window. The straight line is the power law fit, with  $b=0.40$ , estimated by linear regression in the  $40\text{-}10^6$   $m^3$  volume range; the reduced  $\chi^2$  is 0.58 (b) Yosemite Valley. Rock falls occur on a granite cliffs of 100 km length. We used 101 events on the 1915-1992 time window. The straight line is the power law fit, with  $b=0.46$ , estimated by linear regression in the  $50\text{-}10^6$   $m^3$  volume range. The reduced  $\chi^2$  is 0.72. (c) World wide inventory, 142 records in the last 10.000 years. The straight line is the power law fit, with  $b=0.58$ , estimated by linear regression in the  $3 \times 10^7\text{-}2 \times 10^{10}$   $m^3$  volume range. The reduced  $\chi^2$  is 1.07. See text for details.

a distance between these two histograms, as defined by,

$$\chi^2 = \sum_{i=1}^k \frac{(n_i - n_i^*)^2}{n_i^*}, \quad (14.4)$$

where  $n_i$  is the observed number of events in the  $i$ th bin, and  $n_i^*$  is the expected number for the hypothesized distribution function. Equation (14.4) follows a so-called  $\chi^2$  probability law, that allows evaluating the probability to overpass the  $\chi^2$  value when the tested hypothesis is true. We use the reduced  $\chi^2$  value [Press *et al.*, 1992; Taylor, 1997], obtained by dividing the  $\chi^2$  value by the number of degrees of freedom of the system,  $n_f$  defined by,

$$n_f = (\text{number of bins}) - c, \quad (14.5)$$

where  $c$  is the number of constraints applied for the  $\chi^2$  test. For our application,  $c = 2$ , with one constrain for the parameter of the law in the case of the power law, and one for the binning of the data in equiprobable classes [Press *et al.*, 1992; Taylor, 1997]. A reduced  $\chi^2 \gg 1$  rejects the tested distribution as a possible description of the data.

Because the  $\chi^2$  test requires Gaussian-distributed numbers of objects per bin, we have a trade off between the appropriate number of bins and the number of objects within each class. Using 11 bins, corresponding to 5 events per bin, we obtain a reduced  $\chi^2$  value of 0.58. The power-law distribution is thus accepted by the test with a 95% confidence value. We have tested different values of bin numbers between 5 and 18. The reduced  $\chi^2$  value is always close to 1, so that the power-law distribution is always accepted at the 95% confidence level. With the same type of analysis, we reject other distribution functions, such as the exponential, Weillbull and Gumbel distributions, to fit the Grenoble rock fall volume distribution in the same volume range.

## Yosemite inventory

The rock fall volume distribution from the Yosemite inventory is built with 101 events that occurred in the 1915-1992 period (Figure 14.5). As for the Grenoble data set, we recover (i) a roughly linear pattern on a log-log plot for volumes larger  $50 \text{ m}^3$ , (ii) a downward departure from the linear pattern for small volumes. For the 56 events of volume above  $50 \text{ m}^3$ , we obtain  $b=0.45$  from a linear regression of the cumulative volume distribution, with a standard deviation of 0.06. Using the maximum likelihood method we recover a similar  $b$ -value (Table 14.1). The  $b$ -value is not sensitive to changes in either the time period or the minimum volume above  $50 \text{ m}^3$ .

Using 11 bins, corresponding to 5 events per bin, we obtain a reduced  $\chi^2$  value of 0.72. Therefore, the hypothesis that the rock fall volumes follow a power law is accepted at the 90% confidence level.

## World wide inventory

The 142 events of the worldwide inventory range in size from  $10^4$  to  $10^{10}$  m<sup>3</sup>. The cumulative volume distribution shown in Figure 14.5 mimics the 2 previously analysed data sets. For the 54 events with a volume greater than  $3 \cdot 10^7$  m<sup>3</sup>, the observed distribution is well fitted by a power law distribution with  $b=0.51$ , in agreement with the other data sets ( Table 14.1). Using 10 bins, corresponding to 5 events per bin, we obtain a reduced  $\chi^2$  value of 1.07. Therefore, the hypothesis that the rock fall volumes follow a power law distribution above  $10^7$  m<sup>3</sup> is accepted at the 90% confidence level. Similar results are obtained when testing different bin numbers between 5 and 10.

## 14.4 Discussion

### Synthesis of observed rock falls volume distributions

The three originally analysed data sets display power law distributions of rock fall volumes, with similar power law exponents, i.e., close to  $0.45 \pm 0.06$ . The Yosemite and Grenoble cliffs have similar global morphological patterns, with common lengths of steep cliffs made of strong rock matrix. The geometries of the discontinuity patterns are different for the two cliffs. Sub-vertical fractures across gently dipping stratification characterize the Grenoble sedimentary cliffs, while exfoliation and sheeting of granitic domes are reported for Yosemite cliffs. This suggests that the geometry of the fracturing pattern does not influence the exponent of the power law distribution of rock fall volumes.

When taking together the three catalogs studied here, and the other results for rock falls on subvertical cliffs, including natural rock slopes and road-cuts (Table 14.2), it suggests that rock fall volume distributions follow a power law distribution, with an average exponent of  $0.5 \pm 0.2$  on a  $10^{-3}$  m<sup>3</sup> to  $10^{10}$  m<sup>3</sup> volume range. For the data sets listed on Table 14.2, even the largest events fit the power law distribution, without any cut-off. No finite size effect is thus observable. However, a possible finite size effect would come from the finite geometry of the rock slopes or cliffs. In particular, the height of cliff is a saturation length for the maximum available rock fall volumes on any given site.

Except for the seismically instrumented cliff on the Reunion island [*Rousseau, 1999*], all the reported rock fall volumes come from field evaluation (Table 14.2). As events are reported mainly when they induce damage to man-build or natural structures, the sampling is not uniform in the size domain. This sampling bias results in an underestimation of the number of small events. This bias is the best candidate to account for the re-currently observed deficit of small events relatively to the power law distribution for large volumes (Figure 14.5). There is no evidence that this bias may induce spurious power law behavior. However, it may lead to underestimate the exponent of the power law [e.g. *Stark and Hovius, 2001*; for tests on landslides].

TAB. 14.2 – Characteristics of Rock Fall Volume Distributions on subvertical cliffs

Site	Geological Setting	Duration	$N$	$V_{fit}$ m <sup>3</sup>	$b^a$	Ref
Grenoble, French Alps	Calcareous Cliffs	1935-1995	87	$40 - 10^6$	0.41	6 <sup>1</sup>
Yosemite, California	Granitic Cliffs	1915-1992	101	$50 - 10^6$	0.45	6 <sup>2</sup>
Worldwide	Undifferentiated Cliffs	10 000 yrs	142	$3 \times 10^7 - 2 \times 10^{10}$	0.51	6 <sup>3</sup>
Reunion Island, Indian Ocean	Basaltic Cliffs	May–Aug. 1998	370	$\leq 9 \times 10^6$	$0.5^b - 1^b$	1, 5
Himalaya, India	Road cuts		200	$10 - 10^6$	0.19	4
Himalaya, India	Road cuts		200	$10 - 10^7$	0.23	4
Alberta, Canada	Calcareous and quartzitic Cliffs	2 summers	409	$10^{-2} - 10$	0.72	2
B. Columbia, Canada	Massive felsic rock, road cuts <sup>c1</sup>	30 yrs	389	$10^{-2} - 10^7$	0.43	3 <sup>c1</sup>
B.Columbia, Canada	Massive felsic rock, road cuts <sup>c2</sup>	13 yrs	123	$1 - 10^7$	0.40	3 <sup>c2</sup>
B.Columbia, Canada	Jointed metamorphic, rock, road cuts <sup>c3</sup>		64	$1 - 10^7$	0.70	3 <sup>c3</sup>
B.Columbia, Canada	Jointed metamorphic, rock, road cuts <sup>c4</sup>	22 yrs	122	$1 - 10^7$	0.65	3 <sup>c4</sup>

Reference : 1, *Aki* [personnal communication, 2002]; 2, *Gardner* [1970]; 3, *Hungr et al.* [1999]; 4, *Noever* [1993]; 5, *Rousseau* [1999]; 6, (*This study*), data from <sup>1</sup>*RTM* [1996]; <sup>2</sup>*Wiezoreck* [1992]; <sup>3</sup>*Couture* [1998].

<sup>a</sup> Exponent for cumulative volume distribution.

<sup>b</sup> Exponent deduced from amplitude of seismic signals usng different models, see text for details; accordingly the absolute volumes are dependent of the exponent values for each of the seismic model.

<sup>c</sup> Studies on different locations in the same area : <sup>c1</sup>Highway 99, bands A and B, <sup>c2</sup>BCR, <sup>c3</sup>Highway 1, <sup>c4</sup>CP.

As noted above, one study uses a continuous seismic monitoring to detect rock fall events and to size up rock fall volumes on a single, well defined cliff [Rousseau, 1999]. This sampling method and the measurement technique provide a catalog that is not affected by the same biases as the data previously described. The volume distribution derived from Rousseau's catalog also follows a power law distribution (Table 14.2). First, this result supports the hypothesis that the power-law derived from volumes estimated by field evaluations is not a measurement artifact. Second, it shows that a single cliff displays a power law volume distribution. It argues against the power law distribution to result from a geometrical effect, i.e. the power law does not result from an integration process over cliffs of different heights. Using the seismic monitoring technique, the exponent value of the power law is the largest reported value in the available catalogs for rock falls on sub-vertical cliffs (Table 14.2). It may be due to the assumption made to derive the rock fall volume from the seismic amplitude. Seismological volume estimates are supposed to scale with the amplitude of seismic signals [Rousseau, 1999], but this relation may be incorrect. Assuming that seismic amplitude scales with the square root of the rock fall volume, as also proposed by Aki [personal communication, 2002], the exponent of rock fall volume distribution would be 0.5 instead of 1, in agreement with other studies reported on Table 14.2. Comparisons of both seismological signals and rock falls volumes are necessary to validate the relation between volumes and amplitudes of seismic signals.

The power-law distribution has also been reported for mixed landslides (Table 14.3 and references therein). From our study, which focus on the rock fall volumes that occurred on sub vertical cliffs of stiff rock mass, we derive a  $b$ -value that is significantly smaller than the  $1.2 \pm 0.3$  average exponent value estimated from studies that mixed different types of landslides (Table 14.3). For all the cases listed on Table 14.3, reported landslides occur either on less steep topography or involve softer unconsolidated material than rockfalls reported in Table (14.2).

### Implication for rock fall hazard

From the examples analysed in the previous sections, the hypothesis that the volume distributions of natural rock falls follow a power law distribution is accepted at a 90% confidence level. This distribution law provides the probability of occurrence of a given volume in a given time period on a given area, and has been used for hazard assessment by Hungr *et al.* [1999] for rock falls on man made slopes. Using the Grenoble data set as a test example, we can derive the occurrence rate of a given volume range by using the power law,

$$\frac{dN(V)}{dt} = \frac{N_0}{T} \left( \frac{V}{V_0} \right)^{-b}, \quad (14.6)$$

$N(V)$  being the number of events with a volume larger than  $V$  during a time period  $t$ .  $N_0$  is the number of events with a volume larger than  $V_0$ . For the Grenoble inventory,  $V_0 = 40 \text{ m}^3$ ,  $N_0 = 55$ , the time period we analysed is  $T=60$  yrs.

TAB. 14.3 – Characteristics of volume distributions for mixed landslide types

Site	Geological Setting	N	V m <sup>3</sup>	b <sup>a</sup>	Ref.
Southern Alps, New Zealand	35° mean slope	4984	10 <sup>6</sup> -3 × 10 <sup>7</sup>	0.8	4
Japan,		650	3 × 10 <sup>4</sup> -3 × 10 <sup>7</sup>	0.66	4
Akaishi Mountains, Japan	non vertical slope	3243	10 <sup>4</sup> -10 <sup>6</sup>	0.64	4
Akaishi Mountains, Japan	non vertical slope	3243	10 <sup>4</sup> -10 <sup>6</sup>	1.25	5,7
Challana Valley, Bolivian Andes	non vertical slope	1130		1.07	5,7
Challana Valley, Bolivian Andes	non vertical slope	1130		1.25	5
Northridge, California, earthquake triggered	uncons. earth & debris materials	11000		0.86	5
Northridge, California earthquake triggered	uncons. earth & debris materials	11000		1.07	7
Eden Canyon USA	10-35° slope, uncons. materials	709		1.4	5

Reference : 1, *Blodgett et al.*, [1996]; 2, *Fuyii*, [1969]; 3, *Harp and Jibson*, [1995]; 4, *Hovius et al.*, [1997]; 5, *Malamud and Turcotte*, [1999]; 6, *Nielsen et al.*, [1975]; 7, *Pelletier et al.*, [1997]; 8, *Sugai et al.*, [1994].

<sup>a</sup> All the exponent values are for the cumulative volume distributions. They are derived from surface size distributions according to the rule that thickness scales with Area<sup>1/2</sup> [*Hovius et al.*, 1997]. Accordingly,  $b = (\text{cumulative surface exponent}) \times 2/3$ . When there is no data in the Volume column it corresponds to catalogs where just surface sizes are available. It corresponds to aerial landslide mapping on medium steep slope.

The return period of a fall of volume larger than or equal to  $V$  is given by,

$$t(V) = \frac{1}{N(V)}, \quad (14.7)$$

We obtain a 10 years return period for a  $10^4 \text{ m}^3$  event, or an average of four  $10^5 \text{ m}^3$  events within a century. The largest historical event reported in the last thousand years in the Grenoble area is the 1248 Mt Granier rock avalanche of  $5.10^8 \text{ m}^3$ . From the power law distribution based on the 1935-1995 data, we derive a return period of 870 yrs for a Mt Granier size event. Therefore the largest observed event on a thousand-year period agrees with the return period for this volume. For this region the saturation volume for which the scaling law could change is roughly  $(h_{max})^3$ ,  $h_{max}$  being the maximum cliff height, with  $(h_{max})^3 \sim 10^9 \text{ m}^3$  for Grenoble cliffs. This value is a first order estimate which includes the two levels of the Grenoble cliffs (Figure 14.1). Accordingly, the distribution must not be extrapolated to volumes larger than  $10^9 \text{ m}^3$ . Regarding the space domain, the presently limited number of data does not allow us to investigate spatial variations of rock fall occurrence rate. We can just provide the probability of occurrence for the whole studied area [Vengeon *et al.*, 2001].

### Possible models for power law distributions of rockfall volumes

There has not been yet any model which simulates specifically rock fall dynamics. One class of numerical models examines erosion; it can also apply to rock fall or landslide simulations [Hergarten and Neugebauer, 1998; Densmore *et al.*, 1998]. The second class of models includes generic models that can apply to a large range of phenomena that exhibit scale invariant behavior, i.e. fragmentation and sand piles models.

#### Erosion type model

Densmore *et al.* [1998] proposed a numerical model that uses a slope stability criterion to simulate mechanics of hill slope failures. They obtain a power law distribution of volumes of mass movements. The exponent value of the simulated cumulative distribution varies as a function of the mechanical properties of the rock mass (cohesion and friction angle), from 1.2 for soft rock to 0.8 for hard rock. The authors suggest in their numerical simulation that a higher strength leads to steeper critical hill slope heights. Because in this model [Densmore *et al.*, 1998; Champel *et al.*, 2002] a higher strength corresponds to a steeper topography, simulations with stiff rock parameters may be related to rock fall circumstances on a sub vertical cliffs. Alternatively, we propose that other landslide types, which occurred on gentler slopes could be related to simulations with low strength materials that induce a lower exponent value for the power law distribution of volumes.

For mixed landslide types, the observed  $b$ -values (the exponents of the cumulative volume distributions), are in the range 0.7-1.3, with an average value  $b = 1.2 \pm 0.3$  (Table 14.3). These

values are significantly larger than those reported for rock falls on sub vertical cliffs. For rock fall settings (Table 14.2), i.e. stiff rock on sub vertical cliffs characterized by a friction angle close to  $35\text{-}45^\circ$  [Hoek and Brown, 1980], the corresponding  $b$ -values range from 0.2 to 1, with an average value of  $0.5 \pm 0.2$ . Therefore, the models of [Densmore *et al.*, 1998; Champel *et al.*, 2002] qualitatively predict the observed changes in exponents between mixed landslide types that occurred on gentle slope topography (Table 14.3) and rock falls on sub vertical cliffs (Table 14.2). According to this model, the change in exponent values is driven by changes in the mechanical properties (e.g. internal friction angle or cohesion) of the involved rock mass. Stiff rocks, with a higher friction angle, generate steeper topographic slopes and lower exponent values than softer rocks.

### Fragmentation model

From a generic point of view, the rock fall volume distributions are also similar to the observed fragment distributions. A power law distribution is admitted to characterize the distribution of fragments for a variety of rocks in laboratory experiments [e.g. Turcotte, 1986, and references therein]. Observed exponent values for cumulative volume distributions of fragments range from 0.5 to 1.2, with 0.8 as an average value. A generic model of fragmentation generates a power distribution of fragments, with a  $b$  exponent of the cumulative volume distribution defined by,

$$b = \frac{\log(8p)}{\log(8)}, \quad (14.8)$$

where  $p$  is the probability of a given cell of size  $l$  to break in 8 fragments of size  $l/2$ . This breaking rule is scale invariant, i.e. each sub cell whatever its size has the same probability  $p$  to break in 8 smaller cells [Turcotte, 1986]. Tuning of  $p$  values allows recovering observed exponent values for rock fragmentation with  $b < 1$  for  $p$  ranging from 0 to 1. In this way, the power law distribution of rock fall volumes, with an exponent value ranging from 0.2 to 1 (Table 14.2), can be reproduced by this generic fragmentation model. Note that the observed exponents for rock falls,  $0.5 \pm 0.2$ , are in the same ranges of those reported for fragmentation.

Using the fragmentation model, the rock fall exponent value would correspond to a lower  $p$  value, hence a less brittle behavior for rock cliffs than for rock fragmentation experiments. This is in agreement with the weaker geomechanical values proposed by Hoek and Brown [1980] for in situ rock masses when compared to rock samples. It argues for the rock fall sizes to be possibly driven by the fragmentation process of the cliff, i.e. the pre-existing discontinuity pattern. Accordingly, the rock mass fragment size should control the rock fall volume size, while neither cascade nor avalanche process should influence the rock fall volume distribution. This model can reproduce the observed rock fall volume distribution if the largest fragment is larger than the rock fall volume considered. Although the pre-existing discontinuity pattern that controls the fragment size distribution is not extensively known for the studied cliffs, we observe that the number of rock blocks cut by discontinuities decreases rapidly when their size increases.

It argues for possible large fragment sizes on our studied cliff.

### Sand-pile type model

Another alternative to generate power law distributions is the conceptual sand-pile model of *Bak et al.* [1987]. For rock fall dynamics, the scale invariant rock fall distribution could arise solely from the dynamic of mechanical processes without requiring any pre-existing scale invariant heterogeneity. Cellular automata models simulate avalanches on a sand-pile. 3D numerical simulations yield an exponent value of 0.37 [*Bak et al.*, 1987; 1989], close to those we report for natural rock falls. However this 3D model generates avalanches which take place in the bulk of a volume. Accordingly the mapping on the whole rock avalanches is difficult. The model that is usually interpreted in terms of sand pile is the 2D version of the model which yields a power law distribution with an exponent close to zero [*Bak et al.*, 1987; 1989]. This later exponent value is further away from the observed rock fall size distribution. However, a variety of cellular automata models can account for a change in exponent value when modifying the interaction rules or the loading rules of the generic sand pile model from *Bak et al.* [1987], e.g. *Olami et al.* [1992], *Amaral and Lauritsen* [1997]. Therefore these models could explain the  $b$ -value observed for the distribution of rock fall volumes.

Contrary to the fragmentation model, the sand-pile model simulates a power law distribution of volumes that emerges solely from the dynamics without any input of quenched heterogeneity [e.g. *Bak et al.*, 1987]. This model can be applied to any dynamic system characterized by a threshold dynamic, a stationary state, a slow exogeneous driving when compared to the energy released, and a power law distribution of energy released. Within this context, the driven forces for a rock fall dynamical system are both the slow tectonic uplift rate, the fluvial down cutting and the constant gravity force. They have characteristic time scales, which are well separated from the time life of one single rock fall event. On such a basis, the dynamics of rock fall process share the same properties as the one proposed for earthquakes, i.e. a slow driving relatively to the relaxation process and a power distribution of relaxed energy [*Bak et al.*, 1989; *Sornette and Sornette*, 1989; *Main*, 1996; *Grasso and Sornette*, 1998, *Vespignani and Zapperi*, 1998]. As suggested for landslides of unconsolidated material on moderate slope by *Hergarten and Neugebauer*, [1998], it argues for rock fall dynamics to be another example of out of equilibrium, scale free phenomena that could be generic to earth crust deformation processes.

As a tentative mapping of each class of models on rock fall dynamics from sub vertical cliffs and other landslide types respectively, we summarize the advantages and drawbacks of each model (14.4). If a fragmentation model is generically acceptable for rock falls on sub-vertical cliffs, including simulated exponent values, it is rejected as a model for the soft unconsolidated material involved in other landslide types. Similarly, the soil erosion model of *Hergarten and Neugebauer*, [1998] is well suited to simulate landslides of layered soft material, but the exponent value and the layered model assumption itself reject the possibility for this model to reproduce

TAB. 14.4 – Possible conceptual models for rock fall and landslide distributions

Generic type		Model inputs		Model output	
	Ref	Loading	Breaking rules	$b$ -value <sup>a</sup>	mapping
Rock erosion	2	Tectonic uplift,	Slope stability =	0.8	rock fall
	2	gravity, fluvial cut	f(friction, cohesion)	1.2	landslide
Soil erosion (layered)	3	Tectonic uplift gravity, fluvial cut.	Slope Gradient = f(layer thickness)	0.73	landslide
Sand-pile	1	Additional sand grains	Critical slope angle	$\approx 0$ (2D) 0.37 (3D)	landslide and rock fall
Fragmentation	4	no loading	Fragmentation probability law ( $p$ )	$< 1$ $f(p)$	rock fall

Reference : 1, *Bak et al.*, [1987]; 2, *Densmore et al.*, [1998]; 3, *Hergarten and Neugebauer* [1998]; 4, *Turcotte.*, [1986].

<sup>a</sup> All the exponent values are cumulative exponents of volume distributions.

rock falls dynamics of sub vertical cliffs. The erosion model from *Densmore et al.* [1998] is able to reproduce a change in exponent values that is observed when switching from events which originate on sub vertical cliffs of stiff rock to event occurring on gentle slopes of softer materials [*Densmore et al.*, 1998; *Champel et al.*, 2002].

## 14.5 Conclusion

We have analysed three rock fall data sets on sub vertical cliffs and we have shown that the rock fall volume distribution follows a power-law distribution for volumes ranging from  $10^2$  to  $10^{10}$  m<sup>3</sup>, with the same exponent  $b = 0.45 \pm 0.07$  for the three catalogs. This exponent is also in agreement with previous studies of rock falls along road-cuts. We suggest two classes of models than can reproduce the power-law distribution of rock fall volumes.

First, the conceptual sand-pile model of [*Bak et al.*, 1987; 1989] can reproduce the avalanche-like behavior of the rock fall activity. Accordingly the power-law distribution of rock fall volumes is the avalanche like response to a slow loading rate, as driven by tectonic deformation and fluvial incision rates, when compared to the time scales of rock avalanches. This argues for the rock fall dynamics to be another class of out of equilibrium, scale free phenomena as suggested for a large variety of earth crust deformation processes. In this context, the power-law distribution of

rock fall volumes would arise solely from the dynamic of the system, and would not be affected by the pre-existing heterogeneity pattern.

Second, the observed power law distribution of rock fall volumes is similar to the one reported for both fragmentation experiments and fragmentation models. This argues for the in-situ rock mass fragment sizes to possibly control the rock fall volumes. In this context, the rock fall volume distribution should be similar to the fragment size distribution, and neither cascade nor avalanche processes would influence the rock fall volume distribution.

When comparing our observations of rock falls on sub-vertical cliffs with different types of landslides, the exponent of the volume distribution is smaller for rock falls than for landslides involving unconsolidated material occurring on less steep slopes. It argues for the rock mass properties, which constrain the topography slope in numerical simulation [*Densmore et al.*, 1998; *Champel et al.*, 2002], to drive the change in exponent values for different landslide types and geomechanical settings.

### **Acknowledgments**

We gratefully thank R. Couture, J.P. Requillard and G. Wieczorek, who made the data available for the three inventories we used in this study, world wide inventory, Grenoble area and Yosemite Valley respectively. Unpublished detailed comments on their own landslides and rock falls studies by K. Aki, B. Champel, N. Hovius, D. Keefer, J. Pelletier, N. Rousseau and C. Stark helped clarifying the final version of the paper. Reviews by A. Densmore, S. Hergarten and G. Wieczorek, improved the quality of the manuscript. J.M. Vengeon is acknowledged for his fruitful discussions and R. Archuleta for their comments on an initial version of the manuscript.

# Chapitre 15

## Slider-block friction model for landslides : implication for prediction of mountain collapse

Agnès Helmstetter<sup>1</sup>, Didier Sornette<sup>2-4</sup>, Jean-Robert Grasso<sup>1</sup>, Jorgen Vitting Andersen<sup>2,5</sup>, Simon Gluzman<sup>4</sup>, and Vladimir Pisarenko<sup>6</sup>

<sup>1</sup> LGIT, Observatoire de Grenoble, Université Joseph Fourier, France

<sup>2</sup> LPMC, CNRS UMR 6622 and Université de Nice-Sophia Antipolis  
Parc Valrose, 06108 Nice, France

<sup>3</sup> Department of Earth and Space Sciences  
University of California, Los Angeles, California 90095-1567

<sup>4</sup> Institute of Geophysics and Planetary Physics  
University of California, Los Angeles, California 90095-1567

<sup>5</sup> U. F. R. de Sciences Economiques, Gestion, Mathématiques et Informatique,  
CNRS UMR7536 and Université Paris X-Nanterre  
92001 Nanterre Cedex, France

<sup>6</sup> International Institute of Earthquake Prediction Theory and Mathematical Geophysics  
Russian Ac. Sci. Warshavskoye sh., 79, kor. 2, Moscow 113556, Russia

Submitted to *Journal of Geophysical Research*, 2002.

### Abstract

Accelerating displacements preceding some catastrophic landslides has been found empirically to follow a time-to-failure power law, corresponding to a finite-time singularity of the ve-

locity  $v \sim 1/(t_c - t)$  [Voight, 1988]. Here, we provide a physical basis for this phenomenological law based on a slider-block model using a state and velocity dependent friction law established in the laboratory and used to model earthquake friction. This physical model accounts for and generalizes Voight's observation : depending on the ratio  $B/A$  of two parameters of the rate and state friction law and on the initial frictional state of the sliding surfaces characterized by a reduced parameter  $x_i$ , four possible regimes are found. Two regimes can account for an acceleration of the displacement. For  $B/A > 1$  (velocity weakening) and  $x_i < 1$ , the slider block exhibits an unstable acceleration leading to a finite-time singularity of the displacement and of the velocity  $v \sim 1/(t_c - t)$ , thus rationalizing Voight's empirical law. An acceleration of the displacement can also be reproduced in the velocity strengthening regime, for  $B/A < 1$  and  $x_i > 1$ . In this case, the acceleration of the displacement evolves toward a stable sliding with a constant sliding velocity. The two others cases ( $B/A < 1$  and  $x_i < 1$ , and  $B/A > 1$  and  $x_i > 1$ ) give a deceleration of the displacement. We use the slider-block friction model to analyze quantitatively the displacement and velocity data preceding two landslides, Vaiont and La Clapière. The Vaiont landslide was the catastrophic culmination of an accelerated slope velocity. La Clapière landslide was characterized by a strong slope acceleration over a two years period, succeeded by a restabilizing phase. Our inversion of the slider-block model on these data sets shows good fits and suggest to classify the Vaiont (respectively La Clapière) landslide as belonging to the velocity weakening unstable (respectively strengthening stable) sliding regime. We cannot however exclude that La Clapière might also belong to the unstable velocity weakening regime ; its deceleration observed after 1988 may then be interpreted as a change of surface properties that modifies the friction law parameters. For the Vaiont landslide, this model provides good predictions of the critical time of failure up to 20 days before the collapse. Tests are also presented on the prediction of the time of the change of regime for la Clapière landslide.

## 15.1 Introduction

Landslides constitute a major geologic hazard of strong concern in most parts of the world. The force of rocks, soil, or other debris moving down a slope can devastate anything in its path. In the United States for instance, landslides occur in all 50 states and cause \$1-2 billion in damages and more than 25 fatalities on average each year. The situation is very similar with similar costs and casualty rates in the European Union. Landslides occur in a wide variety of geomechanical contexts, geological and structural settings, and as a response to various loading and triggering processes. They are often associated with other major natural disasters such as earthquakes, floods and volcanic eruptions.

Landslides sometimes strike without discernible warning. There are however well-documented cases of precursory signals, showing accelerating slip over time scales of weeks to decades (see [Voight (ed), 1978] for a review). While only a few such cases have been monitored in the past,

modern monitoring techniques are bound to provide a wealth of new quantitative observations based on GPS and SAR (synthetic aperture radar) technology to map the surface velocity field [Mantovani *et al.*, 1996; Fruneau *et al.*, 1996; Malet *et al.*, 2002; Parise, 2001] and seismic monitoring of slide quake activity [Gomberg *et al.*, 1995; Xu *et al.*, 1996; Rousseau, 1999; Caplan-Auerbach *et al.*, 2001]. Derived from the civil-engineering methods developed for the safety of human-built structures, including dams and bridges, the standard approach to slope instability is to identify the conditions under which a slope becomes unstable [e.g. Hoek and Bray, 1997]. In this class of approach, geomechanical data and properties are inserted in finite elements or discrete elements numerical codes to predict the possible departure from static equilibrium or the distance to a failure threshold. The results of such analyses are expressed using a safety factor  $F$ , defined as the ratio between the maximum retaining force to the driving forces. According to this approach, a slope becomes unstable when  $F < 1$ . This approach is at the basis of landslide hazard maps.

By their nature, standard stability analysis cannot account for acceleration in slope movement [e.g. Hoek and Brown, 1980]. The problem is that this modeling strategy gives a nothing-or-all signal. In this view, any specific landslide is essentially unpredictable, and the focus is on the recognition of landslide prone areas. This approach is very similar to the practice in seismology called “time-independent hazard” where earthquake prone areas are located in association with active faults for instance, while the prediction of individual earthquake is recognized to be much more difficult if not unattainable. This “time-independent hazard” essentially amounts to assume that landslides are a random (Poisson) process in time, and uses geomechanical modeling to constrain the future long-term landslide hazard. The approaches in terms of a safety factor do not address the preparatory stage leading to the catastrophic collapse, if any. In contrast, “time-dependent hazard” would accept a degree of predictability in the process, in that the landslide hazard varies with time, maybe in association with varying external forcing (rain, snow, earthquake, volcano). The next level in the hierarchy would be “landslide forecasting”, which require significant better understanding to allow for the prediction of some of the features of an impending landslide, usually on the basis of the observation of precursory signals. Practical difficulties include identifying and measuring reliable, unambiguous precursors, and the acceptance of an inherent proportion of missed events or false alarms. Other studies of landslides analyze the propagation of a landslide and try to predict the maximum runout length of a landslide [Heim, 1932, Campbell, 1989; 1990]. These studies do not describe the initiation of a catastrophic collapse.

To account for a progressive slope failure, i.e., a time dependence in stability analysis, previous works have taken a quasi-static approach in which some parameters are taken to slowly vary to account for slow changes of external conditions and/or external loading. For instance, the accelerated motions have been linked to pore pressure changes [e.g. Vangenuchten and Derijcke, 1989; Van Asch *et al.*, 1999]. According to this approach, an instability occurs when the gravitational pull on a slope overpass the resistance of a particular subsurface level. This resis-

tance on a subsurface level is controlled by the friction coefficient of the interacting surfaces. Since pore pressure acts at the level of submicroscopic to macroscopic discontinuities, which themselves control the global friction coefficient, circulating water can hasten chemical alteration of the interface roughness, and pore pressure itself can force adjacent surface apart. Both effects can lead to a reduction in the friction coefficient that leads, when constant loading applies, to accelerating movement. However, this explanation has not yielded a quantitative method for forecasting slope movement.

Other studies proposed that (i) rates of slope movements are controlled by microscopic slow cracking, and (ii) when a major failure plane is developed, the abrupt decrease in shear resistance may provide a sufficiently large force imbalance to trigger a catastrophic slope rupture [Kilburn and Petley, 2002]. Such a mechanism, with a proper law of input of new cracks, may reproduce the acceleration preceding the collapse that occurred at Vaiont, Mt Toc, Italy [Kilburn and Petley, 2002].

An alternative modeling strategy consists in viewing the accelerating displacement of the slope prior to the collapse as the final stage of the tertiary creep preceding failure [Saito and Uezawa, 1961; Saito, 1965, 1969; Kennedy and Niermeyer, 1971; Kilburn and Petley, 2002]. Further progress in exploring the relevance of this mechanism requires a reasonable knowledge of the geology of the sliding surfaces, their stress-strain history, the mode of failure, the time-dependent shear strength and the piezometric water level values along the surface of failure [Bhandari, 1988]. Unfortunately, this information is not available. This mechanism is therefore used mainly as a justification for the establishment of empirical criteria of impending landslide instability. Controlled experiments on landslides driven by a monotonic load increase have been quantified by a scaling law relating the surface acceleration  $d\dot{\delta}/dt$  to the surface velocity  $\dot{\delta}$  according to

$$d\dot{\delta}/dt = A\dot{\delta}^\alpha, \quad (15.1)$$

where  $A$  and  $\alpha$  are empirical constants [Fukuzono, 1985]. For  $\alpha > 1$ , this relationship predicts a divergence of the sliding velocity in finite time at some critical time  $t_c$ . The divergence is of course not to be taken literally: it signals a bifurcation from accelerated creep to complete slope instability for which inertia is no more negligible. Several cases have been quantified ex-post with this law, usually for  $\alpha = 2$ , by plotting the time  $t_c - t$  to failure as a function of the inverse of the creep velocity (see for a review [Bhandari, 1988]). Indeed, integrating (15.1) gives

$$t_c - t \sim \left(\frac{1}{\dot{\delta}}\right)^{\frac{1}{\alpha-1}}. \quad (15.2)$$

These fits suggest that it might be possible to forecast impending landslides by recording accelerated precursory slope displacements. Indeed, for the Mont Toc, Vaiont landslide revisited here, Voight [1988] mentioned that a prediction of the failure date could have been made more than 10 days before the actual failure, by using a linear relation linking the inverse velocity and the time to failure, as found from (15.2) for  $\alpha = 2$ . Our goal will be to avoid such an a priori

postulate by calibrating a more general physically-based model for the purpose of forecasting. *Voight* [1988, 1989] proposed that the relation (15.1), which generalizes damage mechanics laws [*Rabotnov*, 1969; *Gluzman and Sornette*, 2001], can be used with other variables (including strain and/or seismic energy release) for a large variety of materials and loading conditions. Expression (15.1) seems to apply as well to diverse types of landslides occurring in rock and soil, including first-time and reactivated slides [*Voight*, 1988]. It may be seen as a special case of a general expression for failure [*Voight*, 1988, 1989]. Recently, such time-to-failure laws have been interpreted as resulting from cooperative critical phenomena and have been applied to the prediction of failure of heterogeneous composite materials [*Anifrani et al.*, 1995] and to precursory increase of seismic activity prior to main shocks [*Sornette and Sammis*, 1995; *Jaume and Sykes*, 1999; *Sammis and Sornette*, 2002]. See also [*Sornette*, 2002] for extensions to other fields.

Here, we focus on two case studies, La Clapière sliding system in the French Alps and the Vaiont landslide in the Italian Alps. The latter landslide led to a catastrophic collapse after 70 days of recorded velocity increase. In the former case study, decades of accelerating motion aborted and gave way to a slow down of the system. First, we should stress that, as for earthquakes for instance, it is extremely difficult to obtain all relevant geophysical parameters that may be germane to a given landslide instability. Furthermore, it is also a delicate exercise to scale up the results and insights obtained from experiments performed in the laboratory to the scale of mountain slopes. Having said that, probably the simplest model of landslides considers the moving part of the landslide as a block sliding over a surface endowed with some given topography. Within such a conceptual model, the complexity of the landsliding behavior emerges from (i) the dynamics of the block behavior (ii) the dynamics of interactions between the block and the substratum, (iii) the history of the external loading (e.g. rain, earthquake). In the following, we test how the friction law of a rigid block driven by constant gravity force can be useful for understanding the apparent transition between slow stable sliding and fast unstable sliding leading to slope collapse. We develop a simple model of sliding instability based on rate and state dependent solid friction laws and use it to assess the degree to which such events can be forecasted.

Previous modeling efforts of landslides in terms of a rigid slider-block have taken either a constant friction coefficient or a slip- or velocity-dependent friction coefficient between the rigid block and the surface. A constant solid friction coefficient (Mohr-Coulomb law) is often taken to simulate bed- over bed-rock sliding. *Heim* [1932] proposed this model as an attempt to predict the propagation length of rock avalanches. In this pioneering study to forecast extreme runout length, the constant friction coefficient was interpreted as an effective average friction coefficient. In contrast, a slip-dependent friction coefficient model is taken to simulate the yield-plastic behavior of a brittle material beyond the maximum of its strain-stress characteristics. For rock avalanches, *Eisbacher* [1979] suggested that the evolution from a static to a dynamic friction coefficient is induced by the emergence of a basal gouge. Studies using a velocity-dependent

friction coefficient have mostly focused on the establishment of empirical relationships between shear stress  $\tau$  and block velocity  $v$ , such as  $v \sim \exp(a\tau)$  [Davis *et al.*, 1990] or  $v \sim \tau^{1/2}$  [Korner, 1976], however with not definite understanding of the possible mechanism [see for instance Durville, 1992].

Compared to previous models, the innovation considered here is to account for the interaction between the block and the underlying slope by a solid friction law encompassing both state and velocity dependence, as established by numerous laboratory experiments (see for instance [Scholz, 1990, 1998; Marone, 1998; Gomberg *et al.*, 2000] for reviews). The sliding velocities used in laboratory to establish the rate and state friction laws are of the same order,  $10^{-4} - 10^2 \mu\text{m/s}$ , than those observed for landslides before the catastrophic collapse. On the one hand, state- and velocity-dependent friction laws have been developed and used extensively to model the preparatory as well as the elasto-dynamical phases of earthquakes. On the other hand, analogies between landslide faults and tectonic faults have been noted [Gomberg *et al.*, 1995] and the use of the static friction coefficient is ubiquitous in the analysis of slope stability. However, to our knowledge, no one has yet pushed any further the analogy between sliding rupture and earthquakes and no one has used the physics of state- and velocity-dependent friction to bear on the problem of landslides and their precursory phases. Such standard friction laws have been shown to lead to an asymptotic time-to-failure power law with  $\alpha = 2$  in the late stage of frictional sliding motion between two solid surfaces preceding the elasto-dynamic rupture instability [Dieterich, 1992]. This model therefore accounts for the finite-time singularity of the sliding velocity (15.2) observed for landslides and rationalizes the empirical time-to-failure laws proposed by Voight [1988, 1989]. In addition, this model also describes the stable sliding regime, the situation where the time-to-failure behavior is absent.

In the first section, we derive the four different sliding regimes of this model which depend on the ratio  $B/A$  of two parameters of the rate and state friction law and on the initial conditions of the reduced state variable. Sections 3 and 4 analyze the Vaiont and La Clapière landslides, respectively. In particular, we calibrate the slider-block model to the two landslide slip data and invert the key parameters. Of particular interest is the possibility of distinguishing between an unstable and a stable sliding regime. We also test the predictability of the failure time using different methods, and how long in advance a prediction could have been issued. The results suggest the Vaiont landslide (respectively La Clapière landslide) as belonging to the velocity weakening unstable (respectively strengthening stable) sliding regime. We also investigate the alternative possibility that La Clapière might also belong to the unstable velocity weakening regime; its deceleration observed after 1988 may then be interpreted as a change of surface properties that reset the state variable from  $x < 1$  to  $x > 1$ . Section 5 concludes.

## 15.2 Slider-Block model with state and velocity dependent friction

### Basic formulation

Following [Heim, 1932; Korner, 1976; Eisbacher, 1979; Davis et al., 1990; Durville, 1992], we model the future landslide as a block resting on an inclined slope forming an angle  $\phi$  with respect to the horizontal. In general, the solid friction coefficient  $\mu$  between two surfaces is a function of the cumulative slip  $\delta$  and the slip velocity  $\dot{\delta}$ . There are several forms of rate/state-variable constitutive law that have been used to model laboratory observations of solid friction. The version currently in best agreement with experimental data, known as the Dieterich-Ruina or ‘slowness’ law [Dieterich, 1978; Ruina, 1983], is expressed as

$$\mu = \mu_0 + A \ln \frac{\dot{\delta}}{\dot{\delta}_0} + B \ln \frac{\theta}{\theta_0}, \quad (15.3)$$

where the state variable  $\theta$  is usually interpreted as proportional to the surface of contact between asperities of the two surfaces.  $\mu_0$  is the friction coefficient for a sliding velocity  $\dot{\delta}_0$  and a state variable  $\theta_0$ . The state variable  $\theta$  evolves with time according to

$$\frac{d\theta}{dt} = 1 - \frac{\theta \dot{\delta}}{D_c}, \quad (15.4)$$

where  $D_c$  is a characteristic slip distance, usually interpreted as the typical size of asperities. Expression (15.4) can be rewritten as

$$\frac{d\theta}{d\delta} = \frac{1}{\dot{\delta}} - \frac{\theta}{D_c}. \quad (15.5)$$

As reviewed in [Scholz, 1998], the friction at steady state is :

$$\mu_S = \hat{\mu}_0 + (A - B) \ln \frac{\dot{\delta}}{\dot{\delta}_0}, \quad (15.6)$$

where  $\hat{\mu}_0 = \mu_0 + B \ln \frac{D_c}{\theta_0 \dot{\delta}_0}$ . Thus, the derivative of the steady-state friction coefficient with respect to the logarithm of the reduced slip velocity is  $A - B$ . If  $A > B$ , this derivative is positive : friction increases with slip velocity and the system is stable as more resistance occurs which tends to react against the increasing velocity. In contrast, for  $A < B$ , friction exhibits the phenomenon of velocity-weakening and is unstable.

The primary parameter that determines stability,  $A - B$ , is a material property. For instance, for granite,  $A - B$  is negative at low temperatures and becomes positive for temperatures above about 300° C. In general, for low-porosity crystalline rocks, the transition from negative to positive  $A - B$  corresponds to a change from elastic-brittle deformation to crystal plasticity in the micro-mechanics of friction [Scholz, 1998]. For the application to landslides, we should in addition consider that sliding surfaces are not only contacts of bare rock surfaces : they are usually lined

with wear detritus, called cataclastic or fault gouge. The shearing of such granular material involves an additional hardening mechanism (involving dilatancy), which tends to make  $A - B$  more positive. For such materials,  $A - B$  is positive when the material is poorly consolidated, but decreases at elevated pressure and temperature as the material becomes lithified. See also section 2.4 of Scholz's book [Scholz, 1990].

The friction law (15.3) with (15.4) accounts for the fundamental properties of a broad range of surfaces in contact, namely that they strengthen logarithmically when aging at rest, and weaken (rejuvenate) when sliding [Scholz, 1998].

To make explicit the proposed model, let us represent schematically a mountain flank as a system made of a block and of its basal surface in which it is encased. The block represents the part of the slope which may be potentially unstable. For a constant gravity loading, the two parameters controlling the stability of the block are the dip angle  $\phi$  between the surface on which the block stands and the horizontal and the solid friction coefficient  $\mu$ . The block exerts stresses that are normal ( $\sigma$ ) as well as tangential ( $\tau$ ) to this surface of contact. The angle  $\phi$  controls the ratio of the shear over normal stress :  $\tan \phi = \tau/\sigma$ . In a first step, we assume for simplicity that the usual solid friction law  $\tau = \mu\sigma$  holds for all times, expressing that the shear stress  $\tau$  exerted on the block is proportional to the normal stress with a coefficient of proportionality defining the friction coefficient  $\mu$ . This assumption expresses a constant geometry of the block and of the surface of sliding. For the two landslides that we study in this paper, a rigid block sliding on a slope with a constant dip angle is a good first order approximate of these landslide behaviors.

## Solution of the dynamical equation

### Asymptotic power law regime for $A - B < 0$

As the sliding accelerates, the sliding velocity becomes sufficiently large such that  $\dot{\delta} \gg D_c/\theta$  and we can neglect the first term  $1/\dot{\delta}$  in the right-hand-side of (15.5) [Dieterich, 1992]. This yields

$$\theta = \theta_0 \exp(-\delta/D_c) , \quad (15.7)$$

which means that  $\theta$  evolves toward zero. The friction law then reads

$$\frac{\tau}{\sigma} = \mu_0 + A \ln \frac{\dot{\delta}}{\dot{\delta}_0} - \frac{B\delta}{D_c} , \quad (15.8)$$

where we have inserted (15.7) into (15.3). In this equation,  $\tau$  and  $\sigma$  result from the mass of the block and are constant. The solution of (15.8) is [Dieterich, 1992]

$$\delta(t) = -\frac{AD_c}{B} \ln \left[ \frac{B\dot{\delta}_0 e^{\frac{\tau - \mu_0}{A}}}{AD_c} (t_c - t) \right] , \quad (15.9)$$

where  $t_c$  is determined by the initial condition  $\delta(t=0) \equiv \delta_i$  :

$$t_c = \frac{AD_c}{B\dot{\delta}_0} e^{-\left(\frac{B\delta_i}{AD_c} + \frac{\tau - \mu_0}{A}\right)} \quad (15.10)$$

The logarithmic blow up of the cumulative slip in finite time is associated with the divergence of the slip velocity

$$\dot{\delta} = \frac{AD_c}{B} \frac{1}{t_c - t}, \quad (15.11)$$

which recovers (15.2) for  $\alpha = 2$ .

### The complete solution for the frictional problem

The solution (15.9) is valid only for  $A - B < 0$  and sufficiently close to  $t_c$  for which the slip velocity  $\dot{\delta}$  is large, ensuring the validity of the approximation leading to (15.7). However, even in the unstable case  $A - B < 0$ , the early time behavior, far from  $t_c$ , cannot be described by using the approximation established for  $t$  close to  $t_c$  and requires a description different from (15.9) and (15.11). Furthermore, we are interested in different situations, in which the sliding may not result always into a catastrophic instability, as for instance for the mountain slope La Clapière, which started to slip but did not reach the full instability, a situation which can be interpreted as the stable regime  $A - B > 0$ . The complete solution for the frictional problem is derived in Appendix A.

### Synthesis of the different slipping regimes

The block sliding displays different regimes as a function of the friction law parameters and of the initial conditions. These regimes are controlled by the value of the friction law parameters, i.e.,  $m = B/A$  (by definition (15.17)), of the initial condition  $x_i$  on  $\theta$  and of the material parameter  $S$ .  $A$  and  $B$  are defined in (15.3) and are determined by material properties.  $x_i$  is the initial value of the reduced state variable  $\theta$  defined in (15.19). The parameter  $S$  is defined by (15.16) and is independent of the initial conditions. As derived from the complete solution in Appendix A, the different regimes are summarized below and in Table 15.1 and illustrated in Figure 15.1.

#### For $0 < m < 1$

the sliding is always stable. Depending of the initial value for  $t = 0$  of the reduced state variable  $x_i$ , the sliding velocity either increases (if  $x_i > 1$ ) or decreases (if  $x_i < 1$ ) toward a constant value.

#### For $m > 1$

the sliding is always unstable. When  $x_i < 1$ , the sliding velocity increases toward a finite-time singularity. The slip velocity diverges as  $1/(t_c - t)$  corresponding to a logarithmic singularity of the cumulative slip. For  $x_i > 1$ , the velocity decreases toward a vanishingly small value.

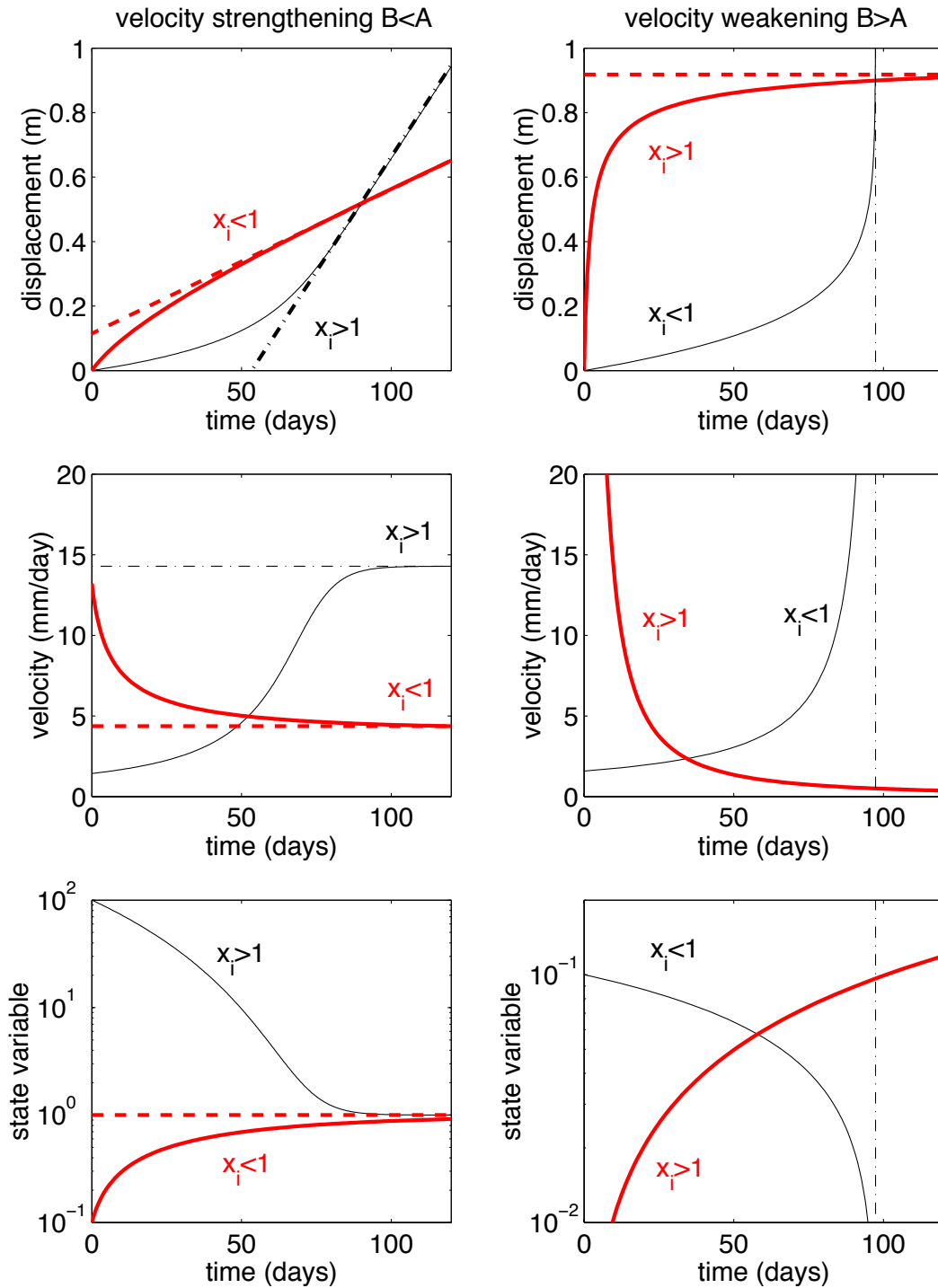


FIG. 15.1 – Schematic classification of the different regimes of sliding discussed in the text. The left column of three panels correspond to the stable regime  $m = B/A < 1$  and the right column of three panels describes the unstable regime  $m = B/A > 1$ . In each case, the displacement, velocity and state variables are shown as a function of time. Each regime (stable and unstable) are divided into two cases, depending on the dimensionless initial value  $x_i \propto \theta_i$  of the state variable. The thick lines corresponds to decreasing velocities and increasing state variables. The thin lines correspond to increasing velocities and decreasing state variables.

TAB. 15.1 – Synthesis of the different regimes of slip as a function of  $m = B/A$  (by definition (15.17)), of the initial condition  $x_i$  on  $\theta$  and of the material parameter  $S$ .  $A$  and  $B$  are defined in (15.3) and are determined by material properties.  $x_i$  is the initial value of the reduced state variable  $\theta$  defined in (15.19). FTS stands for “finite-time singularity.” The parenthesis ( $x_i$ ) and ( $S$ ) in the first column indicates which is the control parameter determining the nature of the slip. The parameter  $S$  is defined by (15.16) and is independent of the initial conditions. While  $A$  is always found positive in laboratory experiments, negative  $B$ -values are sometimes found [Blanpied *et al.*, 1995] leading to the possibility of having  $m < 0$  : this rather special case corresponds to a friction coefficient decreasing with the increase of the surface of contacts.

	$x_i, S < 1$	$x_i, S > 1$
$m > 1$ ( $x_i$ )	FTS (15.9,15.10,15.11)	power law plasticity hardening (15.26)
$m = 1$ ( $S$ )	$\dot{\delta} \sim 1/t$ and $\delta \sim \ln t$	FTS (15.9,15.10,15.11)
$0 < m < 1$ ( $x_i$ )	$\theta \downarrow \text{const}, \dot{\delta} \uparrow \text{const}$	$\theta \uparrow \text{const}, \dot{\delta} \downarrow \text{const}$
$m < 0$ ( $x_i$ )	$\theta \downarrow \text{const}, \dot{\delta} \downarrow \text{const}$	$\theta \uparrow \text{const}, \dot{\delta} \uparrow \text{const}$

## Analysis of landslide observations

In the sequel, we test how this model can reproduce the observed acceleration of the displacement for Vaiont and La Clapière landslides. The Vaiont landslide was the catastrophic culmination of an accelerated slope velocity over a two months period [Muller, 1964]. La Clapière landslide was characterized by a strong slope acceleration over a two years period, succeeded by a restabilizing phase [Susella and Zanolini, 1996]. An acceleration of the displacement can arise from the friction model in two regimes, either in the stable regime with  $m < 1$  and  $x_i > 1$  or in the unstable regime with  $m > 1$  and  $x_i < 1$ . In the first case, the acceleration evolves toward a stable sliding. In the unstable case, the acceleration leads to a finite-time singularity of the displacement and of the velocity. However, these two regimes are very similar in the early time regime before the critical time (see Figure 15.1). It is therefore very difficult to distinguish from limited observations a landslide in the stable regime from a landslide in the unstable regime when far from the rupture.

We assume that the friction law parameters, the geometry of the landslide and the gravity forces are constant. Within this conceptual model, the complexity of the landsliding behavior solely emerges from the friction law. We are aware of neglecting in this first order analysis any possible complexity inherent either to the geometry and rheology of a larger set of blocks, or the geometry and rheology of the substratum or the history of the external loading (e.g. earthquake, rainfalls). We invert the friction law parameters from the velocity and displacement data of the Vaiont and La Clapière landslides. Our goal is (i) to test if this model is useful for distinguishing an unstable accelerating sliding characterized by  $B > A$  from a stable accelerating regime occurring for  $B < A$  and (ii) to test the predictive skills of this model and compare with

other methods of prediction.

## 15.3 The Vaiont landslide

### Historical and geo-mechanical overview

On October 9, 1963, a 2 km-wide landslide initiating at an elevation of 1100-1200 m, that is 500-600 m above the valley floor, on the Mt Toc slope in the Dolomite region in the Italian Alps about 100 km north of Venice, ended up 70 days later in a 20 m/s run-away of about 0.3 km<sup>3</sup> of rocks sliding into a dam reservoir. The high velocity of the slide triggered a water surge within the reservoir, overtopping the dam and killing 2000 people in the village downstream.

This landslide has a rather complex history. The landslide concerned a portion of the mountain above a newly built dam reservoir. The first attempt to fill up the reservoir dam was made between March and November 1960. It induced recurrent observations of creeping motions of a large mass of rock above the reservoir, and led to several small and rather slow slides [Muller, 1964]. Lowering the reservoir water level induced the rock mass velocities to drop from the order of 40 mm/day to less than 1 mm/day. A progressive step by step approach to slowly raise the water level as well as cycling of the water level were performed in order to slowly and cautiously fill the reservoir. A second peak of creeping velocity, at about 10 mm/day, that is four time less than the first 1960 peak, was induced by the 1962 filling cycle. The 1963 filling cycle started in April 1963. From May 1963, recurrent increases of the creep velocity was measured. It ended up abruptly in the 20 m/s downward rush of a volume of 0.3 km<sup>3</sup> of rocks slipping in the reservoir.

The Landslide geometry is a rough rectangular shape, 2 km wide and 1.3 km in length. Velocity measurements are available for four benchmarks, corresponding to four different positions on the mountain slope, respectively denoted 5, 50, 63 and 67 in the Vaiont nomenclature. Benchmarks 63 and 67 are located at the same elevation in the upper part of the landslide a few hundred meters from the submittal scarp. The distance between the 2 benchmarks is 1.1 km. The benchmark 5 and 50 are 700 m downward the 63-67 benchmark level.

Figure 15.2 shows the velocity of the four benchmarks on the block as a function of time prior to the Vaiont landslide. For these four benchmarks, the deformation of the sliding zone prior to rupture is not homogeneous, as the cumulative displacement in the period from August 2<sup>nd</sup>, 1963 to October 8, 1963 ranges from 0.8 to 4 m. However, the low degree of disintegration for distal deposit [Erisman and Abele, 2000] argue for a possible homogeneous block behavior during the 1963 sliding collapse.

It was recognized later that limestones and clay beds dipping into the valley provide conditions favorable for dip-slope failures [Muller, 1964, 1968; Broili, 1967]. There is now a general agreement on the collapse history of the 1963 Vaiont landslide (see e.g., [Erisman and Abele, 2000]). The failure occurred along bands of clays within the limestone mass at depths between

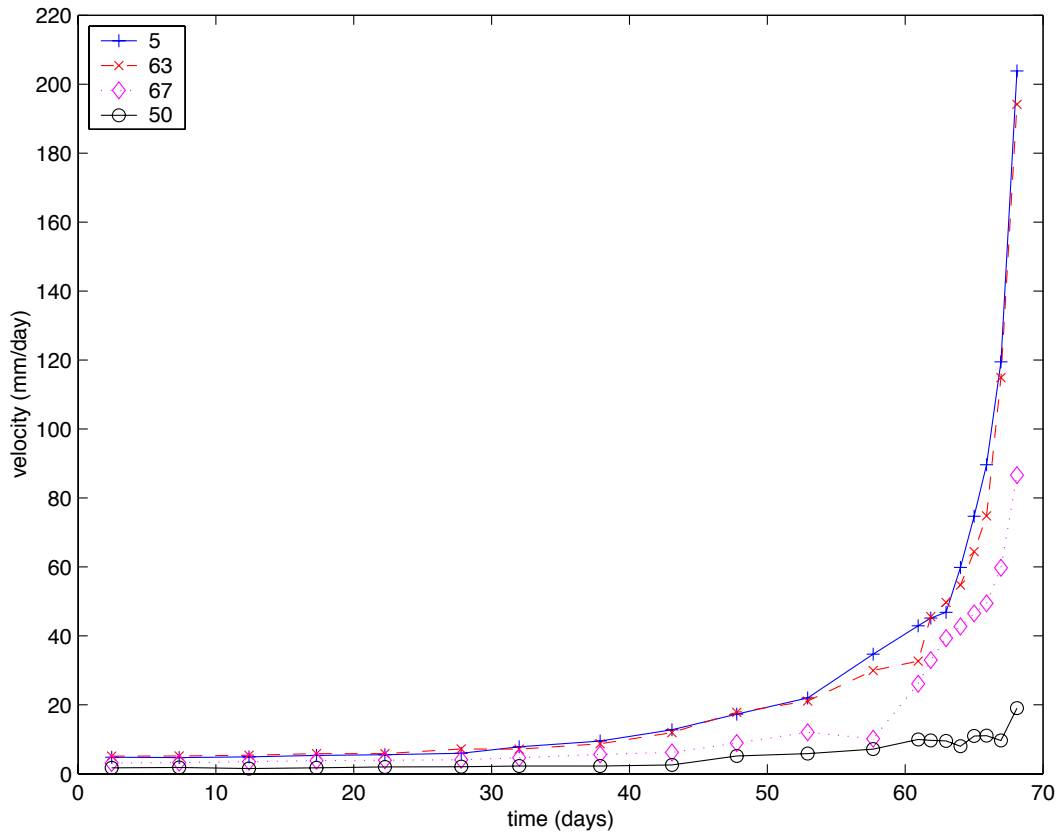


FIG. 15.2 – Benchmarks 5 and 63 exhibit almost the same strong acceleration. Benchmark 50 is the only one which shows only a relatively small acceleration in absolute values at the end of the 60 days accelerating phase. Its acceleration is however significant in relative values, as seen in Figure 15.4. Data from [Muller, 1964].

100-200 m below the surface [Hendron and Patton, 1985]. Raising the reservoir level increased water pore pressure in the slope flank, that triggered the clays layer failure. Final sliding occurred after 70 days of down-slope accelerating movement. The rock mass velocity progressively increased from 5 mm/day to more than 20 cm/day, corresponding to a cumulative displacement of a few meters over this 70 days period [Muller, 1964].

### Analysis of the cumulative displacement and velocity data with the slider-block model parameters.

Figure 15.3 shows the inverse of the velocity shown in Figure 15.2 to test the finite-time-singularity hypothesis (15.2,15.11). Note that this figure does not require the knowledge of the critical time  $t_c$  and is not a fit to the data. The curves for all benchmarks are almost linear in this representation, in agreement with a finite-time singularity of the velocity (15.2) with  $\alpha = 2$ . It was the observations presented in Figure 15.2 that led Voight to suggest that a prediction could have been issued more than 10 days before the collapse [Voight, 1988]. We note that the

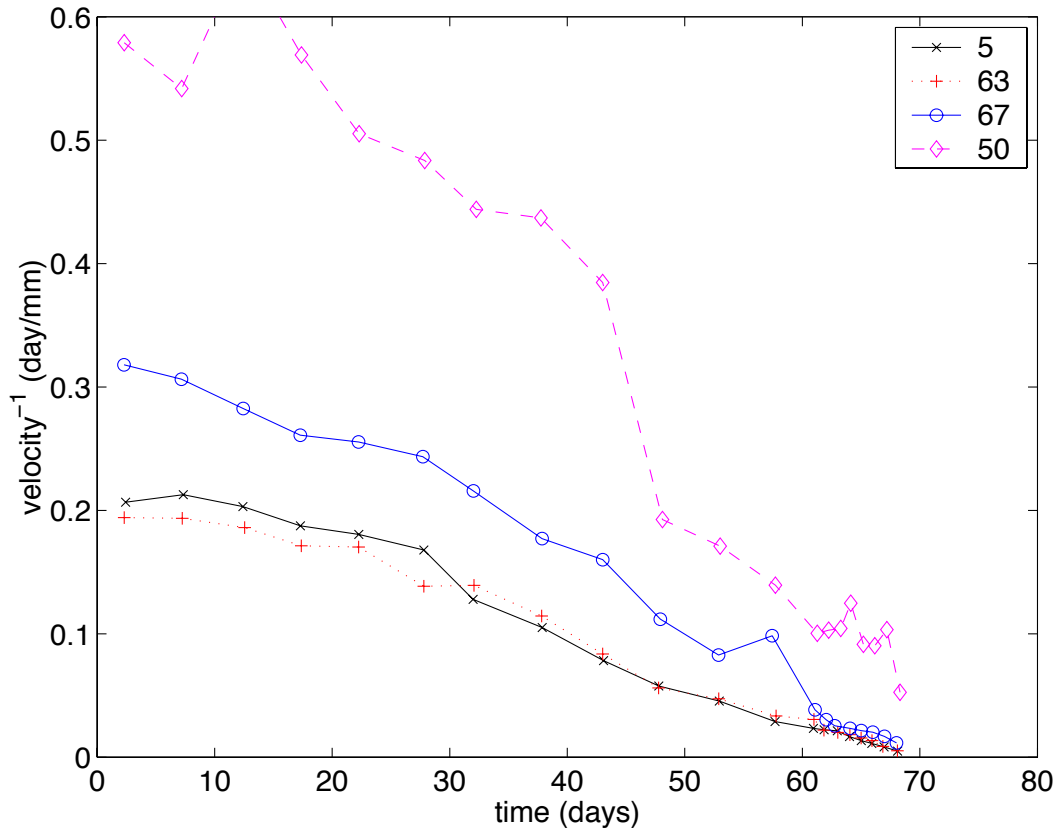


FIG. 15.3 – Same as Figure 15.2 by plotting the inverse of the velocity as a time  $t$ . All curves are approximately linear, showing that the velocity exhibits a finite-time singularity  $v \sim 1/(t_c - t)$  with  $t_c \approx 69.5$  days for all benchmarks, estimated as the intercept of the extrapolation of these curves with the horizontal axis.

law  $\dot{\delta} \propto 1/(t_c - t)$  requires the adjustment of  $\alpha$  to the special value 2 in the phenomenological approach [Voight, 1988] underlying (15.2) while it is a robust and universal result in our model leading to (15.11) in the velocity-weakening regime  $B > A$ ,  $m > 1$  and for a normalized initial state variable larger than 1 (see equation (15.11) and Table 15.1).

In order to invert the parameters  $m$ ,  $D$ ,  $T$  of the friction model and the initial condition of the state variable  $x_i$  from the velocity data, we minimize the *rms* (root-mean-square) of the residual between the observed velocity  $\dot{\delta}_{obs}$  and the velocity  $\dot{\delta}$  from the friction model (15.22) and (15.21). The constant  $D$  in (15.21) is obtained by taking the derivative of the *rms* with respect to  $D$

$$D = \frac{\sum_{t_i} \dot{\delta}(t_i) \dot{\delta}_{obs}(t_i)}{\sum_{t_i} \dot{\delta}(t_i)^2} \quad (15.12)$$

where the velocity  $\dot{\delta}$  in (15.12) is evaluated for  $D = 1$  in (15.21). We use a simplex algorithm (matlab subroutine) to invert the three other parameters. For each data set, we use different starting points (initial parameter values for the simplex algorithm) in the inversion to test for the sensitivity of the results on the starting point.

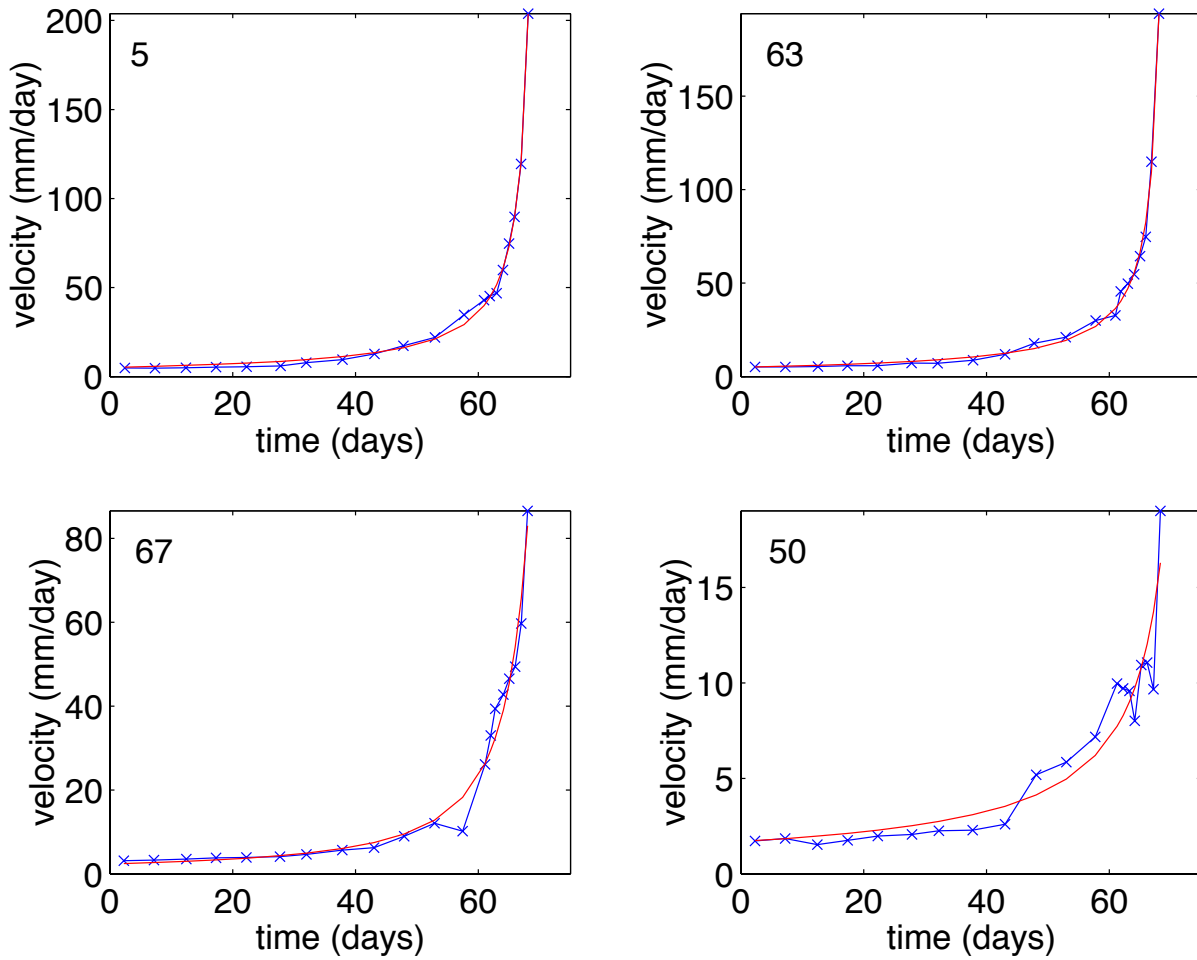


FIG. 15.4 – For each of the four Vaiont benchmarks, the velocity data of Figure 15.2 is fitted with the slider-block model with the state and velocity friction law (15.22) and (15.21) by adjusting the set of parameters  $m$ ,  $D$ ,  $T$  and the initial condition of the state variable  $x_i$ . The data is shown as the crosses linked by straight segments and the fit is the thin continuous line. The fitted  $m$  are respectively  $m = 1.35$  (benchmark 5),  $m = 1.24$  (benchmark 63),  $m = 0.99$  (benchmark 67) and  $m = 1.00$  (benchmark 50).

Figure 15.4 shows the fits to the velocity data using the slider-block model with the state and velocity friction law (15.21) and (15.22). The values of  $m = B/A$  are respectively  $m = 1.35$  (benchmark 5),  $m = 1.24$  (benchmark 63),  $m = 0.99$  (benchmark 67) and  $m = 1.00$  (benchmark 50). Most values are larger than or equal to 1, which is compatible with the finite-time-singularity regime summarized in Table 15.1. The parameters of the friction law are very poorly constrained by the inversion. In particular, even for those benchmarks where the best fit gives  $m > 1$ , other models with  $m < 1$  provide a good fit to the velocity with only slightly larger rms.

We have also tried to invert the friction law parameters using only data up to a time  $t_{max}$  smaller than the last available point to mimic a real-time situation. Changing  $t_{max}$  between 30 and 70 days, we obtain a large variability of the parameters. Most values  $m$  are found larger than 1 for  $30 < t_{max} < 55$  days, and then become smaller than one, and return to  $m \geq 1$  for 3 benchmarks when using the full velocity data. Similar fluctuations are found when using a synthetic data set generated with the friction model. We have generated a synthetic data set using the same parameters as those of the best fit of benchmark 5, and added a white noise with the same standard deviation as that of the residue of the fit of benchmark 5. Although this synthetic data set was generated with  $m = 1.35$ , both  $m > 1$  and  $m < 1$  (for 2 points over 15 points) values are obtained when inverting the parameters up to  $t_{max}$  and changing  $t_{max}$  between 30 and 70 days. However, values with  $m < 1$  for this synthetic data set are much less frequent than for the Vaiont velocity data in relative terms.

Figure 15.5 gives another representation of Figure 15.4 showing the inverse of the velocity as a function of time. A saturation of the velocity before the critical time can be observed for all benchmarks, which may explain the values  $m < 1$  sometimes obtained by the inversion.

It is instructive to contrast these results with those obtained by fitting the cumulative displacement (rather than the velocity) with the slider-block model with the state and velocity friction law (15.21) and (15.22). The results are shown in Figure 15.6. The fitted  $m$  are respectively  $m = 0.99$  (benchmark 5),  $m = 0.85$  (benchmark 63),  $m = 0.68$  (benchmark 67) and  $m = 0.17$  (benchmark 50). These values differ significantly from those obtained by the inversion of the velocity data and, to make things worse, they all correspond to the velocity-strengthening regime  $m < 1$ . At first sight, these results are quite surprising since we fit the same data, the only difference being that the cumulative displacement is the integral of the velocity. We think that the reason for these discrepancies lies in the fact that, assuming that the velocity-weakening regime  $m > 1$  holds, the corresponding logarithmic dependence (15.9) of the displacement  $\delta$  is extremely degenerate in that it predicts an acceleration of the displacement which is significant only very close to the critical time  $t_c$ . Therefore, a cross-over from a low velocity to a larger velocity described by the regime  $m < 1$  may be selected by the inversion, as we witness here. This is the curse of logarithmic singularities, which are so weak as providing poor constraints, notwithstanding the a priori reduction of noise obtained by constructing a cumulative quantity. It may actually be the case that the red noise deriving from the integral of the velocity is en-

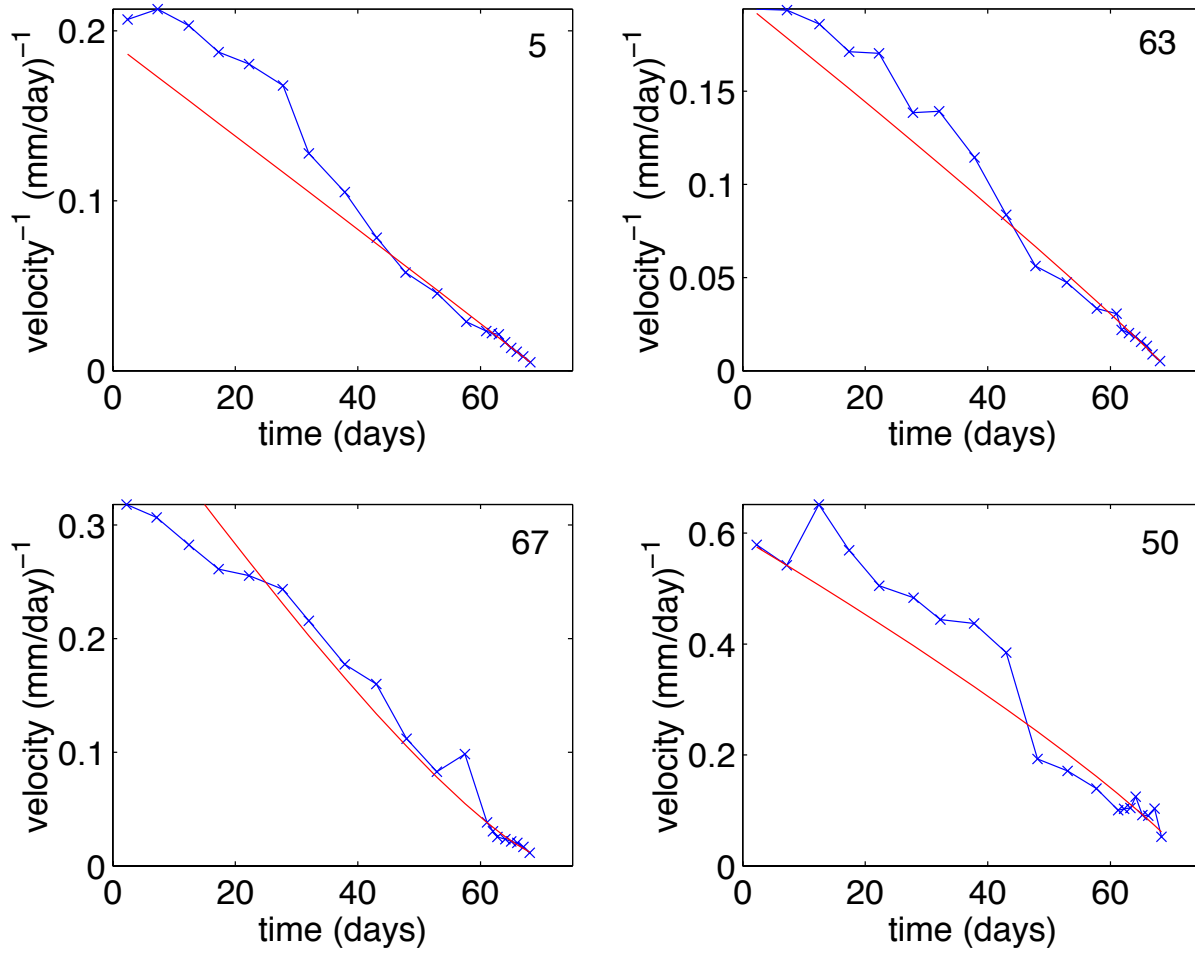


FIG. 15.5 – Same as Figure 15.4 but showing the inverse of the velocity. The upward bending of the curve for benchmark 67 reflects the saturation of the velocity in the stable regime  $B < A$ . The fit for the three other benchmarks characterized by  $m \geq 1$  is very close to the asymptotic solution  $v \sim 1/(t_c - t)$  (15.11).

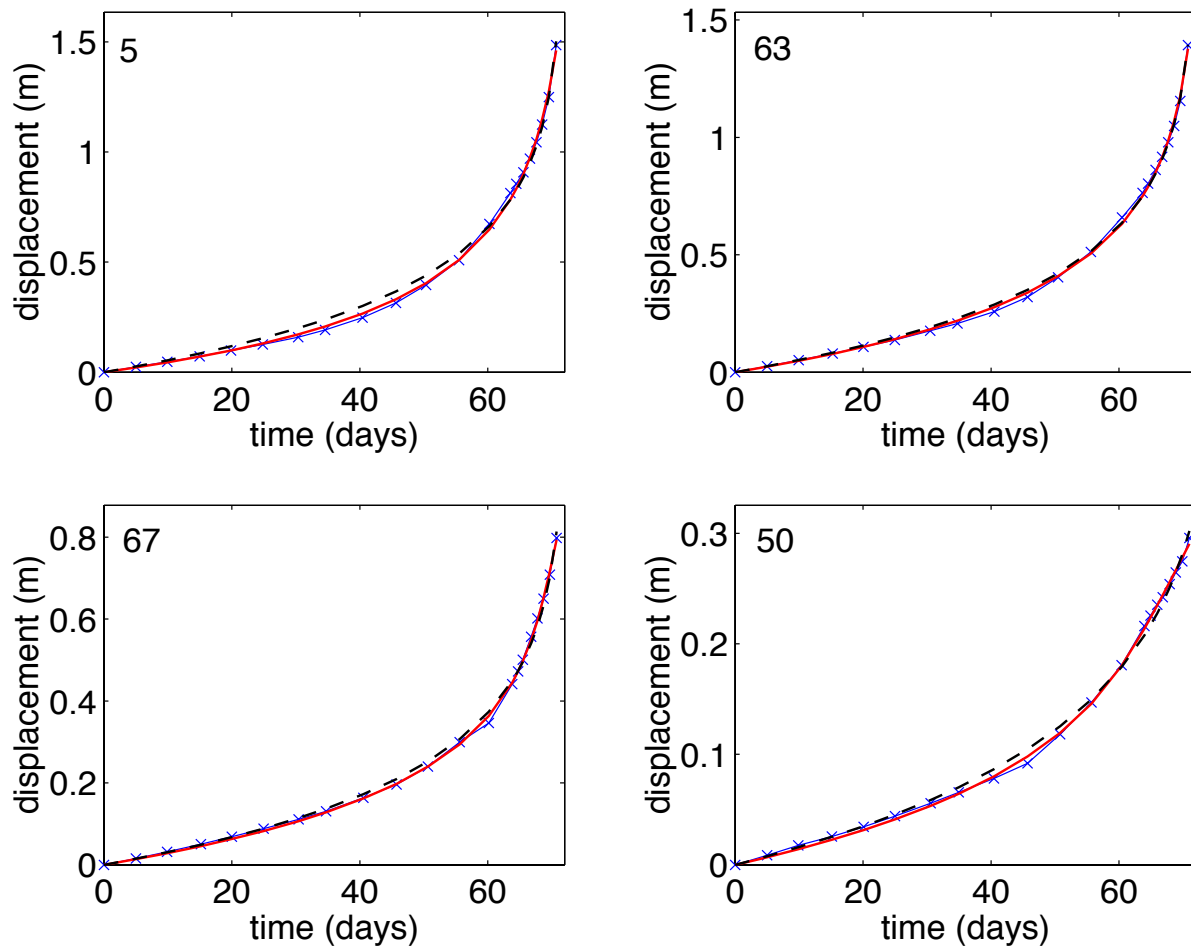


FIG. 15.6 – For each of the four Vaiont benchmarks, the cumulative displacement data is fitted with the slider-block model with the state and velocity friction law (15.22) and (15.21) by adjusting the set of parameters  $m$ ,  $D/T$  and the initial condition of the state variable  $x_i$ . The data is shown as the crosses linked by straight segments and the fit is the thin continuous line. The fitted  $m$  are respectively  $m = 0.99$  (benchmark 5),  $m = 0.85$  (benchmark 63),  $m = 0.68$  (benchmark 67) and  $m = 0.17$  (benchmark 50). The fits with the slider-block model obtained by imposing the value  $m = 1.5$  are shown with the dashed line for comparison.

ough to spoil the weak logarithmic singularity : the resulting correlated noise seems to select a milder behavior. We are thus led to conclude that fits to the sliding velocity which involves stronger power law singularities should be more reliable and we shall use them exclusively in our prediction tests reported below.

The alternation of phases of accelerating and decelerating velocity in the 1960-1962 period implies that some friction parameters have changed, maybe due to changes in water level, resulting in a change of sliding regime. The change of water level may have modified the material properties of the underlying solid contacts at the base of the moving rock mass [e.g. *Erismann and Abele*, 2000], therefore changing the parameter  $A/B$  from the stable to the unstable regime. Another possibility is that changes in water level have modified the population of contacts at the basis of the rock mass, therefore changing the parameters of the friction law, and changing the sliding regime from the decelerating regime to to the accelerating regime. One possible simple change of the parameters of the friction law correspond to a change of the initial condition on the state variable  $x_i$ , which may induce a change of the sliding regime from the decelerating regime for  $m > 1$  and  $x_i > 1$  to the accelerating regime for  $m > 1$  and  $x_i < 1$  and vice-versa.

## Predictions and ex-post skills

We present a series of attempts at predicting in advance the critical time  $t_c$  of the catastrophic Vaiont landslide instability. These attempts rely solely on the analysis of the four benchmarks velocity data up to various times  $t_{\max} < t_c$  mimicking a real-time situation. Therefore, we truncate the data at some time  $t_{\max} < t_c$  and use only the data up to  $t_{\max}$ . Our goal is i) to investigate whether a prediction in advance could have been issued, as suggested by *Voight* [1988], ii) to establish the reliability and the precision limits of such predictions and iii) to test various prediction schemes that we have developed in the recent past for other applications or specifically for this problem. We use and compare 3 methods to predict the critical time  $t_c = 69$  days of the collapse

- the slider block model with the state and velocity friction law described above ;
- an approximation of the slider block model based on the functional renormalization method described below ;
- a simple finite-time singularity (15.2) with  $\alpha = 2$  as proposed by *Voight* [1988].

### Prediction using the slider-block model with the state and velocity friction law

The prediction of the critical time  $t_c$  is obtained by fitting the slider-block model on the velocity time series of the four benchmarks up to a time  $t_{\max}$ . For  $m \geq 1$ ,  $t_c$  is the time of the divergence. The divergence of the velocity exists only in the unstable regime  $m > 1$ . Therefore, we choose the best fit with  $m > 1$ , even if the best model gives sometimes  $m < 1$ .

## Functional renormalization of the friction law

We are dealing with noisy time series with relatively few data points for which the detection of a singularity is a difficult task. Rather than using the full solution of a model assumed to be a good representation of reality as done in the previous sections, it may be profitable to develop prediction schemes that are less constrained by the necessarily restricting physical assumptions underlying the model and that are more specifically designed from a mathematical point of view to be resilient to noise and to the scarcity of data. Such a method is the so-called functional renormalization method, which constructs the extrapolation for future time  $t > t_{\max}$  from a re-summation of the time series represented by a simple polynomial expansion in powers of time  $t$ . Its mathematical foundation has been developed in a series of papers [Yukalov and Gluzman, 1997; Gluzman and Yukalov, 1997, 1998]. The application of this method to detect and predict finite-time singularities has been already investigated by Gluzman *et al.* [2001] and Gluzman and Sornette [2002]. We refer to these papers for a presentation of the method and restrict ourselves here to the concrete application of the method to the friction law (15.21) and (15.22).

The first input of the functional renormalization approach is an expansion of the variable to be predicted in increasing powers of time. In our case, we use the functional renormalization approach to provide an approximate analytical solution of the differential equation of the friction model (15.18). This method is much more efficient numerically than the numerical resolution of the differential equation (15.18). The friction model (15.18) gives the time evolution of the state variable from which the sliding velocity  $\dot{\delta}$  derives using (15.15).

The needed expansion of  $y \equiv \theta/\theta_0$  in powers of time  $t$  is obtained from a Taylor expansion whose coefficients are derived from successive differentiation of (15.18). Up to fourth order  $t^4$ , calling  $y_0 = \theta(t=0)/\theta_0$ , we obtain

$$y_k(t) \simeq \sum_{n=0}^k a_n t^n, \quad t \rightarrow 0, \quad k = 1, 2, 3, 4, \quad (15.13)$$

where the coefficients  $a_n$  are given in the Appendix B as a function of the friction parameters and of the initial condition.

The functional renormalization approach is in principle able to derive an extrapolation to the future from the form (15.13). However, in order to obtain an optimal stabilization, it is essential to incorporate as much available information as possible. In particular, in our case, we know the functional form of the dependence of the state variable as a function of time in the asymptotic regime (large times for  $m < 1$  and close to the singularity for  $m > 1$ ). Therefore, the second input of our implementation of the functional renormalization approach is the following. For  $m < 1$ , in a long-time limit, it is easy to show that equation (15.18) has an asymptotic solution in the form,

$$y_{t \rightarrow \infty}(t) \simeq y^* + A_1 \exp\left(-\frac{t}{t^*}\right) + A_2 \exp\left(-\frac{2t}{t^*}\right) + \text{h.o.t.} \quad (15.14)$$

where  $1/t^* = (1-m)/T = (1-m)(S\theta_0)^{1/(1-m)}$  was already defined in (15.29) and h.o.t. stands

for higher-order terms. The coefficients  $A_1$  and  $A_2$  are unspecified at this stage and can be determined using the crossover technique of *Gluzman and Yukalov [1998]*, in order to optimize the stability of the solution. For  $m \geq 1$ , the asymptotic expression as  $t \rightarrow t_c$  is of the form (15.24), but we shall allow the prefactor and  $t_c$  to be adjusted to ensure maximum stability. Specifically, the determined value of  $t_c$  will be a primary result of the crossover technique.

Our goal is thus to construct a function  $y(t)$  which incorporates the short and long time asymptotics of the solution as given by expressions (15.13) and (15.14) for  $m < 1$  and by (15.13) and (15.24) for  $m \geq 1$ , while possibly departing from it at intermediate times to allow for a maximum stability. The general mathematical formulas that are solution of this problem are given in Appendix B for the two cases  $m < 1$  and for  $m \geq 1$  respectively.

For the application to the Vaiont landslide, and for each “present time”  $t_{\max}$ , we assume that  $m > 1$  so that  $t_c$  exists and we fit the expression of the fourth-order approximate  $y_4^*(t)$  given by (15.47) to the velocity of each of the four benchmarks, extract the corresponding parameters and put them in equation (15.48) for the critical time  $t_{c4}$ . We stress that the function thus reconstructed is essentially indistinguishable with the naked eye from the fit with the slider-block friction model. Solving (15.48) for  $t_{c4}$  allows us to construct the predicted critical time as a function of the “present time”  $t_{\max}$ . We also estimate the value of  $m$  as a function of  $t_{\max}$ . Apart from some large jumps that may be attributed to the sensitivity of specific noisy points as  $t_{\max}$  is scanned, we observe that most fits are compatible with a value of  $m$  in the range 1.3 – 1.5.

### Finite-time singularity (15.2) with $\alpha = 2$

We use a simple linear regression of the inverse of the velocity as a function of time, as proposed by *Voight [1988]*. We have found that, in order to have more stable parameters, it is necessary to give less weight to the early times where the velocity is small and contains little information on the critical time. We find that weighting each data point proportionally to its velocity seems close to optimal. The critical time  $t_c$  is then given as the time at which the fitted straight line of the  $1/\dot{\delta}$  data intersects with the time axis. Recall that a linear relation between  $1/\dot{\delta}$  and time  $t$  is equivalent to a power law singularity of the velocity  $\dot{\delta} \sim 1/(t_c - t)$ , as discussed previously, which is expected asymptotically close to  $t_c$  for the friction model in the case  $m > 1$  and  $x_i < 1$ .

### Comparison of three different methods of prediction of $t_c$ as a function of the “present time” $t_{\max}$

The predictions of the critical time obtained from the three methods are shown in Figure 15.7. A prediction for  $t_c$  with an uncertainty of a few days is obtained for the 4 benchmarks within 20 days before the catastrophic failure. The reliability of the prediction is confirmed by

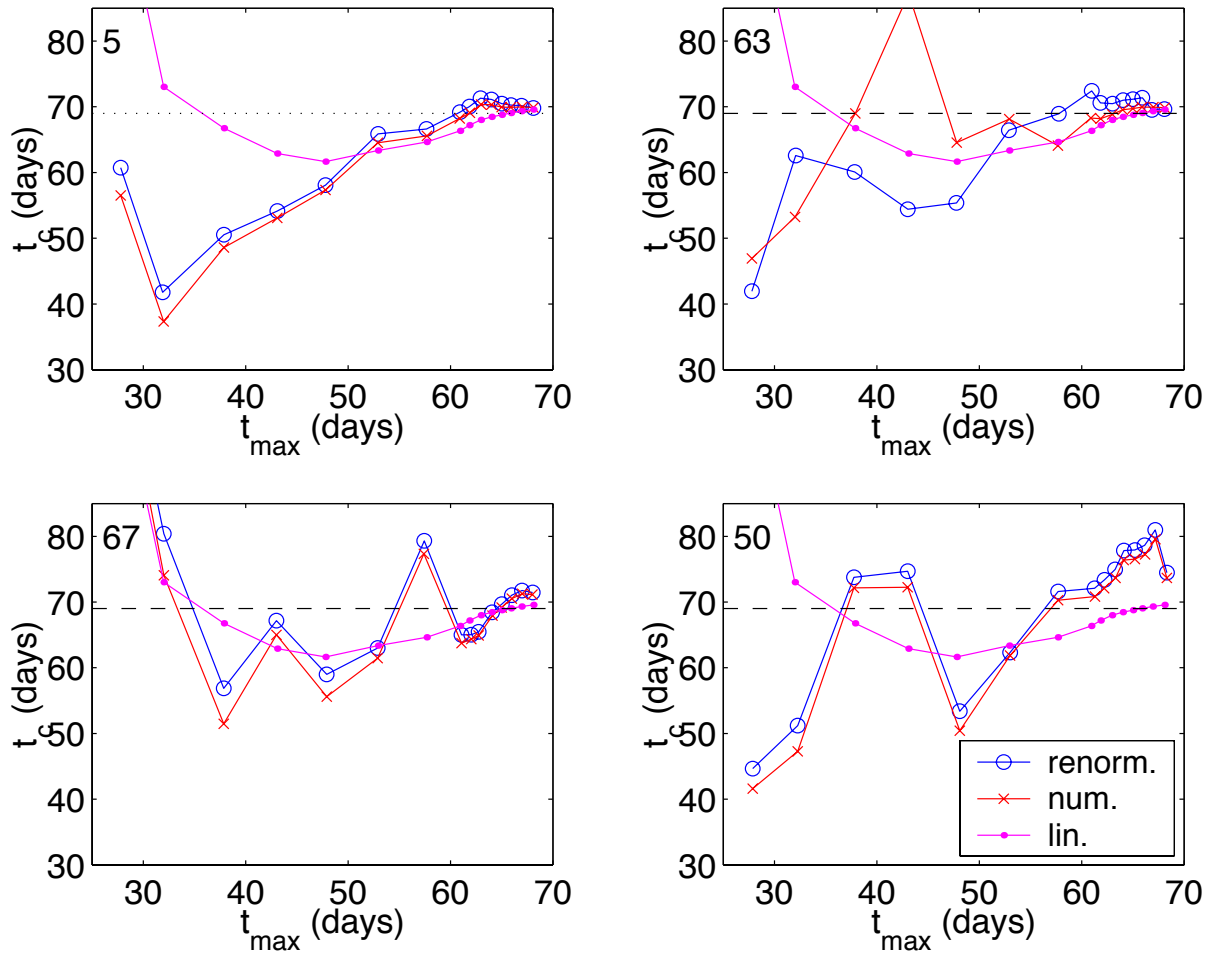


FIG. 15.7 – Predicted critical time  $t_c$  as a function of the “present time”  $t_{max}$  (last point used for the fit) for all four benchmarks of the Vaiont landslide, using three different methods of prediction described in the text : renormalization method (circles), numerical evaluation of the friction model (15.22) (crosses), and linear regression of the inverse velocity as a function of time performed by removing the first point (early time) of the curve and using a weight proportional to the velocity (dots). The horizontal dashed line indicated the true critical time  $t_c = 69.5$  days (for an arbitrary origin of time from which the fits are performed to the catastrophic landslide. All methods impose  $m > 1$ , but in some cases a better fit may be obtained in the stable regime  $m < 1$ ).

the coherence and agreement between the three methods. Starting approximately at  $t_{\max} = 45$  days, one can observe that, using the friction model, all four time series provide a reasonable  $t_c$  prediction which however tends to increase and to follow the value of the “present time”  $t_{\max}$ . This is unfortunately a common feature of fits to power law singularities in which the last data points close to the “present” tends to dominate the rest of the time series and produce a predicted time of singularity close to the “present time”  $t_{\max}$  [Huang *et al.*, 2000 ; Sornette and Johansen, 2001]. The  $t_c$  value obtained using the fourth-order approximate is always a little smaller than the  $t_c$  estimated from the exact friction model. The renormalization method is therefore a little better at early times, but the exact friction model works better at the end. The  $t_c$  value obtained by the linear regression of  $1/\dot{\delta}$  is too large for small  $t_{\max}$ , because it is only an asymptotic solution of the friction model for  $t \approx t_c$ . However, this method provides very good estimates of  $t_c$  close to  $t_c$ .

To test whether the relative value of these three methods result from a genuine difference in their stability with respect to noise or rather reflects an inadequacy of the slider-block friction model to fit the data, we have generated a synthetic velocity time series obtained by using the slider-block friction equations with the same parameters as found in the fit to the full data set of benchmark 5 and adding white noise with the same standard deviation as that of the real data set. We then applied the three prediction methods to this synthetic data set. In principle and by construction, we should expect a priori that the prediction based on the slider-block friction model should always perform best since it is the *true* model. This is not what we find, as shown in Figure 15.8. At times far from  $t_c$ , i.e.  $40 \text{ days} < t_{\max} < 60 \text{ days}$ , the friction model is the best, as expected. However, the prediction based on the asymptotic linear relation between  $1/\dot{\delta}$  and time  $t$  is slightly better than the friction model, starting approximately 9 days before the landslide.

The overall conclusion is that the least sophisticated approach, that is the linear regression of  $1/\dot{\delta}$ , seems to perform as well as or slightly better than the sophisticated renormalization method or the exact friction model for “present times” sufficiently close to the critical time  $t_c$ . For times further away from  $t_c$ , the renormalization method and the exact friction model are better. Although the corresponding power-law is only an asymptotic solution of the friction model for times close to  $t_c$ , the linear regression of  $1/\dot{\delta}$  gives significantly better predictions than the exact model or the renormalization method. However, we must keep in mind that the use of the linear regression of  $1/\dot{\delta}$  as a function of time contains two hidden and rather strong assumptions : the power law and the value of its exponent. Without the slider-block friction model, these assumptions are just guesses and are a priori unjustified.

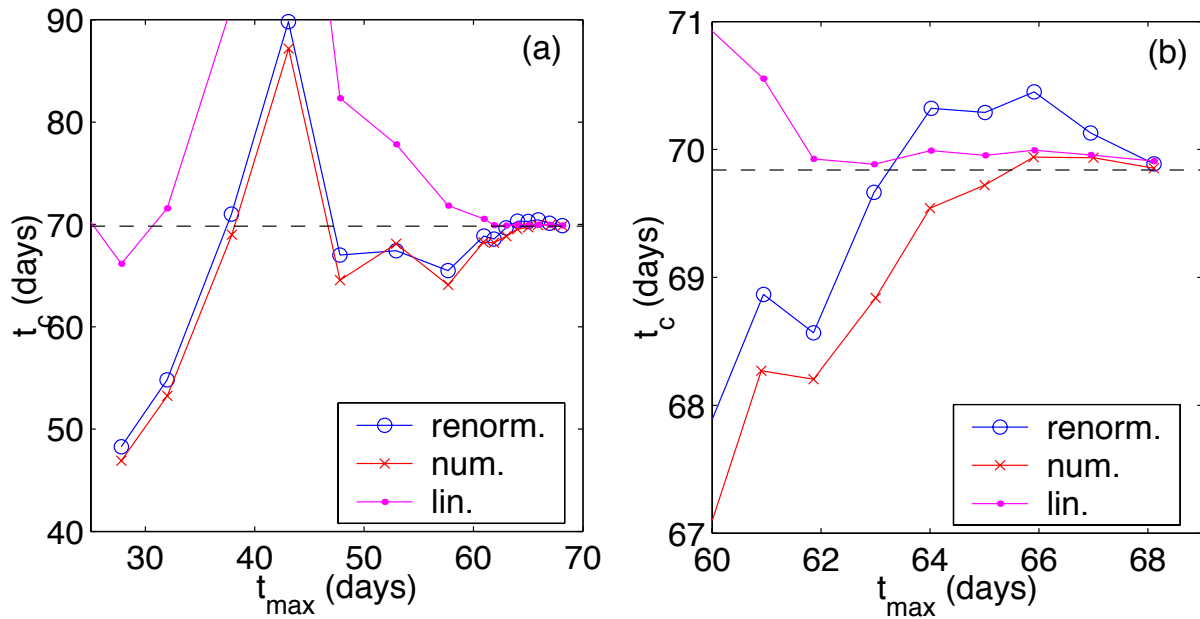


FIG. 15.8 – Same as Figure 15.7 for a synthetic data set with the same parameters and noise as those obtained for benchmark 5 of the Vaiont landslide, using the same three different methods of prediction. The right panel is a zoom of the left panel close to  $t_c$ . The horizontal dashed line indicated the true critical time  $t_c = 69.8$  of the catastrophic landslide.

## 15.4 La Clapière landslide : the aborted 1986-1987 peak acceleration

We now report results on another case which exhibited a transient acceleration which did not result in a catastrophic failure but re-stabilized. This example provides what is maybe an example of the  $m < 1$  stable slip regime, i.e.  $B < A$ , as interpreted within the friction model.

### Historical and geo-mechanical overview

#### Geo-mechanical setting and Displacement history : 1950-2000

La Clapière landslide is located at an elevation between 1100 m and 1800 m on a slope that culminates at 3000 m high and has a width of about 1000 m. The summit of the main scarp ranges in elevation between 1550 and 1735 m. Figure 15.9 shows La Clapière landslide in 1979 before the acceleration of the displacement, and in 1999 after the end of the crisis. The volume of mostly gneiss rocks implied in the landslide is estimated to be around  $50 \times 10^6 \text{ m}^3$ . At an elevation of about 1300 m, a 80 m thick bed provides a more massive and relatively stronger level compared with the rest of relatively weak and fractured gneiss. The two lithological entities are characterized by a change in mica content which is associated with a change of the peak strength

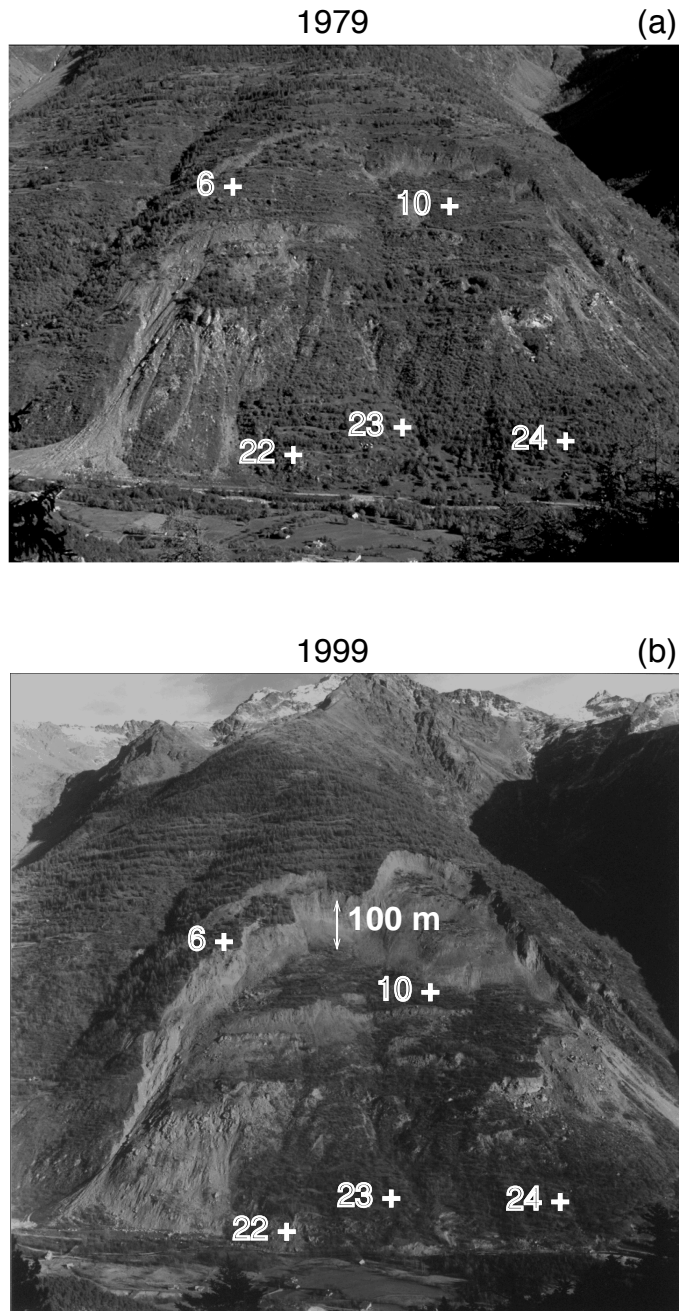


FIG. 15.9 – a) Picture of La Clapière landslide taken in 1979. It is located at an elevation between 1100 m and 1800 m on a slope that culminates at 3000 m high and has a width of about 1000 m. The summit of the main scarp ranges in elevation between 1550 and 1735 m. The volume of mostly gneiss rocks implied in the landslide is estimated to be around  $50 \times 10^6 \text{ m}^3$ . The summit scarp are not connected. b) Picture of La Clapière landslide taken in 1999. Geomorphological criteria allow one to distinguish three distinct sub-entities within the landslide, NW, Central and SW respectively [Follacci *et al.*, 1988]. The global surfacial pattern is preserved. The main feature related to the 1982-1988 crisis is a new summit scarp with a total displacement of about 100 m in 1999, indicated by an arrow in panel (b).

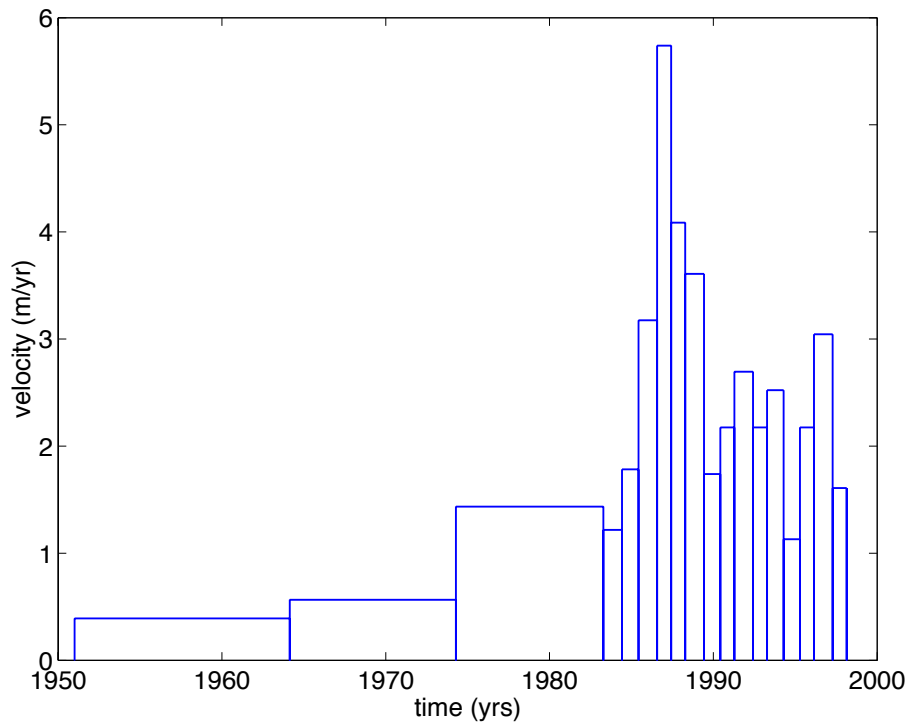


FIG. 15.10 – Velocity in meters/year of the side of La Clapière mount over almost 50 years, showing that the dangerous velocity peak in 1987 was preceded by a progressing build-up extending over several decades. Before 1982, the velocity is inferred from aerial photographs in 1951, 1964, 1974 and 1982. After 1982, the velocity is obtained from automated triangulation and geodesy. Data from *CETE* [1999].

and of the elastic modulus by a factor two [Follacci *et al.*, 1990, 1993]. Geomorphological criteria allow one to distinguish three distinct sub-entities within the landslide, NW, Central and SW respectively [Follacci *et al.*, 1988].

There is some historical evidence that the rock mass started to be active before the beginning of the 20th century. In 1938, photographic documents attest the existence of a scarp at 1700 m elevation [Follacci, 2000]. In the 1950-1980 period, triangulation and aerial photogrammetric surveys provide constraints on the evolution of the geometry and the kinematics of the landslide (Figure 15.10). The displacement rate measured by aerial photogrammetric survey increased from 0.5 m/yrs in the 1950-1960 period to 1.5 m/yrs in the 1975-1982 period [Follacci *et al.*, 1988]. Starting in 1982, the displacements of 43 benchmarks have been monitored on a monthly basis using distance meters [Follacci *et al.*, 1988, 1993; Susella and Zanolini, 1996]. The displacement data for the 5 benchmarks in Figure 15.9 is shown in Figure 15.11. The velocity is shown in Figure 15.12. The rock mass velocities exhibited a dramatic increase between January 1986 and January 1988, that culminated in the 80 mm/day velocity during the 1987 summer and to 90 mm/day in October 1987. The homogeneity of benchmark trajectories and the synchronous acceleration phase for most benchmark, attest of a global deep seated behavior of this landslide [e.g. Follacci *et al.*, 1988]. However, a partitioning of deformation occurred, as reflected by the

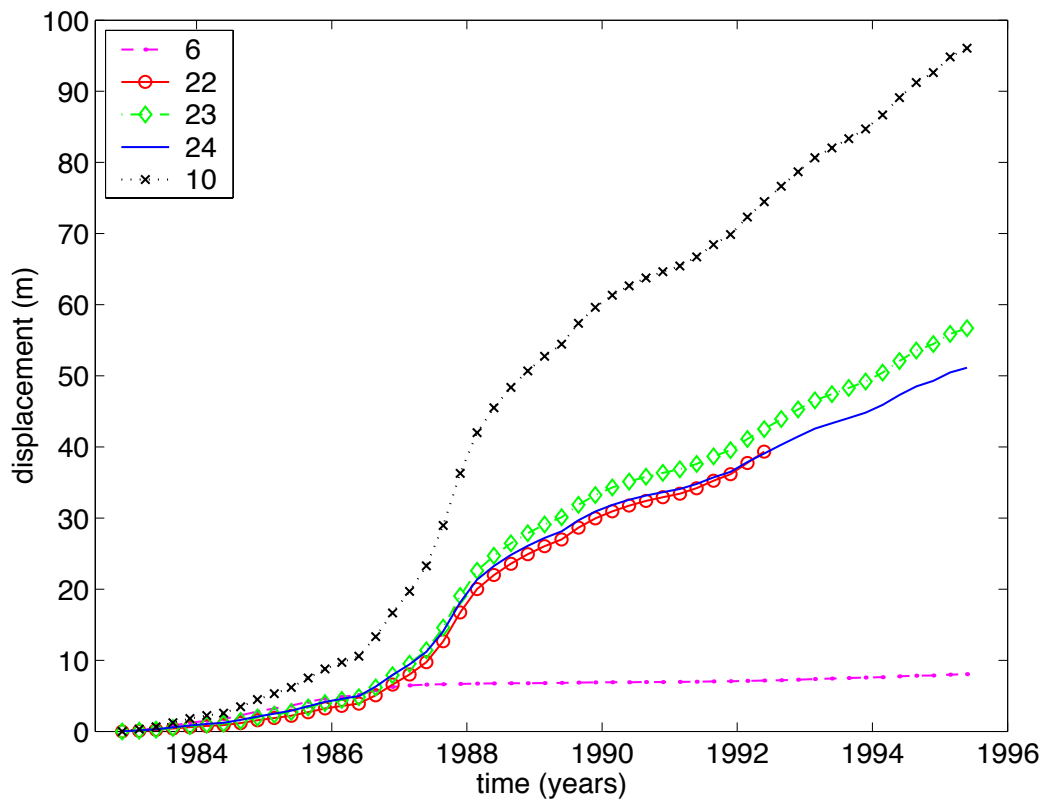


FIG. 15.11 – Displacement for the 5 benchmarks on La Clapière site shown in Figure 15.9.

difference in absolute values of benchmark displacements (Figure 15.11). The upper part of the landslide moved slightly faster than the lower part and the NW block. The observed decrease in displacement rate since 1988 attest of a change in landsliding regime at the end of 1987 (Figure 15.11) .

### Correlations between the landslide velocity and the river flow

The velocity displays large fluctuations correlated with fluctuations of the river flow in the valley as shown in Figure 15.13. There is a seasonal increase of the slope velocity which reaches a maximum  $V_{\max}$  of the order of or less than 30 mm/days. The slope velocity increases in the spring due to snow melting and over a few days after heavy precipitations concentrated in the fall of each year [Follacci *et al.*, 1988 ; Susella and Zanolini, 1996]. During the 1986-1988 period, the snow melt and rainfalls were not anomalously high but the maximum value of the velocity,  $V_{\max} = 90$  mm/day, was much larger than the velocities reached during the 1982-1985 period for comparable rainfalls and river flows [Follacci *et al.*, 1988 ; 1993]. This strongly suggests that the hydrological conditions are not the sole control parameters explaining both the strong 1986-1987 accelerating and the equally strong slowdown in 1988-1990. During the interval 1988-1990, the monthly recorded velocities slowed down to a level slightly higher than the pre-1986 values. Since 1988, the seasonal variations of the average velocity never recovered the level established during the 1982-1985 period [Follacci *et al.*, 1993 ; David and ATM, 2000]. Rat [1988] derives a relationship between the river flow and the landslide velocity by adjusting an hydrological model

to the velocity data in the period 1982 to 1986. This model tuned to this time period does not reproduce the acceleration of the velocity after 1986.

In order to study quantitatively the effect of the precipitations on the landslide velocity, we need to remove the long-term fluctuations of the velocity that may not correlated to changes in the precipitations. We divide the data of benchmark 10 of La Clapière into three different intervals : [1982.917, 1987.833], [1987.833, 1991.25] and [1991.25, 1995.5]. The initial values of the time and of the displacement are fixed to 0 at the beginning of each time period. In the first interval, the velocity rises (with fluctuations) ; in the second interval, the velocity decreases (with fluctuations) ; in the third interval, the velocity fluctuates around a constant. We used non-linear Least-Square fits with different fitting functions separately within each interval. The results of the fits are the following.

1. In the first interval [1982.917, 1987.833], we fit the displacement by  $d(t) = a(|1-t/t_0|^{-b}-1)$  with  $a = 8.96, b = 1.01$  and  $t_0 = 6.26$  years.
2. For the second interval [1987.833, 1991.25], we use the same functional form with  $a = 10.42, b = 0.4106$  and  $t_0 = -0.1081$ . The negative value of  $t_0$  implies a decay of the displacement.

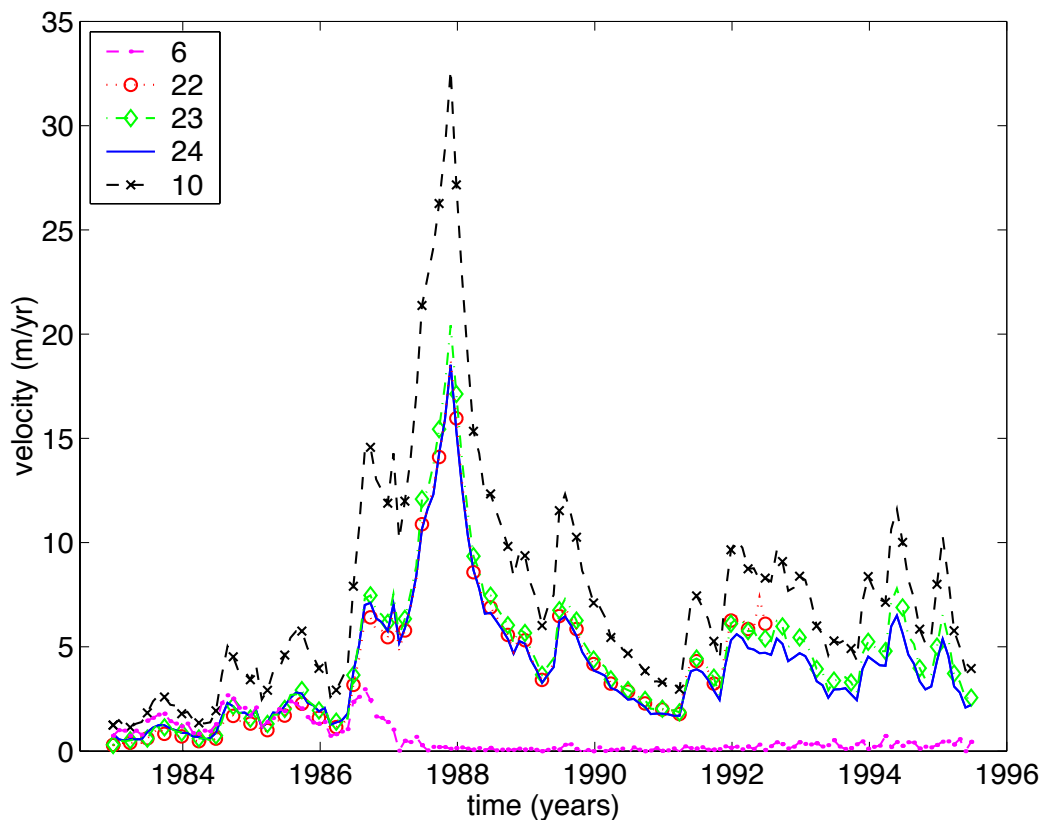


FIG. 15.12 – Velocity for the same data as shown in Figure 15.11. Annual fluctuations of the velocity is due to the seasonal variations of the precipitations.

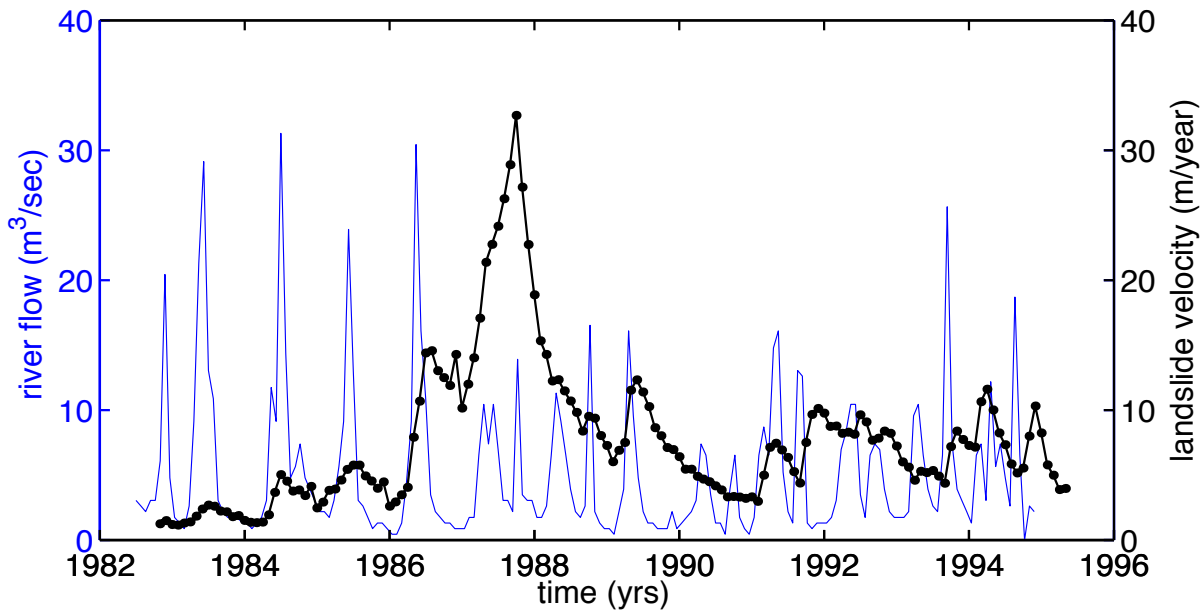


FIG. 15.13 – Velocity pattern for benchmark 10 of La Clapière landslide (solid line and dots) and flow rates (thin solid line) of the Tinée river on the 1982-1995 period. Because the Tinée river runs at the basis of the La Clapière landslide, the river flow rate reflects the water flow within the landslide [Follacci *et al.*, 1993; Susella and Zanolini, 1996]. The flow rates are measured at St Etienne village, 2 km upstream the landslide site. There is no stream network on the landslide site. The Tinée flow drains a 170 km<sup>2</sup> basin. This tiny basin is homogeneous both in terms of slopes and elevation (in the 1000-3000 m range). Accordingly the seasonal fluctuations of the river flow is admitted to reflect the evolution of the amount of water that is available within the landslide slope due to rainfalls and snow melting. Data from *CETE*, [1996].

3. For the third interval [1991.25, 1995.5], we use a fit by  $d(t) = at^b$  which has only two parameters  $a = 7.4687$  and  $b = 0.989$ .

The goodness of fit is very good in all three regimes : the standard deviations of the residuals being of the order of 0.4 while the magnitude of the displacement is about 30, this yields a signal-over-noise ratio of 75, which is very good.

Figure 15.14 compares the the Burg's power spectrum of the flow rates of the Tinée river and of the detrended velocity residuals. The Burg spectrum is a kind of smoothed FFT (fast-Fourier transform) obtained by approximating the true spectrum by that of an autoregressive process of a finite order. The top panel of figure 15.14 exhibits the Burg's power spectrum of the flow rates of the Tinée river on the 1982-1988 and on the 1988-1996 periods, which are proxies of the cycle of precipitations and snow melting. The bottom panel of figure 15.14 shows the Burg's power spectrum of the detrended velocity residuals for these two periods.

In the first time interval 1982-1988, a strong peak at the period of 1 year appears both for the velocity residuals and for the river flow. This correspondence is confirmed by the strong

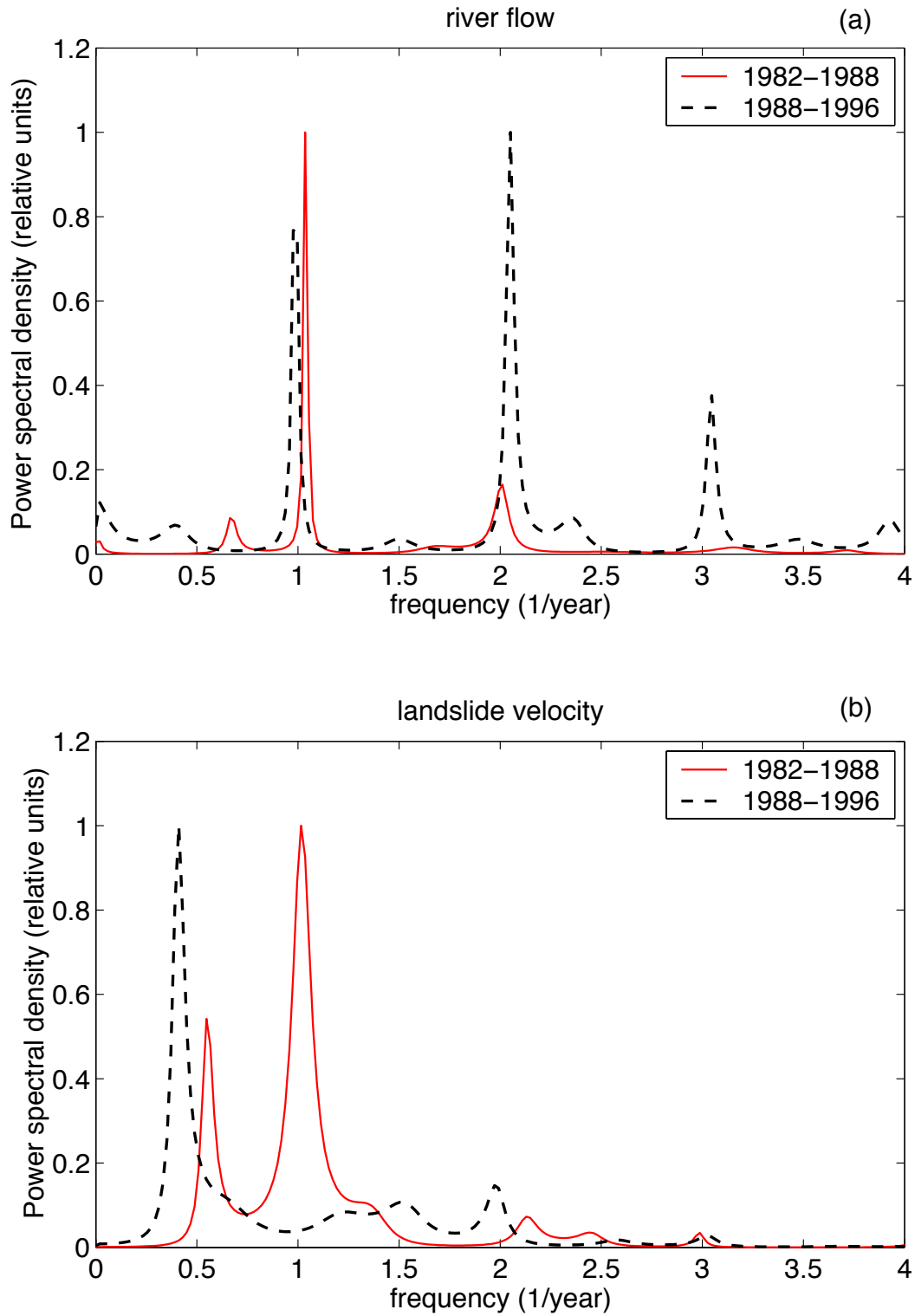


FIG. 15.14 – Top panel : Burg's power spectrum of the flow rates of the Tinée river on the 1982-1988 and on the 1988-1996 periods which are aggregated from the periods shown in Figure 15.13. Bottom panel : Burg's power spectrum of the detrended velocity residuals for the same two periods.

cross-correlation between the river flow and the landslide velocity, which is also directly apparent visually in Figure 15.13. Let us use the language of system theory and consider the river flow as an input (or a forcing) and the landslide velocity as an output of the system. These observations of a common spectral peak and of a strong cross-correlation are then compatible with a view of the system as being linear or only weakly non-linear.

In contrast, the (linear) correlation between the river flow input and the landslide velocity output disappears in the second time interval 1988-1996, as can be seen from the absence of a spectral peak at the period of 1 years and a very weak peak at the period 6 months ( $f = 2 \text{ year}^{-1}$ ) in the (output) landslide velocity spectrum compared with the two strong peaks at the same periods of 1 years and 6 months observed in the (input) river flow spectrum. This breakdown of linear correlation seems to be associated with the birth of a strong peak close to the sub-harmonic period of 2 years ( $f = 0.5 \text{ year}^{-1}$ ), which is absent in the river flow rate. This suggests the following interpretation. Frequency doubling or more generally frequency multiplications are the results of simple nonlinearities. Indeed, higher frequency overtones in river runoff is very common feature of hydrological regime (see for instance [Pisarenko *et al.*, 2002]). In contrast, the creation of sub-harmonics requires bifurcations or period-doubling, for instance involving nonlinear processes with time delays. It thus seems that the input of rain and snow melting is transformed by the system during the second time interval via the process of such delayed period-doubling nonlinearities. It is intriguing that the change of sliding regime to a reduction of velocity in the second time interval seems here to be associated with such a sub-harmonic non-linearity, which could be the result of a change of topology of the block structures (through fragmentation) and of the solicitation of novel fresh surfaces of sliding.

### **Fracturing patterns contemporary to the 1986-1987 accelerating regime**

In 1985-1986, a transverse crack initiated in the upper part of the NW block. It reaches 50 m of vertical offset in 1989. The maximum rate of change of the fracture size and of its opening occurred in 1987 [Follacci *et al.*, 1993]. This new transverse crack uncoupled the NW block from the upper part of the mountain, which moved at a much smaller velocity below 1 mm/day since 1985-86 [Follacci *et al.*, 1993] (Figures 15.9 and 15.15). Since summer 1988, an homogenization of the surface morphological faces and a regression of the main summit scarp were reported. The regression of the summit scarp was observed as a new crack started to open in September 1988. Its length increased steadily to reach 500 m and its width reached 1.75 m in November 1988. Accordingly, the new elevation of main scarp in the SE block reaches 1780 m. This crack, which defined a new entity, that is the upper SE block, has remained locked since then (Figures 15.9 and 15.15).

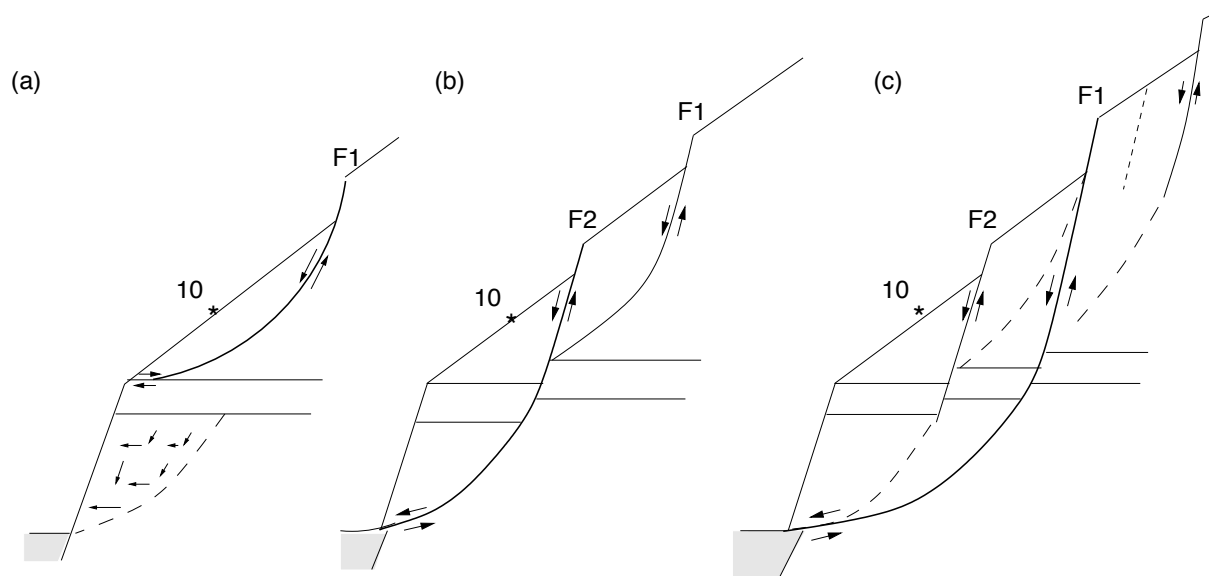


FIG. 15.15 – Schematic structural interpretation of one possible mechanism involved in the 1986-1988 crisis. The 3 schematic cross sections are the proposed landslide geometries, before 1986 (a), during the 1987 acceleration (b), and after 1988 (c). *Follacci et al.* [1993] argue for the failure of the strong gneiss bed (F2 fault) in the NW block as the driving force behind the 1986-1987 accelerating phase (b). In the same period, the development of the upper NW crack, (F1 fault on central cross section), that released the landslide from its head driving force, appears as the key parameter to slow down the accelerating slide. Note that for the global landslide structural pattern. *Guglielmi and Vengeon.* [2002] argue for all the surface faulting patterns to converge at shallow depth as listric faults that define a decollement level which is the sliding surface. The arrow shows the location of benchmark 10 (adapted from [*Follacci et al.*, 1993]).

### Current understanding of the La Clapière acceleration

On the basis of these observations and simple numerical models, an interpretative model for the 1986-1988 regime change was proposed by *Follacci et al.*, [1993] [see also for a review *Susella and Zanolini*, 1996]. In fact, these models do not explain the origin of the acceleration but rather try to rationalize kinematically the different changes of velocity and why the acceleration did not lead to a catastrophic sliding but re-stabilized. The reasoning is based on the fact that the existing and rather strong correlation between the river flow in the valley at the bottom and the slope motion (see Figure 15.13) is not sufficient to explain both the de-stabilizing phase and its re-stabilization. This strongly suggests that the hydrological conditions are not the sole control parameters explaining both the strong 1986-1987 accelerating and the equally strong slowdown in 1988-1990.

*Follacci et al.* [1988, 1993] argue that the failure of the strong gneiss bed in the NW block was the main driving force of the acceleration in 1986-1987. According to this view, the failure

of this bed induced changes in both the mechanical boundary conditions and in the local hydrogeological setting (Figure 15.15). Simultaneously, the development of the upper NW crack, that freed the landslide from its main driving force, appears as a key parameter to slow down the accelerating slide. The hypothesized changes in hydrological boundary conditions can further stabilize the slide after the 1986-1987 transient leak off.

Several works have attempted to fit the velocity time series of La Clapière landslide and predict its future evolution, in a spirit similar to the Vaiont landslide discussed above. The displacement of different benchmarks over the 1982-1986 period has been analysed. An exponential law has been fitted to the 1985-1986 period [*Vibert et al.*, 1988]. Using the exponential fit and a failure criterion that the landslide will collapse when the velocity reaches a given threshold, the predicted collapse time for the landslide ranges from 1988 for NW benchmark to 1990 for the SE benchmarks. Plotting the inverse of the velocity as a function of time as in (15.2) has been tried, hoping that this law holds with  $\alpha = 2$  providing a straightforward estimation of  $t_c$ . This approach applied to La Clapière velocity data predicts a collapse in 1990 for the upper NW part and in 1988-1989 for the SE part of the landslide. To remove the fluctuations of the velocity induced by changes in river flow, an ad-hoc weighting of the velocity data was used by [*Vibert et al.*, 1988]. An attempt to more quantitatively estimate the relation between the river flow and the landslide velocity was proposed by [*Rat*, 1988]. *Rat* [1988] stresses the importance of removing the fluctuations of the velocity induced by changes in the river flow before any attempt to predict the collapse time.

### **Analysis of the cumulative displacement and velocity data with the slider-block model**

The simple rigid block model defined with a single block and with velocity and state dependent friction law cannot account for what happened after the velocity peak, without invoking additional ingredients. Departure from the model prediction can be used as a guide to infer in-situ landslide behavior. Recall that, during the interval 1988-1990, the monthly recorded velocities slowed down to velocity 6 times smaller than the 1987 peak values. This deceleration cannot be explained with the friction model using constant friction parameters. Indeed, for  $B/A = m < 1$ , under a constant geometry and fixed boundary conditions, the velocity increases and then saturates at its maximum value. In order to explain the deceleration of the landslide, one needs to invoke either a change of material properties embodied for example in the parameter  $m = B/A$  or a change of the state variable  $\theta$  that describes the duration of frictional contacts, maybe due to a change in the sliding surfaces.

We have not attempted in this study to fit both the accelerating and the decelerating phases with the slider-block model due to the large number of free parameters it will imply relatively to the small number of points available. Further modeling would allow block partitioning, fluctuations of the slope angle and change with time of the friction parameters. Our purpose is

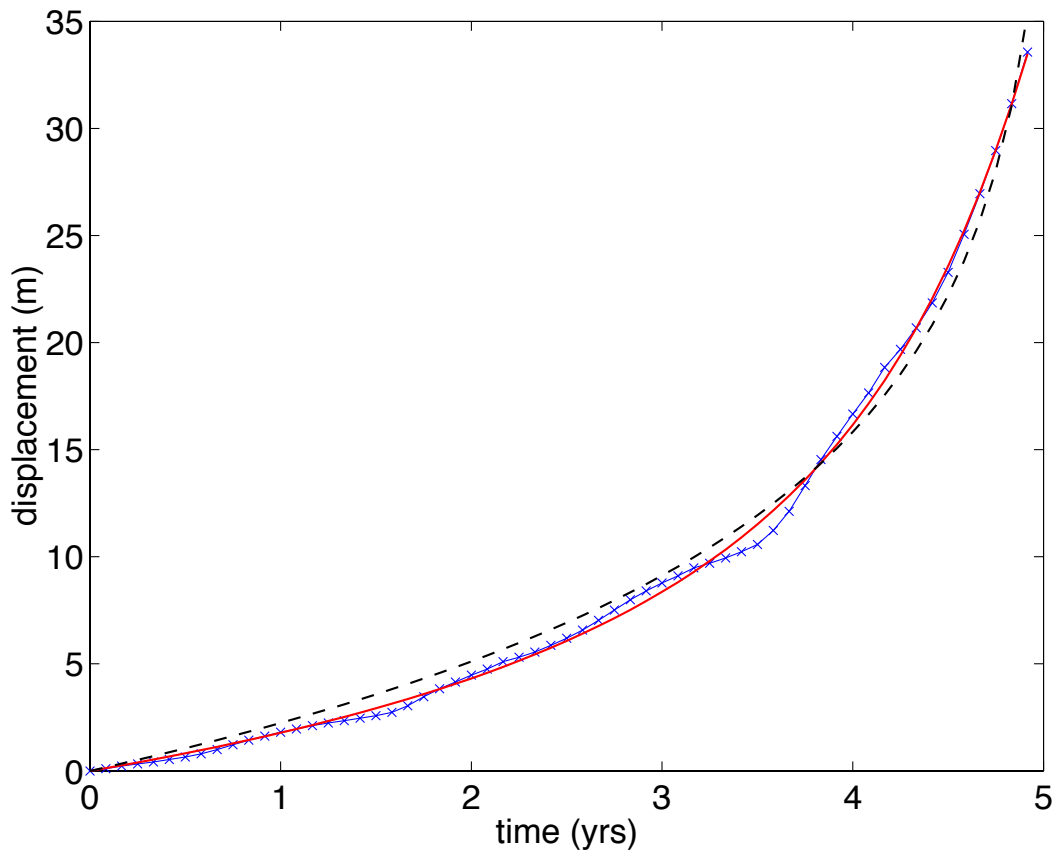


FIG. 15.16 – Displacement for benchmark 10 of la Clapière landslide (crosses) and fit using the friction model. The best fit gives  $m = 0.98$  (black line). The gray line shows the best fit obtained when imposing  $m = 1.5$  for comparison.

here to point out how different landsliding regimes can be highlighted by the introduction of a velocity and state friction law in this basic rigid block model. It would also be interesting to add a periodic forcing to our models to better capture the time-dependence of the velocity and study its possible nonlinear consequences. This is left for a future work, together with a complete description of the three time intervals by the slider-block friction model.

### La Clapière sliding regime : 1982-1987

We fit the monthly measurements of the displacement of several representative benchmarks with the slider-block friction model. In the sequel, we will show results for benchmark 10 which is located in the central part of the landslide (Figure 15.9), and which is representative of the average landslide behavior during the 1982-1995 period [Follacci, personal communication 2001]. We have also obtained similar results for benchmark 22.

We consider only the accelerating phase in the time interval [1982.92; 1987.9]. As for the Vaiont landslide, the inversion provides the values of the parameters  $m$ ,  $T$ ,  $D$ , and the initial condition  $x_i$  of the state variable. The best fit to the displacement of benchmark 10 is shown

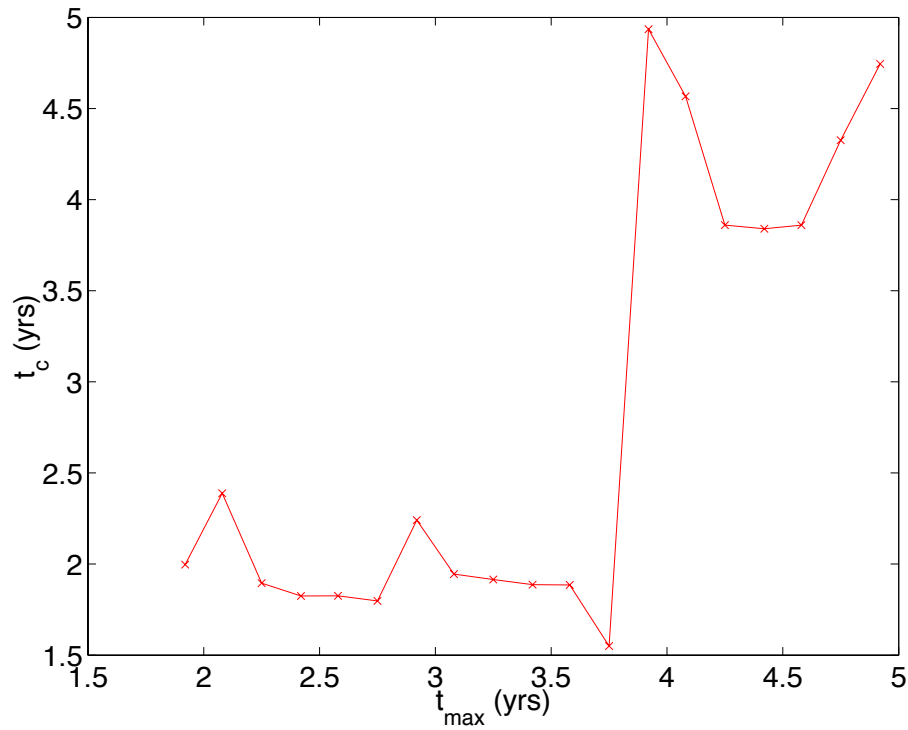


FIG. 15.17 – Predicted value of the time  $t_c$  of the inflection point of the velocity for La Clapière landslide, using a fit of the displacement data with the friction model. All points correspond to the stable regime  $m < 1$ . In this regime there is no finite-time singularity of the velocity but a transition from an accelerating sliding to a stable sliding for times larger than the inflection point  $t_c$ . This parameter is poorly constrained by the fit and increases with the time of the last point  $t_{\max}$  used in the fit.

in Figure 15.16. The model parameters are  $m = B/A=0.98$  and the initial value of the reduced state variable is  $x_i = 39$ . While  $m$  is very close to one, the value of  $x_i$  significantly larger than 1 argues for La Clapière landslide to be in the stable regime (see Figure 15.1 and Table 15.1). Similar results are obtained for the other benchmarks. Since the landslide underwent different regimes, it is important to perform these inversions for different time periods, that is, the fits are done from the first measurement denoted time  $t = 0$  (year 1982.92) to a later  $t = t_{\max}$ , where  $t_{\max}$  is increased from approximately 2 years to 5 years after the initial starting date. This last time  $t \approx 5$  years (end of 1987) corresponds to the time at which the slope velocity reached its peak. For all inversions except the first two point with  $t_{\max} \approx 2$  yrs, the best fit always select an exponent  $0 < m < 1$  and an initial state variable  $x_i \gg 1$ , corresponding to a stable asymptotic sliding without finite-time singularity. For  $t_{\max} < 4$  years (that is, using data before the end of 1986), a few secondary best solutions are found with very different values, from  $m = -3000$  to  $m = 29$ , indicating that  $m$  is poorly constrained. We have also performed sensitivity tests using synthetic data sets generated with the friction model with the same parameters as those obtained for La Clapière. These tests show that a precise determination of  $m$  is impossible but that the inversion recovers the true regime  $m < 1$ .

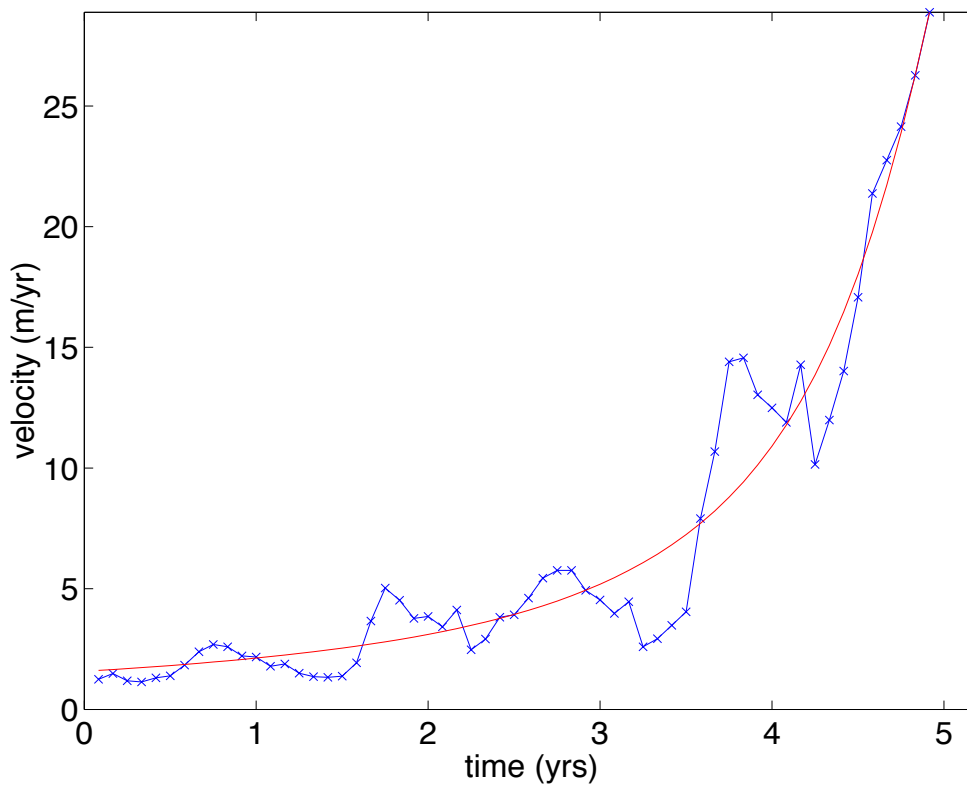


FIG. 15.18 – Velocity for benchmark 10 of la Clapière landslide (crosses) and fit of the velocity data with the friction model. The best fit gives  $m = 0.99$  (black line).

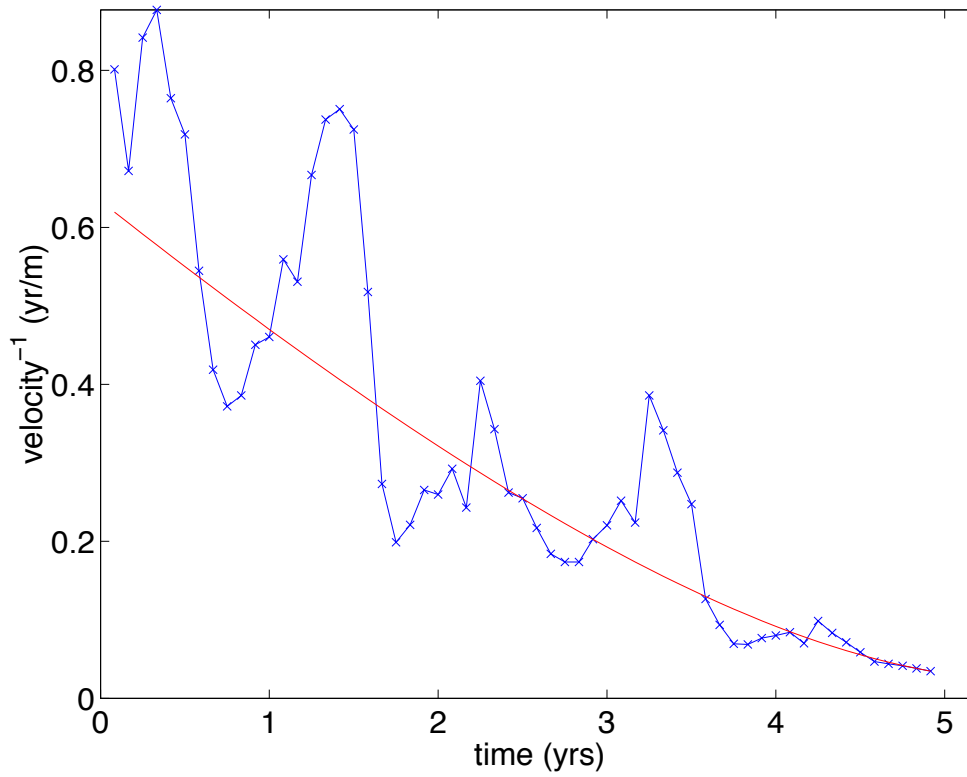


FIG. 15.19 – Same as Figure 15.18 showing the inverse of the velocity.

The transition time (defined by the inflection point of the velocity) is found to increase with  $t_{max}$  (see Figure 15.17). This may argue for a change of regime from an acceleration regime to a restabilization before the time  $t = 1988$  of the velocity peak. The parameters  $S$  and  $x_i$  are also not well constrained. Similar results are obtained for different benchmarks as well as when fitting the velocity data instead of the displacement. A fit to the velocity of benchmark 10 is shown in Figures 15.18 and 15.19. The velocity data show large fluctuations, in part due to yearly fluctuations of the precipitations. The inversion is therefore even more unstable than the inversion of the displacement, but almost all points give  $m < 1$  and  $x_i > 1$ . Such fluctuations of the inverted solution may indicate that the use of constant friction parameters to describe a period where 2 regimes interact, i.e., an accelerating phase up to 1987 followed by a decrease in sliding rate since 1988, does not describe adequately the landslide behavior for the whole time period 1983-1988. Observed changes in morphology as suggested in Figure 15.15 provide evidence for changes both in driving forces and in the geometry of the landslide, including possible new sliding surfaces.

### An alternative interpretation

While a fit to the displacement or to the velocity data for the whole time period 1983-1988 suggests that the landslide was in the stable regime  $m < 1$ , an alternative interpretation is that the early acceleration was in the unstable regime  $m > 1$  but did not reach the instability due to a change of morphology, block partition and the creation of new active surfaces of sliding. This interpretation is suggested by the plot of the inverse of the velocity shown in Figure 15.19, which is close to linear at early times. Over the route toward the finite-time singularity, the landslide did not succeed in accommodating the velocity increase and degenerated by changing geometry and loading conditions (block partitioning). In other words, the solution shown in Figure 15.16 with  $m < 1$  may rather describe a transient from an unstable state to a stable regime. In particular, we cannot exclude the possibility that the surfaces have been all along characterized by the regime  $B > A$  and then a change of geometry and surfaces of sliding may have reset the reduced state variable  $x$  given by expression (15.19). Another possibility is that the friction parameter  $m$  has changed from  $m > 1$  to  $m < 1$ , leading to a stable deceleration of the displacement after 1988. It is not unreasonable to conjecture that the internal stresses associated with and created by the accelerating phase may have led to its fragmentation into several sub-entities, creating fresh surfaces and resetting the state variable or the  $m$ -value characterizing the surfaces of contact. This is in qualitative agreement with field observations of new faulting patterns since 1987, which signal a change in the geometry of the landslide involving the regression of the main scarp and locked sub-entities (Figure 15.15). These observations provide evidence for a change in both the head driven force (mass push from the top) and the activated basal surfaces. These morphological changes suggest that the 1987-1988 period has been a transition period for the evolution of La Clapière sliding system over the last 50 years. In the block-slider model, this

amounts to modifying the variables  $S$  and  $\theta_i$  and thus to reset  $x$ . In this interpretation, the change of regime observed for La Clapière could then be due to a change from  $x_i < 1$  (unstable acceleration) to  $x_i > 1$  (stable deceleration) (see Figure 15.1). This change from  $x_i < 1$  to  $x_i > 1$  may be interpreted as either an increase of applied shear stress, a decrease of normal stress, or an increase of the surface of contacts between the sliding surfaces. Thus, within the slider-block model, one can characterize the post 1988 landslide evolution in terms of new sliding surfaces being mobilized which are more stable than the previous ones due to more numerous and/or efficient contacts.

Appendix C explores what would have been the predicted critical time  $t_c$  estimated in real time prior to the velocity peak, according to this scenario of an unstable acceleration towards a finite-time singularity. We have seen that, while the slider-block model as well as the power law formula (15.2) provide excellent fits to the data, they do not lead to very stable predictions of the critical time  $t_c$  on the Vaiont data as well as on synthetic tests generated in the unstable regime  $m > 1$ . It may thus be valuable to test the approach of [Gluzman *et al.*, 2001] in terms of a version of the functional renormalization approach already discussed in relation with the Vaiont landslide. It is our hope that this approach could provide in a more robust determination of  $t_c$ .

Figure 15.20 compares the prediction of a fit using a polynomial of order two in time to the inverse of the velocity (panel (a)) with the prediction of the renormalization approach (panel (b)). In each panel, two curves are presented corresponding to two different starting points of the data taken into account in the predictions : the leftmost points correspond to the first date taken into account in the predictions ; therefore, the predictions corresponding to the crosses  $\times$  use approximately two years fewer data than the predictions shown with the open circles. This allows us to compare the effect of missing data or alternatively the effect of a non-critical behavior at the beginning of the time series. The abscissa  $t_{\max}$  is the running “present time”, that is, the last time of the data taken into account to issue a prediction. The prediction with the polynomial shown in panel (a) of Figure 15.20 can be seen as an improvement in methodology over the Voight formula (15.2) which corresponds to a linear fit of the inverse velocity with time for  $\alpha = 2$ . Comparing panels (a) and (b), the renormalization method seems to present a smaller dispersion and better convergence : in particular, about half-a-year prior to the time of the maximum realized velocity indicated by the horizontal dashed line, the prediction of this date by the renormalization method using the longer time series becomes very precise. Thus, a critical time close to the time of the velocity peak would have been predicted starting approximately half-a-year year from it. It is then not unreasonable to consider the velocity peak as a proxy for the ghost critical time, since on the approach of the later the largest internal stresses may develop and may fragment the block and modify the morphology of the landslide, thus resetting the geometry and some of the parameters of the model. In this scenario, we would thus expect that the time of the peak velocity should be not far from what would have been the critical time

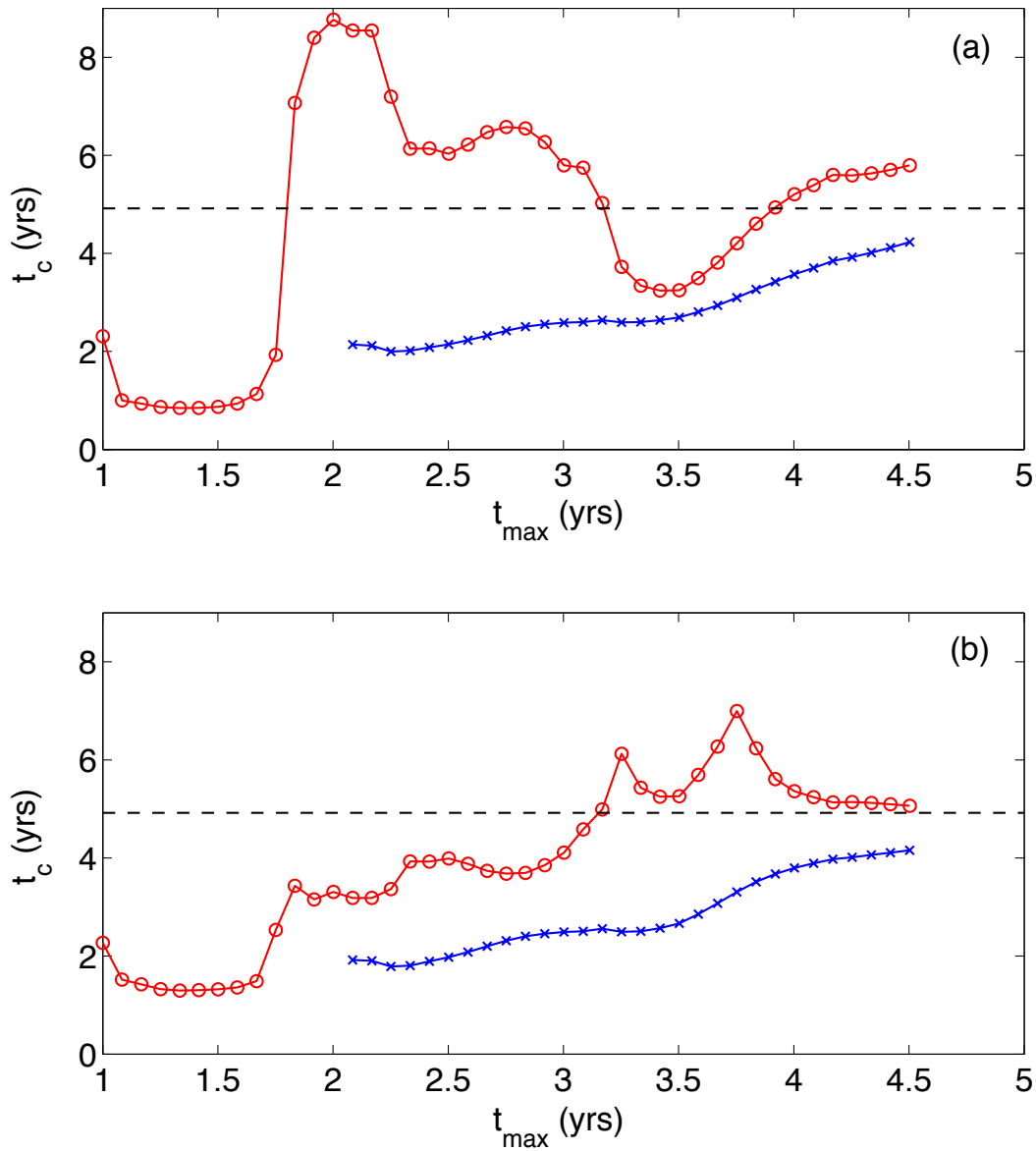


FIG. 15.20 – Panel (a) : prediction of a critical time using a fit with a polynomial of order two in time to the inverse of the velocity; panel (b) : prediction of the renormalization approach described in Appendix C. In each panel, two curves are presented corresponding to two different starting points of the data taken into account in the predictions : the leftmost points correspond to the first date taken into account in the predictions; the predictions corresponding to the crosses  $\times$  use approximately two years fewer data than the predictions shown with the open circles. The abscissa  $t_{\max}$  is the running “present time”, that is, the last time of the data taken into account to issue a prediction. The maximum realized velocity occurred at a time indicated by the horizontal dashed line. This time is thus a proxy for the ghost-like critical time of the landslide.

of catastrophic failure of the landslide.

We should however point out that the functional renormalization method used in this Appendix C does not work for the Vaiont landslide because of a technical instability whose fundamental origin is not understood by these authors. Technically, the numerical instability comes from the absence of alternating signs in the polynomial expansion at early times. This technical problem thus casts some shadow on the usefulness of the approach described here which is unable to tackle the regime which is undoubtedly unstable. This limitation suggests again the importance of working with several alternative and competing models, as further discussed in the following concluding section.

## 15.5 Discussion and conclusion

We have presented a quantitative analysis of the displacement history for two landslides, Vaiont and La Clapière, using a different set of techniques. We have tried to go beyond the time-independent hazard analysis provided by the standard stability analysis to include time dependent predictions. While our present inversion methods provide a single estimate of the critical time  $t_c$  of the collapse for each inversion, a better formulation should be to translate these results in terms of a probability of failure, as for instance done by *Vere-Jones et al.* [2001].

A first innovative concept proposed here was to apply to landslides the state and velocity dependent friction law established in the laboratory and used to model earthquake friction. Our inversion of this simple slider-block friction model shows that the observed movements can be well reproduced with this simple model and suggest the Vaiont landslide (respectively La Clapière landslide) as belonging to the velocity weakening unstable (respectively strengthening stable) regime. Our friction model assumes that the material properties embodied in the key parameters  $m = B/A$  and/or the initial value of the state variable of the friction law control the sliding regime.

Our purpose was here to point out how different landsliding regimes can be highlighted by the introduction of a velocity and state friction law in a basic rigid block model. Even if the displacement is not homogeneous for the two landslides, the rigid block model provides a good fit to the observations and a first step towards a better understanding of the different sliding regimes and the potential for their prediction.

For the Vaiont landslide, this physically-based model suggests that this landslide was in the unstable regime. The friction model provides good predictions of the time-to-failure up to 20 days before the collapse. A pure phenomenological model suggested by *Voight* [1988] postulating a power law finite-time singularity  $v \sim 1/(t_c - t)$  with unit exponent obtains similar results. Our approach can be seen as providing a physically-based derivation of this phenomenological model as well as a generalization to capture three other possible regimes.

For la Clapière landslide, the inversion of the displacement data for the accelerating phase

1983-1988 up to the maximum of the velocity gives  $m < 1$ , corresponding to the stable regime. The deceleration observed after 1988 implies that, not only is la Clapière landslide in the stable regime but in addition, some parameters of the friction law have changed, resulting in a change of sliding regime from a stable regime to another one characterized by a smaller velocity, as if some healing process was occurring. Possible candidates for a change in landsliding regime include the average dip slope angle, the partitioning of blocks, new sliding surfaces and changes in interface properties. However, another possible interpretation is that this landslide was initially in the unstable regime, but did not reach the instability due to a change of geometry and of sliding surfaces. The best fit obtained with  $m < 1$  for the accelerating phase 1983-1988 would then describe a transient regime between the unstable regime and the stable regime, due to a progressive change in the model parameters. This second scenario seems less parsimonious but cannot be completely excluded.

The present work has offered the important insight and novel conceptual framework and language of the slider-block model, which can be used to classify the relative merits and performance of other models. For an assessment in real time of the upcoming risks of a catastrophic failure, one should then consider both scenarios (stable versus unstable which are encoded respectively by the range of parameters  $m < 1$  and  $m > 1$  in the slider-block model) and test the data using the available associated theoretical models, some of which have been presented in this paper. Such an approach in terms of multiple scenarios [Smith *et al.*, 1999; Yukalov and Gluzman, 1999; Ziehm *et al.*, 2000] can add a contribution to the assessment of societal risks. A systematic exploration of such approaches will extend the preliminary investigation and results offered here. In this spirit, the major innovation of the frictional slider-block model that should be explored further is to embody the two regimes (stable versus unstable) in the same physically-based framework, and to offer a way of distinguishing empirically between the two regimes, as shown by our analysis of the two cases provided by the Vaiont and La Clapière landslides.

## 15.6 Appendix A : Derivation of the full solution of the frictional problem

### Complete solution

We now provide the full solution of the frictional problem. First, we rewrite (15.3) as

$$\dot{\delta} = S D_c \left( \frac{\theta}{\theta_0} \right)^{-m}, \quad (15.15)$$

where

$$S \equiv \frac{\dot{\delta}_0 e^{\frac{\tau}{\sigma} - \mu_0}}{D_c} \quad (15.16)$$

and

$$m \equiv \frac{B}{A} . \quad (15.17)$$

Putting (15.15) in (15.4) gives

$$\frac{d(\theta/\theta_0)}{dt} = \frac{1}{\theta_0} - S (\theta/\theta_0)^{1-m} . \quad (15.18)$$

The case  $m = 1$  requires a special treatment since the dependence in  $\theta$  disappears in the right-hand-side of (15.18) and  $\frac{d\theta}{dt}$  is constant.

For  $m \neq 1$ , it is convenient to introduce the reduced variables

$$x \equiv (S\theta_0)^{1/(1-m)} \frac{\theta}{\theta_0} , \quad (15.19)$$

and

$$D \equiv D_c (S\theta_0^m)^{\frac{1}{1-m}} . \quad (15.20)$$

Then, (15.15) reads

$$\frac{\dot{\delta}}{\delta_0} = D x^{-m} . \quad (15.21)$$

Putting (15.15) in (15.4) to eliminate the dependence in  $\delta$ , we obtain

$$\frac{dx}{dt'} = 1 - x^{1-m} , \quad (15.22)$$

where  $t' = t/T$  with

$$T = \frac{D_c}{D} = \left[ \frac{D_c}{\dot{\delta}_0 \theta_0^m} \right]^{1/(1-m)} e^{\frac{\frac{\tau}{\theta} - \mu_0}{B-A}} . \quad (15.23)$$

In the sequel, we shall drop the prime and use the dimensionless time  $t'$ , meaning that time is expressed in units of  $T$  except stated otherwise.

The block sliding behavior is determined by first solving the equation (15.22) for the normalized state variable  $x(t)$  and then by inserting this solution in (15.21) to get the slip velocity. Equation (15.22) displays different regimes as a function of  $m$  and of the initial value  $x_i$  compared to 1 that we now classify.

### Case $m = B/A > 1$

For  $m > 1$  and  $x_i < 1$ , the initial rate of change  $\frac{dx}{dt}$  of the state variable is negative. The initial decay of  $x$  accelerates with time and  $x$  reaches 0 in finite time. Expression (15.21) shows that  $\delta(t)$  continuously accelerates and reaches infinity in finite time. Close to the singularity, we can neglect the first term 1 in the right-hand-side of (15.22) and we recover the asymptotic solution (15.9,15.10,15.11) :

$$x(t) \simeq m^{\frac{1}{m}} (t_c - t)^{\frac{1}{m}} , \quad (15.24)$$

where the critical time  $t_c$  is determined by the initial condition  $x(t = 0) = x_i$

$$t_c = \frac{x_i^m}{m} . \quad (15.25)$$

For  $m > 1$  and  $x_i > 1$ , the initial rate of change  $\frac{dx}{dt}$  of the state variable is positive, thus  $x$  initially increases. This growth goes on, fed by the positive feedback embodied in (15.22). At large times,  $x$  increases asymptotically at the constant rate  $\frac{dx}{dt} = 1$  leading to  $x(t) \approx t$ . Integrating equation (15.21) gives

$$\delta(t) = \delta_\infty - \frac{\dot{\delta}_0 D}{m-1} \frac{1}{t^{m-1}}, \quad (15.26)$$

at large times. The asymptotic value of the displacement  $\delta_\infty$  is determined by the initial condition. This regime thus describes a decelerating slip slowing down as an inverse power of time. It does not correspond to a de-stabilizing landslide but to a power law plasticity hardening.

### Case $m = B/A = 1$

In this case, the variables (15.19) and (15.20) are not defined and we go back to (15.4) (which uses the unnormalized state variable  $\theta$  and time  $t$ ) to obtain

$$\frac{d\theta}{dt} = 1 - S\theta_0, \quad (15.27)$$

where  $S$  is defined by (15.16) and depends on the material properties but not on the initial conditions. If  $S\theta_0 > 1$ ,  $\theta$  decays linearly and reaches 0 in finite time. This retrieves the finite-time singularity, with the slip velocity diverging as  $1/(t_c - t)$  corresponding to a logarithmic singularity of the cumulative slip. If  $S\theta_0 < 1$ ,  $\theta$  increases linearly with time. As a consequence, the slip velocity decays as  $\dot{\delta} \sim 1/t$  at large times and the cumulative slip grows asymptotically logarithmically as  $\ln t$ . This corresponds to a standard plastic hardening behavior.

### Case $m = B/A < 1$

For  $x_i > 1$ , the initial rate of change  $\frac{dx}{dt}$  of the state variable is negative, thus  $x$  decreases and converges to the stable fixed point  $x = 1$  exponentially as

$$x = 1 + ae^{-\frac{t}{t^*}}, \quad (15.28)$$

where the relaxation time  $t^*$  is given by

$$t^* = \frac{1}{1-m} \quad (15.29)$$

in units of  $T$  and  $a$  is a constant determined by the initial condition. Starting from some initial value, the slip velocity increases for  $0 < m < 1$  (respectively decreases for  $m < 0$ ) and converges to a constant, according to (15.15,15.21).

For  $x_i < 1$ , the initial rate of change  $\frac{dx}{dt}$  of the state variable is positive, and  $x$  converges exponentially toward the asymptotic stable fixed point  $x = 1$ . As  $\theta$  increases toward a fixed value, this implies that the slip velocity decreases for  $0 < m < 1$  (respectively increases for  $m < 0$ ) toward a constant value

## 15.7 Appendix B : Functional renormalization group formulas for the friction law (15.21) and (15.22)

Consider an expansion as in (15.13) of an observable  $x(t)$  in powers of a variable  $u$  given by  $x_k(u) = \sum_{n=0}^k a_n u^n$ . The method of algebraic self-similar renormalization constructs so-called “approximants”, which are reconstructed functions that best satisfy the imposed asymptotic constraints while obeying criteria of functional self-similarity and of maximum stability in the space of functions [Yukalov and Gluzman, 1997; Gluzman and Yukalov, 1997; 1998]. These approximants are given by the following general recurrence formula for the approximate  $x_k^*(u)$  of order  $k$  as a function of the expansion  $x_{k-1}(u)$  up to order  $k-1$  :

$$x_k^*(u) = \left[ x_{k-1}^{-k/s}(u) - \frac{k a_k}{s} u^k \right]^{-s/k} . \quad (15.30)$$

The crossover index  $s$  is determined by the condition that the leading terms of the expansion of  $x_k^*(t)$  as  $t \rightarrow 0$  must agree with the expansion of  $x_k(u)$ .

For the friction model (15.21) and (15.22), the coefficients  $a_k$  in (15.13) and (15.30) are determined by the friction parameters and the initial conditions

$$a_0 = y_0, \quad (15.31)$$

$$a_1 = \theta_0^{-1} - S y_0^{1-m}, \quad (15.32)$$

$$a_2 = \frac{1}{2} S (m-1) a_1 y_0^{-m}, \quad (15.33)$$

$$a_3 = \frac{1}{6} \alpha (m-1) [-m a_1^2 y_0^{-m-1} + 2a_2 x_0^{-m}], \quad (15.34)$$

$$a_4 = \frac{1}{24} S (m-1) [(1+m) m a_1^3 y_0^{-m-2} - 6m a_2 a_1 y_0^{-m-1} + 6a_3 y_0^{-m}]. \quad (15.35)$$

### Case $m < 1$

As we see from (15.14), the natural expansion variable is  $u = \exp(-\frac{t}{t^*})$ .

The first-order and simplest approximate is

$$x_1^*(u) = x^* (1 + cu)^{-s} = x^* \left( 1 + c \exp\left(-\frac{t}{t^*}\right) \right)^{-s}, \quad (15.36)$$

with  $x^* = 1/T$  where  $T$  is given by (15.23). The crossover amplitude  $c$  and the crossover index  $s$  are determined by the condition that the expansion of  $x_1^*(t)$  as  $t \rightarrow 0$  must agree with the first two terms of expression (15.13), leading to the following system of equations,

$$x^* (1 + c)^{-s} = x_0, \quad (15.37)$$

$$x_0 s c \frac{1}{t^*(1+c)} = a_1. \quad (15.38)$$

The crossover index  $s$  is then given by

$$s = -\frac{\ln(x_0/x^*)}{\ln(1+c)}, \quad (15.39)$$

while the crossover amplitude  $c$  satisfies the following equation :

$$\frac{\ln(x_0/x^*)}{\ln(1+c)} \frac{c}{(1+c)} = -\frac{a_1 t^*}{x_0}. \quad (15.40)$$

The second-order approximate is given by

$$\begin{aligned} x_2^*(u) &= x^* [(1+c_2 u)^{-s_2} + c_1 u^2]^{-s_1} \\ &= x^* \left[ \left( 1 + c_2 \exp\left(-\frac{t}{t^*}\right) \right)^{-s_2} + c_1 \exp\left(-\frac{2t}{t^*}\right) \right]^{-s_1}. \end{aligned} \quad (15.41)$$

The crossover amplitudes  $c_1, c_2$  and crossover index  $s_1$  and  $s_2$  are obtained from the condition that the expansion of  $x_2^*(t)$  as  $t \rightarrow 0$  must recover the first four terms of expression (15.13). The corresponding expressions are rather long and will not be presented here explicitly. Interestingly, for  $m = 0$ , the second-order approximate recovers the exact solution.

### Case $m \geq 1$

In this case, the natural variable in the expansion is  $u = t$ . Our goal is to obtain the critical time  $t_c$  as a function of  $m$ . Using the crossover technique of [Gluzman and Yukalov, 1998] for the two asymptotic expressions (15.13) at short time and (15.24) close to  $t_c$ , we obtain a sequence of approximants  $x_1^*(t)$ ,  $x_2^*(t)$ ,  $x_3^*(t)$  and  $x_4^*(t)$  associated with a sequence of improving approximations for the critical time,  $t_{c1}(m)$ ,  $t_{c2}(m)$ ,  $t_{c3}(m)$  and  $t_{c4}(m)$ . All approximants agree term-by-term with the corresponding short time expansion and lead to the critical behavior (15.24) as  $t$  goes to the corresponding critical time. The first-order approximate is

$$x_1^*(t) = x_0 \left( 1 + \frac{a_1}{x_0} m t \right)^{1/m}, \quad \text{with } t_{c1} = -\frac{x_0}{m a_1}. \quad (15.42)$$

Interestingly,  $x_1^*(t)$  coincides with the exact solution in the limit  $m \rightarrow \infty$ , which takes the form  $x = x^* ((x_0/x^*)^m - (t/t^*))^{\frac{1}{m}}$ .

In the next order, we obtain the second-order approximate

$$x_2^*(t) = x_0 \left[ \left( 1 + \frac{a_1}{x_0} t \right)^m + \frac{m a_2}{x_0} t^2 \right]^{1/m}, \quad (15.43)$$

and  $t_{c2}$  is solution of the following equation

$$\left( 1 + \frac{a_1}{x_0} t_{c2} \right)^m + \frac{m a_2}{x_0} t_{c2}^2 = 0. \quad (15.44)$$

The third order approximate reads

$$x_3^*(t) = x_0 \left[ \left( 1 + \frac{a_1}{x_0} t + \frac{a_2}{x_0} t^2 \right)^m + \frac{m a_3}{x_0} t^3 \right]^{1/m}, \quad (15.45)$$

and  $t_{c3}$  satisfies the following equation

$$\left(1 + \frac{a_1}{x_0} t_{c3} + \frac{a_2}{x_0} t_{c3}^2\right)^m + \frac{m a_3}{x_0} t_{c3}^3 = 0 . \quad (15.46)$$

The fourth-order approximate is given by

$$x_4^*(t) = x_0 \left[ \left(1 + \frac{a_1}{x_0} t + \frac{a_2}{x_0} t^2 + \frac{a_3}{x_0} t^3\right)^m + \frac{m a_4}{x_0} t^4 \right]^{1/m} , \quad (15.47)$$

with  $t_{c4}$  solution of the equation

$$\left(1 + \frac{a_1}{x_0} t_{c4} + \frac{a_2}{x_0} t_{c4}^2 + \frac{a_3}{x_0} t_{c4}^3\right)^m + \frac{m a_4}{x_0} t_{c4}^4 = 0 . \quad (15.48)$$

Note that for  $m = 1$ , all approximants are identical and equal to the exact solution.

## 15.8 Appendix C : Functional renormalization of polynomials expansions for the prediction of $t_c$ as a function of the “present time” $t_{\max}$ for La Clapière landslide

This appendix present tests of the prediction of the time at which the velocity peaked, following the hypothesis discussed in the main text that the ensuing deceleration resulted from a change from  $x_i < 1$  to  $x_i > 1$  in the velocity weakening regime  $B > A$ . According to this interpretation, the first accelerating phase should be described by an increasing velocity  $\propto 1/(t_c - t)$ . The critical time  $t_c$  can be approximated by the time of the peak of the velocity, in other words,  $t_c$  is close to the inflection point of the displacement as a function of time.

Rather than using the version of the functional renormalization method described for the Vaiont landslide based on the slider-block equations of motion, we use here a simpler version that has been tested earlier in another rupture problem [*Gluzman et al.*, 2001]. This choice is governed by the fact that we can not rely entirely on the friction model with fixed parameters since we know that a change of regime occurred. We thus follow a more general approach which is not dependent upon a specialized specification of the equations of motion. The previous investigation on a model system [*Gluzman et al.*, 2001] developed theoretical formulas for the prediction of the singular time of systems which are a priori known to exhibit a critical behavior, based solely on the knowledge of the early time evolution of an observable. From the parameterization of such early time evolution in terms of a low-order polynomial of the time variable, the functional renormalization approach introduced by *Yukalov and Gluzman* [1997] allows one to transform this polynomial into a function which is asymptotically a power law. The value of the critical time  $t_c$ , *conditioned* on the assumption that  $t_c$  exists, can then be determined from the knowledge of the coefficients of the polynomials. *Gluzman et al.* [2001] have tested with success this prediction scheme on a specific example and showed that this approach gives more precise and reliable

predictions than through the use of the asymptotic power law model, but is probably not better than the true model when the later is known.

The input of the method is the inverse of La Clapière block velocity  $\dot{\delta}$  as a function of time up to the “present time”  $t_{\max}$ . One starts with a simple polynomial fit of  $1/\dot{\delta}$  as a function of time from some starting time up to  $t_{\max}$ . One then applies the functional renormalization method explained in *Gluzman et al.* [2001] to this polynomial expansion. We restrict our analysis to expansions of up to second-order in time :

$$1/\dot{\delta} = 1 + b_1 t + b_2 t^2 , \quad (15.49)$$

where the zeroth-order coefficient  $b_0$  has been put equal to 1 by a suitable normalization of the data.

The first order approximant for the inverse velocity reads [*Gluzman et al.*, 2001]

$$F_1^*(t) = \left(1 - \frac{b_1 t}{s_1}\right)^{-s_1} . \quad (15.50)$$

The second order approximant is

$$F_2^*(t) = 1 + b_1 t \left(1 - \frac{b_2 t}{b_1 s_2}\right)^{-s_2} . \quad (15.51)$$

The exponents  $s_1$  and  $s_2$  are control parameters that are determined from an optimal stability criterion. We follow [*Gluzman et al.*, 2001] and impose  $s_1 = s_2 = s$ , which is a condition of consistency between the two approximants.  $s$  is now the single control parameter, and plays the role of the critical exponent at the critical point  $t_c$ . The condition of the existence of a critical point is that both approximants  $F_1^*(t)$  and  $F_2^*(t)$  of the inverse velocity should vanish at  $t = t_c$ . This yields two equations determining  $t_c$  and  $s$ , which can be solved numerically.

The numerical estimates of  $(t_c, s)$  depends on the time interval over which the polynomial coefficients  $b_1$  and  $b_2$  are determined. Let  $t_{\max}$  denote the last point used in the polynomial fit. Figure 15.20 shows the numerical estimate of  $t_c$  as a function of  $t_{\max}$ . More precisely, Figure 15.20 compares the prediction of a fit using a polynomial of order two in time to the inverse of the velocity (panel (a)) with the prediction of the renormalization approach (panel (b)).

We have also fitted a power law to the data to extract an estimate of  $t_c$  as a function of  $t_{\max}$  and find an extremely unstable prediction where  $t_c$  fluctuates wildly ranging from two years before the end of 1987 to 25 years after 1987. Clearly, predicting the change of regime from a power law fit of the acceleration in the first phase of La Clapière is completely unreliable. In contrast, the renormalized approximants provide a more reasonable stable estimate.

## Acknowledgments

We thanks C. Scavia and Y. Guglielmi for key supports to capture archive data for Vaiont and La Clapière landslide respectively. We are very grateful to N. Beeler, J. Dieterich, Y. Guglielmi,

D. Keefer, J.P. Follacci, J.M. Vengeon for useful suggestions and discussions. AH and JRG were supported by INSU french grants, Gravitationnal Instability ACI. SG and DS acknowledge support from the James S. Mc Donnell Foundation 21st century scientist award/studying complex systems.

# Conclusion générale et perspectives

On présente ici des conclusions et perspectives globales relatives aux séismes et aux instabilités gravitaires. Une conclusion plus détaillée de la première partie sur le déclenchement des séismes est présentée dans le chapitre 13.

## Prédictabilité des risques naturels

L'étude des tremblements de terre et des instabilités gravitaires réalisée dans ce travail montre qu'il existe une certaine prédictabilité de ces catastrophes naturelles, qui permet d'aller au delà de l'estimation du risque indépendante du temps couramment utilisée. Ces deux instabilités sont précédées, au moins pour certains exemples, d'une accélération de la déformation qui diverge en loi de puissance au moment de la rupture finale (séisme majeur ou glissement de terrain catastrophique). Cette accélération peut-être liée à des processus physiques très différents.

Pour les séismes, on propose dans ce travail une alternative au modèle de point critique invoqué pour décrire l'accélération de l'activité sismique avant un séisme majeur. On montre que la loi d'Omori inverse (accélération en loi de puissance du nombre de séismes avant un choc principal) résulte d'un modèle simple de déclenchement de séismes (ETAS) qui incorpore uniquement les propriétés des aftershocks. La loi d'Omori inverse apparaît comme la trajectoire moyenne de la sismicité quand on conditionne l'activité sismique à conduire à un pic d'activité sismique au moment du choc principal. La principale différence entre cette approche et les modèles de point critique est que, dans le modèle ETAS la loi d'Omori inverse est une loi *statistique moyenne*, observée uniquement en superposant un grand nombre de séquences. De plus, la loi d'Omori inverse est observée dans le modèle ETAS avant n'importe quel événement indépendamment de sa taille. Les analyses préliminaires de catalogues de sismicité semblent être en accord avec nos résultats théoriques : on observe en superposant un grand nombre de séquences une accélération en loi de puissance avant chaque séisme indépendamment de sa taille. Une étude plus poussée doit être réalisée pour tester le modèle de point critique et les algorithmes de prédiction basés sur la reconnaissance de précurseurs, pour mettre en évidence ou rejeter l'existence de précurseurs sismiques non reproduits par le modèle ETAS. En particulier, certaines études suggèrent l'existence de précurseurs à des échelles de temps et d'espace bien plus grandes que les distances et les temps d'interactions entre un séisme et ses aftershocks,

qui ne peuvent donc pas être expliqués par le modèle étudié ici. On propose pour poursuivre ce travail d'utiliser le modèle ETAS comme une hypothèse nulle pour tester la validité d'autres modèles ou l'existence de précurseurs. L'objectif est de complexifier le modèle pour le rendre le plus réaliste possible et pour incorporer toutes les propriétés de l'activité sismique observées, tout en gardant un modèle le plus parcimonieux possible. L'étude de la prédictabilité du modèle ETAS réalisée dans le chapitre 7 donne une borne inférieure de la prédictabilité de l'activité sismique, qui est déjà très significative et bien meilleure que pour un processus poissonien. On devrait obtenir une prédictabilité beaucoup plus forte en incorporant la distribution spatiale de la sismicité dans la méthode de prédiction présentée dans le chapitre 7. La prédictabilité de l'activité sismique peut être plus forte que celle du modèle ETAS, s'ils existent des phénomènes précurseurs non pris en compte par ce modèle.

Pour les instabilités gravitaires, on a montré qu'un modèle de bloc avec une loi de friction dépendante de la vitesse permet de reproduire l'accélération des glissements de terrains précédant l'instabilité finale (chapitre 15). Ce modèle permet de reproduire l'accélération en loi de puissance de la vitesse de glissement qui a précédé l'effondrement du glissement de terrain de Vaiont en 1963 (Alpes italiennes). Ce modèle permet de prédire la rupture 20 jours à l'avance, et justifie par un modèle physique le fit par une loi de puissance de la vitesse de glissement  $v \sim 1/(t_c - t)$  qui était utilisée avant empiriquement pour prédire les glissements de terrain [Voight, 1988].

## Validation des modèles et inversion des paramètres

La validation des modèles étudiés tant pour les séismes que pour les instabilités gravitaires et l'estimation des paramètres de ces modèles sont très difficiles à cause de la pauvreté des données. En conséquence, des modèles très différents donnent une description satisfaisante des données, sans qu'il soit possible de les distinguer.

Pour les séismes, nous n'avons pas abordé dans ce travail le problème de l'estimation des paramètres du modèle ETAS. Deux problèmes restent à résoudre avant d'aborder l'inversion des paramètres du modèle dans les catalogues de sismicité, afin de pouvoir utiliser le modèle ETAS pour faire des prédictions de l'activité sismique :

- Comment tenir compte des séismes les plus petits, qui ne sont pas observés mais qui ont un rôle prépondérant dans le déclenchement de la sismicité (chapitre 2)? Ce problème se pose pour l'estimation des paramètres du modèle ETAS à partir d'un catalogue incomplet pour les plus petits séismes, et ultérieurement pour la prédiction du taux de sismicité. La méthode d'inversion couramment utilisée [Ogata, 1988; Kagan, 1991] néglige le rôle des petits séismes en dessous du seuil de détection. Nous avons réalisés des tests sur des catalogues synthétiques qui montrent que cette méthode est incorrecte et ne permet pas de retrouver les paramètres du modèle quand le seuil de détection est plus élevé que la magnitude minimum des événements dans le catalogue synthétique. L'approche analytique développée ici devrait nous permettre de développer une nouvelle méthode d'inversion

prenant en compte les séismes en dessous du seuil de détection. Notre approche devrait aussi nous permettre de prendre en compte l'influence de ces petits séismes dans l'activité sismique future dans le but de prédire l'activité sismique.

- Les résultats théoriques dérivés dans ce travail ne sont valables que pour certaines valeurs des paramètres du modèle ( $\alpha < b/2$ ), qui ne sont pas réalistes pour décrire la sismicité (chapitre 2). Les résultats obtenus dans le régime  $b/2 < \alpha < b$  pour des simulations numériques montrent que le phénomène de renormalisation de la loi d'Omori et le rôle des aftershocks secondaires sont plus faibles que dans le régime  $\alpha < b/2$ , mais que les résultats obtenus analytiquement pour  $\alpha < b/2$  sont encore qualitativement valables dans le régime  $b/2 < \alpha < b$ . Des résultats analytiques ont été obtenus dans ce régime qui donnent les comportements limites pour  $\alpha = b/2$  et  $\alpha = b$  (chapitre 10), en bon accord avec les résultats numériques. Ces résultats sont un premier pas vers l'étude analytique du modèle ETAS dans le régime  $b/2 < \alpha < b$  et l'application du modèle à la sismicité.

Pour les glissement de terrain, le seul paramètre accessible par l'analyse du déplacement est la valeur du rapport  $B/A$  des paramètres de la loi de friction. L'inversion de ce paramètre  $B/A$  est très mal contrainte par les données, des valeurs très différentes de ce paramètre  $B/A$  donnant des résultats très semblables pour l'évolution temporelle du glissement. L'analyse de deux glissements de terrains suggère que ce modèle est quand même capable de distinguer une accélération dans le régime stable ( $B/A < 1$ , cas du glissement de la Clapière) d'une accélération instable ( $B/A > 1$ , cas du glissement de terrain de Vaiont). On espère pouvoir étudier un plus grand nombre de glissements de terrains pour valider le modèle. Une perspective pour mieux contraindre le modèle et pour améliorer l'accord entre le modèle et les observations est d'inclure dans ce modèle l'effet des précipitations sur la vitesse de glissement, en reliant les paramètres de la loi de friction au niveau d'eau dans le glissement. Des mesures précises et plus nombreuses que celles étudiées dans ce travail devrait permettre de caler la relation entre les précipitations et les paramètres de la loi de friction, et de mieux contraindre le modèle.



# Bibliographie

- Abercrombie, R. E., and J. Mori, Occurrence patterns of foreshocks to large earthquakes in the western United States, *Nature*, 381, 303-307, 1996.
- Abramowitz, M. and I. A. Stegun, *Handbook of Mathematical Functions* Dover Publications, New York, 1964.
- Agnew, D. C. and L. M. Jones, Prediction probabilities from foreshocks, *J. Geophys. Res.*, 96, 11,959-11971, 1991.
- Aki, K., Maximum likelihood estimate of  $b$  in the formula  $\log N = a - bM$  and its confidence limits, *Bull. Earthquakes Res. Institute*, 43, 237-239, 1965.
- Aki, K., A probabilistic synthesis of precursory phenomena, in *Earthquake Prediction*, edited by D. W. Simpson and P. G. Richards, AGU Maurice Ewing series : 4, Washington, D.C., pp 556-574, 1981.
- Allen, J.C., W.M. Schaffer and D. Rosko, Chaos reduces species extinction by amplifying local population noise, *Nature* 364, 229-232, 1993.
- Amaral, L. A. N., and K. B. Lauritsen, Universality classes for rice-pile models, *Phys. Rev. E*, 56, 231-234, 1997.
- Andersen, J. V., D. Sornette and K.-T. Leung, Tri-critical behavior in rupture induced by disorder, *Phys. Rev. Lett.* 78, 2140-2143, 1997.
- Anderson, D.L., The San Andreas fault, *Sci. Am.* 225 (5), 52-68, 1971.
- Anghel, M. et al., *EOS Trans. Am. Geophys. Union* 80, F923; preprint cond-mat/0002459; Sá Martins, J.C. et al., preprint cond-mat/0101343, 1999.
- Anifrani, J.-C., C. Le Floch and D. Sornette, Prédiction de la rupture de réservoirs composites de haute pression à l'aide de l'émission acoustique, *Contrôle Industriel* 220, 43-45, 1999.
- Atkinson, B. K., A fracture mechanics study of subcritical tensile cracking of quartz in wet environments, *Pure Appl. Geophys.*, 117, 1011-1024, 1979.
- Atkinson, B. K., Subcritical crack growth in geological materials. *J. Geophys. Res.*, 89, 4077-4114, 1984.
- Aviles, C.A., C. H. Scholz and J. Boatwright, Fractal analysis applied to characteristic segments of the San Andreas fault, *J. Geophys. Res.*, 92, 331-344, 1987.

- Bak, P., C. Tang and K. Wiesenfeld, Self-organized criticality : an explanation of  $1/f$  noise, Phys. Rev. Lett., 59, 381-384, 1997.
- Bak, P. and C. Tang, Earthquakes as a self-organized critical phenomena, J. Geophys. Res. 94, 15,635-15,637, 1989.
- Bak, P., How nature works : the science of self-organized criticality, New York, NY, USA : Copernicus, 1996.
- Barkai, E., Fractional Fokker-Planck equation, solution and application, Phys. Rev. E 63, 046118, 2001a.
- Barkai, E., CTRW pathways to the fractional diffusion equation, preprint cond-mat/0108024, 2001b.
- Barkai, E., R. Metzler and J. Klafter, From continuous time random walks to the fractional Fokker-Planck equation, Phys. Rev. E 61, 132-138, 2000.
- Barton C.A. and M.D. Zoback, Self-similar distribution and properties of macroscopic fractures at depth in crystalline rock in the Cajon Pass scientific drill hole, J. Geophys. Res. 97, 5181-5200, 1992.
- Barton, C.C. and P. R. La Pointe, eds., Fractals in the Earth Sciences, Plenum Press, New York and London, 1995.
- Bath, M., Lateral inhomogeneities in the upper mantel, Tectonophysics 2, 483-514, 1965.
- Bath, M. and C.F. Richter, Mechanisms of the aftershocks of the Kern County, California earthquake of 1952, Bull. Seism. Soc. Am. 48, 133-146, 1958.
- Bender, C. M. and S. Orzag, *Advanced Mathematical Methods for Scientists and Engineers*, Mc. Graw-Hill, 1978.
- Ben-zion, Y. and J. Rice, Earthquake failure sequences along a cellular fault zone in a 3-dimensional elastic solid containing asperity and nonasperity regions, J. Geophys. Res. 93, 14109-14131, 1993.
- Ben-zion Y. and Rice J., Slip patterns and earthquake populations along different classes of faults in elastic solids, J. Geophys. Res.100, 12959-12983, 1995.
- Ben-Zion, Y., K. Dahmen, V. Lyakhovsky, D. Ertas and D. Fisher, Self-driven mode switching of earthquake activity on a fault system, Earth and Planetary Science Letters 172, 11-21, 1999.
- Ben-Zion, Y. and V. Lyakhovsky, Accelerated seismic release and related aspects of seismicity patterns on earthquake faults, submitted to Pure Appl. Geophys, 2001.
- Berg, E., Relation between earthquake foreshocks, stress and mainshocks, Nature, 219, 1141-1143, 1968.
- Berkowitz, B. and H. Scher, The role of probabilistic approaches to transport theory in heterogeneous media, Transport in Porous Media 42 (1-2), 241-263, 2001.
- Beroza, G.C. and M.D. Zoback, Mechanism diversity of the Loma-Prieta aftershocks and the mechanics of mainshock-aftershock interaction, Science 259, 210-213, 1993.

- Bhandari R. K., Some lessons in the investigation and field monitoring of landslides, *Proceedings 5th Int. Symp. Landslides lausanne 1988*, eds C. Bonnard , 3, 1435-1457, Balkema, 1988.
- Bird, P., and R. W. Rosenstock, Kinematics of present crust and mantle flow in southern California, *Geol. Soc. Am. Bull.*, 95, 946-957, 1984.
- Blanpied, M. L., D. A. Lockner and J. D. Byerlee, Frictional slip of granite at hydrothermal conditions, *J. Geophys. Res.*, 100, 13045-13064, 1995.
- Blanter, E.M., M.G. Shnirman, J.-L. Le Mouél and C.J. Allègre, Scaling laws in blocks dynamics and dynamic self-organized criticality, *Phys. Earth Planet. Int.*, 99, 295-307, 1997.
- Blodgett, T.A., B.L. Isacks, E.J. Fielding, J.G. Masek, and A.S. Warner, Erosion attributed to landslides in the Cordillera Real, Bolivia, *Eos Trans. AGU*, 17, Spring Meet. Suppl. S261, 1996.
- Bonnet, E., O. Bour, N. E. Odling, P. Davy, I. Main, P. Cowie and B. Bekowitz, Scaling of fracture systems in geological media, *Reviews of Geophysics* 39, 347-383, 2001.
- Bouchaud, J.-P. and A. Georges, Anomalous diffusion in disordered media : Statistical mechanisms, models and physical applications, *Physics Reports* 195, 127-293, 1990.
- Bowman, J. R., A seismicity precursor to a sequence of Ms 6.3-6.7 midplate earthquakes in Australia, *Pure Appl. Geophys.*, 149, 61-78, 1997.
- Bowman, J. R. and K. Kisslinger, A test of foreshocks occurrence in the central Aleutian island arc, *Bull. Seism. Soc. Am.*, 74, 181-197, 1984.
- Bowman, D. D., G. Ouillon, C. G. Sammis, A. Sornette and D. Sornette, An observational test of the critical earthquake concept, *J. Geophys. Res.* 103, 24359-24372, 1998.
- Bowman, D. D. and G. C. P. King, Accelerating seismicity and stress accumulation before large earthquakes, *Geophys. Res. Lett.* 28, 4039-4042, 2001.
- Bowman, D. D. and G. C. P. King, Stress transfer and seismicity changes before large earthquakes, *Comptes Rend. Acad. Sci. II (A) Paris*, 333, 591-599, 2001.
- Bowman, J.R., A seismicity precursor to a sequence of Ms 6.3-6.7 midplate earthquakes in Australia, *Pure Appl. Geophys.* 149, 61-78, 1997.
- Bowman, J. R. and K. Kisslinger, A test of foreshocks occurrence in the central Aleutian island arc, *Bull. Seism. Soc. Am.*, 74, 181-197, 1984.
- Brehm, D.J. and L. W. Braile, Intermediate-term earthquake prediction using precursory events in the new Madrid seismic zone, *Bull. Seism. Soc. Am.* 88, 564-580, 1998.
- Brehm, D.J. and L. W. Braile, Intermediate-term earthquake prediction using the modified time-to-failure method in southern California, *Bull. Seism. Soc. Am.* 89, 275-293, 1999.
- Brehm, D.J. and L. W. Braile, Refinement of the modified time-to-failure method for intermediate-term earthquake prediction, *Journal of Seismology* 3, 121-138, 2000.

- Broili, L., New knowledge on the geomorphology of the Vaiont slide slip surfaces, *Rock mechanics and Engineering*, 5, 38-88, 1967.
- Budde, C., D. Prato and M. Re, Superdiffusion in decoupled continuous time random walks, *Phys. Lett. A*. 283, 309-312, 2001.
- Bufe, C. G., Frequency magnitude variations during the 1970 Danville earthquake swarm, *Earthquake Notes*, 41, 3-7, 1970.
- Bufe, C.G. and Varnes, D.J., Predictive modeling of the seismic cycle of the greater San-Francisco Bay region, *J. Geophys. Res.* 98, 9871-9883, 1993.
- Cagnetti, V. and V. Pasquale, The earthquake sequence in Frieli, Italy, 1976, *Bull. Seism. Soc. Am.*, 69, 1797-1818, 1979
- Campbell, C.S., Self-lubrication for long runout landslides, *Journal of Geology*, 97, 653-665, 1989.
- Campbell, C.S., Rapid granular flow, *Annu. Rev. of Fluid Mech.*, 22, 57-92, 1990.
- Caplan-Auerbach, J., C. G. Fox and F. K. Duennebieer Hydroacoustic detection of submarine landslides on Kilauea volcano, *Geophys. Res. Letts*, 28, 1811-1813, 2001.
- Champel, B., P. Van der Beek, J.L. Mugnier and P. Leturmy, Growth and lateral propagation of fault-related folds in the Siwaliks of western Nepal : Rates, mechanisms and geomorphic signature, in press *J. Geophys. Res.*, 2002.
- Chatelain, J.-L., Cardwell, R.K. and Isacks, B.L., Expansion of the aftershock zone following the Vanuatu (New Hebrides) earthquake on 15 July 1981, *Geophys. Res. Lett.* 10, 385-388, 1983.
- Christensen, K. and Z. Olami, Variation of the Gutenberg-Richter *b*-values and non-trivial temporal correlation in a spring-block model for earthquakes, *J. Geophys. Res.* 97, 8729-8735, 1992.
- Cochard A. and Madariaga R., Dynamic faulting under rate-dependent friction, *Pure Appl. Geophys.* 142, 419-445, 1994.
- Coleman, B. D., Time dependence of mechanical breakdown in bundles of fibers, *J. Appl. Phys.*, 28, 1058, 1957.
- Console, R., M. Murru and B. Alessandrini, Foreshocks statistics and their possible relationship to earthquake prediction in the Italian region, *Bull. Seism. Soc. Am.*, 83, 1248-1263, 1983.
- Console, R. and M. Murru, A simple and testable model for earthquake clustering, *J. Geophys. Res.* 166, 8699-8711, 2001.
- Console, R., A.M. Lombardi, M. Murru and D. Rhoades, Bath's law and the self-similarity of earthquakes, in press in *J. Geophys. Res.*, 2002.
- Correig, A.M., Urquizu, M., Vila, J. and Manrubia, S.C., Aftershock series of event February 18, 1996 : An interpretation in terms of self-organized criticality, *J. Geophys. Res.* 102, 27407-27420, 1997.
- Costa, P., D.S. Harned and J.T. Lundquist, Rethinking the aviation industry, *McKinsey Quarterly* 2, Risk and resilience, 2002,  
[http://www.mckinseyquarterly.com/article\\_page.asp?ar=1190&L2=23&L3=79](http://www.mckinseyquarterly.com/article_page.asp?ar=1190&L2=23&L3=79).

- Courtillot, V.E., A volcanic eruption, *Scientific American* 263 N4 :85-92, 1990.
- Courtillot, V.E., *Evolutionary catastrophes : the science of mass extinction*, New York : Cambridge University Press, 1999.
- Courtillot, V. and Y. Gaudemer, Effects of mass extinctions on biodiversity, *Nature* 381, 146-148, 1996.
- Couture, R., *Contribution aux aspects mécaniques et physiques des écroulements rocheux. Génie géologique, PhD Thesis, Saint-Foy, Quebec, U. Laval, 56-65, 1998.*
- Cowie, P., D. Sornette and C. Vanneste Statistical physics model for the spatio-temporal evolution of faults, *J. Geophys. Res.* 98, 21809-21821, 1993.
- Cowie, P., D. Sornette and C. Vanneste, Multifractal scaling properties of a growing fault population, *Geophys. J. Int.* 122, 457-469, 1995.
- Daley, D.J. and Vere-Jones, D., *An Introduction to the Theory of Point Processes*, Springer, 1988.
- Das, S. and Scholz, C.H., Theory of time-dependent rupture in the Earth, *J. Geophys. Res.* 86, 6039-51, 1981.
- David, E. and ATM, Glissement de La Clapière, St Etienne de Tinée, Etude cinématique, géomorphologique et de stabilité, *rapport CETE Nice, France, 88 pp., 2000.*
- Davis, R.O., N. R. Smith and G. Salt, Pore fluid frictional heating and stability of creeping landslides, *Int. J. Num. Anal. Meth. Geomechanics*, 14, 427-443, 1990.
- Davis, S.D. and C. Frohlich, Single-link cluster analysis of earthquake aftershocks : decay laws and regional variations, *J. Geophys. Res.* 96, 6335-6350, 1991a.
- Davis, S. D. and C. Frohlich, Single link cluster analysis, synthetic earthquake catalogues, and aftershock identification, *Geophys. J. Int.* 104, 289-306, 1991.
- Davy, P., Sornette A. and Sornette D., Some consequences of a proposed fractal nature of continental faulting, *Nature* 348, 56-58, 1990.
- Davy, P., A. Sornette and D. Sornette, Experimental discovery of scaling laws relating fractal dimensions and the length distribution exponent of fault systems, *Geophys. Res. Lett.* 19, 361-364, 1992.
- Densmore, A., M. Ellis, and R. Anderson, Landsliding and the evolution of normal-fault-bounded mountains, *J. Geophys. Res.*, 103, 15,203-15,219, 1998.
- Dieterich, J., Time dependent friction and the mechanics of stick slip, *Pure Appl. Geophys.*, 116, 790-806, 1978.
- Dieterich, J. H., Earthquake nucleation on faults with rate- and state-dependent strength, *Tectonophysics*, 211, 115-134, 1992.
- Dieterich, J., A constitutive law for rate of earthquake production and its application to earthquake clustering, *J. Geophys. Res.* 99, 2601-2618, 1994.

- Dieterich, J. H., Earthquake simulation with time-dependent nucleation and long-range interactions, *Journal of Nonlinear Processes in Geophysics*, 2, 109-120, 1995.
- Dieterich, J. H. and B. Kilgore, Implications of fault constitutive properties for earthquake prediction, *Proc. Nat. Acad. Sci USA*, 93, 3787-3794, 1996.
- Di Luccio, F., Console, R., Imoto, M. and Murru, M., Analysis of short time-space range seismicity patterns in Italy, *Annali di Geofisica* 40, 783-797, 1997.
- Dodge, D. D., G. C. Beroza and W.L. Ellsworth, Detailed observations of California foreshock sequence : implications for the earthquake initiation process, *J. Geophys. Res.*, 101, 22,371-22,392, 1996.
- Drakatos, G., Relative seismic quiescence before large aftershocks, *Pure Appl. Geophys.* 15, 1407-1421, 2000.
- Drakatos, G. and J. Latoussakis, A catalog of aftershock sequence in Greece (1971-1997) : Their spatial and temporal characteristics, *Journal of Seismology* 5, 137-145, 2001.
- Dreger, D. and B. Savage, Aftershocks of the 1952 Kern County, California, earthquake sequence, *Bull. Seism. Soc. Am.* 89, 1094-1108, 1999.
- Durville, J.L., Study of mechanisms and modeling of large slope movements, *Bull. Int. Ass. Engineering Geology*, 45, 25-42, 1992.
- Eisbacher, G.H., Cliff collapse and rock avalanches in the Mackenzie Mountains, Northwestern Canada, *Can. Geot. J.*, 16, 309-334, 1979.
- Enescu, B. and K. Ito, Some premonitory phenomena of the 1995 Hyogo-Ken Nanbu (Kobe) earthquake : seismicity, *b*-value and fractal dimension, *Tectonophysics*, 338, 297-314, 2001.
- Eneva, M., Effect of limited data sets in evaluating the scaling properties of spatially distributed data – An example from mining-induced seismic activity, *Geophys. J. Int.* 124, 773-786, 1996.
- Erismann, T. H. and G. Abele, *Dynamics of Rockslides and Rockfalls*, Springer, 300 pp, 2000.
- Evison, F. F., The precursory earthquake swarm, *Phys. Earth Planet. Inter.*, 15, 19-23, 1977.
- Evison, F. F. and D. A. Rhoades, The precursory earthquake swarm in Japan : hypothesis test, *Earth Planets and Space*, 51, 1267-1277, 1999.
- Fedotov S. A., A. A. Gusev and S. A. Boldiev, Progress in earthquake prediction in Kamchatka, in E.F. Savarensky and T. Rikitake (Eds), *Forerunners of strong earthquakes*, *Tectonophysics*, 14, 279-286, 1972.
- Feller, W. *An Introduction to Probability Theory and its Applications*, II, John Willey and sons, New-York, 1971.
- Felzer, K.R., T.W. Becker, R.E. Abercrombie, G. Ekström and J.R. Rice, Triggering of the 1999  $M_W$  7.1 Hector Mine earthquake by aftershocks of the 1992  $M_W$  7.3 Landers earthquake, in press in *J. Geophys. Res.*, 2002.
- Follacci, J. P. Photographic album of La Clapière landslide, *CETE Méditerranée*, 2000.

- Follacci J. P., P. Guardia and J. P. Ivaldi, La Clapière landslide in its geodynamical setting, *Bonnard eds, Proc. 5th Int. Symp. on Landslides, 3*, 1323-1327, 1988.
- Follacci, J.-P., L. Rochet and J.-F. Serratrice, Glissement de La Clapière, St Etienne de Tinée, Synthèse des connaissances et actualisation des risques, *rapport 92/PP/UN/I/DRM/03/AI/01, Ministère Environnement, 76 pp.*, 1993.
- Fréchet, J., Sismicité du Sud-Est de la France et une nouvelle méthode de zonage sismique, *Thèse 3ème cycle, Université de Grenoble, 159 pp*, 1978.
- Fruneau, B., J. Achache and C. Delacourt, Observation and modeling of the Saint-Etienne-de-Tinée landslide using SAR interferometry, *Tectonophysics, 265*, 181-190, 1996.
- Fukuzono, T., Method for predicting the failure time of a slope, *Proceedings of the 4th Int. Conf. Field Workshop on Landslides*, National Research Center for Disaster prevention, Tokyo, 145-150, 1985.
- Fuyii, Y., Frequency distribution of the landslides caused by heavy rain-fall, *Seismological Society of Japan Journal, 22*, 244-247, 1969.
- Gabrielov, A., Keilis-Borok, V. and Jackson, D. D., Geometric incompatibility in a fault System, *Proc. Natl. Acad. Sci. USA 93*, 3838-3842, 1996.
- Gabrielov, A., I. Zaliapin, W. I. Newman and V. I. Keilis-Borok, Colliding cascades model for earthquake prediction, *Geophys. J. Int. 143*, 427-437, 2000a.
- Gabrielov, A., V. Keilis-Borok, I. Zaliapin and W. I. Newman, Critical transitions in colliding cascades, *Phys. Rev. E 62*, 237-249, 2000b.
- Garcimartin, A., A. Guarino, L. Bellon and S. Ciliberto, Statistical properties of fracture precursors, *Phys. Rev. Lett. 79*, 3202-3205, 1997.
- Gardner, J., Rockfall : a geomorphic process in high mountain terrain, *The Albertan Geographer, 6*, 15-20, 1970.
- Gardner, J.K. and L. Knopoff, Is the sequence of earthquakes in Southern California, with aftershocks removed, Poissonian ?, *Bull. Seis. Soc. Am. 64*, 1363-1367, 1974.
- Gelfand, I.M., Guberman, Sh.A., Keilis-Borok, V.I., Knopoff, L., Press, F., Ranzman, E.Ya., Rotwain, I.M. and A.M. Sadovsky, Pattern recognition applied to earthquake epicenters in California, *Physics of the Earth and Planetary Interiors 11*, 227-283, 1976.
- Glöckle, W. and T. F. Nonnenmacher, Fox function representation of non-Debye relaxation processes, *J. Stat. Phys., 71*, 741-757, 1993.
- Gluzman, S. and V. I. Yukalov, Algebraic self-similar renormalization in the theory of critical phenomena, *Phys. Rev. E, 55*, 3983-3999, 1997.
- Gluzman, S. and V. I. Yukalov, Unified approach to crossover phenomena, *Phys. Rev. E, 58*, 4197-4209, 1998.

- Gluzman, S. and D. Sornette, Self-Consistent theory of rupture by progressive diffuse damage, *Physical Review E* V63 06 N6 PT2 :6129, 241-250, 2001.
- Gluzman, S. and D. Sornette, Classification of possible finite-Time singularities by functional renormalization, in press in *Phys. Rev. E*, 2002. (<http://arXiv.org/abs/cond-mat/0111181>).
- Gluzman, S., J. V. Andersen and D. Sornette, Functional renormalization prediction of rupture, *Computational Seismology* 32, 122-137, 2001.
- Gnedenko, B. V. and A. N. Kolmogorov, *Limit Distributions for Sum of Independent Random Variables*, Addison Wesley, Reading MA, 1954.
- Goguel, J., and A. Pachoud, Géologie et dynamique de l'éroulement du Mont Granier, dans le massif de la Chartreuse, en novembre 1248, *Bulletin du BRGM* III(1), 29-38, 1972.
- Goltz, C., Decomposing spatio-temporal seismicity patterns, *Natural Hazards and Earth System Sciences* 1, 83-92, 2001.
- Gomberg, J., The failure of earthquake failure models, *J. Geophys. Res.* 106, 16,253-16,263, 2001.
- Gomberg, J., P. Bodin, W. Savage and M. E. Jackson, Landslide faults and tectonic faults, Analogs ? – The slumgullion earthflow, Colorado, *Geology*, 23, 41-44, 1995.
- Gomberg, J., N. Beeler and M. Blanpied, On rate-state and Coulomb failure models, *J. Geophys. Res.* 105, 7857-7871, 2000.
- Gomberg, J., Reasenberg, P.A., Bodin, P. and Harris, R.A., Earthquake triggering by seismic waves following the Landers and Hector Mine earthquakes, *Nature* 411, 462-466, 2001.
- Gorshkov, A.I., Keilis-Borok, V.I., Rotwain, I.M., Soloviev, A.A. and Vorobieva, I.A., On dynamics of seismicity simulated by the models of blocks-and-faults systems, *Annali di Geofisica* 40 (5), 1217-1232, 1997.
- Gorshkov, A.I., Kossobokov, V.G., Rantsman, E.Ya. and Soloviev, A.A., Recognition of earthquake prone areas : validity of results obtained from 1972 to 2000, *Computational Seismology* 32, 48-57, Eds. A. Levshin, G. Molchan, B. Naimark, Moscow, GEOS, 2001.
- Grasso, J.-R., F. Guyoton, J. Fréchet and J.F. Gamond, Triggered earthquakes as stress gauge : Implication for the uppercrust behavior in the Grenoble area, France, *Pure Appl. Geophys.*, 139, 579-605, 1992.
- Grasso, J.-R. and D. Sornette, Testing self-organized criticality by induced seismicity, *J. Geophys. Res.*, 103,29,965-29,987, 1998.
- Gross, S. and C. Kisslinger, Tests of models of aftershocks rate decay, *Bull. Seism. Soc. Am.* 84, 1571-1579, 1994.
- Gross, S. and Rundle, J., A systematic test of time-to-failure analysis, *Geophys. J. Int.* 133, 57-64, 1998.
- Guarino, A, S. Ciliberto, A. Garcimartin, M. Zei and R. Scorretti, Failure time and critical behaviour of fracture precursors in heterogeneous materials, *European Physical Journal B*, 26, 141-151, 2002.

- Guglielmi, J., and J. M. Vengeon, Interrelation between gravitational patterns and structural fractures La Clapière, French Alps, submitted to *Geomorphology*, 2002.
- Guillot, P. and R. Duband, La méthode du GRADEX pour le calcul de la probabilité de crues partir des pluies, *IASH Publication, n° 84*, 1967.
- Guo, Z. and Y. Ogata, Correlations between characteristic parameters of aftershock distributions in time, space and magnitude, *Geophys. Res. Lett.* 22, 993-996, 1995.
- Guo, Z. and Y. Ogata, Statistical relations between the parameters of aftershocks in time, space and magnitude, *J. Geophys. Res.*, 102, 2857-2873, 1997.
- Gutenberg, B. and C.F. Richter, Frequency of earthquakes in California, *Bull. Seism. Soc. Am.* 34, 185-188, 1944.
- Gutenberg, B. and C. F. Richter, *Seismicity of the Earth and Associated Phenomena*, Princeton Univ. Press, Princeton, NJ, 1949.
- Hainzl, S., G. Zoller and J. Kurths, Similar power laws for foreshock and aftershock sequences in a spring-block model for earthquakes, *J. Geophys. Res.* 104, 7243-7253.
- Hainzl, S., G. Zoller and J. Kurths, Self-organization of spatio-temporal earthquake clusters, *Nonlinear Processes in Geophysics*, 7, 21-29, 2000.
- Hamburger, D., Biham, O and Avnir, D., Apparent fractality emerging from models of random distributions, *Phys. Rev. E* 53, 3342-3358, 1996.
- Hanks, T. C., Small earthquakes, tectonic forces, *Science* 256, 1430-1431, 1992.
- Harp E.L. and R.L. Jibson, Inventory of landslide triggered by the 1994 Northridge California earthquake, U.S. Geol. Survey, Open-file report, 95-213, 1995.
- Harris, T.E., *The theory of branching processes*, Springer, Berlin, 1963.
- Harris, R.A., Earthquake stress triggers, stress shadows, and seismic hazard, in *International Handbook of Earthquake and Engineering Seismology*, edited by W. H. L. Lee et al., Chapter 73, 48 pages (Chapman and Hall, New-York), 2001.
- Harris, R.A. and Simpson, R.W., Change in static stress on Southern California faults after the 1992 Landers earthquake, *Nature* 360, 251-254, 1992.
- Harris, R.A. and Simpson, R.W., In the shadow of 1857 – The effect of the great Ft Tejon earthquake on subsequent earthquakes in Southern California, *Geophys. Res. Lett.* 23, 229-232, 1996.
- Harris, R.A., Simpson, R.W. and Reasenberg, P.A., Influence of static stress changes on earthquake locations in Southern California, *Nature* 375, 221-224, 1995.
- Harris, R.A. and Simpson, R.W., Suppression of large earthquakes by stress shadows : A comparison of Coulomb and rate-and-state failure, *J. Geophys. Res.* 103, 24439-24451, 1998.
- Harris, R.A., Dolan, J.F., Hartleb, R. and Day, S.M., The 1999 Izmit, Turkey, earthquake : A 3D dynamic stress transfer model of intraearthquake triggering, *Bull. Seism. Soc. Am.* 92, 245-255, 2002.

- Hawkes, A.G., Point spectra of some mutually exciting point processes. *J. Roy. Stat. Soc. B* 33, 438-443, 1971.
- Hawkes, A.G., Spectra of some mutually exciting point processes with associated variables, In *Stochastic Point Processes*, ed. P.A.W. Lewis, Wiley, 261-271, 1972.
- Hawkes, A.G. and Adamopoulos, L., Cluster models for earthquakes - regional comparisons, *Bull Internat. Stat. Inst.* 45, 454-461, 1973.
- Hawkes, A. G. and Oakes D., A cluster representation of a self-exciting process, *Journal Appl. Prob.*, 11, 493-503, 1974.
- Heim A., *Bergsturz and Menschenleben*, Zurich, 1932.
- Heimpel, M., Critical behaviour and the evolution of fault strength during earthquake cycles, *Nature* 388, N6645, 865-868, 1997.
- Helmstetter, A., Is earthquake triggering driven by small earthquakes ?, submitted to *Geophys. Res. Lett.*, 2002.
- Helmstetter, A. and D. Sornette, Sub-critical and super-critical regimes in epidemic models of earthquake aftershocks, in press in *J. Geophys. Res.* (<http://arXiv.org/abs/cond-mat/0109318>), 2002a
- Helmstetter, A. and D. Sornette, Diffusion of earthquake aftershock epicenters and Omori's law : exact mapping to generalized continuous-time random walk models, in press in *Phys. Rev. E* (<http://arXiv.org/abs/cond-mat/0203505>), 2002b.
- Helmstetter, A., D. Sornette and J.-R. Grasso, Mainshocks are aftershocks of conditional foreshocks : how do foreshock statistical properties emerge from aftershock laws, in press in *J. Geophys. Res.* (<http://arXiv.org/abs/cond-mat/0205499>), 2002.
- Hendron, A. J. and F. D. Patton, The Vaiont slide, a geotechnical analysis based on new geologic observations of the failure surface, *US Army Corps of Engineers Technical Report GL-85-5 (2 volumes)*, 1985.
- Hergarten, S., and J. Neugebauer, Self-organized criticality in a landslide model, *Geophys. Res. Lett.*, 25, 801-804, 1998.
- Hill, D.P., Reasenberg, P.A., Michael, A., Arabaz, W.J. et al., Seismicity remotely triggered by the magnitude 7.3 Landers, California earthquake, *Science* 260 N5114, 1617-1623, 1993.
- Hirata, T., Fractal geometry of fault systems in Japan – Fractal structure in rock fracture geometry at various scales, *Pure Appl. Geophys.* 131, 157-170, 1989.
- Hoek, E., and E.T. Brown, Underground excavations in rock, *Institution of Mining and Metallurgy*, London, 1980.
- Hoek, E., and J. W. Bray, *Rock slope engineering*, 3rd Edn (rev), Institution of Mining and Metallurgy and E&FN Spon, London, pp 358, 1997.

- Hough, S.E. and L.M. Jones, Aftershocks ; Are they earthquakes or afterthoughts? EOS, Transactions, American Geophysical Union 78, N45, 505-508, 1997.
- Hovius, N., C.P. Stark, and P.A. Allen, Sediment flux from a mountain belt derived by landslide mapping, *Geology* 25, 231-234, 1997.
- Huang, Y., Saleur, H., Sammis, C. and Sornette, D., Precursors, aftershocks, criticality and self-organized criticality, *Europhys. Lett.* 41, 43-48, 1998.
- Huang, Y., A. Johansen, M. W. Lee, H. Saleur and D. Sornette, Artifactual log-periodicity in finite-size data : relevance for earthquake aftershocks, *J. Geophys. Res.* 105, 25451-25471, 2000.
- Huber, N. K., The geologic story of Yosemite national Park, *U.S. Geological Survey Bulletin*, 1595, pp. 59, 1987.
- Hudnut K.W., L. Seeber and J. Pacheco, Cross-fault triggering in the November 1987 Superstition Hill earthquake sequence, southern California, *Geophys. Res. Lett.* 16, 199-203, 1989.
- Hughes, B.D. Random walks and random environments, Oxford University Press, 1995.
- Hungr, O., S.G. Evans, and J. Hazzard, Magnitude and frequency of rock falls along the main transportation corridors of southwestern British Columbia, *Canadian Geotechnical Journal*, 36, 224-238, 1999.
- Hurst, H.E., Long term storage capacity of reservoirs, *Transactions of the American Society of Civil Engineers*, 116, 770-808, 1951.
- Ikegami, R, *Bull. Earth. Res. Inst.*, 45, 328-345, 1967.
- Imoto, M., On migration phenomena of afterschocks following large thrust earthquakes in subduction zones, *Kokuritsu Bosai Kagaku Gijutsu Senta Kenkyu Hokoku (Report of the National Research Center for Disaster Prevention)* 25, 29-86, 1981.
- Imoto, M., Changes in the magnitude frequency  $b$ -value prior to large ( $M \geq 6.0$ ) earthquakes in Japan, *Tectonophysics*, 193, 311-325, 1991.
- Imoto, M. and Kishimoto, Y., Statistical search for migrations of aftershock sequences, *Bulletin of the Disaster Prevention Research Institute* 27, Part 3, 93-111, 1977.
- Jacod, J. and A. N. Shiryaev, *Limit Theorems for Stochastic Processes*, Springer, Berlin, 1987.
- Jacques, E., J.C. Ruegg, J.C. Lepine, P. Tapponnier, G.C.P. King, GCP and A. Omar, Relocation of  $M \geq 2$  events of the 1989 Dobi seismic sequence in Afar : evidence for earthquake migration, *Geophys. J. Int.* 138, 447-469, 1999.
- Jaumé, S.C. and L. R. Sykes, Evolving towards a critical point : A review of accelerating seismic moment/energy release prior to large and great earthquakes, *Pure Appl. Geophys.* 155, 279-305, 1999.
- Jefferies, P., D. Lamper and N. F. Johnson, Anatomy of extreme events in a complex adaptative system, e-print at cond-mat/0201540.

- Johansen, A., D. Sornette, H. Wakita, U. Tsunogai, W. I. Newman and H. Saleur, Discrete scaling in earthquake precursory phenomena : evidence in the Kobe earthquake, Japan, *J. Phys. I France*, 6, 1391-1402, 1996.
- Johansen, A. and D. Sornette, Critical ruptures, *Eur. Phys. J. B* 18, 163-181, 2000.
- Jones, L. M., Foreshocks (1966-1980) in the San Andreas system, California, *Bull. Seis. Soc. Am.*, 74, 1361-1380, 1984.
- Jones, L. M., and P. Molnar, Frequency of foreshocks, *Nature* 262, 677, 1976.
- Jones, L. M., and P. Molnar, Some characteristics of foreshocks and their possible relationship to earthquake prediction and premonitory slip on fault, *J. Geophys. Res.*, 84, 3596-3608, 1979.
- Jones, L. M., and E. Hauksson, The seismic cycle in southern California : Precursor or response? *Geophys. Res. Lett.* 24, 469-472, 1997.
- Jones, L. M., R. Console, F. Di Luccio and M. Murru, Are foreshocks mainshocks whose aftershocks happen to be big?  
preprint 1999 available at <http://pasadena.wr.usgs.gov/office/jones/italy-bssa.html>
- Kagan, Y.Y., Point sources of elastic deformation : elementary sources, static displacements, *Geophys. J. Royal Astron. Soc.* 90, 1-34, 1987.
- Kagan, Y.Y., Multipole expansions of extended sources of elastic deformation, *Geophys. J.* 93, 101-14, 1988a.
- Kagan, Y.Y., Static sources of elastic deformation in a homogeneous half-space, *J. Geophys. Res.* 93, 10560-10574, 1988b.
- Kagan, Y.Y., Random stress and earthquake statistics – Spatial dependence, *Geophys. J. Int.* 102, 573-583, 1990.
- Kagan, Y.Y., Likelihood analysis of earthquake catalogues, *Geophys. J. Int.* 106, 135-148, 1991a.
- Kagan, Y.Y., 3-D rotation of double-couple earthquake sources, *Geophys. J. Int.* 106, 709-716, 1991b.
- Kagan Y.Y., Geometry of earthquake faulting *Eos, Transactions, American Geophysical Union*, 72 (17) 58, 1991c.
- Kagan, Y.Y., Seismicity – Turbulence of solids, *Nonlinear Science Today*, 2 (N1), 1-1, 1992.
- Kagan, Y.Y., Observational evidence for earthquakes as a nonlinear dynamic process, *Physica D* 77, 160-192, 1994.
- Kagan, Y.Y., Is earthquake seismology a hard, quantitative science? *Pure Appl. Geophys.* 155, 233-258, 1999a.
- Kagan, Y. Y., Universality of the seismic moment-frequency relation, *Pure Appl. Geophys.* 155, 537-573, 1999b.
- Kagan, Y. Y., Aftershock zone scaling, *Bull. Seism. Soc. Am.*, 92, 641-655, 2002.
- Kagan, Y. Y. and L. Knopoff, Statistical search for non-random features of the seismicity of strong earthquakes, *Phys. Earth Planet. Int.*, 12, 291-318, 1976.

- Kagan, Y., and L. Knopoff, Earthquake risk prediction as a stochastic process, *Phys. Earth Planet. Inter.*, 14, 97-108, 1977.
- Kagan, Y. Y. and L. Knopoff, Statistical study of the occurrence of shallow earthquakes, *Geophys. J. R. Astr. Soc.*, 55, 67-86, 1978.
- Kagan Y.Y. and L. Knopoff, Spatial distribution of earthquakes : the two-point correlation function, *Geophys. J. R. astr. Soc.* 62, 303-320, 1980.
- Kagan, Y. Y. and L. Knopoff, Stochastic synthesis of earthquake catalogs, *J. Geophys. Res.*, 86, 2853-2862, 1981.
- Kagan, Y.Y. and Knopoff, L., The first-order statistical moment of the seismic moment tensor, *Geophys. J. Royal Astron. Soc.* 81, 429-44, 1985.
- Kagan, Y.Y. and L. Knopoff, Statistical short-term earthquake prediction, *Science* 236, 1563-1467, 1987.
- Kagan, Y.Y. and D.D. Jackson, Spatial aftershock distribution : Effect of normal stress, *J. Geophys. Res.* 103, 24453-24467, 1998.
- Kagan, Y.Y. and Jackson, D.D., Probabilistic forecasting of earthquakes, *Geophys. J. Int.* 143, 438-453, 2000.
- Kanamori, H. and D. Anderson, Theoretical basis of some empirical relations in seismology, *Bull. Seism. Soc. Am.*, 65, 1073-1095, 1975.
- Keefer, D.K., Rock avalanches caused by earthquakes :Source characteristics, *Science*, 223, 1288-1290, 1984.
- Keefer, D.K., Earthquake-induced landslides and their effects on alluvial fans, *J. Sedimentary Research*, 69.1, 84-104, 1999.
- Keilis-Borok, V. I. and L. N. Malinovskaya, One regularity in the occurrence of strong earthquakes, *J. Geophys. Res.*, 69, 3019-3024, 1964.
- Keilis-Borok, V.I., I.M. Rotvain and T.V. Sidorenko, Intensified sequence of aftershocks as a precursor of strong earthquake, *Dokl. Akad. Nauk. SSSR*, 242(3), 567-569, 1978.
- Keilis-Borok, V. I., L. Knopoff, I.M. Rotvain and T.M. Sidorenko, Burst of seismicity as long-term precursors of strong earthquake, *J. Geophys. Res.*, 85, 803-811, 1980a.
- Keilis-Borok, V. I., L. Knopoff and C.R. Allen, Long-term premonitory seismicity patterns in Tibet and the Himalayas, *J. Geophys. Res.*, 85, 813-820, 1980b.
- Keilis-Borok, V. and V. G. Kossobokov, Premonitory activation of earthquake flow - Algorithm M8, *Phys. Earth Planet. Int.*, 61, 73-83, 1990a.
- Keilis-Borok V. I. and V. G. Kossobokov, Times of increased probability of strong earthquakes ( $M \geq 7.5$ ) diagnosed by algorithm M8 in Japan and adjacent territories, *J. Geophys. Res.*, 85, 12413-12422, 1990b.

- Keilis-Borok, V., A. Ismail-Zadeh, V. Kossobokov and P. Shebalin, Non-linear dynamics of the lithosphere and intermediate-term earthquake prediction, *Tectonophysics*, 338, 247-260, 2001.
- Kenkre, E.W. Montroll and M.F. Shlesinger, *J. Stat. Phys.* 9, 45, 1973.
- Kennedy, B. A. and K. E. Niermeyer, Slope monitoring systems used in the prediction of a major slope failure at the Chuquicamata Mine, Chile, *Proc. on Planning Open Pit Mines, Johannesburg*, Balkema, 215-225, 1971.
- Kilburn, C. R. J., and D. N. Petley, Forecasting giant, catastrophic slope collapse : lessons from Vajont, Northern Italy, in press in *Geomorphology*, 2002.
- King G.C.P., Stein R.S. and Lin J., Change in failure stress on the southern San-Andreas fault system caused by the 1992 Magnitude = 7.4 Landers earthquake, *Science* 258, 1328-1332, 1992.
- King G.C.P., Stein R.S. and Lin J., Static stress changes and the triggering of earthquakes, *Bull. Seismol. Soc. Am.* 84, 935-953, 1994.
- Kirchner, J.W. and Weil, A., No fractals in fossil extinction statistics, *Nature* 395 N6700, 337-338, 1998.
- Kisslinger, C., The stretched exponential function as an alternative model for aftershock decay rate, *J. Geophys. Res.* 98, 1913-1921, 1993.
- Kisslinger, C. and L.M. Jones, Properties of aftershocks sequences in Southern California, *J. Geophys. Res.* 96, 11947-11958, 1991.
- Knopoff, L., The magnitude distribution of declustered earthquakes in Southern California, *Proc. Nat. Acad. Sci. USA*, 97, 11880-11884, 2000.
- Knopoff, L., Y.Y. Kagan and R. Knopoff, *b*-values for fore- and aftershocks in real and simulated earthquakes sequences, *Bull. Seism. Soc. Am.* 72, 1663-1676, 1982.
- Knopoff, L., Levshina, T., Keilis-Borok, V. and Mattoni, C., Increased long-range intermediate-magnitude earthquake activity prior to strong earthquakes in California, *J. Geophys. Res.* 101, 5779-5796, 1996.
- Korner, H. J., Reichweite und Geschwindigkeit von Bergstürzen und Fleisscheneelawinen, *Rock mechanics*, 8, 2256-256, 1976.
- Kossobokov, V. G., J. H. Healy and J. W. Dewey, Testing an earthquake prediction algorithm, *Pure Appl. Geophys.* 149, 219-232, 1997.
- Kossobokov, V. G., L. L. Romashkova, V. I., Keilis-Borok and J. H. Healy, Testing earthquake prediction algorithms : statistically significant advance prediction of the largest earthquakes in the Circum-Pacific, 1992-1997, *Phys. Earth Planet. Inter.*, 111, 187-196, 1999.
- Kossobokov, V.G., Keilis-Borok, V.I. and Cheng, B.L., Similarities of multiple fracturing on a neutron star and on the Earth, *Phys. Rev. E* 61, 3529-3533, 2000.
- Kotulski, M., Asymptotic distributions of continuous-time random walks - A probabilistic approach, *J. Stat. Phys.* 81, 777-792, 1995a.

- Kotulski, M., Chaos the interplay between stochastic and deterministic behavior, eds. P. Garbaczewski, M. Wolf and A. Weron, Lecture Notes in Physics 457, 471, 1995b.
- Krajcinovic, D., Damage mechanics, North-Holland Series in Applied Mathematics and Mechanics, Elsevier, Amsterdam, 1996.
- Krishnamurthy, S., Tanguy, A., Abry, P. and Roux, S., A stochastic description of extremal dynamics, Europhysics Lett. 51, 1-7, 2000.
- Kutner, R., Hierarchical spatio-temporal coupling in fractional wanderings. (I) - Continuous-time Weierstrass flights, Physica A 264, 84-106, 1999.
- Kutner, R. and Regulski, M., Hierarchical spatio-temporal coupling in fractional wanderings. (II). Diffusion phase diagram for Weierstrass walks, Physica A 264, 107-133, 1999.
- Kyte, F.T., A meteorite from the Cretaceous/Tertiary boundary, Nature, 396 N6708 :237-239, 1998.
- Lahaie, F. and J.-R. Grasso, A fluid-rock interaction cellular automaton of volcano mechanics : Application to the Piton de la Fournaise, J. Geophys. Res, 103, 9637-9649, 1998.
- Laherrère, J. and D. Sornette, Stretched exponential distributions in Nature and Economy : "Fat tails" with characteristic scales, European Physical Journal B, 2, 525-539, 1998.
- Lamainière, L., F. Carmona and D. Sornette, Experimental realization of a critical thermal fuse network, Phys. Rev. Lett. 77, 2738-2741, 1996.
- Lapusta, N., Rice, J.R., Ben-Zion, Y. and Zheng, G.T., Elastodynamic analysis for slow tectonic loading with spontaneous rupture episodes on faults with rate- and state-dependent friction, J. Geophys. Res. 105, 23765-23789, 2000.
- Lavin, P.M. and Alexander, S.S., Evidence for block tectonic structural elements in the eastern United States and their present tectonic significance, Earthquake Notes 52 (3), 19, 1981.
- Lee, M.W., Unstable fault interactions and earthquake self-organization, Ph.D. thesis, Univ. of Calif., Los Angeles, 1999.
- Lee, M.W. and D. Sornette, Novel mechanism for discrete scale invariance in sandpile models, Eur. Phys. J. B 15, 193-197, 2000.
- Lee, M.W., D. Sornette and L. Knopoff, Persistence and quiescence of seismicity on fault systems, Phys. Rev. Lett. 83, 4219-4222, 1999.
- Li, Q. L., J. B. Chen, L. Yu, and B. L. Hao, Time and space scanning of the  $b$ -value : A method for monitoring the development of catastrophic earthquakes, Acta Geophys. Sinica, 21, 101-125, 1978.
- Lindh, A. G., and M. R. Lim, A clarification, correction and updating of Parkfield California, earthquakes prediction scenarios and response plans, U.S. Geol. Surv. Open File Rep., 95-695, 1995.
- Liu, Z.R., Earthquake frequency and prediction, Bull. Seism. Soc. Am. 74, 255-265, 1984.

- Lomnitz, C., *Global Tectonics and Earthquake Risk (Chapter 7 Modelling the earthquake process)*, Elsevier, 1974.
- Ma, H., Variation of the  $b$ -values before several large earthquakes that occurred in North China, *Acta Geophysica Sinica.*, 21, 126-141, 1978 (in chinese).
- Ma, Z., Fu Z., Zhang Y., Wang C., Zhang G. and D. Liu, Earthquake prediction, nine major cas in China, Seismological Press Beijing, Springer Verlag, 332 pp, 1990.
- Maeda, K., Time distribution of immediate foreshocks obtained by a stacking method, *Pure Appl. Geophys.*, 155, 381-384, 1999.
- Main, I., Statistical physics, seismogenesis and seismic hazard, *Review of Geophysics* 34, 433-462, 1996.
- Main, I.G., P.G. Meredith and P.R. Sammonds, Temporal variation in seismic event rate and  $b$ -values from stress corrosion constitutive laws, *Tectonophysics* 211, 233-246, 1992.
- Mainardi, F., Y. Luchko and G. Pagnini, The fundamental solution of the space-time fractional diffusion equation, *Fractional Calculus and Applied Analysis* 4, 153-192, 2001.
- Malamud, B.D. and D.L. Turcotte, Self organized criticality applied to natural hazards, *Natural Hazards*, 20, 93-116, 1999.
- Malcai, O., Lidar, D.A., Biham, O. and Avnir, D., Scaling range and cutoffs in empirical fractals, *Phys. Rev. E* 56, 2817-2828, 1997.
- Malet, J. P., O. Maquaire and E. Calais, The use of Global Positioning System techniques for the continuous monitoring of landslides : application to the Super-Sauze earthflow (Alpes-de-Haute-Provence, France), *Geomorphology*, 43, 33-54, 2002.
- Mandelbrot, B.B. and J.W. Van Ness, Fractional Brownian motions, fractional noise and applications, *Society for Industrial and Applied Mathematics Review*, 10, 422-437, 1968.
- Mantovani, F., R. Soeters and C. J. Vanwesten, Remote sensing techniques for landslide studies and hazard zonation in Europe, *Geomorphology* 15, 213-225, 1996.
- Marcellini, A., Arrhenius behavior of aftershock sequences, *J. Geophys. Res.*, 100, 6443-6468, 1995.
- Marcellini, A., Physical model of aftershock temporal behavior, *Tectonophysics*, 277, 137-146, 1997.
- Margolin, G. and B. Berkowitz, Application of continuous time random walks to transport in porous media, *J. Phys. Chem.* 104, 3942-3947, 2000.
- Marone, C., Laboratory-derived friction laws and their application to seismic faulting, *Ann. Rev. Earth Planet. Sci.*, 26, 643-696, 1998.
- Marsan, D., C.J. Bean, S. Steacy and J. McCloskey, Spatio-temporal analysis of stress diffusion in a mining-induced seismicity system. *Geophys. Res. Lett.* 26, 3697-3700, 1999.
- Marsan, D., C.J. Bean, S. Steacy and J. McCloskey, Observation of diffusion processes in earthquake populations and implications for the predictability of seismicity systems, *J. Geophys. Res.* 105, 28,081-28,094, 2000.

- Marsan, D. and C.J. Bean, Average dynamical seismicity changes following a stress perturbation, for a world-wide catalogue, Submitted to *Geophys. J. Int.*, 2001.
- Marshall, C.R. Palaeobiology - Mass extinction probed, *Nature* 392 N6671 :17-19 (1998).
- Marshall, C.R. and P.D. Ward, Sudden and gradual extinctions in the latest Cretaceous of Western European Tethys, *Science* 274, 1360-1363, 1996.
- Martinod J., F. Jouanne, J. Taverna, G. Menard, J.F. Gamond, X. Darmantrail, J.C. Notter, and C. Basile, Present day deformation of the Dauphine (SE France) Alpine and Subalpine massifs, *Geophys. J. Int.*, 127, 189-200, 1996.
- Mathai, A.M. and R.K.Saxena, the H-function with applications in statistics and other disciplines, Wiley Eastern Limited, New Delhi, 1978.
- Matsu'ura, S.R., Precursory quiescence and recovery of aftershock activities before some large aftershocks, *Bull. Earthquake Res. Inst., Univ. Tokyo* 61, 1-65, 1986.
- Maveyraud, C., J.P. Vila, D. Sornette, C. Le Floch, J.M. Dupillier, R. Salomé, Numerical modelling of the behaviour of high-pressure vessels under a hypervelocity impact, *Mec. Ind.* 2, 57-62, 2001.
- Meltzner, A.J. and D.J. Wald, Foreshocks and aftershocks of the great 1857 California earthquake, *Bull. Seism. Soc. Am.* 89, 1109-1120, 1999.
- Metzler, R. and J. Klafter, The random walk's guide to anomalous diffusion :a fractional dynamics approach, *Physics Reports* 339, 1-77, 2000.
- Mendoza, C. and S. H. Hartzell, Aftershock patterns and mainshock faulting, *Bull. Seism. Am. Soc.* 78, 1438-1449, 1988.
- Meredith, P.G., I.G. Main and C. Jones, Temporal variation in seismicity during quasi-static and dynamic rock failure, *Tectonophysics* 175, 249-268, 1990.
- Michael, A. J. and L. M. Jones, Seismicity alert probabilities at Parkfield, California, revisited, *Bull. Seis. Soc. Am.*, 88, 117-130, 1998.
- Mikumo, T. and T. Miyatake, Earthquake sequences on a frictional fault model with non-uniform strengths and relaxation times, *Geophysical Journal of the Royal Astronomical Society*, 59, 497-522, 1979.
- Miltenberger, P., D. Sornette and C. Vanneste, Fault self-organization as optimal random paths selected by spatio-temporal dynamics of earthquakes, *Phys. Rev. Lett.* 71, 3604-3607, 1993.
- Milton, J.G. and J. Belair, Chaos, noise and extinction in models of population growth, *Theor. Population Biol.* 37, 273-290, 1990.
- Mogi, K., Some discussions on aftershocks, foreshocks and earthquake swarms, *Bull. Res. Inst., Tokyo, Univ.*, 41, 595-614, 1963.
- Mogi, K., Earthquakes and fractures, *Tectonophysics*, 5, 35-55, 1967.
- Mogi K., Sequential occurrences of recent great earthquakes, *J. Phys. Earth* 16, 30-36, 1968.

- Molchan, G. M., Structure of optimal strategies in earthquake prediction, *Tectonophysics*, 193, 267-276, 1991.
- Molchan, G. M., Earthquake prediction as a decision-making problem, *Pure Appl. Geophys.*, 149, 233-247, 1997.
- Molchan, G.M., O.E. Dmitrieva, I.M. Rotwain and J. Dewey, Statistical analysis of the results of earthquake prediction, based on bursts of aftershocks, *Phys. Earth and Planetary Interiors* 61, 128-139, 1990.
- Molchan, G. M. and O. Dmitrieva, Dynamics of the magnitude frequency relation for foreshocks *Phys. Earth. Plan. Inter.*, 61, 99-112, 1990.
- Molchan, G.M. and O.E. Dmitrieva, Aftershock identification – Methods and new approaches, *Geophys. J. Int.* 109, 501-516, 1992.
- Molchan, G. M. and Y. Y. Kagan, Earthquake prediction and its optimization, *J. Geophys. Res.*, 97, 4823-4838, 1992.
- Molchan, G. M., T.L. Konrod and A.K. Nekrasova, Immediate foreshocks : time variation of the  $b$ -value, *Phys. Earth. Plan. Inter.*, 111, 229-240, 1999.
- Montroll, E.W. and G.H. Weiss, *J. Math. Phys.*, 6, 167, 1965.
- Montroll, E.W. and Scher, *J. Stat. Phys.*, 9 (2), 101-135, 1973.
- Mora, P. et al., in “Geocomplexity and the Physics of Earthquakes”, eds Rundle, J. B., Turcotte, D. L. and Klein, W. (Am. Geophys. Union, Washington, 2000).
- Mora, P. and D. Place, Stress correlation function evolution in lattice solid elastodynamic models of shear and fracture zones and earthquake prediction, *Pure Appl. Geophys.*, in press (preprint at <http://www.quakes.uq.edu.au/research/PDF/Mora1PAG01.pdf>), 2001.
- Moreno, Y., A. M. Correig, J. B. Gomez and A. F. Pacheco, A model for complexe aftershock sequences, *J. Geophys. Res* 106, 6609-6619, 2001.
- Morse, P. M. and H. Feshbach, *Methods in Theoretical Physics*, McGraw-Hill, New-York, 1953.
- Moyal, J.E., Multiplicative population chains, *Proc Royal Soc Lond, series A* 266, 518-526, 1962.
- Muller L., The rock slide in the Vaiont valley, *Felsmechanik und Ingenieurgeologie*, 2, 148-212, 1964.
- Muller L., News consideration on the Vaiont slide, *Felsmechanik und Ingenieurgeologie*, 6, 1-91, 1968.
- Muzy, J.F., J. Delour and E. Bacry, Modeling fluctuations of financial time series : from cascade process to stochastic volatility model, *The European physical Journal B* 17, 537-548, 2000.
- Nanjo, K. and H. Nagahama, Spatial distribution of aftershocks *Tectonophysics*, 287, 173-186, 1998.
- Narteau, C., Shebalin, P., Holschneider, M., Le Mouel, J.L. and C. Allègre, Direct simulations of the stress redistribution in the scaling organization of fracture tectonics (SOFT) model, *Geophys. J. Int.* 141, 115-135, 2000.

- Nielsen, T.H., J.A., Bartow, Jr., V.A., Frizell, and J.D., Sims, Preliminary photointerpretation maps of landslides and other superficial deposits of 567minutes quadrangle in the southeastern San Francisco Bay region, Alameda, Contra costa and Santa Clara countries, *California, U.S. Geol Sur. Open-file report 75-0277*, 1975.
- Noever, D. A., Himalayan sandpiles, *Phys. Rev. E*, 47, 724-725, 1993.
- Noir, J., E. Jacques, S. Bekri, P.M. Adler, P. Tapponnier, and G.C.P. King, Fluid flow triggered migration of events in the 1989 Dobi earthquake sequence of Central Afar, *Geophys. Res. Lett.* 24, 2335-2338, 1997.
- Nur A. and J.R. Booker, Aftershocks caused by pore fluid flow? *Science* 175, 885-888, 1972
- Ogata, Y., Statistical models for earthquake occurrences and residual analysis for point processes, *Research Memo. (Technical report), No. 288*, The Institute of Statistical Mathematics, Tokyo, 1985.
- Ogata, Y., Long-term dependence of earthquake occurrences and statistical models for standard seismic activity, *Suri Zisin Gaku (Mathematical Seismology) II* (ed. Saito, M.), Cooperative Research Report, vol. 3, Institute of Statistical Mathematics, Tokyo, pp. 115-125, 1987 (in Japanese).
- Ogata, Y., Statistical models for earthquake occurrence and residual analysis for point processes, *J. Am. Stat. Assoc.* 83, 9-27, 1988.
- Ogata, Y., Statistical model for standard seismicity and detection of anomalies by residual analysis, *Tectonophysics* 169, 159-174, 1989.
- Ogata, Y., Detection of precursory relative quiescence before great earthquakes through a statistical model, *J. Geophys. Res.* 97, 19845-19871, 1992.
- Ogata, Y., Space-time point process models for earthquake occurrences, *Ann. Inst. Stat. Math.* 50, 379-402, 1998.
- Ogata, Y., Seismicity analysis through point-process modeling : a review, *Pure Appl. Geophys.* 155, 471-507, 1999.
- Ogata, Y., Increased probability of large earthquakes near aftershock regions with relative quiescence, *J. Geophys. Res.* 106, 8729-8744, 2001.
- Ogata, Y., T. Utsu and K. Katsura, Statistical features of foreshocks in comparison with others earthquakes clusters, *Geophys. J. Int.*, 121, 233-254, 1995.
- Ogata, Y., T. Utsu and K. Katsura, Statistical discrimination of foreshocks from other earthquakes clusters, *Geophys. J. Int.*, 127, 17-30, 1996.
- Ogata, Y., L. Jones and S. Toda, When and where the aftershocks activity was depressed : contrasting decay patterns of the proximate large earthquakes in southern California, *J. Geophys. Res.* 108, 2318, doi :10.1029/2002JB002009, 2003.

- Okubo P.G. and Aki K., Fractal geometry in the San Andreas fault system, *J. Geophys. Res.* 92, 345-355, 1987.
- Olami, Z., H. J. S. Feder and K. Christensen, Self-organized criticality in a continuous, non-conservative cellular automaton modeling earthquakes, *Phys. Rev. Lett.*, 68, 1244-1247, 1992.
- Olver, F. W. J. *Asymptotics and Special Functions*, 572 pp., Academic Press, N.Y. and London, 1974.
- Omori, F., On the aftershocks of earthquakes, *J. Coll. Sci. Imp. Univ. Tokyo*, 7, 111-120, 1894.
- Ouchi, T. and T. Uekawa, Statistical analysis of the spatial distribution of earthquakes - variation of the spatial distribution of earthquakes before and after large earthquakes, *Phys. Earth Planet. Inter.* 44, 211-225, 1986.
- Ouillon, G., *Application de l'Analyse Multifractale et de la Transformée en Ondelettes Anisotropes : la Caractérisation Géométrique Multi-Echelle des Réseaux de Failles et de Fractures*, Editions du BRGM, Orléans, France, 1995.
- Ouillon G., C. Castaing and D. Sornette, Organization of joints and faults from 1 cm to 100 km scales revealed by optimized anisotropic wavelet coefficient method and multifractal analysis, *Nonlinear Processes in Geophysics* 2, 158-177, 1995.
- Ouillon, G. and Sornette, D., Unbiased multifractal analysis : application to fault patterns, *Geophys. Res. Lett.* 23, 3409-3412, 1996.
- Ouillon G., D. Sornette and C. Castaing, Hierarchical scaling of faulting, *J. Geophys. Res.* 101, 5477-5487, 1996.
- Ouillon G., D. Sornette, The concept of 'critical earthquakes' applied to mine rockbursts with time-to-failure analysis, *Geophys. J. Int.* 143, 454-468, 2000.
- Page, R.A., Comments on "earthquake frequency and prediction" by Liu Z.R., *Bull. Seis. Soc. Am.*, 74, 1491-1496, 1986.
- Panza, G.F., Soloviev, A.A. and Vorobieva, I.A., Numerical modelling of block-structure dynamics : Application to the Vrancea region, *Pure Appl. Geophys.* 149, 313-336, 1997.
- Papazachos, B. C., The time distribution of reservoir-associated foreshocks and its importance to the prediction of the principal shock, *Bull. Seis. Soc. Am.*, 63, 1973-1978, 1973.
- Papazachos, B. C., On certain aftershock and foreshock parameters in the area of Greece, *Ann., Geofis.*, 28, 497-515, 1975a.
- Papazachos, B., Foreshocks and earthquakes prediction, *Tectonophysics*, 28, 213-216, 1975b.
- Papazachos, B., M. Delibasis, N. Liapis, G. Moumoulis and G. Purcaru, Aftershock sequences of some large earthquakes in the region of Greece, *Ann. Geofis.*, 20, 1-93, 1967.
- Parise, M., Landslide mapping techniques and their use in the assessment of the landslide hazard, *Phys. Chem. Earth, Part C- Solar-Terr. Plan. Sci.*, 26, 697-703, 2001

- Parsons, T., Stein, R.S., Simpson, R.W. and Reasenberg, P.A., Stress sensitivity of fault seismicity : A comparison between limited-offset oblique and major strike-slip faults, *J. Geophys. Res.* 104, 20183-20202, 1999.
- Pelletier, J.D., B.D. Malamud, T.A. Blodgett and D.L. Turcotte, Scale invariance of soil moisture variability and its implications for the frequency size distribution of landslides, *Eng. Geol.*, 48, 255-268, 1997.
- Pelletier, J. D., Spring-block models of seismicity/ Review and analysis of a structurally heterogeneous model coupled to a viscous asthenosphere, in *Geocomplexity and the physics of earthquakes*, edited by J.B. Rundle, D. L. Turcotte, and W. Klein, AGU, geophysical monograph 120, Washington D.C., 27-42, 2000.
- Pepke, S. L. and J. M. Carlson, Predictability of self-organizing systems, *Phys. Rev. E.*, 50, 1994.
- Phillips, J.C., Stretched exponential relaxation in molecular and electronic glasses, *Rep. Prog. Phys.* 59, 1133-1208, 1996.
- Pisarenko, V.F., A. A. Lyubushin, S. Canu, M. F. Kanevsky, E. A. Savelieya, V. V. Demianov, M. V. Bolgov, T. A. Rukavishnikova, and I. V. Zalyapin, Statistical methods for river's runoff forecast, 2002, submitted to *Water Resources Research*. (this paper was presented at the 4-th INTAS Interdisciplinary Symposium on Physical and Chemical Methods in Biology, Medicine and Environment, Moscow, May 30 - June 3, 2001).
- Pisarenko, V.F. and D. Sornette, Characterization of the frequency of extreme events by the Generalized Pareto Distribution, in press in *Pure and Appl. Geophys.*, 2002 (e-print cond-mat/0011168)
- Press, W.H., S.A. Teukolsky, W.T. Vetterling and B.P. Flannery, Numerical recipes in C, *Cambridge Univeristy Press*, pp. 994, 1992.
- Rabotnov, Y. N., *Creep problems in Structural Members, North-Holland eds*, Amsterdam, 1969.
- Ramselaar, P. A., The mean behavior of the Ogata earthquake process, Master's thesis, Dept of Mathematics, Univ. Utrecht, 1990.
- Ranalli, G., A statistical study of aftershock sequences, *Annali di Geofisica* 22, 359-397, 1969.
- Rat, M. Difficulties in foreseeing failure in landslides - La Clapière, French Alps, *Proceedings 5th Int. Symp. Landslides lausanne 1988*, eds C. Bonnard, vol 3, 1503-1504, Balkema, 1988.
- Reasenberg, P., Second-order moment of central California seismicity, 1969-82, *J. Geophys. Res.* 90, 5479-95, 1985.
- Reasenberg, P. A., Foreshocks occurrence before large earthquakes, *J. Geophys. Res.* 104, 4755-4768, 1999.
- Reasenberg, P. A. and L. M. Jones, earthquake hazard after a mainshock in California, *Science*, 243, 1173-1176, 1989.
- Redner, S., Fragmentation, in "Statistical models for the fracture of disordered media", H. J. Hermann and S. Roux Eds. (Elsevier Science Publishers, 1990a).

- Redner, S., Random multiplicative processes : An elementary tutorial, *Am. J. Phys.*, 58, 267-273, 1990b.
- Reuschlé, T., Slow crack growth and aftershock sequences, *Geophys. Res. Lett.*, 17, 1525-1528, 1990.
- Rice, J.R. and Benzon, Y., Slip complexity in earthquake fault models, *Proc. Nat. Acad. Sci. USA* 93, 3811-3818, 1996.
- Richter, C. F., *Elementary seismology*, 758 pp., W.H. Freeman and Co, San Francisco, 1968.
- Robinson, R. and Benites, R., Synthetic seismicity models of multiple interacting faults, *J. Geophys. Res.* 100, 18229-18238, 1995.
- Roman, H.E. and P.A. Alemany, Continuous-time random walks and the fractional diffusion equation, *J. Phys. A* 27, 3407-3410, 1994.
- Rotwain, I., V. Keilis-Borok and L. Botvina, Premonitory transformation of steel fracturing and seismicity, *Phys. Earth Planet. Int.*, 101, 61-71, 1997.
- Rousseau, N., Study of seismic signals associated with rockfalls at 2 sites on the Reunion island (Mahavel Cascade and Souffriere cavity), *PhD thesis*, IPG Paris, 1999.
- RTM, Isère, Inventaire des mouvements rocheux, Secteur de l'Y grenoblois. Grenoble, France, *Service de Restauration des Terrains en Montagne de l'Isère*, 1996.
- Ruina, A. L., Slip instability and state variable frictions laws, *J. Geophys. Res.*, 88, 10,359-10,370, 1983.
- Rundle, J.B. and W. Klein, New ideas about the physics of earthquakes, *Reviews of Geophysics* 33, 283-286, 1995.
- Rundle, P.B. Rundle, J.B. Tiampo, K.F., Martins, J.S.S. and Klein, W., Nonlinear network dynamics on earthquake fault systems, *Phys. Rev. Lett.* 8714 (N14), 8501, 141-143, 2001.
- Rundle, J.B., K. F. Tiampo, W. Klein and J. S. S. Martins, Self-organization in leaky threshold systems : The influence of near-mean field dynamics and its implications for earthquakes, neurobiology, and forecasting, *Proc. Nat. Acad. Sci. USA*, 99, 2514-2521, 2002.
- Rundquist, D.V. and Soloviev, A.A., Numerical modeling of block structure dynamics : an arc subduction zone, *Physics of the Earth and Planetary interiors* 111, 241-252, 1999.
- Rydelek, P.A. and Sacks, I.S., Migration of large earthquakes along the San Jacinto fault ; stress diffusion from the 1857 Fort Tejon earthquake, *Geophys. Res. Lett.* 28, 3079-3082, 2001.
- Sahimi, M. and S. Arbabi, Scaling laws for fracture in disordered solids and granular media : approach to a fixed point, *Phys. Rev. Lett.* 77, 3689-3692, 1996.
- Saichev, A.I. and G.M. Zaslavsky, Fractional kinetic equations : solution and applications, *Chaos* 7 (4), 753-764, 1997.
- Saito, M., Forecasting the Time of occurrence of a Slope Failure, *Proc. 6th Int. Conf. Soil Mech. & Found. Eng., Montreal, vol.2*, 537-541, 1965.

- Saito, M., Forecasting time of Slope Failure by Tertiary Creep, *Proc. of 7th Int. Conf. Soil Mech. & Found. Eng.*, Mexico City, vol. 2, 677-683, 1969.
- Saito, M. and H. Uezawa, Failure of soil due to creep, *Proc of 6th Int. Conf. Soil Mech. & Found. Eng., Montreal, vol. 1*, 315-318, 1961.
- Saleur, H., C.G. Sammis, and D. Sornette, Discrete scale invariance, complex fractal dimensions, and log-periodic fluctuations in seismicity, *J. Geophys. Res.* 101, 17661-17677, 1996.
- Sá Martins, J. S. S., J. B. Rundle, M. Anghel and W. Klein, Precursory dynamics in threshold systems, *Phys. Rev. E* 64, 056117(1-4), 2002.
- Sammis, C.G. and S.W. Smith, Seismic cycles and the evolution of stress correlation in cellular automaton models of finite fault networks, *Pure appl. geophys.* 155, 307-334, 1999.
- Sammis, S.G. and D. Sornette, Positive feedback, memory and the predictability of earthquakes, *Proceedings of the National Academy of Sciences*, 99, 2501-2508, 2002.
- Scholz, C.H., Mechanism of creep in brittle rocks, *J. Geophys. Res.*, 73, 3295-3302, 1968a.
- Scholz, C.H., Microfracturing and the inelastic deformation of rocks in compression, *J. Geophys. Res.* 73, 1417-1432, 1968b.
- Scholz, C. H., Microfractures, aftershocks, and seismicity. *Seismological Society of America Bulletin*, 58, 1117-1130, 1968c.
- Scholz, C.H., *The Mechanics of Earthquakes and Faulting*, Cambridge University Press, 1990.
- Scholz, C. H., Earthquakes and friction laws, *Nature*, 391, 37-42, 1998.
- Scholz C.H. and Mandelbrot B.B., eds., *Fractals in Geophysics*, Birkhauser, 1989.
- von Seggern, D., S. S. Alexander and C-B Baag, Seismicity parameters presceding moderate to major earthquakes *J. Geophys. Res.*, 86, 9325-9351, 1981.
- Shaw B.E., Generalized Omori law for aftershocks and foreshocks from a simple dynamics, *Geophys. Res. Lett.* 20, 907-910, 1993.
- Shebalin, P., Zaliapin, I. and Keilis-Borok, V., Premonitory raise of the earthquakes' correlation range : Lesser Antilles, *Physics of the Earth and Planetary Interiors* 122, 241-249, 2000.
- Scher, H. and E.W. Montroll, Anomalous transit-time dispersion in amorphous solids, *Phys. Rev. B* 12, 2455, 1975.
- Scher, H. G. Margolin, R. Metzler, J. Klafter and B. Berkowitz, The dynamical foundation of fractal stream chemistry : the origin of extremely long retention times, accepted to *Geophys. Res. Lett*, e-print at cond-mat/0202326
- Shlesinger, M.F., Asymptotic solutions of continuous-time random walks, *J. Stat. Phys.* 10, 421-433, 1974.
- Shlesinger, M.F., J. Klafter and Y.M. Wong, Random walks with infinite spatial and temporal moments, *J. Stat. Phys.* 27, 499-512, 1982

- Simeonova, S. and D. Solakov, Temporal characteristics of some aftershocks sequences in Bulgaria, *Annali di Geofisica*, 42, 821-832, 1999.
- Singh, S.K. and G. Suarez, Regional variation in the number of aftershocks ( $m_b \geq 5$ ) of large, subduction-zone earthquakes ( $M_w \geq 7.0$ ), *Bull. Seism. Soc. Am.* 78, 230-242, 1988.
- Smith, W.D., The  $b$ -value as an earthquake precursor, *Nature*, 289, 131-139, 1981.
- Smith, W.D., Evidence for precursory changes in the frequency-magnitude  $b$ -value, *Geophys. J. Roy. Astr. Soc.*, 86, 815-838, 1986.
- Smith, L.A., C. Ziehmann and K. Fraedrich, Uncertainty dynamics and predictability in chaotic systems, *Quarterly J. Royal Meteor. Soc.*, 125, 2855-2886, 1999.
- Sole, R.V., Manrubia, S.C., Benton, M. and Bak, P., Self-similarity of extinction statistics in the fossil record, *Nature* 388, 764-767, 1997.
- Sokolov, I.M., Levy flights from a continuous-time process, *Phys. Rev. E* 63, 011104, 2001.
- Sokolov, I.M., A. Blumen and J. Klafter, Linear response in complex systems : CTRW and the fractional Fokker-Planck equations, preprint cond-mat/0107632, 2001.
- Soloviev, A.A., Vorobieva, I.A. and Panza, G.F., Modeling of block-structure dynamics : Parametric study for Vrancea, *Pure Appl. Geophys.* 156, 395-420, 1999.
- Soloviev, A.A., Vorobieva, I.A. and Panza, G.F., Modeling of block structure dynamics for the Vrancea region : Source mechanisms of the synthetic earthquakes, *Pure Appl. Geophys.* 157, 97-110, 2000.
- Sornette, D., Self-organized criticality in plate tectonics in the proceedings of the NATO ASI *Spontaneous formation of space-time structures and criticality*, T. Riste and D. Sherrington Editors, Kluwer Academic Publishers, 57-106, 1991.
- Sornette, D., Sweeping of an instability : an alternative to self-organized criticality to get power-laws without parameter tuning, *J. Phys. I France* 4, 209-221, 1994.
- Sornette, D., Earthquakes : from chemical alteration to mechanical rupture, *Physics Reports* 313, 238-292, 1999a.
- Sornette, D., Complexity, catastrophe and physics, *Physics World* 12, 57-57, 1999b.
- Sornette, D., *Critical Phenomena in Natural Sciences (Chaos, Fractals, Self-organization and Disorder : Concepts and Tools)* Springer Series in Synergetics, Heidelberg, 2000a.
- Sornette, D., Mechanochemistry : an hypothesis for shallow earthquakes, in *Earthquake thermodynamics and phase transformations in the earth's interior*, edited by R. Teisseyre and E. Majewski, International Geophysics Series, Vol. 76, pp. 329-366, Cambridge University Press, 2000b.
- Sornette, D., Predictability of catastrophic events : material rupture, earthquakes, turbulence, financial crashes and human birth, *Proc. Nat. Acad. Sci. USA* 99 SUPP1, 2522-2529, 2002.
- Sornette, A. and Sornette, D., Self-organized criticality and earthquakes. *Europhys. Lett.* 9, 197-202, 1989.

- Sornette, A., Davy, P., Sornette, D., Growth of fractal fault patterns, *Phys. Rev. Lett.* 65, 2266-2269, 1990.
- Sornette, D. and C. Vanneste, Dynamics and memory effects in rupture of thermal fuse networks, *Phys. Rev. Lett.* 68, 612-615, 1992.
- Sornette, D., C. Vanneste and L. Knopoff, Statistical model of earthquake foreshocks, *Phys. Rev. A* 45, 8351-8357, 1992.
- Sornette A., Davy P. and Sornette D., Fault growth in brittle-ductile experiments and the mechanics of continental collisions, *J. Geophys. Res.* 98, 12111-12139, 1993.
- Sornette D., P. Miltenberger and C. Vanneste, Statistical physics of fault patterns self-organized by repeated earthquakes, *Pure Appl. Geophys.* 142, 491-527, 1994.
- Sornette D., P. Miltenberger and C. Vanneste, Statistical physics of fault patterns self-organized by repeated earthquakes : synchronization versus self-organized criticality, in *Proceedings of the conference 'Statistical Mechanics and Quantum Field Theory'*, USC, Los Angeles, May 16-21, 1994, eds. P. Bouwknecht, P. Fendley, J. Minahan, D. Nemeschansky, K. Pilch, H. Saleur and N. Warner, World Scientific, Singapore, p.313-332, 1995.
- Sornette, D. and C.G. Sammis, Complex critical exponents from renormalization group theory of earthquakes : Implications for earthquake predictions, *J. Phys. I France* 5, 607-619, 1995.
- Sornette, D., L. Knopoff, Y. Y. Kagan and C. Vanneste, Rank-ordering statistics of extreme events : applications to the distribution of large earthquakes, *J. Geophys. Res.* 101, 13883-13893, 1996.
- Sornette, A. and D. Sornette, Renormalization of earthquake aftershocks, *Geophys. Res. Lett.* 26, 1981-1984, 1999a.
- Sornette, D. and Sornette, A., General theory of the modified Gutenberg-Richter law for large seismic moments, *Bull. Seism. Soc. Am.* 89 1121-1130, 1999b.
- Sornette, D. and A. Johansen, Significance of log-periodic precursors to financial crashes, *Quantitative Finance* 1, 452-471, 2001.
- Sornette, D. and A. Helmstetter, On the occurrence of finite-time-singularity in epidemic models of earthquakes and starquakes, *Phys. Rev. Lett.* 89, 158501, 2002 (<http://arXiv.org/abs/cond-mat/0112043>).
- Sornette, D., Y. Malevergne and J.F. Muzy, Volatility fingerprints of large shocks : Endogenous versus exogeneous, submitted to *Risk Magazine*, 2002 (<http://arXiv.org/abs/cond-mat/0204626>).
- Sotolongo-Costa, O., J.C. Antoranz, A. Posadas, F. Vidal and A. Vásquez, Lévy flights and earthquakes, *Geophys. Res. Lett.* 27, 1965-1968, 2000.
- Stark, C.P. and N. Hovius, The characterization of landslides size distributions, *Geophys. Res. Lett.*, 28, 1091-1094, 2001.

- Steeple, D.W. and D.D. Steeples, Far-field aftershocks of the 1906 earthquake, *Bull. Seism. Soc. Am.* 86, 921-924, 1996.
- Stein, R.S., The role of stress transfer in earthquake occurrence, *Nature* 402, 605-609, 1999.
- Stein, R.S., G.C.P. King and J. Lin, Stress triggering of the 1994 M=6.7 Northridge, California, earthquakes by its predecessors, *Science* 265, 1432-1435, 1994.
- Stephens, C. D., J. C. Lahr, K. A. Fogleman and R.B. Horner, The St-Helias, Alaska, earthquake of february 28, 1979 : regional recording of aftershocks and short-term, pre-earthquake seismicity *Bull. Seis. Soc. Am.*, 70, 1607-1633, 1980.
- Sugai, T., H. Ohmori, and M. Hirano, Rock control on magnitude-frequency distribution of landslides, *Transactions of Japanese Geomorphological Union*, 15, 233-351, 1994.
- Susella, G. and F. Zanolini, Risques générés par les grands mouvements de terrains, *eds, Programme Interreg 1, France-Italie*, 207 pp., 1996.
- Suyehiro, S., Difference between aftershocks and foreshocks in the relationship of magnitude frequency of occurrence for the great chilean earthquake of 1960, *Bull. Seis. Soc. Am.*, 56, 185-200, 1966.
- Sykes, L.R. and S.C. Jaumé, Seismic activity on neighboring faults as a long-term precursor to large earthquakes in the San-Francisco Bay region, *Nature* 348, 595-599, 1990.
- Tajima, F. and H. Kanamori, Global survey of aftershock area expansion patterns, *Phys. Earth Planet. Inter.* 40, 77-134, 1985a.
- Tajima, F. and H. Kanamori, Aftershock area expansion and mechanical heterogeneity of fault zone within subduction zone, *Geophys. Res. Lett.* 12, 345-348, 1985b.
- Taylor, J. R., An introduction to error analysis, *University science Books*, Sausalito, California, 2nd ed., pp 327, 1997.
- Tiampo, K.F., Rundle, J.B., McGinnis, S. and Gross, S. J., Observation of systematic variations in non-local seismicity patterns from Southern California, in : *GeoComplexity and the Physics of Earthquakes*, AGU, Washington, 211-218, 2000.
- Turcotte, D.L., Self-organized criticality, *Reports on Progress in Physics* 62, 1377-1429, 1999.
- U.S. Water Resources Council, Guidelines for determining flood flow frequency, *Bulletin 17B : Hydrology subcommittee, Office of Water Data Coordination*, U.S. Geological Survey, Reston, VA, 182p, 1982.
- Utsu, T., A statistical study of the occurrence of aftershocks, *Geophys. Magazine* 30, 521-605, 1961.
- Utsu, T., Aftershocks and earthquake statistics (I) : source parameters which characterize an aftershock sequence and their interrelations, *J. Fac. Sci.Hokkaido Univ., Ser.VII*, 3, 129-195, 1969.
- Utsu, T., Aftershocks and earthquake statistics (II) : Further investigation of aftershocks and other earthquake sequence based on a new classification of earthquake sequences, *J. Faculty Sci. Hokkaido Univ. Ser. VII* 3, pp. 379-441, 1970.

- Utsu, T., A review of seismicity, *Suri Zisin Gaku (Mathematical Seismology) II* (ed. Saito, M.), Cooperative Research Report, vol. 34, Institute of Statistical Mathematics, Tokyo, pp. 139-157, 1992 (in Japanese).
- Utsu, T., Y. Ogata and S. Matsu'ura, The centenary of the Omori formula for a decay law of aftershock activity, *J. Phys. Earth* 43, 1-33, 1995.
- Van Asch, T. W. J., J. Buma and L. P. H. Van Beek, A view on some hydrological triggering systems in landslides, *Geomorphology*, 30, 25-32, 1999.
- Vangenuchten, P. M. B. and H. Derijke, Pore water pressure variations causing slide velocities and accelerations observed in a seasonally active landslide, *Earth Surface Processes and Landforms*, 14, 577-586, 1989.
- Vanneste, C. and D. Sornette, Dynamics of rupture in thermal fuse models, *J. Phys. I France* 2, 1621-1644, 1992.
- Varnes D. J., Slope movements : types and processes. In : *Landslide analysis and control*. Edited by Schuster R. L. & Krizek R. J., *Transp. Research Board, Special Report 176*, 11-33, Nat. Ac. Sci., Washington, 1978.
- Vengeon, J.M., D. Hantz, and C. Dussauge, Predictabilité des éboulements rocheux : approche probabiliste par combinaison d'études historiques et géomécaniques, *Revue Francaise Géotechnique*, 95-96, 143-153, 2001.
- Vere-Jones, D., A note on the statistical interpretation of Bath' s Law, *Bull. Seism. Soc. Am.* 59, 1535-1541, 1969.
- Vere-Jones, D., Statistical theories of crack propagation, *Mathematical Geology*, 9, 455-481, 1977.
- Vere-Jones, D., Probabilities and information gain for earthquake forecasting, *Computational Seismology* 30, 248-263, 1998.
- Vere-Jones, D., R. Robinson and W. Yang, Remarks on the accelerated moment release model : problems of model formulation, simulation and estimation, *Geophys. J. Int.* 144, 517-531, 2001.
- Vespignani, A. and S. Zapperi, How self-organized criticality works : A unified mean-field picture, *Phys. Rev. E*, 57, 6345-6363, 1998.
- Vibert C., M. Arnould, R. Cojean, J. M. Cleac'h, An attempt to predict the failure of a mountainous slope at St Etienne de Tinée, France, *Proceedings 5th Int. Symp. Landslides lausanne 1988*, eds C. Bonnard, vol 2, 789-792, Balkema, 1990.
- Viljoen, H.J., L.L.Lauderback and D. Sornette, Solitary waves and supersonic reaction front in metastable solids, *Phys. Rev. E* 65, 026609, 1-13, 2002 (<http://arXiv.org/abs/cond-mat/0012496>).
- Voight, B. eds, 2, *Engg. Sites, Development in Geotech. Engg.*, vol. 14b, 595-632, 1978.
- Voight, B., A method for prediction of Volcanic Eruption, *Nature*, 332, 125-130, 1988.
- Voight, B. A., A relation to describe rate-dependent material failure, *Science*, 243, 200-203, 1989.

- Voight B., Materials Science Laws applies to time forecast of slope failure, *Proceedings 5th Int. Symp. Landslides lausanne 1988*, eds C. Bonnard, vol 3, 1471-1472, Balkema, 1988.
- Weiss, G.H., Aspects and Applications of random Walk, North Holland, 1994.
- Weiss, G.H. and P.P. Calabrese, Occupation times of a CTRW on a lattice with anomalous sites, *Physica A* 234, 443-454, 1996.
- Wesnousky, S., C. Scholz, K. Shimazaki, and T. Matsuda, Earthquake frequency distribution and the mechanics of faulting, *J. Geophys. Res.*, 88, 9331-9340, 1983.
- Wesson, R.L., Modeling aftershock migration and afterslip of the San Juan Bautista, California, earthquake of October 3, 1972, *Tectonophysics* 144, 215-229, 1987.
- Wiederhorn, S. M. and L. H. Bolz, Stress corrosion and static fatigue of glass, *J. Am. Ceram. Soc.*, 50, 543, 1970.
- Wieczorek, G.F., J.B. Snyder, C.S. Alger and K.A. Isaacson, Yosemite historical rockfall inventory, *U.S Geological Survey, Open File Report 92-387*, pp.38, 1992.
- Wieczorek, G. F., S. P. Nishenko, and D. J. Varnes, Analysis of rock falls in the Yosemite Valley, California, *Proceedings of 35th U.S. Symposium on Rock Mechanics*, Daemen, J.J., and Schultz, R.A., eds., A.A. Balkema, p 85-89, 1995.
- Wiemer, S. and K. Katsumata, Spatial variability of seismicity parameters in aftershock zones, *J. Geophys. Res.*, 104, 13,135-13,151, 1999.
- Wiemer, S, Introducing probabilistic aftershock hazard mapping, *Geophys. Res. Lett.*, 27, 3405-3408, 2000.
- Wilson, K.G., Problems in physics with many scales of length, *Scientific American* 241, August, 158-179, 1979.
- Wu, K.T., Yue, M.S., Wu, H.Y., Chao, S.L., Chen, H.T., Huang, W.Q., Tien, K.Y and S.D. Lu, Certain characteristics of the Haicheng earthquake (M=7.3) sequence, *Chinese Geophysics*, AGU, 1, 289-308, 1978.
- Wu, R.-S. and Aki K., The fractal nature of the inhomogeneities in the lithosphere evidenced from seismic wave scattering, *Pure Appl. Geophys.* 123, 806-817, 1985.
- Wyss, M. and W. H. K. Lee, Time variations of the average magnitude in central California, *Proceedings of the conference on Tectonic Problems of the San Andreas Fault System*, edited by Kocach and Nur, *Stanford University Geol. Sci.*, 13, 24-42, 1973.
- Wyss, M. and R. E. Habermann, Precursory seismic quiescence, *Pure Appl. Geophys.*, 126, 319-322, 1988.
- Wyss, M., Shimazaki, K., and Ito, A. Eds., *Seismicity Patterns, their Statistical Significance and Physical Meaning* (Birkhäuser, Basel), 1999.
- Xu Z. Y., S. Y. Schwartz and T. Lay, Seismic wave-field observations at a dense small-aperture array located on a landslide in the Santa Cruz Mountains, California, *Bull. Seis. Soc. Am.*, 86, 655-669, 1996.

- Yamanaka, Y. and K. Shimazaki, Scaling relationship between the number of aftershocks and the size of the main shock, *J. Phys. Earth* 38, 305-324, 1990.
- Yamashita, T. and L. Knopoff, Models of aftershock occurrence, *Geophys. J. R. Astron. Soc.* 91, 13-26, 1987.
- Yamashita, T. and L. Knopoff, A model of foreshock occurrence, *Geophys. Journal* 96, 389-399, 1989.
- Yamashita, T. and L. Knopoff, Model for intermediate-term precursory clustering of earthquakes, *J. Geophys. Res.* 97, 19873-19879, 1992.
- Yin, X-C., Load-Unload Response Ratio and Accelerating Moment/Energy Release Critical Region Scaling and Earthquake Prediction, preprint 2001.
- Yiou, P., D. Sornette and M. Ghil, Data-adaptive wavelets and multi-scale singular spectrum analysis, *Physica D* 142, 254-290, 2000.
- Yukalov, V. I. and S. Gluzman, Self-similar bootstrap of divergent series, *Phys. Rev. E*, 55, 6552-6565, 1997.
- Yukalov V.I. and S. Gluzman, Weighted fixed points in self-similar Analysis of Time Series, *International Journal of Modern Physics B*, 13, 1463-1476, 1999.
- Zhang G., Zhu L., Song, X., Li, Z., Yang, M., SU, N., X. Chen, Predictions of the 1997 strong earthquakes in Jiashi, Xinjiang, China, *Bull. Seis. Soc. Am.*, 89, 1171-1183, 1999.
- Zhurkov, S. N., Kinetic concept of the strength of solids, *Int J. Fract. Mech.* 1, 311-323, 1965.
- Ziehmann, C., L. A. Smith and J. Kurths, Localized Lyapunov exponents and the prediction of predictability, *Phys. Lett. A*, 271, 237-251, 2000.
- Ziv, A. and A. M. Rubin, Implications of rate-and-state friction for properties of aftershock sequences : quasi-static inherently discrete simulations, *J. Geophys Res.* 108, 2051, doi :10.1029/2001JB001219, 2003.
- Zoller, G., S. Hainzl, and J. Kurths, Observation of growing correlation length as an indicator for critical point behavior prior to large earthquakes, *J. Geophys. Res.*, 106, 2167-2175, 2001.
- Zoller, G. and S. Hainzl, A systematic spatio-temporal test of the critical point hypothesis for large earthquakes, *Geophys. Res. Lett.* 29, 10.1029/2002GL014856, 2002.

[The following text is a dense block of illegible text, likely a list of references or a table of contents, which has been rendered as a single large block due to the low resolution and blurriness of the image. It contains numerous lines of text, some appearing to be names and dates, but they are not legible.]

## Ruptures et instabilités : sismicité et mouvements gravitaires

**Résumé** - On s'intéresse à la rupture associée à deux classes de phénomènes naturels, les séismes et les instabilités gravitaires.

Pour les séismes, on étudie un modèle stochastique de sismicité, basé sur les deux lois les mieux établies pour la sismicité, la décroissance en loi de puissance du taux de sismicité après un séisme, et la distribution en loi de puissance des énergies des séismes. Dans ce modèle, on suppose que chaque séisme déclenche d'autres séismes, dont le nombre augmente avec l'énergie du choc principal. Le taux de sismicité global résulte de la cascade de déclenchements de séismes directs et indirects. On analyse l'organisation spatiale et temporelle de la sismicité dans les différents régimes sous- et sur-critiques du modèle. Ce modèle permet de reproduire un grand nombre de propriétés de l'activité sismique, telles que la variabilité de la décroissance des séquences d'aftershocks, l'augmentation de l'activité sismique avant un séisme, la diffusion des aftershocks, la migration des foreshocks et la modification de la distribution des magnitudes avant un séisme. On obtient avec ce modèle une bonne prédictabilité d'une fraction des séismes qui sont déclenchés à court terme après un grand séisme. Nos résultats démontrent le rôle essentiel des cascades de déclenchement de séismes à toutes les échelles dans l'organisation de l'activité sismique. Concernant l'étude des instabilités gravitaires, une étude statistique de plusieurs catalogues d'éboulements rocheux montre que la distribution des volumes de roches suit une loi de puissance. On propose que cette distribution en loi de puissance résulte soit de l'hétérogénéité initiale de la matrice rocheuse, soit de la dynamique d'un système critique auto-organisé. Certains glissements de terrains sont précédés par une accélération de la vitesse de glissement avant la rupture finale. On peut reproduire l'évolution temporelle du glissement à l'aide d'un modèle de bloc rigide avec une loi de friction dépendante de la vitesse de glissement et de l'état de contact entre le bloc et sa surface de glissement. L'analyse de deux glissements de terrains avec ce modèle permet de distinguer une accélération du glissement dans le régime stable, d'une accélération instable qui évolue vers une rupture catastrophique.

**Mots-clés** - Sismicité, Prédiction, Modèle statistique, Déclenchement, Foreshock, Aftershock, Rupture, Instabilités gravitaires.

## Rupture and instabilities : seismicity and landslides

**Abstract** - We analyze the rupture associated with two natural phenomena, earthquakes and landslides.

In the first part, we study a simple stochastic model of seismicity, based on the two best-established empirical laws for earthquakes, the power law decay of seismicity after an earthquake and the power law distribution of earthquake energies. This model assumes that each earthquake can trigger aftershocks, with a rate increasing with its magnitude. The seismicity rate is in this model the result of the whole cascade of direct and secondary aftershocks. We analyze the space-time organization of the seismic activity in the different sub- and super-critical regimes of the model. We show that this simple model can reproduce many properties of real seismicity, such as the variability of the aftershocks decay law, the acceleration of the seismic activity before large earthquakes, the diffusion of aftershocks, the migration of foreshocks, and the modification of the magnitude distribution before large earthquakes. We find that this model provides a good predictability for a fraction of earthquakes that are triggered by a previous large event. We demonstrate the essential role played by the cascades of earthquake triggering at all scales in controlling the seismic activity.

The second part is devoted to the analysis of landslides. A study of several catalogs of rock falls shows that the distribution of rockfall volumes follows a power-law distribution, arising either from the scale invariant heterogeneity of the rock-mass, or from the dynamics of a self-organized critical system.

We propose that the precursory acceleration of the displacement before some catastrophic landslides can be reproduced using a slider block model with a rate-and-state dependent friction law. Application of this model to two landslide slip histories suggests that we can distinguish an acceleration of the sliding velocity in the stable regime from an unstable acceleration leading to a catastrophic collapse.

**Keywords** - Seismicity, Prediction, Statistical model, Triggering, Foreshock, Aftershock, Rupture, Landslide.